BUOYANT JETS WITH TWO AND THREE-DIMENSIONAL TRAJECTORIES

A thesis

submitted in partial fulfilment

of the requirements for the Degree

of

Doctor of Philosophy in Civil Engineering

at the

University of Canterbury

by

Gustaaf Adriaan Kikkert

University of Canterbury

Christchurch, New Zealand

2006

Abstract

Extensive experimental data is available from previous research into the behaviour of buoyant jets released into an unstratified ambient. The experimental data has been the basis for theoretical and numerical modelling work, and currently several numerical models exist that are employed in the design of engineering structures built for the disposal of wastewater in the ocean. However there are still flow configurations with limited or no available experimental data, and hence confidence in the use of the models under some circumstances is limited. These circumstances include two-dimensional trajectory flows that are discharged at oblique angles to the ambient and buoyant jet flows with three-dimensional trajectories. As part of the current project an experimental investigation is conducted into the behaviour of discharges that have either two-dimensional or three-dimensional trajectories, focussing particularly on those configurations with currently limited available experimental data.

A light attenuation technique is developed for the investigation of such flows, largely because it enables the behaviour of discharges with three-dimensional trajectories to be recorded with relative ease. However, this technique provides integrated views of the flow and hence the interpretation of the integrated concentration data is aided by assumed mean cross-sectional concentration profiles. In the strongly advected region (with the exception of the weak-jet) a double-Gaussian approximation is shown to provide a reasonable representation of mean concentration profiles. In the weakly advected regions and the weak-jet region, it is well-known that a single Gaussian adequately represents the mean flow structure.

A new numerical model, the Momentum Model, is developed to assist in the design and to monitor the performance of the experimental investigation. Unlike other models, the behaviour of the flow is determined by the relative magnitudes of the initial excess momentum flux, the buoyancy-generated momentum flux and the entrained ambient momentum flux. It is shown that ratios of these momentum fluxes are equivalent to the length-scales traditionally employed for this task.

Predictions from the Momentum Model are compared with data from the current and previous experimental investigations and, in addition, predictions from two representative numerical models, VisJet and CorJet. Predictions from the Momentum Model are shown to be consistent with data for a wide variety of discharge configurations. These predictions are also generally consistent with those of VisJet and CorJet. However, the experimental results from the

buoyant jet discharged in a moving ambient show that the spreading rates of the strongly advected flows (puffs and thermals) differ, and while this difference is incorporated into the Momentum Model, it is not evident in the VisJet and CorJet predictions.

Numerical model predictions of negatively buoyant discharges are shown to be inadequate. This discharge configuration is investigated in some detail experimentally and additional analytical solutions of the flow behaviour are developed to aid in the interpretation of the flow behaviour. The experimental results show that buoyancy-induced instabilities on the inner side of the jets, which generate additional vertical mixing, significantly alter the form of the mean concentration profiles in this region. This results in considerably higher integrated dilutions along the flow centreline.

Another significant difference between the newly developed Momentum Model and the existing numerical models (VisJet and CorJet), is the approach taken to dealing with oblique discharges in a cross-flow. Experimental results in combination with additional analytical solutions show that for initial discharge angles of 20° and less, an oblique discharge in a cross-flow becomes a weak-jet in the strongly advected region, and for angles of 40° and above, the flow becomes a puff. The strongly advected behaviour predicted by the Momentum Model changes abruptly at the transition angle, and is reasonably consistent with the data. The gradual change in strongly advected behaviour employed by VisJet and CorJet does not appear to be appropriate in the puff region.

Finally a preliminary experimental investigation of discharges with three-dimensional trajectories shows that there are significant discrepancies between the predicted behaviour and the experimental data. This is surprising given the numerical models are, for the most part, able to predict the behaviour of flows with two-dimensional paths with reasonable accuracy. It is evident that flows with three-dimensional paths are modified more severely by the different directions of the initial, buoyancy-generated, and entrained ambient momentum fluxes than the current models suggest.

Acknowledgements

From day 1, the intension of the research was to investigate buoyant jets with a three-dimensional path. With this aim in mind, time was spent developing a flow visualization technique and an alternative numerical model to aid in the investigation. Both the flow visualization technique and the model were verified with experimental data obtained from buoyant jets with a two-dimensional path. This process included some major distractions in the form of the investigations of the negatively buoyant jet and obliquely discharged non-buoyant jets in a moving ambient. However, when it was time for the investigation of the buoyant jets with a three-dimensional path, all the knowledge that was gained from the flows with a two-dimensional path was applied in the design and analysis of that investigation.

I would like to sincerely thank my supervisor, Dr. Mark Davidson, not just for suggesting the topic by presenting it as a challenge, but also for his continuous commitment, support and invaluable advice during the length of the investigation. I especially appreciate his honest insights into the wider research community, giving me a right perspective from which to grow as a researcher.

I would like to thank my co-supervisor, Dr. Roger Nokes. His enthusiasm developed my interest in fluid mechanics as an under-graduate student. His comments as an expert in fluid dynamics slightly outside the current area of study were especially helpful in increasing the standard of the project. I am also grateful for his willingness to upgrade computer software at a moment's notice.

The laboratory staff, under the leadership of Mr. Ian Sheppard and including Mr. Colin Bliss, Mr. Ray Allan and Mr. Kevin Wines, have given me much support with the experimental investigation. Without their problem solving solutions and extra pair of hands, it would not have been possible to conclude the experimental investigation in time. Beside their help with research related issues I also appreciate the advice on and help with fixing anything from bicycles to vacuum cleaners.

I would like to thank my fellow post-graduate students, Caroline, Dave, Langford, Bill and James, for being the first to complain to when computers, software or anything else that could go wrong, went wrong. I also appreciate the many small, but useful, time-wasters, which helped keep me sane during the many hours spent in the laboratory.

Finally I would like to express my gratitude to my family, friends, and especially my wife, Heather. Their support from the outside made it possible for me to spend three years working on a single project. However they also helped me remember what is really important in life.

Table of Contents

List of Figures

List of Tables

List of Notations

a	Calibration constant
b, b_1, b_2, b_3, b_4, b_{jp}, b_{mt}, b_{wj}	Velocity spread
b_c	Concentration spread
b_{th}	Average Gaussian velocity spread
$b_{th\text{-}mt}$	Average double-Gaussian velocity spread
C	Local tracer concentration
C_0	Initial tracer concentration
C_{0rp}	Trajectory coefficient
c_1	Constant in empirical relationship for h
c_2-c_7	Transition constants
C_1-C_6	Reflection loss constants
C_{air}, C_{glass}, $C_{perspex}$, C_{water}, C_{dye}	Absorption loss constants
C_c	Tracer concentration at centre of double-Gaussian approximation
C_i	Local integrated tracer concentration
C_{i0}	Integrated initial tracer concentration
C_{ii}	Double-integrated tracer concentration
C_{ii0}	Double-integrated initial tracer concentration
C_{il}, $C_{il\text{-}assumed}$, $C_{il\text{-}actual}$	Integrated centreline tracer concentration
C_{ily}	Integrated single-Gaussian centreline tracer concentration in the y-direction
C_{ilz}	Integrated single-Gaussian centreline tracer concentration in the z-direction
C_{iy}	Local integrated tracer concentration in the y-direction
C_{iz}	Local integrated tracer concentration in the z-direction
$C_{iz\text{-}peak}$	Integrated peak tracer concentration in the z-direction
C_{jk}	Constant in weak-jet spread assumption
C_l, $C_{l\text{-}1}$	Centreline tracer concentration
$C_{l\text{-}vortex}$	Tracer concentration at centre of double-Gaussian approximation
C_m	Experimental maximum tracer concentration within cross-section
C_{peak}	Tracer concentration at peak of double-Gaussian approximation
$C_{th\text{-}m}$	Average tracer concentration in the advected line momentum puff region
$C_{th\text{-}t}$	Average tracer concentration in advected thermal region

c_{wj1}, c_{wj2}	Constants in derivation of weak-jet trajectory equation
d	Diameter of the source
f	Double-Gaussian approximation constant
Fr, Fr_0	Initial Froude number
g	Gravitational constant
h	Double-Gaussian approximation constant
h^*	Asymptotic value of h
I_{cam}	Intensity of ray of light at camera
I_{green}	Intensity of green gun
I_m, I_q, I_c, I_{qc}, I_{cdg}, I_{qdg},	Shape constants
I_{ref}	Intensity of reference with no dye present
I_{ref_green}	Intensity of reference green gun
I_{source}	Intensity of ray of light at source
k	Gaussian spread constant
k_{cm}	Dilution relationship coefficient
k_{me}, k_{xm}, k_{x0R}, k_{zm}	Trajectory relationship coefficients
k_{sg}	Concentration spread-rate for the single-Gaussian of the double-Gaussian approximation divided by λ
k_{th}	Average Gaussian spread constant
L, L_1	Distance from source along trajectory in angled jet experiment
l_{jp}	Length-scale for the transition between the strong-jet and advected plume regions
l_{jm}	Length-scale for the transition between the strong-jet and advected line momentum puff regions
l_{mt}	Length-scale for the transition between the advected line momentum puff region and the advected thermal region
L_{mz^*}	Length-scale for the transition between weakly advected and strongly advected regions for the trajectory data of the obliquely discharged non-buoyant jet in a moving ambient
M_0	Initial momentum flux
M_0'	Reflection of M_0 in the x-y plane
M_a	Entrained ambient momentum flux
M_{a0}	Initial ambient momentum flux
M_b	Buoyancy-generated momentum flux
M_e	Excess momentum flux
M_{e0}	Initial excess momentum flux
M_{e0x}, M_{e0y}, M_{e0z}	Components of the initial excess momentum flux in the x, y and z-directions

M_s	Total momentum flux
M_{s0}	Initial total momentum flux
m_{th}	Average double-Gaussian spread constant
$m_{th\text{-}m}$	Average double-Gaussian advected line momentum puff spread constant
$m_{th\text{-}t}$	Average double-Gaussian advected thermal spread constant
M_x	Momentum flux in the x-direction
M_y	Momentum flux in the y-direction
M_z	Momentum flux in the z-direction
n	Coordinate representing distances in the direction perpendicular to the initial velocity
p	Instantaneous modified pressure
P	Mean Modified Pressure
p'	Fluctuating modified pressure
Q_0	Initial flow rate
$Q_{\Delta 0}$	Initial density deficit flux
r	Radial coordinate
Re, Re_0	Discharge Reynolds number
s	Distance from source along trajectory
s_i	Coordinate representing distances in the direction of the initial velocity
S_{jp}	Length-scale for the transition between jet and plume regions
S_m	Distance from source to the maximum centreline height in the s-direction
s_{yz}	Distance from the source, travelled along the projection of the direction of the initial discharge in the y-z plane
t	Time
u	Local velocity
U_0	Initial velocity
U_a	Ambient velocity
u_e	Entrainment velocity
U_e	Excess velocity
U_{e0}	Initial excess velocity
U_{eth}	Average excess velocity
u_i	Instantaneous velocity
U_i	Mean velocity
u_i'	Fluctuating velocity
U_l	Single-Gaussian cross-sectional centreline velocity
U_r	Ratio of ambient velocity over the initial velocity
w	Substitute variable in derivation of weak-jet trajectory equation

x	Cartesian coordinate in the same direction as the ambient velocity; (in the direction of the horizontal component of the initial velocity for still ambient flows)
x_{amp}	Horizontal distance from advected line momentum puff virtual source
x_{0r}	Horizontal distance from source to impact point
x_{0rj}	Horizontal distance from source to impact point in the jet region
x_{0rp}	Horizontal distance from source to impact point in the plume region
x_{jp}	Horizontal distance from source to jet to plume transition point
x_m	Horizontal distance from source to maximum centreline height
x_{trp}	Horizontal distance from transition point to impact point in the plume region
x_{wj}	Horizontal distance from weak-jet virtual source
y	Cartesian coordinate perpendicular to the x-coordinate in the horizontal plane
y'	Distance in y-direction from centre of double-Gaussian cross-sectional profile
y_l	Distance in y-direction from source to centre of double-Gaussian cross-sectional profile
z	Cartesian coordinate in the same direction as the vertical component of the initial velocity
z'	Distance in z-direction from centre of double-Gaussian cross-sectional profile
z_{amp}	Vertical distance from advected line momentum puff virtual source
z_{jp}	Vertical distance from source to jet to plume transition point
z_l	Distance in z-direction from source to centre of double-Gaussian cross-sectional profile
z_m	Vertical distance from source to maximum centreline height
z_{me}	Vertical distance from source to edge of flow at maximum centreline height
z_t	Vertical distance from source to the point of transition
z_v	Vertical distance from the point of transition to the virtual source
z_{wj}	Vertical distance from weak-jet virtual source
α	Angle between the total momentum flux and its reflection in the x-*y* plane
α_0	Angle between the initial excess momentum flux and the horizontal plane (3D trajectory flow)
β	Angle between the reflection of the total momentum flux in the *x*-*y* plane and the ambient momentum flux
β_{amp}	Ratio of the puff edge radius to the nominal radius *b*
β_0	Angle between the projection of the initial excess momentum flux in the *x*-*y* plane and x-axis (3D trajectory flow)
β_{wj}	Ratio of the weak-jet edge radius to the nominal radius *b*
Δ	Local density deficit
ε	Entrainment coefficient
ϕ_0	Angle between the excess momentum flux and the ambient momentum flux

γ	Angle between the assumed camera position and the actual camera position in relation to parallax issues
ν	Kinematic viscosity of water
θ	Angle between the trajectory and the velocity spread
ρ	Density of jet fluid
ρ_a	Density of ambient fluid
λ	Ratio of the spread of the mean concentration distribution to the spread of the mean velocity distribution
λ_r	Ratio of λ-values of the weak-jet region to the puff region

Chapter 1 – Introduction

1.1 – General Introduction

In the modern society urban areas are expanding rapidly and at the same time the environmental awareness of its citizens has increased. Both these processes have lead to a more critical point of view with respect to the effluent disposal problem.

Of all the major cities in the world, about 80% of them are near the coast. This makes the disposal of wastewater into the ocean an attractive option. It is close-by, it is well buffered for both pH and temperature changes, and vast quantities of dissolved oxygen are available to biodegrade the organics. Also the concentration of the contaminants can be reduced with the help of initial dilution and the dilution capabilities of the ocean.

Engineering structures have been built for years to dispose of wastewater into the ocean. The wastewater is normally disposed of through an outfall. The main purpose of the outfall is to enhance the dilution as it is released into the receiving water and thus reduce the impact on the local environment. Models of the outfall are needed to determine whether or not the outfall meets the environmental requirements set by the local agencies. Communities are now generally favouring higher degrees of land-based treatment and in many cases the environmental requirements can be met at the end of the initial dilution zone. This is the region where the essentially fresh water effluent rises to the surface of the higher density oceanic waters. Extensive mixing takes place in this region. If it can be shown that the environmental requirements are satisfied within this region then the need to model the behaviour of the effluent in the ocean mixing region is largely eliminated. The development of ocean mixing models is an expensive option, because these models require extensive quantities of field data for calibration and validation procedures, if reasonable predictions are to be obtained. A decision as to whether or not such models are needed is based on the degree of confidence with which predictions of dilution in the initial dilution zone can be made. The accuracy of the initial dilution zone models is therefore of particular importance.

The release of fast flowing wastewater into a large body of stagnant or slow moving unstratified ocean water, creates a jet flow. The body of water is normally large enough so

that the boundaries do not interfere with the flow of the jet. The fluid of the jet is fully turbulent when the Reynolds number, based on the initial conditions of the jet (source diameter, initial velocity), is larger than approximately two thousand. The relative densities of the two fluids determine whether the flow is buoyant or non-buoyant. During the initial dilution phase the wastewater will generally go through three distinct regions. The first one is the jet-region where the initial momentum flux of the wastewater dominates its behaviour. The second region is the plume region, where the buoyancy forces dominate the behaviour of the flow. The third phase is the advected thermal region, where the ambient current dominates the behaviour. Many experiments have been conducted to understand the behaviour of the flow released into a stagnant unstratified ambient, and a large amount of knowledge is now available. However a high percentage of this work has focused on the jet fluid being released into the ambient horizontally or vertically. Fewer experimental investigations have been carried out for discharges that are released into a moving unstratified ambient current. In most cases these experiments were carried out with the source flow either released vertically or in the same direction as the ambient current. The flow trajectories in these stagnant and moving discharge configurations are all two-dimensional and, as a result of previous studies, reasonably well understood. However, in general effluent is released at some angle to the ambient current and the trajectory of the discharge is three-dimensional. Few studies have focussed on this type of discharge.

1.2 – Problem Overview

To be able to estimate the dilution and trajectories of the wastewater plume released into an unstratified ambient, relatively simple integral methods are routinely employed to predict the behaviour of the plume with two- and three-dimensional trajectories. Experimental investigations provide data to which the model predictions can be compared. Positive matches between experimental data and model prediction build confidence in the use of the model. However due to gaps in experimental evidence the confidence in the use of the models under some circumstances is limited. These circumstances include two-dimensional trajectory flows in a still ambient that are discharged at oblique angles and buoyant jet flows with three-dimensional trajectories. As part of this project an experimental investigation will be conducted into the behaviour of discharges with two-dimensional trajectories (including jets and plumes) and three-dimensional trajectories.

1.3 – Scope of Research

For the past century researchers have actively investigated the phenomenon of the buoyant jet. In the last 50 years several mathematical models have been presented to predict the trajectory and dilution of buoyant jets with different discharge configurations. An overview of the different models as well as their mathematical background is given in Chapter 2.

All models have been verified by laboratory and field data. Experimental studies into the behaviour of buoyant jets started at approximately the same time the first model was presented, and the database has been expanding ever since. Considerable amounts of laboratory and field data are now available for particular flow regions and these are summarized in Chapter 2, where discharge configurations for which there is very limited experimental data are also discussed.

To create a high quality data set two quantitative flow visualizations techniques are used. These are presented in Chapter 3. The first is LIF or Laser Induced Fluorescence. LIF has been used for nearly two decades and has been used to visualize buoyant jets for the past decade. LIF performs well for investigations into the behaviour of flows with two-dimensional trajectories and is used in the present study during the investigation of discharges in a still ambient fluid (in particular the negatively buoyant jet). An alternative flow visualization technique is developed to help with the investigation into the behaviour of three-dimensional trajectory flows. It is referred to as LA or Light Attenuation and is also employed for the two-dimensional trajectory flow experiments. The technique is based on a linear relationship between the increase in concentration of dye in the water and decrease in the intensity of the light passing through it.

A new model has been set up to aid in the design and to monitor the performance of the experiments. The model is based on a relatively simple framework when compared to existing models. The behaviour of the discharge at any particular location is determined by the relative magnitudes of three distinct forms of momentum flux (the initial momentum flux, buoyancy-generated momentum flux, and the entrained ambient momentum flux). Hence the new model is called the Momentum Model. The development of the model is outlined in Chapter 4. Its performance is verified by comparing it with existing experimental data for different flow configurations.

A wide range of LA experiments have been conducted. This is firstly done to verify the visualization technique, secondly to provide additional insight into the behaviour of discharges with two-dimensional trajectories, and finally to investigate the behaviour of discharges with three-dimensional trajectories. In Chapter 5 results for a range of initial discharge configurations are presented and comparisons are made with existing data and model predictions, as well as predictions from the Momentum Model.

A more detailed investigation is carried out into the behaviour of negatively buoyant jets and this is described in Chapter 6. There is a growing interest in the process of desalination to produce drinking water, because of increased uncertainties in water supply associated with unstable weather patterns. Discharges from desalination plants are in the form of negatively buoyant jets (wastewater with a higher density than the receiving ambient). Earlier investigations have primarily focused on a single angle of discharge (60º). The present investigation expands that to a range of angles and includes a comparison with both analytical and numerical model predictions.

Another flow with a two-dimensional trajectory that is investigated in more detail is the non-buoyant oblique discharge in a moving ambient. Both horizontally and vertically released non-buoyant discharges in a moving ambient have been studied in the past and the influence of the ambient on the flow in the strongly advected region was found to be significantly different for the two cases. The attention of the current investigation is focused on the transition angle that defines the distinctly different final forms of flow behaviour. The theoretical and experimental investigations can be found in Chapter 7.

Finally, the results of the experimental investigation into the behaviour of three-dimensional trajectory flows are presented in Chapter 8. As the knowledge of these flows is limited, the main purpose of the study is to observe these flows in general, comment on their behaviour and compare the results with predictions from current models.

Conclusions from the current research and possible suggestions for future work are put forward in Chapter 9.

Chapter 2 – Review of Previous Research

2.1 – Introduction

In this chapter an overview is given of relevant research undertaken into the behaviour of buoyant jets released into an unstratified ambient. For over a century research into this topic has been carried out and this has resulted in extensive knowledge about the theory of buoyant jets. The theories developed have formed the basis for several mathematical models and a summary of the models as well as their theoretical background is presented. Experimental investigations have led to considerable quantities of relevant experimental data on buoyant jets. Previous experimental investigations are discussed in this chapter and flow configurations with very limited experimental data are highlighted.

2.2– Problem Formulation of the Buoyant Jet

A (buoyant) jet is generated when relatively fast flowing fluid, from a continuous source, is discharged in a reservoir of relatively slow flowing fluid and the density difference between the two fluids is small. The high velocity gradients at the interface between jet and the ambient fluid make it highly unstable, and cause the jet fluid to rotate. These turbulent vortices entrain the ambient fluid into the jet, causing the mixing processes and the dissipation of the energy from the discharge.

Previous studies suggest that a buoyant jet flow can be divided into distinct flow regions (for example Pun (1998) and Jirka (2004)). These flow regions are the initial region, strong jet region, weak jet region, advected line momentum puff region, advected plume region, and the advected thermal region, however the influence of the initial region on the overall behaviour of the flow is minimal. In each of these regions the flow is dominated by a group of independent flow parameters, and the overall flow behaviour can therefore be described by a sequence of these distinct flow regions. Research, both experimental and theoretical modelling, has therefore focused on increasing the understanding of the behaviour of the flow within the distinct flow regions, and to a lesser extend on the transition regions that connect the flow regions.

As the distinct flow regions are the same for buoyant jet flows with two-dimensional and three-dimensional paths, it is assumed that the understanding of the behaviour of the flow, gained from experiments with two-dimensional trajectories, can also be applied to buoyant discharges with three-dimensional trajectories. Models based on this approach are assumed to predict with reasonable accuracy the behaviour of discharges with two-dimensional and three-dimensional paths (Cheung et al. 2000; Jirka 2004).

2.3 - Research History

Buoyant jets have been observed and commented on since the beginning of modern science, for example, they were observed coming out of smokestacks and volcanoes. Jirka (2004) gives an extended overview of the history of research on the buoyant jet. Some key features are given here.

It was not until the beginning of the twentieth century that the first detailed experimental measurements and an analytical explanation were completed on the subject. The investigation was lead by L. Prandtl in the 1920's; he applied boundary layer theory to the jet flow. Soon it was followed by measurements on the round non-buoyant jet (Zimm 1921) and the plane non-buoyant jet (Förthmann 1934). These measurements were the basis for the development of the similarity solutions for the spread and the velocity decay of the jet (Görtler 1942; Reichardt 1942; Tollmien 1926). Prandtl's turbulent mixing length hypothesis was used to relate the shear stresses to the mean flow of the jet and this method was taken a step further to include a pure vertically rising plume by Schmidt (1941). Reichardt (1943) was the first to determine that the cross-sectional properties of the jet could be approximated by Gaussian profiles, forming the foundation of the jet-integral method. The method was further developed into a jet integral model with the results of more detailed experiments carried out on the simple jet (Albertson et al. 1949) and the pure plume (Rouse et al. 1952).

Morton et al. (1956) introduced the idea that fluid momentum, vorticity and scalars in a jet are spread by turbulent entrainment rather than turbulent diffusion. They hypothesised that non-turbulent, irrotational fluid from outside the jet was entrained into the turbulent jet. This viewpoint was quickly incorporated into the already existing jet-integral methods. Jordinson (1956) and Keffer and Baines (1963) included a cross flowing ambient current in their experimental studies of the pure jet. Scorer (1959) introduced dimensional analysis and the use of length scales to separate regions of strong and weak deflections. With a similar analysis

Turner (1960) and Richards (1963) showed that an internal double vortex pair significantly affected the velocity and scalar distributions when the jet or plume flow was strongly deflected by the ambient current.

2.4 – Previous Experimental Investigations

Over the past six decades many experimental studies have been carried out in the field of buoyant jets. Most of these studies have been carried out in the laboratory. Data from field studies is available, but it was not possible to measure all the major factors influencing the flow behaviour and therefore the data is difficult to interpret. Because of the less-controlled environment outside the laboratory the results were less accurate. Inside the laboratory it is possible to separate the important independent parameters, the initial momentum flux, the buoyancy-generated momentum flux and the ambient momentum flux, from outside influences and from each other. This enables the researcher to carefully determine the influence of each of the factors on the flow. The laboratory studies differed in the use of measurement techniques, aims and types of flow. Because of the increase in the technology available to researchers over time, the studies have become more detailed; the flow measurement techniques more accurate and more complex flow configurations have been monitored. Data from experimental investigations has been used for verification of models as well as determination of the empirical parameters in the length-scale and integral models (see section 2.5).

2.4.1 – Flow measurement techniques

An overview of the main techniques used to measure velocity and concentrations in buoyant jets is given below.

Mean velocity measurements in an air jet where made by Albertson et al (1949) using pitot tubes. Rouse et al. (1952) measured velocities above a heated air plume using a vane anemometer (a thermocouple was used to measure temperatures). Pitot tubes were subsequently replaced by Hot-Wire Anemometry (Lassiter 1957) and Laser-Doppler Anemometry (LDA) (Abbis et al. 1975; Capp 1983). These changes expanded the research into the turbulent properties of the flow, as the newer techniques were capable of measuring the fluctuating components. The Hot-Wire Anemometry (HWA) was later upgraded to reduce

the high local turbulence intensity, caused by the flow around the stationary wires, with the Flying Hot-Wire anemometry (FHW) (Hussein et al. 1994). With the introduction of Particle Image Velocimetry (PIV) (Simoens and Ayrault 1994), velocity measurements were no longer confined to a point, but a planar velocity field could be observed and measured

Concentration measurements were made by Ayoub (1971) using conductivity probes, which were used to determine mean cross-sectional concentration profiles, and a black and white still camera in combination with potassium permanganate dye was used to determine the flow trajectory. For the buoyant jet in a cross-flow experiments a second black and white camera was added to record the trajectory in both the *x*-*y* and *x*-*z* planes. Papanicolau (1984) investigated the concentration profiles of a buoyant jet in a still ambient using laser-induced fluorescence (LIF), a non-intrusive optical technique, giving both trajectory and instantaneous concentration measurements. Knudsen (1988) added red dye to her experiments and recorded the trajectory using either a photographic or video camera. The trajectory of the centreline was determined by the averaging the two points defining the visible edges of the flow. With the known trajectory, a set of suction probes was inserted into the flow to measure the concentration at a pre-determined location. The upgrade of LIF to Planar Laser-Induced Fluorescence (PLIF) (van Cruyningen et al. 1990) did for the concentration measurements what PIV has done for the velocity measurements. Hereafter Laser Induced Fluorescence and Planar Laser-Induced Fluorescence are both referred to as LIF. However, simpler techniques continue to provide valuable information. For example, Cheung (1991) used hot water, rather than salt water, to create a difference in density between ambient and jet fluid. Rows of thermistor probes or a single thermilinear probe were then used to find the cross-sectional concentration field. The centre of mass of the concentration field defined the trajectory.

Experimental studies have also employed more than one measurement technique to obtain both velocity and concentration data, or to compare results from more than one technique as an internal verification. Examples are Papanicolau (1984) and Chu (1996) using both LDA and LIF, and Wang (2000a) using both PIV and LIF.

2.4.2 – Flow configurations

In this section several different flow configurations are discussed and sources of experimental data listed. These sources are not described in detail here, but data from these studies is

incorporated into subsequent chapters where appropriate. Note that x is the Cartesian coordinate in the same direction as the ambient velocity; or in the direction of the horizontal component of the initial velocity for still ambient flow, z is the Cartesian coordinate in the same direction as the vertical component of the initial velocity, and y is the Cartesian coordinate perpendicular to the x-coordinate in the horizontal plane. The angle ϕ_0 is the angle between the excess momentum flux and the ambient momentum flux; or between the excess momentum flux and the x-axis for still ambient flows, and s is the distance from the source along the trajectory of the flow.

2.4.2.1 - Jets

The first experimental investigations were on the behaviour of the simple jet. A simple jet flow has no buoyancy flux, as the density of the fluid in the jet (ρ) and the density of the ambient fluid (ρ_a) are the same, and the ambient environment is stationary (the ambient velocity (U_a) is zero). The behaviour of the flow is therefore dominated by the initial momentum flux ($M_0 = Q_0 U_0$, where U_0 is the initial (uniform) velocity of the flow, and Q_0 is the flow rate of the discharge) and is independent of the initial angle of discharge (ϕ_0). Investigations by Corrsin (1943), Hinze and van der Hegge Zijnen (1949), Albertson et al (1949), Corrsin and Uberoi (1950), Forstall and GayLord (1954), Sunavala et al. (1957), Ricou and Spalding (1961), Kiser (1963), Rosler and Bankoff (1963), Becker et al. (1967), Wygnanski and Fiedler (1969), Crow and Champagne (1971), Labus and Symons (1972), Birch et al. (1978), Capp (1983), Hussein et al. (1994), Pun (1998), Law and Wang (2000) and others have led to a firm understanding of the spread, velocity and dilution profiles as well as the rate of entrainment of the simple jet. The mean cross-sectional velocity and concentration profiles were both shown to fit the Gaussian shape well. Later experiments involving a simple jet have been carried out as a first step towards more complicated flow configurations or to investigate the instantaneous behaviour, including the turbulent properties of the jet. A schematic representation of a jet flow can be seen in Figure 2.1, including a mean cross-sectional velocity profile at some distance away from the source. The cross-sectional centreline velocity is represented by U_l, the local velocity in the cross-section by u, and the cross-sectional velocity spread by b. By defining b as the distance from the centre of the cross-section to the $e^{-1}U_l$ contour, the total width of the jet is approximately $4b$. C_0 is the

initial concentration of an inert pollutant added to the jet fluid, and *d* is the diameter of the source.

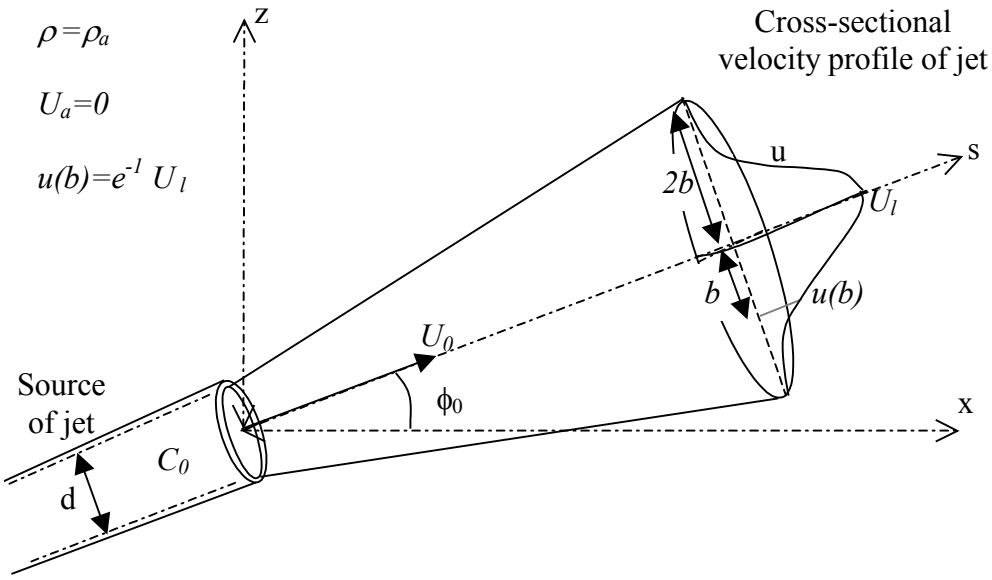

Figure 2.1 - Initial conditions and cross-sectional velocity profile for jet experiment

2.4.2.2 – Pure Plumes

Like the simple jet, the pure plume flows into a still ambient. But unlike the simple jet there is a buoyancy flux due to the difference in density between the ambient fluid and the plume fluid, and the initial velocity of the flow is almost negligible (Figure 2.2). Due to the low initial velocity of the flow, the source direction does not influence the behaviour of the flow. In the environment the ambient fluid is generally more dense than the pure plume fluid and therefore the buoyancy flux acts vertically upwards. Examples are heated air released from a vertical smokestack or wastewater (fresh water) released into an ocean (salt water). Adding salt to the pure plume fluid most often generates the density difference in the laboratory and therefore the buoyancy force is acting vertically downwards. Due to the relatively small density differences used (up to approximately three percent) it is appropriate to use Boussinesq's assumption and the results of the laboratory experiments can be used to describe the phenomena in the outside world. The mean cross-sectional concentration and velocity profiles of pure-plumes have also been shown to fit the Gaussian assumption. It is worth noting that generally pure plume experiments are not conducted in the laboratory, because laboratory flows normally have a notable initial momentum flux.

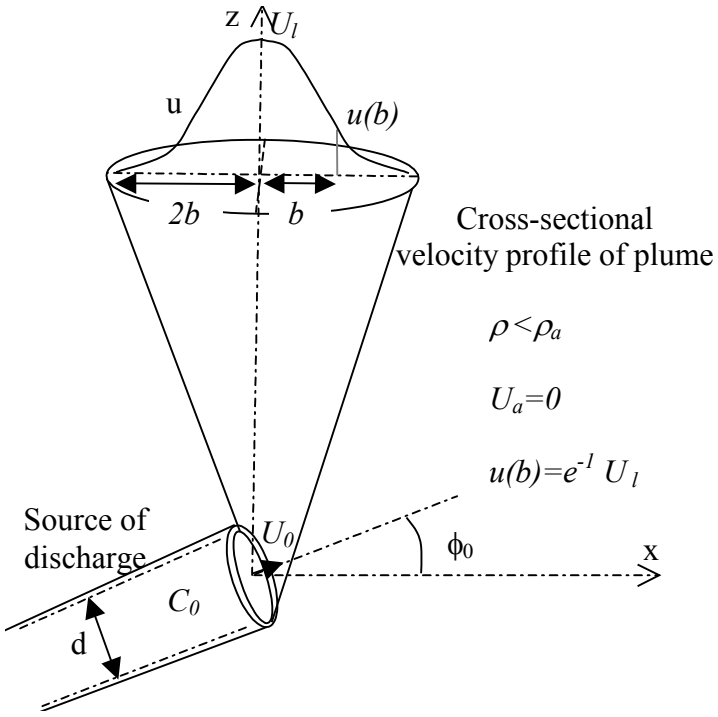

Figure 2.2 - Initial conditions and cross-sectional velocity profile for pure plume

2.4.2.3 – Buoyant Jets

As indicated, most plume experiments have a significant initial momentum flux and these experiments are better described as buoyant jet flows. The flow travels firstly through a region where the initial momentum flux dominates and the behaviour of the flow is jet-like. In the region where the flow is driven by the buoyancy force, the buoyancy-generated momentum flux dominates and the behaviour is plume-like (see Figure 2.3). In this region the flow starts to rise or fall more dramatically depending on the relative densities of the two fluids. Dimensional analysis has been used to determine the approximate location of the transition between the jet-like region and the plume-like region (see Table 2.2). This jet to plume transition length-scale collapses all trajectory, spread or dilution data for a particular discharge angle (ϕ_0) onto a single line (independent of the initial conditions). The mean velocity and concentration profiles of the buoyant jet are similar to those of the jet and plume.

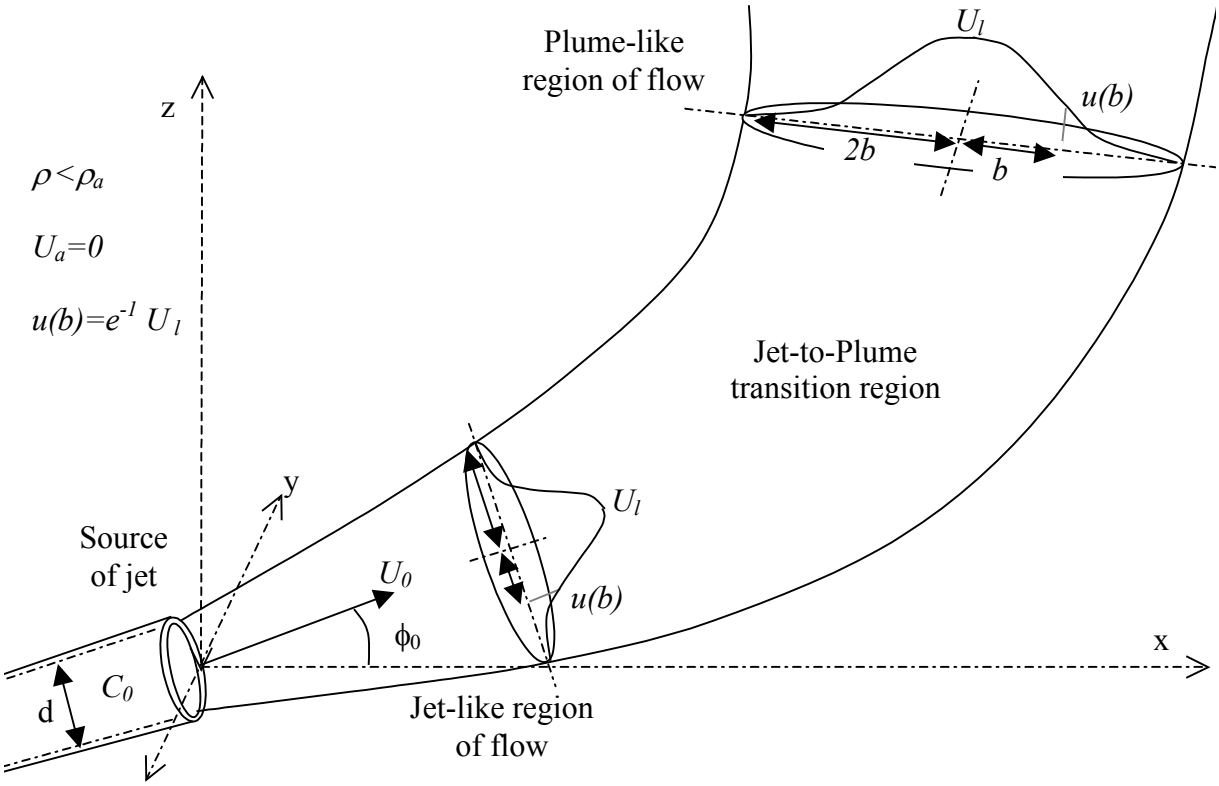

Figure 2.3 - Flow regions of a buoyant jet

Vertically discharged buoyant jets are commonly released such that the initial momentum flux acts in the same direction as the buoyancy-generated momentum flux. Extensive knowledge is available on the behaviour of these vertically discharged buoyant jets because of studies by Rouse et al. (1952), Abraham, (1960), Ricou and Spalding (1961), Abraham (1963), Frankel and Cumming (1965), Anwar (1969), George et al. (1977), Nakagome and Hirata (1977), Papanicolaou and List (1988), Fisher (1995), Pun (1998), Wang and Law (2002) and others.

Changing the source configuration to a horizontal position creates a horizontal buoyant jet. This buoyant jet configuration has been studied by, amongst others, Hanson and Schroder (1968), Anwar (1969), Ayoub (1971), Fan (1967), Hofer and Hutter (1981), Papanicolaou (1984), Papantoniou and List (1989), Davidson (1989), Gaskin and Wood (1993), and Papps (1995).

Buoyant jet flows with initial discharge angles falling between the vertical and horizontal cases above are called positively buoyant jets, because the vertical component of the initial momentum flux acts in the same direction as the buoyancy force. The remaining initial discharge angles create negatively buoyant jet flows, because the vertical component of the

initial momentum flux acts in the opposite direction of the buoyancy force. Zeitoun et al. (1972), Roberts and Toms (1987), Roberts et al. (1997) and Cipollina et al. (2005) have studied negatively buoyant jets with an initial discharge angle of -60°. Zeitoun et al. and Cipollina et al. also included initial discharge angles of -30° and -45°. The vertically discharged negatively buoyant jet is commonly referred to as a fountain. Here the flow reaches a maximum height before reversing direction. Turner (1966), Abraham (1967), James et al. (1983), McLellan and Randal (1986), Baines et al. (1990) and Zhang and Baddour (1998) have investigated the vertically discharged negatively buoyant jet.

2.4.2.4 – Advected Jets

Removing the buoyancy flux and introducing a moving ambient results in an advected jet. The discharge can be in the same direction as the ambient motion, in the opposite direction, perpendicular to the ambient motion, or at some intermediate angle. These flows are referred to as a jet in a co-flow, jet in a counter-flow, jet in a cross-flow and oblique discharged advected jet respectively. During an advected jet experiment, the initial momentum flux generally dominates the behaviour close to the source. This type of flow is called a strong jet and is weakly advected. The behaviour of the flow is similar to that of the simple jet. Further away from the source the entrained ambient momentum flux dominates the flow and the type of flow changes. The flow is now said to be strongly advected. Depending on the initial angle of discharge the flow either changes to an advected line momentum puff for a jet in a cross-flow (Figure 2.4a) or a weak jet for a jet in a co-flow (Figure 2.4b). The angle that determines the transition from the strong jet to either the advected line momentum puff or a weak jet is as yet unknown (Pun 1998). The concentration and velocity distributions in the region of the advected line momentum puff are no longer Gaussian but resemble a counter-rotating vortex pair with self-similarity perpendicular to the flow direction (Chu and Lee 1996). Data on the advected jet in a co-flow is available from studies by Ayoub (1971), Antonia and Bilger (1973), Smith and Hughes (1977), Biringen (1986), Knudsen (1988), Nickels and Perry (1996), Chu et al (1999), and Davidson and Wang (2002). Data on the advected jet in a cross-flow is available from studies by Jordinson (1956), Keffer and Baines (1963), Pratte and Baines (1967), Platten and Keffer (1971), Chu (1975a), Wright (1977), Chu (1996), Hung (1998) and Davidson and Pun (1999). Experimental studies investigating oblique discharges have been carried out by Margason (1968), Platten and Keffer (1971), Chu (1975a) and Hung

(1998). Advected jets in a counter-flow have been investigated by Yoda and Fielder (1996) and Lam and Chan (2002).

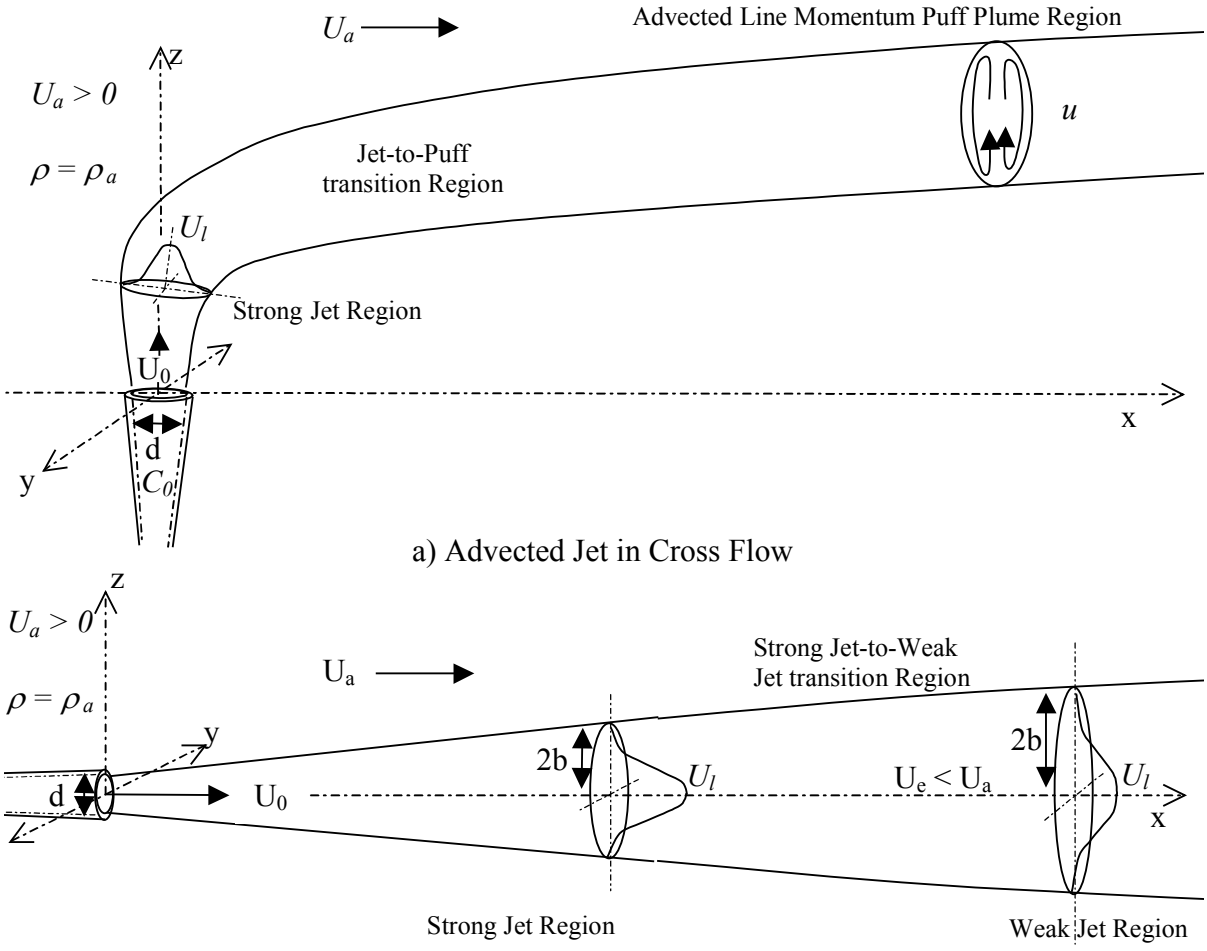

Figure 2.4 - Different flow regions of advected jet

2.4.2.5 – Buoyant Discharges in an Ambient Flow

All previously discussed flows can be described as two-dimensional trajectory flows (including jets and plumes). In all cases it was possible to define a plane that encompasses the complete trajectory of the flow. This may no longer be possible for some configurations of the buoyant jet in an ambient flow, because the densities of the ambient and the source fluid are no longer the same and hence three different forms of momentum flux are generated in the flow. As the buoyancy-generated momentum flux and the entrained ambient momentum flux act in perpendicular directions, the initial momentum flux determines whether a two-

dimensional or a three-dimensional trajectory flow is created. If the initial momentum flux acts in the same plane as the buoyancy-generated and ambient entrained momentum flux, the resulting flow has a two-dimensional trajectory. The focus of past experimental investigations for buoyant discharges in an ambient flow has largely been on 2D trajectory flows, and in particular on either the vertically discharged buoyant jet (Figure 2.5a) or the co-flowing case where the flow is discharged horizontally (Figure 2.5b).

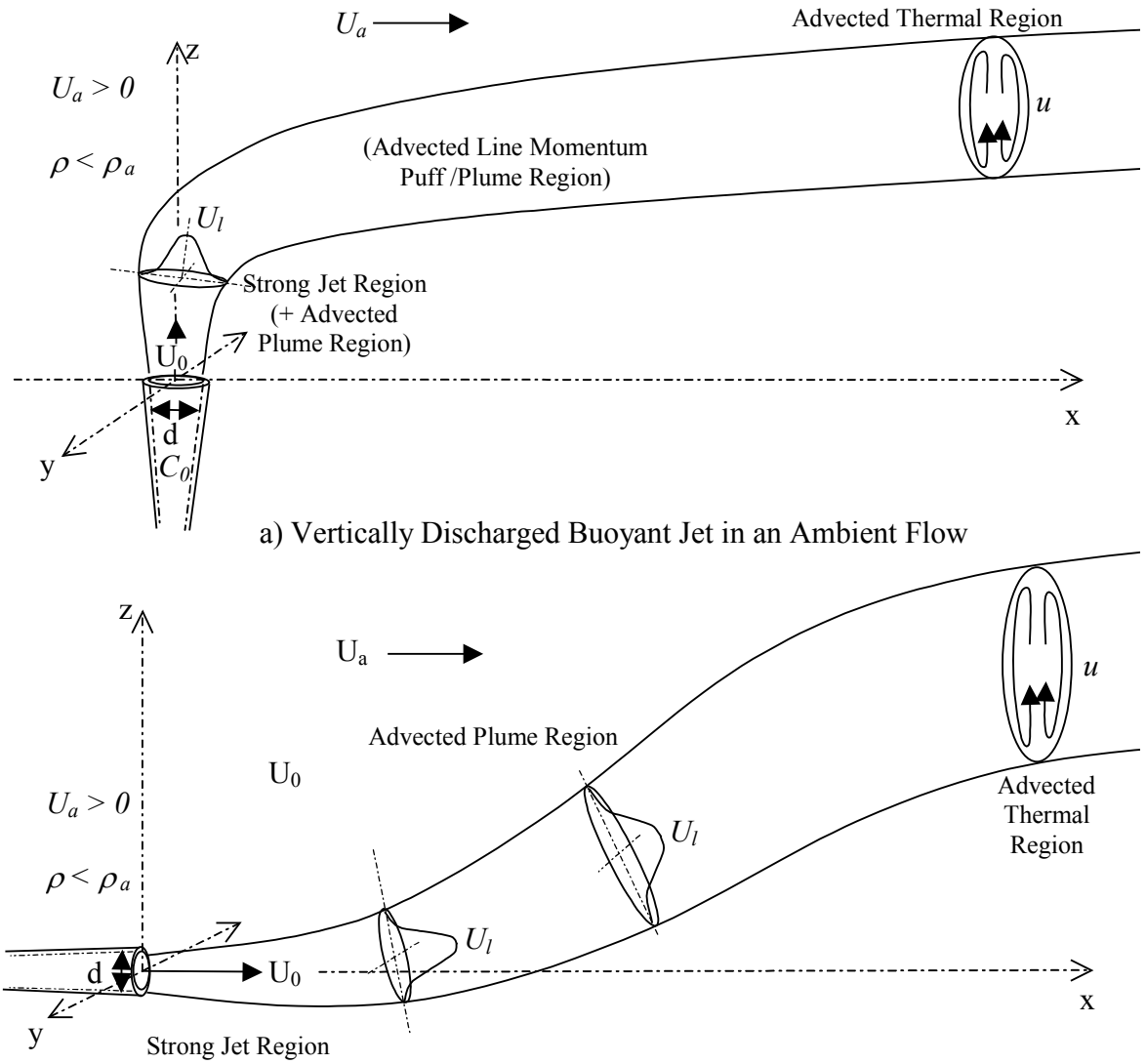

Figure 2.5 – Flow regions of buoyant jet in flowing ambient with a 2D-trajectory

The vertically discharged buoyant jet in an ambient flow moves through three regions. At first the flow has jet-like behaviour (the strong jet). In the strong jet region, both the buoyancy-generated momentum flux and the entrained ambient momentum flux increase in size. If the buoyancy-generated momentum flux dominates after the strong jet region, the flow behaves like a plume. However, if the entrained ambient momentum flux dominates the flow after the

strong jet region, the flow is an advected line momentum puff. After either the plume or puff regions a second flow transition takes place and the flow is then in the advected thermal region where both the buoyancy-generated and the entrained ambient momentum flux dominate the flow. In the weakly advected flow regions (strong jet and plume regions) the deflections due to the ambient current are small. In the strongly advected region (advected line momentum puff and advected thermal regions) the flow is noticeably bent over due to the ambient current and the velocity and concentration profiles resemble a counter-rotating vortex pair. Experimental investigations into this flow configuration have been carried out by Fan (1967), Chu and Goldberg (1974), Wright (1977) and Cheung (1991). Hewett (1971) investigated the vertical heated jet in a cross-flow.

By changing the angle of release of the discharge so that it is in line with the ambient current a buoyant jet in a co-flow is produced (Figure 2.5b). In this situation it is not possible for an advected line momentum puff to form and the presence of buoyancy effectively eliminates the possibility of the formation of a weak jet. Thus only three different flow regions are possible (strong-jet, plume, advected thermal), making their identification relatively simple. Ayoub (1971), Knudsen (1988), Davidson et al (1991) , Wong and Lee (1991) and Gaskin and Wood (1993) have studied the horizontal buoyant jet in a coflow.

Experimental studies into the behaviour of buoyant jets with two-dimensional trajectories in an ambient flow with discharge configurations that differ from the two mentioned above are less common. Knudsen (1988) studied the horizontal buoyant jet in a counter-flow. Chu (1975b) and Anderson et al. (1973) have investigated the behaviour of negatively buoyant jets in a cross-flow. Chu released the initial momentum flux perpendicular to the ambient flow; Anderson et al. released the initial momentum flux at 60° to the cross-flow.

If the source outlet is not lying in the plane of the ambient motion and buoyancy force, the initial momentum flux is not in the direction of the buoyancy-generated and entrained ambient momentum flux plane. The flow trajectory is therefore three-dimensional and the flow is called a buoyant jet in a cross-flow (Figure 2.6). The flow can pass through the same regions as the equivalent two-dimensional trajectory flow, but the transformations take place along a three-dimensional path. Experimental investigations into these flows are inherently difficult because the flow measurement techniques employed to investigate buoyant jet flows are not easily adapted for measuring concentration and velocity profiles along a three-dimensional path. The early techniques (Ayoub 1971; Chu 1975a) measured the concentration

or velocity profiles of the flow at one or several points, setting up the measuring equipment at the point of interest (perpendicular to the direction of flow). However with none of the trajectory co-ordinates fixed, locating the trajectory and the direction of flow required a separate investigation. The introduction of LIF made it possible to obtain more detailed information at a particular cross-section, but locating the cross-section so that it was perpendicular to the flow direction remained problematic. Determining the trajectory co-ordinates from photographs or video images is difficult because of the changing calibration length-scales, due to the flow not travelling perpendicular to the plane of view. However, the above-mentioned constraints are largely eliminated for areas of the flow that travel predominantly in a single direction, reducing the flow to one with an essentially two-dimensional trajectory (Cheung 1991). Ayoub (1971), Chu (1975a) and Cheung (1991) studied the horizontally discharged buoyant jet in a cross-flow and Wallingford Hydraulic Research Station (1977) the horizontally discharged heated jet in a cross-flow.

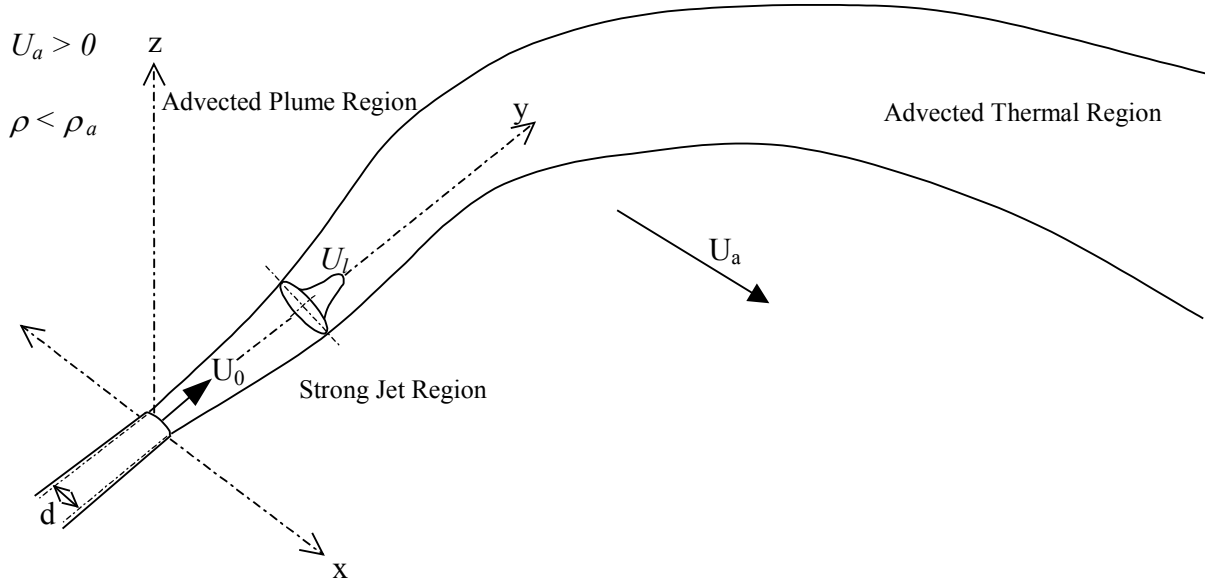

Figure 2.6 – Flow configuration horizontally discharged buoyant jet in a cross-flow

2.4.3 – Missing Experimental Data

Even though there is extensive experimental data available for the two-dimensional trajectory flows as a whole, there still remain flow configurations with limited or no available data. The horizontal and vertical flow configurations have dominated past experimental investigations. Relatively few studies have focussed on discharges with oblique angles. Those studies that

have investigated these flows have largely been limited to trajectory results. These flows are of particular interest because they provide an opportunity to study more closely the nature of transitions between the different strongly advected regions. In the non-buoyant case these regions are the weak-jet and the advected line momentum puff. More generally, currently available models predict oblique discharge behaviour and validation of these predictions with experimental data is desirable.

With the increase in the demand for clean water as well as decreasing costs for the desalination process, desalination plants are becoming an increasingly viable option as a supplementary reliable main water supply for many communities. The effluent from desalination plants has relatively high salinity concentrations. Discharging the effluent into less dense surrounding fluid makes the effluent fall rather than rise. If the ambient motion is relatively small or non-existent the discharge essentially becomes a negatively buoyant jet. Except for the vertical discharge configuration, the negatively buoyant jet has not received a great deal of attention. Past experimental investigators have primarily studied the behaviour of the discharge with a 60° angle, and to a lesser extent the 30° and 45°. The experimental results have focused on the rise height of the flow, the distance from the point of release to the impact point (the point at which the flow returns to the source height), and the dilution at the impact point. Widening the scope of the investigation into the behaviour of the negatively buoyant jets (including a range of discharge angles and determining spread and dilution data along the trajectory of the flow), will increase the knowledge of the mixing characteristics of these flows. This understanding can eventually lead to more effective discharge techniques.

As indicated, relatively few studies have focused on the three-dimensional flow trajectory, in part because of the difficulties described previously. While the more recent study by Cheung (1991) provides valuable information about these flows, the study was necessarily limited in its coverage of flow regions. In addition, the experiments were carried out in a flume where the influence of mean shear and ambient turbulence was difficult to assess. Two earlier studies (Ayoub 1971; Chu 1975a) were completed over thirty years ago and hence limited information could be obtained from the flows. Coverage of flow regions was again also limited. With current technology more detailed information can be obtained and a broader range of discharge configurations more easily explored. The past studies have been limited to a single discharge configuration. The source outlet was horizontal and perpendicular to the ambient current.

2.5 - Existing Models

The considerable research activity in this area over the past 50 years has resulted in a number of different models to mathematically describe the trajectory and dilution of buoyant discharges. Over time these models have expanded to incorporate more complex flow configurations. Most models are now able to predict the behaviour of a buoyant jet with a three-dimensional flow trajectory. The different models can generally be split into three different categories, the length-scale models, the integral models, and the models that use a combination of both length-scales and integral techniques.

2.5.1 – Length-Scale Models

The first group of models is based on the length-scale approach (for a more detailed explanation, see Pun (1998)). The first step in this approach is to determine the different flow regions. For buoyant jets in a cross-flow, the different flow regions or limiting cases are the initial, strong jet, weak jet, line momentum puff, advected plume and advected thermal. These flow regions are determined by the relative magnitude of the independent parameters of the flow. The independent parameters are the initial flow rate (Q_0), initial excess momentum flux (M_{e0}), the initial density deficit flux ($Q_{\Delta 0}$) and the ambient velocity (U_a). Table 2.1 shows the dominant parameters for each of the different flow regions. U_0 represents the initial (uniform) velocity of the flow at the end of the round source, d the diameter of the source, g the gravitational constant, ρ_a the density of the ambient fluid, ρ the density of the jet fluid, and ϕ_0 the initial discharge angle.

By combining the dominant parameters of two neighbouring flow regions different length-scales can be formed. The length-scales are along the predominant direction of movement of the flow before the transition (with the exception of the weak-jet to advected thermal length-scale which is along the direction of the secondary movement), and determine approximate locations where the flow transforms from one flow region into another (Table 2.2). Length-scales are compared to determine the form of the flow at a particular location. If the independent parameters are all non-zero then buoyant jet discharges start in the initial flow region and end up as an advected thermal. The relative magnitudes of the independent parameters determine the sequence of flow regions that form as the flow develops. Transition points are located more accurately through the introduction of transition constants into the

transition length-scale relationships. These constant are obtained from comparisons with experimental data.

Table 2.1 - Dominant parameters in flow regions

Flow Region	Dominant Parameters
Initial	$Q_0 \left(= \pi/4\, d^2 U_0\right)$
Strong Jet	$M_{e0} \left(= Q_0 U_{e0} = Q_0 \left[U_0 - U_a\right]\right)$
Weak Jet	M_{e0} and U_a
Line Momentum Puff	M_{e0} and U_a
Advected Plume	$Q_{\Delta 0} \left(= Q_0 g \left(\rho_a - \rho\right)/\rho\right)$
Advected Thermal	$Q_{\Delta 0}$ and U_a

Table 2.2 – Transition length-scales for transition between flow regions

Flow Region Transition	Transition Length-Scale
Initial – Strong Jet	$\sim \frac{Q_0}{M_{e0}^{1/2}}$
Initial – Advected Plume	$\sim \frac{Q_0^{3/5}}{Q_{\Delta 0}^{1/5}}$
Initial – Advected Thermal	$\sim \frac{Q_0 U_a^{\,2}}{Q_{\Delta 0}}$
Strong Jet – Weak Jet	$\sim \frac{M_{e0}^{1/2}}{U_a} \left\lvert \cos\phi_0 \right\rvert$
Strong Jet – Advected Line Momentum Puff	$\sim \frac{M_{e0}^{1/2}}{U_a} \left\lvert \sin\phi_0 \right\rvert$
Strong Jet – Advected Plume	$\sim \frac{M_{e0}^{3/4}}{Q_{\Delta 0}}$
Weak Jet – Advected Thermal	$\sim \frac{M_{e0} U_a}{Q_{\Delta 0}} \left\lvert \cos\phi_0 \right\rvert$
Advected Plume – Advected Thermal	$\sim \frac{Q_{\Delta 0}}{U_a^{\,3}}$
Advected Line Momentum Puff – Advected Thermal	$\sim \frac{M_{e0} U_a}{Q_{\Delta 0}} \left\lvert \sin\phi_0 \right\rvert$

The second step involves working out relationships that describe flow behaviour within a flow region using dimensional analysis. With the help of the Buckingham Π theorem the trajectory, spread, velocity and dilution can be related to the distance from the source or the virtual source (see Table 2.3). The virtual source of a flow region is the location of the source if the flow was released in that particular flow region. Appropriate constants are introduced that can again be obtained from experimental data.

Table 2.3 – Characteristic relations of flow parameters with distance within flow regions

Flow Region	Trajectory	Spread	Velocity	Dilution
Strong Jet (vertical discharge)	$z \sim x^{1/2}$	$\sim z^{1}$	$\sim z^{-1}$	$\sim z^{1}$
Weak Jet (horizontal discharge)	-	$\sim x^{1/3}$	$\sim x^{-2/3}$	$\sim x^{2/3}$
Line Momentum Puff (vertical discharge)	$z \sim x^{1/3}$	$\sim z^{1}$	$\sim z^{-2}$	$\sim z^{2}$
Advected Plume	$z \sim x^{3/4}$	$\sim z^{1}$	$\sim z^{-1/3}$	$\sim z^{5/3}$
Advected Thermal	$z \sim x^{2/3}$	$\sim z^{1}$	$\sim z^{-1/2}$	$\sim z^{2}$

The length-scale approach has been used by Scorer (1959), Hoult et al. (1969), Chu and Goldberg (1974), Wright (1977), Knudsen (1988) and Doneker and Jirka (1990). The commercially available outfall model CorMix (Doneker and Jirka 1990) is also based on the length-scale approach. The main advantage of this approach is its simplicity and it enhances the physical insight into the flow. But it relies heavily on empirical data and is unable to predict flow behaviour in the transition zones. Nevertheless the models based on the length-scale approach are considered accurate enough to be used for engineering applications.

2.5.2 – Integral Models

All incompressible fluid dynamical phenomena are governed by the Navier Stokes equations. Equation 2.1 is the conservation of mass equation using index notation. Equation 2.2 is the conservation of momentum equation using index notation. The gravity term is absorbed into the pressure term, thus p is the modified pressure.

$$\frac{\partial u_i}{\partial x_i} = 0 \tag{2.1}$$

$$\frac{\partial u_i}{\partial t} + u_j \frac{\partial u_i}{\partial x_j} = -\frac{1}{\rho}\frac{\partial p}{\partial x_i} + \nu \frac{\partial^2 u_i}{\partial x_j \partial x_j} \tag{2.2}$$

At this moment in time it is difficult to solve the Navier Stokes equation directly for a turbulent flow, as the equations are four non-linear partial differential equations with four dependent and four independent parameters. Osborne Reynolds suggested solving the Navier Stokes equations for average values of the velocity and pressure rather than the instantaneous values. For turbulent flows that are steady in the mean, the parameters u_i and p randomly change in time around some mean value. These parameters can be decomposed into a mean (U_i and P) and a fluctuating part (u_i` and $p$`). This is known as Reynolds decomposition.

$$u_i = U_i + u_i' \tag{2.3}$$

$$p = P + p' \tag{2.4}$$

Inserting equation 2.3 and 2.4 into the Navier Stokes equations and averaging gives the average continuity equation (2.5) and the Reynolds equation (2.6). The Reynolds equation governs the mean velocity and pressure fields in a turbulent flow.

$$\frac{\partial U_i}{\partial x_i} = 0 \tag{2.5}$$

$$\frac{\partial U_i}{\partial t} + U_j \frac{\partial U_i}{\partial x_j} = -\frac{1}{\rho}\frac{\partial P}{\partial x_i} + \frac{\partial}{\partial x_j}\left(\nu \frac{\partial U_i}{\partial x_j} - \overline{u_i' u_j'}\right) \tag{2.6}$$

When comparing equations (2.1) with (2.5) and equation (2.2) with (2.6), it can be noted that the terms in the average equation are almost the same as in the instantaneous equation. The only extra term in the Reynolds equation is $-\overline{u_i' u_j'}$, the turbulent stress per unit density. When multiplied by ρ it is also known as the Reynolds stress. This term came into the equation because of the averaging of the non-linear advection term in the original equation. The term involves the product of the fluctuating components. The Reynolds stress is a symmetric second order tensor and non-zero. Thus the averaging process produces six new unknowns. Together with four mean flow parameters this gives a total of ten unknown parameters and only four equations. This problem is known as the closure problem of turbulence: how to relate the turbulent stress terms to the mean velocity and pressure terms, or provide additional equations.

As a solution to the buoyant jet problem the assumption of self-similarity for all cross-sectional properties, velocities or concentration, was proposed by Morton et al. (1956). The self-similarity of the cross-sectional properties was used to integrate across the cross-section

and then solve for the velocity and concentration distributions along the flow. The unknown parameters velocity, spread, density of jet fluid and concentration of the tracer were all related to the entrainment of ambient fluid into the jet. This simplified the problem to finding just one equation, the relationship between the entrainment and the mean flow parameters. Morton et al. arrived at the entrainment assumption. It stated that the entrainment velocity is proportional to the centreline velocity of the buoyant jet.

$$u_e = \varepsilon U_l \tag{2.7}$$

where u_e is the entrainment velocity and U_l the centreline velocity. The entrainment coefficient (ε) has been shown experimentally to be approximately 0.055 for a strong jet based on Gaussian cross-sectional profiles; but this changes for different flow configurations, for example, if the flow is dominated by the buoyancy-generated momentum flux (a plume forms) the value for the entrainment coefficient is 0.083. Morton et al. developed the integral model of the buoyant jet by using the entrainment assumption and integrating the equations of motion over a control volume.

Abraham (1963) arrived at the spread assumption using a second approach to solve the set of equations. It stated that the rate of spread of a jet is a constant.

$$b = kx \tag{2.8}$$

where b is velocity spread and x the distance from the source, the spread constant (k) is approximately 0.11 for the strong jet. The advantage of the spread assumption over the entrainment assumption is that it can be generalized more easily. The rate of spread of a plume is also a constant and not dissimilar to that of the jet. Abraham was the first to present a more general jet-integral model that included different source and ambient conditions.

Abraham's model was however based on the jet-diffusion approximation (fluid momentum and vorticity spread by turbulent diffusion) rather than turbulent entrainment. The first to incorporate the entrainment approach into a general jet model was Fan (1967). He used an Eulerian integral method, in which the flow passes through a fixed control volume, and integrated the equations of motion over that control volume. Others who have used this approach are Fan and Brooks (1969), Muellenhoff et al. (1985), Wood (1993) and Chu and Lee (1996) and Jirka (2004) [CorJet]. Cheung et al (2000) [VisJet] and Baumgartner et al (1993) used the Lagrangian integral method for the development of their models. The Lagrangian integral method integrates the equations of motion over a control volume that moves with the flow. Both CorJet and VisJet are commercially available models.

2.5.3 – Hybrid Models

A significant benefit of the Length Scale approach is that the problem is simplified, while the results predicted by the Length Scale models are still acceptable for engineering applications. However that is at the same time their weakness: Length Scale models are unable to accurately predict the behaviour of flow, especially in the zones of transition between different regions, because of their simplicity and their dependence on experimental data. The integral models are more sophisticated, and at the same time this can be a drawback with the need for numerical solutions. They are, however, capable of producing relatively accurate results and do not have a high dependence on experimental data. Attempts have been made to combine the two approaches. An example is the hybrid model of Davidson & Pun (1998) and Davidson & Pun (2000). The Length Scale approach was used to define the different flow regions and analytical integral solutions were used to define the flow behaviour within the flow regions. Thus combining the simplicity of a length-scale model with the reduced empirical dependence of the integral solutions.

2.6 – Summary

For over a century researchers have investigated the behaviour of the buoyant jet. The observations and quantitative results from early experimental research led to the formulation of empirical and analytical solutions. These solutions formed the basis of the mathematical models that are used today to predict the behaviour of these flows. Later experimental studies have benefited from newer flow measurement techniques that have increased the accuracy and detail of the data available. The new results have been used to verify the output of the models, as well as increasing the general knowledge of flows, particularly with respect to instantaneous behaviour.

However, as pointed out above, when considering mean flow behaviour several important experimental data sets are missing, and these are the focus of the current study. In the current study, separate investigations have been carried out into the behaviour of negatively buoyant jets, the non-buoyant oblique discharge in a moving ambient flow, and the buoyant jet with three-dimensional trajectories. The results of these investigations can be found in Chapters 6, 7 and 8. In Chapter 5 experimental results from other two-dimensional trajectory flows that

were carried out, with a view to creating a more complete experimental data set for buoyant jet discharges, are presented. These included simple jets, plumes, positively buoyant jets, non-buoyant discharges released perpendicular to the ambient flow and oblique buoyant discharges in a moving ambient.

Chapter 3 – Flow Visualization Techniques

3.1 - Introduction

As indicated in the previous chapter, buoyant jet flows can be classified based on their trajectory. For those flows with two-dimensional trajectories (including jets and plumes) it is possible to observe the flow through a camera located such that it is perpendicular to the flow path. Flows in the second group have three-dimensional trajectories. For these flows it is no longer possible to set the camera up in such a way that it is perpendicular to the central flow path at all points. An example of a flow from this group is a buoyant jet in a cross-flow, discharged horizontally and perpendicular to the ambient flow.

LIF (Laser Induced Fluorescence) has been used for the last two decades to investigate two-dimensional trajectory flows in a qualitative as well as a quantitative way (Papanicolaou 1984; Papantoniou and List 1989). LIF is a flow visualization technique that is well suited to these types of flows, because the laser sheet used for LIF can be set up in such a way that it coincides with the central trajectory plane. As this is no longer possible for the three-dimensional trajectory buoyant jet flows, LIF is not suitable unless the laser sheet is rapidly scanned in the third dimension and image recording is coordinated with that scan (Tian and Robert 2003). Although traditional planar LIF can be employed to obtain cross-sections from these flows, large numbers of these would be required to adequately characterize each flow.

A relatively simple alternative approach, employed here, is to use the light attenuation (LA) technique. LA is based upon the relationship between the increase in dye concentration in the fluid and the decrease of intensity of the light passing through the dyed fluid. Cenedese and Dalziel (1998) showed that attenuation of light that passes through a dyed fluid could be used to measure the concentration of dye in the fluid or the thickness of a fluid layer. The technique has been successfully applied to 2 dimensional fluid flows (Zhang and Chu 2003; Gaskin et al. 2004). In the present study a LA system has been developed to study 3 dimensional fluid flows and the technique is then applied to problems of interest with both two-dimensional and three-dimensional trajectories.

LA and LIF are not strictly alternatives as LA provides information that has been integrated over a flow depth, whereas LIF provides information that has been integrated over the width of the laser sheet (typically of the same scale as the source). Due to the integrated nature of the LA concentration data, the signal does not diminish as quickly with increasing distance from the source, when compared to the point concentration data from LIF. Thus the LA system can provide high quality quantitative information for the flow as a whole. However this same integrated nature makes the interpretation of the data obtained more challenging.

This chapter firstly presents the details of the LA technique developed for the buoyant jet flows with three-dimensional trajectories, including the limitations and interpretation of the results from LA experiments. A LIF system employed for parts of the present study is also briefly outlined at the end of the chapter.

3.2 - LA

An overview of the light attenuation flow visualization technique and its application to the problem at hand is given below. Initially the experimental and theoretical aspects of the LA system are discussed. This is followed by the set up, method and results of the calibration experiments; which were carried out to explore the experimental configuration and the limitations of the method for the current application. The data acquired from a LA experiment is integrated concentration data. The interpretation of the integrated concentration data is discussed for weakly advected (strong-jet and plume) and strongly advected flows (puff, thermal and weak-jet). In addition a flow angled towards the camera is also dealt with and this in turn is used to explore parallax issues. Finally the upgrade from the standard LA system (used for two-dimensional trajectory flows), to the 3D LA system (used for three-dimensional trajectory flows), is presented. This includes verification of the results using a weakly advected and a strongly advected flow.

3.2.1 – Light Attenuation System

As indicated, LA is based upon the relationship between the increase in dye concentration in the fluid and the decrease of intensity of the light passing through the dyed fluid. This is explained in some detail when discussing the theoretical background of the light attenuation

technique. The experimental configuration of a typical LA experiment is used as an aid in that explanation and is therefore discussed first.

3.2.1.1 – LA Experimental Configuration

The light attenuation technique requires controlled lighting conditions and hence the LA experiments were carried out in a darkroom. The tank used for the experiments had inside dimensions of (length x width x height) 6220mm x 1540mm x 1080mm. Both the ends and the sides of the tank were made up of glass windows with a viewable area of (width x height) 700mm x 980mm. The ends had two such windows, the sides eight. A trolley-system with a variable speed control was mounted on top of the tank, driving along the length of the tank. The source was attached to the trolley and a magnetic flow meter and timer were situated on top of the trolley. The trolley-system included a cable-tray that was used to feed through the electrical cables and hoses to the source. A schematic diagram of the tank can be seen in Figure 3.1. The results of the magnetic flow meter calibration test can be seen in Figure 3.2. The error was within 2%.

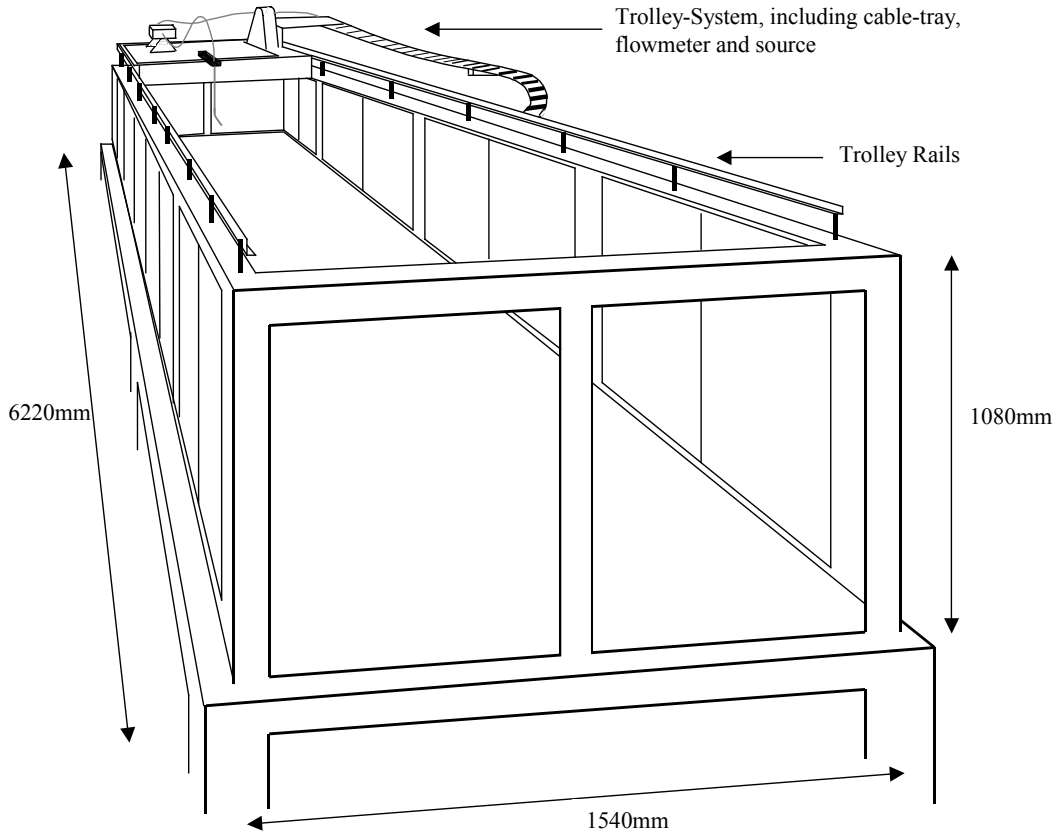

Figure 3.1 - Schematic Diagram of main tank

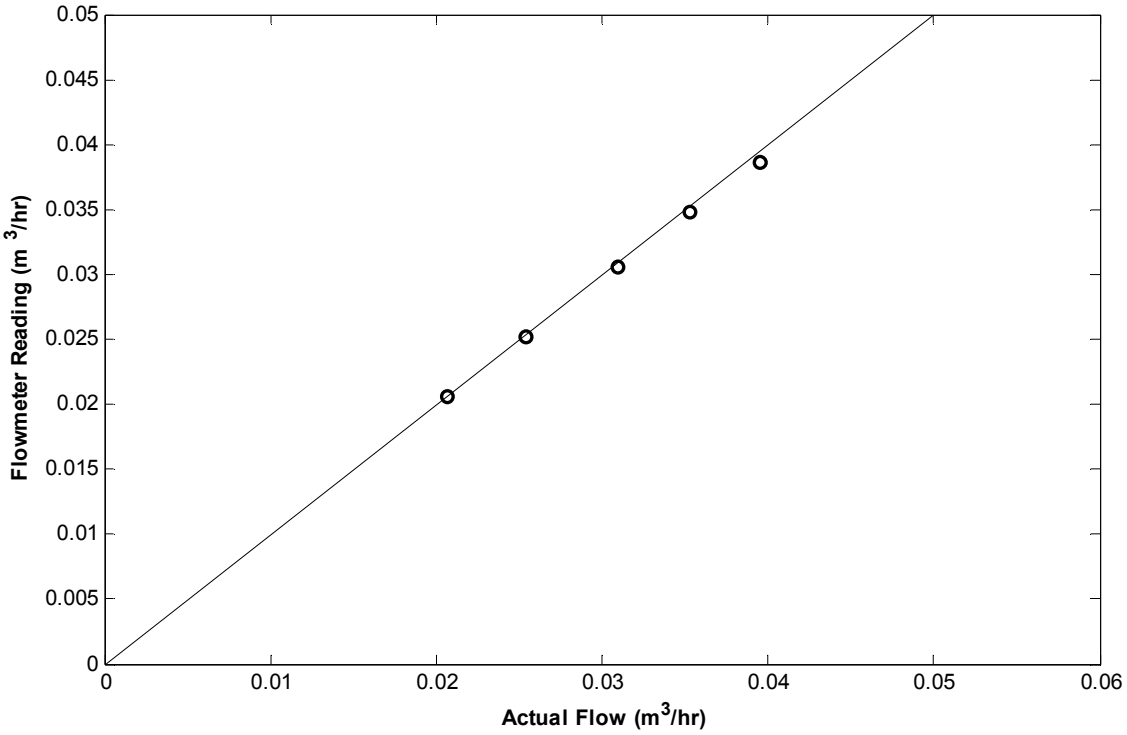

Figure 3.2 - Magnetic flow meter calibration test results

A second, smaller tank with a volume of 320 litres was situated next to the main tank. This tank was filled with the source solution. The temperature of the solution was controlled with cooling cells, so that the source fluid had the same temperature as the water in the main tank. Before and during experiments, frequent temperature measurements of the source fluid, at the source, and the water in the main tank were carried out to make sure the temperature variations were within 0.1^{o} C. Covering the tank when not in use minimized evaporation of the source solution. The source solution was pumped up to a constant head tank, 3870mm above the floor of the main tank. From the constant head tank, the solution ran back down through the flow meter and out the source. A second outlet was inserted in the system to enable draining of the hoses before each experiment to make sure the temperature of the source solution matched the temperature of the water in the main tank. The overflow of the constant head tank ran back into the source tank. After each experiment the source fluid left in the constant head tank was pumped back into the source tank.

The light source for the light attenuation experiments was a white-light bank consisting of twelve 100Hz fluorescent tubes. This light bank was positioned behind the third window of the main tank (see Figure 3.3). The light bank was supported by a dexion frame, and placed at a height so that the light bank covered the complete viewable area of the window. An opaque

Perspex diffusion sheet with a thickness of 2mm was placed in between the lights and the window. The Perspex sheet acted as a diffuser creating a more uniform light sheet. The light bank was covered with black cloth to minimize the chance of light reaching the camera other than through the selected window.

On the opposite side of the tank a digital video camera was positioned up to approximately 5 metres from the middle of the tank. The camera was either a Canon MV4i DV (or MV30 DV) or Jai CV M7+(or Jai CV M7+ CL). The video camera was mounted on a tri-pod and positioned in such a way that the lens of the camera was in the middle of, and perpendicular to the third window. The camera was connected to the computer via a data-cable and either a IEEE Firewire (for the Canon cameras) or Bitflow video board (for the Jai cameras). The ImageStream Software (Nokes 2005) was used to analyse the data.

Two calibration cells were placed inside the tank. These calibration cells consisted of a glass picture frame and its supports, including wheels. The visible area of the glass had dimensions of 770mm x 550mm. The width between the glass plates was 32mm (±0.3%). The wheels of the calibration cells were set inside two L-shaped rails that were positioned lengthwise on the bottom of the tank. The rails were fixed in place using magnets. The first calibration cell was left empty, with its valves open. Therefore the main tank and this cell were filled simultaneously. The second calibration cell was filled with diluted source solution and then closed. Figure 3.3 shows the positions of the light source, video camera and the calibration cells relative to the main tank.

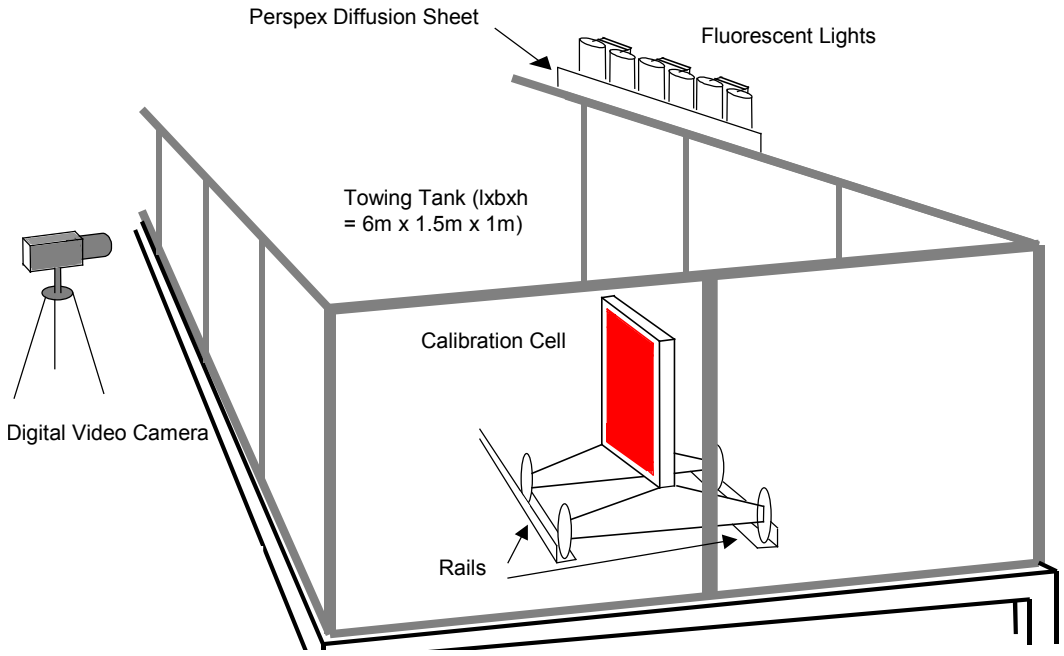

Figure 3.3 - Schematic diagram of experimental equipment

The source solution was made up from water, red food dye and salt. The relative quantity of each depended on the type of discharge. After mixing the source solution was left alone for at least one day so that the salt was properly dissolved, and the air bubbles were dissolved.

A cross-sectional cut at the third window creates Figure 3.4, the set up for a typical LA experiment.

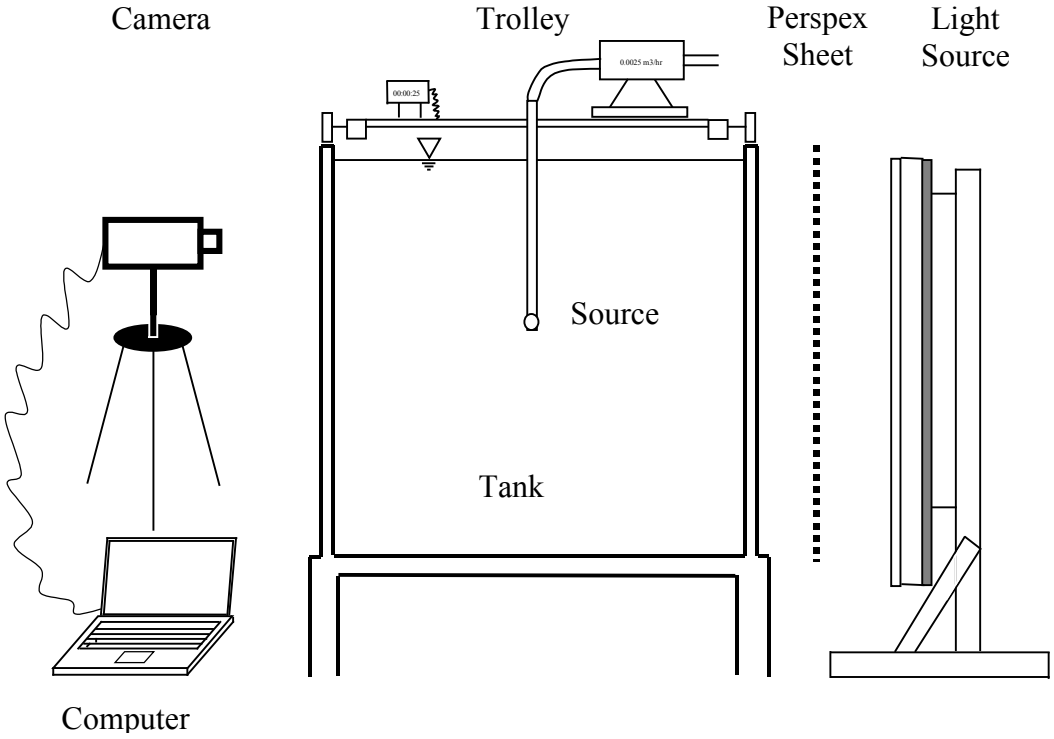

Figure 3.4 - Typical LA experimental set up

3.2.1.2 – Theoretical Background

The attenuation of light intensity and the operation of a digital video camera and computer are combined to form the basis for the flow visualization technique. Additional details of the attenuation of light technique can be found in a paper by Cenedese and Dalziel (1998) and the operation of a digital video camera is described in depth by Poynton (1996)

In Figure 3.4, light travels from the light source through the Perspex diffuser sheet and the tank and is caught by the digital video camera located at the other side of the tank. The camera sends the data to the computer. The computer stores the data and is the tool used to analyse the recorded data.

Looking in more detail at the individual components of the system, one can consider what happens to a ray of light from when it departs the light source until it is analysed using the computer (see Figure 3.5). After leaving the light source the ray of light will immediately start to decrease in intensity. The air absorbs the light and thus the further away from the light source the less bright it appears. Absorption of light also occurs when the ray is travelling through the Perspex diffuser sheet, the glass walls of the tank and the water in the tank. Upon hitting the Perspex sheet some of the incident ray of light will be reflected back due to the air/Perspex interface, and the ray loses some of its intensity. Similar reflections occurs when the ray hits the Perspex/air, air/glass interface, glass/water interface, water/glass interface and glass/air interface. If these losses were calculated as the intensity of the light after the loss divided by the intensity before the loss occurred, ten constants with a value between zero and one would be determined. These constants can be referred to as C_{air}, $C_{Perspex}$, C_{glass} and C_{water} for the four different absorption losses and C_1, C_2, C_3, C_4, C_5 and C_6 for the reflection losses as mentioned above. Figure 3.5 shows the path of the ray of light for a typical system including the losses of intensity along the way.

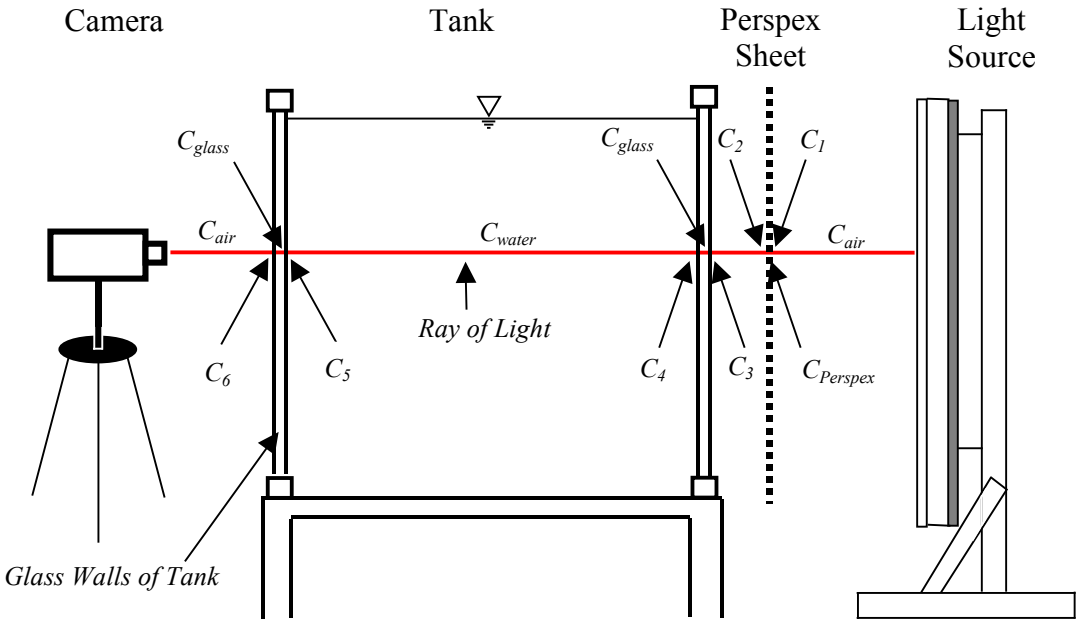

Figure 3.5 - Path of a ray of light

The intensity of the ray of light at the camera (I_{cam}) is then related to the intensity of the ray at the light source (I_{source}) by taking into account all the loss terms along its path. This gives equation (3.1). In LA experiments the intensity of the light at the camera will be used as a reference intensity, I_{ref}. Substituting I_{ref} for I_{cam} in equation (3.1) gives equation (3.2).

$$I_{cam} = C_1 * C_2 * C_3 * C_4 * C_5 * C_6 * C_{air} * C_{Perspex} * C_{glass} * C_{water} * I_{source} \quad (3.1)$$

$$I_{ref} = C_1 * C_2 * C_3 * C_4 * C_5 * C_6 * C_{air} * C_{Perspex} * C_{glass} * C_{water} * I_{source} \quad (3.2)$$

Upon receiving the light, the camera codes the colours by assigning three values to represent each colour. The three values correspond to the red, blue and green intensities of the colour. The camera sends the codes to the computer via a data-cable. The computer receives the data and converts it back to colours to reproduce the image. An introduction to the processes involved can be found in Appendix A

Figure 3.6 is as Figure 3.5 but with the addition of some dyed fluid in the path of the ray of light. This dyed fluid can be thought of as a jet-flow in the middle of the tank or a stationary dyed fluid covering the whole tank. The image recorded in this situation is similar to an image recorded during a typical LA calibration experiment. However, due to the added dye in the path of the light, there is an extra loss term, C_{dye}, as the dye will absorb some of the intensity of the ray while it is passing through the dye. If the colour of the dye is red and the concentration of the dye is low enough, the red signal transmitted through the fluid is unaltered, but part of the green and blue signals will be absorbed. If the dye is green, the green signal is unaltered but the red and blue signals attenuate etc. This extra loss term changes the relationship between the intensity at the camera and the intensity at the light source. The relationship is shown in equation (3.3).

$$I_{cam} = C_1 * C_2 * C_3 * C_4 * C_5 * C_6 * C_{air} * C_{Perspex} * C_{glass} * C_{water} * C_{dye} * I_{source} \quad (3.3)$$

Dividing equation (3.3) by equation (3.2) gives

$$\frac{I_{cam}}{I_{ref}} = \frac{C_1 * C_2 * C_3 * C_4 * C_5 * C_6 * C_{air} * C_{Perspex} * C_{glass} * C_{water} * C_{dye} * I_{source}}{C_1 * C_2 * C_3 * C_4 * C_5 * C_6 * C_{air} * C_{Perspex} * C_{glass} * C_{water} * I_{source}} = C_{dye} \quad (3.4)$$

Equation (3.4) shows the relationship between the intensity at the camera of the image during an experiment and the intensity at the camera of a reference image, recorded when the dye is not present. The dye loss term can therefore be used as a quantitative measure of dye concentration, but if and only if there is a known relationship between the increase in dye concentration in the flow, and decrease of intensity of the light.

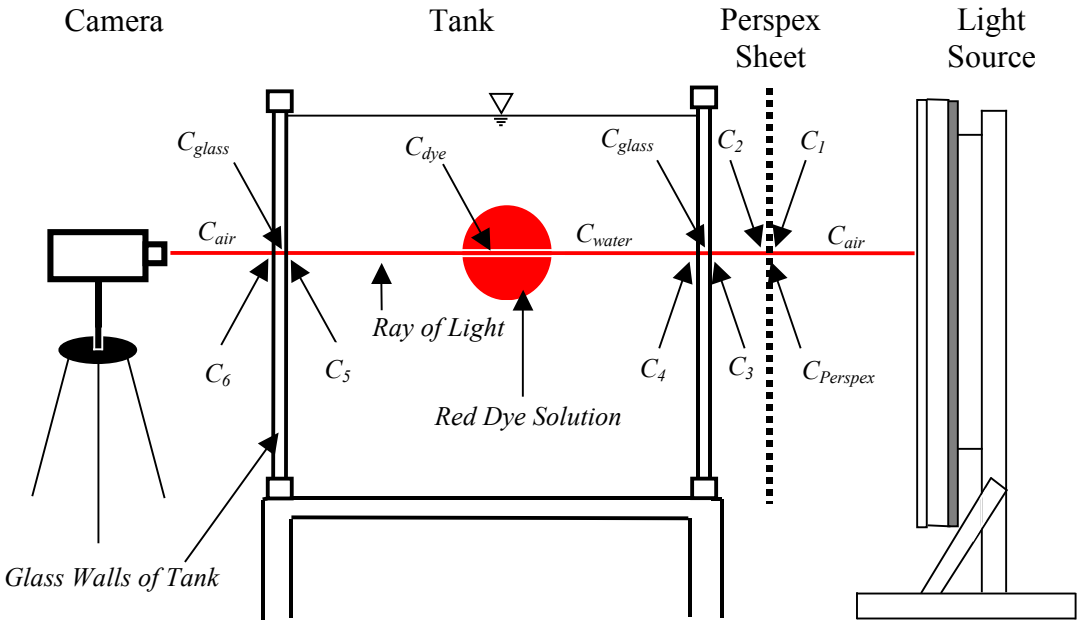

Figure 3.6 - Path of a ray of light including dyed solution

3.2.2 - Calibration experiments

To determine the relationship between the increase in dye concentration and the loss term C_{dye}, calibration experiments were carried out. These experiments were designed to explore the best possible set up and to provide insights into the limitations of the method. The specific experimental set up (including the video cameras, light source and dye), employed to carry out the calibration experiments is discussed below, and this is followed by the method for these experiments. The results from the calibration experiments demonstrate the repeatability of the LA technique. They also confirm the exponential relationship between the increase in dye concentration and the decrease of light passing through it (Cenedese and Dalziel 1998). The constant in this exponential relationship is determined from the calibration data. Finally the response of the red dye under different circumstances is determined with a separate set of experiments.

3.2.2.1 – Experimental Set Up

The experimental set up was similar to that as shown in Figure 3.4. To record the experiments three different cameras were used. Two of them were Canon Digital Video Cameras, the Canon MV30i DV (720x576 pixels, progressive scan, firewire enabled) and the Canon MV4i

DV (720x576 pixels, progressive scan, firewire enabled). Both cameras are so-called handycams and designed for home-videoing. They set most of their parameters automatically to make it easier for inexperienced people to get reasonable images. This affected the experiments in a negative way, as the camera altered some of the parameters during an experiment making the results inconclusive. This issue was resolved by manually setting some of the camera's parameters.

During an experiment it was important that the only change in intensity recorded by the camera was due to the increase in dye concentration in the tank. Therefore the room was blackened so that only the light from the light source was able to reach the camera. The camera automatically changed the shutter-speed and the exposure if less light reached the camera. In order to avoid this the shutter-speed was set to 1/120, and the exposure was set so that the intensity signal was close to 255 (normally between 230-240). If the exposure was set such that the intensity signal was at 255 the image was over-exposed, and the colour was saturated. The closer the maximum intensity was set to 255, the bigger the range of intensity recorded. A bigger range of intensity increased the accuracy of the measurement technique. The camera also changed the recorded intensity by altering the white-balance during an experiment. The camera itself set the white-balance so that pure-white consisted of blue, green and red guns with the same intensity. As only red dye was added to the water the camera attempted to compensate and create a more uniform picture by adjusting the relative magnitude, the gain, of the other two guns (colours). The white-balance could be set manually. The camera had to be focussed on a pure-white background and the camera would adjust the relative magnitudes, of the red, green and blue guns at each pixel so that they all had the same value at that pixel. As the pure-white background strongly depended on the lighting conditions and the relative position of the camera, it was difficult to recreate and thus the experiments using the manually set white-balance were not repeatable. An alternative approach involved setting the white-balance manually using one of the camera's two pre-sets white-balances; one was for recording inside and one for recording outside. These set the white-balances independently of outside light sources and thus the experiments were repeatable. Because the lighting conditions during the experiments were substantially different from normal lighting conditions, neither pre-set white-balance gave an image that represented the original flow well in terms of colour. But the green signal was adequate for analysis purposes. The last parameter to set manually was the focus.

The third camera used was the Jai CV M7+ in combination with a Cosmicar/Pentax Precision 12.5 – 75mm zoom lens. The Jai is a more expensive scientific camera and gives the user full control over exposure, shutterspeed and white-balance (by adjusting the black-level and the gain). The shutter-speed was set to 1/100s and the maximum intensity of 255 was accomplished by setting the black level to 250, the gain to 67 and the lens aperture to 16mm. The camera records 1292x1028 pixels at a frame rate of 24Hz and has the ability to record at higher frame rates by sampling a portion of the image. Just as with the Canon handycams, the Jai camera is a bayer filter camera, meaning that at each pixel one colour is recorded. In every 2x2 matrix of pixels, the pixels on one diagonal both record a value of the green gun and the pixels on the other diagonal record one value of the blue and one value of the red gun. The whole image consists of a multiple of these 2x2 matrices. The actual image can be recreated by calculating the values of the missing guns at each pixel by linearly interpolating the values of the guns surrounding the pixel. The Canon cameras have a built in feature that does the conversion from recorded image to actual image automatically. The data recorded with the Jai were converted using ImageStream (Nokes 2005).

During the calibration experiments several light sources were tested. The chosen light source was to give the most constant and uniform light intensity and had to be independent of time. The combination of the camera with the fluorescent lights at 100Hz had the least variation and was the most uniform. Eight tubes were used to make up a light bank of 1.5 meters by wide 0.5 high meters. It had less variation then the fluorescent lights at 50Hz, because the 100Hz lights had a frequency that was further removed from the approximately 25Hz at which the camera recorded images. Both OHP-lamps and Halogen lights had more variation, because it was not possible to configure these lamps to create a relatively uniform light sheet. It was important that the air temperature surrounding the lights was constant as the light intensity depends on this temperature. The heat from the lights was the main factor influencing the temperature of the surrounding air. The lights were turned on at least half an hour before an experiment for the temperature of the surrounding air to reach a steady state. This steady state was checked by comparing the intensity results of a blank image recorded before and after the experiment.

In order for the relationship between the increase in dye concentration and C_{dye} to be useful, the dye employed as the tracer should have a constant absorption response with different wavelengths, so that the absorption of dye is independent of wavelength. Figure 3.7 (Figure 7, Cenedese and Dalziel (1998)) shows the absorption spectrum for red dye (a), blue dye (b),

green dye (c) and potassium permanganate solution (d). The concentrations of red, green and blue dye are from the top 0.05ml/l, 0.1ml/l, 0.2ml/l and 0.4 ml/l respectively. The concentration of potassium permanganate is from the top 0.6ml/l, 1.2ml/l, 2.4 ml/l and 4.8ml/l respectively. From Figure 3.7 it can be seen that, for low concentrations, only the red-dye and the potassium permanganate have a region where the absorption is more or less constant and thus independent of the wavelength (between 4500-5600 and 5200-5800 Angstroms respectively). The absorption responses of the blue and green dyes show large gradients, and therefore strongly depend on the wavelength. For the experiments the red dye was chosen over potassium permanganate because of the toxic nature of the latter.

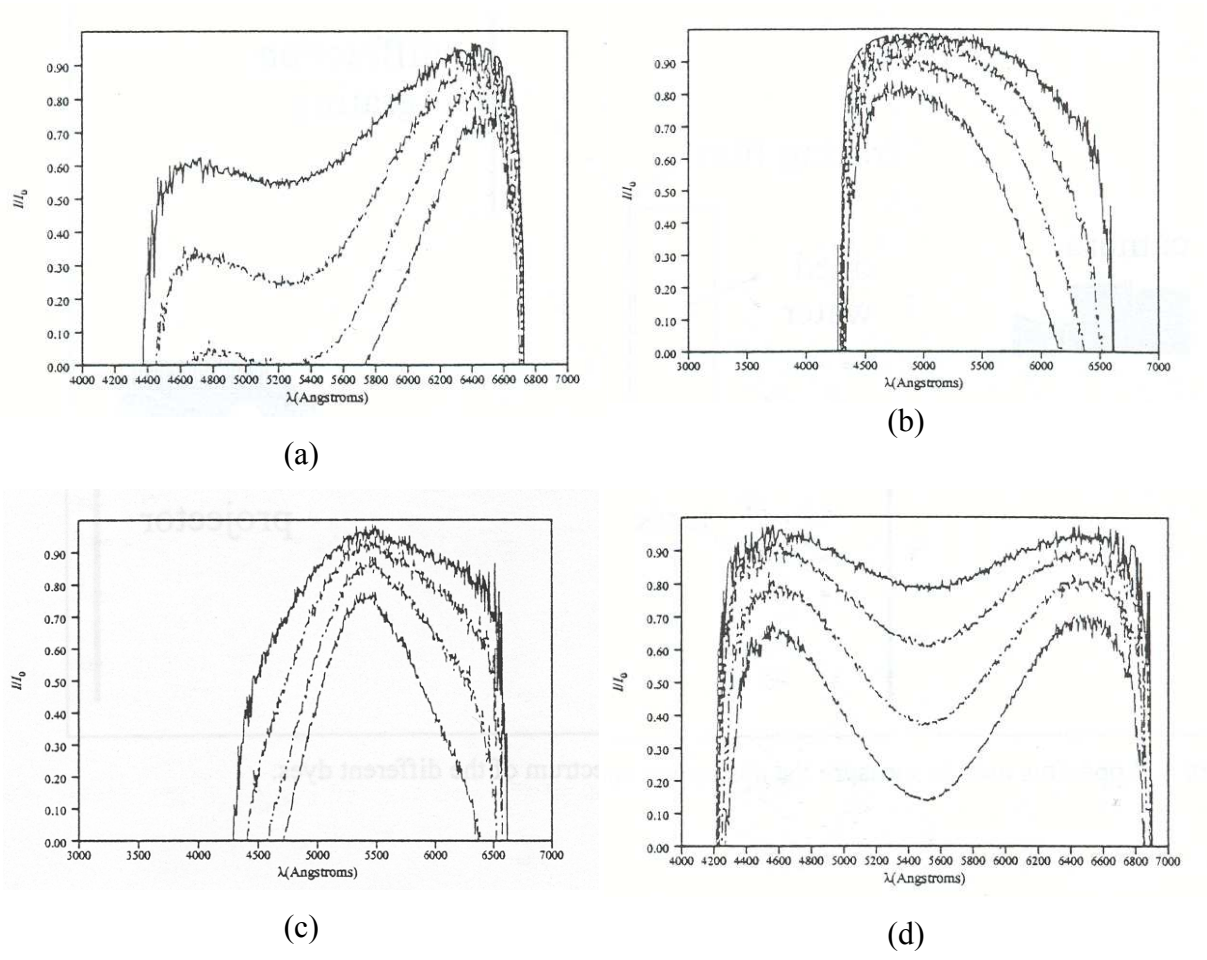

Figure 3.7 - Absorption spectrum for four different tracers, (a) red dye (λ (4000-7000 Angstroms) vs I/I_0 (0-1)) with concentrations of (from top) 0.05ml/l, 0.1ml/l, 0.2ml/l and 0.4 ml/l, (b) green dye (λ (3000-7000 Angstroms) vs I/I_0 (0-1)) with concentrations of (from top) 0.05ml/l, 0.1ml/l, 0.2ml/l and 0.4 ml/l, (c) blue dye (λ (3000-7000 Angstroms) vs I/I_0 (0-1)) with concentrations of (from top) 0.05ml/l, 0.1ml/l, 0.2ml/l and 0.4 ml/l, (d) potassium permanganate (λ (4000-7000 Angstroms) vs I/I_0 (0-1)) with concentrations of (from top) 0.6ml/l, 1.2ml/l, 2.4ml/l and 4.8ml/l

With red-dye as the tracer, red light was transmitted through the discharge and thus the intensity of the red signal is unaltered by the presence of the red-dye (for low concentrations of red-dye). Therefore, only the blue and green light was attenuated, and given the relatively constant response of the absorption spectrum of the green signal it was used to determine the attenuation of the light during an experiment. Evidence that the absorption spectrum of the green light was relatively constant for the red dye is evident in Figure 3.8 (Figure 10, (Cenedese and Dalziel 1998)). Cenedese and Dalziel (1998) set up a green filter between the video camera and the flow. This filter only let light through with a wavelength between 450-610 nm. The continuous line is the absorption spectrum without filter; the dotted line is the absorption spectrum with filter. The filtered response was significantly improved in this context when compared to the unfiltered response. For the calibration experiments described here no physical filter was used, but instead the camera and the computer-software were able to effectively isolate the green signal as indicated earlier. Therefore C_{dye} from equation (3.4) is calculated by dividing the green component during an experiment $\left(I_{green}\right)$ by the green component of the reference image $\left(I_{ref\_green}\right)$ at the same pixel.

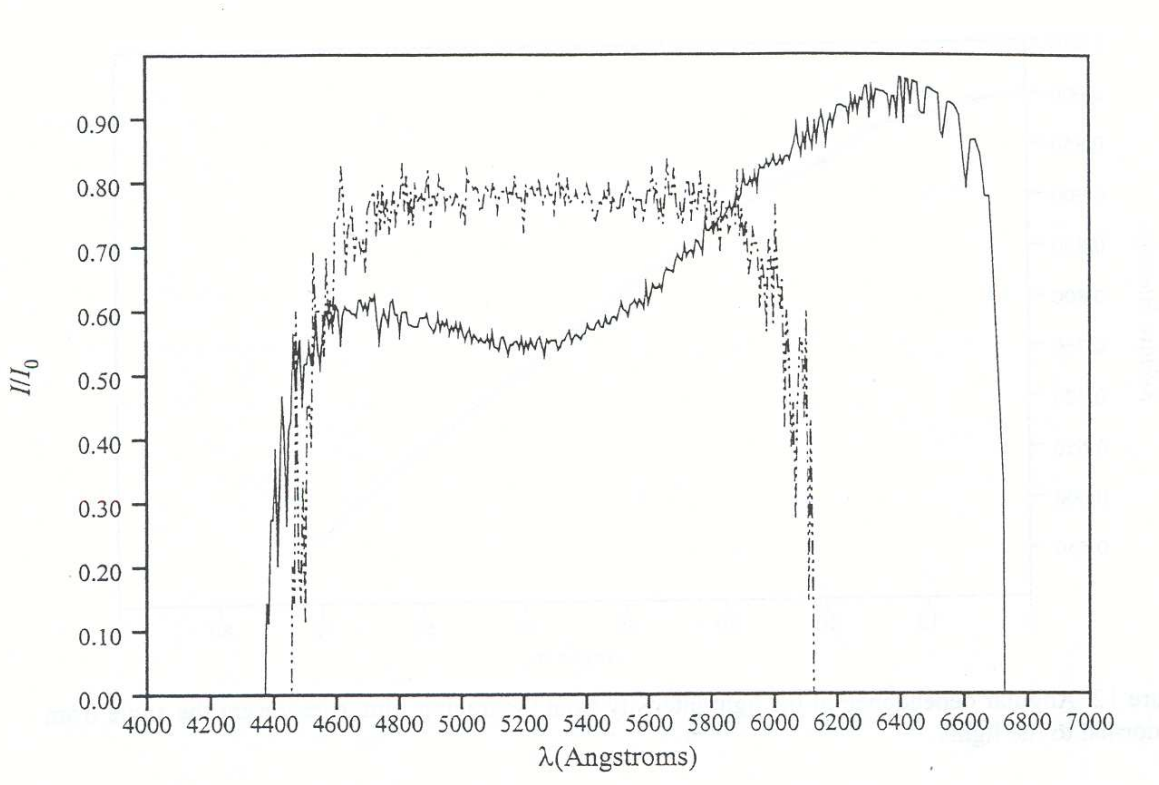

Figure 3.8 - Red Dye Absorption Spectrum with and without green filter

The investigation could also have been carried out with the results from the blue signal, but the blue signal is not as strong as the green one. Seventy two percent of the energy of light is in the green colour (Poynton 1996). Use of the weaker blue signal therefore amplifies errors.

3.2.2.2 – Experimental Method

The calibration experiments were conducted by mixing a volume of red dye solution (with a known concentration) in a tank of water, recording a video of the tank using Adobe Premier 6.0 or Labview ImageGrabber, and analysing it using ImageStream,

The red food dye used for the calibration experiments was Ariavit Carmoisine manufactured by Quest International, Auckland, New Zealand. It is also known as Food Additive Code No 122. Two litres of red dye solution were made up with a nominal concentration of 0.05 g/l. The weight of dye in the dyed solution was determined to a precision of 0.0001g (0.1%) and the volume of the solution to a precision of 0.7ml (0.035%).

The tank used during the experiments was a rectangular based Perspex tank with inside dimensions (length x base x height) of 751mm x 100mm x 382mm. A Perspex diffusion sheet with a thickness of approximately 2mm was placed behind the Perspex tank, and in front of the bank of lights. The tank was filled with approximately 24 litres of filtered water. The weight of the water in the tank was determined using a set of scales to a precision of 0.5 gram (0.002%). The weight of water was converted to a volume based on the density at the measured temperature. The temperature was measured using a thermometer. For the duration of the experiment the temperature of the water in the tank was kept constant (within 0.1 of a degree). The attenuation of green light due to a fixed amount of red dye depended on temperature. This is demonstrated in Figure 3.9. It shows the response of the green signal for four different experiments each with an increased water temperature and a corresponding increase in green intensity.

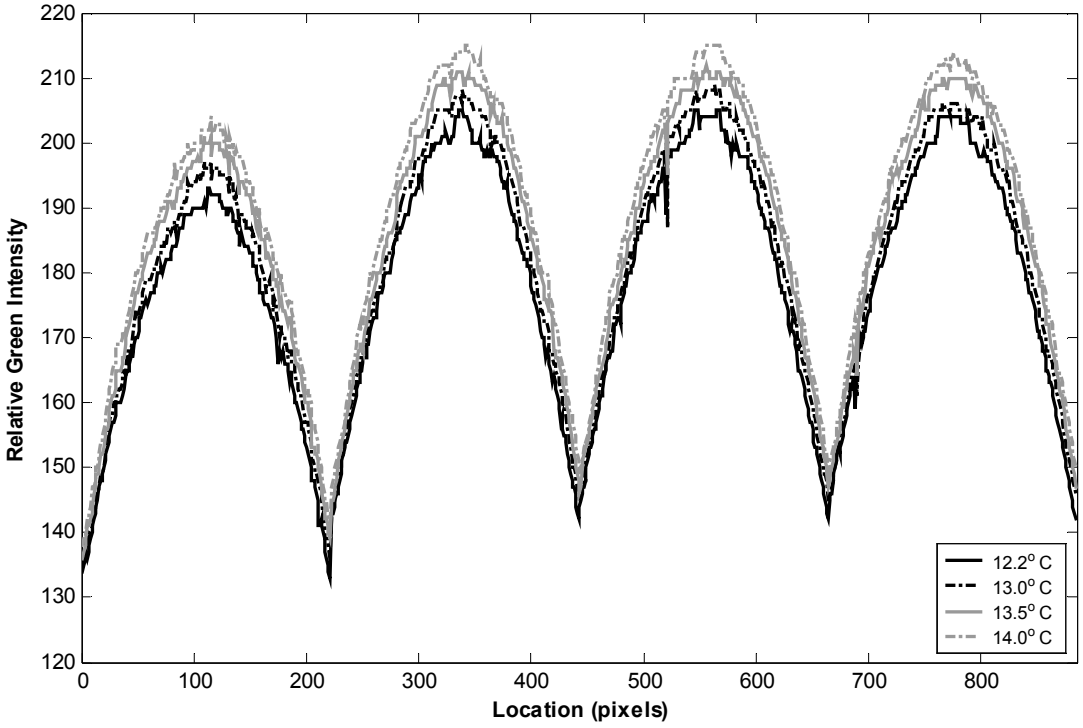

Figure 3.9 - Temperature influence on green intensity response

The camera was set at a distance that provided a view of the complete tank. During an experiment the distance between the light source and the tank and the distance between the tank and the camera were not altered. At least two background videos were recorded before the start of each experiment. The background videos showed the tank filled with water, without red dye solution. Two videos were necessary to confirm that the fluorescent lights had properly warmed up and the emitted light intensity was constant. From the two litres of red dye solution 50ml was taken with a pipette to a precision of 0.053ml (0.1%) and added to the water in the tank. After it had been mixed in properly another video sequence was recorded. The process of adding 50ml of the red dye solution and recording videos was repeated until 1.5 litres was added to the water in total. The videos consisted of 100 frames with a frame rate of approximately 24 frames per second. These frames were exported as .tif files and used to create time-averaged images in ImageStream. At each step the integrated concentration was calculated to define the amount of red dye present between the light source and the camera. For the calibration experiments the integrated concentration was calculated by dividing the mass of the added red dye by the total volume of water in the tank and multiplying this concentration by the width of the tank (100mm).

3.2.2.3 – Calibration Results

For the planned buoyant jet experiments the Jai camera had significant advantages over the Canon handycams. The total manual control of the camera gave better repeatability and its higher resolution would give more detailed results. Therefore all results of calibration experiments presented here come from runs using the Jai camera.

Figure 3.10a is an image from one of the calibration experiments. Here 12 litres of water was mixed with 12 litres of red dye solution of a certain concentration and repeatability issues were explored. This image clearly shows the tank, the red coloured water, the white background and the non-uniformity of the intensity due to the non-uniformity of the background lighting. One hundred of these images were recorded and averaged to create one average colour image. This average image was used to create an intensity field based on the green intensity. The processed image is shown in Figure 3.10b. Again it clearly shows the non-uniformity of the background lighting. The green intensity values at the pixels along the black line in Figure 3.10b have been plotted in Figure 3.11. The results of a second experiment have been plotted as well, the experiment used the same set up as the one mentioned above including the same temperature of both the water and the red dye solution. Comparing the two data sets shows that the repeatability of the experiments is reasonable when the temperature of the water as well as the temperature of the lights do not change between experiments.

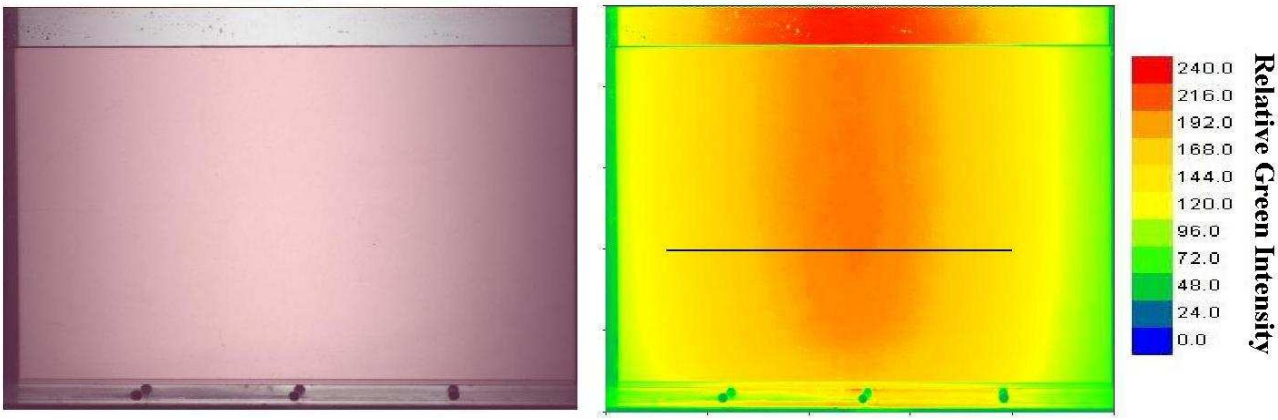

(a) **(b)**

Figure 3.10 - The recorded image (a) and processed image (b)

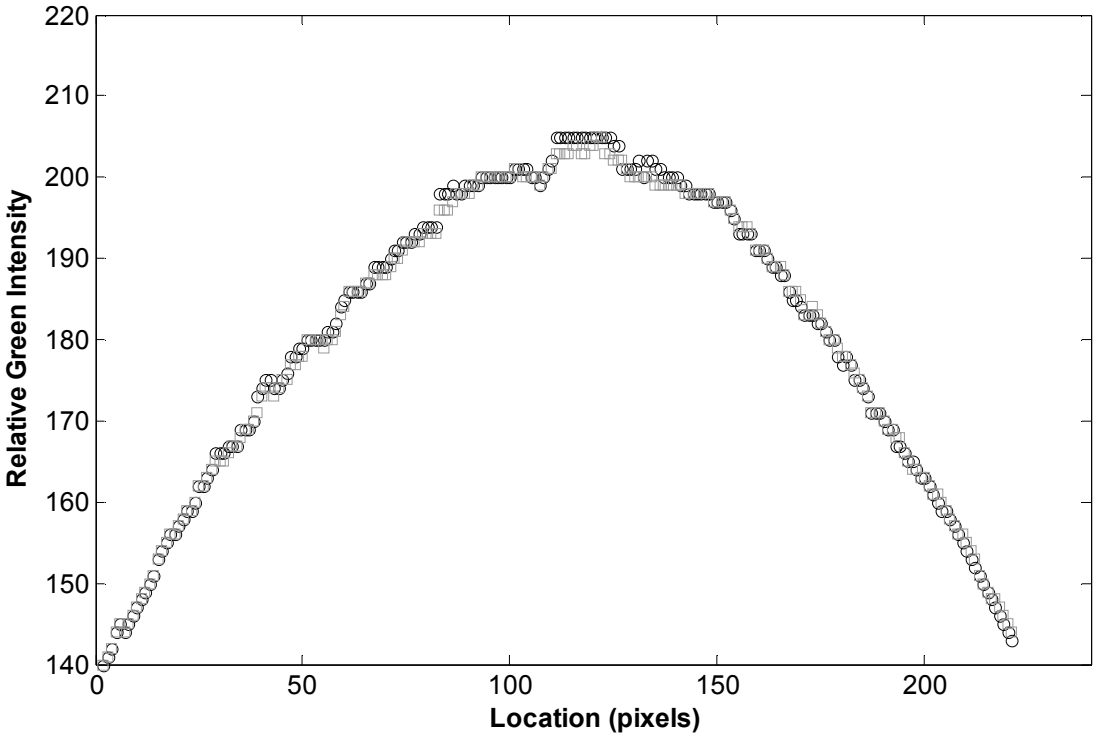

Figure 3.11 - Comparison of green intensity response of two separate experiments

Figure 3.12 shows the response of the green gun for a complete calibration experiment at two pixels with different background intensities $\left(I_{ref\_green}\right)$. As expected, the intensity of the green gun decreases with an increase of dye in the tank, and the decrease reduces the lower the background intensity. Thus the initial slope for the green intensity response is steeper for pixels with higher background intensities.

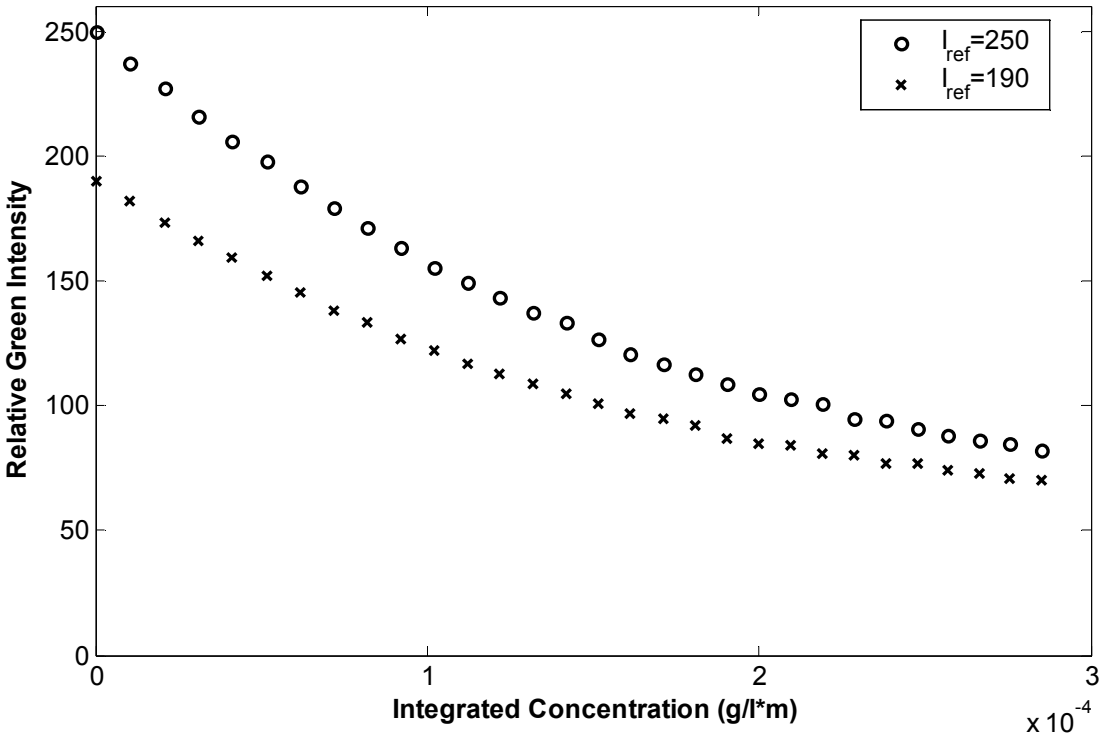

Figure 3.12 - Response of the green gun for two different background intensities

Figure 3.13 shows C_{dye} versus the volume of dyed solution added, C_{dye} being the ratio of the green intensity with the red dye present divided by the green intensity of the background. As expected there is no loss at 0ml, thus C_{dye} was 1. C_{dye} decreases towards zero for increasing intensity. It also shows this ratio depends weakly on the background intensity as the slopes for the two experiments in the initial region of the plot are not the same, resulting in diverging curves for higher concentrations. Thus C_{dye} at a particular pixel is a function of the background intensity. This can be written as

$$C_i = f\left(\frac{I_{green}}{I_{ref\_green}}, I_{ref}\right) \tag{3.5}$$

where C_i is the integrated concentration.

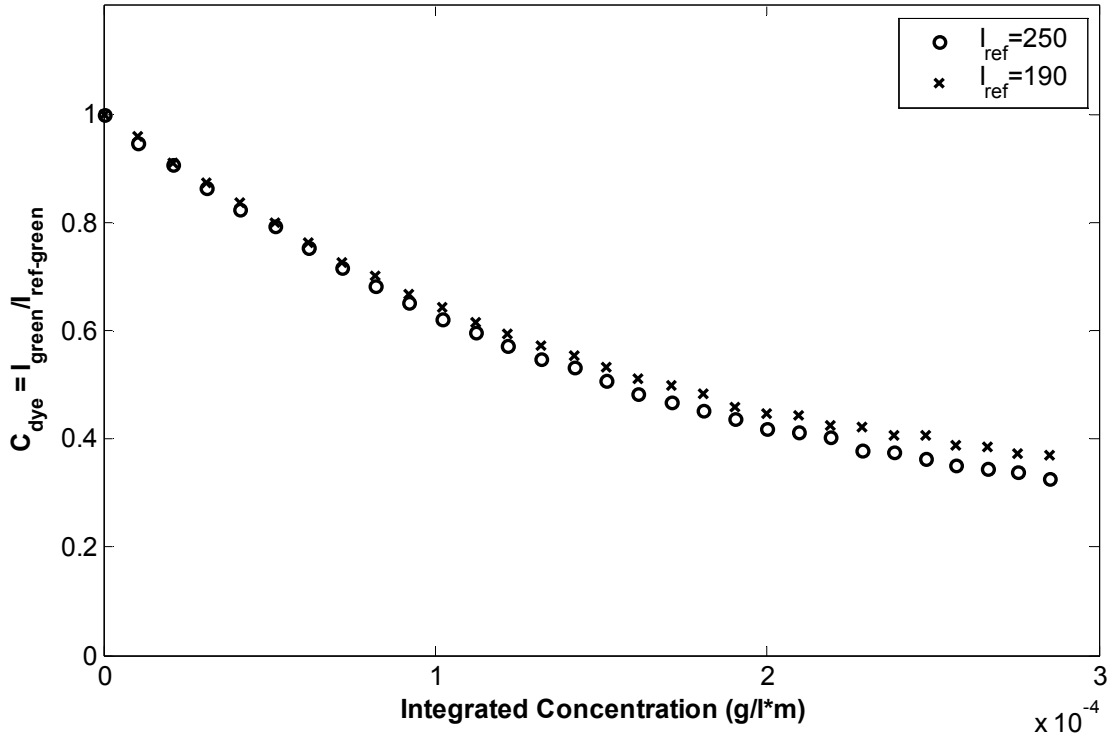

Figure 3.13 - Response of C_{dye} for two pixel with different background intensities

The decay of light intensity of the green gun is exponential (Cenedese and Dalziel 1998), therefore an extra transformation is applied to the data. This is called the green absorption transformation. In Figure 3.14 the natural logarithm of the inverse of C_{dye} is plotted versus the integrated concentration, this value is called the green absorption value *(GA)*. The background green intensity at this particular pixel was 240. This graph confirms that there is a linear relationship between increase of dye and decrease of intensity, but only for low integrated concentrations. With red dye as the tracer, red light is transmitted through the buoyant jet, however only for low concentrations of red dye. At some point there is enough red dye in the water to decrease the intensity of the red gun as well. Prior to this equation (3.5) can be re-written as

$$C_i = a \ln\left(\frac{I_{ref\_green}}{I_{green}}\right) \tag{3.6}$$

where a is a constant determining the slope of the linear relationship. The value of the constant depends on the background intensity. The upper limit was found by fitting a straight line through the data using the first and the last point of the dataset. This was repeated for multiple datasets; including pixels with the maximum and minimum expected background green intensity during a LA experiment. The error of this approximation was calculated for all points in between and if the error at any of the points from any of the datasets was more than

five percent the last point in the datasets was removed and a straight line was fitted through the remaining data. This process was necessary because the actual calibration before the LA experiments would be a two-point calibration. The process was repeated until the error at all points was less than five percent. An example of the result of this process can be seen in Figure 3.14, the upper integrated concentration limit was 0.00016 g/l*m.

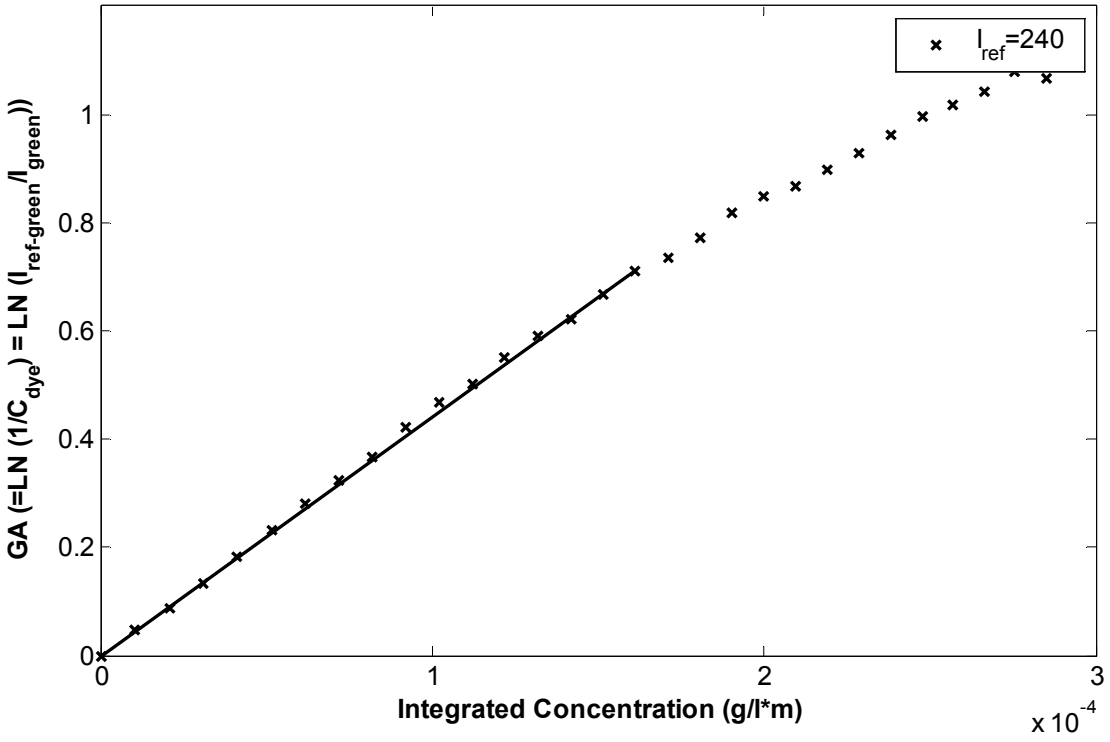

Figure 3.14 - Response using Green Absorption Filter for pixel with Iref = 240

During the experimental investigation into the behaviour of simple jets, the integrated initial concentration (C_{i0}) was set lower than the upper integrated concentration limit. Due to the internal structure of the simple jet and the turbulent fluctuations during the flow, the maximum instantaneous integrated concentration is approximately 48% higher than C_{i0} $((1+0.1*2)/0.812=1.48$, see equation (3.16) and Figure 3.25 and including 2 standard deviations (95%)). The integrated initial concentration was set at 0.00014g/l*m and therefore the maximum integrated concentration during a jet experiment was 0.00021 g/l*m. Using the same approximation as before, the maximum instantaneous error at the maximum integrated concentration was between 5% and 9% depending on the pixel. However for values up to 0.00018 g/l*m (29% above C_{i0}) the instantaneous error remained within 5%. Due to the small time-scales, the instantaneous error at the maximum integrated concentration is believed not

to have a significant effect on the mean integrated concentration values and it is reasonable to assume that the error remained less than five percent at all points.

For the investigation into all other buoyant jet flows the same integrated initial concentration was used as for the simple jet flows. The turbulent fluctuations were no longer as much of a concern as the centreline-integrated concentration decreased with distance downstream and was therefore no longer in the vicinity of the upper limit. To increase the accuracy of the data at a location far downstream, the initial integrated concentration can be significantly increased. During the analysis any points with an integrated concentration of more than 0.00018g/l*m would then be discarded.

As mentioned previously the slope of the straight line depends on the background green intensity, but repeating the straight line fit procedure for a pixel with a background green intensity of 190 gave the same upper-limit for the integrated concentration. As the slope of the line represents the actual relationship between the increase in dye concentration in the flow and decrease of intensity of the light, the value of the slope must be known at each pixel.

Before a LA experiment, the value of the slope of the line at each pixel *(a)* was found using two calibration cells (see section 3.2.1.1). The first calibration cell was filled with water from the main tank; the second calibration cell was filled with diluted source solution. The source solution was diluted down to an integrated concentration of 0.00014g/l*m. The width between the glass panels was 32mm; therefore the concentration in the calibration cell was 0.0044g/l. The green intensity had a temporal variability of ±2, therefore four hundred frames were recorded of both cells and then averaged. A third series of four hundred images was recorded of the background lighting (no cells or dye present) and this series too was averaged. This averaged image was called the reference image. The average calibration cell images were converted into GA images using the reference image. The slope of the calibration line at each pixel is solely related to the attenuation due to the red dye. However, the glass plates of the calibration cell also attenuated some of the light. To compensate for this the GA value from the red dye solution calibration cell was reduced by the value obtained from the calibration cell filled with clear water. The resulting image gave the initial GA value at each pixel.

To determine the integrated concentration values at each pixel for a particular LA image, firstly the GA values for the image are calculated using the background green intensity. With the GA values known at all pixels for the integrated initial concentration and for the zero

integrated concentration, the GA value at a particular pixel can be converted into the integrated concentration value using linear interpolation.

3.2.2.4 – Response of the Red Dye

To be able to carry out a set of experiments in succession it was important that the concentration of red food dye, in both the secondary (storage) tank and the calibration cells, did not change over time. Therefore the red dye solution was tested for variations in light attenuation with time. The two calibration cells were filled with the red dye solution and the tank was filled with water. At each time interval the digital camera recorded 200 images of both calibration cells and 200 reference images. These were averaged over time and GA images were created. From the GA images a square area of approximately $0.09m^2$ was taken and the GA values averaged. The values were plotted versus the elapsed time since filling the calibration cell, and the results of these tests can be seen in Figure 3.15.

The tests are divided by the method of composing the red dye solution in the calibration cell. It was either done by diluting the red dye solution in the secondary tank by the appropriate amount (the dilution tests), or by mixing dry red dye matter into water to create the same concentration as above (the solution tests). The red dye solution for dilution test 1 was made at the same time as the red dye solution in the secondary tank was made. The results of the test do not show a decrease in light attenuation. The red dye solution for dilution test 2 was made 5 days later from the same batch of red dye solution in the secondary tank as dilution test 1. As the result from test 2 matches the one from test 1, it can also be concluded that there had been no decrease of concentration of red dye in the secondary tank during that period. During the dilution process for dilution test 3, Sodium Chloride $(NaCl)$ was added to the solution to create a density difference of approximately 2.5% with the water in the tank. The results show that the light attenuation for dilution test 3 is slightly lower than for tests 1 and 2, however the light attenuation does not decrease with time. The lower initial light attenuation is taken into account by the field calibration and that makes *NaCl* suitable to be used in conjunction with the red dye.

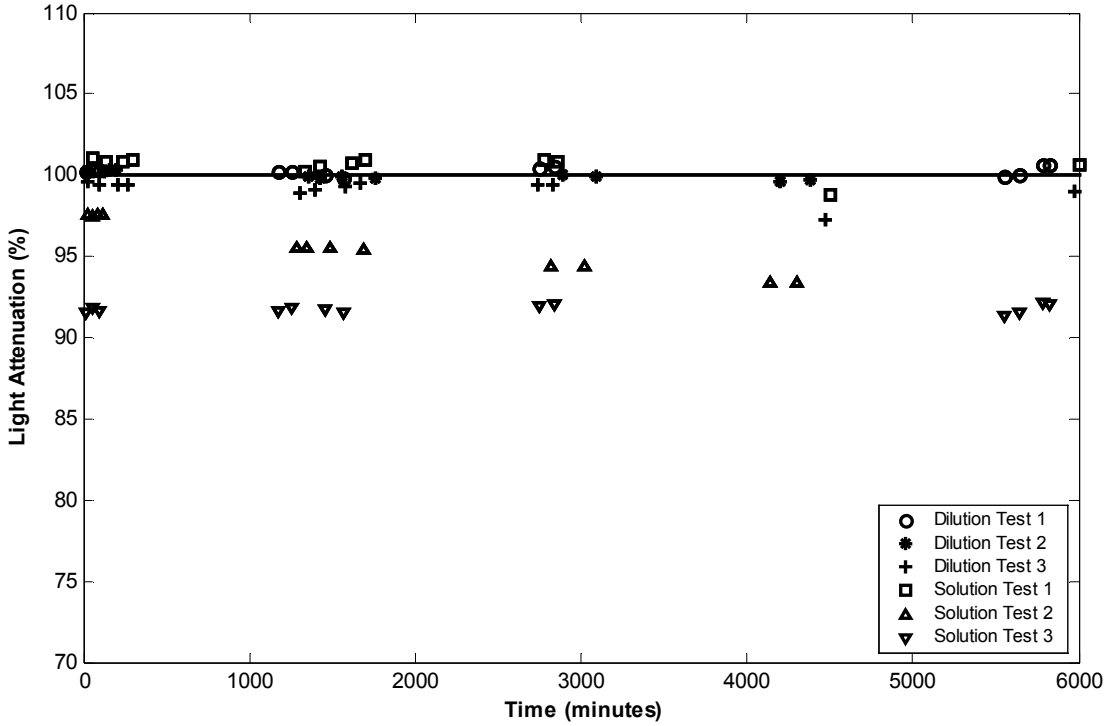

Figure 3.15 – Red Dye Experiment Results

For solution test 1 the red dye solution was made up from water and red dye. The results from solution test 1 match the results from dilution test 1 and 2. For the second solution test, Sodium Sulphite $\left(Na_2SO_3\right)$ was added to the red dye solution. The Sodium Sulphite reacts with the dissolved oxygen in the water used to create the red dye solution, stopping bubbles forming on the inside of the calibration cells. However Figure 3.15 shows that the light attenuation results from solution test 2 are lower than expected initially and that they decrease during the remainder of the test, making it difficult to use the Sodium Sulphite for the LA experiments. Solution test 3 used a similar red dye solution as solution test 2, but at a time of zero minutes it had already been in the calibration cell for approximately 50 days. It confirms the results of solution test 2 and shows that the maximum decrease of the light attenuation due to the Sodium Sulphite is about 9 percent.

The red dye in combination with Sodium Chloride showed very little variation in light attenuation over time. The maximum error was 2.8%, but most of the results fell within 1% of the average recorded integrated concentration. However the error in the test results was difficult to assess. Both the changing water temperature and the purity of the ambient water had an influence on the results. By comparing the results from the Sodium Chloride test with Solution test 1 (which was recorded at the same time as the Sodium Chloride test) part of

these uncertainties could be assessed. This comparison determined that the variation was consistent, between 1.4% and 1.7%, throughout the recording period. The changes in ambient temperature and purity do not have an influence on the results of a jet experiment as the field calibration takes them into account. But to reduce the possible error due to variations in light attenuation further, the red dye solution in the calibration tanks was replaced every week.

3.2.3 – Interpretation of the integrated information

When using the LIF flow visualization technique for a buoyant jet experiment, the thickness of the plane illuminated by the laser is in the order of millimetres. Because of the finite thickness of the plane, the data received from a LIF experiment is in principle integrated concentration data. The error involved in assuming the data to be point-values is small, given that the data is typically integrated over a source diameter. This assumption does not hold for data received from a LA experiment as the data is integrated over the depth of the flow. To be able to use the integrated concentration data, a method for relating the integrated to the non-integrated data is required. This can either be done by integrating the governing equations and comparing the data with the predictions of the new equations, or by transforming the integrated data to non-integrated data and comparing the converted data with the existing equations and data.

As the data is integrated over the flow, the interpretation of the integrated data depends on the internal concentration structure of the flow. The study of axi-symmetric buoyant discharges has identified two distinct types of internal structures; for weakly advected flows the mean cross-sectional concentration distributions are found to be Gaussian, and for strongly advected flows the mean concentration distributions resemble those of a vortex pair. Here two example experiments, a simple jet flow as an example of a weakly advected flow and a momentum puff flow as an example of a strongly advected flow, are used to investigate the interpretation of the integrated information. These experiments will also be used to examine how well the quantitative flow visualization technique performs.

In addition a third flow is investigated, that of a jet where the source discharges at an angle to the camera. This flow is an example of a flow that is no longer flowing perpendicular to the camera view. Although it is possible to carefully choose the position of the source for flows with two-dimensional trajectories so that they flow perpendicular to the camera axis, this is

not possible for flows with three-dimensional trajectories. Therefore it is important to investigate the LA technique under those circumstances.

Parallax issues are assumed to have a negligible effect on the results of the experiments that are used to investigate the interpretation of the integrated information. In section 3.2.3.4 the angled jet flow analysis will be used to verify this assumption.

For the interpretation of the integrated information the following subscripts are used: *i*, integrated; *iy*, integrated in the *y*-direction; *iz*, integrated in the *z*-direction; *l*, centreline of single-Gaussian; *c*, centreline of vortex pair; *peak*, maximum in vortex pair cross-section; *0*, initial; *dg*, double-Gaussian; *sg*, single Gaussian.

3.2.3.1 – Weakly Advected-Flow, a Simple Jet Experiment

A simple jet experiment was set up using the experimental system as shown in Figure 3.4. For a more precise description of the experimental set up see section 3.2.1.1. The dimensions of the tank were (length x base x height) 6220mm x 1540mm x 1080mm. The source of the jet was mounted on a frame situated above the tank. It pointed vertically down into the tank and was positioned approximately in the middle of the tank, so that the boundaries were not having a significant effect on the flow. The port diameter used was 2.45mm and the initial velocity 1.47 m/s. This gave a Reynolds number for the flow of approximately 3600.

A red dye solution was made up to a concentration (C_0) of 0.0571g/l. This takes into account both the 0.00014g/l*m upper concentration limit (C_{i0}) as well as the 0.00245m diameter of the source (d). More information about this relationship can be found in section 3.2.2.3. As the camera was set further back than during the calibration experiments to reduce parallax issues, the gain was increased to 200 so that initial background green values were between 190 and 250. The other parameters were the same as those employed for the calibration experiments.

The first video sequence recorded was of a cross-shaped ruler inserted vertically down into the tank at the position where the jet would be. During the analysis this image was used to deduce the calibration length-scales in the horizontal and the vertical direction of the images. The second video sequence recorded was the reference video. The cross-shaped ruler had

been removed from the tank, but the jet source had not been opened at this stage, and this created a background image. To eliminate the influence of small light fluctuations with time, 400 frames were recorded and later averaged. With about 24 frames being recorded per second, the length of the reference video was approximately 16 seconds. The third video sequence was of the calibration cell filled with the red dye solution with a uniform integrated concentration of 0.00014g/l*m. Video sequence four was of a second calibration cell, but this time filled with just water. The last video sequence was of the jet itself after the source had been opened. About a minute of footage was recorded, approximately 1300 frames. A single frame can be seen in Figure 3.16. The 1300 frames were used to create the averaged image, independent of time, shown in Figure 3.17.

Figure 3.16 - Single frame of jet video

Figure 3.17 - Average image of jet

In ImageStream the average image of the jet, as well as the average background image, and the average images of both calibration cells were used to calculate the integrated concentration values at each pixel. Figure 3.18 shows the integrated concentration image of the jet. The upper integrated concentration limit of the image is 0.18mg/l*m and the lower limit is –0.02mg/l*m. Values outside this range show up as white on the image. The image appears to match expectations as the integrated concentration values are the highest in the middle of the jet and fall away towards zero on the edges. Also the integrated concentration values along the centre line of the jet are constant. This can be explained by the fact that the integrated concentration is made up of two parts, the concentration of the dye (C_l) and the distance of the light path through the dye ($\approx 2*2b_c$, where b_c is the concentration spread, and $2b_c$ is generally associated with the distance from the centreline to the edge of the jet). For a jet, the spread increases linearly with distance and the concentration decreases linearly with distance. Multiplying these together ($\approx C_l * 4\ b_c$) gives a constant value (see equation (3.16)).

The trajectory of the flow was defined as the point with the maximum integrated concentration value in a cross-section, and a cross-section of the flow was taken perpendicular to the trajectory. The integrated concentration image was saved as a txt-file and opened in

MatLab. A MatLab algorithm was written to analyse the file and find the position of the trajectory and the corresponding maximum values, and also the cross-sectional position and values. An example of the algorithm can be found in Appendix B.

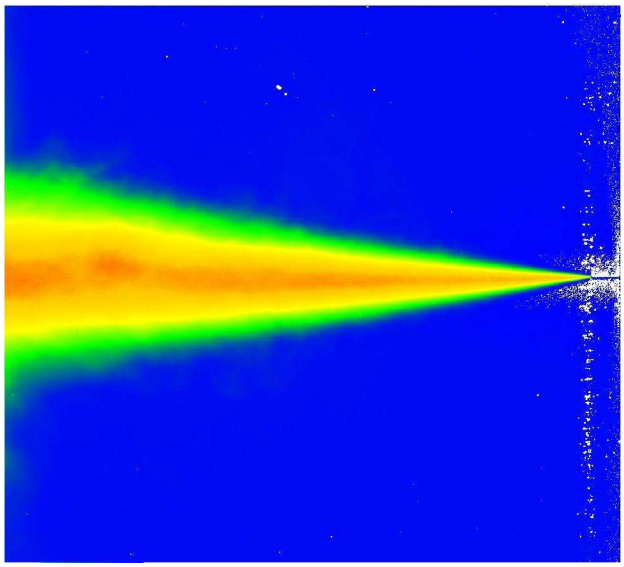

Figure 3.18 – Integrated concentration image of jet

In theory the integrated concentration values outside the jet should be zero as nothing should change from the reference image to the jet image. The blue colour outside the jet seen in Figure 3.18 is an indication that this was indeed what was found. To provide a more thorough review of the values outside the jet, the upper and lower bounds of the colours were narrowed to –1% of the maximum integrated concentration (blue regions) for the lower limit of the colour map and 1% for the upper limit (red regions). The result can be seen in Figure 3.19. The colours cover almost the entire image, except where the jet is located. The yellow colour shows regions where the background noise is less than ±0.1% of the maximum integrated concentration.

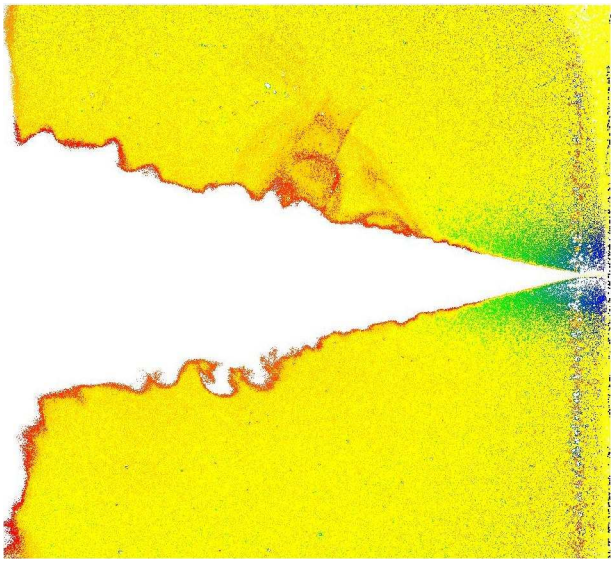

Figure 3.19 - Green absorption image of jet, boundaries –1% to 1%

The jet problem has been studied experimentally and analytically over many years and hence its expected behaviour is well known. Work by Morton et al.(1956), Abraham (1963), Fan and Brook (1969) and others led to the integral methods commonly used now to predict the behaviour of buoyant jet discharges using the assumption that the mean cross-sectional concentration distributions are Gaussian. A coordinate system can be defined as shown in Figure 3.20 where the jet is discharged along the x- axis.

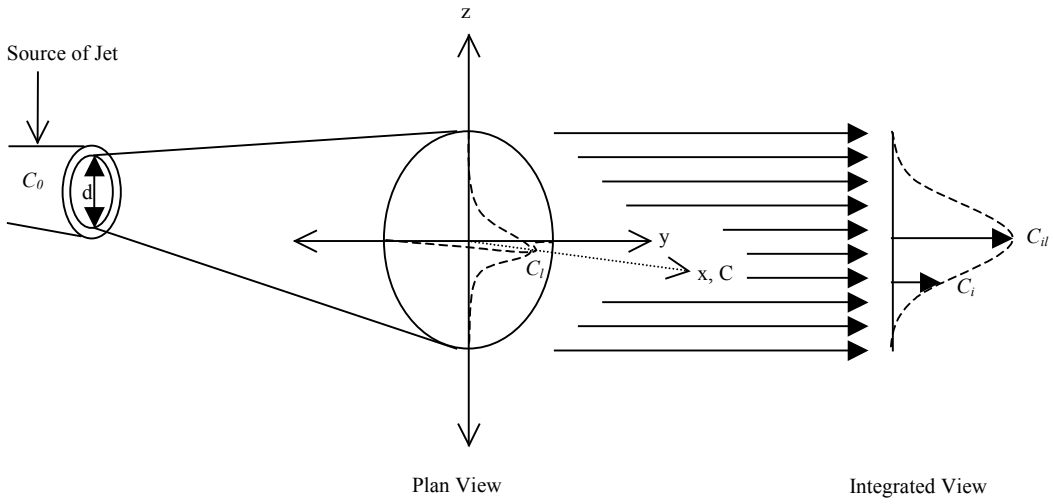

Figure 3.20 - Plan and integrated view of concentration profiles for a simple jet

In this coordinate system the Gaussian assumption relates the local concentration in a cross-section (C) to the centreline concentration (C_l). This relationship is:

$$C = C_l e^{-\left(\frac{y}{b_c}\right)^2} e^{-\left(\frac{z}{b_c}\right)^2} \tag{3.7}$$

where b_c is the concentration spread of the flow. Integrating this equation in the y-direction gives the relationship between the local integrated concentration (C_i) and the centreline concentration.

$$C_i = \int_{-\infty}^{\infty} C_l e^{-\left(\frac{y}{b_c}\right)^2} e^{-\left(\frac{z}{b_c}\right)^2} dy = C_l b_c \sqrt{\pi} e^{-\left(\frac{z}{b_c}\right)^2} \tag{3.8}$$

The integrated centreline concentration (C_{il}) is then:

$$C_{il} = C_l b_c \sqrt{\pi} \tag{3.9}$$

or alternatively

$$C_l = \frac{C_{il}}{b_c \sqrt{\pi}} \tag{3.10}$$

Substituting equation (3.10) back into equation (3.8) to find a relationship between local integrated concentration and the centreline integrated concentration gives:

$$C_i = C_{il} e^{-\left(\frac{z}{b_c}\right)^2} \tag{3.11}$$

Figure 3.21 shows concentration profiles for the jet. Seven different cross-sections were used from 14 port-diameters downstream to 132 port-diameters downstream. As expected, with appropriate scaling, the profiles are self-similar and there is a good match to the Gaussian curve of equation (3.11).

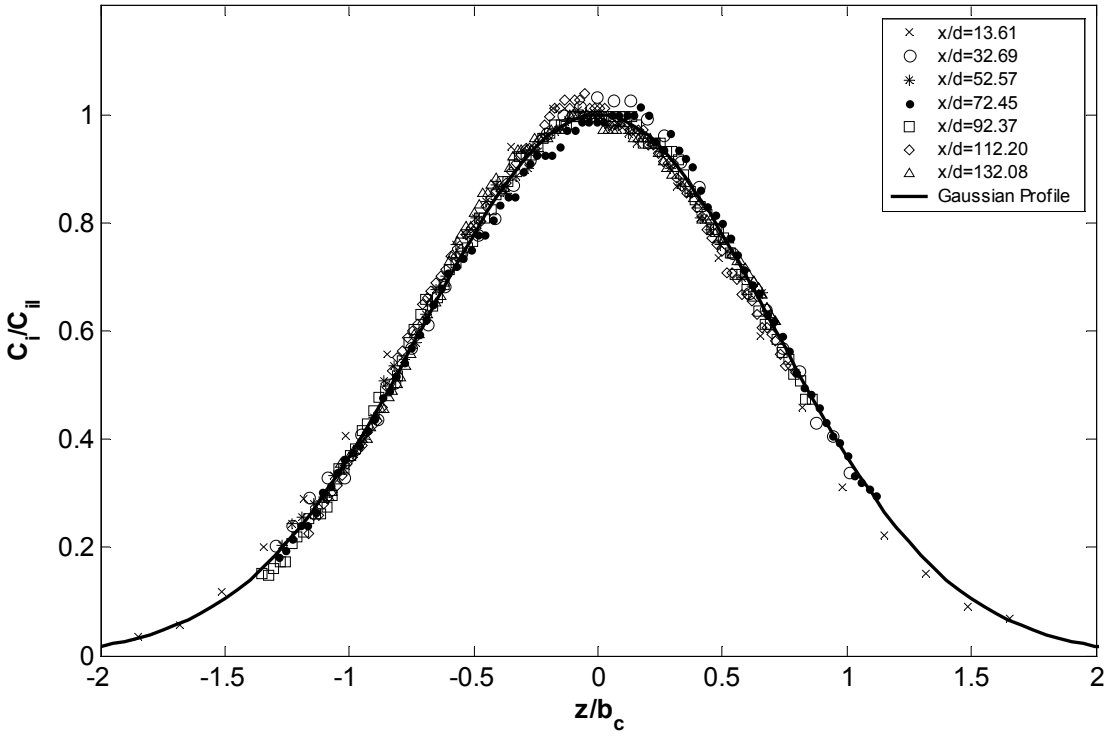

Figure 3.21 - Self-similarity of integrated cross-sectional profiles of jet

From the Eulerian Integral method comes the relationship between the centreline concentration and the initial concentration (C_0).

$$C_l = C_0 \frac{\sqrt{I_m}}{I_{qc} k} \sqrt{\frac{\pi}{4}} \frac{d}{x} \tag{3.12}$$

where d is the diameter of the source of the flow, k is the velocity spread value, and I_m and I_{qc} are both shape factors (Pun 1998). Table 3.1 shows the experimental values found by various researchers for both the velocity spread and the concentration spread. Note that the values by Fischer et al. (1979) were an average of all experimental spread data that was available at the time of publishing. In the process of averaging the spread values, the results from the most recent studies were given the most significance, as the newer measuring techniques used in those studies increased the accuracy of the results. With an average value for k of 0.106 and a value for $k\lambda$ of 0.129, the value for λ is 1.22. Both Papanicolau (1984) and Wang (2000a) found that 7% of the total mass flux was carried by turbulence, therefore I_{qc} can be calculated to have a value of 2.03. The jet experiments by Hussein et al. (1994) gave a value of approximately 10% for that part of the total momentum flux that is carried by turbulence. Similar experiments carried out by Wang (2000a) gave a value of approximately 9%. I_m can therefore calculated to be approximately 1.7.

Table 3.1 - Comparison of velocity and concentration spread values

	k (velocity spread)	$k\lambda$ (concentration spread)
(Fischer et al. 1979)	0.107	0.127
(Chen and Rodi 1980)	0.103	0.136
(Papanicolaou 1984)	0.112	0.139
(Papanicolaou and List 1988)	0.104	0.126
(Panchapakesan and Lumley 1993)	0.115	
(Hussein et al. 1994)	0.106	
(Wang 2000a)	0.105	0.127
Weighted-Average spread values	0.106	0.129

The above determined concentration spread value is verified using experimental concentration spread results, non-dimensionalised by the port diameter, shown in Figure 3.22 The experimental data was found by fitting Gaussian curves through the cross-sectional integrated concentration values. The cross-sectional profile was perpendicular to the direction of the

trajectory at that point. The theoretical line was calculated as *k* times the distance from the source times λ (the spread assumption). The figure shows that theory is consistent with the experimental data.

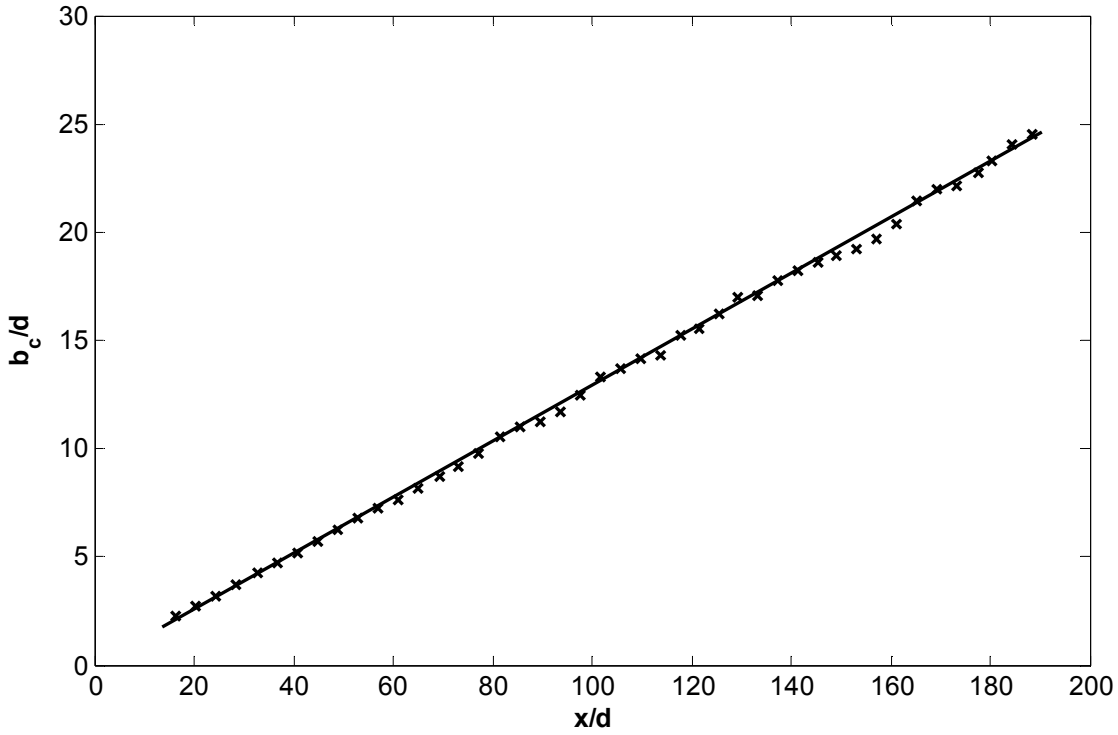

Figure 3.22 – Concentration spread of jet

As indicated in second paragraph of section 3.2.3.1., the before the relationship between the maximum integrated initial concentration $\left(C_{i0}\right)$ and the initial concentration is

$$C_{i0} = C_0 * d \tag{3.13}$$

where *d* is the diameter of the source. Substituting equation (3.13) into equation (3.12) gives

$$C_l = \frac{C_{i0}}{d}\frac{\sqrt{I_m}}{I_{qc}k}\sqrt{\frac{\pi}{4}}\frac{d}{x} = C_{i0}\frac{\sqrt{I_m}}{I_{qc}k}\sqrt{\frac{\pi}{4}}\frac{1}{x} \tag{3.14}$$

To find the relationship between the integrated centreline concentration and the integrated initial concentration, equation (3.14) is substituted into (3.10)

$$C_{il} = C_{i0}\frac{\sqrt{I_m}}{I_{qc}k}\sqrt{\frac{\pi}{4}}\frac{1}{x}b_c\sqrt{\pi} = C_{i0}\frac{\sqrt{I_m}}{I_{qc}}\frac{\pi}{2}\lambda \tag{3.15}$$

or

$$\frac{C_{i0}}{C_{il}} = \frac{I_{qc}}{\lambda\sqrt{I_m}}\frac{2}{\pi} \tag{3.16}$$

The experimentally determined ratio of the initial integrated concentration and the integrated centreline concentration has been plotted versus non-dimensional distance downstream in

Figure 3.23. The figure confirms that the integrated centreline dilution is indeed constant with distance downstream. A least squares fit line was plotted through the integrated centreline dilution data from seven jet experiments (see Chapter 5) to determine an average dilution value of 0.829 (see Figure 3.23). Equation (3.16) and the above-determined values for λ, I_m and I_{qc} combine to give a theoretical value for the integrated dilution of 0.812. The difference between the experimental and the theoretical value is associated with a decrease of approximately 2.0% in the value of the ratio $I_{qc}/\sqrt{I_m}$ (from 1.59 to 1.56). This suggests a lower value for the total mass flux carried by turbulence and/or a higher value for the part of the total momentum flux that is carried by turbulence.

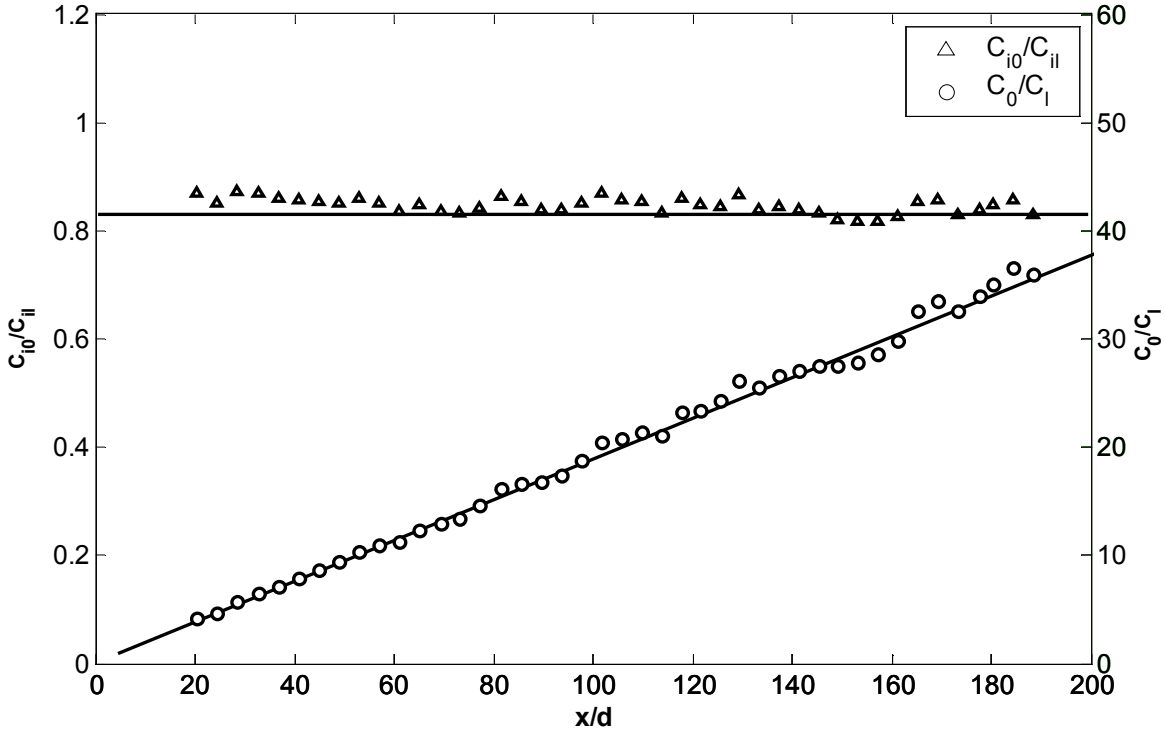

Figure 3.23 – Integrated centreline and point centreline dilution

Close to the source the values for the ratio of the integrated dilution increase. This is due to the small jet scale relative to the pixel resolution. In this situation the pixels smooth the peak concentration significantly, and significantly affected data was discarded.

Equation (3.10) can also be used to convert the integrated concentration data back to point concentration data, by combining it with equation (3.13) to give:

$$d\frac{C_{il}}{C_{i0}} = \frac{C_l}{C_0} b_c \sqrt{\pi} \tag{3.17}$$

or alternatively to calculate the dilution

$$\frac{C_0}{C_l} = \frac{C_{i0}}{C_{il}} \frac{b_c \sqrt{\pi}}{d} \tag{3.18}$$

The data from the simple jet experiment was converted using the above equation and plotted versus non-dimensional distance downstream in Figure 3.23. The experimental data depended on a second experimental value (b_c)(as seen in Figure 3.22). Theoretical predictions are shown for comparison (equation (3.12)). There is a good agreement between the theoretical predictions and experimental results.

The opposite of converting the integrated dilution data into point dilution data is to convert the data into double integrated dilution data. This can again be done using the spread at the cross-section or by calculating the area under the cross-sectional profile.

The theoretical relationship between the double integrated concentration $(C_{ii})$and the centreline concentration is found by integrating equation (3.7) in both the *y*-direction and *z*-direction.

$$C_{ii} = C_l \int_{-\infty}^{\infty} \int_{-\infty}^{\infty} e^{-\left(\frac{y}{b_c}\right)^2} e^{-\left(\frac{z}{b_c}\right)^2} dydz = C_l {b_c}^2 \pi \tag{3.19}$$

The double-integrated initial condition (C_{ii0}) is defined as

$$C_{ii0} = C_0 \frac{\pi}{4} d^2 = C_{i0} \frac{\pi}{4} d \tag{3.20}$$

Substituting equations (3.19) and (3.20) into equation (3.12) gives the relationship for the double-integrated dilution.

$$\frac{C_{ii0}}{C_{ii}} = \frac{I_{qc}}{I_m^{1/2}} \frac{1}{2\sqrt{\pi}} \frac{1}{\lambda^2 k} \frac{d}{x} \tag{3.21}$$

The experimental results are compared with equation (3.21) in Figure 3.24. Here again the experimental results match the predictions.

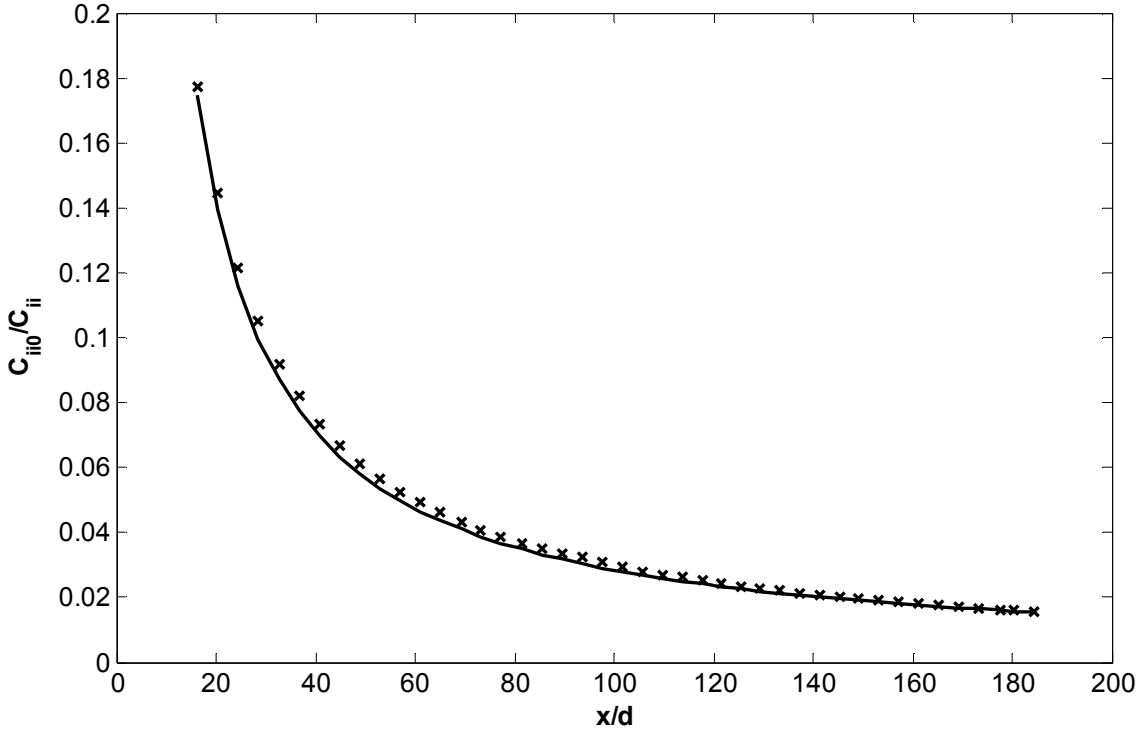

Figure 3.24 – Double-integrated jet dilution

By creating integrated concentration images from the instantaneous jet images before the images are averaged, the integrated turbulent statistics can be investigated. Previous investigators have shown that the dimensionless turbulent intensity of the concentration fluctuations along the centreline of the jet is approximately 0.225 (Papanicolaou 1984; Wang 2000a). Figure 3.25 shows that the intensity of the dimensionless integrated concentration fluctuations along the flow centreline was approximately 0.12 for these experiments. The instantaneous jet consists of multiple rotating eddies of different sizes, entraining the surrounding ambient fluid. Large eddies dominate the flow and therefore have a major influence on the turbulent fluctuations. The relatively good correlation between the centreline and integrated turbulent intensity confirms the presence of the large eddies. If the instantaneous flow had existed out of numerous small eddies, the reduction in turbulent intensity, due to the integrated view, would have been significantly greater.

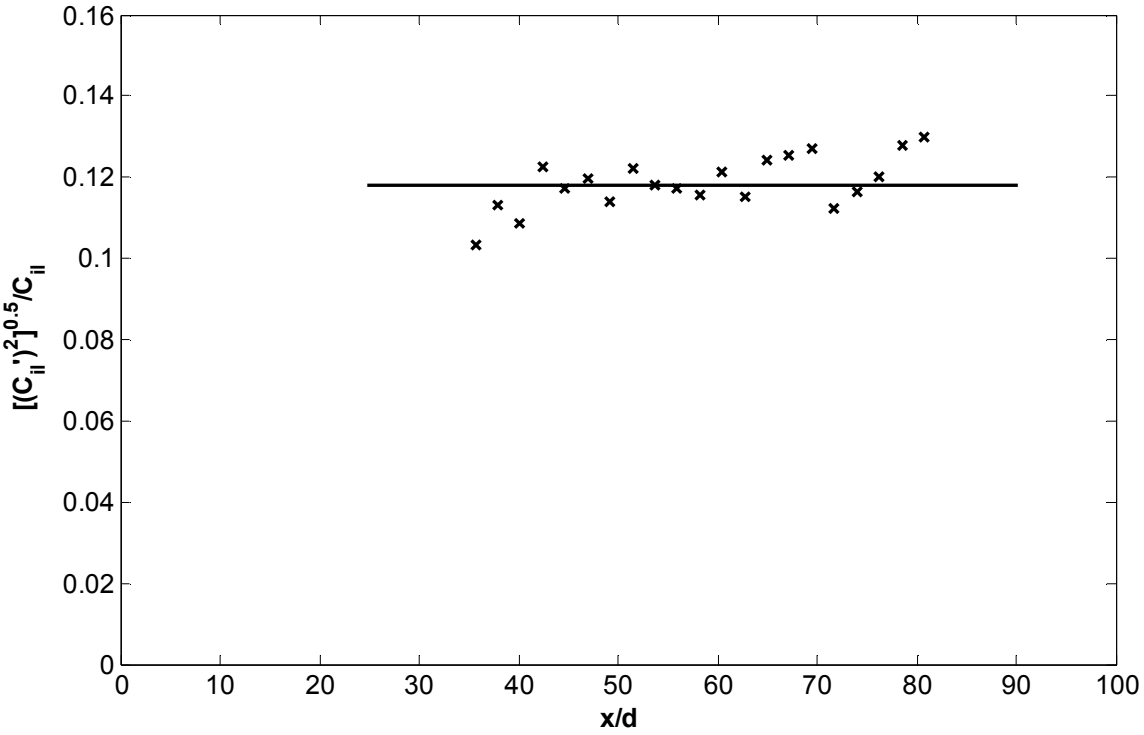

Figure 3.25 – Integrated concentration fluctuation along the jet centreline

The cross-sectional variation of the integrated turbulent fluctuations can be seen in Figure 3.26. The double peak shaped profile matches the cross sectional variations found by previous researchers for the point turbulent concentration fluctuations. However the peaks are more pronounced for the integrated case. Moving away from the centreline of the jet, the distance over which the integration takes place becomes smaller and therefore the dampening effect of the integrated view decreases. Hence, the maximum difference in the turbulent intensity between the point and integrated values, happens at the centreline. Moving away from the centreline the integrated values increase more than the point intensity values, so that these values are more closely matched. The ratio of the integrated turbulent fluctuation to the non-integrated turbulent fluctuation (Papanicolaou 1984; Wang 2000a) increases from 0.53 at the centreline to 0.61 and 0.67 at z/x = 0.1 and 0.2 respectively.

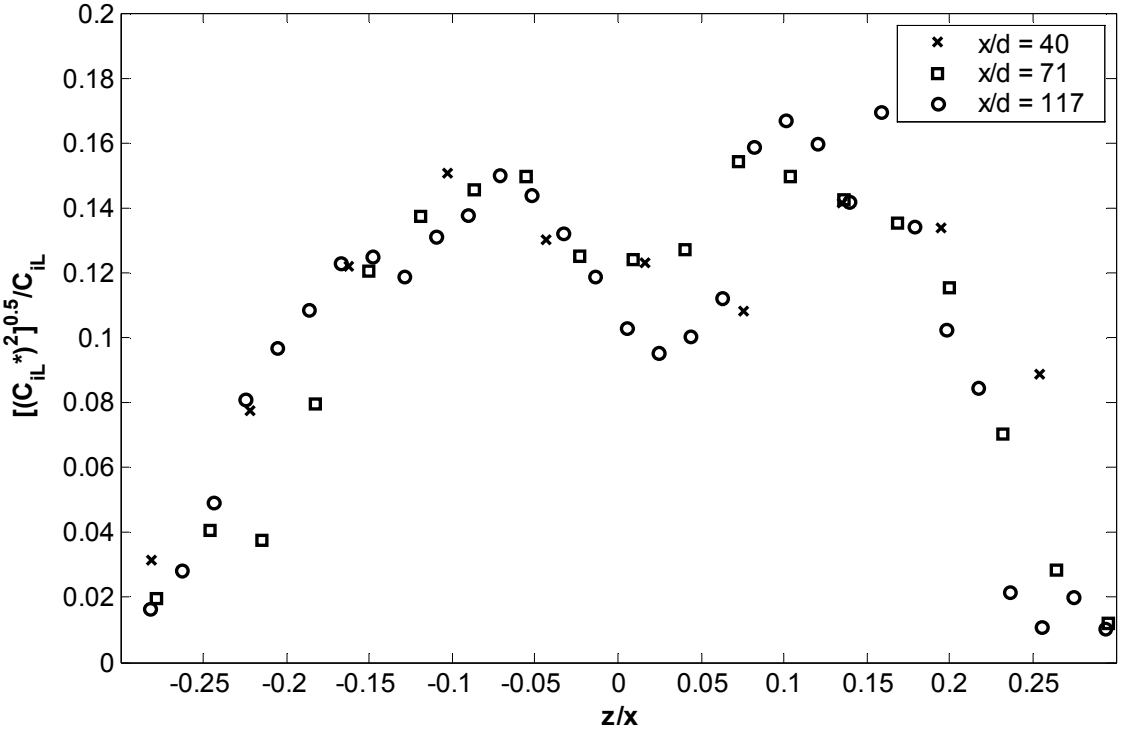

Figure 3.26 – Integrated cross-sectional profiles of turbulent concentration fluctuations

3.2.3.2 – Strongly Advected Flow, a Momentum Puff Experiment

For the momentum puff experiments, two separate series of runs were required to characterize the flow, providing perpendicular views of the discharge. One series provided a side view (see Figure 3.27a), the camera view is along the *y*-axis of the flow and therefore records the *y*-integrated view of the flow. The experimental set up for the side view experiment was similar to that for the simple jet experiment described above. However, in this case the source was attached to a trolley that moved through the camera view during the experiment. These experiments will be referred to as *y*-integrated momentum puff experiments. More details about the experimental set up of the camera recording the *y*-integrated view can be found in section 3.2.1.1. For the second series the view was along the *z*-axis of the flow (see Figure 3.27b) such that the initial discharge was facing towards the camera. These experiments will be referred to as *z*-integrated momentum puff experiments, and more details about the recording of the *z*-integrated view can be found in section 3.2.4.1. The momentum puff flow is independent of the discharge angle as long as the flow is discharged perpendicular to the ambient. Therefore by rotating the source and the coordinate system by 90^{o}, the *z*-integrated momentum puff experiments could be recorded without altering the position of the camera.

The calibration length-scales change with the changing distance between camera and flow trajectory during the *z*-integrated momentum puff experiments. Details of the method used to determine the calibration length-scales for the *z*-integrated momentum puff experiments can be found in section 3.2.4.2.

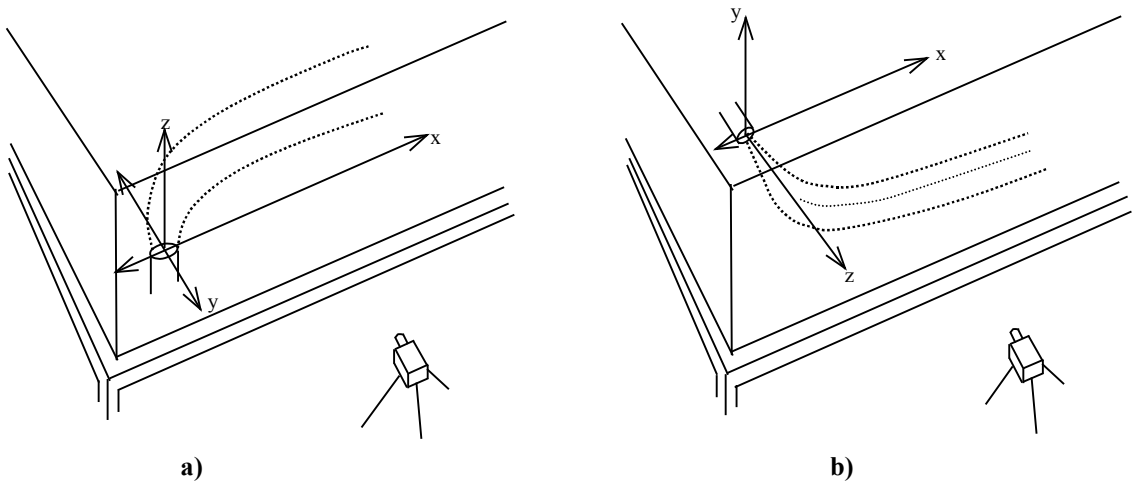

Figure 3.27 - y-integrated (a) and z-integrated (b) momentum puff views

The source diameter for the momentum puff experiment was either 2.45mm or 3.00mm. The Reynolds number ranged between 2600 and 5100, and the ambient velocity (the velocity of the trolley) ranged between 33mm/s and 98mm/s.

Again videos were recorded of the background and both calibration cells before the experiments. The videos of the momentum puff were approximately 1500 frames long. In ImageStream the images were converted into integrated concentration images and then transformed into a reference frame moving with the source. Figure 3.28 and Figure 3.29 show the integrated concentration plots for the *y*-integrated view and *z*-integrated view respectively. The white colour indicates an integrated concentration of 0 and the black approximately 0.00014 g/l*m.

Figure 3.28 – Integrated concentration image of a *y*-integrated momentum puff

Figure 3.29 – Integrated concentration image of a *z*-integrated momentum puff

In the strongly advected phase of the line momentum puff the internal concentration structure no longer has a Gaussian shape, but the structure resembles that of a vortex pair. This can be seen in Figure 3.29, where the integrated concentration values are clearly lower in the centre of the flow. It has been shown (Richards 1963; Knudsen 1988; Wong and Lee 1991; Gaskin 1995; Chu 1996) that the fully developed vortex pair is self-similar in the mean. To date the vortex pair distribution has not been approximated by a relatively simple function. This is necessary to be able to relate the integrated concentration to the point concentration values of the vortex pair and is achieved with a pair of stretched, merging Gaussians. This approximation is not particularly good near the edges of the flow, but it allows for the peaks to be resolved with reasonable accuracy. A schematic of the approximation can be seen in Figure 3.30. Figure 3.30a shows the approximation of the vortex-pair by the double-Gaussian and its integrated counterpart in the *z*-direction. The integration in the *y*-direction can be seen in Figure 3.30b. The *x*-coordinate is in the direction of the ambient flow and perpendicular to the cross-sectional plane. Note that the spread value b_c is the spread of the single Gaussian and *f* and *h* are constants if the distribution is self-similar. Plotting least-squares fit double-Gaussian curves through the *y*-integrated and *z*-integrated cross-sectional concentration data at certain locations can determine values for *f* and *h*. The value for *h* is the ratio of the *y*-integrated spread in the *z*-direction to the *z*-integrated spread in the *y*-direction, and *f* is the ratio of the distance between the centreline and peak of a single Gaussian to the concentration spread of the single Gaussian.

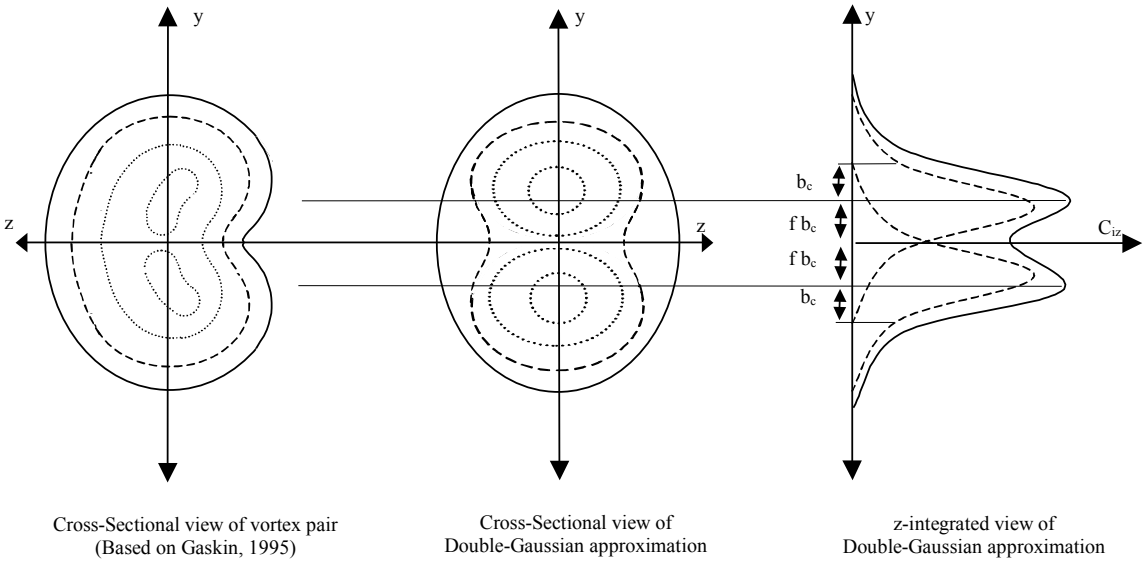

Cross-Sectional view of vortex pair (Based on Gaskin, 1995) | Cross-Sectional view of Double-Gaussian approximation | z-integrated view of Double-Gaussian approximation

a)

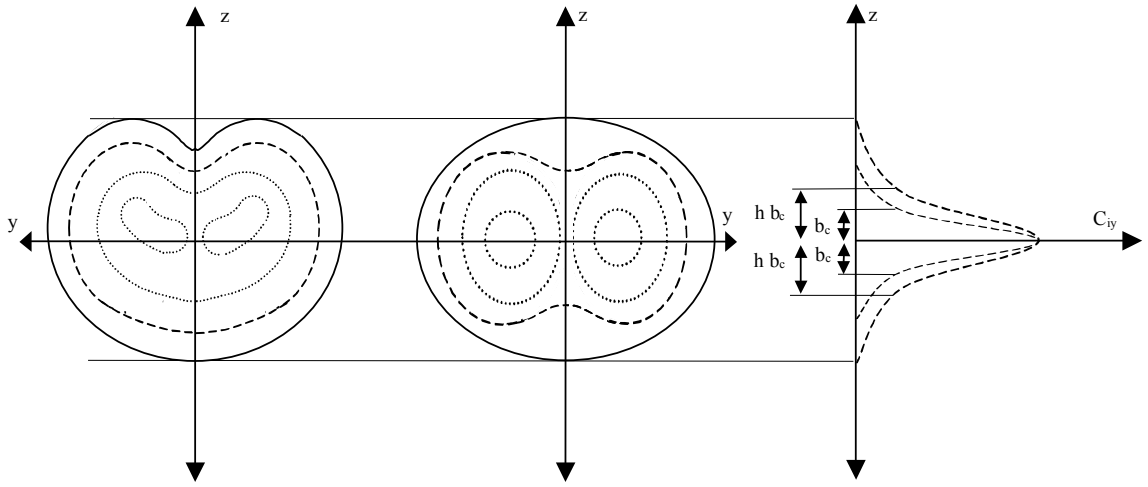

Cross-Sectional view of vortex pair (Based on Gaskin, 1995) | Cross-Sectional view of Double-Gaussian approximation | y-integrated view of Double-Gaussian approximation

b)

Figure 3.30 – Vortex pair and double-Gaussian approximation

Using this approximation, the equation relating the local concentration to the centreline concentration in a cross-section (equation (3.7)) can be rewritten to incorporate the double Gaussian.

$$C = C_l \left[e^{-\left(\frac{y-fb_c}{b_c}\right)^2} + e^{-\left(\frac{y+fb_c}{b_c}\right)^2} \right] e^{-\left(\frac{z}{hb_c}\right)^2} \tag{3.22}$$

For a given experiment the assumed location of the centreline of the vortex pair and the actual location may differ. To allow for this the following adjustment is made:

$$y' = y - y_l \tag{3.23}$$

and

$$z' = z - z_l \tag{3.24}$$

where y_l and z_l are the coordinates of the actual flow centreline. Replacing y and z in equation (3.22) with y' and z' gives:

$$C = C_l\left[e^{-\left(\frac{y'-fb_c}{b_c}\right)^2} + e^{-\left(\frac{y'+fb_c}{b_c}\right)^2}\right]e^{-\left(\frac{z'}{hb_c}\right)^2} \tag{3.25}$$

Again this equation can be integrated, but the distribution is no longer axi-symmetric and therefore integrations in the y and z-directions must be dealt with separately. Integrating in the y-direction gives the relationship between the local integrated concentration in the y-direction $\left(C_{iy}\right)$ and the centreline concentration. The result is equation (3.26).

$$\begin{aligned} C_{iy} &= C_l\left[\int_{-\infty}^{\infty}\left(e^{-\left(\frac{y'-fb_c}{b_c}\right)^2} + e^{-\left(\frac{y'+fb_c}{b_c}\right)^2}\right)dy\right]e^{-\left(\frac{z'}{hb_c}\right)^2} = C_l\left[\int_{-\infty}^{\infty} e^{-\left(\frac{y'-fb_c}{b_c}\right)^2}dy + \int_{-\infty}^{\infty} e^{-\left(\frac{y'+fb_c}{b_c}\right)^2}dy\right]e^{-\left(\frac{z'}{hb_c}\right)^2} \\ &= C_l\left(b_c\sqrt{\pi} + b_c\sqrt{\pi}\right)e^{-\left(\frac{z'}{hb_c}\right)^2} = C_l 2b_c\sqrt{\pi}e^{-\left(\frac{z'}{hb_c}\right)^2} \end{aligned} \tag{3.26}$$

or alternatively

$$C_{iy} = C_{ily}e^{-\left(\frac{z'}{hb_c}\right)^2} \tag{3.27}$$

Substituting $z' = 0$ into equation (3.26) gives the relationship between C_{ily} (y-integrated centreline concentration) and C_l

$$C_{ily} = C_l 2b_c\sqrt{\pi} \tag{3.28}$$

Note that the centreline concentration $\left(C_l\right)$ in equation (3.28) is based on the single Gaussian distribution and does not represent either the centreline value or the peak value of the vortex pair. To find the relationship between C_{ily} and the concentration at the centreline of the vortex pair $\left(C_c\right)$, first the relationship between C_l and C_c is found by substituting $y' = 0$ and $z' = 0$ into equation (3.25) to create equation (3.29). Then equation (3.29) is rearranged for C_l and substituted into equation (3.28) to form equation (3.30)

$$C_c = C_l\left(e^{-f^2} + e^{-f^2}\right) \tag{3.29}$$

$$C_{ily} = C_c b_c \sqrt{\pi} e^{f^2} \tag{3.30}$$

The same approach leads to the relationship between C_{ily} and the peak concentration of the vortex pair $\left(C_{peak}\right)$. This time $y' = f\lambda b$ and $z' = 0$ are substituted into equation (3.25)

$$C_{peak} = C_l \left(1 + e^{-(2f)^2}\right) \tag{3.31}$$

$$C_{ily} = C_{peak} \frac{2b_c\sqrt{\pi}}{1 + e^{-(2f)^2}} \tag{3.32}$$

Integrating equation (3.25) in the *z*-direction gives the relationship between the local integrated concentration in the *z*-direction $\left(C_{iz}\right)$ and the centreline concentration of the single Gaussian.

$$C_{iz} = C_l \left(e^{-\left(\frac{y'-fb_c}{b_c}\right)^2} + e^{-\left(\frac{y'+fb_c}{b_c}\right)^2} \right) \int_{-\infty}^{\infty} e^{-\left(\frac{z'}{hb_c}\right)^2} dz = C_l h b_c \sqrt{\pi} \left(e^{-\left(\frac{y'-fb_c}{b_c}\right)^2} + e^{-\left(\frac{y'+fb_c}{b_c}\right)^2} \right) \tag{3.33}$$

or

$$\frac{C_{iz}}{C_{ilz}} = \left(e^{-\left(\frac{y'-fb_c}{b_c}\right)^2} + e^{-\left(\frac{y'+fb_c}{b_c}\right)^2} \right) \tag{3.34}$$

Pun (1998) gives the relationship between the initial concentration and the centreline concentration. Modified to include the double-Gaussian assumption, this can be written as:

$$\frac{U_a}{U_0}\frac{C_0}{C_l} = I_{cdg} k_{sg}{}^2 \left(\frac{z}{M_{e0}{}^{0.5}/U_a} \right)^2 \tag{3.35}$$

where U_a is the ambient velocity, U_0 the initial velocity, k_{sg} the concentration spread-rate for the single Gaussian divided by λ, M_{e0} the initial excess momentum flux and I_{cdg} a shape constant defined by the integral

$$I_{cdg} = \int_{-\infty}^{\infty}\int_{-\infty}^{\infty} e^{-\left(\frac{z'}{hb_c}\right)^2} \left(e^{-\left(\frac{y'}{b_c}-f\right)^2} + e^{-\left(\frac{y'}{b_c}+f\right)^2} \right) d\frac{y}{b} d\frac{z}{b} \tag{3.36}$$

I_{cdg} has a value of $2h\lambda^2\pi$. Note that by defining I_{cdg} by equation (3.36), C_l in equation (3.35) is again based on the single Gaussian distribution and I_{cdg} is a constant value if the

cross-sections are self-similar. Rearranging equation (3.25) for C_l and inserting it into equation (3.35) gives

$$\frac{C_0}{C} = \left[\frac{U_0 I_{cdg} k_{sg}{}^2}{U_a} \left(\frac{z}{M_{e0}{}^{0.5}/U_a} \right)^2 \right] \Bigg/ \left(\left[e^{-\left(\frac{y'-fb_c}{b_c}\right)^2} + e^{-\left(\frac{y'+fb_c}{b_c}\right)^2} \right] e^{-\left(\frac{z'}{hb_c}\right)^2} \right) \tag{3.37}$$

Integrating in the *y*-direction gives the relationship between initial concentration and C_{iy}.

$$\frac{C_0}{C_{iy}} = \left[\frac{U_0 I_{cdg} k_{sg}{}^2}{U_a} \left(\frac{z}{M_{e0}{}^{0.5}/U_a} \right)^2 \right] \Bigg/ \left(2b_c \sqrt{\pi} e^{-\left(\frac{z'}{hb_c}\right)^2} \right) \tag{3.38}$$

Inserting $z' = 0$, and combining equations (3.13) and (3.38) gives the relationship between the integrated initial condition and the integrated centreline concentration in the *y*-direction

$$\frac{C_{i0}}{C_{ily}} = \frac{dU_0 I_{cdg} k_{sg}{}^2}{2b_c \sqrt{\pi} U_a} \left(\frac{z}{M_{e0}{}^{0.5}/U_a} \right)^2 = 2h\lambda k_{sg} \frac{z}{M_{e0}{}^{0.5}/U_a} \tag{3.39}$$

Integrating equation (3.37) in the z-direction gives the relationship between initial condition and C_{iz}

$$\frac{C_0}{C_{iz}} = \left[\frac{U_0 I_{cdg} k_{sg}{}^2}{U_a} \left(\frac{z}{M_{e0}{}^{0.5}/U_a} \right)^2 \right] \Bigg/ \left(hb_c \sqrt{\pi} \left[e^{-\left(\frac{y'-fb_c}{b_c}\right)^2} + e^{-\left(\frac{y'+fb_c}{b_c}\right)^2} \right] \right) \tag{3.40}$$

Inserting $y' = 0$, and combining equations (3.13) and (3.40) gives the relationship between the integrated initial condition and the integrated centreline concentration in the *z*-direction

$$\frac{C_{i0}}{C_{ilz}} = \frac{dU_0 I_{cdg} k_{sg}{}^2}{hb_c \sqrt{\pi} U_a} \left(\frac{z}{M_{e0}{}^{0.5}/U_a} \right)^2 \frac{e^{f^2}}{2} = 2\lambda k_{sg} \frac{z}{M_{e0}{}^{0.5}/U_a} e^{f^2} \tag{3.41}$$

Combining equations (3.39) and (3.41) gives a second experimental means (the first being the ratio of the spread at a cross-section) to find an estimate for *h*

$$h = e^{f^2} \frac{C_{i0}/C_{ily}}{C_{i0}/C_{ilz}} \tag{3.42}$$

An assessment of the value of the double-Gaussian approximation is determined through comparisons with experimental data from the momentum puff using the LA technique. At 20 different points along the trajectory of the flow, cross-sections were taken from a *y*-integrated momentum puff experiments (Re = 4363, U_r = 0.0289). The cross-sectional values were non-dimensionalised, using the strong jet to advected line momentum puff transition length-scale $(M_{e0}{}^{0.5}/U_a)$, and plotted versus the Gaussian theory of equation (3.27). The results are shown

in Figure 3.31. The double-Gaussian assumption matches the cross-sectional experimental data well. It also shows that the cross-sections are self-similar which is consistent with the observations of Knudsen (1988), Wong and Lee (1991), Gaskin (1995) and Chu (1996)

For a comparison of the *z*-integrated double-Gaussian assumption, ten non-dimensional integrated cross-sectional concentration profiles from a *z*-integrated momentum puff experiment (Re = 4042, U_r = 0.0317) were compared with the theory of equation (3.34) in Figure 3.32. There is good agreement between the assumed and experimental profiles and this agreement suggests that the double-Gaussian approximation for tracer profiles is reasonable in the strongly advected region of the flow.

The assumed profile in Figure 3.32 used a value for *f* of 0.88. Values of the parameter *f* determined from least-squares fits to the profiles in the strongly advected region, such as those shown in Figure 3.32, are presented in Figure 3.33. The value for *f* is reasonably constant in the strongly advected region, but did have a slight downward trend in some of the datasets. The average value for *f* is 0.88 with an error of ± 0.05. The error reduced with increasing distance from the source.

Much of the error is believed to be caused by the sensitivity of the flow to the generated turbulence, especially in the region close to the transition. Richards (1963) carried out line thermal experiments in a still ambient. A horizontal cylinder of fluid with a higher density than the surrounding fluid was released and carried away by buoyancy forces. His work clearly showed the presence of a vortex pair. He also showed that the flow was approximately self-similar in the mean and the width of the line-thermal was proportional to the (vertical) distance travelled. However the proportionality constant he found was heavily dependent on the method of release. In the present experimental set up, it is possible that the random nature of the turbulence in the transition zone to the puff region generates different circumstances under which the vortex pair is formed, influencing both the position and the behaviour of the vortex pair.

Using equations (3.29) and (3.31) the theoretical ratio of maximum concentration to centreline concentration is determined to be 1.13. This is lower than the 1.18 that Chu (1996) found experimentally. However as Figure 3.32 shows the double-Gaussian curve has a tendency to smooth the peaks and troughs of the experimental cross-sectional data, decreasing the expected ratio of maximum to centreline concentration.

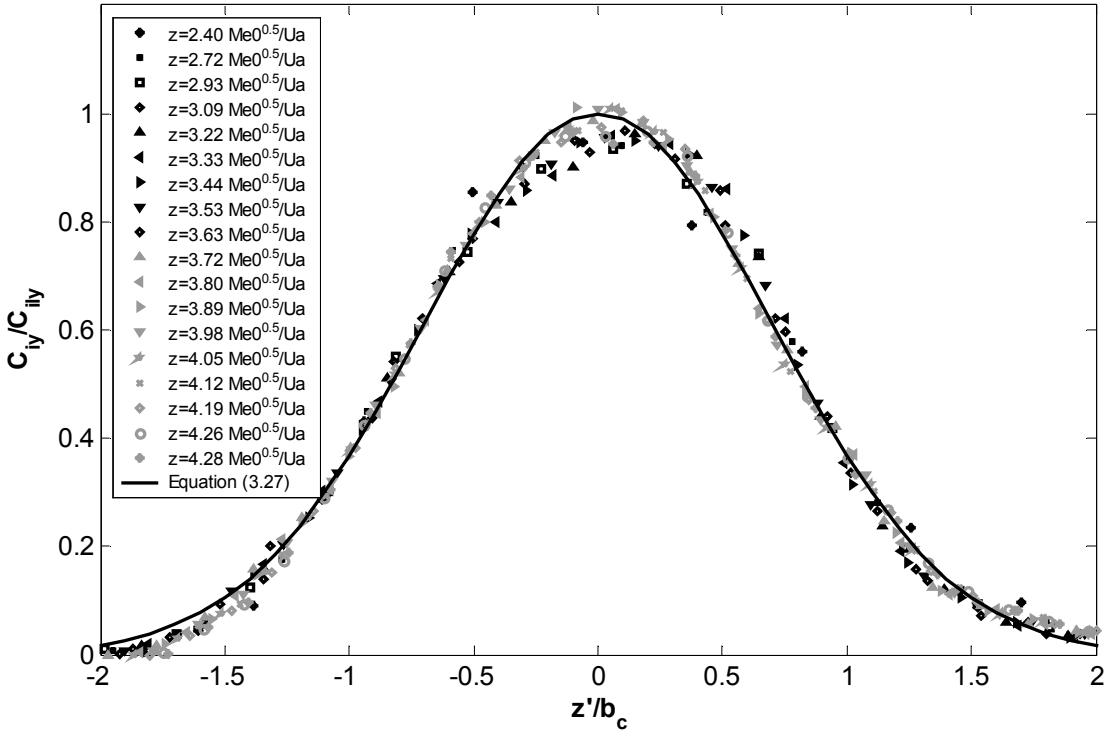

Figure 3.31 - Cross-Sectional Integrated Concentration profiles integrated in the y-direction

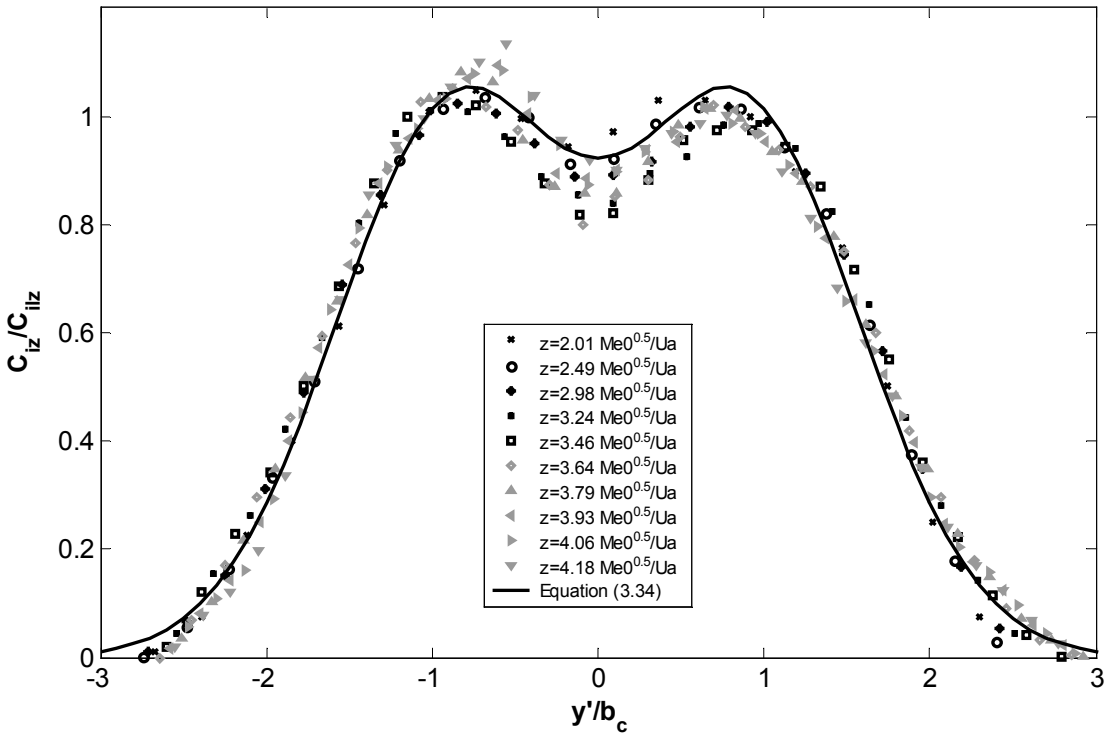

Figure 3.32 - Cross-Sectional Integrated Concentration profiles integrated in the z-direction

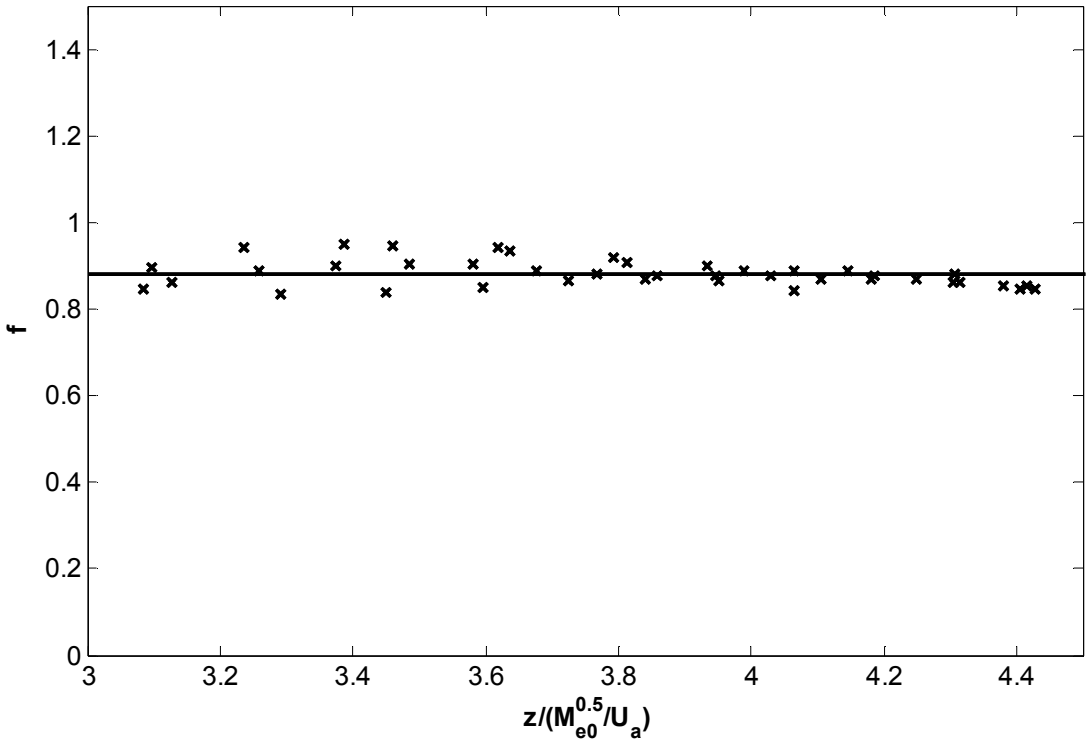

Figure 3.33 - Value of *f* as a function of vertical distance away from source

The double integrated concentration results from both the *y* and *z*-directions are presented in Figure 3.34. For most runs the results were within 5% of the expected results. Part of that error came from the determined calibration length scale for the *z*-integrated runs (see section 3.2.4.2). However for some runs the error was much larger. This was related to the use of Sodium Sulphite during the experimental investigation (see section 3.2.2.4). To take the influence of the Sodium Sulphite into account, a correction based on the double integrated results was applied to the experimental integrated concentration data. The double integrated dilution equation can be calculated from the conservation of mass equation for the momentum puff $\left(C_0 Q_0 = C_{ii} U_a\right)$ or by double integrating equation (3.37),

$$\frac{U_0}{U_a}\frac{C_{ii0}}{C_{ii}} = 1 \tag{3.43}$$

where C_{ii0} is the double integrated initial concentration and C_{ii} is the double integrated concentration. The theoretical solution in the jet region was determined by modifying equation (3.21) to include the velocity ratio. Of interest is the location of the transition from weakly to strongly advected behaviour, which appears to occur gradually and not be complete until at least 3.5 length-scales from the source in the *z*-direction. Comparing Figure 3.24 with Figure 3.34 it can be noted that, in the jet region, the current results are over predicted by the

double-integrated theory while the theory under predicted the results shown in Figure 3.24. In section 5.3.1.2 this is investigated further.

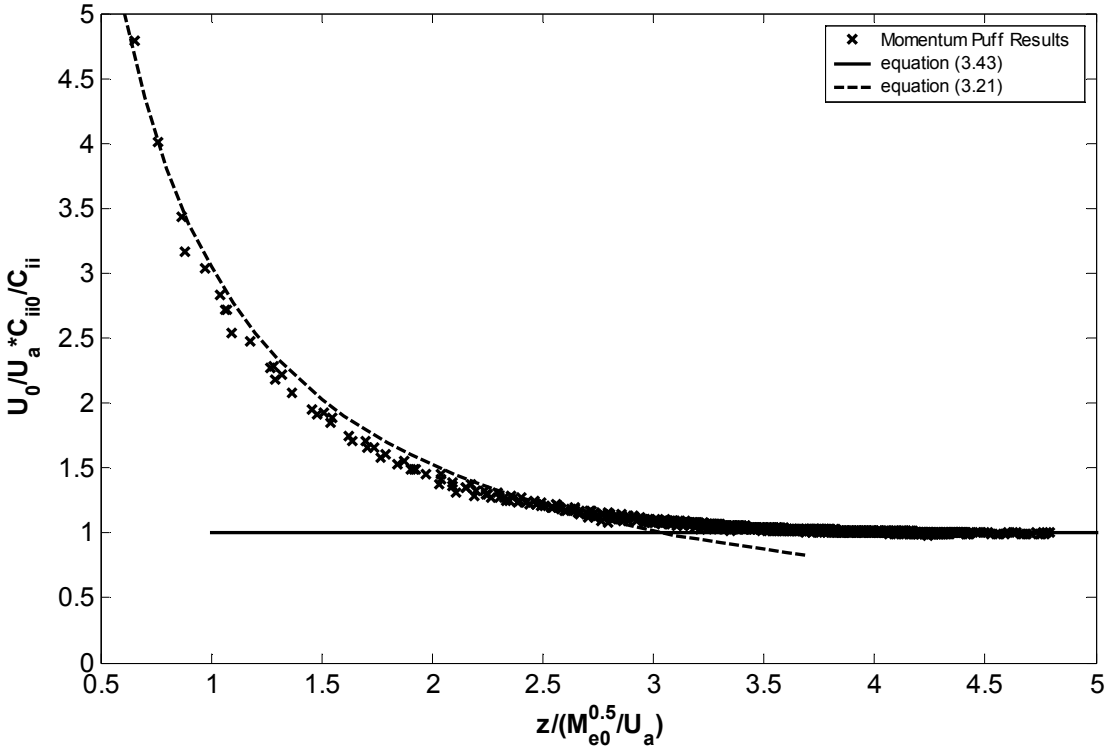

Figure 3.34 – Double integrated dilution results for momentum puff experiments

The distortion of the individual Gaussians is taken into account by the value *h*, where *h* is the ratio of the *y*-integrated spread in the *z*-direction to the *z*-integrated spread in the *y*-direction of the single Gaussian. As mentioned before the ratio of the integrated centreline dilutions provides information with respect to this distortion (equation (3.42)). Ratios of the centreline *z*-integrated dilution to the *y*-integrated centreline dilution are shown in Figure 3.35. A direct measure of the distortion is given by the ratio of the spread in the *z*-direction to that in the *y*-direction as determined from least-squares fits of the double-Gaussian approximation to the integrated profiles. This data is also shown in Figure 3.35.

The two sets of data are consistent and show the profiles are more distorted near the transition region and that this distortion eases in the strongly advected region where the value of *h* approaches 1.46 (Figure 3.35). These variations in *h* can be approximated empirically with the relationship

$$h = h^* + \frac{c_1}{b_c}\frac{M_{e0}^{0.5}}{U_a} \tag{3.44}$$

where h^* is equal to 1.46 and c_1 is equal to 0.04. It is worth noting that for distances less than three length-scales from the source the angle of the cross-sectional profiles is more than 10° from the vertical. With the vertical cross-sectional assumption that is built into the experimental technique this leads to significantly increasing errors closer to the source

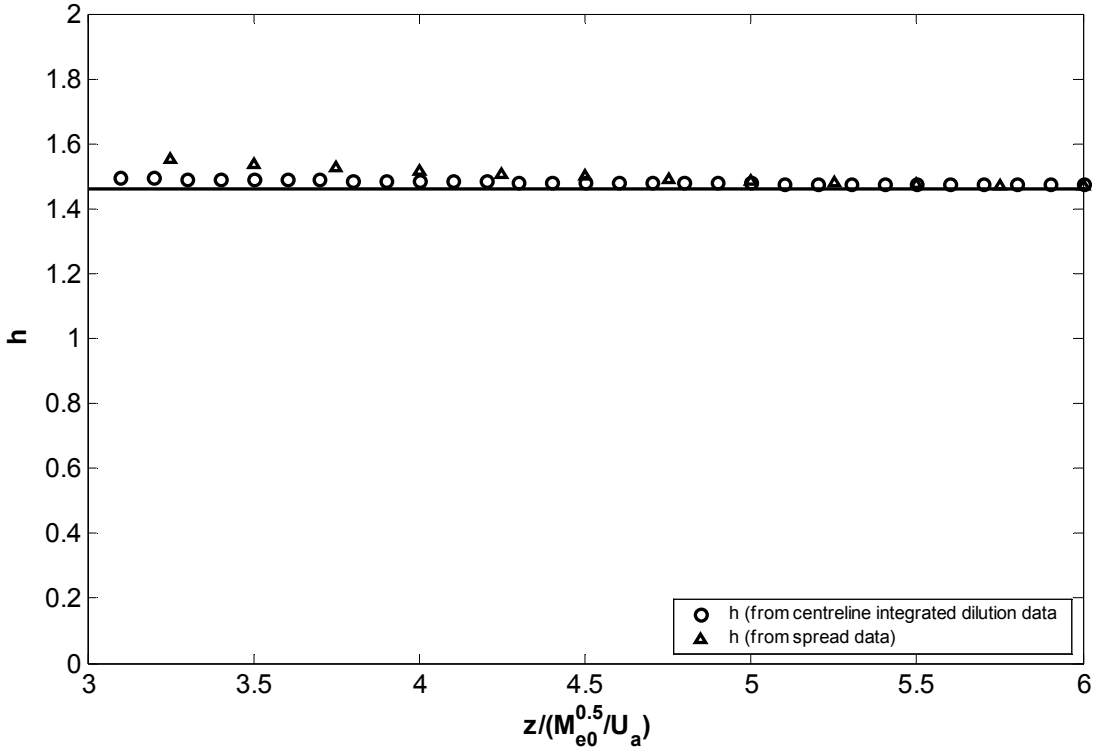

Figure 3.35 – Double-Gaussian parameter *h* as a function of vertical distance from the source

Figure 3.36 compares the *y*-integrated concentration spread in the *z*-directions and the *z*-integrated concentration spread in the *y*-direction. Fitting linear least-square fit lines to both data sets gives concentration spread constants of 0.36 and 0.24 for the concentration spread in the *y* and *z*-directions respectively. Relationships predicting the dilution are based on the concentration spread divided by λ of one of the single Gaussians (k_{sg}, equation (3.35)), and this is given as $k_{sg} = 0.24/\lambda = 0.20$.

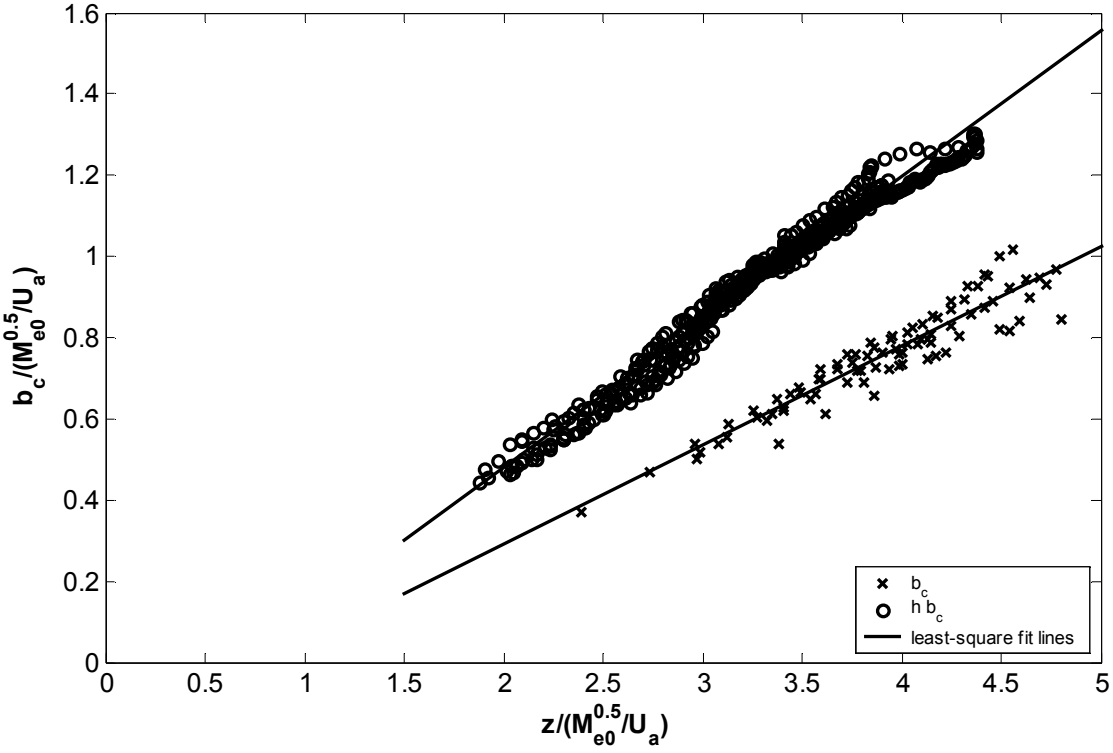

Figure 3.36 - Spread comparison of top and side view momentum puff experiments

As the vortex pair distribution has not been approximated by a relatively simple function definitions of the characteristic width of the momentum puff have differed in the past (Gaskin 1995). The *y*-integrated spread constant can be compared with previous data from point cross-sectional concentration profiles measured in the *z*-direction over the whole cross-section. The value for the *y*-integrated spread constant compares well with the value found by Knudsen (1988) of 0.36 and to a lesser degree with 0.41 found by Gaskin (1995).

Wong and Lee (1991) calculated a ratio of horizontal to vertical width for a strongly advected cross-section. The boundary of the cross-section was defined by a $C = e^{-1}C_m$ contour, where C_m is the maximum concentration in the cross-section. The experiments they carried out showed that the ratio increased from 1 (in the jet region of the flow) to about 1.1-1.3. The average value they found was 1.2. Chu (1996) determined an average value for the puff aspect ratio of 1.23. Using the definition of the aspect ratio as explained above, the double-Gaussian cross-sectional assumption gives a value for the width ratio of 1.26, comparing well with the experimental values found by Wong and Lee, and Chu.

Figure 3.37 shows the results of a comparison between the experimental results and the integrated dilution equations. The Reynolds numbers ranged between 2631 and 5100 and the ambient velocity between 33mm/s and 98mm/s. Integrating in the *y*-direction gives a more comprehensive view as the complete flow has been recorded by the camera and thus the two different regions, the jet and momentum puff regions were visible. On Figure 3.37 only the strongly advected results have been plotted. The flow recorded from the *z*-integrated direction has the limitation that it cannot be interpreted clearly until it is sufficiently bent over so that the vertical cross-section assumption is reasonable. Both data sets collapse well onto a single line, although there is more scatter in the *z*-integrated data. The theory of equation (3.39) matches the experimental data from 3.5 length-scales onwards. This is consistent with the end of the transition zone determined with the double-integrated data. Up to the transition the theoretical integrated dilution value is 0.812 (see section 3.2.3.1). The *y*-integrated dilution results therefore suggest a transition point at a distance of 1.9 length-scales in the *z*-direction, the *z*-integrated results suggest a transition point at 1.7 length-scales.

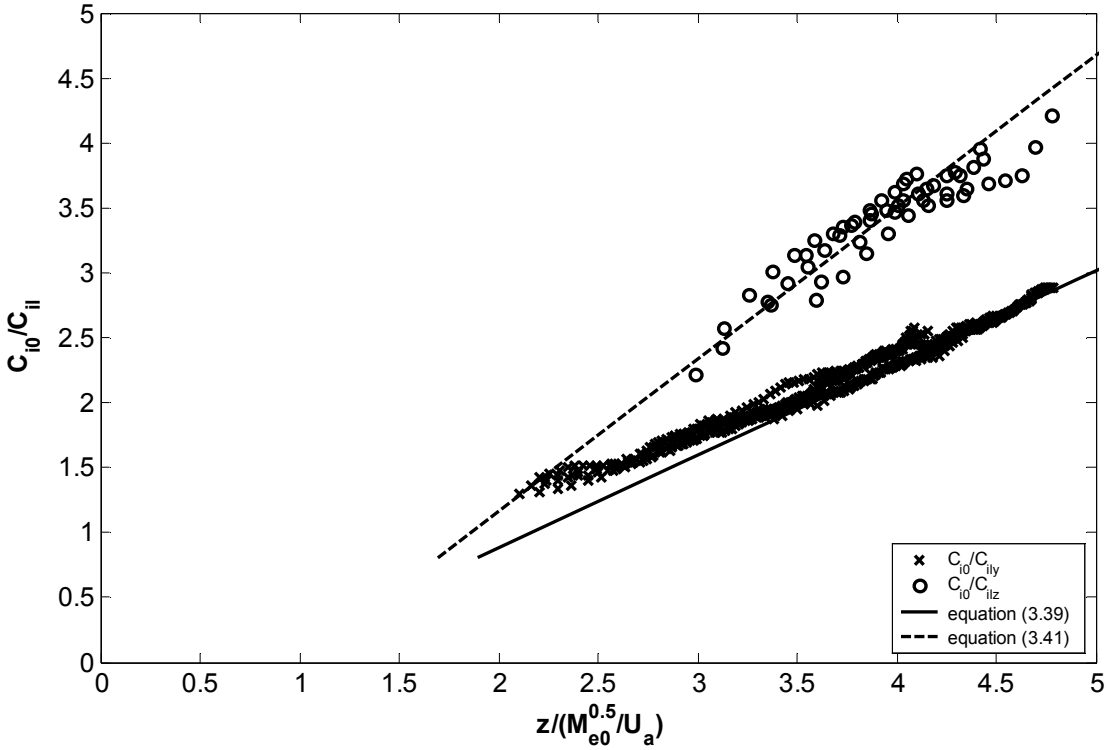

Figure 3.37 - Integrated Dilution results

Within the puff region the integrated dilution in the *y*-direction can be converted into point dilution. The minimum point dilution occurs at the peaks. The theoretical equation for the minimum dilution can be found by inserting equation (3.31) into equation (3.35). Rearranging gives

$$\frac{U_a}{U_0}\frac{C_0}{C_{peak}} = \frac{I_{cdg}k_{sg}^{\ 2}}{\left(1+e^{-(2f)^2}\right)}\left(\frac{z}{M_{e0}^{\ 0.5}/U_a}\right)^2 \tag{3.45}$$

The experimental *y*-integrated dilution data can be converted into minimum point dilution data by combining equation (3.28), equation (3.13) and equation (3.31). Solving the equation for the actual dilution gives

$$\frac{U_a}{U_0}\frac{C_0}{C_{peak}} = \frac{C_{i0}}{C_{ily}}\frac{2\sqrt{\pi}}{\left(1+e^{-(2f)^2}\right)}\frac{b_c}{d}\frac{U_a}{U_0} = \frac{C_{i0}}{C_{ily}}\frac{\pi b_c}{\left(M_{e0}^{\ 0.5}/U_a\right)}\frac{1}{\left(1+e^{-(2f)^2}\right)} \tag{3.46}$$

Similarly combining equation (3.33) $\left(y' = fb_c\right)$, equation (3.13) and equation (3.31) gives the relationship between the minimum point dilution and the integrated dilution when integrating in the *z*-direction

$$\frac{U_a}{U_0}\frac{C_0}{C_{peak}} = \frac{C_{i0}}{C_{iz-peak}}\frac{b_c h\sqrt{\pi}}{d}\frac{U_a}{U_0} = \frac{C_{i0}}{C_{iz-peak}}\frac{h\pi b_c}{2\left(M_{e0}^{\ 0.5}/U_a\right)} \tag{3.47}$$

Figure 3.38 shows the minimum point dilution of the momentum puff. The figure presents the experimental results from the *y*-integrated momentum puff experiments converted into point peak dilution data using equation (3.46) and the experimental results from the *z*-integrated momentum puff experiments converted into point peak dilution data using equation (3.47). The data is compared with predictions based on equation (3.45), with appropriate allowance for a virtual source, and those of VisJet (Cheung et al. 2000) and CorJet (Jirka 2004). The model prediction from VisJet overestimates the dilution in the strongly advected region and the prediction from CorJet underestimates the dilution. All experimental data collapses onto a single line that matches the theory well. The agreement between the data obtained from two different integrated perspectives further indicates the value of the double-Gaussian approximation in interpreting the strongly advected behaviour of these flows.

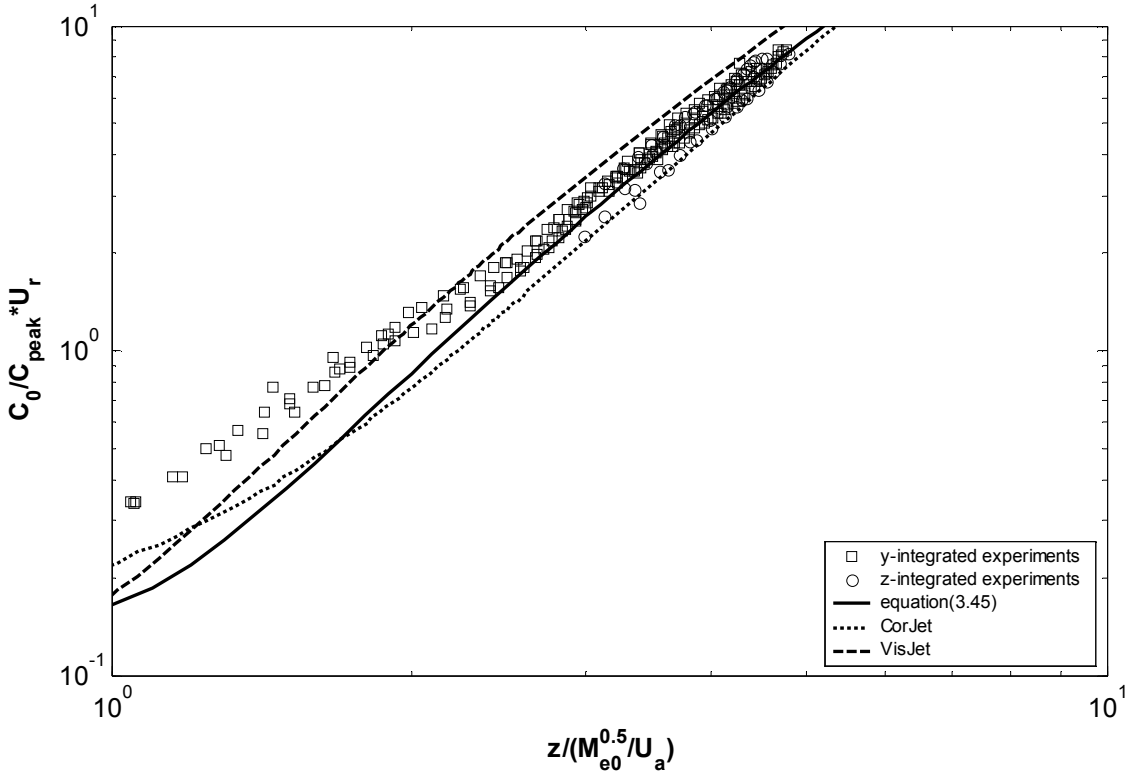

Figure 3.38 - Converted peak dilution data using far-field and near-field values for h

For the present experimental configurations the trajectory of the momentum puff can only be seen using the *y*-integrated view. It is defined as the location with the maximum integrated concentration value in a cross-section, taken perpendicular to the flow trajectory. The result of a *y*-integrated experiment is plotted in Figure 3.39 and it is compared with trajectory predictions from two different mathematical models. The experimental data agrees well with the experimental data of Hung (1998) and Pratte and Baines (1967), however there is less agreement with the experimental data of Jordinson (1956), and Keffer and Baines (1963). Model prediction from CorJet and VisJet appear to match the experimental data reasonably well, but the CorJet predictions have a tendency to under predict the data further downstream, whereas VisJet tends to under predict initially, but is more consistent with the data further downstream.

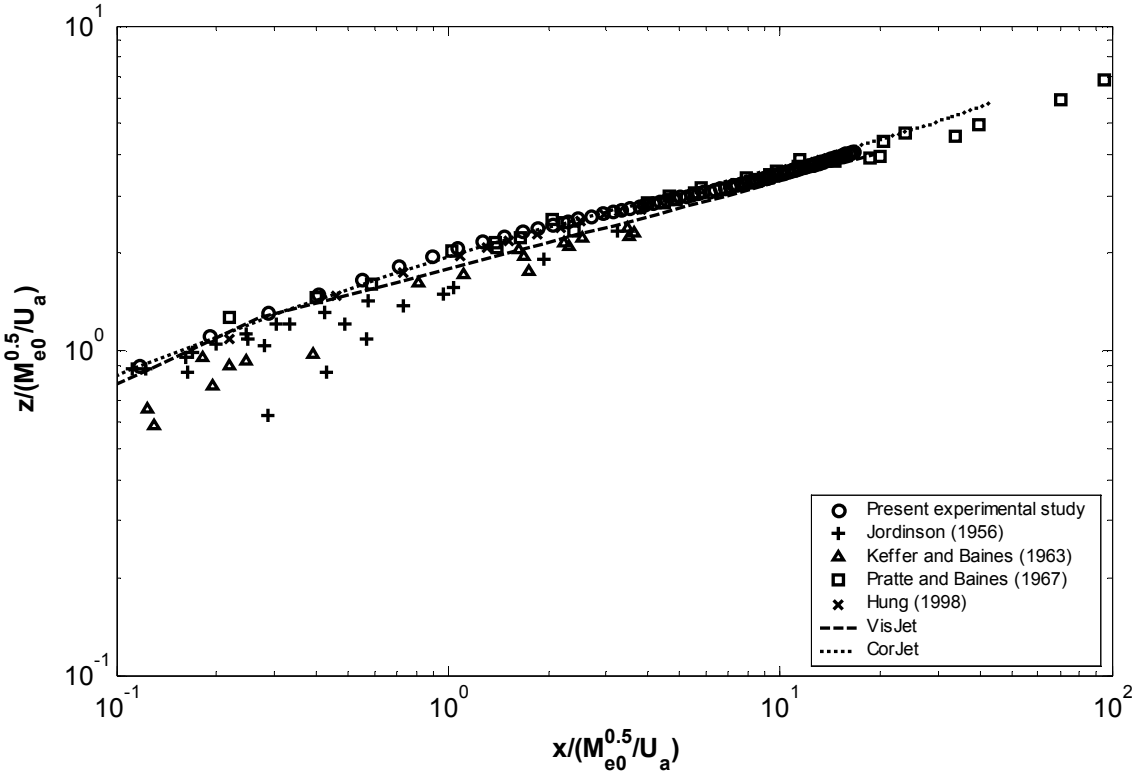

Figure 3.39 - Momentum puff trajectory, comparing experimental data with model predictions

3.2.3.3 – Angled Jet

As mentioned previously the angled jet flow is an example of a flow that is no longer flowing perpendicular to the camera view. The experimental set up for the angled jet experiment is the same as for the simple jet with the exception of the source position. It was no longer positioned vertically downwards, but makes a certain angle, ϕ_0, with the horizontal. This can be seen in Figure 3.40. The angle ϕ_o was 65^o for these experiments, determined to a precision of 0.25 of a degree. The diameter of the source was 3mm and Q_0 was 0.010l/s.

To be able to convert the integrated concentration values, obtained from the angled jet experiment, into centreline concentration values, the internal concentration structure along the ray of light that reached the camera has to be known. The cross-sectional view of the angled jet in Figure 3.41 has been cut through the centre of the jet. Therefore the integrated centreline concentration has been integrated over the local concentration along dimensionless distance $b_1 + b_2$. At a certain distance $L = s/d = b/k\lambda d$ downstream, where s/d is the non-dimensional distance downstream from the source along the trajectory of the jet, b_1 and b_2

can be written as function of angles ϕ_0, θ and L. The value of θ is approximately equal to $k\lambda$.

$$b_1 = L\frac{\sin(\theta)}{\cos\left(\frac{\pi}{2}-\phi_0-\theta\right)} \tag{3.48}$$

$$b_2 = L\frac{\sin(\theta)}{\cos\left(\frac{\pi}{2}-\phi_0+\theta\right)} \tag{3.49}$$

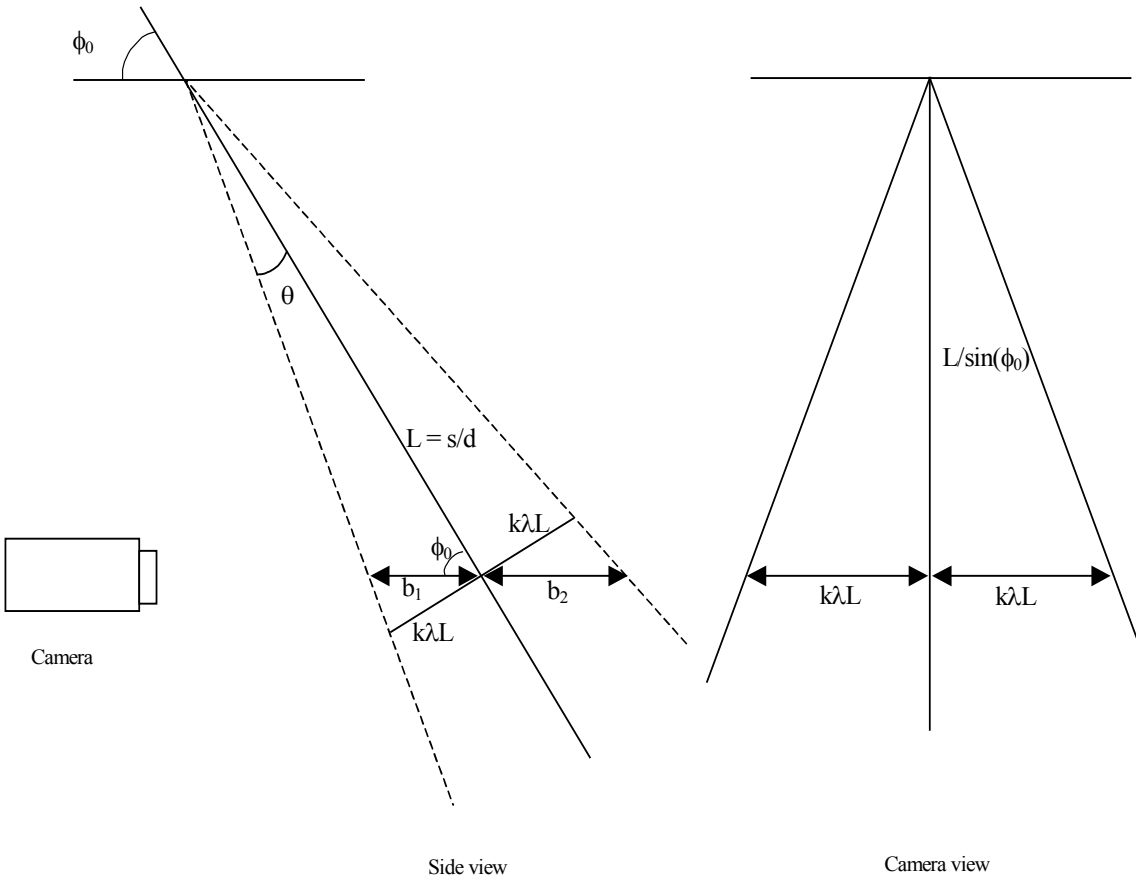

Figure 3.40 - Vertical cross-sectional and frontal view of angled jet experiment

Using the above derived non-dimensional distances for b_1 and b_2, a horizontal cross-section of the flow in the plane of the camera can be drawn (Figure 3.41). A coordinate system with the origin at the maximum concentration value has been added. The cross-section consists out of two half ovals meeting at the *y*-axis and can be mathematically described by equations (3.50) and (3.51).

$$\text{for} \quad x \le 0 \quad : \quad \frac{x^2}{\left(\dfrac{L\sin(\theta)}{\cos\left(\dfrac{\pi}{2}-\phi_0-\theta\right)}\right)^2}+\frac{y^2}{(k\lambda L)^2}=1 \tag{3.50}$$

$$\text{for} \quad x \ge 0 \quad : \quad \frac{x^2}{\left(\dfrac{L\sin(\theta)}{\cos\left(\dfrac{\pi}{2}-\phi_0+\theta\right)}\right)^2}+\frac{y^2}{(k\lambda L)^2}=1 \tag{3.51}$$

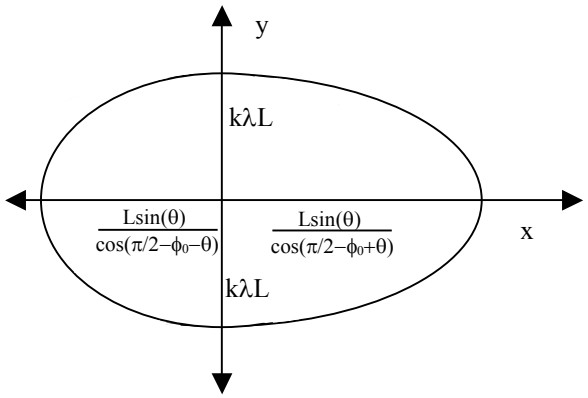

Figure 3.41 – Horizontal cross-section

The cross-sectional centreline concentration profiles of a simple jet are known to have a Gaussian shape, therefore the cross-sectional concentration profiles of the angled jet can be described by two half Gaussians, again meeting at the *y*-axis. Equation (3.7) is split up into two integrals, from minus infinity to zero and zero to infinity, and used to calculate the theoretical integrated centreline concentration.

$$C_{il} = C_l\left[\int_{-\infty}^{0} e^{\left(\frac{x}{b_1}\right)^2} dx + \int_{0}^{\infty} e^{\left(\frac{x}{b_2}\right)^2} dx\right] = \frac{1}{2}C_l\sqrt{\pi}L\sin(\theta)\left[\frac{1}{\cos\left(\dfrac{\pi}{2}-\phi_0-\theta\right)}+\frac{1}{\cos\left(\dfrac{\pi}{2}-\phi_0+\theta\right)}\right] \tag{3.52}$$

or alternatively to convert the integrated value into the actual centreline concentration

$$C_l = C_{il}\frac{2}{\sqrt{\pi}L\sin(\theta)}\frac{1}{\left(\frac{1}{\cos\left(\frac{\pi}{2}-\phi_0-\theta\right)}+\frac{1}{\cos\left(\frac{\pi}{2}-\phi_0+\theta\right)}\right)} \tag{3.53}$$

Combining equation (3.53) with equation (3.13) gives the following relationship for dilution.

$$\frac{C_0}{C_l} = \frac{C_{i0}}{C_{il}}\frac{\sqrt{\pi}L\sin(\theta)}{2d}\left[\frac{1}{\cos\left(\frac{\pi}{2}-\phi_0-\theta\right)}+\frac{1}{\cos\left(\frac{\pi}{2}-\phi_0+\theta\right)}\right] \tag{3.54}$$

Figure 3.42 compares the dilution results (converted using equation (3.54)) from the angled jet experiment with the theoretical equation (3.12). Just as in the simple jet case the accuracy of the dilution results is affected by the need to use the concentration spread values to convert the integrated values to point values and in this case a value for θ must also be calculated at each point. However the agreement with theory is reasonable and this shows that LA can be used under these circumstances as long as the internal concentration structure is known.

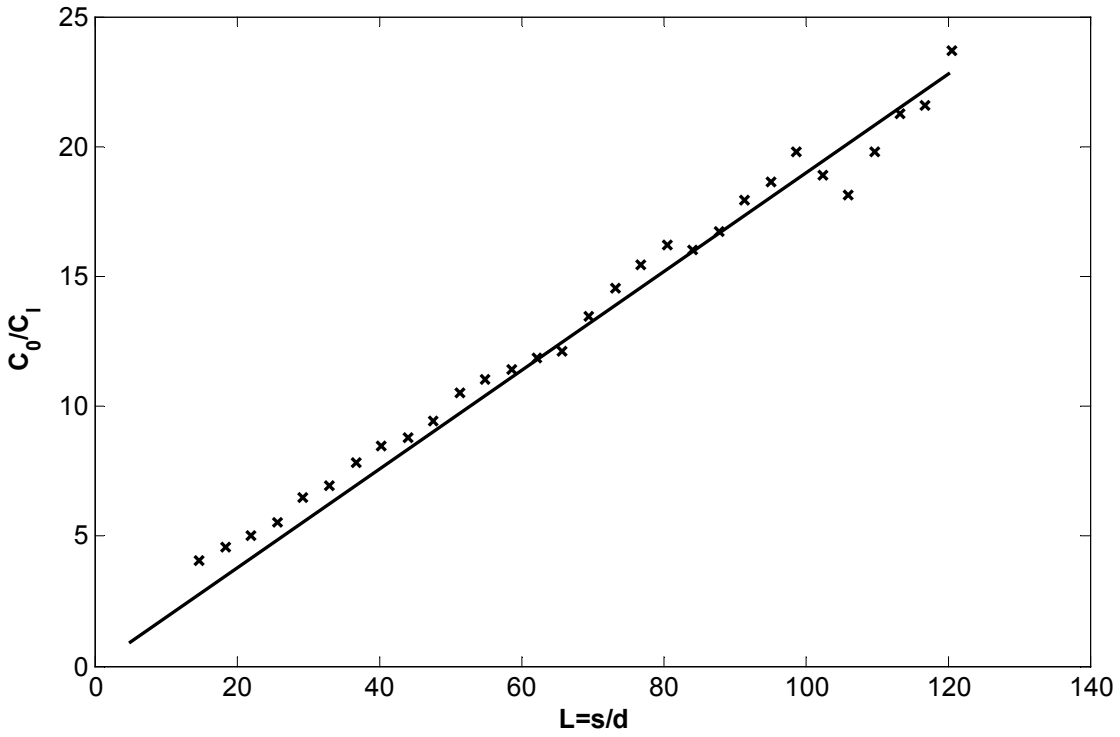

Figure 3.42 – Experimental versus theoretical dilution of angled jet

3.2.3.4 – Parallax Issues

The above derived equations can be used to calculate the errors that are involved in LA due to parallax. The dimensions of the recorded camera view are approximately 570mm x 700mm (horizontal x vertical). The highest error due to parallax will occur when a flow is recorded in the corner of the screen. For these experiments, the maximum vertical distance from the image centre is 350mm and the maximum horizontal distance is 285mm. Therefore the distance to the corner is approximately 450mm. The averaged distance of the camera from the flow in the tank was 4000mm. The two camera positions, where the camera is assumed to be and where it actually is can be seen on the left hand side of Figure 3.43, creating the angle γ. Returning to the angled jet, rotating the source of the flow over an angle γ generates the same parallax issue. The result can be seen on the right hand side of Figure 3.43. Note that

$$\phi_0 = \frac{\pi}{2} - \gamma \tag{3.55}$$

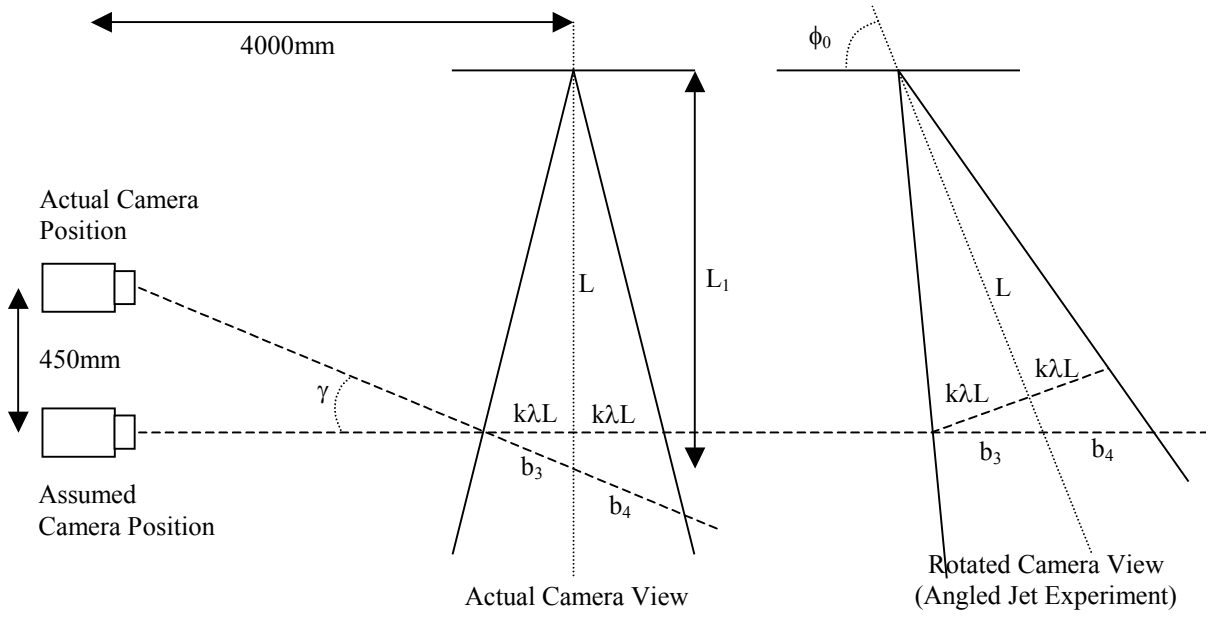

Figure 3.43 – Cross sectional view of simple jet experiment including the effects of parallax

To measure the error involved in neglecting the effects of parallax, the ratio of the assumed integrated centreline concentration over the actual integrated centreline concentration is

calculated. The assumed integrated centreline concentration $C_{il-assumed}$ can be calculated using equation (3.9) rewritten as

$$C_{il-assumed} = C_l \lambda b \sqrt{\pi} = C_l \lambda k L \sqrt{\pi} \tag{3.56}$$

The actual integrated centreline concentration can be found using equation (3.52), but as the centreline distance from the source has increased form L to L_1, the centreline concentration has decreased from C_l to C_{l-1}. Inserting into equation (3.52) gives

$$C_{il-actual} = \frac{1}{2} C_{l-1} \sqrt{\pi} L_1 \sin(\theta) \left[\frac{1}{\cos(\gamma - \theta)} + \frac{1}{\cos(\gamma + \theta)} \right] \tag{3.57}$$

and therefore the error involved is

$$error = 1 - \frac{C_{il-assumed}}{C_{il-actual}} = 1 - \frac{C_l L}{C_{l-1} L_1} \frac{2\lambda k \sqrt{\pi}}{\sqrt{\pi} \sin(\theta) \left[\frac{1}{\cos(\gamma - \theta)} + \frac{1}{\cos(\gamma + \theta)} \right]} \tag{3.58}$$

As mentioned before the spread of a jet increases linearly with distance and the concentration decreases linearly with distance. As the spread is linearly related to the distance downstream from source, $C_l L$ is a constant and therefore the ratio of $C_l L$ over $C_{l-1} L_1$ is 1 and equation (3.58) can be simplified to

$$error = 1 - \frac{2\lambda k}{\sin(\theta) \left[\frac{1}{\cos(\gamma - \theta)} + \frac{1}{\cos(\gamma + \theta)} \right]} \tag{3.59}$$

This gives a maximum error in the measured integrated centreline concentration value due to the effects of parallax of 0.0099 or 0.99%. Using a different experimental set up will slightly alter the error involved, but will still be well within the maximum 5% error of the linear intensity versus concentration assumption used for calibration and therefore parallax issues are not considered significant.

3.2.4 – 3D LA

The established LA flow visualization technique was upgraded and used to visualize buoyant jet flows with three-dimensional trajectories. The upgraded experimental set up is discussed including a section on the issues surrounding calibration length-scales of the flows with three-dimensional trajectories. The system is verified by presenting experimental data from two 3D LA experiments, a weakly advected simple jet experiment and a strongly advected momentum puff experiment.

3.2.4.1 – 3D LA Equipment and Experimental Set Up

As the trajectory of a three-dimensional trajectory flow is no longer located in a plane perpendicular to a single camera, a second camera is needed to establish where the trajectory is at any given point. The second camera records a perpendicular view relative to the first camera, and both cameras are positioned perpendicular to the direction of the ambient flow. The camera locations during the experimental investigation can be seen in Figure 3.44. The digital video camera on the side of the tank, recording the *y*-integrated view of the experiment, was the Jai CV M7+, recording a maximum of 1400 images per experiment. The digital video camera situated above the tank, recording the *z*-integrated view of the flow, was the Jai CV M7+ CL, recording a maximum of 1046 images per experiment. When the tank was filled with water both cameras were approximately 3.7 metres away from the centre of the body of water.

The light source for the *z*-integrated view, a set of twelve 100Hz fluorescent light bulbs were mounted on an aluminium frame and placed on the floor of the main tank (see Figure 3.44). The light bulbs were spaced 55mm apart, the total length and width of the light sheet were 1.60 and 0.84 metres respectively. Extension cords were attached to either end of the bulbs. They connected the submerged light bulb with the light fitting situated outside the tank. To generate enough heat for the submerged light bulbs to reach standard operating temperatures the bulbs were inserted into clear plastic tubes. The air in the tube worked as a layer of insulation protecting the submerged light bulbs from the cold water. A second aluminium frame was built to fit over top of the lights and support the Perspex diffusion sheet. The distance between the frame supporting the light bulbs and the frame supporting the diffusion sheet was approximately 110mm. A significant gap was needed to stop the lights from overheating. The sides along the length of the light bulbs were also covered with diffusion sheets to reduce reflections of the light in the glass panels of the tank.

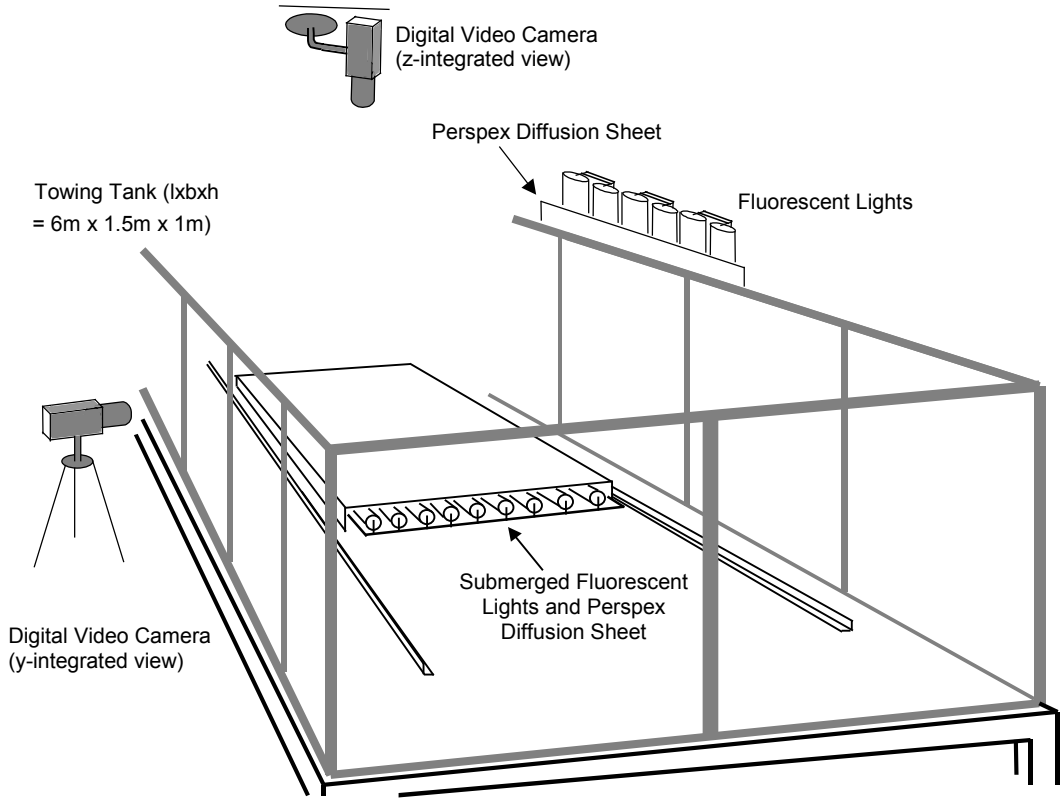

Figure 3.44 - 3D LA system – set up of experimental equipment

For the 3D LA system, the calibration cells had to be upgraded. Due to the size of the submerged light sheet the distance between the rails had to be increased and therefore the trolleys needed an increase in track width. The trolleys also had to be able to be driven over the top of the light sheet and therefore needed increased ground clearance, however the glass picture frame had to stay at the same height above the floor of the tank. With two directions of view a vertical and horizontal field calibration needed to be carried out before each experiment. Therefore one of the calibration trolleys was rebuilt and used for the field calibration in the *z*-integrated direction (see Figure 3.45). As there was only enough room in the tank for two trolleys, the upgraded trolleys were filled with clear water before a set of experiment to record the attenuation due to the glass, and during the experiments the trolleys were filled with the diluted red dye mixture, to be used for the field calibration. A comparison of several GA images, recorded at different times, displaying the attenuation due to the glass plates, showed that the error involved by not having a recording of the attenuation due to the glass before each single experiment was minimal (<<1%).

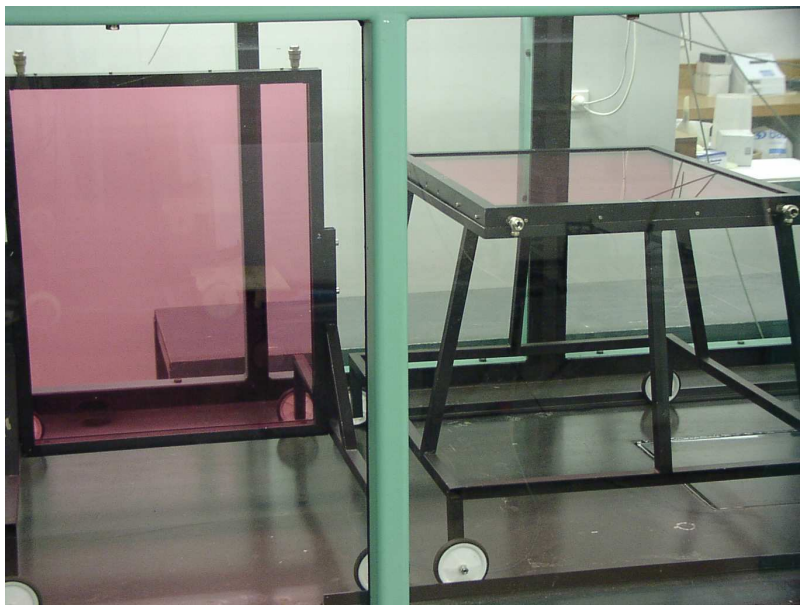

Figure 3.45 – Upgraded calibration cells

During the recording of the field calibration images in the *z*-integrated direction, the frame of the calibration cell created a shadow. This could be remedied during the recording of the background images for the attenuation of the glass by placing a piece of aluminium framing on the trolley to recreate the shadow. However, this was not possible during the recording of the background images when determining the attenuation of the red dye during an experiment. The result was a slightly overestimated attenuation due to the red dye in the ten percent of the field calibration closest to the vertical light sheet. During the experimental investigation, the flow configurations were chosen so as to minimize its impact.

3.2.4.2 – Calibration Length Scales

For the standard LA system the calibration length-scales were found by inserting a cross-shaped ruler in the trajectory plane of the flow. This approach is no longer sufficient for the 3D LA system as the flow is travelling either towards or away from the camera during the length of the experiment, and the calibration length-scales change with the changing distance between camera and flow trajectory. To be able to define the length-scales in both the *y* and *z*-integrated directions, the length-scales were found as a function of distance from the camera. The results can be seen in Figure 3.46.

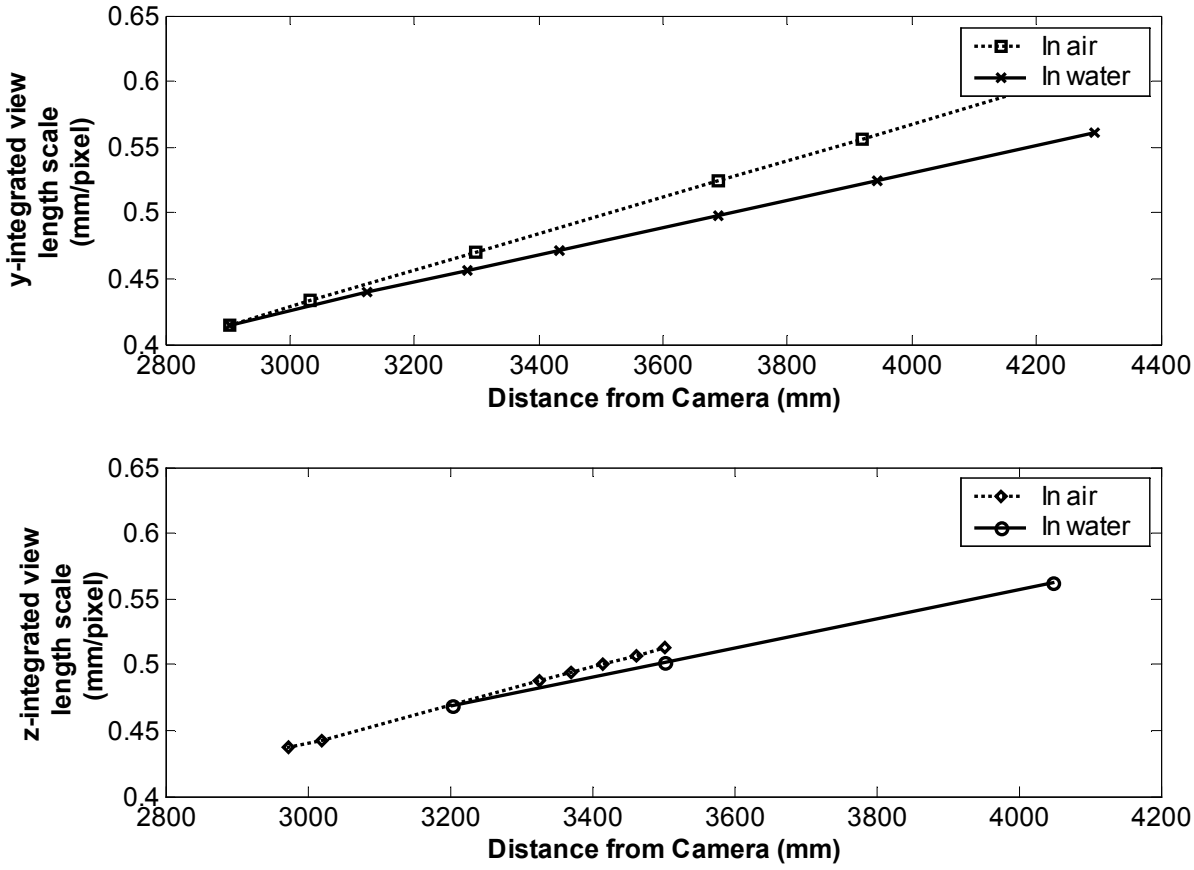

Figure 3.46 - *y* and *z* integrated view length scales versus distance away from camera

As it is not possible to change the calibration length-scales for individual images during the creation of the transformed average image, two calibration length-scales were used to analyse each experiment, creating two different transformed average integrated concentration images. The first one was the initial length scale at the source. The distance between the camera and the source was found and with the help of the results in Figure 3.46 transformed into a calibration length-scale. The second calibration length-scale was the final length scale at the end of the experiment. Because the camera situated above the tank recorded fewer images than the one on the side, the end of the experiment was defined by image 1040 for both recordings. From image 1040 the distance in pixels that the flow had travelled from the source was determined. Using these distances, the length-scales at the source, and the equations from the least-squares fit lines from the data in Figure 3.46, four equations with four unknown were determined. These equations were solved simultaneously and the results were the distances from the cameras to the end points of the flow and the corresponding calibration length-scales. The two transformed average integrated concentration images were both analysed in MatLab. The results from the MatLab analysis for both the *y*-direction and the *z*-direction

were then combined using an iterative process to determine the results at intermediate locations. The iterative process reduced the error due to the inaccuracies in the length-scales at any point of the flow to less than 1%.

3.2.4.3 – Verification of 3D LA system

The first experiment testing the 3D LA system was a simple jet experiment. The Reynolds number of the flow was 3479, the source diameter 2.45 millimetres and the initial velocity 1.42m/s. As the flow is axi-symmetric in the mean the results were expected to be the same from both cameras. Figure 3.47 shows the concentration spread results for both the *y*-integrated and *z*-integrated results. The two data series match each other and the theoretical prediction very well, indicating that the correct length-scales were used in both directions. Figure 3.48 shows the integrated dilution results of the same experiment. Again the two data series collapse onto the same line, the theoretical prediction is slightly lower as explained in 3.2.3.1. The collapse of the integrated dilution results indicates that the field calibration for both the horizontal and vertical direction was successful.

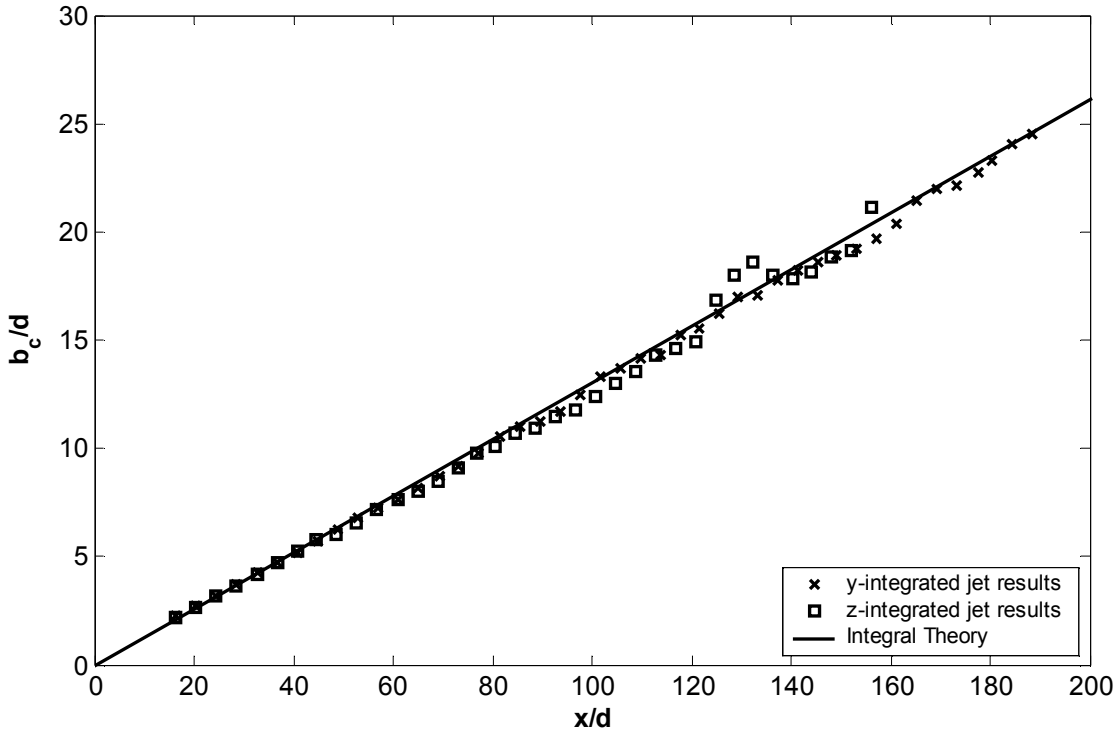

Figure 3.47 – Concentration spread results for *y* and *z*-integrated simple jet experiment

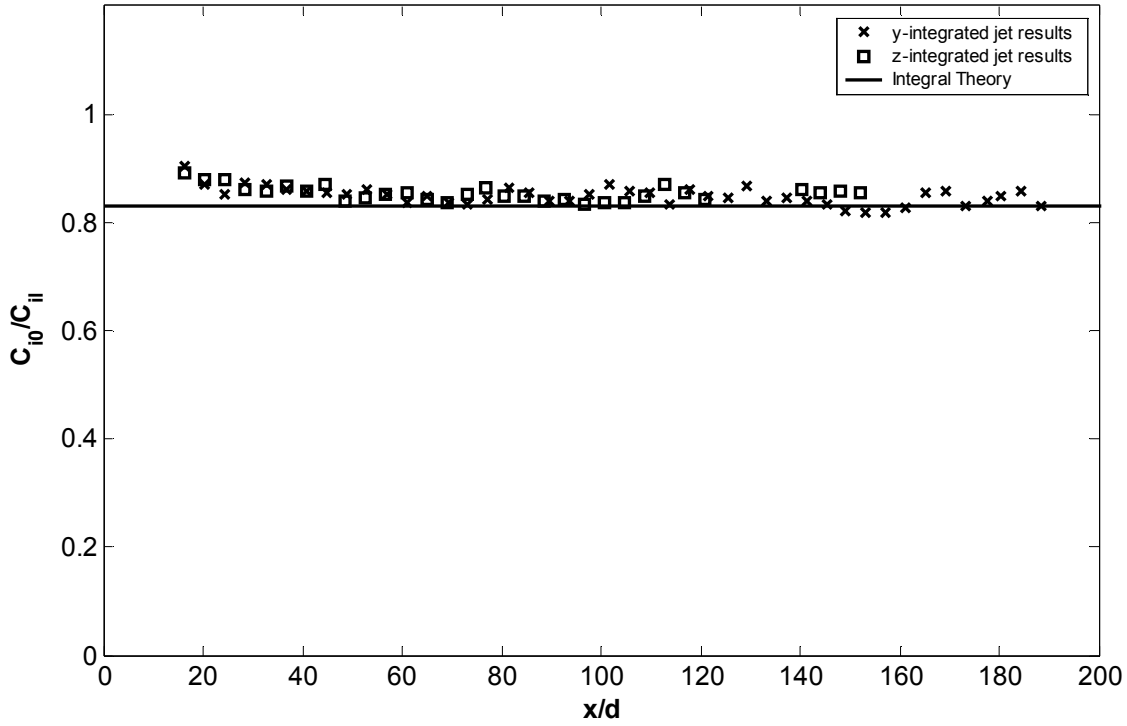

Figure 3.48 – Integrated dilution results for *y* and *z*-integrated simple jet experiment

Here again the vertically discharged momentum puff is used as an example of a strongly advected flow. These flows are no longer axi-symmetric, however the double integrated dilution results are still expected to be the same for both in the *y* and the *z*-directions when the ambient momentum flux is dominating the flow. Figure 3.49 shows the double integrated dilution results for a vertically discharged momentum puff recorded in both the *y* and the *z*-direction. The Reynolds number of the flow was 4340, the velocity ratio 0.029 and the source diameter 2.45 millimetre. Up to a non-dimensional vertical distance of two, the results are very different. This can be explained by the source discharging the red-dye straight towards the *z*-integrated camera. The flow is still in the jet-like region and can therefore only be properly analysed with the *y*-integrated data. However with the influence of the ambient momentum flux growing, the flow becomes more bent over and thus flows more parallel to the camera recording the *z*-integrated view. The error due to the assumption of horizontal cross-sectional profiles is negligible by a non-dimensional vertical distance of 2.5, as at that point the double integrated dilutions of the two different viewpoints match. This happens in the middle of the transition zone from jet to puff. The transition zone is not complete until a non-dimensional vertical distance of approximately 3.5. The three-dimensional trajectory flows are constantly moving towards or away from the camera, and both cameras will be recording views similar to the *z*-integrated momentum puff view. The results from this *z*-

integrated momentum puff experiment show that the three-dimensional trajectory flows can also be analysed quantitatively with reasonable accuracy as long as the flow direction is predominantly perpendicular to the line of sight of the camera.

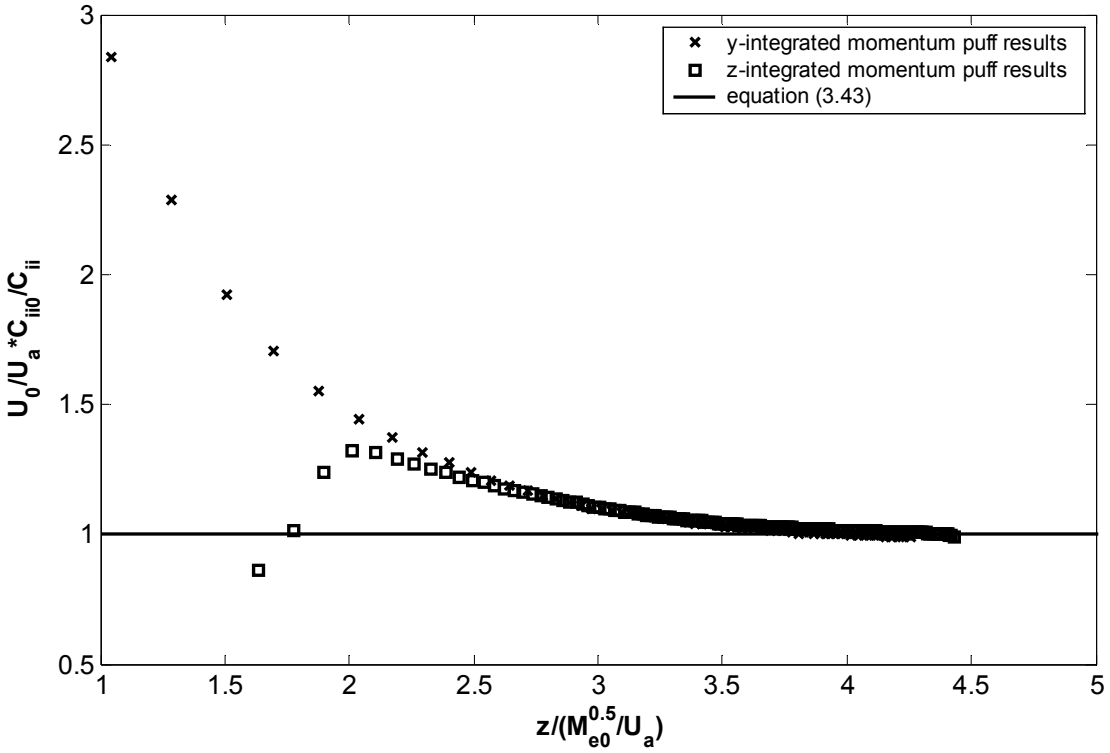

Figure 3.49 – Double integrated dilution results for *y* and *z*-integrated momentum puff experiment

3.2.5 - Summary

The Light Attenuation flow visualization technique is an alternative technique based on the relationship between the increase in dye concentration and the corresponding decrease of light intensity that reaches the camera. The technique can be applied to visualize buoyant jet flows with two- and three-dimensional trajectories and provides integrated concentration data for the flow as a whole. However, it cannot be used to directly acquire cross-sectional data.

The calibration experiments and the jet and puff experiments show that LA is a quantitative flow visualization technique that provides very good results with very little background noise and errors due to parallax. The main limitation is the relatively low upper limit of concentration of the red dye. In flow situations where high dilutions occur this upper limit could be a constraint on the accuracy of the data.

The results for the simple jet experiment show that LA can be used for weakly advected flows. For other weakly advected flows such as the plume and the buoyant jet the equations derived above have to be altered to incorporate the specific dilution rates of the flows. The same is true for the strongly advected flows such as the advected thermal. As both the advected flows as well as the angled jet show good agreement with the theory, LA can be confidently used for more complex flows with three-dimensional trajectories.

The challenge with LA is related to the fact that the internal concentration distribution has to be known to be able to calculate point dilutions. For weakly advected flows this was shown to be straightforward as the distribution is well documented, however this was not the case for strongly advected flows. The double-Gaussian approximation has been shown to be an effective representation of the distribution for strongly advected flows.

3.3 - LIF

The laser induced fluorescent flow visualization technique is an established technique to investigate buoyant jet flows with two-dimensional trajectories. In the present study the LIF system was employed for the investigation of negatively buoyant jets (see Chapter 6). The LIF system was used to provide comparisons with LA results and to also provide additional information on the flow structure.

The LIF system that was used during these experiments is described below in two parts. In the first part the equipment used and the experimental set up of the system are explained and in the second part the calibration method used is explained. Because it was only used for the investigation of negatively buoyant jets, the discussion of the system relates directly to those experiments.

3.3.1 – Laser Induced Fluorescent System

A schematic overview of the LIF system can be seen in Figure 3.50. The LIF experiments were carried out under controlled lighting conditions in a darkroom. The tank for these experiments had inside dimensions of (length x width x height) 1070mm x 1070mm x 610mm. The bottom of the tank was approximately 810mm above the floor. The source with a diameter of 2.45mm was set to the desired angle using a setsquare with a precision of 0.25°. The source fluid was stored in a 300 litre tank positioned approximately 2300mm above the end of the source. The source tank was connected to the source via a magnetic flow meter.

The Laser system used during the LIF experiments was a Millennia IIs, diode-pumped, cw Visible Laser, which has a maximum output of 2Watts at 532nm. The Laser Head was connected to a laser sheet generator via a fibre-optic cable. The maximum output from the cable was approximately 1 Watt. The laser sheet generator consisted of a cylindrical lens producing a non-uniform fan-like laser sheet. The laser sheet generator was set up in such a way that it was vertical, and in line with the centre of the source, therefore displaying the centreline of the flow during an experiment.

Before an experiment the storage tank was filled with 150 litres of water up to a precision of 0.05 litres (0.033%). Salt was added to the water to create a density difference of approximately 2.5%. The actual density difference was checked before and after a series of experiments with an Anton Paar density meter. The tracer was initially made up as two litres of Rhodamine 6G dye solution with a concentration of 50mg/l using distilled water. The weight of dye in the dyed solution was determined to a precision of 0.0001g (0.1%) and the volume of the solution to a precision of 0.7ml (0.035%). From the two litres of solution 400ml (precision 1ml or 0.25%) was added to the salt-water solution. When illuminated by the laser sheet the Rhodamine 6G fluorescent molecules emitted light with a wavelength of 590nm.

A 10-bit Pulnix 1010 DV digital video camera was used for recording the flows. For most of the experiments it was set up approximately 2.5 metres away from the side of the tank and perpendicular to the laser sheet. A Cosmicar/Pentax 50mm F/1.4 TV lens was attached to the camera while in that position. An alternative set up was used for recording non-vertical cross-sections of the flow. For those experiments the camera was positioned approximately one meter above the tank and set to an angle so that the camera was perpendicular to the recorded cross-section. The lens used was a Cosmicar/Pentax 25mm F/1.4 CCTV camera lens. At all times a Heliopan ES 46 filter was placed in front of the lens. This (532nm) filter reduced the amount of laser light reflected from particulate matter reaching the camera.

The camera recorded 1008x1008 pixels at a rate of 15Hz. The height of the camera was adjusted to be approximately in between the maximum and the minimum height of the flow. The camera was connected to the computer via a data-cable and a Bitflow video board. Due to the size of the 10-bit images, 888 images could be recorded per experiment. To increase the recording time and therefore the time over which an average was taken only every second or third image displayed was recorded.

A software based control programme, Pulnix TM-1010 Controller v1.02, was used to set the camera's manual parameters. The intensity signal of the 10-bit camera had a range between zero and 1023, where zero is black and 1023 saturation. The manual parameters were set so that the intensity of the camera was not saturated at any pixel, but still gave the largest practical range of intensity. For the LIF experiments the camera had an open shutter, the Gain was set to 50, the white-level (VRef) was set to 170, and the black-level (URef) to 70. The recorded images were analysed in ImageStream (Nokes 2005).

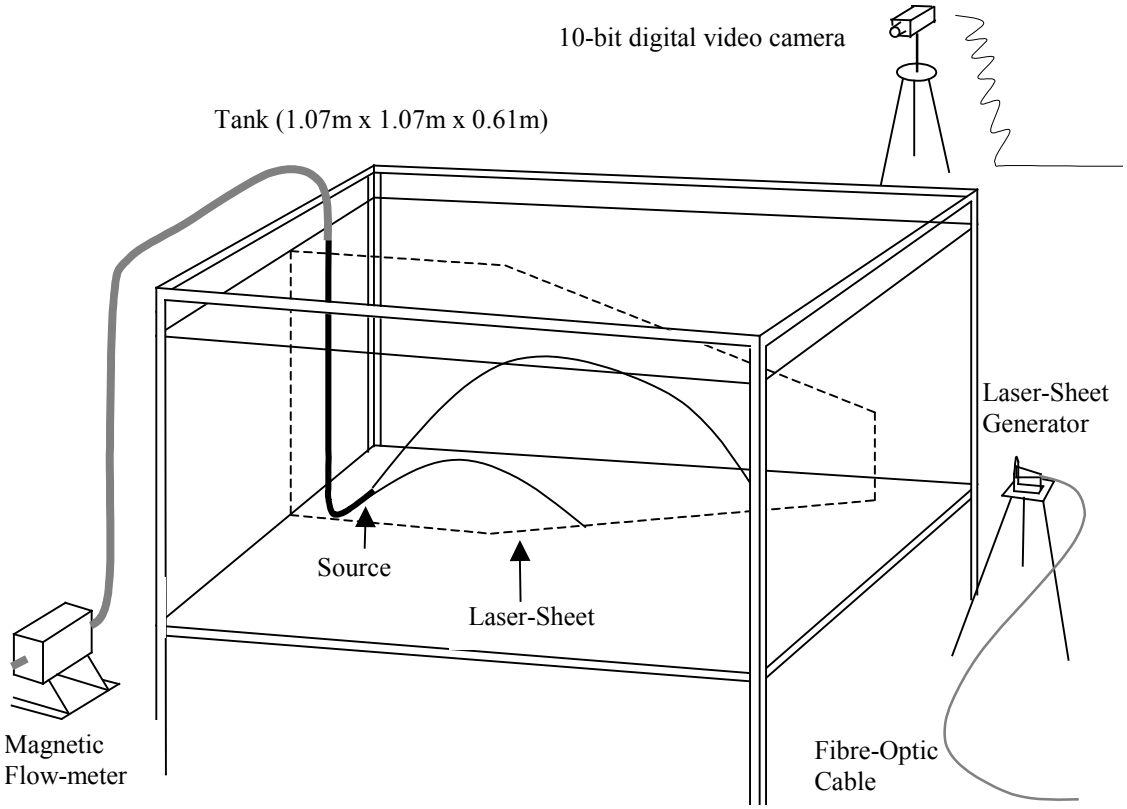

Figure 3.50 - LIF experimental set up

3.3.2 – LIF Calibration Methods

The LIF system was calibrated before each series of LIF experiments so the results from the experiments could give quantitative as well as qualitative information. The relationship between light intensity and Rhodamine dye concentration is linear (Pun 1998). However the response of the camera was non-linear and to correct for the camera response a multipoint calibration was carried out. Due to the fan-like appearance of the laser sheet, the light intensity of the sheet decreased with distance from the laser sheet generator. Therefore the system had to be calibrated for each pixel separately.

Before a series of experiments, the tank was filled with approximately 660l of water up to a precision of 0.05l. Then 175ml, ±1ml, of the Rhodamine 6G solution was stirred into the tank. When the dyed solution was uniformly mixed through the water the laser was turned on and set to the maximum setting of 2 Watts. A hundred images were recorded of the tank at this setting, then the output of the laser was reduced to 1.8 Watts and another hundred images

were recorded. This process was repeated until the output of the laser was 0 Watts. This gave eleven series of one hundred images that were transformed into eleven averaged images. These images were plotted versus their respective laser output and provided a field calibration for each pixel. The result of one pixel can be seen in Figure 3.51, note that the laser output has been non-dimensionalised by the maximum output. A second order polynomial was fitted through the data as it was found to better match the data than a linear fit, especially through the lower quarter of the data. The calibration error was within 4%. The second order polynomial at each pixel was used to transform the 10-bit intensity data into relative concentration data.

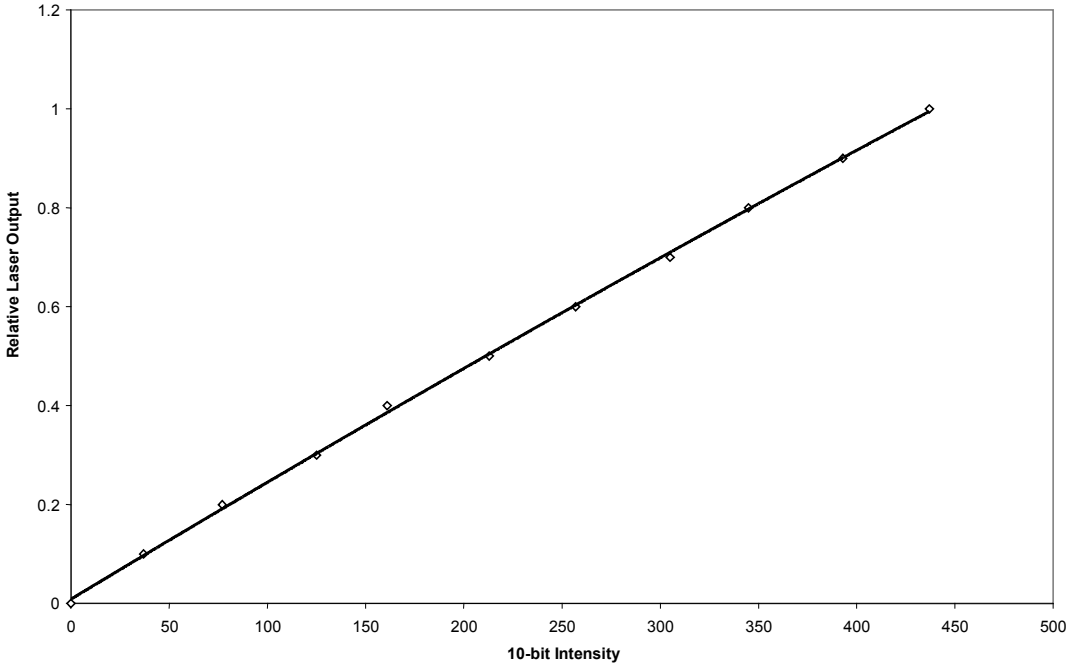

Figure 3.51 - Polynomial Field Calibration at pixel (178,196)

The relative concentration found after applying the polynomial field calibration to the raw data was converted into the actual concentration by multiplying the relative concentration by the ratio in concentration between the source fluid and the concentration of the fluid during the recording of the calibration images. This was found in two different ways. The first was to calculate the concentration of Rhodamine 6G dye in the source fluid and divide it by the calculated value for the concentration of dye in the tank during calibration. The second method was using the TD-700 Laboratory Fluorometer. The Fluorometer was firstly calibrated so that no sample exceeded the value 999 and water with no fluorescent dye gave a value of zero. Then a sample from both the source fluid as well as the tank (during calibration) was taken and inserted into the fluorometer. The respective values were noted and

the first was divided by the second. The fluorometer experienced drift and hence each sample had to be referenced to a zero value. The error involved in comparing the values from the two methods was approximately 6%. As the concentration of fluorescent dye is known to decrease over time when mixed in tap-water (Pun 1998), a sample was taken from the source fluid every day.

3.3.3 – Summary

The LIF system as used during the negative buoyant jet experiments is presented above. The error due to the second order polynomial assumption is of the same order as the error in the LA system when determining relative concentrations. However this is increased when the actual concentration values are calculated. The results of the negative buoyant jet experiments can be found in chapter 6.

Chapter 4 – Momentum Model

4.1 - Introduction

To assist in the design and to monitor the performance of the experiments a new numerical model was set up. The new model also provided the opportunity to independently confirm parameters currently used to model buoyant discharges, as well as the ability to isolate issues that required more detailed investigations. The model is referred to as the Momentum Model and is based on the integral approach, similar to VisJet (Cheung et al. 2000) and CorJet (Jirka 2004). However unlike the other models, the behaviour of the discharge at any particular location is determined by the relative magnitudes of three distinct forms of momentum flux. The three distinct forms of momentum flux are the entrained ambient momentum flux per unit density, M_a, the buoyancy-generated momentum flux per unit density, M_b, and the initial momentum flux per unit density, M_0. Hereafter the momentum flux per unit density is referred to as the momentum flux. Employing momentum fluxes to determine the behaviour of the flow is both simplistic and physically consistent with the real flow. It therefore potentially gives a greater insight into the behaviour of the flow. Nine differential equations are set up in MatLab, and the set of equations is closed by the spread assumption. An ODE-solver is employed to solve the ten differential equations simultaneously. A comparison between the Momentum Model and previous experimental studies is carried out to confirm the accuracy of the new model. The results of this comparison can be found in Chapter 5.

4.2 – Model Configuration and Initial Conditions

A coordinate system is defined so that the ambient fluid (U_a) flows in the same direction as the *x*-axis (Figure 4.1). The *z*-axis is defined to be in line with the buoyancy force and thus vertical. As the ambient flow is assumed to flow horizontally or perpendicular to the buoyancy force, the y-axis can be defined as perpendicular to both the ambient flow and the buoyancy force. The direction of the initial momentum flux is related to the coordinate system by angles α_0 and β_0. The angle α_0 is defined in the z-M_0 plane, that is, between the initial

momentum flux and its projection in the *x*-*y* plane $\left(M_0^{'}\right)$. The second angle, β_0, is the angle in the x-y plane between $M_0^{'}$ and the x-axis.

Further downstream, away from the source, M_s is the total momentum flux at a distance *s* from the source along the trajectory of the flow. This total momentum flux is calculated by taking into account the magnitudes of the different forms of momentum flux. The direction of the total momentum flux is related to the coordinate system by angles α and β. Angle α is the angle between the total momentum flux and its projection in the x-*y* plane. Angle β is the angle between this projection of the total momentum flux and the ambient momentum flux.

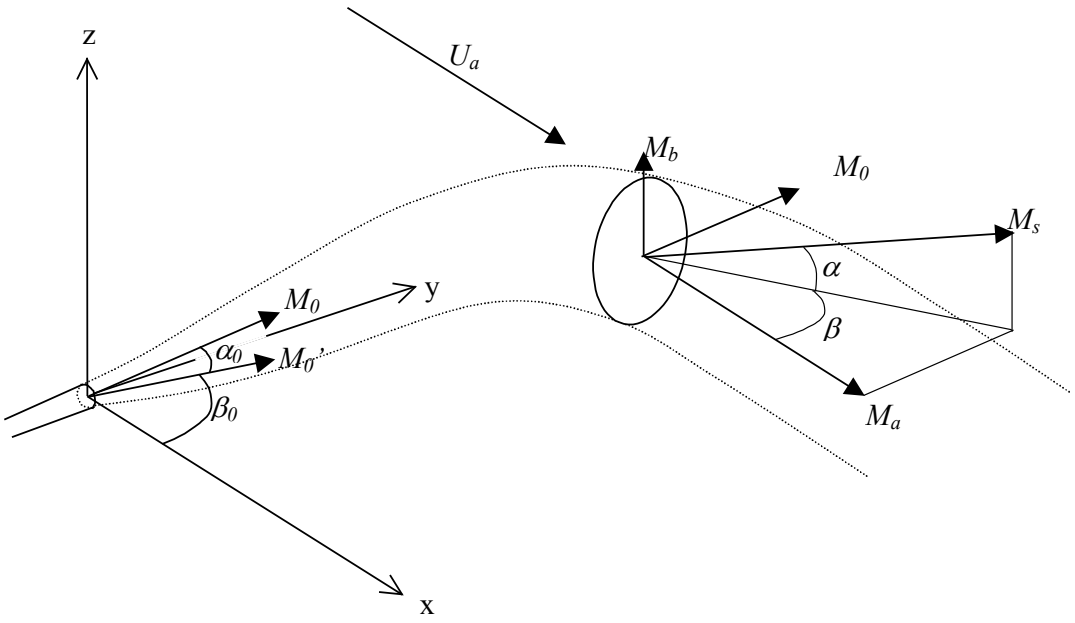

Figure 4.1 – Schematic diagram of coordinate system of Momentum Model

The entrained ambient momentum flux, M_a, and the initial momentum flux, M_0 are defined as follows:

$$M_a = U_a Q_\alpha \quad \text{where } Q_\alpha = Q - Q_0 \tag{4.1}$$

$$M_0 = U_0 Q_0 = U_0^{\,2} \frac{d^2}{4}\pi \tag{4.2}$$

where Q is the flow rate. The initial zone of establishment has not been modelled due to its negligible effect on the flow away from the source.

An excess momentum flux, M_e, is calculated as well. This excess momentum flux represents the initial plus buoyancy-generated momentum fluxes in excess of the entrained ambient

momentum flux (Figure 4.2). Angle ϕ is the angle between the excess momentum flux and the ambient momentum flux. The initial excess momentum flux (Figure 4.3) includes the assumption that coflowing discharges are immediately aware of the ambient flow (a jet only forms because of the initial excess velocity), but cross-flowing discharges are not aware of the ambient flow until ambient fluid is entrained. The initial excess momentum flux can therefore be written as:

$$M_{e0} = U_0 Q_0 - U_a Q_0 \cos(\phi_0) \tag{4.3}$$

and $$\phi_0 = \cos^{-1}\left[\cos(\alpha_0)\cos(\beta_0)\right] \tag{4.4}$$

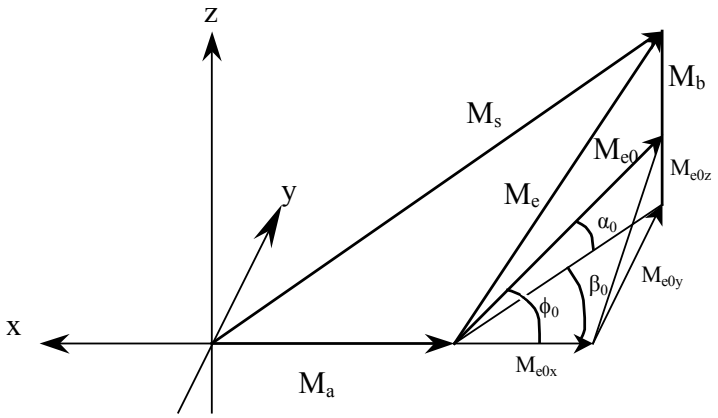

Figure 4.2 - Schematic diagram of excess momentum flux

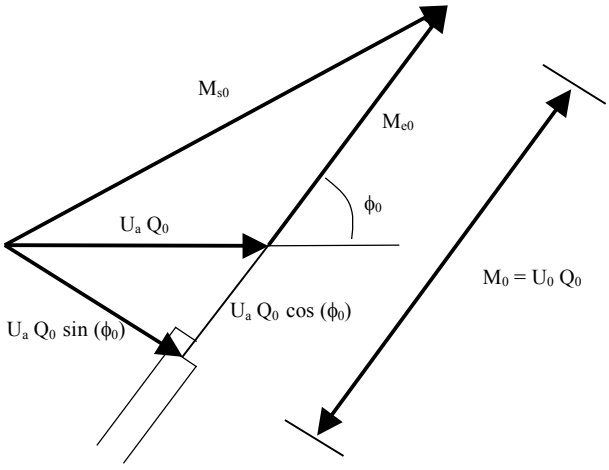

Figure 4.3 - Schematic diagram of the initial excess momentum flux discharge configuration

The initial excess momentum flux can be split up into three different vectors in the *x*, *y* and *z* direction respectively using angles α_0 and β_0. This is shown in Figure 4.2.

$$M_{e0x} = \left[U_0 Q_0 - U_a Q_0 \cos(\phi_0)\right] \cdot \cos(\alpha_0)\cos(\beta_0) \tag{4.5}$$

$$M_{e0y} = \left[U_0 Q_0 - U_a Q_0 \cos(\phi_0)\right] \cdot \cos(\alpha_0)\sin(\beta_0) \tag{4.6}$$

$$M_{e0z} = \left[U_0 Q_0 - U_a Q_0 \cos\left(\phi_0\right)\right] \cdot \sin\left(\alpha_0\right) \tag{4.7}$$

Applying the same assumption as for the initial excess momentum flux, the initial ambient momentum flux is given by

$$M_{a0} = U_a Q_0 \cos\left(\phi_0\right) \tag{4.8}$$

Assuming there is no significant drag on the buoyant fluid, the momentum flux of the flow increases with distance downstream because of increases in the entrained ambient momentum flux and the buoyancy-generated momentum flux.

4.3 – Ordinary Differential Equations

Six parameters are needed to describe the behaviour of the flow at any particular location. The *x*, *y* and *z* coordinates give the location of the flow centreline, *b* is spread of the flow, *Q* the volume flux of the flow and *Δ* the buoyancy at the particular location. In addition four different forms of momentum fluxes, that indicate the flow condition, are determined, that is, the entrained ambient momentum flux, the buoyancy-generated momentum flux, the excess momentum flux and the total momentum flux, giving ten unknowns. To solve the problem in this form, ten equations are needed. These ten equations are set up as ordinary differential equations with respect to the step-size, *s*, along the flow trajectory and rewritten in dimensionless form. The velocity and the concentration in a cross-section of the flow are assumed to have top-hat distributions.

4.3.1 – Deriving Equations

The equations for the location of the flow centreline can be derived by comparison of the different forms of momentum flux in a particular direction to the total momentum flux at a specific location. The relative change in the *x*-direction along the trajectory is equal to the momentum flux in the *x*-direction over the total momentum flux. There are two possible sources of momentum flux in the *x*-direction, the entrained ambient momentum flux and the initial excess momentum flux in the *x*-direction. The change in the *y*-direction with respect to the step-size is equal to the momentum flux in the *y*-direction over the total momentum flux. There is only one possible source of momentum flux in the *y*-direction, the initial excess momentum flux in that direction. In the *z*-direction there are again two possible sources of

momentum flux, the buoyancy-generated momentum flux and the initial excess momentum flux in the *z*-direction. This gives the following equations for the change in location due to a step along the trajectory.

$$\frac{\Delta x}{\Delta s} \approx \frac{M_x}{M_s} = \frac{M_{e0x} + M_a}{M_s} \tag{4.9}$$

$$\frac{\Delta y}{\Delta s} \approx \frac{M_y}{M_s} = \frac{M_{e0y}}{M_s} \tag{4.10}$$

$$\frac{\Delta z}{\Delta s} \approx \frac{M_z}{M_s} = \frac{M_{e0z} + M_b}{M_s} \tag{4.11}$$

Letting the step-size approach zero gives the ordinary differential equations for the location of the flow.

$$\frac{dx}{ds} = \frac{M_{e0x} + M_a}{M_s} \tag{4.12}$$

$$\frac{dy}{ds} = \frac{M_{e0y}}{M_s} \tag{4.13}$$

$$\frac{dz}{ds} = \frac{M_{e0z} + M_b}{M_s} \tag{4.14}$$

The buoyancy-generated momentum flux can be calculated by determining the buoyancy force. The buoyancy force is generated by the density deficit Δ (also known as reduced gravity), and can be calculated as

$$\Delta = \frac{(\rho_a - \rho)}{\rho} g \tag{4.15}$$

The change in buoyancy-generated momentum flux is then given by:

$$\Delta M_b \approx \Delta \cdot b^2 \pi \cdot \Delta s \tag{4.16}$$

Dividing both sides by Δs and letting the step-size go to zero gives the ODE for the buoyancy-generated momentum flux.

$$\frac{dM_b}{ds} = \pi \Delta b^2 \tag{4.17}$$

The conservation of density deficit, the mass flux relationship, shows that there cannot be a change in the total amount of buoyancy flux in the flow. Therefore

$$\frac{d(\Delta Q)}{ds} = 0 \tag{4.18}$$

where Q is the total volume flux of the flow. The product in equation (4.18) can be split up into two parts

$$Q\frac{d\Delta}{ds}+\Delta\frac{dQ}{ds}=0 \tag{4.19}$$

Rearranging the above equation gives the fifth ODE, the change in buoyancy with distance downstream

$$\frac{d\Delta}{ds}=-\frac{\Delta}{Q}\frac{dQ}{ds} \tag{4.20}$$

The change in volume flux along the trajectory of the flow can be found by relating the total volume flux to the total momentum flux.

$$M_s=\pi U^2b^2=\frac{Q^2}{\pi b^2} \tag{4.21}$$

or

$$Q^2=M_sb^2\pi \tag{4.22}$$

Differentiating both sides of the equation with respect to the distance along the trajectory, s, and rearranging gives the sixth ODE, which describes the change in volume flux:

$$\frac{dQ}{ds}=\frac{\pi b^2}{2Q}\frac{dM_s}{ds}+\frac{\pi M_sb}{Q}\frac{db}{ds} \tag{4.23}$$

The total momentum flux is equal to the square root of the momentum fluxes in the x, y and z-direction squared. The ODE for the second of the four different kinds of momentum flux, M_s, can be found by a differentiation with respect to s of that relationship

$$\frac{dM_s}{ds}=\frac{1}{2}\frac{1}{\sqrt{\left(M_x{}^2+M_y{}^2+M_z{}^2\right)}}\frac{d}{ds}\sqrt{\left(M_x{}^2+M_y{}^2+M_z{}^2\right)} \tag{4.24}$$

or

$$\frac{dM_s}{ds}=\frac{M_x}{M_s}\frac{dM_x}{ds}+\frac{M_y}{M_s}\frac{dM_y}{ds}+\frac{M_z}{M_s}\frac{dM_z}{ds} \tag{4.25}$$

The change in momentum flux in the x-direction will solely be caused by the change in entrained ambient momentum flux, as the initial excess momentum flux in the x-direction is constant. As the initial excess momentum flux is the only momentum in the y-direction, there will be no change in momentum flux in the y-direction and the change in the z-direction will be caused by the change in buoyancy-generated momentum flux. Therefore the ODE for the total momentum flux becomes

$$\frac{dM_s}{ds}=\frac{\left(M_{e0x}+M_a\right)}{M_s}\frac{dM_a}{ds}+\frac{\left(M_{e0z}+M_b\right)}{M_s}\frac{dM_b}{ds} \tag{4.26}$$

Figure 4.2 can be used to find the ODE for the excess momentum flux. It shows that the total excess momentum flux is equal to the square root of the excess momentum fluxes in the *x*, *y* and *z*-directions. In both the *x* and *y*-directions the only excess momentum flux is the initial excess momentum flux, in the *z*-direction the excess momentum flux is the initial excess momentum flux plus the buoyancy-generated momentum flux . Differentiating both sides with respect to *s* gives

$$\frac{dM_e}{ds} = \frac{1}{2} \frac{1}{\sqrt{\left({M_{e0x}}^2 + {M_{e0y}}^2 + \left(M_{e0z} + M_b \right)^2 \right)}} \frac{d}{ds} \sqrt{\left({M_{e0x}}^2 + {M_{e0y}}^2 + \left(M_{e0z} + M_b \right)^2 \right)} \quad (4.27)$$

or

$$\frac{dM_e}{ds} = \frac{\left(M_b + M_{e0z} \right)}{M_e} \frac{dM_b}{ds} \quad (4.28)$$

The ODE for the entrained ambient momentum flux can be found by differentiating equation (4.1) with respect to the distance along the trajectory

$$\frac{dM_a}{ds} = U_a \frac{dQ}{ds} \quad (4.29)$$

4.3.2 – Spread Relationships

The final differential equation cannot be derived. The spread equation is based on the spread assumption and it is used to solve the closure problem of turbulence (see section 2.5.2). It uses experimentally determined spread ratios to predict the flow spread at a given location. There are essentially three forms of the spread relationship. One is for Gaussian flows and has the following form (Wang 2000b):

$$\frac{db}{ds} = k \frac{U_e}{1.55U_a + U_e} \quad (4.30)$$

where U_e is the centreline excess velocity. The relationship adequately predicts the spreading rates of the weakly advected flows (jet and plumes) where it becomes:

$$\frac{db_{jp}}{ds} = k \quad (4.31)$$

The relevant strongly advected Gaussian flow is the weak-jet and equation (4.30) reduces to the following in this region

$$\frac{db_{wj}}{ds} = k \frac{U_e}{1.55U_a} \quad (4.32)$$

In employing equation (4.30) the assumption is made that in the weak-jet region the initial excess momentum flux rather than the horizontal component of the initial excess momentum flux is the dominant parameter. This assumption has not been verified by experimental evidence. However, the maximum difference in spreading rates is 6% for a discharge angle of 25°, and the difference reduces with the decrease of angle ϕ further downstream. For larger discharge angles a weak-jet is not expected to form (see Chapter 7).

The second spread relationship has been developed (from the standard spread equation used by models, db/dz = m) for the strongly advected line momentum puff region and is based on the double-Gaussian assumption. It has the form:

$$\frac{db_m}{ds} = k_{sg-m}\frac{ds_{yz}}{ds} = k_{sg-m}\left(\frac{y}{\sqrt{y^2+z^2}}\frac{dy}{ds} + \frac{z}{\sqrt{y^2+z^2}}\frac{dz}{ds}\right) \tag{4.33}$$

where s_{yz} is the distance travelled along the projection of the direction of the initial discharge in the *y*-*z* plane. The third spread relationship has been developed for the strongly advected thermal region and has the form:

$$\frac{db_t}{ds} = k_{sg-t}\frac{dz}{ds} \tag{4.34}$$

Note that the experimental results in Chapter 5 indicate that the spreading rate in the advected line momentum puff region of the flow is not equal to the spreading rate in the advected thermal region. Hence the need for separate values for the spreading rate in the momentum puff region ($k_{sg\text{-}m}$) and thermal region ($k_{sg\text{-}t}$).

However these spread relationships were determined using the Gaussian (see 3.2.3.1) or double-Gaussian assumption (see 3.2.3.2). As the velocity and concentration distributions for the Momentum Model were assumed to be top-hat and hence based on the top-hat spread, the values for *k* and k_{sg} (as defined in Chapter 3), have to be converted to be used with the top-hat assumption (k_{th} and m_{th}). Details of these conversions are given in section 4.4. Furthermore, the centreline excess velocity in equation (4.30) has to be converted into the average excess velocity. The conversion equations for the weak-jet region are equations (4.67) and (4.68). Inserting equation (4.68) into (4.67) and solving for the centreline excess velocity gives:

$$U_e = \frac{\pi\beta_{wj}^{\ 2}}{I_q}U_{eth} = \frac{\pi\beta_{wj}^{\ 2}}{I_q}\frac{M_e}{Q} \tag{4.35}$$

where U_{eth} is the average excess velocity, and β_{wj} represents the ratio of the jet edge radius to the nominal radius and has a value of $\sqrt{2}$ (see Chapter 7 for more details). The spread

relationships, using the parameters as defined above, including the assumptions that a jet in a cross-flow is not immediately aware of the ambient flow, and the top-hat conversions, become

$$\frac{db_{th}}{ds} = k_{th}\frac{\pi\beta_{wj}{}^2 M_e}{I_q Q}\frac{1}{\frac{\pi\beta_{wj}{}^2 M_e}{I_q Q} + 1.55U_a\cos\phi_0} = k_{th}\frac{M_e/Q}{\frac{M_e}{Q} + \frac{1.55}{\beta_{wj}{}^2}U_a\cos\phi_0} \tag{4.36}$$

$$\frac{db_{th-m}}{ds} = m_{th-m}\left(\frac{y}{\sqrt{y^2+z^2}}\frac{dy}{ds} + \frac{z}{\sqrt{y^2+z^2}}\frac{dz}{ds}\right) \tag{4.37}$$

$$\frac{db_{th-t}}{ds} = m_{th-t}\frac{dz}{ds} \tag{4.38}$$

In the Momentum Model the application of the relevant spread relationships per region is determined by the relative magnitudes of the momentum fluxes, that control the flow behaviour, and in one instance the initial discharge angle. Table 4.1 shows the momentum flux ratios and corresponding relationships for the regions that are of interest in terms of the spread equation. Therefore only regions before a transition zone are listed.

The momentum flux ratios defined in Table 4.1 are functions of the distance from the source. The momentum flux ratios increase with increasing distance, and at some point the ratio exceeds the transition constant and the flow enters a different region. These transition constants are represented by the symbols c_2 to c_6. Note that the physical transitions are not abrupt, but a transition between region exists. The current approach is an approximation for modelling purposes only. Setting the momentum flux ratios equal to the transition ratios and solving for the distance from the source gives the length-scales in the centre column of Table 4.2. These derived length-scales are compared with the length-scales determined by Pun (1998) using dimensional analysis (column 3, Table 4.2). The exception is the transition from the advected line momentum puff to the advected thermal, where Pun's length-scale was not obtained directly from length-scale analysis, but was obtained from the constraints of a constant momentum flux, dilution, velocity and spread at the transition point. By combining the two results, the constants c_2 to c_6 can be determined. The results can be seen in Table 4.3. The constants C_{sm}, C_{sp}, C_{pt} C_{wt} and C_{mt} come from experimental work and are set to 1, 2.3, 0.5 1.1 and 1.35 respectively (Pun 1998). The transition point between the strong jet and weak jet region has not been calculated because the spread function, as defined by equation (4.35),

automatically changes the spread depending on the relative sizes of both the excess centreline, and the ambient velocity.

Each scenario starts in the strong-jet region. With the first region known, the relevant momentum flux ratios in that region are calculated at each step. If any of the ratios exceeds the value of the transition constants, the flow region changes, and the spread function changes accordingly. If no transition ratios are exceeded the current spread function is retained.

The initial discharge angle (ϕ_0) adds an additional complexity to the strong-jet region. The strongly advected behaviour of a non-buoyant jet discharge in a moving ambient is dependent on the initial discharge angle. For angles close to 90° the strong-jet turns into an advected line momentum puff, for angles close to 0°, the strong-jet turns into a weak-jet. As the discharge angle at which the strongly advected form changes is not known (Pun 1998), an experimental investigation was carried out to determine the angle. Details of the investigation are presented in Chapter 7. Based on this study, the Momentum Model uses a transition discharge angle of 25°.

By comparing the results from the momentum flux analysis with the results from the dimensional analysis for the strong-jet to advected line momentum puff transition it can be noted that c_2 appears to depend on the initial discharge angle. Pun assumed that the dominant parameter in the puff region was the component of the initial excess momentum flux perpendicular to the ambient flow. The results presented in Chapter 7 indicate that this assumption is correct and that the initial discharge angle cannot be ignored. In Table 4.3 the relevant momentum flux ratio has been modified accordingly. Interestingly, Table 4.3 shows that a transition involving the entrained ambient momentum flux is triggered when the momentum flux ratio is approximately one-third, whereas a transition involving the buoyancy-generated momentum flux is triggered when the momentum flux ratio is closer to one.

Using the momentum flux ratios, a spread function flow chart can be set up to show all possible paths through the different flow regions (Figure 4.4). Note that there is no distinct separation between the strong-jet and weak-jet regions, and there is no direct path from the weak-jet region to the advected thermal region. The momentum flux ratio determining the transition from strong-jet to advected plume region is the same as the momentum flux ratio determining the transition from the weak-jet to advected thermal region. The value of the

momentum flux ratio at the transition of the former is lower than that for the latter, and hence a flow in the weak-jet region automatically enters the advected plume region after such a transition. However in moving from the weak-jet region, the flow has already entrained a significant amount of ambient fluid. Therefore the flow immediately exceeds the transition ratio in the advected plume region and enters the advected thermal region.

Table 4.1 - Dominant momentum flux ratios per flow region

Current Flow Region	Dominant Momentum Flux Ratio	Flow Region After Transition
Strong Jet	$\frac{M_a}{M_{e0}} \approx \frac{U_a d}{M_{e0}^{0.5}} \pi^{0.5} k_{th} \frac{s}{d} = c_2$	Advected Line Momentum Puff
	$\frac{M_b}{M_{e0}} = \frac{\Delta_0 d^3}{4 M_{e0}} \pi k_{th} \left(\frac{x}{d} \right)^2 = c_3$	Advected Plume
Advected Plume	$\frac{M_a}{M_b} \approx \left(\frac{16}{3} k_{th}^{\,2} \frac{U_a^{\,3}}{U_0^{\,3}} Fr_0^{\,2} \right)^{1/3} \frac{z}{d}^{1/3} = c_4$	Advected Thermal
Weak Jet	$\frac{M_b}{M_{e0}} = \frac{\Delta_0 d}{U_a U_{e0}} \frac{s}{d} = c_5$	Advected Thermal
Advected Line Momentum Puff	$\frac{M_b}{M_{e0}} = \frac{\Delta_0 d}{U_a U_{e0}} \frac{s}{d} = c_6$	Advected Thermal

Table 4.2 - Transition length-scales for relevant flow transitions

Flow region transition	Momentum flux analysis	Dimensional analysis
Strong Jet – Advected Line Momentum Puff	$\frac{s}{d} = c_2 \frac{1}{\pi^{0.5} k_{th}} \frac{M_{e0}^{\,0.5}}{U_a d}$	$\frac{s}{d} = c_{sm} \frac{M_{e0}^{\,0.5}}{U_a d} \lvert \sin \phi_0 \rvert$
Strong Jet – Advected Plume	$\frac{s}{d} = \sqrt{c_3 \frac{2}{\sqrt{\pi} k_{th}}} \frac{M_{e0}^{\,0.75}}{(Q_0 \Delta_0)^{0.5} d}$	$\frac{s}{d} = c_{sp} \frac{M_{e0}^{\,0.75}}{(Q_0 \Delta_0)^{0.5} d}$
Advected Plume – Advected Thermal	$\frac{z}{d} = c_4^{\,3} \frac{3}{4 \pi k_{th}} \frac{Q_0 \Delta_0}{U_a^{\,3} d}$	$\frac{z}{d} = c_{pt} \frac{Q_0 \Delta_0}{U_a^{\,3} d}$
Weak Jet – Advected Thermal	$\frac{s}{d} = c_5 \frac{M_{e0} U_a}{Q_0 \Delta_0 d}$	$\frac{s}{d} = c_{wt} \frac{M_{e0} U_a}{Q_0 \Delta_0 d}$
Advected Line Momentum Puff – Advected Thermal	$\frac{s}{d} = c_6 \frac{M_{e0} U_a}{Q_0 \Delta_0 d}$	$\frac{s}{d} = c_{mt} \left(\frac{\left[M_{e0} \lvert \sin \phi_0 \rvert \right]^2}{Q_0 \Delta_0 U_a} \right)^{1/3}$

Table 4.3 – Momentum flux ratio at flow transition for relevant flow transition

Flow region transition	Momentum flux ratio
Strong Jet – Advected Line Momentum Puff	$\frac{M_a}{M_{e0}\sin(\phi_0)} = \pi^{0.5} k_{th} c_{sm} = 0.255$
Strong Jet – Advected Plume	$\frac{M_b}{M_{e0}} = \left(\frac{\pi}{4}\right)^{0.5} k_{th} C_{sp}{}^2 = 0.673$
Advected Plume – Advected Thermal	$\frac{M_a}{M_b} = \left(\frac{4\pi}{3} k_{th}{}^2 C_{pt}\right)^{1/3} = 0.351$
Weak Jet – Advected Thermal	$\frac{M_b}{M_{e0}} = C_{wt} = 1.1$
Advected Line Momentum Puff – Advected Thermal	$\frac{M_b}{M_{e0}}\left(\frac{M_{e0} U_a{}^4}{\left[Q_0 \Delta_0 \lvert\sin\phi_0\rvert\right]^2}\right)^{1/3} = C_{mt} = 1.35$ or $\frac{M_b}{M_{e0}} = \left(\frac{\left[Q_0 \Delta_0 \lvert\sin\phi_0\rvert\right]^2}{M_{e0} U_a{}^4}\right)^{1/3} C_{mt} = c_7 C_{mt} = 1.35 c_7$

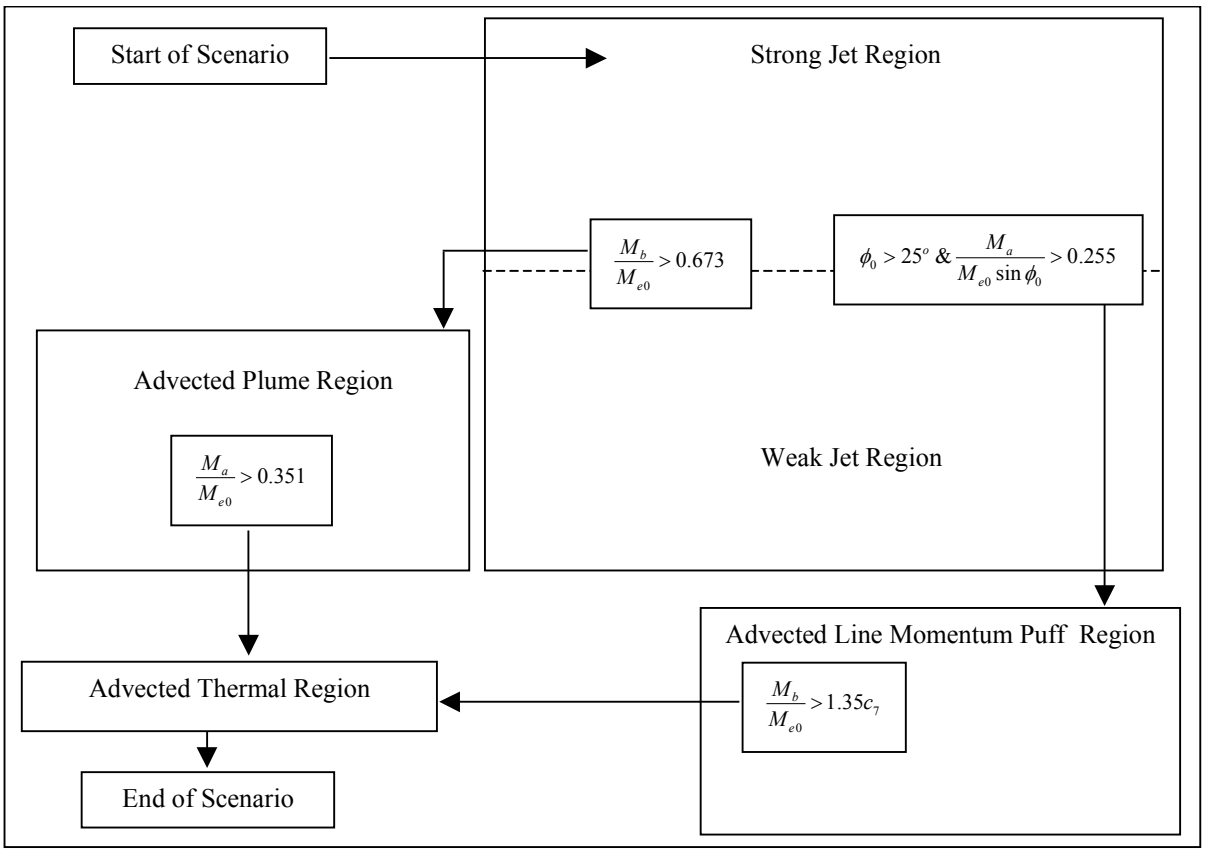

Figure 4.4 – Momentum Model spread function flow chart

4.3.3 – Dimensionless ODEs

Before the equations are entered into MatLab they are first non-dimensionalised. This eases the interpretation of the results when comparing them with either results from other models or experimental data. To make the equations dimensionless the following dimensional scales are used. The length scale is the diameter of the source, *d*, the velocity scale is the initial velocity of the flow, U_0, the discharge scale is the initial volume flux of the flow, Q_0, the momentum flux scale is the initial momentum flux, M_0, and the buoyancy scale is the initial density deficit, Δ_0. The subscript * indicates the non-dimensional variables

The geometric relationships become:

$$\frac{dx_*}{ds_*} = \frac{M_{e0x*} + M_{a*}}{M_{s*}} \tag{4.39}$$

$$\frac{dy_*}{ds_*} = \frac{M_{e0y*}}{M_{s*}} \tag{4.40}$$

$$\frac{dz_*}{ds_*} = \frac{M_{e0z*} + M_{b*}}{M_{s*}} \tag{4.41}$$

The buoyancy-generated momentum flux:

$$\frac{dM_{b*}}{ds_*} = \frac{4}{Fr_0^{\,2}} \Delta_* b_*^{\,2} \tag{4.42}$$

where Fr_0 is the initial Froude number of the flow defined by

$$Fr_0 = \frac{U_0}{\sqrt{\Delta_0 d}} \tag{4.43}$$

The density-deficit flux:

$$\frac{d\Delta_*}{ds_*} = -\frac{\Delta_*}{Q_*}\frac{dQ_*}{ds_*} \tag{4.44}$$

The spread:

$$\frac{db_{th*}}{ds_*} = k_{th}\frac{M_{e*}/Q_*}{\frac{M_{e*}}{Q_*}+\frac{1.55}{\beta_{wj}^{\ 2}}U_{a*}\cos\phi_0}$$

$$\frac{db_{th-m*}}{ds_*} = m_{th-m}\left(\frac{y_*}{\sqrt{y_*^{\ 2}+z_*^{\ 2}}}\frac{dy_*}{ds_*}+\frac{z_*}{\sqrt{y_*^{\ 2}+z_*^{\ 2}}}\frac{dz_*}{ds_*}\right) \tag{4.45}$$

$$\frac{db_{th-t*}}{ds_*} = m_{th-t}\frac{dz_*}{ds_*}$$

The entrained ambient momentum flux:

$$\frac{dM_{a*}}{ds_*} = U_{a*}\frac{dQ_*}{ds_*} \tag{4.46}$$

The excess momentum flux:

$$\frac{dM_{e*}}{ds_*} = \frac{\left(M_{b*}+M_{e0z*}\right)}{M_{e*}}\frac{dM_{b*}}{ds_*} \tag{4.47}$$

The total momentum flux:

$$\frac{dM_{s*}}{ds_*} = \frac{\left(M_{e0x*}+M_{a*}\right)}{M_{s*}}\frac{dM_{a*}}{ds_*}+\frac{\left(M_{e0z*}+M_{b*}\right)}{M_{s*}}\frac{dM_{b*}}{ds_*} \tag{4.48}$$

And the volume flux of the flow:

$$\frac{dQ_*}{ds_*} = \frac{2b_*^{\ 2}}{Q_*}\frac{dM_{s*}}{ds_*}+\frac{4M_{s*}b_*}{Q_*}\frac{db_*}{ds_*} \tag{4.49}$$

4.3.4 – Solving the Equations in MatLab

In MatLab the ten equations are solved simultaneously at a particular location along the trajectory. Simultaneously means that MatLab integrates the system of differential equations and finds answers for all ten variables at a specific location and then checks the error involved in the integration. MatLab only advances a step size if the error is smaller than a maximum tolerance that is specified beforehand. If the error is outside the tolerance level, MatLab shortens the step size and goes through the set of equations again.

The order in which the derivatives are calculated is of importance. The differential equations for x, y, z, M_b and b are calculated first, as these do not depend on the results of any of the other equations. With the buoyancy-generated momentum flux equation now known, the excess momentum flux equation can be calculated and is therefore next. For MatLab to

calculate values for the other equations, the total momentum flux equation (4.48) has to be rewritten so that the result is no longer dependent on the change in ambient momentum flux. The reason for this is that the answer from the entrained ambient momentum flux equation (4.46) depends on the change in volume flux and the answer from the volume flux equation (4.49) depends on the change in total momentum flux, therefore creating a loop that cannot be solved. By inserting equation (4.49) into (4.46) and inserting the result into equation (4.48), the total momentum flux equation can be modified so that it only depends on the results of the spread equation and the buoyancy-generated momentum flux equation. As these results are already known the total momentum flux equation can be determined.

$$\frac{dM_{s*}}{ds_*} = \left(\frac{M_{e0x*} + M_{a*}}{M_{s*}} \right) U_{a*} \left(\frac{2b_*^2}{Q_*} \frac{dM_{s*}}{ds_*} + \frac{4M_{s*}b_*}{Q_*} \frac{db_*}{ds_*} \right) + \frac{\left(M_{e0z*} + M_{b*} \right)}{M_{s*}} \frac{dM_{b*}}{ds_*} \tag{4.50}$$

Solving equation (4.50) for the change in total momentum flux gives the final non-dimensional equation

$$\frac{dM_{s*}}{ds_*} = \frac{\dfrac{4\left(M_{e0x*} + M_{a*} \right) U_{a*} b_*}{Q_*} \dfrac{db_*}{ds_*} + \dfrac{\left(M_{e0z*} + M_{b*} \right)}{M_{s*}} \dfrac{dM_{b*}}{ds_*}}{1 - \dfrac{2\left(M_{e0x*} + M_{a*} \right) U_{a*} b^2}{Q_* M_{s*}}} \tag{4.51}$$

The volume flux equation will be the eighth equation solved, and this is followed by the last two, Δ and M_a, both depending on the change in volume flux.

A MatLab m-file, *MomentumModel7*, is used to enter the initial conditions of a flow scenario, the source diameter, the initial velocity of the flow, the ambient velocity, the density difference used to calculate the initial buoyancy flux, and both the initial angles of the discharge, α_0 and β_0. These initial conditions are used to calculate the scenario dependent constants, ϕ_0, M_{e0}, M_{e0x}, M_{e0y}, M_{e0z}, U_a, Fr_0 and c_7 as well as the first values for the ten dependent variables. The scenario dependent constants and the initial values for the ten dependent variables are then non-dimensionalised. A row-vector is created with the initial values of all the ten non-dimensional ODE's. The *MomentumModel7* m-file calls a second m-file, *dy7*, in which the ten equations are defined in the above-mentioned order. The universal constants for the velocity spread of a weakly advected flow, k_{th}, a strongly advected puff flow , $m_{th\text{-}m}$, and a strongly advected thermal flow, $m_{th\text{-}t}$, are calculated in *dy7* as these do not change from one scenario to another. The MatLab function *ODE45* solves the ten differential equations. This function is specifically programmed to evaluate the right-hand side of differential equations by using an explicit Runge-Kutta (4,5) formula. It is a one-step solver

needing only the solution at the immediately preceding point. The output of the model are the values for the ten parameters at each step size. It stores these values in a matrix for later access and uses them as the initial conditions for the next step. A printed version of both algorithms can be found in Appendix C.

4.4 – Top-Hat Conversions

As indicated in section 4.3.2 it is necessary to relate the Gaussian or double-Gaussian parameters to the top-hat parameters employed by the model. From integral methods the momentum, volume and tracer fluxes using the Gaussian assumption can be determined. These have to be equal to their top-hat counterparts. This is shown below.

Momentum flux: $$I_m U_e^2 b^2 = \pi b_{th}^2 U_{eth}^2 \tag{4.52}$$

Volume flux: $$I_q U_e b^2 = \pi b_{th}^2 U_{eth} \tag{4.53}$$

Tracer flux: $$I_{qc} U_e C_l b^2 = \pi U_{eth} C_{th} b_{th}^2 \tag{4.54}$$

I_m, I_q and I_{qc} are shape factors with values of 1.7, π and 2.03 respectively (see section 3.2.3.1). The momentum flux equation can be divided by the volume flux equation to show the conversion equation for the velocity:

$$U_{eth} = \frac{I_m}{I_q} U_e = \frac{1.7}{\pi} U_e \tag{4.55}$$

Equation (4.52) is inserted into the volume flux equation to find the conversion equation for the spread:

$$b_{th} = \frac{I_q}{\sqrt{\pi I_m}} b = \sqrt{\frac{\pi}{1.7}} b \tag{4.56}$$

and

$$k_{th} = \sqrt{\frac{\pi}{1.7}} k = 0.136k \tag{4.57}$$

Both equation (4.55) and equation (4.56) are inserted into the tracer flux equation to find the conversion equation for the concentration:

$$C_{th} = \frac{I_{qc}}{I_q} C_l = 0.646C \tag{4.58}$$

For the determination of the conversion equations from the double-Gaussian assumption to the top-hat assumption for the momentum puff region, equations for the volume and tracer flux are changed due to the influence of the ambient velocity.

Volume flux: $$I_{qdg} U_a b^2 = \pi U_a m_{th}^{\ 2} \tag{4.59}$$

Tracer flux: $$I_{cdg} U_a C_l b^2 = \pi U_a C_{th} m_{th}^{\ 2} \tag{4.60}$$

The expressions for I_{cdg} can be found in Chapter 3.2.3.2. $I_{qdg} b^2$ is the area under the double-Gaussian. I_{qdg} is determined below, using the double-Gaussian assumption as suggested in Chapter 3. In the calculation of I_{qdg}, the integration limits were $\pm 2b_c$, because $2b_c$ is generally associated with the distance from the centreline to the edge of the single-Gaussian jet. However the spread relationship employs a velocity spreading rate, where the velocity spreading rate is the concentration spreading rate divided by λ. This is taken into account by multiplying a factor $1/\lambda^2$ in the calculation of I_{qdg}.

$$I_{qdg} = \frac{1}{\lambda^2}\frac{8{b_c}^2 h\pi}{b^2} - \frac{1}{\lambda^2}\frac{4}{b^2}\int_{-2b_c+fb_c}^{0} \sqrt{\left(2b_c h\right)^2 - \left(hx - hfb_c\right)^2}\,dx = 4h\left(\pi + \frac{f}{2}\sqrt{4-f^2} + 2\sin^{-1}\left(\frac{f}{2}\right)\right) \tag{4.61}$$

Using the values for f and h, as found in 3.2.3.2, the spread and concentration conversion equations for the momentum puff become

$$b_{th-m} = \sqrt{\frac{I_{qdg}}{\pi}}\,b = 3.00b \tag{4.62}$$

and

$$m_{th-m} = \sqrt{\frac{I_{qdg}}{\pi}}\,k_{sg} = 3.00k_{sg} = 0.60 \tag{4.63}$$

$$C_{th-m} = \frac{I_{cdg}}{I_{qdg}} C_l = 0.482 C_l = 0.482\frac{C_{peak}}{\left(1+e^{-(2f)^2}\right)} = 0.461 C_{peak} \tag{4.64}$$

The experimental results from the buoyant jet in an ambient flow experiments (see section 5.3.2.2) are used to determine the spread in the advected thermal region. It gave the following relationship for the spread equation:

$$m_{th-t} = 0.73 \tag{4.65}$$

Therefore the concentration conversion equation becomes:

$$C_{th-t} = 0.324\frac{C_{peak}}{\left(1+e^{-(2f)^2}\right)} \tag{4.66}$$

Note that due to the influence of the ambient flow, the standard conversion equations based on the Gaussian assumption cannot be applied in the weak jet region. Altering equations (4.52) to (4.54) to take the ambient into account, gives:

Momentum flux: $$I_q U_a U_e b^2 = \pi b_{th}^2 U_{eth} U_a \tag{4.67}$$

Volume flux: $$\pi U_a \left(\beta_{wj} b\right)^2 = \pi b_{th}^2 U_a \tag{4.68}$$

Tracer flux: $$I_c U_a C b^2 = \pi U_a C_{th} b_{th}^2 \tag{4.69}$$

The concentration conversion equation becomes:

$$C_{th} = \frac{I_c}{\pi} \frac{b^2}{b_{th}^2} C_l = \frac{\lambda^2}{\beta_{wj}^2} C_l \tag{4.70}$$

4.5 – Double-Gaussian Dilution Ratios

The use of the double-Gaussian profile as the approximation of the cross-sectional concentration profile in the strongly advected regions makes it possible to determine minimum cross-sectional and minimum centreline dilutions, and convert between the two. It also gives a tool to convert dilution predictions from other models, to make a direct comparison possible.

In the strongly advected regions VisJet gives average dilution results that can be converted to minimum point centreline dilution (C_0/C_c) by dividing the average dilution by 2.3 (Cheung 1991). For the data to be compared with the cross-sectional minimum point dilution experimental data (C_{peak}), the predicted values by VisJet are converted using the following equation:

$$\frac{C_0}{C_{peak}} = \frac{C_0}{C_{ave}} \frac{C_{ave}}{C_c} \frac{C_c}{C_{peak}} = \frac{C_0}{C_{ave}} \frac{2e^{-f^2}}{2.3\left(1+e^{-(2f)^2}\right)} \tag{4.71}$$

The dilution results given by CorJet are centreline minimum dilution results and cross-sectional average dilution results, however no definition is given as to how this relates to the double-vortex concentration distribution (Jirka 2004). For a comparison with the experimental data, the average dilution values are multiplied by 1.4. Assuming the centreline maximum concentration is the maximum expected concentration in the cross-section the conversion equation becomes:

$$\frac{C_0}{C_{peak}} = \frac{C_0}{C_{ave}} \frac{C_{ave}}{C_{peak}} = \frac{C_0}{C_{ave}} \frac{1}{1.4} \tag{4.72}$$

In the strongly advected regions of the flow previous experimental studies have both determined the minimum dilution of the cross-section and the minimum centreline dilution of the cross-section. Using equations (4.64) and (4.66) enables a comparison between the

experimental data and the predictions from the Momentum Model. To find the centreline minimum dilution of the cross-section, $y' = 0$ and $z' = 0$ are entered into the equation for the double-Gaussian approximation to give the equation relating the average dilution with the minimum centreline dilution C_c. For the momentum puff region this becomes:

$$\frac{C_0}{C_c} = 0.482 \frac{C_0}{C_{ave}} \frac{e^{f^2}}{2} \tag{4.73}$$

and for the advected thermal region:

$$\frac{C_0}{C_c} = 0.310 \frac{C_0}{C_{ave}} \frac{e^{f^2}}{2} \tag{4.74}$$

It should be noted that each model has its own definition for C_{ave}. This definition is based on the spread definition used by the model. A more complete discussion of the comparison between models is given in Kikkert et al. (2006a).

4.6 – Summary

Ten ordinary differential equations that describe the dependent parameters of the flow along its trajectory are the basis of the Momentum Model. The behaviour of the discharge at any particular location is determined by the relative magnitudes of three distinct forms of momentum flux, the initial excess, buoyancy-generated and entrained ambient momentum flux. This lead to the derivation of nine ordinary differential equations. The tenth equation, the spread equation, came from empirical relationships and depended on the flow type. Momentum flux ratios within flow regions determined the transition points between flow regions. The equations were solved simultaneously at a particular location along the trajectory. Top-hat profiles were assumed in both the strongly and weakly advected regions of the flow and conversions equations were included to properly interpret the data and make it possible for the results to be compared with previous experimental work.

To assist in the design and to monitor the performance of the experiments the accuracy of the Momentum Model predictions has to be verified. This verification is presented in the following chapter.

Chapter 5 – Two-Dimensional Trajectory Flows

5.1 – Introduction

This chapter gives an overview of the all the experiments with two-dimensional trajectories (including jets and plumes) that were carried out as part of the current investigation. First the flows in a still ambient are discussed followed by the two-dimensional trajectory flows in a moving ambient. As most of these flows have been investigated in the past, in the present study these flows were not studied in detail. However, the present investigation did give special attention to oblique discharge configurations for flows in a stagnant and moving ambient, as data from these flows is limited. The specifics of the experimental set up for each of the flows investigated is discussed, a more thorough discussion of the experimental technique can be found in Chapter 3.

Before the Momentum Model (Chapter 4) can be used as a guide in the design and monitoring of the performance of experimental investigations, the output of the model has to be verified against experimental data. The experimental results obtained include trajectory, concentration spread and dilution data and these are used as part of the verification of the model. One flow region not covered by the current investigation is the weak-jet, because of the large horizontal distances needed to record weak-jet behaviour properly. Momentum Model predictions in the weak-jet region are compared with the most recent weak-jet data by Wang (2000b). Both the new data and the Momentum Model predictions are compared with predictions from VisJet (Cheung et al. 2000) and CorJet (Jirka 2004) and experimental data from previous researchers whenever possible.

The results from the two-dimensional trajectory flow experiments were also used as a verification of the LA flow visualization technique (see Chapter 3) and to provide the foundation for the three-dimensional trajectory experiments (see Chapter 8). A more thorough investigation was carried out into the behaviour of negatively buoyant jets in a still ambient and non-buoyant jets discharged at oblique angles to a moving ambient. The theoretical and experimental findings of these investigations can be found in Chapters 6 and 7 respectively.

5.2 – Still Ambient Flows

The behaviour of a buoyant jet flow in the environment can be separated into weakly advected (close to the source) and strongly advected behaviour. In the strongly advected region the flow is dominated by the influence of the ambient motion. In the weakly advected region the flow is dominated by the initial momentum flux, and the buoyancy-generated momentum flux. In the laboratory a special case can be created by reducing the ambient flow velocity to zero. The entire flow then exhibits the behaviour of the weakly advected region and it can be studied in detail.

Three distinctly different flows can be observed depending on the initial conditions of the flow. The first is the simple jet. Besides having an ambient velocity of zero there is also no density difference between the fluid from the jet and the surrounding fluid. Therefore the behaviour of the simple jet depends only on the initial momentum flux.

The second distinct flow in a still ambient is the plume. Compared with the simple jet there is a density difference between the buoyant jet fluid and the ambient fluid, but the initial velocity is relatively small. The behaviour of the flow is therefore dominated by the buoyancy-generated momentum flux rather than the initial momentum flux.

The third distinct flow is the buoyant jet in a still ambient. It combines the characteristics of the simple jet and the plume. The buoyant jet flow goes through a region where its behaviour is jet-like and dominated by the initial momentum flux, and a region where its behaviour is plume-like and dominated by the buoyancy-generated momentum flux. The two flow regions are connected by a relatively short transition region. Depending on the angle of discharge the buoyant jet flow is either a positively buoyant jet (the vertical component of the initial velocity of the jet acts in the same direction as the buoyancy-generated momentum flux), a horizontal buoyant jet or a negatively buoyant jet. The horizontal buoyant jet has in the past received by far the most attention from researchers.

Simple jet, plume and buoyant jet experiments have been carried out as part of the present study. An overview of the experimental set up and experimental results for the three flows are presented below.

5.2.1 – Simple Jet

Twenty-seven simple jet experiments were carried out as part of the present investigation. First the experimental set up will be discussed, including the initial conditions of each run, and then the results will be presented.

5.2.1.1 – Experimental Design

The light attenuation flow visualization system was used for all jet runs. For more details of the LA technique see section 3.2. The simple jet runs were used as an integral part of the investigation into the LA technique. They enabled the exploration of various parameters that influence the accuracy of the LA technique, and in addition an exploration of how the LA system handled a jet run flowing towards the camera under a pre-determined angle. They were also used to verify the integrated dilution theory, and to investigate and verify the 3D LA technique. The specifics of each run are listed in Table D.1 in Appendix D

The orientation of the source does not affect the behaviour of the flow, because there is no buoyancy-generated momentum flux or ambient flow. Therefore the source could be positioned anywhere in the tank as long as the trajectory of the flow was perpendicular to the camera (with the exception of the Angled Jet experiments – runs 16.2 and 17.2). The source was placed so that it discharged either vertically downwards or horizontally. The advantage of the vertical position was the longer path of the flow that could be recorded, because of the orientation of the camera and calibration cells. But the disadvantage was the potential influence of the bottom boundary on the flow near the tank floor.

The initial conditions of all jet runs can be seen in Table D.1. It shows that the Reynolds numbers ranged from 2988 to 9762, thus ensuring the discharges were turbulent at all times. The source diameter was reduced during the investigation from 10.15mm to 2.45mm. This was partly due to the low concentration of red dye needed for flows with bigger diameter sources and partly due to the fact that with a smaller diameter source the flow could be investigated further downstream in terms of non-dimensional distances. The initial volume flux of the flow, recorded with the magnetic flow meter, varied between 0.0630l/s for the

largest diameter source and 0.0058l/s for the smallest diameter source. Due to the small temperature differences between the fluid of the jet and the ambient fluid, the density differences were minute and the initial Froude number was effectively infinite for all flows.

5.2.1.2 – Experimental Results and Model Predictions

The jet experiments provided concentration spread and centreline dilution results (both point and integrated). The concentration spread and point dilution data from the experiments, and the model predictions of the same quantities depend on the assumption that the cross-sectional profile of the jet has a Gaussian shape. From the Gaussian assumption, the integrated cross-sectional profile is shown to also have a Gaussian shape (equation 3.11). Figure 5.1 shows integrated cross-sectional concentration profiles from jet runs 12, 14 and 15. The location of the cross-sections increases from under 14 port diameters (run 15) to over 175 port diameters (run 14). The results, as expected, show that the Gaussian assumption is a very good representation of the cross-sectional integrated concentration values.

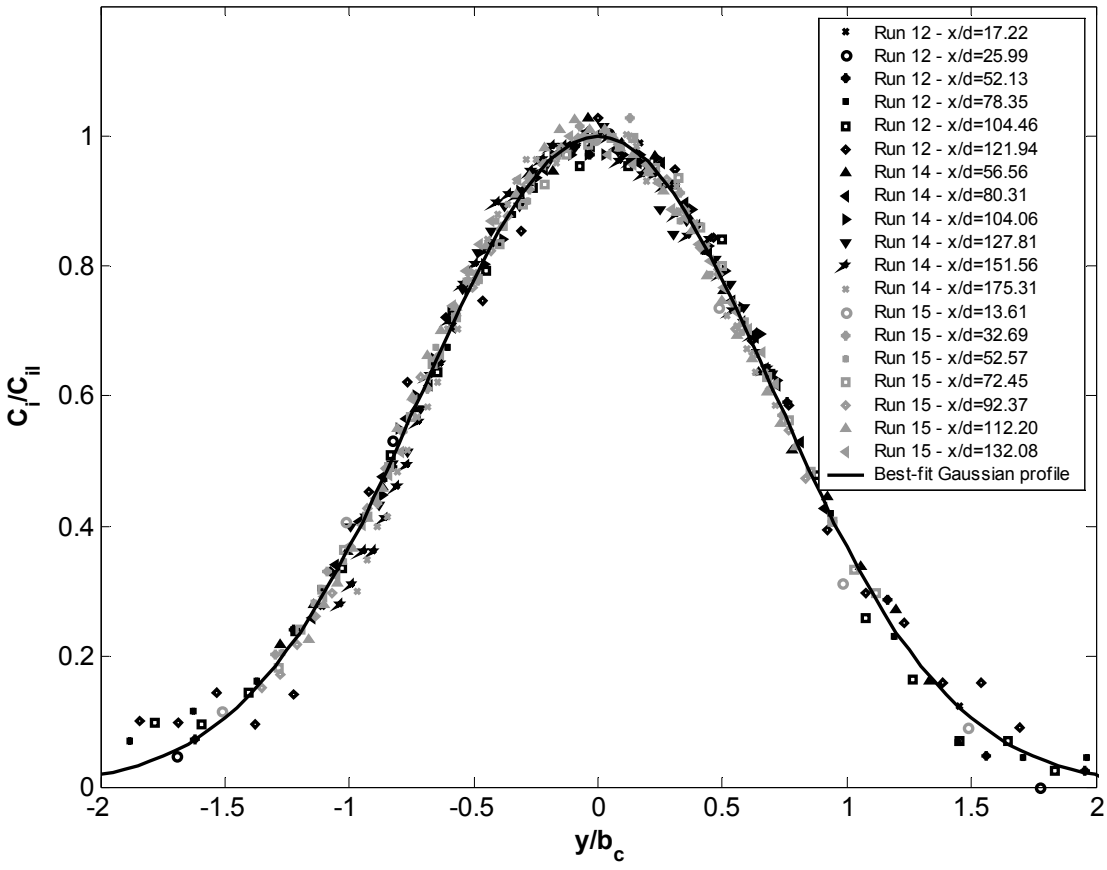

Figure 5.1 – Integrated cross-sectional concentration profiles from Jet Runs 12, 14 & 15 at various location downstream from the source

The concentration spread results (b_c) of the jet experiments, non-dimensionalised by the port diameter (d), can be seen in Figure 5.2. The experimental data collapses very well for the first 100 port diameters downstream, but for increasing distances the data shows more scatter. The increasing scatter can be attributed to the increasing time-scale of the turbulence, and therefore increasing number of frames needed to create a suitable average image. Experimental data from Pun (1998) reached approximately 80 port diameters downstream. This data is consistent with the current results. The model predictions from the Momentum Model and CorJet for the concentration spread are nearly identical, VisJet predicts a higher concentration spread. The difference in predictions can be traced back to the constants employed in the relationship that closes the set of equations in the various models, entrainment constants in CorJet and VisJet, and a spread constant in the Momentum Model The most accurate experimental data, data up to 100 port diameters downstream, is most consistent with the predictions from the Momentum Model and CorJet. Further downstream the average concentration spread value of all the experimental data falls approximately in line with the predicted value by the two models. The predicted values from VisJet appear to be too high when compared to the experimentally determined values. CorJet models the zone of flow establishment and a difference in predictions can be seen in the first 5 port diameters after the fluid has left the source. However this has no discernable effect on the predicted results further downstream when compared to the Momentum Model predictions, validating the assumption in the Momentum Model that the zone of flow establishment has a negligible effect on the flow at distances greater than 10 port-diameters from the source.

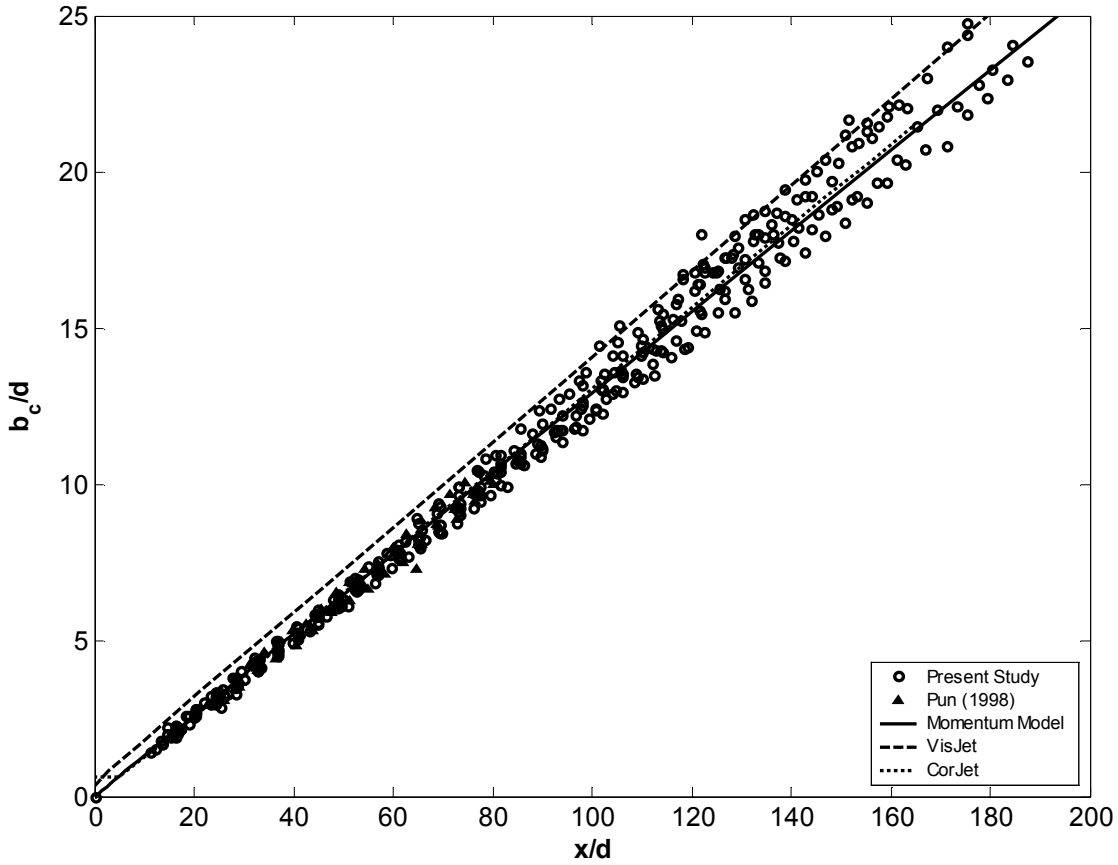

Figure 5.2 - Concentration spread results versus distance downstream, comparing the experimental jet results with the model predictions

The integrated centreline dilution theory for the jet is discussed in section 3.2.3.1. Equation (3.16) shows that the integrated centreline dilution (C_{i0}/C_{il}) for a jet is independent of distance downstream and has a theoretical value of 0.812. Figure 5.3 shows the theoretical line and the comparison with the experimental values found. The experimental results collapse well to form a single horizontal line with an average value of 0.829, and approximately 4% scatter. The numerical models are not designed to give integrated dilution results and therefore have been omitted from Figure 5.3.

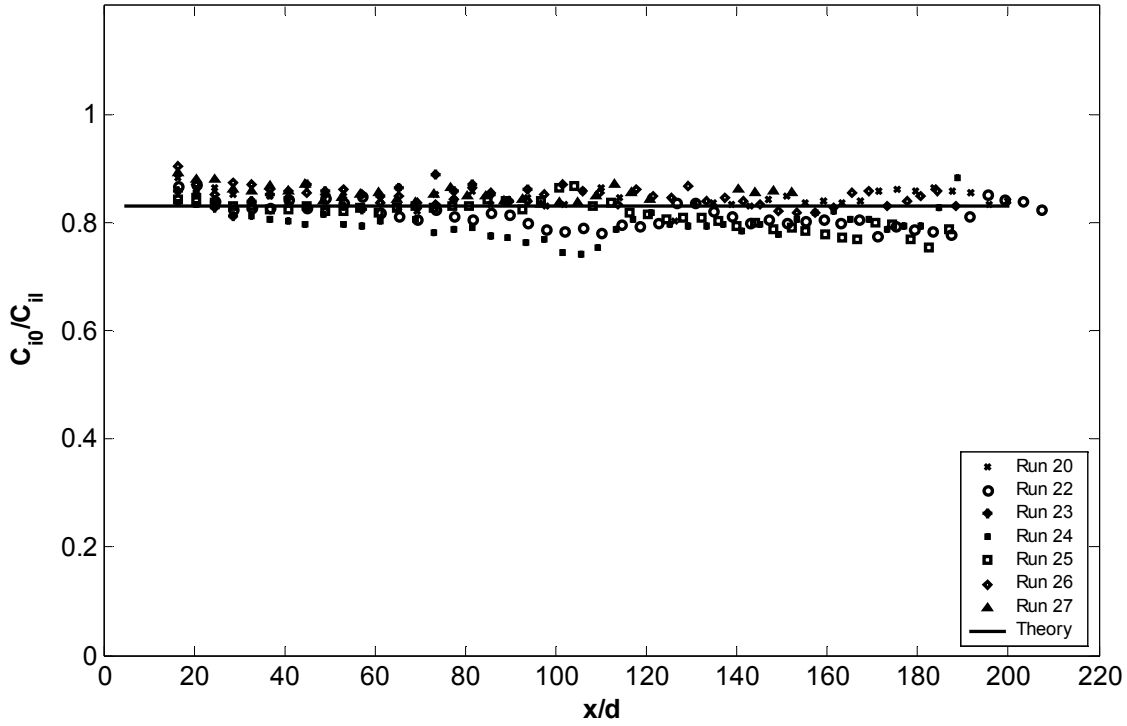

Figure 5.3 - Integrated centreline dilution results versus distance downstream, comparing experimental results with integrated jet theory

The integrated centreline dilution results can be combined with the concentration spread results to find the point centreline dilution (C_0/C_l) in a cross-section. Equation (3.18) describes the relationship between the integrated centreline and the point centreline dilution. The equation was used to convert the integrated dilution data from the jet experiments into point dilution data and the results can be seen in Figure 5.4. The results collapse reasonably well, however the scatter is higher than for the concentration spread results. This is expected as the calculation of the point dilution involves two experimentally determined quantities. As with the concentration spread results, Figure 5.4 shows that the predictions by CorJet and the Momentum Model are very similar, with no noticeable difference due to the omission of the zone of flow establishment in the Momentum Model. They are more consistent with the experimental data than the predictions of VisJet. The experimental values of Pun (1998) fall within the scatter of the present study and also indicate that VisJet is overestimating the dilution.

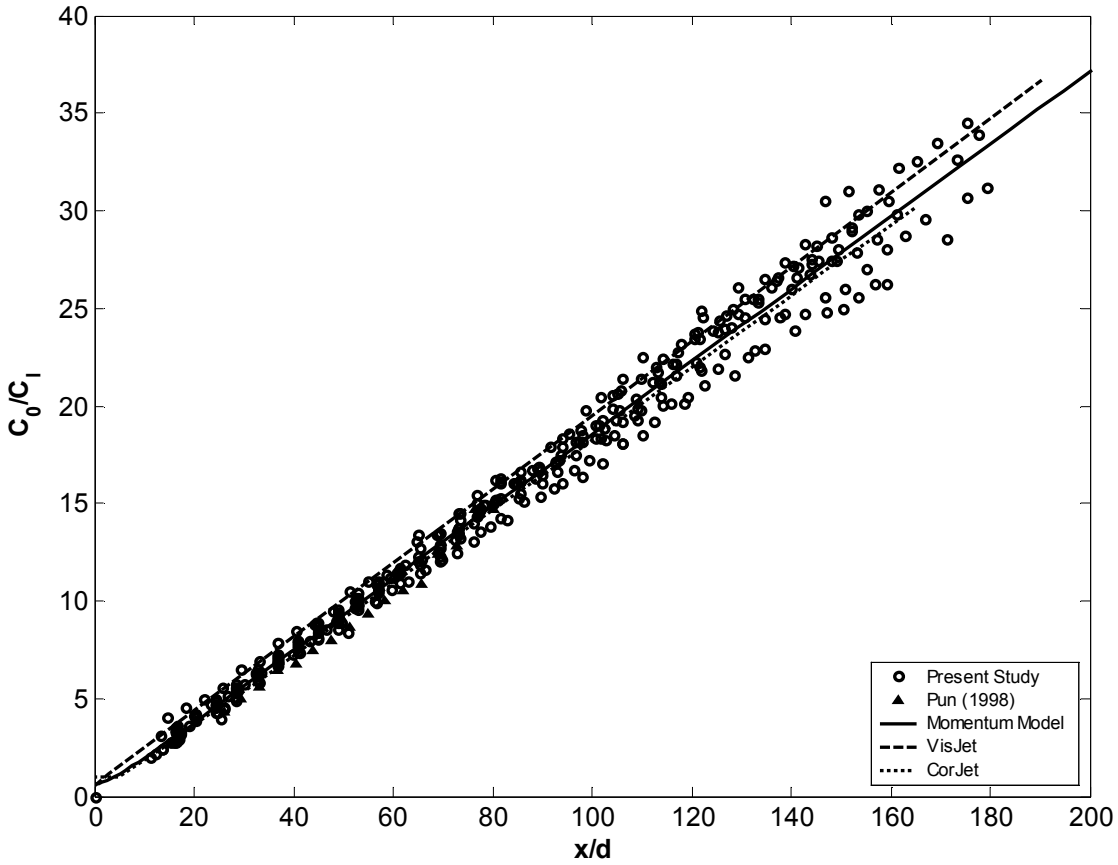

Figure 5.4 - Point centreline dilution results versus distance downstream, comparing the experimental jet results with model predictions and previous experimental results

5.2.2 – Plume

Four plume (or vertically discharged buoyant jet) runs were carried out as part of the present investigation. The experimental set up and results are discussed below.

5.2.2.1 – Experimental Design

The plume experiments were carried out directly after the first series of jet experiments that were used to guide the set up of the LA system. The plume experiments were therefore the first test for the LA system with a different flow configuration. Salt was added to the red-dye solution to create the density difference with the ambient fluid and therefore the source was discharged vertically downwards to create a plume flow. The density difference between source fluid and ambient fluid was checked using an Anton Paar density meter.

Details and initial conditions of each plume run can be seen in Appendix D, Table D.2. To be able to record the plume flow the Froude number had to be low enough so that the jet-to-plume transition length-scale was small. The jet region was then nearly non-existent and the majority of the recorded flow was in the plume-region. Due to the reasonably small port-diameter (3.2mm) and the low Froude number needed to create a plume flow, the Reynolds numbers were not high enough to expect fully turbulent flow at the end of the source. This was confirmed by the experimental results. A virtual source was found for each run by projecting the spread results back to a virtual source. The initial Froude number ranged from 5.66 to 20.63, and the Reynolds number from 557 to 2029. The density difference between the red-dye solution and the ambient fluid was kept constant for the duration of the experiments at just over three percent.

The value for λ, used to convert the velocity spread data predicted by the models into concentration spread data, was set to 1.05 (Papanicolaou and List 1988; Wang 2000a) for the plume flows.

5.2.2.2 – Experimental Results and Model Predictions

As for the simple jet, the cross-sectional velocity and concentration distributions are assumed to be Gaussian and self-similar for the plume, and therefore the integrated cross-sectional profiles are also assumed to be Gaussian. This assumption was verified by collapsing the integrated experimental cross-sectional data and comparing the outcome with the theoretical Gaussian curve. The results can be seen in Figure 5.5. It shows cross-sectional profiles from runs 1, 3 & 4 at various locations downstream from the source, varying between 16 port-diameters (run 3) and 138 port-diameters (run 4). The graph confirms that the Gaussian assumption is a very reasonable approximation of the cross-sectional distribution of the plume. It can therefore be confidently used in the calculation of the point dilution.

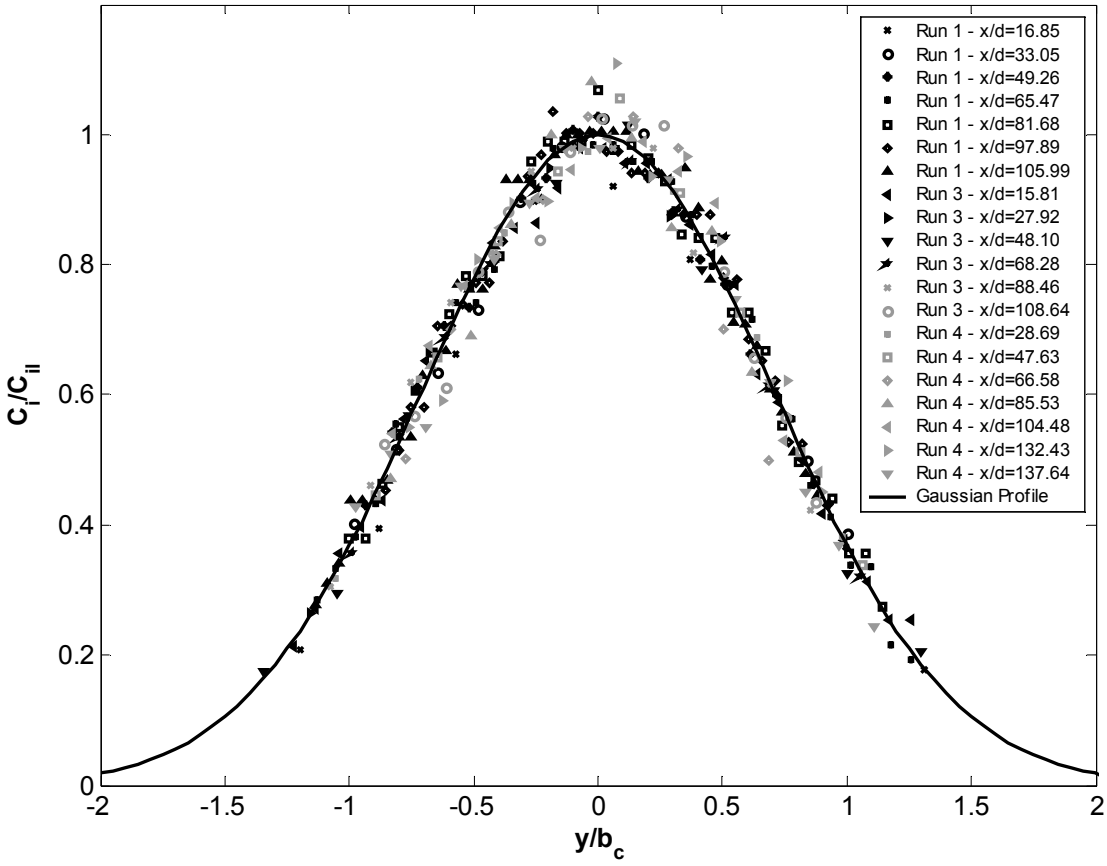

Figure 5.5 – Integrated cross-sectional concentration profiles from plume runs 1, 3 & 4 at various location downstream from the source

The concentration spread results from the plume runs, non-dimensionalised by the port diameter and the Froude number, can be seen in Figure 5.6. The experimental results from the present study collapse well onto a single line, and are consistent with the results of Papanicolaou and List (1988) and Fisher (1995). The results of Pun (1998) are consistently lower than the results found in the present study. The experimental results are most consistent with the predictions of the Momentum Model and VisJet. The predicted spread result of CorJet is lower than the predictions of the other models, but still lies above the data of Pun.

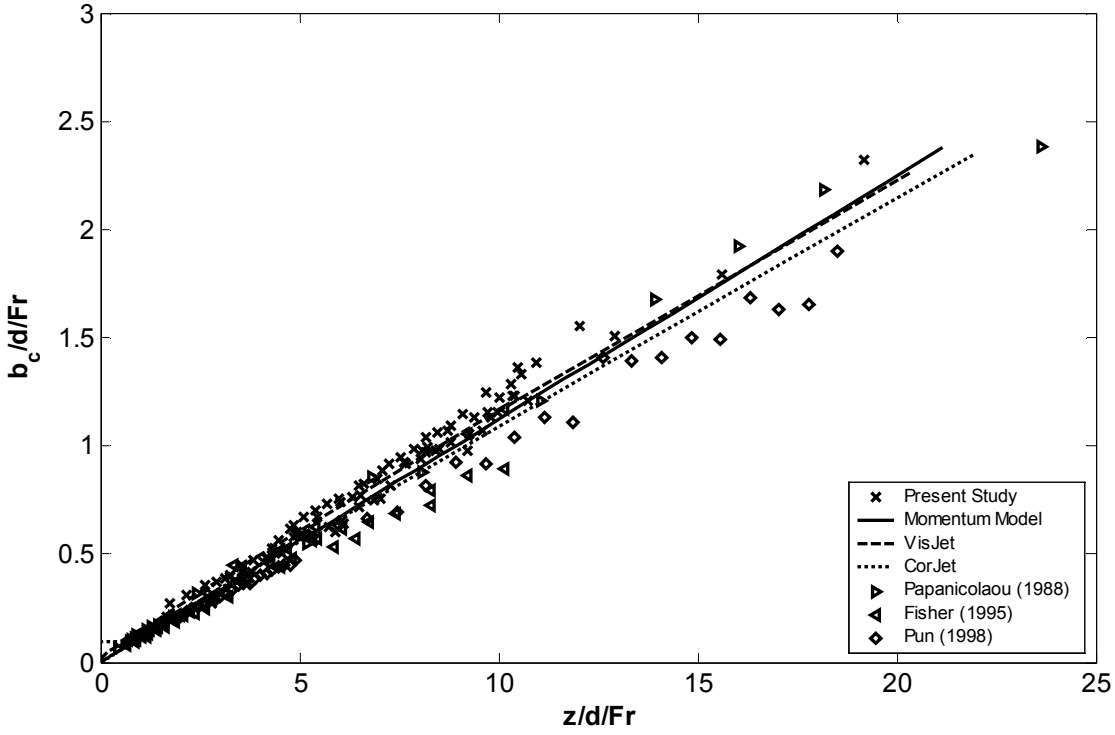

Figure 5.6 - Concentration spread results versus distance downstream, comparing the experimental plume results with the model predictions and previous experimental results

The point centreline dilution data, divided by the Froude number is plotted versus the non-dimensional distance downstream, also divided by the Froude number in Figure 5.7. The experimental values collapse well and are consistent with all the model predictions and the data from Fisher (1995) and Wang (2000a). The experimental values found by Papanicolaou and List and Pun do not match the experimental plume data, and therefore do not agree with the model predictions either.

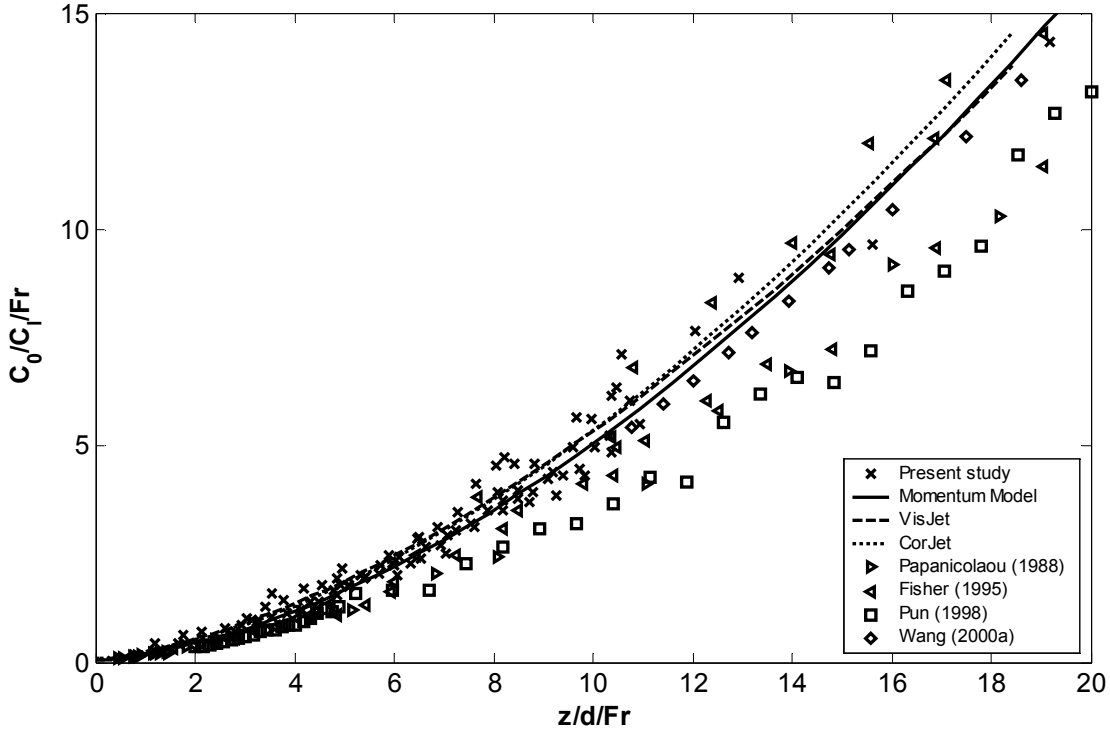

Figure 5.7 - Point centreline dilution results versus distance downstream, comparing the experimental plume results with model predictions and previous experimental results

5.2.3 – Horizontal Buoyant Jet

Three horizontal buoyant jet runs were carried out. The experimental set up is described below, followed by the results of the experiments. The experimental results are compared with the model predictions and data from previous experimental investigations.

5.2.3.1 – Experimental Design

To create the density difference between the source solution and the ambient fluid, salt was added to the red-dye solution. The heavier source solution would therefore fall towards the bottom of the tank and hence the source was positioned horizontally in the top quarter of the image that was recorded by the camera.

Table D.3 in appendix D shows the initial conditions of all horizontal buoyant jet flows. The Froude number ranged from 14 to 50 and the Reynolds number ranged from 1300 to 4900.

The source was not changed during the experiments and had a diameter of 3.2 millimetres. The density difference was just over three percent.

The higher Froude number flows (runs 1 and 3) disappeared from the camera view before having reached the bottom of the recorded image. After the recording of the first part of Runs 1 and 3 the trolley (with the source attached to it) was moved a sufficient amount so that during a second recording of the same flow the lower part of the flow was recorded. The new source location was measured and used during the analysis of the second part of runs 1 and 3. The Reynolds number of run 2 was not sufficiently large for the flow to be fully turbulent by the end of the source. The concentration-spread results from run 2 were used to find a virtual source. The centreline dilution results were used to confirm the location of the virtual source.

The point at which the buoyant jet flow changed its behaviour from that resembling a jet flow into that resembling a plume is called the jet-plume transition point. Using the length-scale method, Pun (1998) defined the distance from the source to the transition point as

$$l_{jp} = 2.3\frac{M_{e0}{}^{3/4}}{(Q_0\Delta_0)^{1/2}} = 2.3\left(\frac{\pi}{4}\right)^{1/4} Fr_0 d \tag{5.1}$$

The values for l_{jp} can be found in the 11th column of Table D.3. The relatively low values for l_{jp} indicate that for each experiment the flow passed from the jet-like region into the plume-like region.

5.2.3.2 – Experimental Results and Model Predictions

Unlike the trajectory of a simple jet, or a pure plume, the trajectory of the horizontal buoyant jet is no longer a straight line. The initial momentum flux drives the flow in the horizontal direction and the buoyancy-generated momentum flux drives the flow in the vertical direction. The experimental trajectory results, non-dimensionalised by the port diameter and the Froude number, can be seen in Figure 5.8. The Figure shows that the experimental data is consistent with results found by previous researchers (Anwar 1969; Davidson 1989; Hansen and Schroder 1968). The prediction of the Momentum Model also matches the experimental data well. The predictions of CorJet and VisJet for the trajectory of the horizontal buoyant jet indicate a higher degree of curvature due to the buoyancy force than the Momentum Model. The prediction by VisJet is still a reasonable prediction of the experimental data, CorJet overestimates the distance travelled in the *z*-direction.

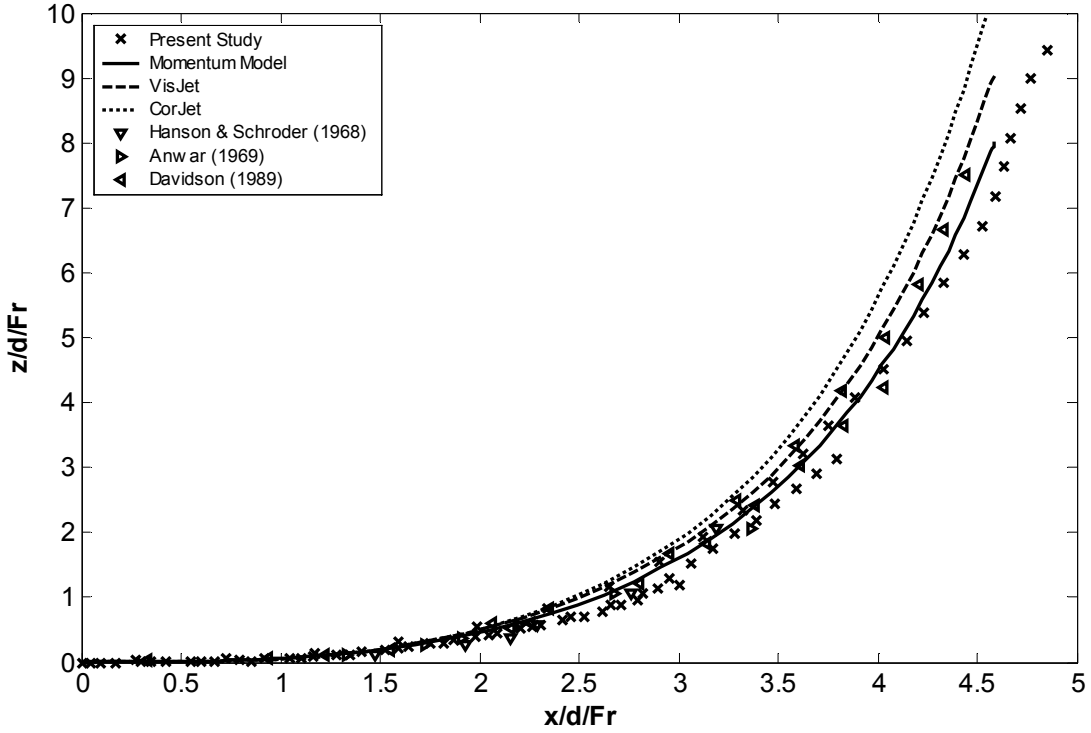

Figure 5.8 – Trajectory results horizontal buoyant jet in still ambient, comparing the experimental results with model predictions and previous experimental results

To predict the trajectory data shown in Figure 5.8, all models use the Gaussian assumption that was used to predict the simple jet and pure plume results. However due to the buoyancy-generated momentum flux and the initial momentum flux no longer acting in the same direction, the inner edge of the jet is inherently unstable, and the cross-sectional profiles are no longer axi-symmetric. Figure 5.9 shows integrated cross-sectional concentration profiles from a horizontal buoyant jet run (this run was part of the investigation into the behaviour of the negatively discharged buoyant jets, for more details see Chapter 6). The cross-sections were located between 0.22 and 1.88 transition length-scales downstream from the source. It confirms that the cross-sectional profiles are clearly no longer axi-symmetric when the distance downstream is greater than approximately 1 transition length-scale. However, the fact that the models all assume axi-symmetrical cross-sectional profiles and still predict the trajectory of the horizontal buoyant jet with reasonable accuracy, suggests that the assumption is also still a reasonable one. It is worth noting that the left-hand side of the cross-sectional profiles, which corresponds with the outside spread of the flow, still matches the Gaussian profile and can be used to calculate the spread and dilution data from the experimental runs.

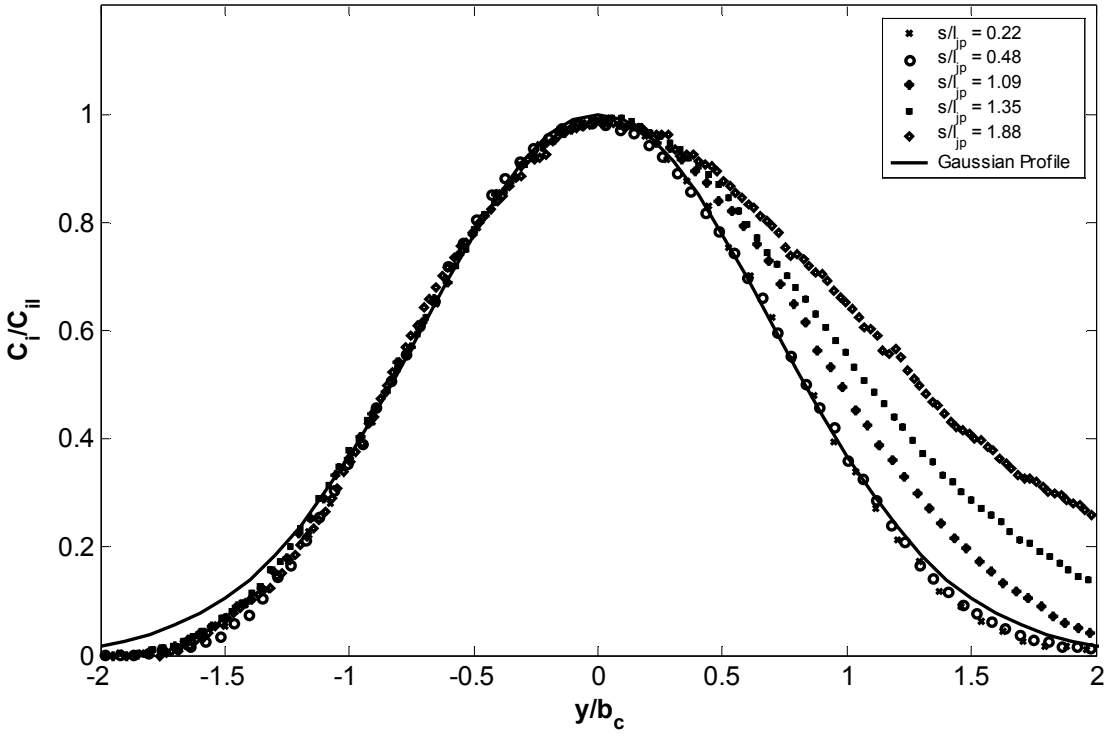

Figure 5.9 - Cross-sectional profiles from negatively discharged buoyant jet run 38, initial conditions: $\phi_0 = 0^o$, $Fr_0 = 56.51$ and $Re_0 = 4704$

The concentration spread results were non-dimensionalised by the jet-plume transition point length scale, l_{jp}, and therefore the jet-like region is the region with $s/l_{jp} < 1$. However, the concentration spread results have been plotted against the distance downstream along the trajectory of the flow (s), rather than the vertical distance away from the source, in order to collapse the data onto a single line. The results can be seen in Figure 5.10. It shows that the experimental data from the three runs overlap each other well and a slight difference in slope can be noted between the two regions. As all the models predict velocity spread data, they had to be modified separately for the jet and the plume regions, because the λ values differ (1.22 for a jet and 1.05 for a plume). A discontinuity therefore exists at the transition point. As expected from the favourable trajectory data, the models also predict the spread with reasonable accuracy. Figure 5.10 is a combination of Figure 5.2 and Figure 5.6. It is therefore not surprising to find that the Momentum Model concentration spread data agrees with the experimental data. It also confirms that CorJet has a tendency to underestimate the spread in the plume region and VisJet has a tendency to overestimate the spread in the jet-region.

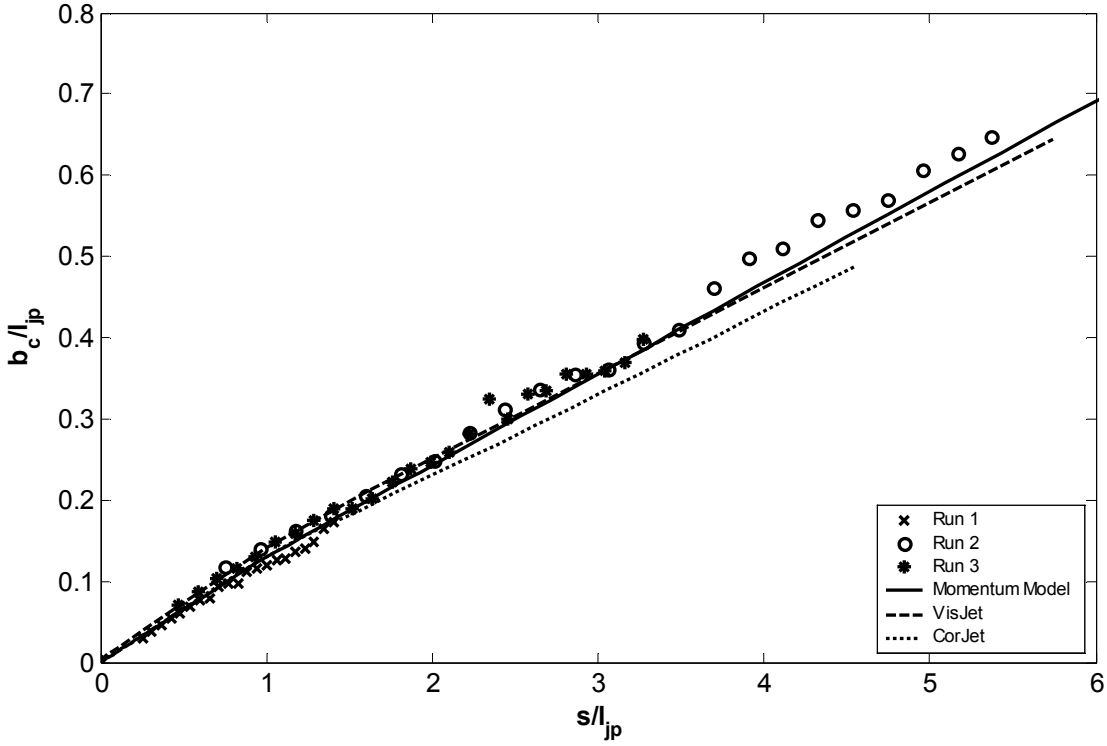

Figure 5.10 – Concentration spread results horizontal buoyant jet in still ambient, comparing the experimental results with model predictions and previous experimental results

The point centreline dilution results for the horizontal buoyant jet in a still ambient are plotted versus the vertical distance away from the source, and are shown in Figure 5.11. The dilution results are plotted versus the vertical distance from the source. Again the overlap of the experimental results with previous experimental results (Cederwall 1968; Hansen and Schroder 1968; Liseth 1970), and the model predictions is reasonable. This indicates that the asymmetry in the cross-section profiles does not affect the flow behaviour to a large extent. Due to the better estimates for the trajectory as well as the spread data, the Momentum Model also gives the best prediction for the point centreline dilution data. Mass conservation and the underestimation of the spread of the buoyant jet leads to dilution predictions by VisJet and CorJet that favour the lower experimental values.

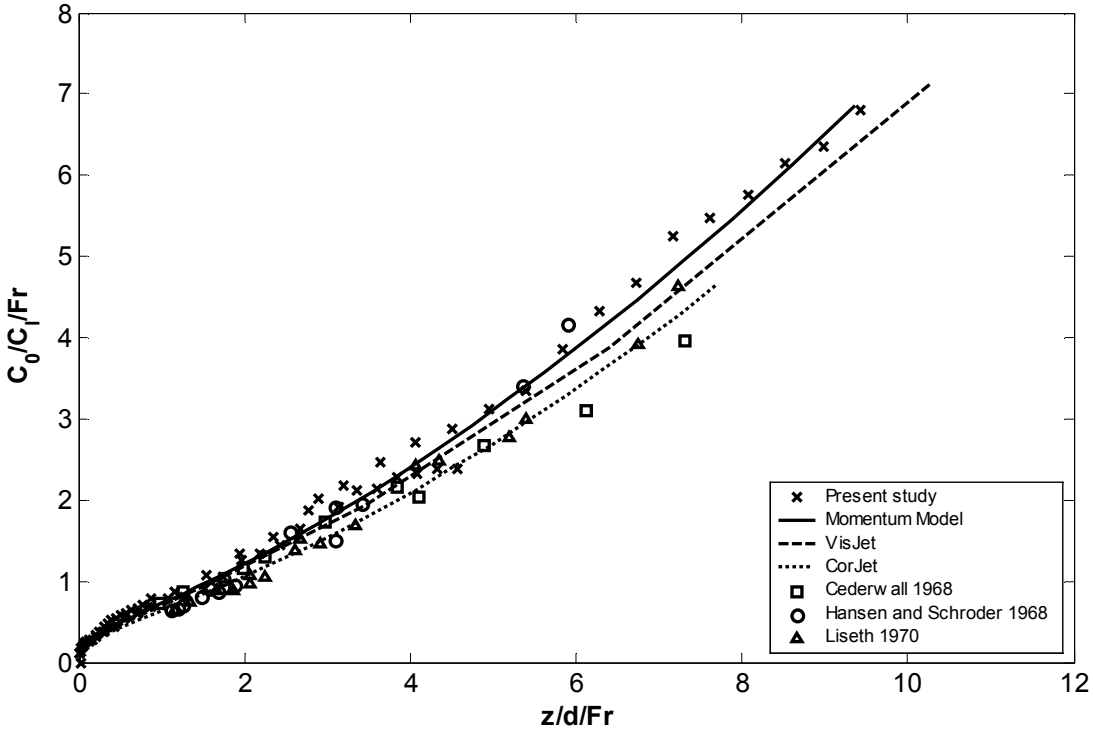

Figure 5.11 – Point centreline dilution results horizontal buoyant jet in still ambient, comparing the experimental results with model predictions and previous experimental results

5.2.4 – Positively Buoyant Jet

Ten experiments were carried out to investigate the behaviour of the positively buoyant jet. The initial angle of the experiments was changed from 0° to 90° in 10° increments. The specifics of the experimental set up and the result can be found below.

5.2.4.1 – Experimental Design

As with the horizontal buoyant jet, salt was added to the red dye solution, and the buoyant jet flow sank to the bottom of the tank. The source was therefore positioned in the top quarter of the image recorded by the camera. The angle of the source was set using a slope-adjustable level and confirmed during the analysis of the experiment. The source angle had an accuracy of 0.25°.

Table D.4 in Appendix D shows the initial conditions of the ten runs. Both the Froude number and the Reynolds number were left unchanged during the series of experiments at 27.15 and 2625 respectively. The port-diameter was 2.91 millimetres and the density different just over three percent. The transition length scale between the jet and plume regions was 67 port-diameters, well within the distance from the source that was captured by the camera. Therefore both the jet-like and plume-like regions of the flow were investigated.

5.2.4.2– Experimental Results and Model Predictions

The results of two of the ten positively buoyant jet experiments, run 5 and run 10, could have been shown as part of the pure plume and horizontal buoyant jet results respectively. As the results of the horizontal buoyant jet and the pure plume were predicted with reasonable accuracy by the three models, it is therefore expected that the predictions for the trajectory of the positively buoyant jet will match the experimental values as well. It is also expected that the asymmetry of the cross-sectional profiles does not have a notable influence on the predicted results. As shown above the asymmetry did not have a sufficient effect on the horizontal buoyant jet, the 0° case, and it is expected that the asymmetry decreases when the angle increases, until it disappears for the 90° case.

The trajectory results of the positively buoyant jet runs can be seen in Figure 5.12 and they are compared with the results predicted by the Momentum Model, VisJet and CorJet. The predicted values are consistent with the experimental values. It is noted that the trajectory predictions from the Momentum Model have the least curvature and those of CorJet the most. This difference in curvature disappears for higher angles.

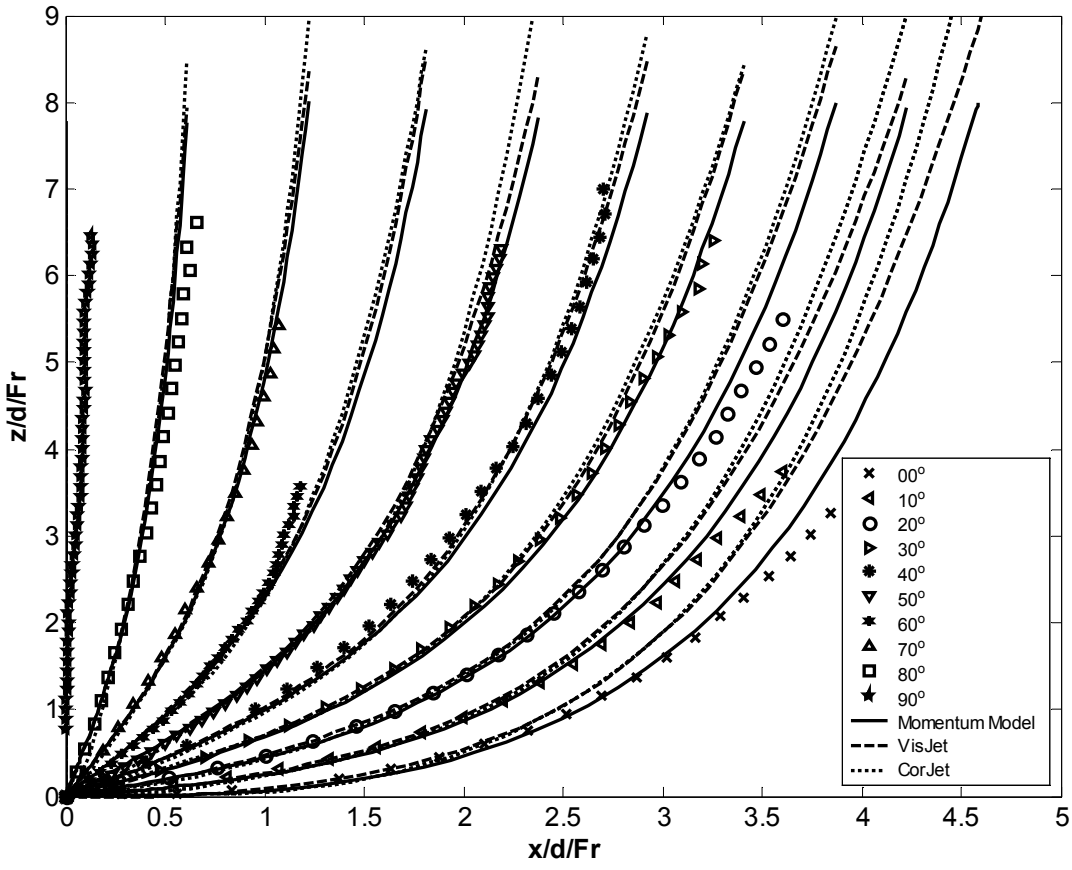

Figure 5.12 - Trajectory results positively buoyant jet experiments, comparing the experimental results with model predictions

The concentration spread data has been non-dimensionalised in the same manner as the horizontal buoyant jet data above, and are plotted versus the distance downstream along the trajectory of the flow. Figure 5.13 is therefore similar to Figure 5.10 and shows the concentration-spread results in the jet and plume region of the buoyant jet as well as comparisons with model values. The comments made regarding Figure 5.10 are again applicable. However, due to the value of l_{jp}, the experimental values shown in Figure 5.13 are relatively close to the source when compared to the values in Figure 5.10. This shows the zone of transition more clearly. At the transition point the experimental values are noticeably lower than the predicted ones, however this difference does not increase further downstream. This is probably related to the distortion of the cross-sectional profiles evident in Figure 5.9. Figure 5.13 shows again the overestimation of the concentration spread by VisJet in the jet region of the flow.

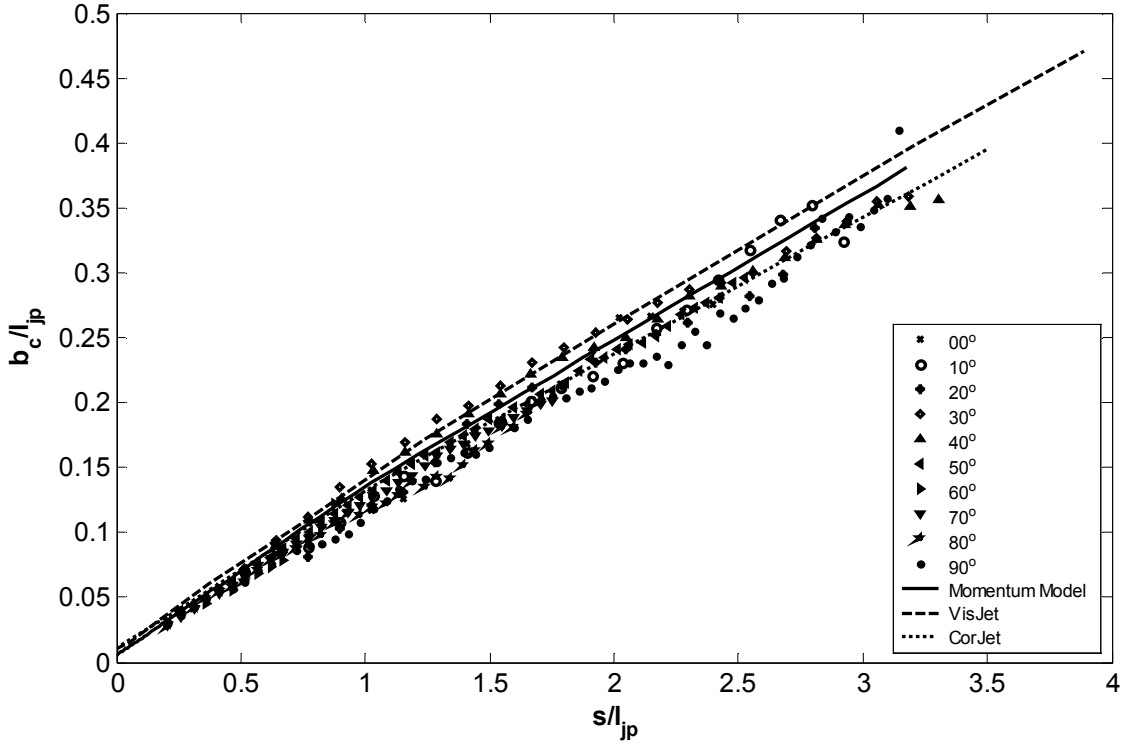

Figure 5.13 – Concentration spread results positively buoyant jet experiments, comparing the experimental results with model predictions

The point centreline dilution results have been plotted against the distance downstream along the trajectory of the flow. The results of the experiments and the models can be seen in Figure 5.14. The collapse of the experimental data is satisfactory. As seen with the concentration spread results, the experimental point centreline dilution values deviate from the predicted values around the transition point (the point of transition is at approximately $s/d/Fr = 2$). Further downstream the deviation diminishes. It can be noted that the dilution predicted by CorJet tends towards the low side. The experimental data is most consistent the predictions of Momentum Model and VisJet.

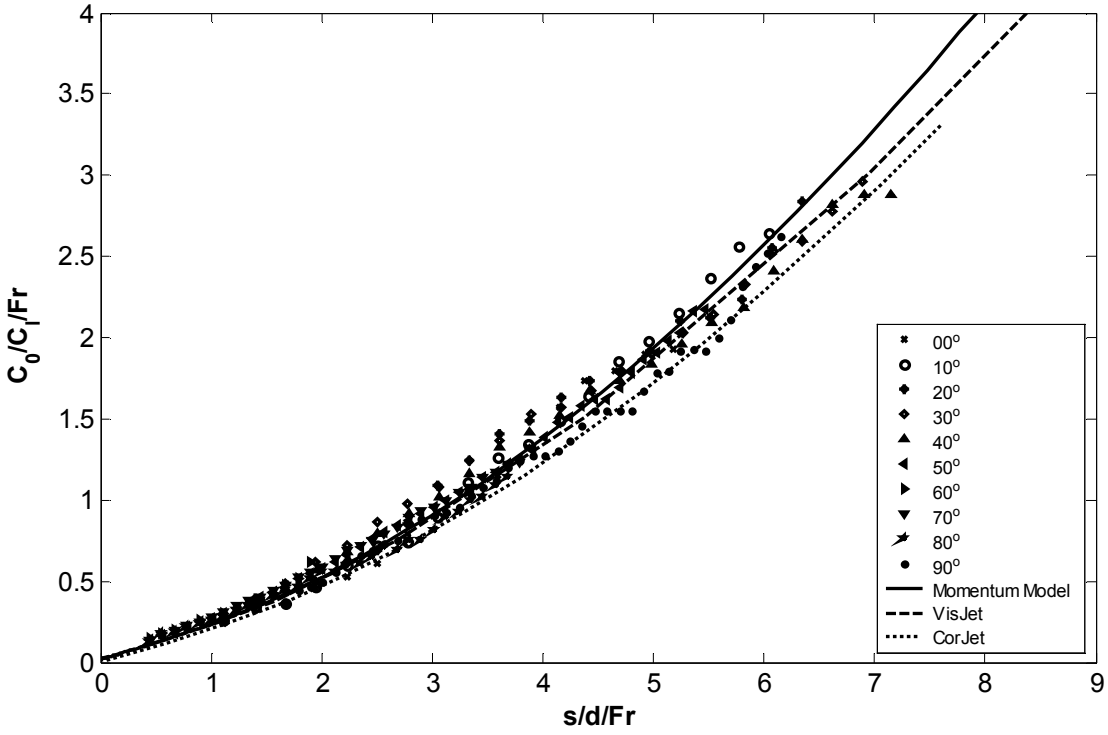

Figure 5.14 – Point centreline dilution results positively discharged buoyant jet experiments, comparing the experimental results with model predictions

5.3 – Moving Ambient Flows

The two-dimensional trajectory flows have been broadly defined in this thesis as flows with a trajectory that lies in a plane. Normally, from an experimental perspective, the source is located so that the trajectory plane is perpendicular to the camera. When the ambient is in motion, the flow trajectory remains two-dimensional only if the ambient moves in the same plane as the discharge. In these circumstances it is convenient to initially consider non-buoyant and buoyant discharges separately.

In the case of non-buoyant discharges the strongly advected behaviour can be either that of a momentum puff or a weak-jet. As discussed in Chapter 4, the strongly advected form of the flow appears to depend on the initial discharge angle. As the discharge angle (relative to the ambient velocity) approaches 90°, the internal mean concentration distribution resembles that of a vortex pair (see section 3.2.3.2) in the strongly advected region, that is, a line momentum puff forms. Whereas for small angles the internal mean concentration distribution remains Gaussian in the strongly advected region, where a weak-jet forms. The experimental investigation into these non-buoyant discharges has been split into two groups. The vertically

discharged momentum puff flows carried out as part of the present investigation are described in section 5.3.1. The flows discharged under oblique angles to the ambient have been studied in more depth and the results are presented in Chapter 7. The Momentum Model predictions in the weak-jet region are verified by comparing the predictions with previous experimental results. These results are presented in section 5.3.3.

As indicated previously, two-dimensional trajectory buoyant discharges in a moving ambient have three distinct regions of flow behaviour. In the first region the initial excess momentum flux dominates the behaviour. In the second region the buoyancy-generated momentum flux or the entrained ambient momentum flux dominates, depending on their relative sizes. In the final region, the advected thermal, the flow is dominated by both the buoyancy-generated momentum flux and the entrained ambient momentum flux. The presence of the buoyancy-generated momentum flux adds an additional constraint to the experimental set up, in that the flow moves in a vertical plane, which must be aligned with the ambient motion to maintain the two-dimensional path. These flows are discussed in more detail in section 5.3.2.

5.3.1 – Vertically Discharged Non-Buoyant Jet in an Ambient Flow

The investigation into the behaviour of the vertically discharged non-buoyant jet in an ambient flow has itself been divided into two different sections. The first group of experiments focused on the weakly advected behaviour where the initial excess momentum flux dominates the flow. These flows are referred to as advected jets. The second group of experiments focused on the strongly advected flows (the advected line momentum puffs). In total six advected jet and 23 advected line momentum puff experiments were carried out.

5.3.1.1 – Experimental Design

The advected line momentum puffs were the first experiments conducted in a moving ambient using the LA flow visualization technique and were an important part of its development. The experiments were used to determine the best set up for the LA system in combination with a moving ambient flow, to investigate the integrated theory (including the double-Gaussian assumption), and to verify the 3D LA system in combination with an ambient flow. The specifics of each run are listed in Table D.5 in Appendix D. This table includes information

on whether the camera recorded the *y*-integrated view or the *z*-integrated view (see Figure 3.27). During the investigation of the integrated theory, the source fluid was discharged horizontally directly away from the camera and thus the camera located alongside the tank recording a *z*-integrated view. During the verification of the 3D LA system, the source fluid was discharged vertically downwards. The camera alongside the tank then recorded the *y*-integrated view and the camera positioned above the tank recorded the *z*-integrated view.

The initial conditions of the advected jet runs are shown in Table D.6. The camera located alongside the tank, recorded the *y*-integrated view. The *z*-integrated view was not recorded for any of these flows. Advected jet runs 5 and 6 doubled as simple jet experiments. For run 5 the advected jet run was recorded first, then the source was brought back into the view of the camera and the stationary jet was recorded. However during the recording of the advected jet red dye was left behind in the camera view, interfering with the recording of the simple jet. For run 6, the order was reversed, alleviating much of the dye problem. These double-experiments were carried out to make a direct comparison between the jet and advected jet results.

In general the camera was fixed in its position during an experiment with the flow travelling through the recorded image. During the analysis the velocity of the trolley (the ambient velocity), and the frame rate of the camera were used to transform the images into a reference frame moving with the source. The main difference for the averaging process when compared with the still ambient flows was the number of images available for the calculation of the average at each particular pixel. This number decreased with increasing ambient velocity. To have enough images to create a reasonable average image some of the experiments were repeated two, three or four times. Those runs created out of multiple experiments are denoted with sub units 1 to 4 in Table D.5 and Table D.6.

The main difference between the advected jet and advected line momentum puff experiments is the distance from the source to the strongly advected transition point. This distance (or strong jet to puff transition length-scale) is given by:

$$l_{jm} = \frac{M_{e0}^{1/2}}{U_a} \tag{5.2}$$

A higher value for the transition length-scale shifts the strongly advected transition point further away from the source. Therefore, increasing the value for the transition length-scale made it possible to investigate the jet region in more detail. The transition length-scale for the

advected jet experiments ranged from 0.050m to 0.359m and the transition length-scale for the advected line momentum puff experiments ranged from 0.023 to 0.059. As there is no density difference between source fluid and ambient fluid, the Froude number was effectively infinite. The Reynolds number ranged from 2631 to 7682, guaranteeing a fully turbulent flow at the end of the source. The diameter of the source was reduced during the investigation from 3.00 mm to 2.45mm, the ambient velocity ratio $\left(U_a/U_0\right)$ varied between 0.003 and 0.049.

5.3.1.2 – Experimental Results and Model Predictions

The trajectory results, non-dimensionalised by the strong jet to puff transition length scale, are shown in Figure 5.15. In the strongly advected region the flow moves predominantly in the *x*-direction because of the influence of the entrained ambient momentum flux. The trajectory results in the strongly advected region are shown in Figure 5.15a and the experimental data is in good agreement with the experimental data from Pratte and Baines (1967) and Hung (1998). The model predictions in the strongly advected region are consistent with the experimental data and each other. In the region dominated by the initial excess momentum flux, the predominant motion is in the *z*-direction. The experimental results from the advected jets are compared with previous studies and the model predictions in Figure 5.15b. The experimental data matches the results from Pratte and Baines (1967) and Hung (1998). Data from Jordinson (1956) and Keffer and Baines (1963) appears to be relatively low in both figures. It is evident that the predictions of the Momentum Model do not match the experimental data in the transition zone from jet to puff. This is because the transition from the jet to the momentum puff region was set to occur at a point, $z/\left(M_{e0}{}^{0.5}/U_a\right)=1.0$, rather than allowing it to happen gradually; thus the trajectory prediction of the Momentum Model bends over too late. However it makes up for overshooting the experimental data by immediately becoming a strongly advected flow and therefore matching the data again at approximately 1.8 length-scales in the *z*-direction. Further downstream the prediction from the Momentum Model is consistent with the experimental data, confirming the determined value of 0.60 for the top-hat spread in the momentum puff region of the flow (see section 4.4). VisJet and CorJet predict the trajectory better near the transition point. Beyond the transition zone, the predicted values from VisJet are lower than the predicted values from the Momentum Model and CorJet.

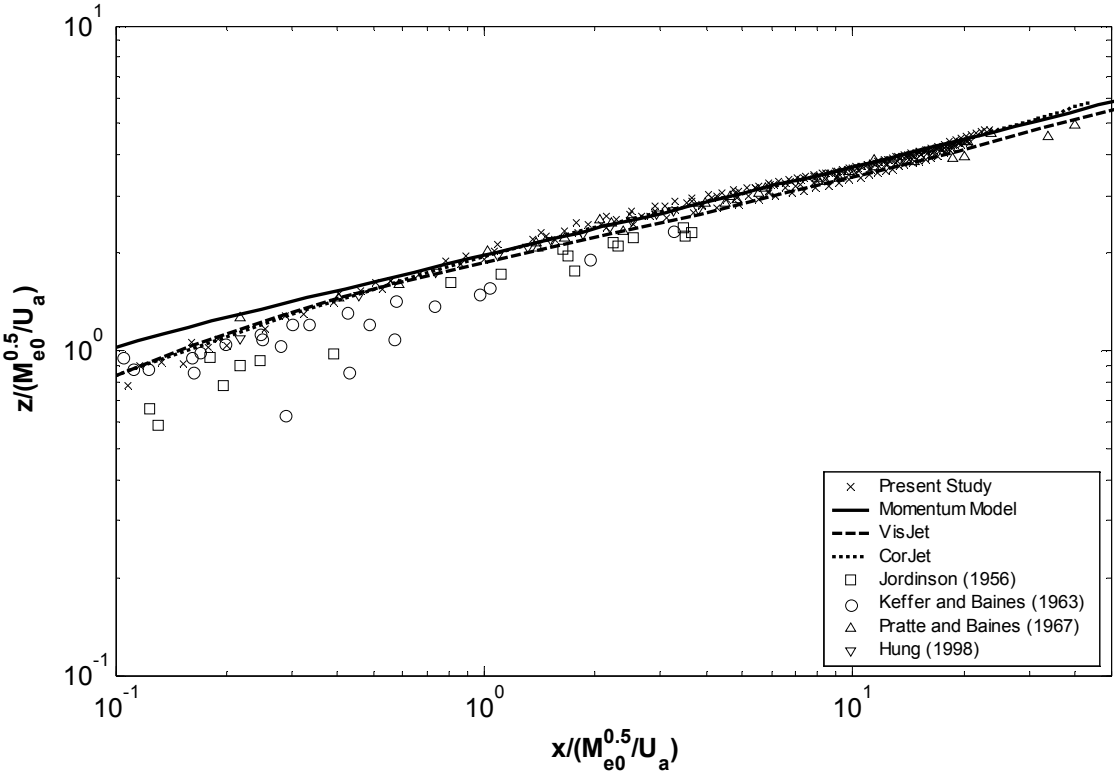

5.15(a) – Trajectory results from advected line momentum puff experiments

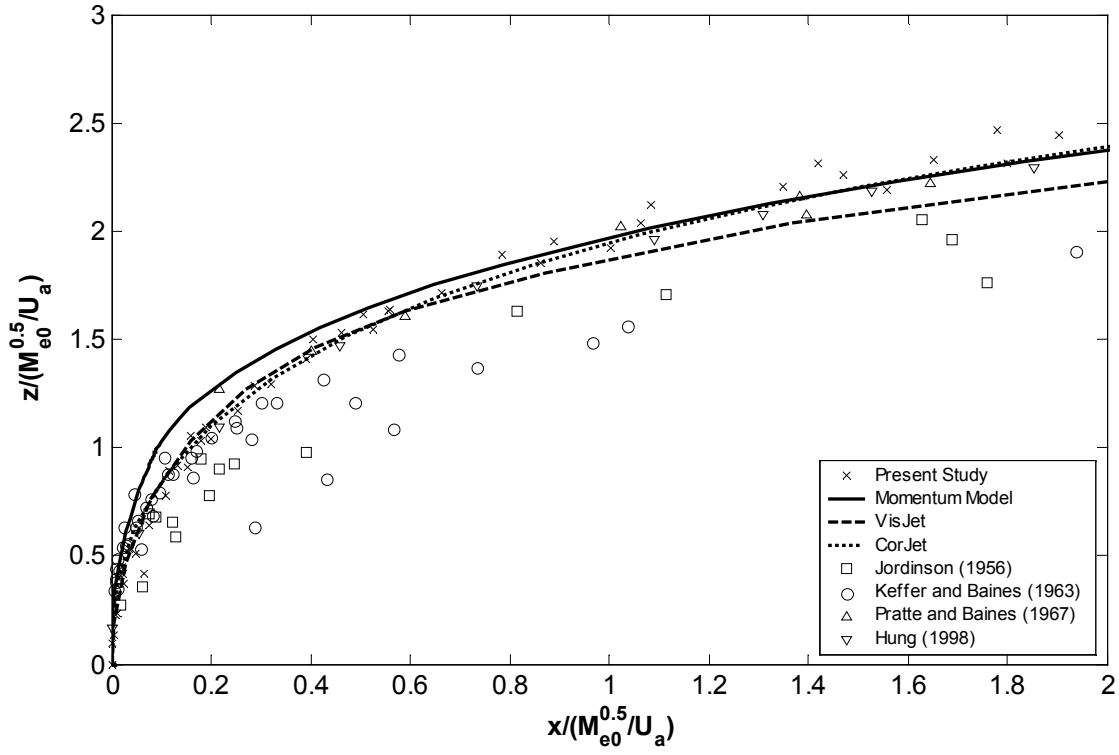

5.15 (b) – Trajectory results from advected jet experiments

Figure 5.15 – Trajectory results from advected line momentum puff and advected jet experiments are compared with previous results and model predictions

Figure 5.16 shows the concentration-spread results from the advected jet (AJet) and advected line momentum puff experiments (AMP). These are compared with predictions from the Momentum Model. However, the predicted values are average velocity spread values, and must therefore be converted into concentration spread values. Again this creates a discontinuity at the transition point, because of different spread conversion rates for the weakly and strongly advected flows (the concentration spread decreases from 0.13 to 0.11 at the transition point). The experimental data in Figure 5.16 is divided into four groups. The first group is the average *y*-integrated concentration spread data. This data was determined by fitting a second order polynomial through the natural logarithm of the concentration spread values at a cross-section and is used in section 3.2.3.2. The outside and inside advected jet concentration spread refer to the *y*-integrated concentration spread on the outer and inner edge of the flow respectively where $C_i = e^{-1} C_{il}$. The results show a lack of symmetry in the jet-region of the flow. The outside spread is significantly lower than the average spread and the inside spread slightly higher. The Momentum Model prediction assumes symmetry in this region and is consistent with the outside concentration spread. The advected jet outside spread deviates from the inside spread at approximately 0.5 length-scales, indicating the start of the transition zone. Following the outside spread into the momentum puff region, the advected line momentum puff results show that the outside spread matches up with the average cross-sectional spread data at approximately 2.7 length-scales.

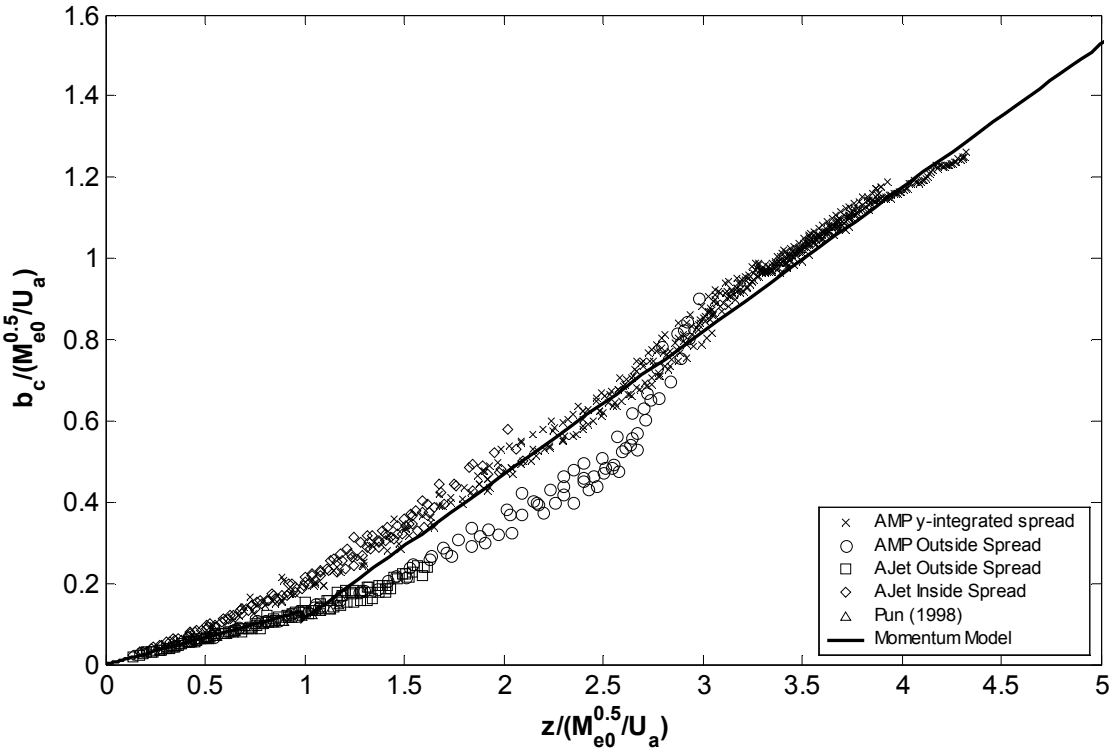

Figure 5.16 – Concentration spread results from the vertically discharged momentum puff and advected jet experiments

The asymmetry in the spread results has an influence on the *y*-integrated dilution results. This is clearly visible in Figure 5.17. The *y*-integrated theory as discussed in Chapter 3 is compared with the *y*-integrated dilution results from both the advected jet and the advected line momentum puff experiments. In the strongly advected region, at least three length-scales in the *z*-direction from the source, the predicted slope of the *y*-integrated dilution theory matches the experimentally determined slope, confirming the earlier determined end of the transition zone. In the weakly advected jet-like region of the flow, the *y*-integrated dilution is constant at approximately 1.20. However the theoretical integrated dilution in the jet region is 0.81, 32% lower than the experimental values.

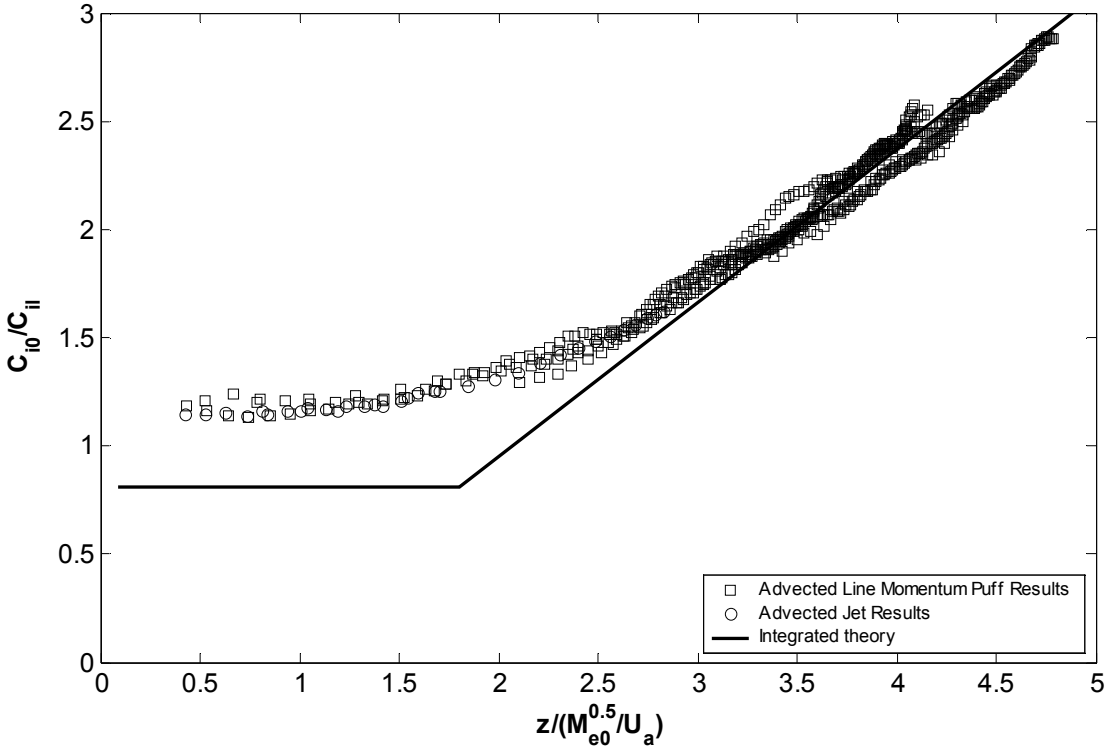

Figure 5.17 - *y*-integrated dilution results from advected line momentum puff and advected jet experiments

The discrepancy in the integrated dilution values in the jet region was investigated further by comparing the double-integrated dilution results (C_{ii0}/C_{ii}) from jet experiments with those of the advected jet. Figure 5.18 shows the double integrated dilution results of the jet and advected jet, including advected jet run 7 doubling as a jet experiment, compared with the theory of equation (3.21). Run 7 was carried out to enable a direct comparison between the jet and advected jet results, and it confirmed the results from the other jet and advected jet experiments. As explained in Chapter 3.2.3.1, the jet results are approximately 2% higher than the theory. The advected jet results initially follow the jet results and thus the theory, but are lower by up to 6% further downstream. However these differences are relatively small and therefore the double-integrated dilution results can be used to confirm that there are no systematic experimental errors in the LA system causing the discrepancy in the integrated dilution. The difference between the theory and the experimental values is therefore real and appears to be related to the distortion of the flow shape, and thus the cross-sectional profiles. The internal concentration distribution in the advected jet region is assumed to have the same distribution as the jet, but this assumption clearly does not hold for the integrated dilution results. The distortions create an internal concentration distribution in the advected jet region that has to be quantified and incorporated into the integrated dilution theory. The higher

integrated dilution values and hence reductions in the integrated concentration are consistent with the results from Davidson and Pun (1999). They indicated that in the advected-jet region the cross-sectional profiles in the *y*-direction were narrower than the Gaussian profile predicted.

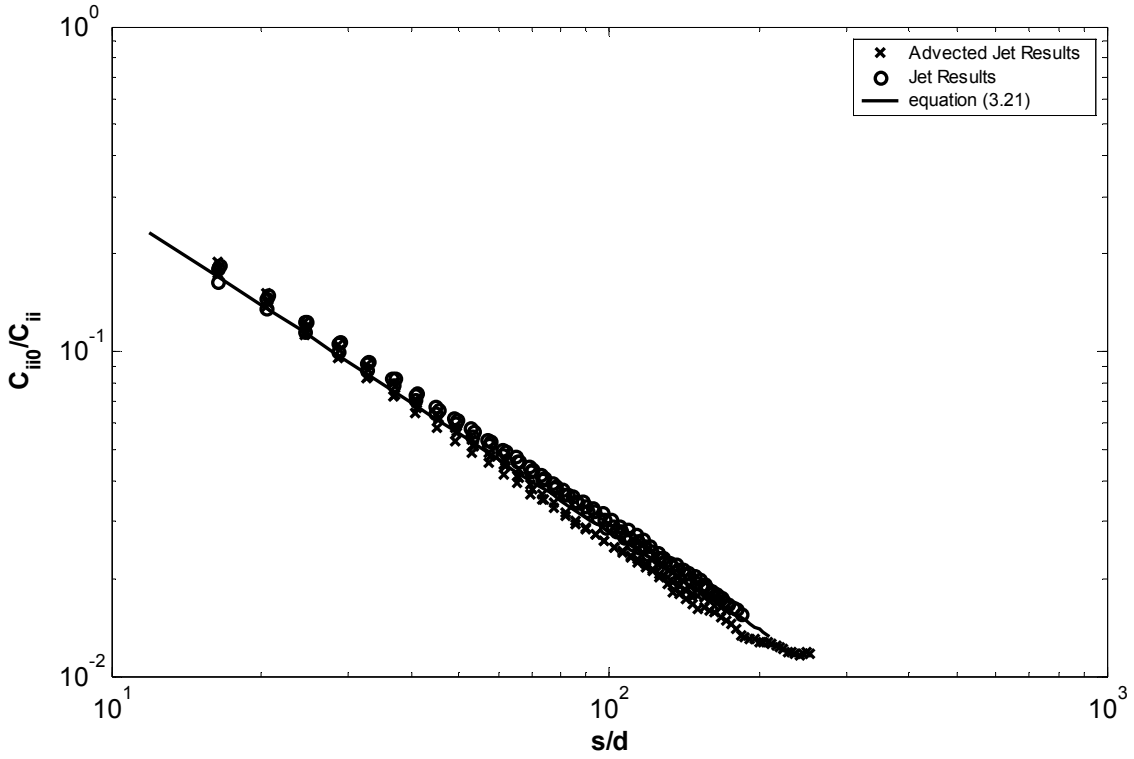

Figure 5.18 – Double integrated dilution results from advected jet and jet experiments

Figure 5.19 compares the minimum point dilution of the three models with the experimental data. The experimental data measured from both directions collapse well onto a single line. Again the error in the Momentum Model prediction, due to the point transition and the subsequent instantaneous change in concentration conversion rate, is clear. The model underestimates the peak dilution in the transition zone. However, in the strongly advected region, from approximately 2.5 length-scales in the *z*-direction onwards, the prediction by the Momentum Model matches the experimental data, again confirming the determined value of 0.60 for the top-hat spread in the momentum puff region of the flow. In the strongly advected region, the experimental values fall in between the model predictions of CorJet and VisJet, with CorJet underestimating the dilution and VisJet overestimating it.

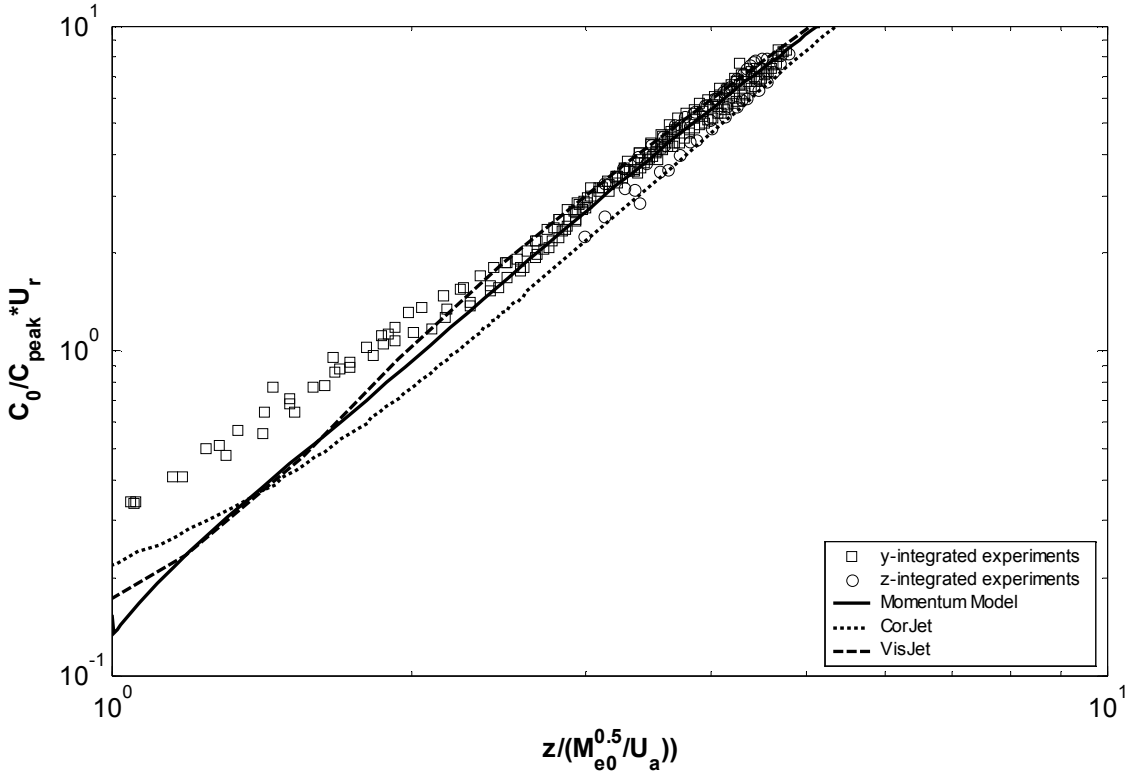

Figure 5.19 – Cross-sectional minimum dilution results from vertically discharged momentum puff experiments

5.3.2 – Buoyant Jet in Moving Ambient Flow

Many previous experimental investigations have focused on the behaviour of the buoyant jet in a moving ambient flow. In most of these studies the angle between the initial momentum flux and the entrained ambient momentum flux was either 0° or 90° (see section 2.4.2.5). The aim of the present investigation was twofold. Firstly to study the trajectory of the flow in the advected thermal region, and secondly to study buoyant discharges with oblique initial discharge angles in a moving ambient.

5.3.2.1 – Experimental Design

The experimental investigation into the behaviour of buoyant jets in moving ambient flows comprised 23 runs. The initial conditions of each of the runs can be found in Table D.7 in Appendix D. Runs 1-18 focussed on the behaviour of obliquely discharged buoyant jets in a moving ambient. The source diameter was left unchanged at 2.91mm for the duration of these

runs and the density difference between the source fluid and the ambient fluid was approximately 3.9% for runs 1 to 11 and 2.7% for runs 12 to 18. The initial Froude number ranged from 27 to 55 and the Reynolds number from 2625 to 4507. Runs 19-23 were used to investigate the trajectory in the advected-thermal region and therefore only trajectory results are available. The source diameter for these runs was 2.43mm, the density difference either approximately 1.9% or 3.9%. The Froude numbers ranged from 17 to 78, and the Reynolds number from 1281 to 4119. The low Reynolds numbers meant the flow was laminar when exiting the source for some of the experiments. However this is shown to have no significant effect on the flow by the time it has reached the advected-thermal region.

5.3.2.2 – Experimental Results and Model Predictions

Starting with the advected thermal trajectory results, it has been noted that for a flow with a two-dimensional trajectory the spread assumption used by the Momentum Model in the advected thermal regions of the flow, is of the form

$$\frac{db}{dz} = m_{th-t} \tag{5.3}$$

where b is based on top-hat profiles. This top-hat assumption can be incorporated into the advected thermal flow trajectory equation (Davidson 1989) to give:

$$\left(\frac{z}{Q_0 \Delta_0 / U_a^{\,3}} \right)^3 = \frac{3}{2\pi} \frac{1}{m_{th-t}^{\,2}} \left(\frac{x}{Q_0 \Delta_0 / U_a^{\,3}} \right)^2 \tag{5.4}$$

Thus, the advected thermal trajectory results can be used to determine a value for the spreading rate in the advected thermal region of the flow.

Figure 5.20 shows the trajectory results of the buoyant jet in a moving ambient experiments, non-dimensionalised by the plume to thermal transition length-scale (see section 2.5.1). In Figure 5.20a the results from the horizontally discharged buoyant jets in a coflow are presented. On the log-log plot, flows in the advected thermal region are identified by having a linear trajectory relationship. Runs 22 and 23 travelled for some distance in the advected thermal region and were used to define the constant of the best-fit line. All the other experiments indicate that at greater distances they would collapse onto this line. The spread constant $m_{th\text{-}t}$ was calculated from the constant of the best-fit line and has a value of 0.73. The value determined for the top-hat spreading rate in the momentum puff region, $m_{th\text{-}m}$, was 0.60, clearly indicating that the spreading rates are not the same in the two regions. It is also worth

noting that the consistency of the results indicates that the initial Reynolds number is insignificant in defining the advected thermal behaviour.

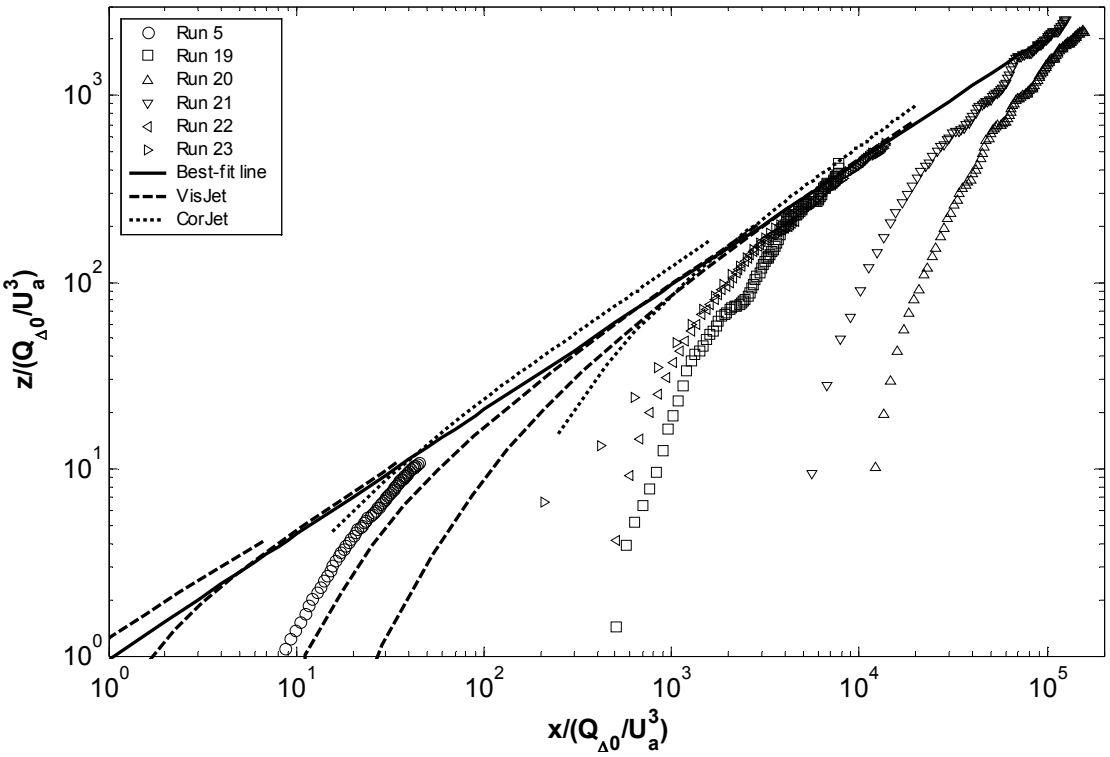

5.20(a) –Trajectory results, comparing experimental results with model predictions

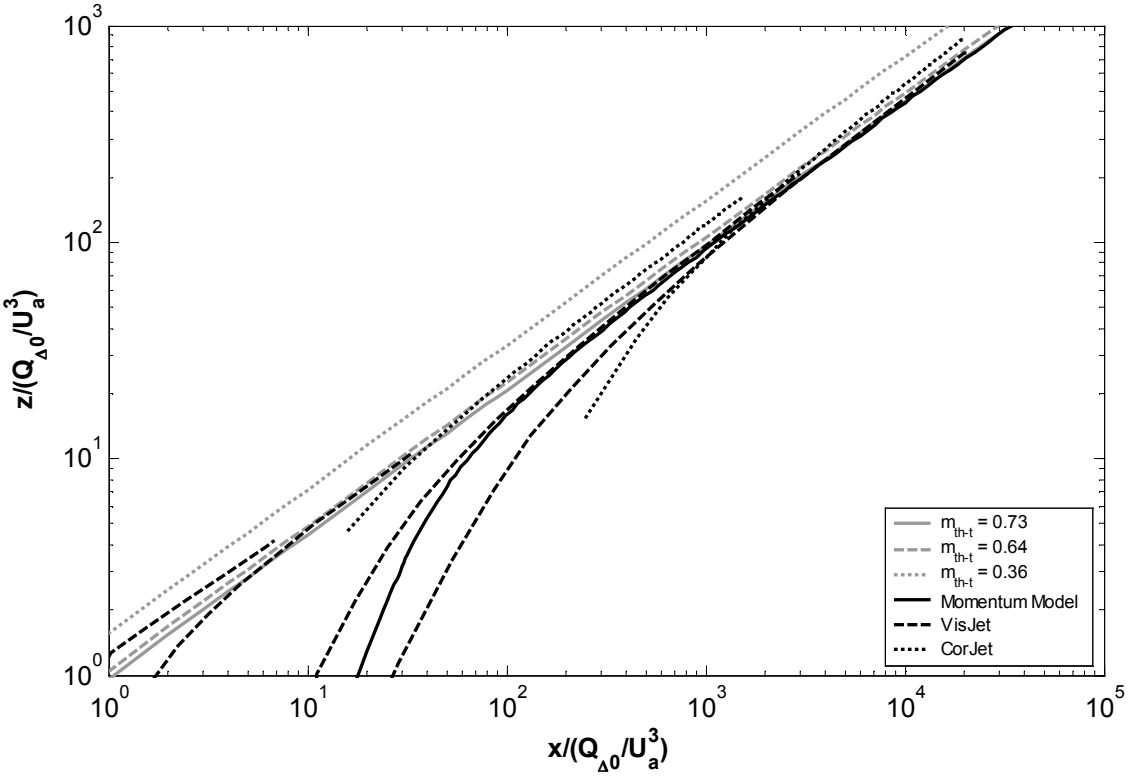

5.20(b) - Trajectory results, model predictions and limiting behaviour

Figure 5.20 - Trajectory results from horizontally discharged buoyant jet in a moving ambient

The predictions from VisJet and CorJet have been added to Figure 5.20a. From the Figure it is clear that both models cross the best-fit line based on the experimental data. VisJet and CorJet employ entrainment rate assumptions to close their set of equations. The entrainment rates in the advected thermal region were converted into the top-hat spreading rates, giving values of 0.64 and 0.36 for VisJet and CorJet respectively. Using equation (5.4) the limiting trajectory behaviour was calculated as predicted by the models. The results are presented in Figure 5.20b and they confirm the results from Figure 5.20a. The entrainment rates employed by VisJet and CorJet are too low and therefore the models overestimate the distance travelled in the z-direction.

As mentioned above the behaviour of the flow in the strongly advected region is expected to be dominated by the advected thermal and thus independent of initial discharge angle. To verify this statement, the experimental trajectory results from the runs with oblique discharges are presented in Figure 5.21. For comparison the predictions from the Momentum Model and VisJet for the 0° and 130° cases and the prediction from CorJet for the 0° case have been added as well. The trajectory results from runs with the same initial angle, but different Froude numbers and velocity ratios, are no longer expected to collapse onto a single line in the weakly advected region for the buoyant jet in a moving ambient flow. It was therefore necessary for previous experimental results to have the exact same initial conditions as the current experiments to make a proper comparison possible, and hence no comparisons with previous experimental results have been presented.

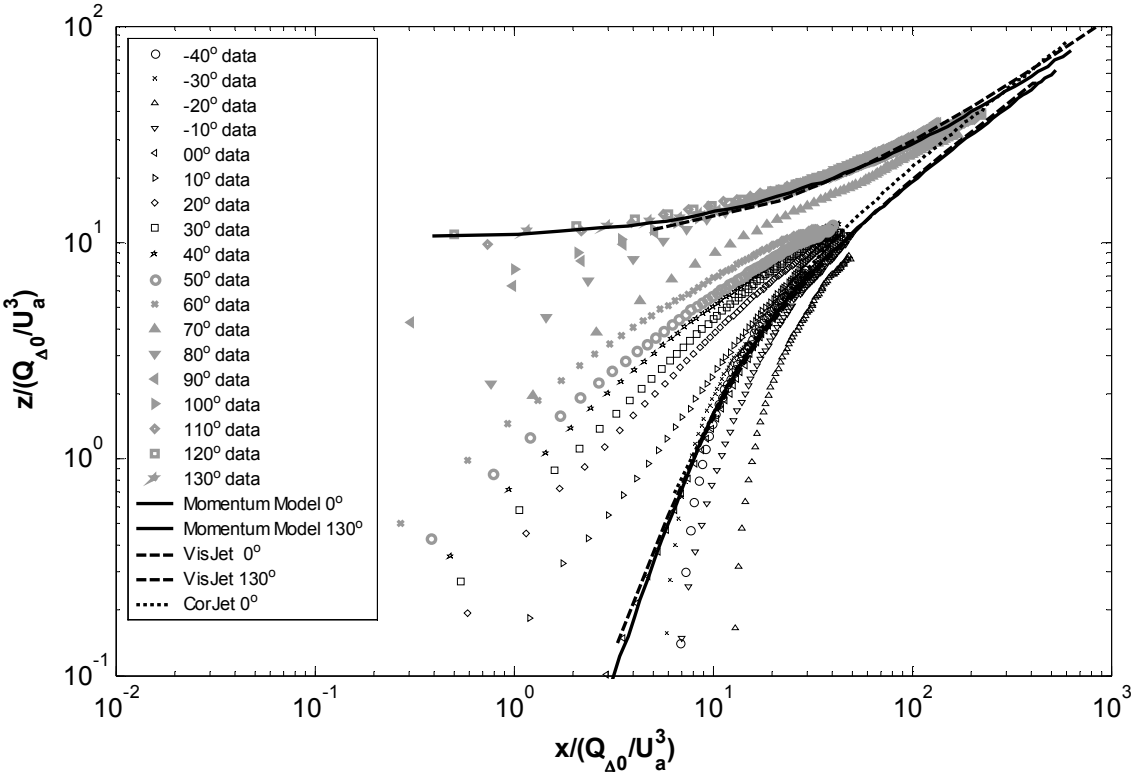

Figure 5.21 - Limiting trajectory results for oblique discharged buoyant jets in a moving ambient

The results in Figure 5.21 indicate that in the advected thermal region of the flow trajectories are independent of the initial discharge angle. The data from the different runs appear to collapse with increasing distance from the source. The results from the runs with an initial discharge angle upwards from 70° actually collapse onto a single line. However, due to different initial conditions for the runs up to 60°, the results for these runs do not extend sufficiently far downstream for this to be seen on the plot, but it is evident that these runs also have a tendency towards a single line. Figure 5.21 also confirms the inconsistencies between the three model predictions in the advected thermal region of the flow. CorJet and VisJet predict that the flow travels a greater distance in the *z*-direction than the Momentum Model.

The trajectory results of a sample of the runs are presented in Figure 5.22. For the lower angles, -20°, 0° and 20 (Figure 5.22a), the model predictions from the Momentum Model and VisJet match the experimental data very well. This indicates that the distortion of the assumed Gaussian cross-sectional profiles due to the ambient motion, in the weakly advected region, is not severe enough to significantly influence the trajectory results. The 0° and 20° data show a divergence between the CorJet and the other model predictions. The relatively low value for $m_{th\text{-}t}$ employed by CorJet results in an underestimate of the influence of the ambient entrainment and therefore the distance travelled in the horizontal.

For the -40° run, shown in Figure 5.22b, the results in the strongly advected region are similar to the 20° run, with the VisJet prediction being higher than the Momentum Model prediction. In the weakly advected region it was observed during the experiment that before reaching maximum depth, some of the eddies that formed on the inside edge of the flow were not re-entrained and appeared to move separately from the main flow. These detached eddies were eventually re-entrained by the flow after it had reversed direction in the vertical. However, the model predictions are still reasonably consistent with the experimental data in the weakly advected region.

The 70° run, shown in Figure 5.22c, has similar problems near the transition zone as the vertically discharged non-buoyant jet in an ambient experiments described earlier. The distance travelled in the z-direction is overestimated because the transition is predicted to occur at a single point. Up to that point the cross-sectional profiles are modelled to be Gaussian, underestimating the influence of the ambient flow on the cross-section and therefore on the trajectory. The prediction from the Momentum Model is consistent with the prediction from VisJet. The influence of the lower spreading rate in the advected thermal region on the trajectory is insignificant in Figure 5.22c because the distance travelled from the source is relatively small. However the effect of the low spreading rate is visible in the predicted results from CorJet. The predictions from the Momentum Model match the 100° and 130° experimental data well, including the data in the weakly advected region of the flow. VisJet overestimates the influence of the entrained ambient momentum flux in the weakly advected region of the flow, and therefore underestimates the distance travelled in the z-direction.

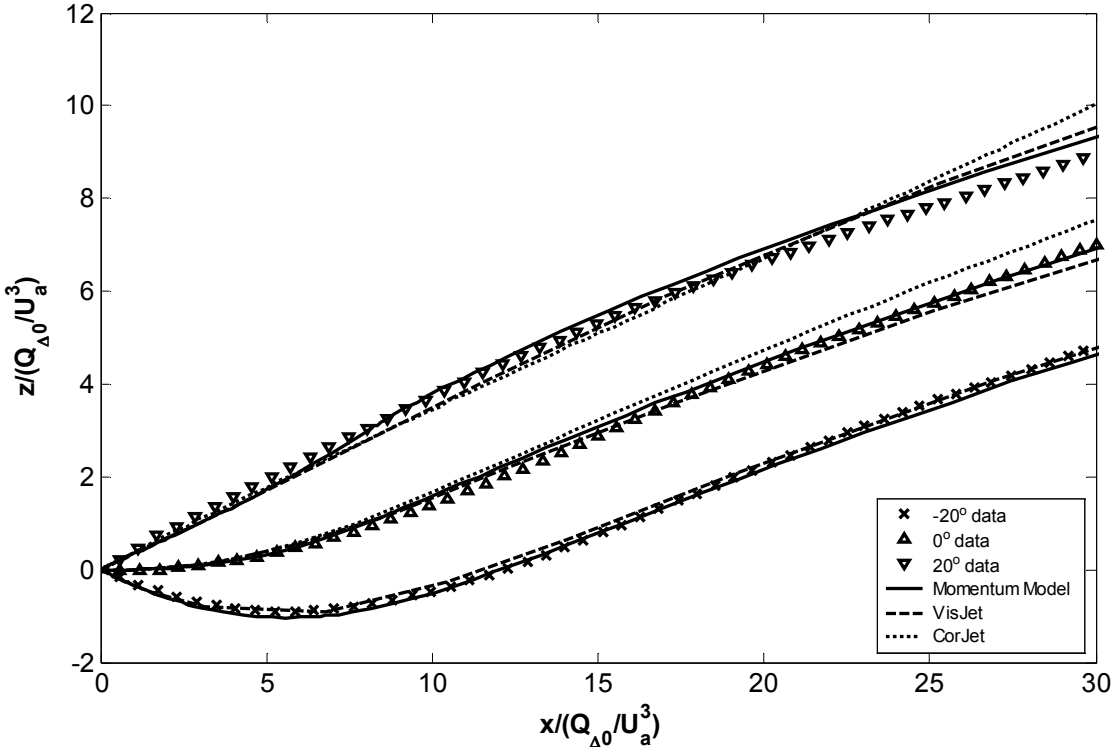

5.22(a) - Trajectory results for runs with initial discharge angles of -20°, 0°, and 20°

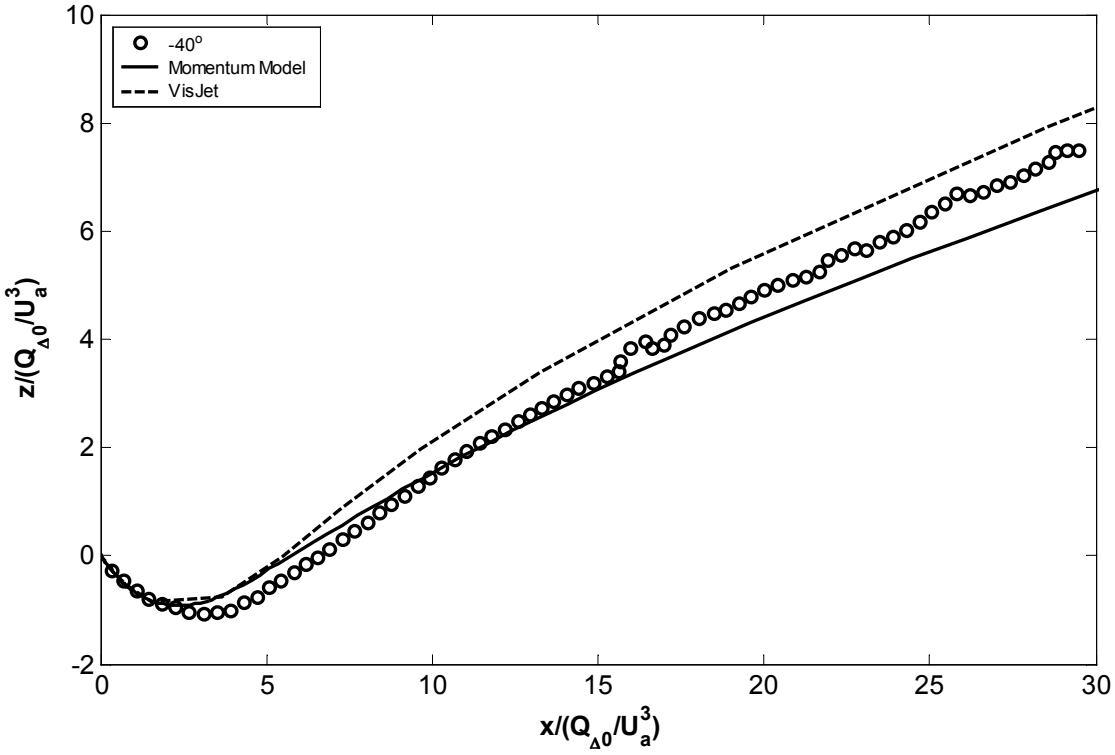

5.22(b) - Trajectory results for runs with initial discharge angles of -40°

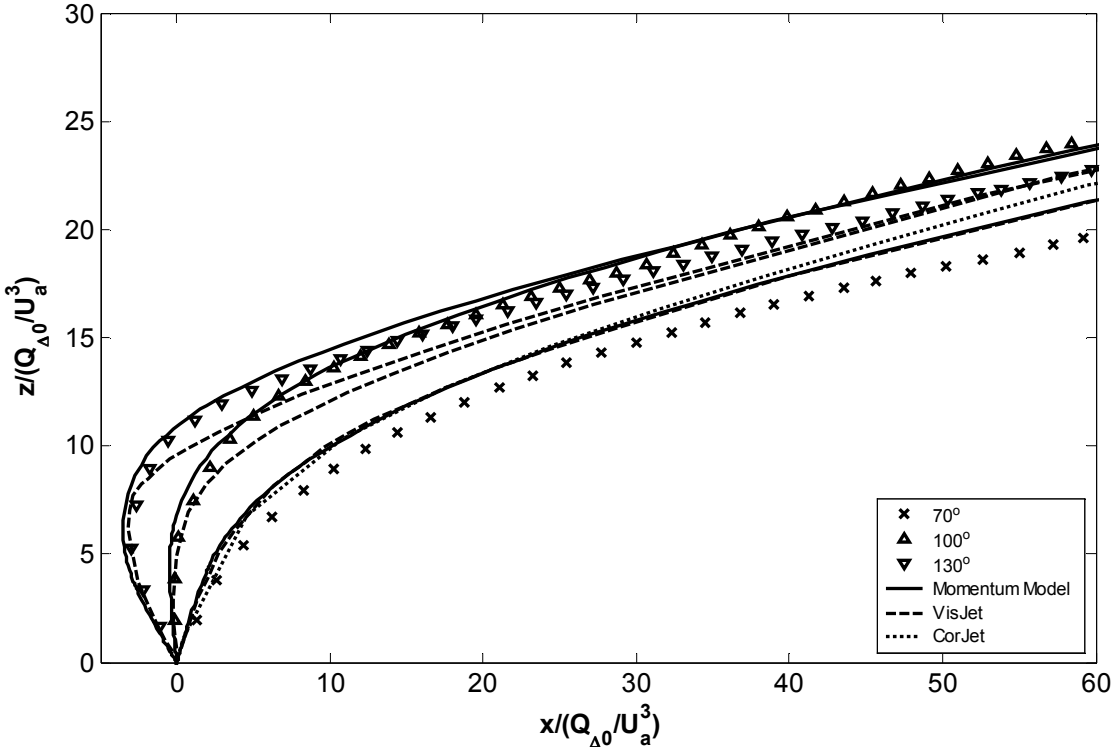

5.22(c) – Trajectory results for runs with initial discharge angles of 70°, 100° and 130°

Figure 5.22 –Trajectory results from buoyant jet in moving ambient experiments

Figure 5.23 and Figure 5.24 present the *y*-integrated concentration spread results. VisJet and CorJet predictions have been omitted from these plots, because the spread data predicted by these model is no longer based on the actual cross-sectional profiles in the strongly advected region. Therefore a direct comparison cannot be made. The spread prediction from the Momentum Model is based on the double-Gaussian assumption (see section 3.2.3.2), and it is therefore possible to convert the predicted data and compare the results directly with the experimental data. Note that the trajectory results show that in the advected thermal region, the rate of spread is higher (by approximately 20%) than in the momentum puff region of the flow. However, during the experimental investigation, only the *y*-integrated concentration spread has been measured. Without detailed information about the concentration spread in the *z*-integrated direction, it is difficult to assess how the increase in entrainment alters the mean cross-sectional concentration profiles (and the values for f, h and k_{sg}), and therefore how the conversion from top-hat to double-Gaussian is affected.

Figure 5.23 shows the *y*-integrated concentration spread data for flows with higher initial discharge angles. The prediction from the Momentum Model for the 90° case has been converted based on the assumption that the increase in entrainment does not alter the overall

shape of the cross-sectional profile, but k_{sg} increases by approximately 20%. Comparing the predicted results with the experimental data, it is clear that the Momentum Model prediction does not match the experimental data. Previous research (for example Jirka (2004)) has used the assumption that the spread in the momentum puff and advected thermal regions were the same. However, most previous investigations have studied the puff and thermal in the y-direction only. This, in combination with the higher spreading rate of the complete cross-section in the thermal region, indicates that the increased entrainment in the thermal region does not affect the y-integrated concentration spread results. An alternative prediction for the 90° experimental data has been added to Figure 5.23 based on this assumption. The figure shows that the alternative prediction from the Momentum Model is reasonably consistent with the experimental data. This indicates that in the advected thermal region the product of k_{sg} times h is the same as that in the momentum puff region even though the values for k_{sg} and h may change. The Momentum Model prediction with the alternative conversion is also a reasonable prediction for the experimental data for the run with an initial discharge angle of 120°.

The Momentum Model prediction with the alternative top-hat conversion rate for the concentration spread discharges was expected to be consistent with the experimental data of the –20° and 0° cases, because of the consistency between the model and experiment in the trajectory results. Figure 5.24 shows that the match between experimental data and model is reasonable close to the source and in the strongly advected region of the flow, increasing the confidence in the use of the double-Gaussian assumption to model the cross-sectional profiles in the strongly advected region, and the alternative top-hat conversion rate. The prediction is the least accurate near the transition from weakly advected to strongly advected flow, because the transition zone is modelled as a point transition, and the top-hat conversion rate from the weakly advected to strongly advected region changes instantaneously at that point. Rather than an abrupt changeover, a changeover region was defined to more accurately compare the model prediction with the data. This region should include the complete transition zone, however it was not possible to accurately determine the starting point of the transition zone. The point of transition, as defined by the Momentum Model, was therefore chosen as the lower limit of the region and the upper limit the end point of the transition determined by the experimental data. Within that region a conversion rate based on the relative distances from either end of the region was applied to the data. The adjusted data has been added to Figure 5.24, showing that conversion adjustment substantially increases the accuracy of the model's prediction.

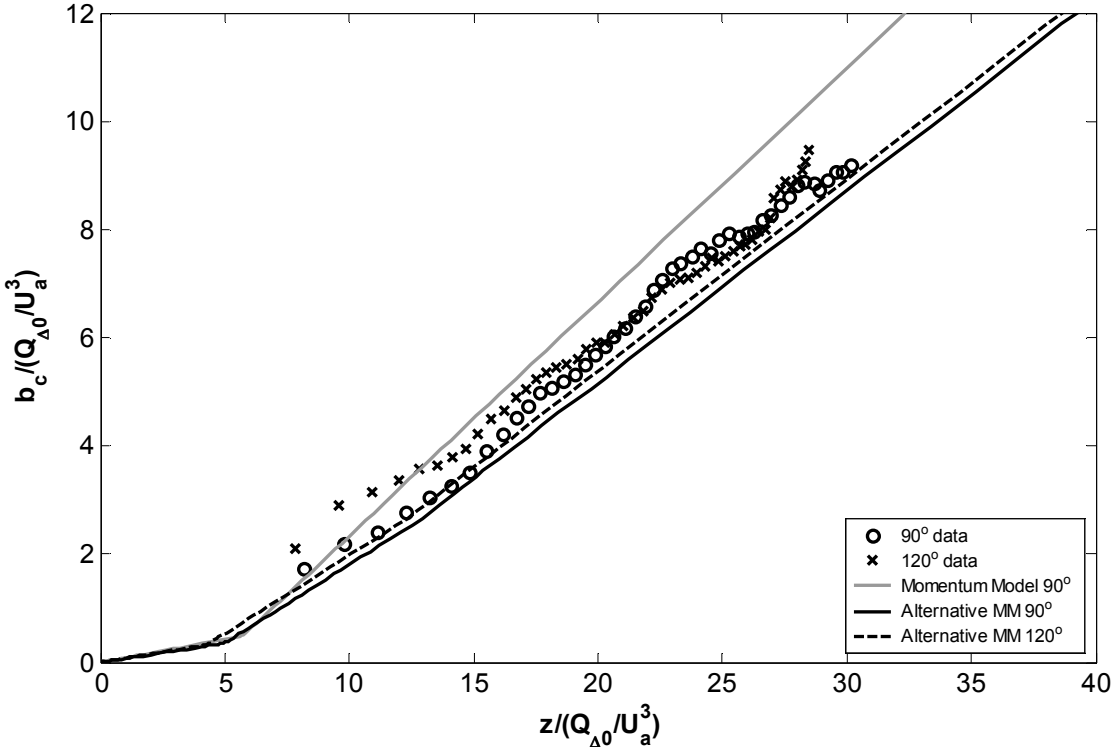

Figure 5.23 - Concentration spread results from buoyant jet in moving ambient experiments with initial discharge angles of 90° & 120°

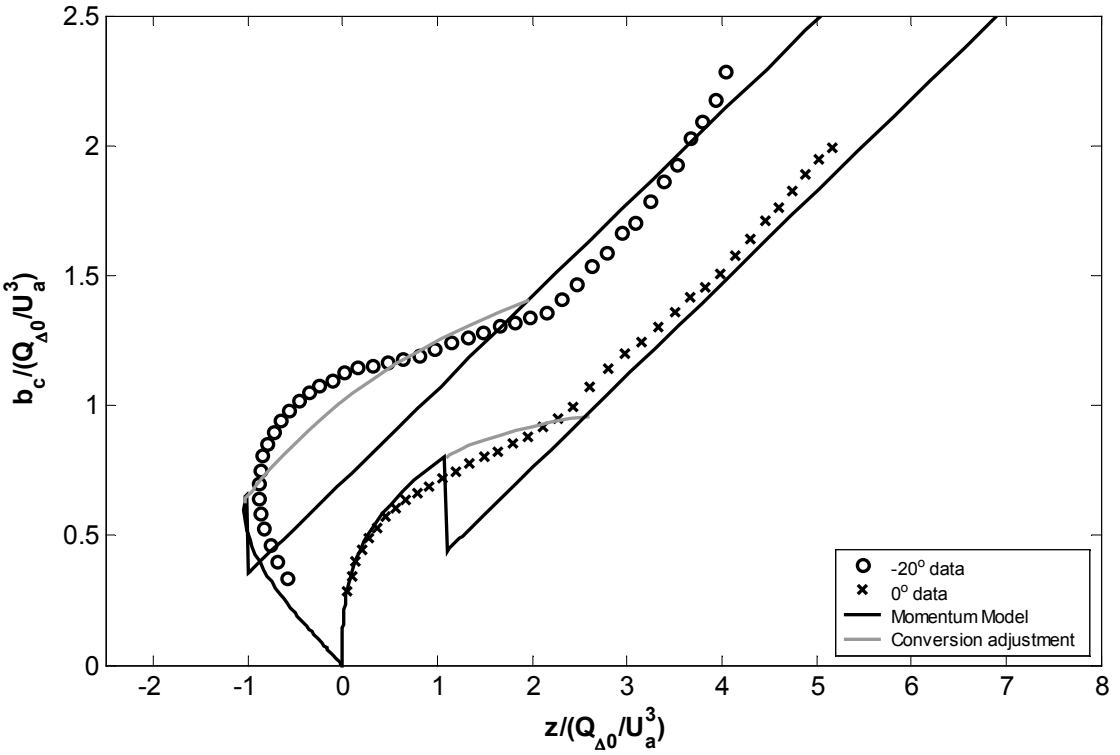

Figure 5.24 - Concentration spread results from buoyant jet in moving ambient experiments with initial discharge angles of -20° and 0°

The experimental minimum dilution results were calculated using the concentration spread results, the experimentally found integrated dilution data and equation (3.46). Both Momentum Model and VisJet give top-hat dilution data. The Momentum Model data was converted using equation (4.66) and VisJet's data using equation (4.71). All these conversion equations depend of *f*. Without information from the *z*-integrated direction it is not possible to estimate a value for *f* in the thermal region, therefore the puff value of 0.88 has been used. No attempts have been made to include a gradual conversion rate between the weakly and strongly advected regions, therefore only a direct comparison between the models and experimental data can be made in the strongly advected region. The minimum dilution results in Figure 5.25a show that in the strongly advected region the Momentum Model prediction is consistent with the experimental data from the –20° and 0° runs. VisJet and CorJet are both overestimating the dilution. Figure 5.25b shows the dilution results from the 90° and 120° runs. The 120° predictions by both VisJet and the Momentum Model are to the left of the 90° predictions, the single prediction from CorJet is discharged vertically. Again the data is most consistent with the prediction of the Momentum Model in the strongly advected region.

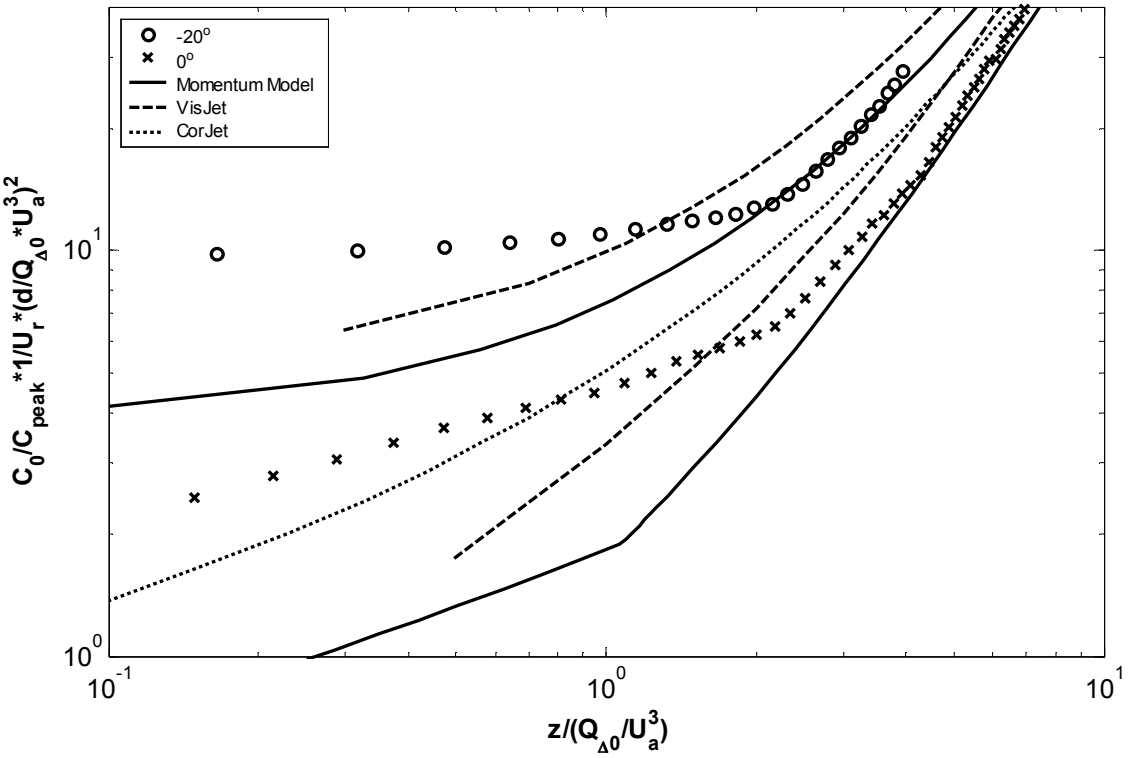

5.25(a) – Minimum dilution results from runs with initial discharge angles of -20° and 0°

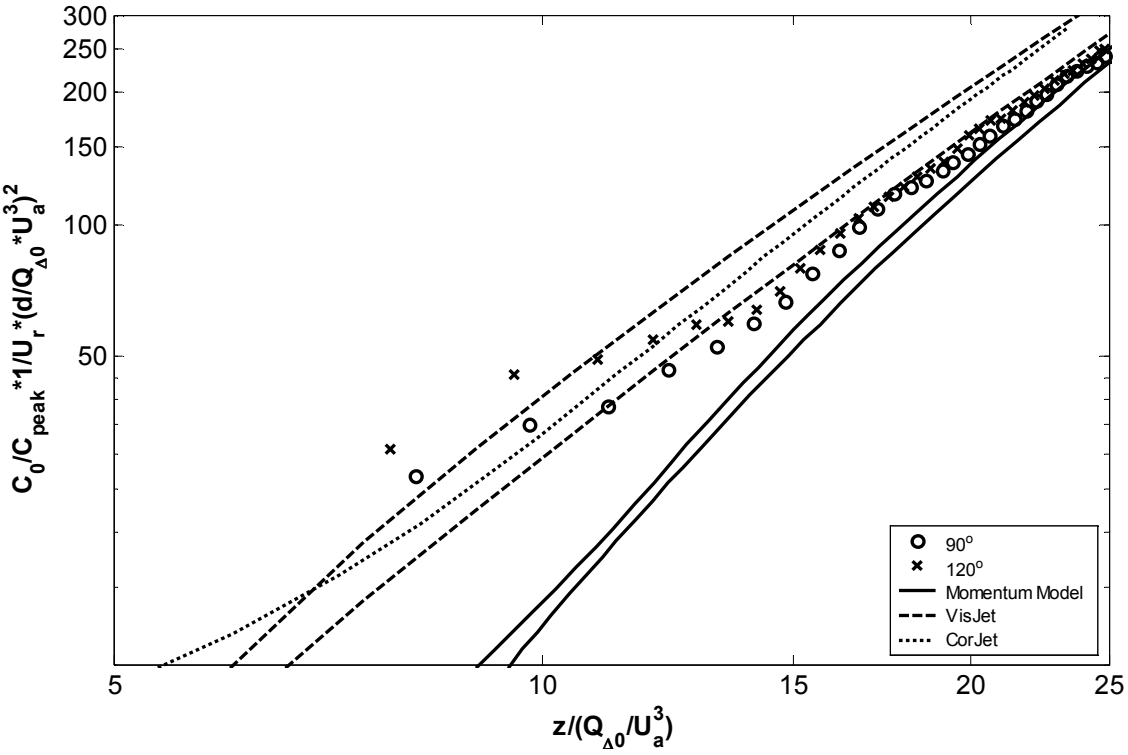

5.25(b) – Minimum dilution results from runs with initial discharge angles of 90°, and 120°

Figure 5.25 –Minimum dilution results from buoyant jet in moving ambient experiments

5.3.3 – Weak Jet

A horizontally discharged non-buoyant discharge in a moving ambient transforms into a weak jet in the strongly advected region. Wang (2000b) carried out detailed experimental work into the behaviour of the weak jet. Her work is the basis for the weak jet spread function used by the Momentum Model, defining the behaviour in the weak jet region. The data from her experimental investigation is therefore expected to match well with the Momentum Model predictions.

Figure 5.26 shows the concentration spread from Wang's experimental data and the Momentum Model. The top-hat values from the model were converted to Gaussian spread values using equation (4.68) and then multiplying by λ to obtain the concentration spread predictions. The value used for λ in the weak jet region was 1.59 (30% higher than in the strong jet region) as suggested by Wang. The match between the model and the experimental data is very reasonable. The predicted concentration data was converted using equation (4.70).

The centreline dilution data is compared with data from Wang in Figure 5.27. Again the model predictions are consistent with the experimental data.

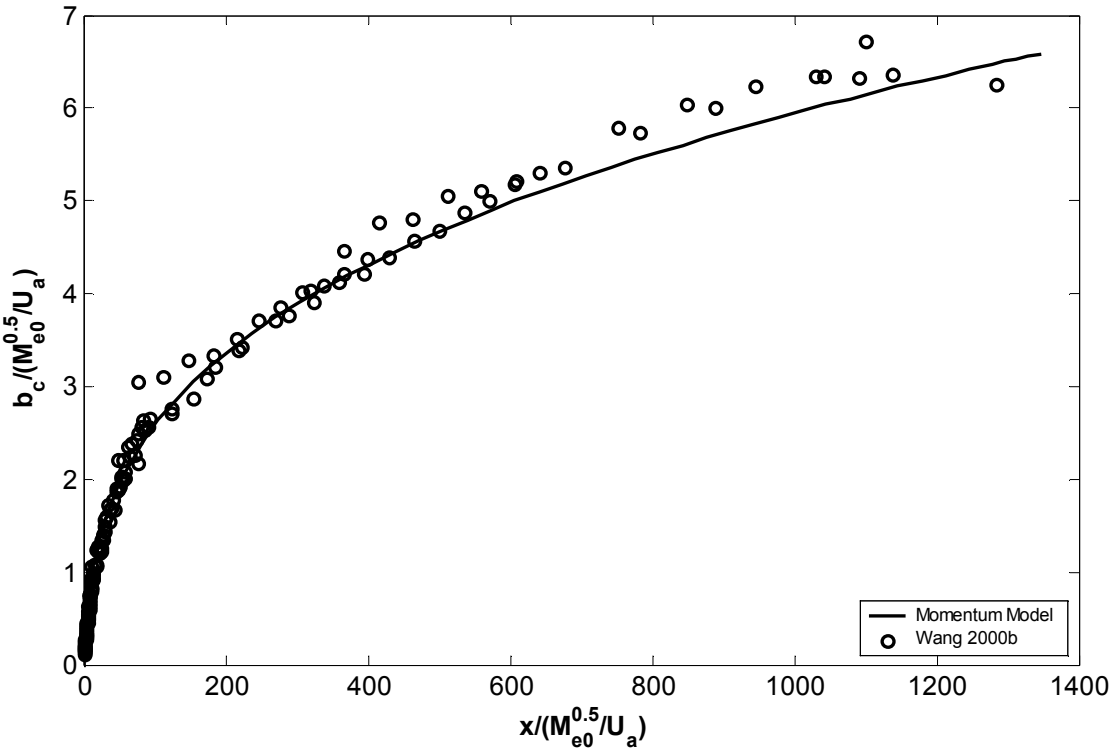

Figure 5.26 – Momentum Model prediction for concentration spread in weak jet region

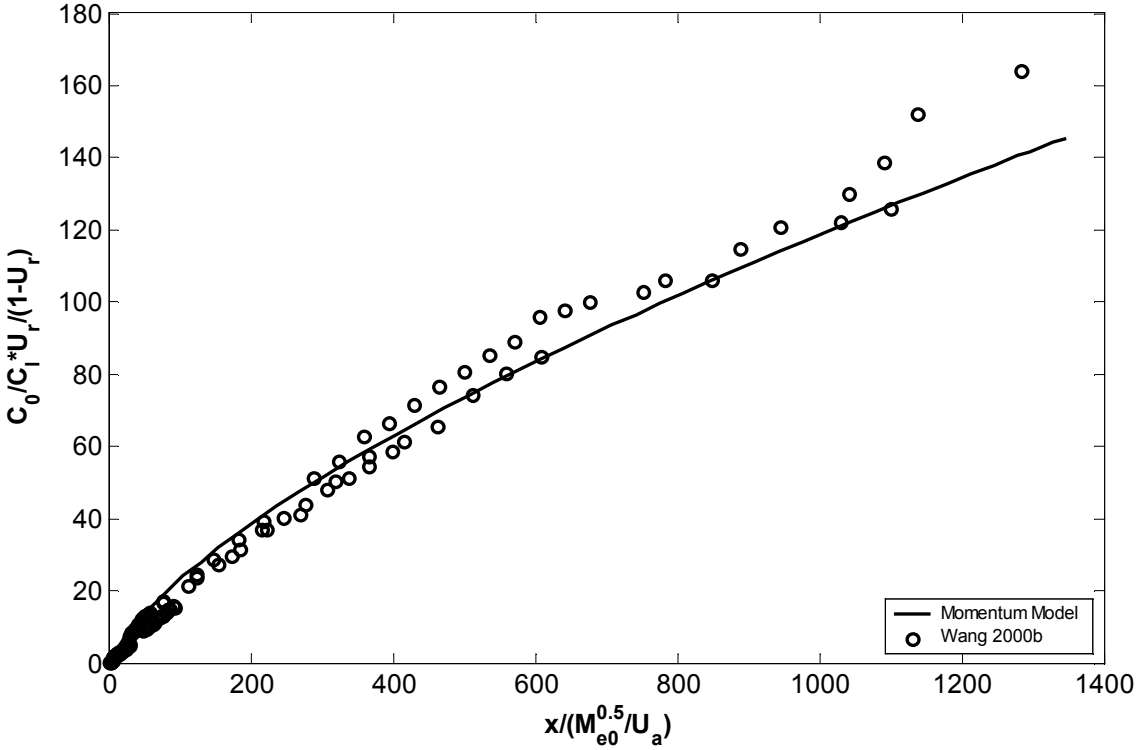

Figure 5.27 – Momentum Model prediction for centreline dilution in weak jet region

5.4 – Summary

A total of 98 runs were carried out as part of the investigation into the behaviour of two-dimensional trajectory flows. Whenever possible the results from these experiments were compared with previous experimental results and predictions from the VisJet and CorJet. At the same time, the experimental results were used to verify the accuracy of the Momentum Model.

The still ambient flows presented in the chapter, with the exception of the positively buoyant jet, have been studied extensively. The results from the current experimental investigation were consistent with earlier work, increasing the confidence in the LA flow visualization technique. All three models were able to predict the still ambient flow results with a high degree of accuracy. No significant differences were found between them. The results from the positively buoyant jet experiments confirm that the models can also accurately predict trajectory, spread and dilution results for the intermediate angles.

The experimental results for the flows in a moving ambient did point out some of the shortcomings of the Momentum Model. The model is unable to predict the behaviour of the flow during the zone of transition from the weakly to the strongly advected flow regions, as the assumed cross-sectional profiles no longer match the actual profiles, and the transition happens more slowly than the transitions within the weakly advected region. However the behaviour of the flow in the transition zone had a small influence on the limiting behaviour of the flow in the strongly advected region. As a result the model was capable of predicting the limiting behaviour with reasonable accuracy.

In the advected thermal region of the flow a comparison between the experimental trajectory results and the predicted trajectory results of the Momentum Model based on the double-Gaussian assumption, VisJet based on top-hat profiles and CorJet based on single Gaussian profiles, showed that both VisJet and CorJet use a spreading rate that is relatively low. The predicted results from the Momentum Model, incorporating the correct rate of spread, were reasonable for the trajectory, concentration spread and dilution for the buoyant jets in a moving ambient. The consistency in the strongly advected region of the Momentum Model with the experimental results provides increased confidence in the use of the double-Gaussian approximation.

Chapter 6 – Negatively Buoyant Jets

6.1 - Introduction

The only flow with a two-dimensional trajectory in a still ambient not discussed in Chapter 5 was the negatively buoyant jet. In many applications, such as domestic and industrial discharges into a marine environment, the effluent is positively buoyant, and hence a large body of research has focused on developing effective tools for modelling the resulting flows. Less common, in both application and research focus, are the so-called negatively buoyant, or dense, discharges. Here the discharge fluid is denser than the surrounding fluid and hence buoyancy forces act to make the effluent fall rather than rise. It was mentioned in Chapter 1 that an example of this type of discharge is the effluent from desalination plants, which have relatively high salinity concentrations. This traditionally expensive water supply alternative is becoming an increasingly viable option for many communities, because of reductions in processing costs and the increased scarcity of secure high quality fresh water supplies.

The review of previous research in Chapter 2 showed that past studies of negatively buoyant flows have had a tendency to focus on vertical discharges (Abraham 1967; Baines et al. 1990; James et al. 1983; McLellan and Randal 1986; Turner 1966; Zhang and Baddour 1998) or alternatively on a particular angle of discharge. Zeitoun et al. (1972) indicated that 60° was the preferred discharge angle because of the relatively high levels of dilution achieved and hence practical applications and research investigations have had a tendency to focus on this discharge configuration (Roberts et al. 1997; Roberts and Toms 1987). More recently Cipollina et al. (2005) have broadened the study of such flows to include flow behaviour at different discharge angles, in particular 30° and 45°. Their study focused on determining empirical relationships to predict key characteristics of the buoyant jet's trajectory, which included the maximum height and point of impact.

This chapter presents details of a new investigation into the behaviour of the negatively buoyant jet. As part of this investigation the previous work has been extended by developing analytical solutions to predict the behaviour of inclined negatively buoyant discharges at discharge angles for which the assumed flow behaviour is valid. In addition the LA and LIF

visualization techniques (see Chapter 3) were used to study the behaviour of negatively buoyant discharges. The data from these experiments provides additional information about the path, mixing characteristics, spread and dilution of these flows.

The work presented in this Chapter formed the basis of a journal article, submitted to the Journal of Hydraulic Engineering, ASCE (Kikkert et al. 2006b). The investigation, and in particular the analytical solutions, has been carried out with major contributions from the co-authors. The journal article defined a single set of integral constants for the jet and plume regions in the derivation of the analytical solutions, because the focus of the article was on the conclusions from the comparison of the analytical solutions and the numerical models with the experimental data. The employment of different integral constants is more accurate, but also adds additional complexity to the solutions. The more accurate results, presented in the chapter, did not alter the main conclusions presented in the article.

6.2 - Analytical Solutions

Analytical solutions for negatively buoyant discharges are developed for comparison with the experimental results in addition to the numerical solution from the Momentum Model, developed in Chapter 4. In comparing the analytical and numerical approaches, it is worth noting that the analytical solutions provide an efficient and direct means of determining the relationships that characterise the flow behaviour for a broad range of initial angles, something that can only be obtained from the numerical models through numerous simulations. The analytical solutions for the behaviour of negatively buoyant discharges are developed with the aim of complementing empirical relationships such as those developed by Cipollina et al. (2005), and to broaden their application to a range of initial discharge angles. The approach taken is similar to that of Davidson and Pun (2000), where analytical solutions for the trajectories of positively buoyant flows were developed.

6.2.1 - Discharge Configuration and Initial Conditions

A schematic diagram of the discharge configuration is shown in Figure 6.1. From a practical perspective, there are three locations of particular interest; the centreline maximum height (x_m, z_m), the maximum elevation of the edge of the jet (z_{me}) and the horizontal distance to what is commonly referred to as the impact point, but is more generally the location at which

the flow returns to the source height $(x_{0R},0)$. The flow is released at an initial angle (ϕ_0), from a source of diameter (d), with a velocity (U_0), and a difference in density between that of the ambient fluid (ρ_a), and the discharge fluid (ρ_0). The flow therefore has an initial momentum flux (M_0), and buoyancy forces act to create buoyancy-generated momentum flux (M_b). Note that where the density differences are small it is common to express the momentum flux per unit density, so the initial momentum flux is defined as $\pi U_0^2 d^2/4$.

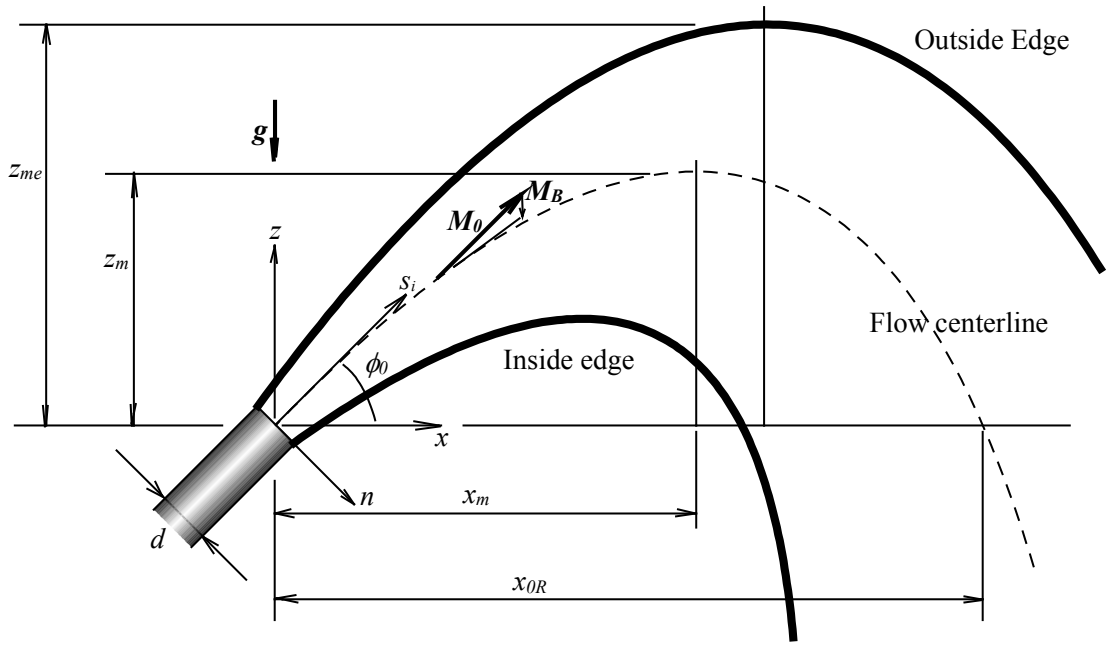

Figure 6.1 - Schematic diagram of the generic discharge configuration for negatively buoyant jet

6.2.2 - Derivation of Equations

Near the source it is assumed that the initial momentum flux is large compared to the buoyancy-generated momentum flux and hence it dominates the flow behaviour. The role of the buoyancy-generated momentum flux in this jet-like region is to deflect the flow downwards and its trajectory can be defined using the relevant momentum flux ratio:

$$\frac{dn_*}{ds_{i*}} = \frac{M_{b*}\cos\phi_0}{1 - M_{b*}\sin\phi_0} \tag{6.1}$$

Where the coordinate s_i is in the direction of the initial momentum flux and the coordinate n is perpendicular to it. Note the subscript $*$ denotes a dimensionless parameter. Appropriate

length and momentum flux scales are the source diameter and the initial momentum flux respectively.

Employing integral techniques, the growth of the buoyancy-generated momentum flux within the jet region can be written as:

$$M_{b*} = \frac{I_c k}{I_{qc}} \left[\frac{I_m}{\pi} \right]^{1/2} \frac{1}{Fr_0^{\,2}} s_{i*}^{\,2} \tag{6.2}$$

where I_{qc} and I_c have values of 2.03 and 4.68 respectively, using the values for λ and turbulent mass fluxes in the jet-like region. Wang (2000a) found that approximately 15% of the total mass flux was carried by turbulence in the plume region. With the plume value for λ, I_{qc} and I_c can be calculated to have values of 1.90 and 3.46 respectively.

The transition from jet-like to plume-like behaviour is expected to occur when the buoyancy-generated momentum flux and the initial momentum flux are of equal magnitude $\left(M_{b*} \approx 1\right)$ and from equation (6.2) the transition length-scale $\left(S_{jp}\right)$ is then given by:

$$S_{jp*} \approx \left[\frac{I_{qc}}{I_c} \frac{1}{k} \left(\frac{\pi}{I_m} \right)^{1/2} \right]^{1/2} Fr_0 \tag{6.3}$$

Davidson and Pun (2000) obtained a similar relationship by equating the buoyancy-generated momentum flux of a plume with the initial momentum flux of discharge; their approach resulting in the inclusion of an additional multiplicative term ($[2/3]^{1/2}$). Thus equation (6.3) provides marginally longer estimates for the transition length-scale.

Substituting equation (6.2) into equation (6.1) and integrating yields:

$$n_* = \frac{1}{\tan\phi_0} \frac{S_{jp*}}{\sin^{1/2}\phi_0} \left[-\frac{s_* \sin^{1/2}\phi_0}{S_{jp*}} + \frac{1}{2} \ln \left(\frac{1 + \dfrac{s_* \sin^{1/2}\phi_0}{S_{jp*}}}{1 - \dfrac{s_* \sin^{1/2}\phi_0}{S_{jp*}}} \right) \right] \tag{6.4}$$

where the x and z coordinates are given by:

$$z_* = s_{i*} \sin\phi_0 - n_* \cos\phi_0 \tag{6.5}$$

$$x_* = s_{i*} \cos\phi_0 + n_* \sin\phi_0 \tag{6.6}$$

These relationships then provide the basis for determining analytical relationships for the locations of practical interest listed above.

The maximum height is reached when the buoyancy-generated momentum flux equals the vertical component of the initial momentum flux, that is $M_{b*} = \sin\phi_0$. This condition indicates that the maximum height will always be reached within the jet region and applying it to equation (6.2) gives:

$$s_{m*} = S_{jp*} \sin^{1/2}\phi_0 \tag{6.7}$$

where s_m is the distance in the initial discharge direction to the location of the centreline maximum of the flow.

Combining equations (6.7) and (6.4) with equations (6.5) and (6.6) gives the following relationships for the coordinates of the centreline maximum:

$$z_{m*} = S_{jp*} \sin^{3/2}\phi_0 \left[1 + \frac{1}{\tan\phi_0}\left(1 - \frac{1}{2\sin\phi_0} \ln\left(\frac{1+\sin\phi_0}{1-\sin\phi_0} \right) \right) \right] \tag{6.8}$$

$$x_{m*} = \frac{S_{jp*}}{2} \frac{\cos\phi_0}{\sin^{1/2}\phi_0} \ln\left(\frac{1+\sin\phi_0}{1-\sin\phi_0} \right) \tag{6.9}$$

The dilution at the centreline maximum height can be determined from the standard relationship for a jet:

$$\frac{C_0}{C_l} = 2 I_{qc} k \left[\frac{1}{\pi I_m} \right]^{1/2} s_{m*} \tag{6.10}$$

The maximum height of the edge of the jet can be estimated by adding the radius of the jet $\left(= 2\lambda k s_m\right)$ to the maximum centreline height. Note the inclusion of the spread ratio λ is consistent with the determination of maximum heights from mean tracer profiles

$$z_{me*} = S_{jp*} \sin^{1/2}\phi_0 \left[\sin\phi_0 \left(1 + \frac{1}{\tan^2\phi_0}\left(1 - \frac{1}{2\sin\phi_0} \ln\left(\frac{1+\sin\phi_0}{1-\sin\phi_0} \right) \right) \right) + 2\lambda k \right] \tag{6.11}$$

It has been assumed here that the difference in the horizontal location of the maximum edge height and centreline maximum height due to spreading of the flow is small.

Determining the location of the point where the centreline of the flow returns to the source height is more complex, because this can occur in either the jet or plume regions. For small

discharge angles it is anticipated that this point will be reached in the jet region and for large angles the flow is expected to be plume-like when it returns to the source height.

In the jet region this location can be determined by recognizing that $z_* = 0$ at this point and by manipulating equations (6.4), (6.5) and (6.6) to yield:

$$x_{0rj*} = \frac{1}{\tan\phi_0}\frac{S_{jp*}}{\sin^{3/2}\phi_0}\left[-\frac{x_{0rj*}}{S_{jp*}}\sin^{1/2}\phi_0\cos\phi_0 + \frac{1}{2}\ln\left(\frac{1+\dfrac{x_{0rj*}}{S_{jp*}}\sin^{1/2}\phi_0\cos\phi_0}{1-\dfrac{x_{0rj*}}{S_{jp*}}\sin^{1/2}\phi_0\cos\phi_0}\right)\right] \tag{6.12}$$

An approximate solution to equation (6.12) can be obtained by expressing the logarithmic term as a series and ignoring higher order terms to give:

$$x_{0rj*} \approx \frac{\left[3\sin\phi_0\right]^{1/2}}{\cos^2\phi_0} S_{jp*} \tag{6.13}$$

At this point the distance travelled in the source direction $s_{0r*} = x_{0rj*}\cos\phi_0$ and the dilution can be estimated with equation (6.10).

In the plume region the location of the flow's return to the source height is determined through the incorporation of analytical solutions for plume behaviour. These solutions are outlined in Davidson and Pun (2000) and in more detail in Pun (1998), as is the method employed for implementing the solutions. The method requires that the momentum fluxes and parameter values are essentially preserved between the jet and plume solutions at the transition point and this requires the creation of a plume virtual source. They show that under these conditions, the vertical distance from the transition point to the plume virtual source is given by the transition length-scale (S_{jp}). The plume solution is then employed beyond the transition point and predictions are determined based on distances from the imaginary (virtual) plume source. The coordinates at a particular location are translated between those making reference to the virtual and real sources as part of this process. Davidson and Pun (2000) also show that models based on this analytical approach are able to predict buoyant jet behaviour with acceptable accuracy.

Adopting this approach to determine conditions at the point where the flow returns to its source height, requires that the horizontal and vertical distances from the transition point to the location of interest (x_{jp*}, z_{jp*}) are determined, which can be achieved by combining equations (6.3) and (6.4) with equations (6.5) and (6.6) to give:

$$z_{jp*} = S_{jp*} \sin\phi_0 \left(1 - \frac{1}{\tan^2 \phi_0} \left(-1 + \frac{1}{2\sin^{1/2} \phi_0} \ln\left(\frac{1+\sin^{1/2} \phi_0}{1-\sin^{1/2} \phi_0} \right) \right) \right) \tag{6.14}$$

$$x_{jp*} = \frac{S_{jp*}}{2} \frac{\cos\phi_0}{\sin^{1/2} \phi_0} \ln\left(\frac{1+\sin^{1/2} \phi_0}{1-\sin^{1/2} \phi_0} \right) \tag{6.15}$$

The distance z_{jp*} can be added to the vertical distance from the plume virtual source to the transition point (S_{jp*}) and substituted into the trajectory relationship for the plume region (Davidson and Pun 2000). The resulting relationship then gives the horizontal location of the return point relative to the transition point, that is:

$$x_{trp*} = 12^{1/3} \left(\left(\frac{\pi}{I_m} \right)^{1/2} \frac{I_{qc}}{I_c k} \right)^{1/2} Fr_0 \cos\theta_0 \left(1 - \left(\frac{1}{C_{0rp}} \right)^{1/3} \right) \tag{6.16}$$

where I_{qc} and I_c are the plume values, and for convenience the coefficient C_{0rp} is defined as:

$$C_{0rp} = 1 + \sin\phi_0 \left(1 - \frac{1}{\tan^2 \phi_0} \left(-1 + \frac{1}{2\sin^{1/2} \phi_0} \ln\left(\frac{1+\sin^{1/2} \phi_0}{1-\sin^{1/2} \phi_0} \right) \right) \right) \tag{6.17}$$

Note that multiplying the coefficient C_{0rp} by the transition length scale gives the vertical distance from the plume virtual source to the point where the flow returns to the source height. In addition note the horizontal location of the transition point and the virtual source are the same in the above trajectory relationship.

Adding equations (6.15) and equation (6.16) gives the horizontal location of the return point relative to the real source:

$$x_{0rp*} = \cos\phi_0 \left[\frac{S_{jp*}}{2\sin^{1/2} \phi_0} \ln\left(\frac{1+\sin^{1/2} \phi_0}{1-\sin^{1/2} \phi_0} \right) + 12^{1/3} \left(\left(\frac{\pi}{I_m} \right)^{1/2} \frac{I_{qc}}{I_c k} \right)^{1/2} Fr_0 \left(1 - \left(\frac{1}{C_{0rp}} \right)^{1/3} \right) \right] \tag{6.18}$$

The dilution at this location is given by:

$$\frac{C_0}{C_l} = 12^{1/3} \left[\frac{1}{\pi I_m{}^3} \right]^{1/4} \left[\frac{I_{qc}{}^3 k}{I_c} \right]^{1/2} C_{0rp}{}^{5/3} Fr_0 \tag{6.19}$$

Equation (6.19) can be integrated in the y-direction under the assumption of a Gaussian concentration distribution to give:

$$\frac{C_{i0}}{C_{il}} = \frac{12^{1/3}}{\pi\lambda} \frac{I_{qc}}{I_m{}^{1/2}} C_{0rp}{}^{2/3} \tag{6.20}$$

It remains to determine under what condition the flow reaches its original height in the jet and plume regions. The critical situation in this regard occurs when the transition from jet to plume behaviour takes place at the source height, that is, $z_{jp*} = 0$. Employing this information along with equations (6.3), (6.4) and (6.5) gives the following condition:

$$1 + \tan^2 \phi_0 = \frac{1}{2\sin^{1/2} \phi_0} \ln\left[\frac{1+\sin^{1/2} \phi_0}{1-\sin^{1/2} \phi_0}\right] \tag{6.21}$$

Expanding the logarithmic function as a series and neglecting higher order terms yields the following approximate condition:

$$\cos^2 \phi_0 \approx 3\sin \phi_0 \tag{6.22}$$

Equation (6.22) indicates that the flow centreline will reach the source height in the jet region for angles less than $\approx 20°$.

6.3 - Experimental Set Up

The solutions presented in the above section can be employed to predict the behaviour of negatively buoyant discharges; however, an assessment of the value of these predictions can only be determined through comparisons with experimental data. Although experimental data for these flows exists, its coverage is limited. Therefore an experimental program was carried out as part of the investigation to enable a more complete comparison to be made. Both the LA and the LIF flow visualization techniques were used. The specifics of the experimental set up for both systems in combination with the negatively buoyant jet runs are discussed below.

6.3.1 - LA Experiments

The LA system is described in detail in Chapter 3.2. Runs 1 to 41 were recorded with the Canon MV4i DV. For runs 40.1 and 40.2 the number of frames recorded was increased from approximately 2000 to 6000 and 12000 respectively, to investigate the effect the increased averaging time would have on the accuracy of the results. However, for increased accuracy, it was decided to change to a camera with a higher resolution and the other runs were recorded using the Jai CV M7+, grabbing 1200 frames per run.

The initial conditions for the LA negatively buoyant jet runs can be seen in Table D.8 in Appendix D. Because the analytical solutions depend on the initial discharge angle and the initial Froude number, the experimental investigation was focused on flows with initial discharge angles of 0°, 15°, 30°, 45°, 60° and 75° (with an error of 0.25˚). For each angle several runs were carried out with different initial Froude numbers. The Froude number ranged from 5.43 to 60.68 and the Reynolds number ranged from 438 to 5207. The lowest Reynolds numbers indicate that the flow was not fully turbulent for some of the experiments. The results of these flows were either discarded or a virtual source was found by projecting the spread data back to the virtual origin. The port diameter was 2.91mm for the flows recorded with the Canon camera and 2.94mm for the experiments recorded with the Jai, the density difference between source fluid and ambient fluid varied between 2.3 and 3.0 percent.

6.3.2 - LIF Experiments

In addition to the LA experiments described above, a LIF system was employed to provide trajectory information and cross-sectional intensity contours. Unlike the integrated perspective gained with an LA system, LIF enables the flow behaviour to be observed within thin planar slices. The latter providing insights into changes to the flow structure as it develops. A detailed description of the LIF flow visualization technique can be found in section 3.3.

Just as with the LA experiments the initial discharge angle was varied during the investigation and runs with different Froude numbers were recorded at each angle. The Froude number ranged from 39.46 to 93.02, and the Reynolds number from 2388 to 5630. The port-diameter was left unchanged during the experiments at 2.45 millimetres and the density difference was approximately 2.5 or 3.0 percent. A complete list of all initial conditions for the LIF experiments can be found in Table D.9 in Appendix D.

For all runs, except the last four, the camera was set up perpendicular to the trajectory plane of the flow to enable it to record an overview of the flow. The last four runs were carried out to get an insight into the distortion of the non-integrated cross-sectional profiles. During runs 37 and 38 the laser-sheet cut across the flow vertically, perpendicular to the direction of flow, at the centreline maximum height. During run 39 the laser sheet was set up horizontally at the source and impact heights with the camera recording vertically downwards, and during run 40

the laser sheet coincided with the cross-sectional profile at the impact point. The angle between the laser sheet and the horizontal was approximately 60°, the camera recorded perpendicular (from above).

6.4 - Experimental Results and Model Predictions

6.4.1 - Gaussian Assumption

It is appropriate to initially discuss the validity of the Gaussian assumption between the point of release and the point of impact or zero crossing, because this is the zone for which the analytical solutions have been developed. An overview of the flow behaviour in this region can be seen in Figure 6.2. Here time averaged centreline LIF intensity contours are presented, and predictions of trajectory and flow spread are shown for comparison. While the model appears to predict the path of the flow and its outer edge with reasonable accuracy, the inner edge of the jet is not well predicted. The inner edge of the jet is inherently unstable and buoyancy driven instabilities in this region generate a significant vertical flux of material out of the buoyant jet as it moves in a predominantly horizontal direction. This flux appears to destroy the typical entrained flows one would expect to see near the edge of a jet, but in turn creates additional mixing in this region and hence additional dilution of the dye tracer.

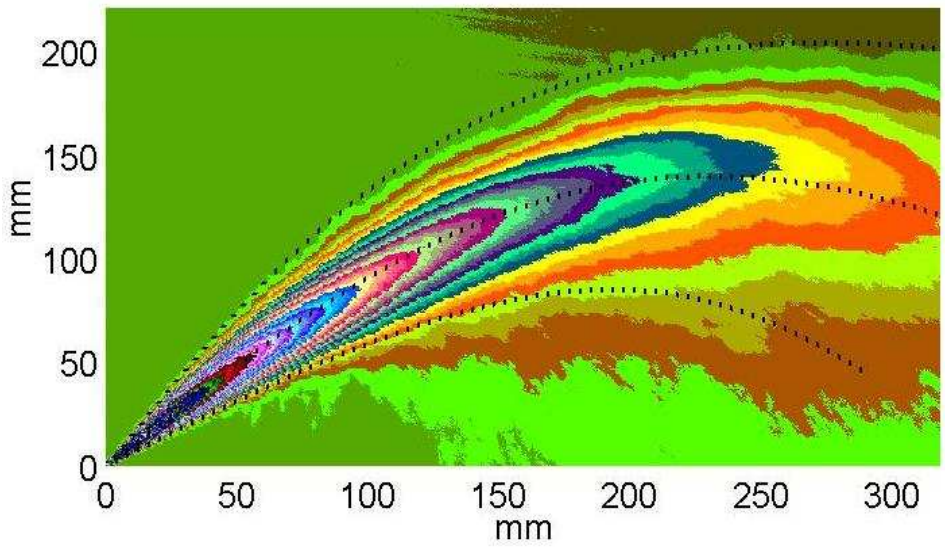

Figure 6.2 - Averaged LIF image showing the path and additional mixing associated with a negatively buoyant discharge. The dashed lines represent analytical model predictions of the flow's path and spread. The initial conditions for this flow are $\phi_0 = 45°$, $Fr_0 = 48.66$ and $Re_0 = 2945$.

It is also worth noting that for cross-sections perpendicular to the flow direction and between the source and point of maximum height, the buoyancy driven instabilities are generating a backflow (opposite to the jet direction). For those perpendicular cross-sections taken between the point of maximum height and the point of impact the buoyancy driven instabilities are creating an additional flux in the same direction as the jet. In the former case the tracer flux within the jet must be enhanced and in the latter case it must be reduced for the flux of tracer to be conserved.

A more detailed assessment of the impact of these buoyancy driven instabilities on the mean flow structure can be seen in the intensity cross-sections shown in Figure 6.3(a). These cross-sections were obtained from Figure 6.2 and are taken perpendicular to the mean flow direction at various distances along the flow centreline. Profiles from the outer edge of the flow are apparently un-affected by the gravitationally stable nature of the fluid in this area, and can be collapsed in a traditional way onto a single Gaussian curve. This is consistent with values of the gradient Richardson number for the outer edge area in the jet region, which increases with the square of distance from the source to reach a maximum value of 0.1 at the jet to plume transition. Gravitational stability is expected to dominate the shear-induced instabilities at gradient Richardson numbers in excess of 0.25. In the outer edge area of the plume this number has a constant value of approximately 0.1.

In contrast the inner side of the jet is initially Gaussian, but becomes increasingly distorted due to the presence of the buoyancy driven instabilities. The distortion appears to increase with distance, until the maximum height is reached. Beyond this the distorted profiles appear to almost collapse. Values of the integral constants employed in the analytical solutions presented in section 6.2 are obtained based on the assumptions of Gaussian and self-similar cross-sectional profiles. The distorted profiles indicate these values should in fact vary with distance from the source and hence the accuracy of predictions reduces with increasing distance from the source, because of the simplified approach taken in generating the analytical solutions. However, the initial indications from Figure 6.2 are that these variations do not have a severe impact on the quality of predictions obtained from the solutions.

The LIF profiles presented in Figure 6.3(a) provide detailed information about the mean flow structure in a plane passing through the flow centreline. Additional information about the overall mean flow structure can be obtained by comparing these profiles with those obtained using the LA technique, the latter providing an integrated view of the mean concentration

distribution. Concentration profiles obtained using the LA technique are presented in Figure 6.3(b). The profiles are generally similar to those in Figure 6.3(a), but there are some notable differences. Beyond a single radius scale (b) in Figure 6.3(b), on the outer side of the jet, the data falls below the Gaussian curve, whereas in Figure 6.3(a) it remains consistent with the Gaussian curve. This indicates a reduction in lateral width near the outer edge of jet, which implies that the stable nature of the fluid in this region is having some influence on the mean flow structure, although the turbulence generated within the flow is clearly dominant. On the inner side of the jet similar changes to the profiles are observed in both figures, although deviations from the Gaussian form are more evident closer to the source in the integrated data (Figure 6.3(b)). The latter detecting relatively small changes to the inner region as a whole close to the source, whereas the planar LIF data shows the influence on the flow centreline is initially negligible.

Figure 6.3(c) shows a second set of integrated profiles that were obtained from the buoyant discharge under similar initial conditions, but with an initial discharge angle of 0°. Profile distortions consistent with those discussed above are evident, but they are clearly less severe. Gaussian plume models are well established for this flow type, which indicates these models remain effective under some degree of change to the mean flow structure. Profiles were obtained from discharges with initial angles ranging from 0° to 75° and similar effects were observed in all cases. It is worth noting that the severity of the distortion on the inside edge of flow increased for discharges with initial angles from 0° to 45°.

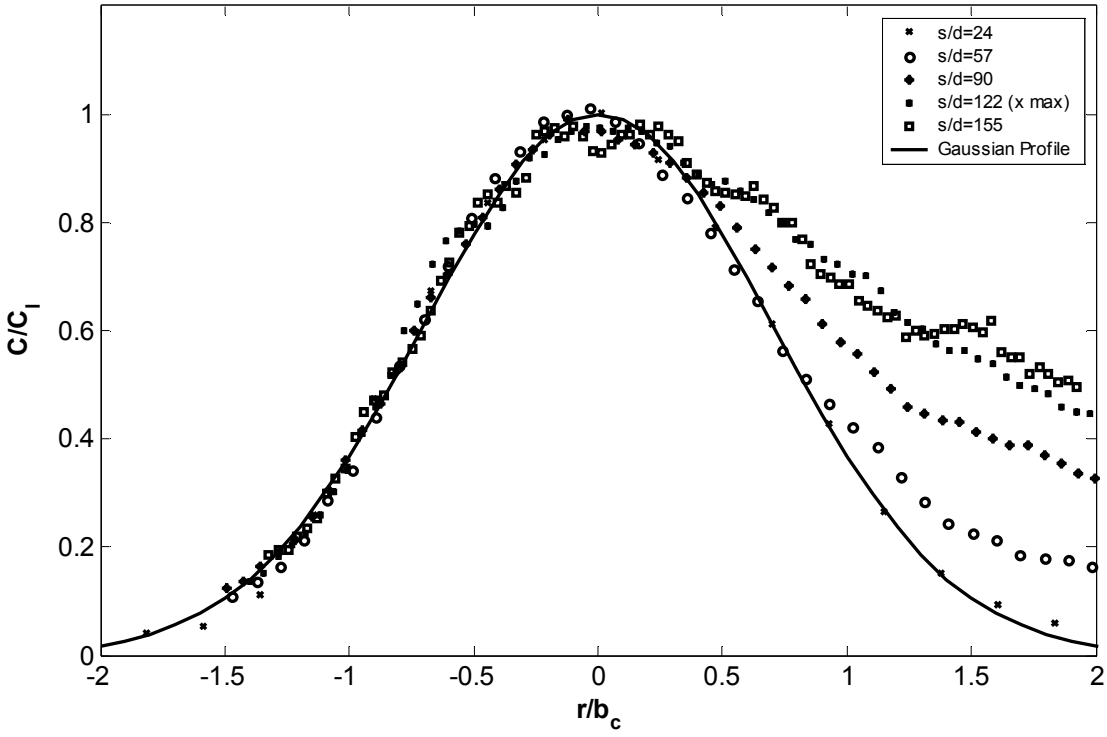

6.3(a) - Initial conditions: $\phi = 45°$, $Fr_0 = 48.66$ and $Re_0 = 2945$

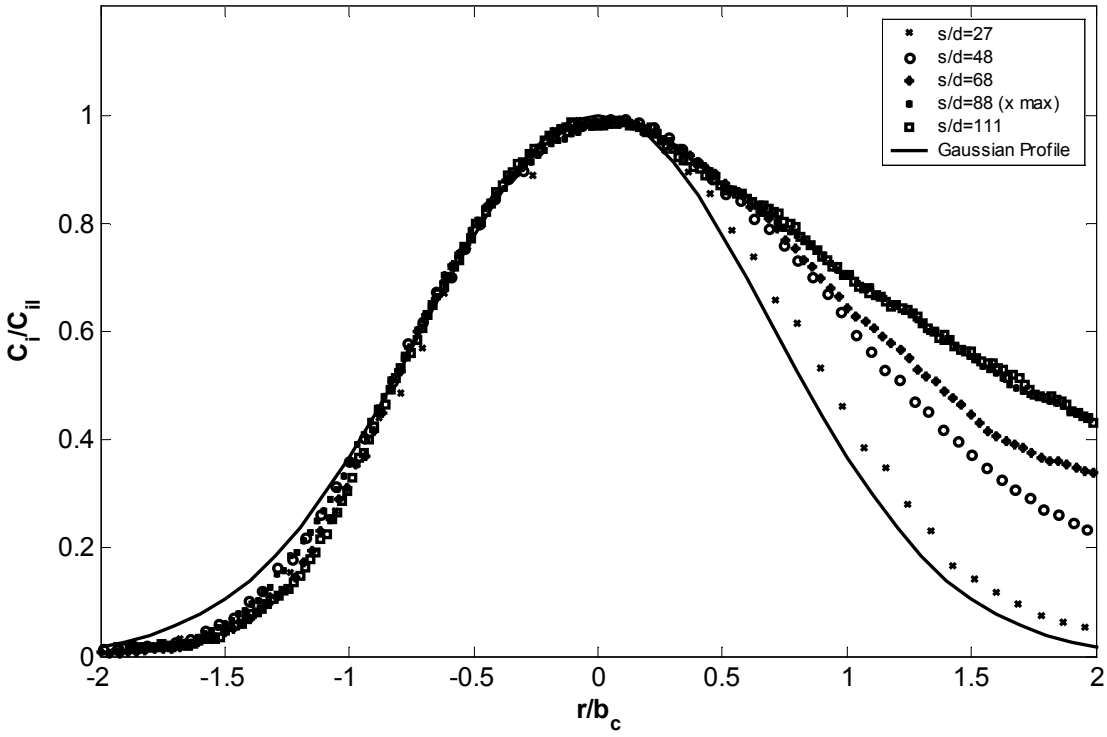

6.3(b) - Initial conditions: $\phi = 45°$, $Fr_0 = 38.53$ and $Re_0 = 3041$.

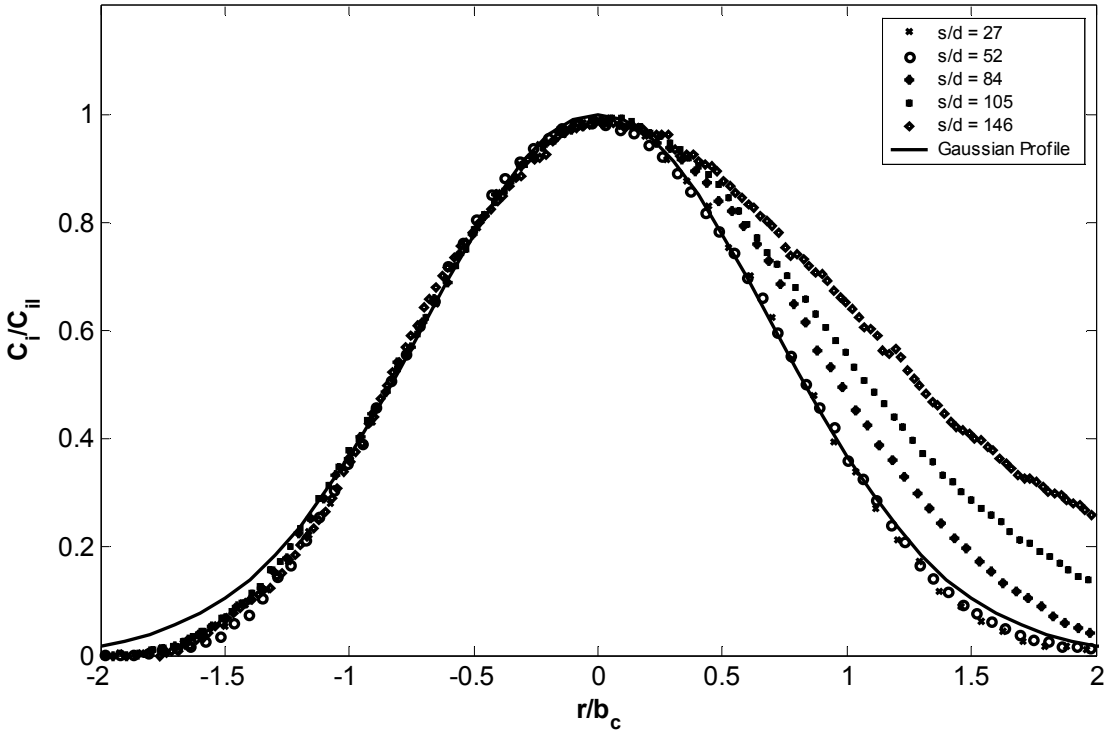

6.3(c) - Initial conditions: $\phi = 0°$, $Fr_0 = 56.51$ and $Re_0 = 4704$.

Figure 6.3 - LIF and LA concentrations profiles from inclined jets

Given the limitations described above, the cross-sectional profiles can be used to determine bulk properties of the flow such as the minimum dilution, outer edge spread and location of the peak concentration. Information obtained at the maximum height and the impact point can then be compared with the analytical solutions developed in section 2.

6.4.2 - Conditions at Maximum Height

The conditions at the maximum height are considered initially and Figure 6.4 to Figure 6.6 show data obtained at this location for a range of initial Froude numbers and a discharge angle of 45°. The data presented are the horizontal location at which the maximum centreline height is reached (Figure 6.4), the maximum centreline height (Figure 6.5) and the maximum height of the edge of the flow (Figure 6.6). Similar Figures for initial discharge angles of 30° and 60° can be found in Appendix E, Figures E.1 to E.3. The appropriate analytical solutions are also presented in the figures, as are data obtained by other authors. Data from the present study are consistent with previously published data. The analytical solutions provide adequate predictions of the location of the peak concentration, although the analytical solutions

underestimate the horizontal location of the maximum height at 30°. In addition the agreement with the analytical solutions for all angles indicates that the analytical solutions are also providing adequate outer edge spread predictions for these flows. It is worth noting that the trajectory data obtained using the planar LIF system is consistently higher than that obtained using the integrated LA technique, although the differences are relatively small. These differences are created by the changes to the mean flow structure described above. Predictions from the CorJet (Jirka 2004) and VisJet (Cheung et al. 2000) numerical models have also been added to Figure 6.4, Figure 6.5 and Figure 6.6. These predictions indicate the numerical models have a tendency to under predict the horizontal and vertical location of the maximum jet height, as well as the maximum height of the edge of the flow. The models do not take into account the effect of the buoyancy-induced instabilities and therefore overestimate the rate of increase of the buoyancy-generated momentum flux. The relative importance of the initial momentum flux is thus smaller, decreasing the horizontal and vertical distance from the source to the point of maximum height.

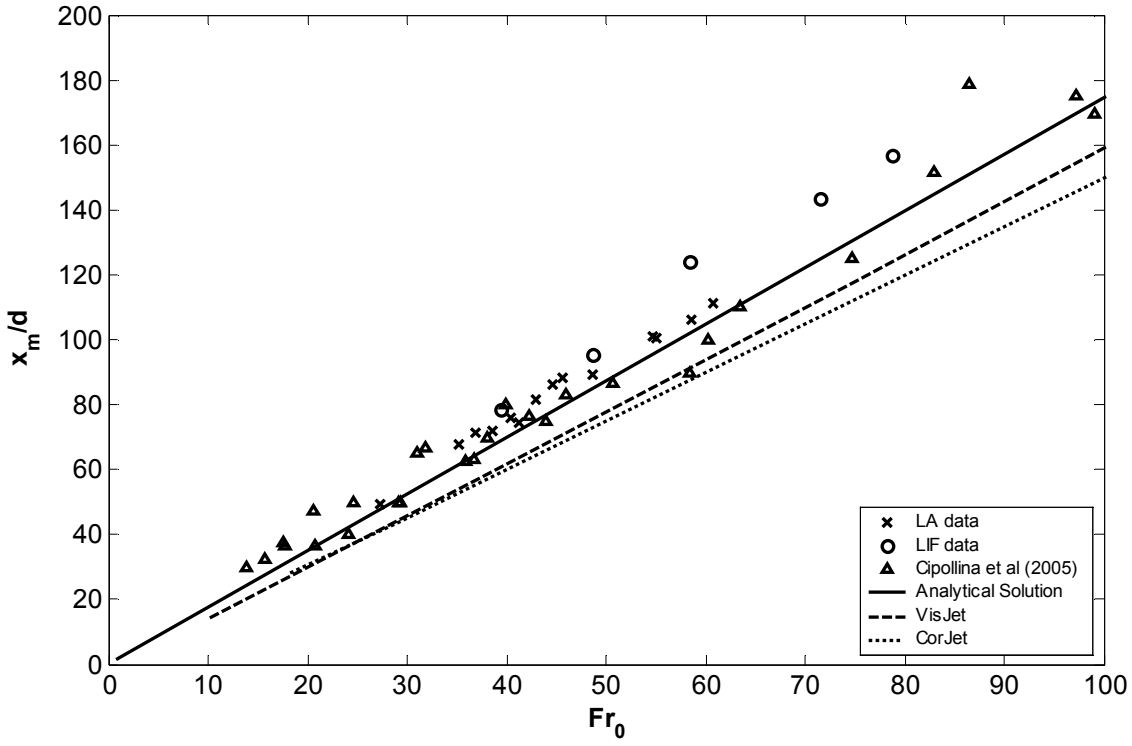

Figure 6.4 – Horizontal location of maximum centreline height for flows with an initial angle of 45° and Reynolds numbers ranging from 2144 to 4639

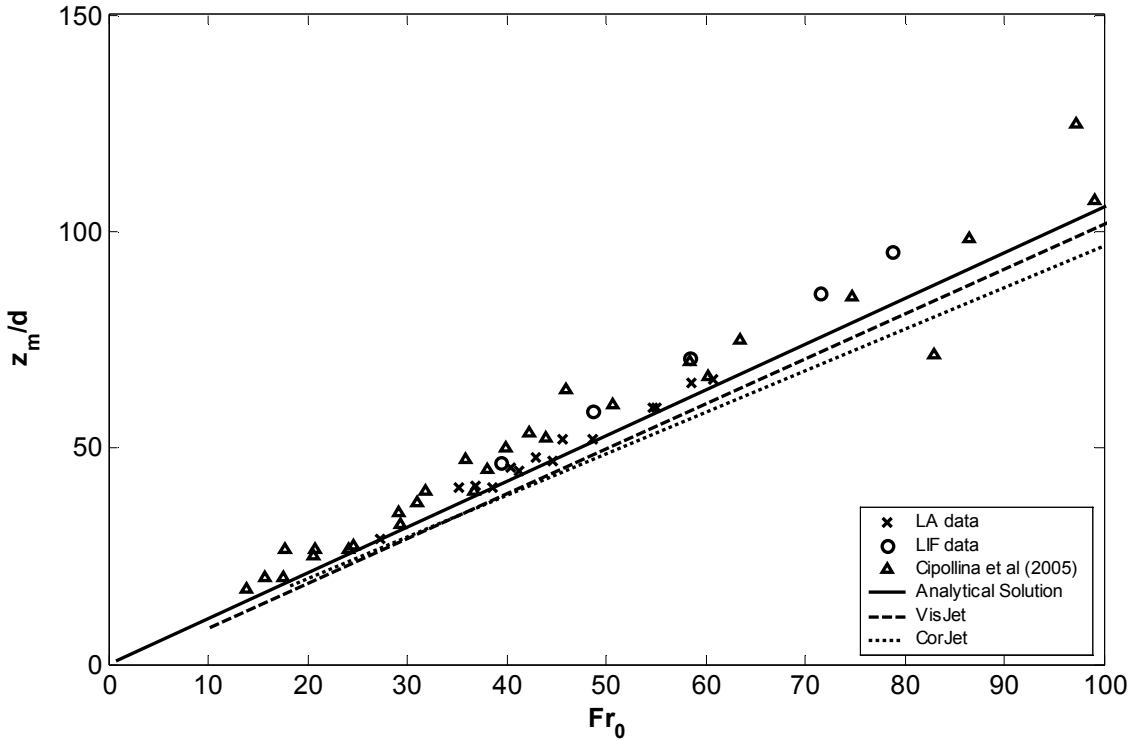

Figure 6.5 - Vertical location of maximum centreline height for discharges with an initial angle of 45° and Reynolds numbers ranging from 2144 to 4639

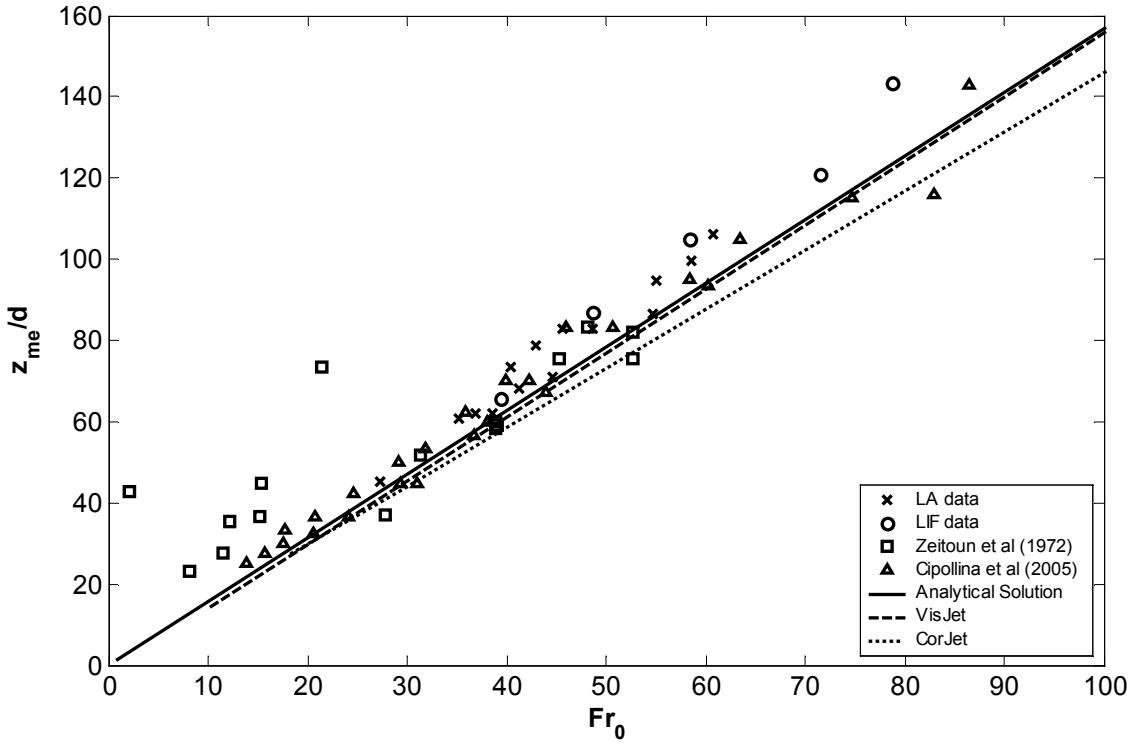

Figure 6.6 - Maximum height of edge of jet for discharges with an initial angle of 45° and Reynolds numbers ranging from 2144 to 4639

Minimum integrated dilution data at this location is shown in Figure 6.7. As indicated previously, at maximum height the flow is a jet and hence the integrated concentration is predicted to be 0.812 for all initial Froude numbers and discharge angles considered here. However, for the range of initial discharge angles and Froude numbers presented in Figure 6.7, the minimum integrated dilution is clearly greater than the predicted value and a least squares fit indicates an integrated value of 1.04 is more realistic. That is an increase of approximately 30%. The dilution data clearly indicates that the buoyancy-induced instabilities on the inner side of the jet are having a significant effect on the mixing processes as it rises to its maximum height.

The integrated dilution predictions from the CorJet and VisJet models, shown in Figure 6.7, are significantly lower than both the data and the analytical solutions, and they also display a dependence on initial discharge angle that is not evident in the analytical solutions or the experimental data. Both models employ entrainment assumptions for closure and it appears that these assumptions result in a reduction in the dilution of the flow as it approaches maximum height. This reduction is dependent on the initial discharge angle and is clearly inconsistent with the measured flow behaviour.

Equations (6.3), (6.7) and (6.10) can be combined to give an estimate of the minimum point dilution at the maximum height for a specific discharge angle and this is commonly written in the form:

$$\frac{C_0}{C_l} = k_{cm} Fr_0 \tag{6.23}$$

where k_{cm} is a constant for which the analytical solutions suggest a value of 0.44 for the 45° case. In contrast, after converting to non-integrated dilution data, the experimental 45° data in Figure 6.7 suggests a value of 0.53, which is consistent with the value of 0.56 determined by Zeitoun et al (1972), but higher than the average value of 0.38 obtained by Roberts and Toms (1987). However Roberts and Toms data show a dependence on initial Froude number, with lower Froude number runs giving a k_{cm} value of approximately 0.5. It is important to note that the estimate of k_{cm}, based on the integrated dilution data in Figure 6.7, assumes a Gaussian cross-sectional form and that the outer spread of the flow is representative of the horizontal spread (perpendicular to flow path) at the flow centreline.

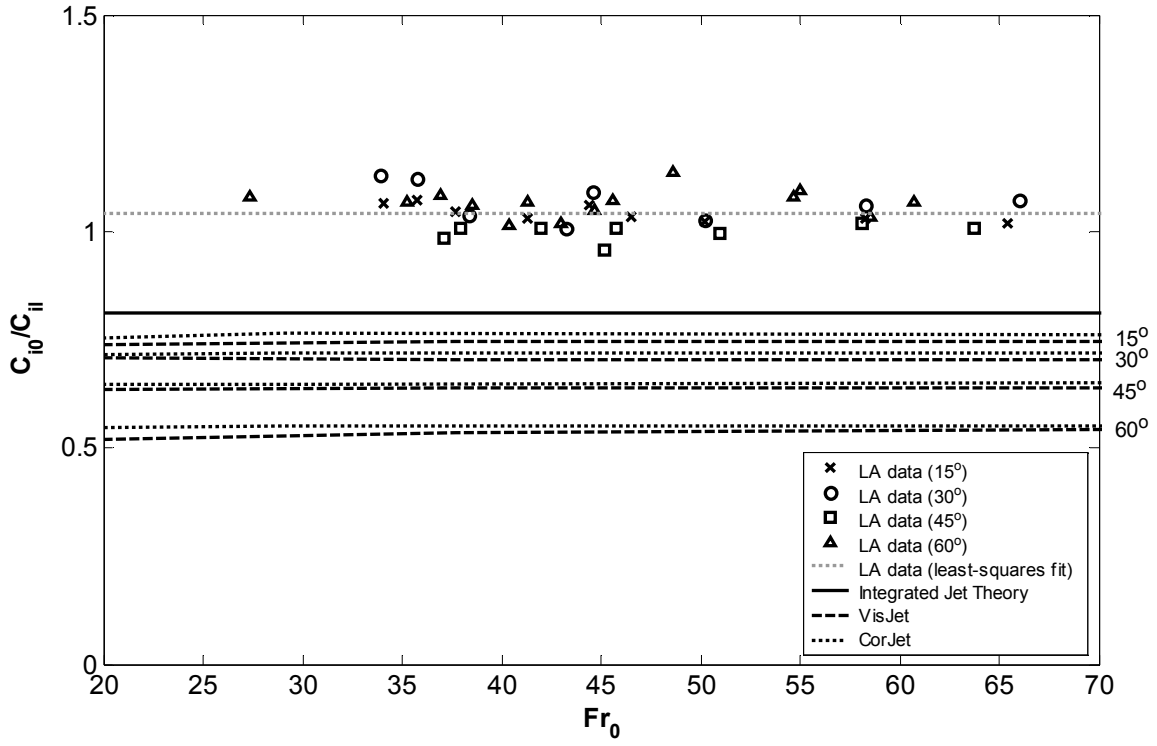

Figure 6.7 - Centreline integrated dilution at maximum height for discharges with Reynolds numbers ranging from 2144 to 5207

The ability of the analytical solutions to predict the jet trajectories for different discharge angles has been evaluated by comparing predictions with data from experiments with initial discharge angles ranging from 5° to 75°. This data is presented in Figure 6.8 to Figure 6.10. In presenting the data it is noted that the relationships for the locations can be written in a similar manner as the point dilution above. Combining equation (6.7) with equation (6.9), for example, enables the relationship to be written in the well-known form:

$$x_{m*} = k_{xm} Fr_0 \tag{6.24}$$

where k_{xm} is a constant coefficient for a particular initial discharge angle. Equations (6.8), (6.11) and (6.14) can be written in a similar form with coefficients of k_{zm}, k_{me} and k_{x0R} respectively. The values of these coefficients can then be compared with those obtained from the experimental data, such as that presented in Figure 6.4 to Figure 6.7, through a least-squares fit. Comparisons of values of these coefficients obtained experimentally with predictions from the appropriate analytical solution are shown in Figure 6.8 to Figure 6.10.

In Figure 6.8 the variation with initial discharge angle of the coefficient for predicting the horizontal location of the maximum point is compared with experimental data. Figure 6.9 and

Figure 6.10 shows similar comparisons for the centreline elevation coefficient and the maximum elevation of the flow edge coefficient. Figure 6.8 confirms that for low initial discharge angles (up to approximately an angle of 45), the analytical solution underestimates the horizontal distance to the location of maximum height. In the other two cases predictions from the analytical solutions fall within the scatter of the available experimental data and hence provide reasonable predictions of the flow behaviour. Beyond discharge angles of 75° the jet will at some angle begin to resemble a fountain, with the rising jet entraining portions of the falling plume and the analytical solutions will no longer be valid. It is interesting to note that Jirka (2004) states that CorJet predicts a maximum jet elevation coefficient of 1.9 for the 60° flows. This compares with the average values of the experimental data of 2.3 and the value from the analytical solution of 2.14.

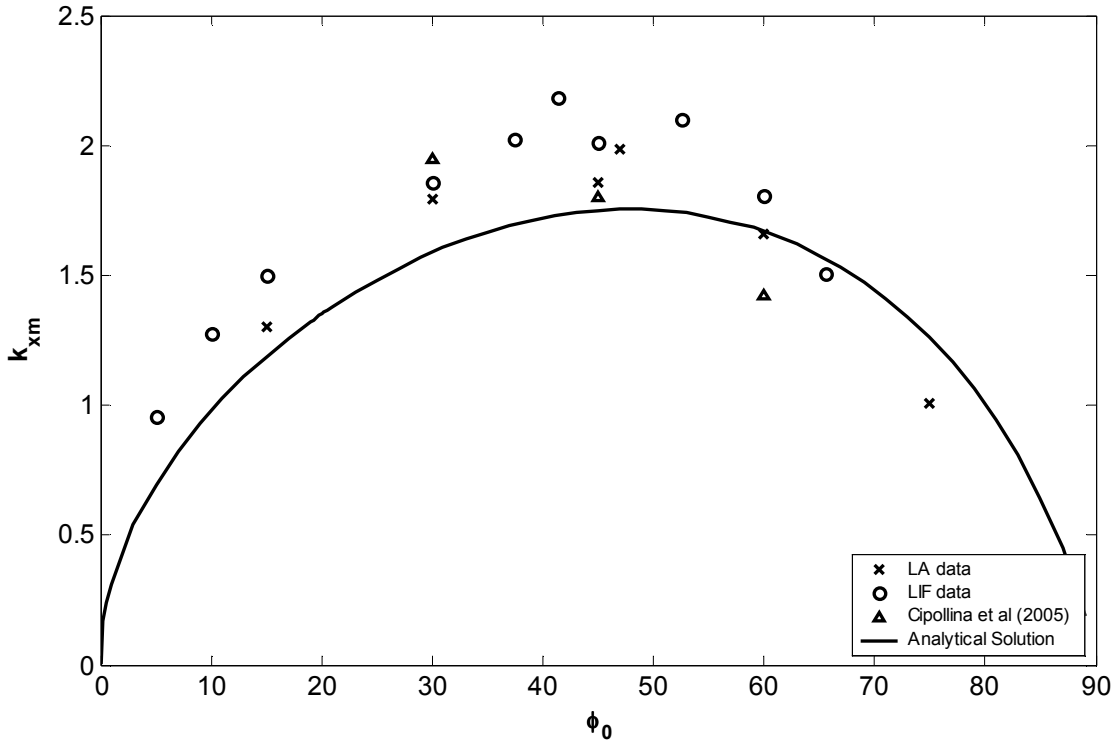

Figure 6.8 - The coefficient for the horizontal centreline location at maximum height as a function of the initial discharge angle

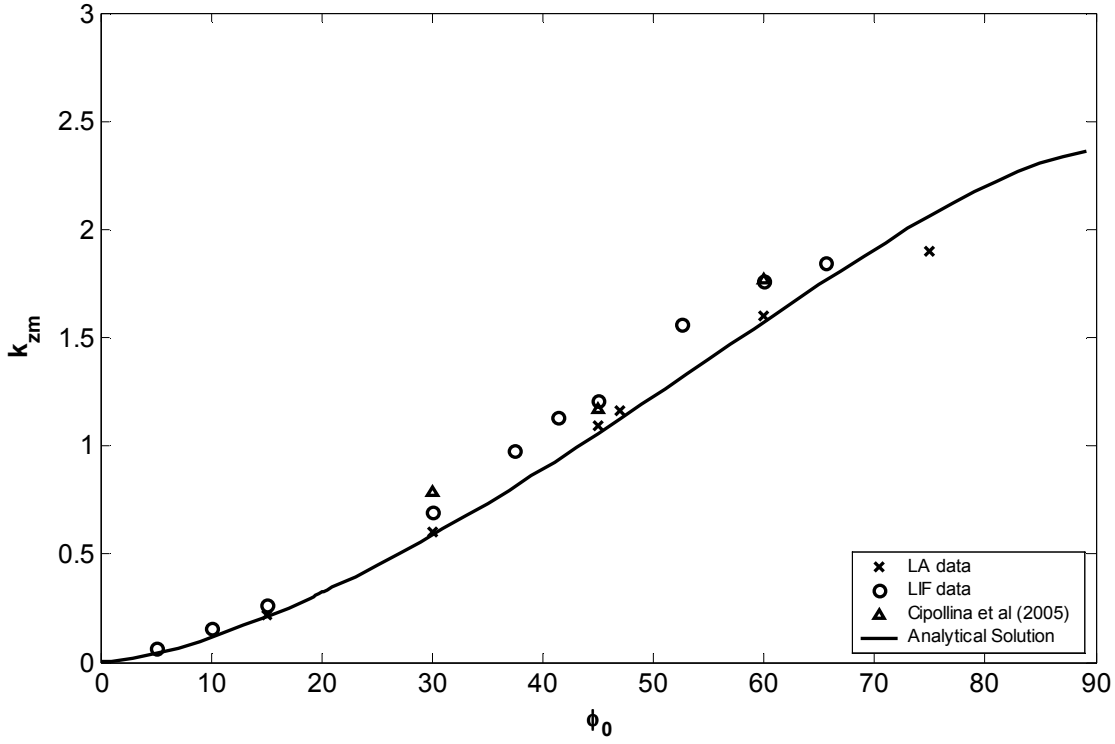

Figure 6.9 - The coefficient for maximum centreline elevation as a function of initial discharge angle

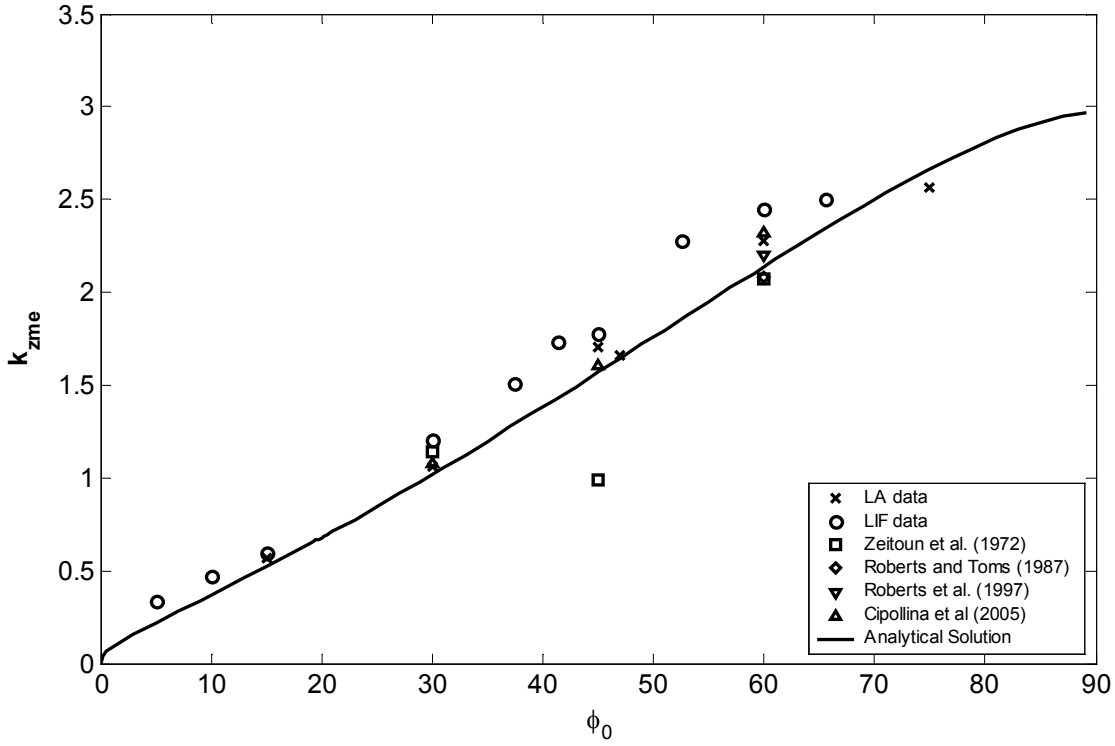

Figure 6.10 - The coefficient for maximum elevation of the flow edge as a function of initial discharge angle

6.4.3 - Conditions at impact point

A similar analysis has been carried out for conditions at the impact point. Figure 6.11 shows the horizontal distance data obtained at this location for a range of initial Froude numbers and discharge angles of 15° and 45°. The 15° discharge (Figure 6.11a) is expected to reach the impact point in the jet region, and the data is therefore compared with the predictions calculated using equation (6.13). The analytical solution is consistent with the data from the current investigation. The 45° discharge (Figure 6.11b) is expected to reach the impact point in the plume region. In Figure 6.11b the data is compared to the appropriate analytical solution (equation 6.18) using the plume values for I_{qc} and I_c. The experimental data is also compared with data obtained by other authors. The results from the present investigation match the experimental results of Zeitoun et al. (1972), but are higher than the results of Cipollina et al. (2005). The predictions of the location of the peak concentration at the point of impact from the analytical solutions are consistent with the results from Cipollina et al., and thus are lower than the results from the current investigation. Similar figures for the 30° and 60° discharges can be found in Appendix E, Figure E.4. The analytical solutions for the 30° and 60° initial discharges shows similar discrepancies, although the analytical solutions at the 60° match the LA data better.

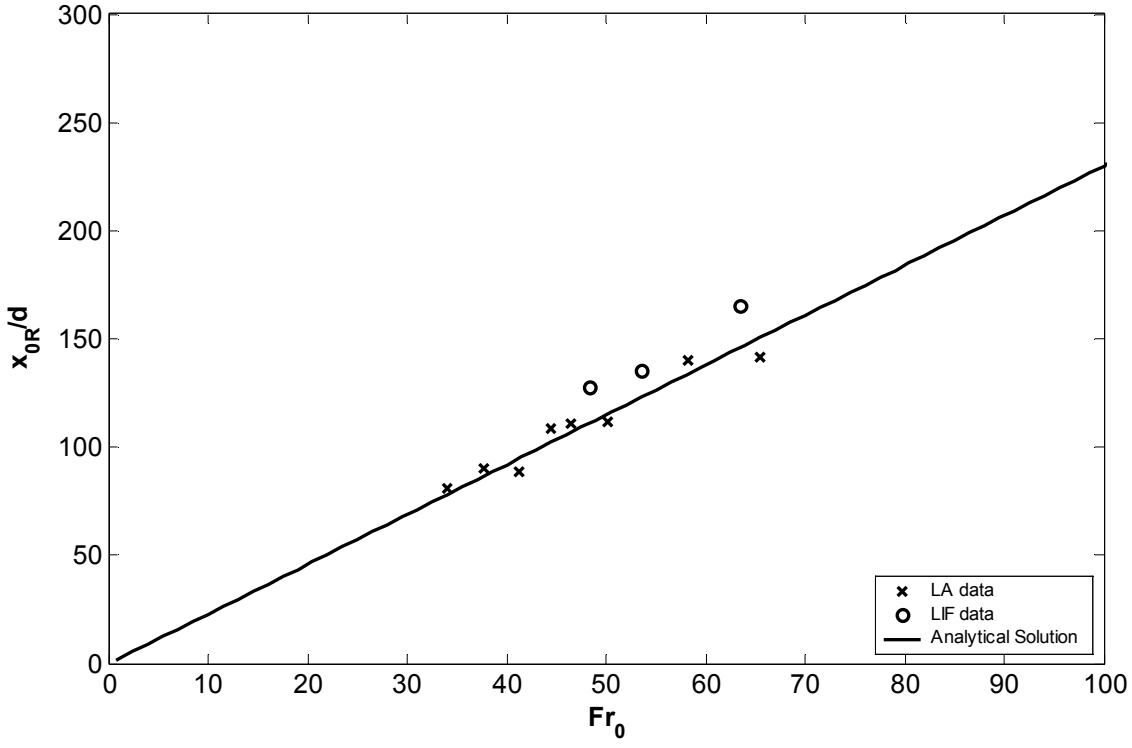

6.11(a) - Initial angle of 15° and Reynolds numbers ranging from 2988 to 5163

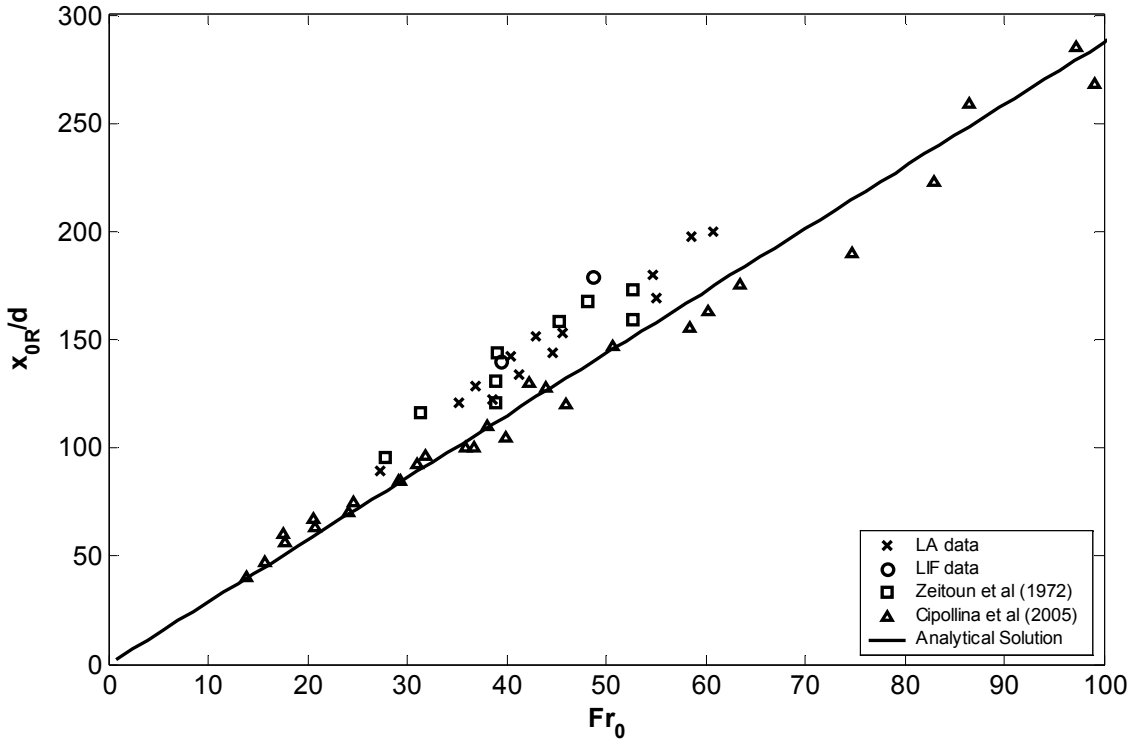

6.11(b) - Initial angle of 45° and Reynolds numbers ranging from 2144 to 4639

Figure 6.11 – Horizontal location of impact point for flows with initial angles of 15° and 45°

Minimum integrated dilution data at the impact point is shown in Figure 6.12. Using equation (6.22) it was found that flows with initial angles less than 20° are still in the jet-like region when passing the impact point. Therefore the minimum integrated dilution for experimental flows with an initial angle of 15° are still compared with the minimum integrated jet dilution value of 0.812. Figure 6.12 shows that the experimental data clearly does not match the theory; the increase of the experimental data over the theory is approximately 50%. For the other angles the analytical integrated dilution solution presented in equation (6.20) was used to determine the integrated dilution at the impact point. The results for the angles 30°, 45° and 60° are shown in Figure 6.12 and compared with the experimental data. Again the experimental integrated dilution is clearly higher than theory, however the difference between experimental results and theory is now approximately 30%.

Comparing the results of the experimental data at the maximum height with the experimental results at the point of impact, a considerable increase in scatter in the data is noticeable. This is perhaps a reflection of the difficulties associated with obtaining experimental data at larger distances from the source. Further downstream the signals are relatively weak and extended temporal averages are required, particularly for higher initial discharge angles. This is

particularly true for the LIF experiments, as the centreline signal decays faster than the integrated signal. Also the smaller size of the tank used during the LIF experiments meant that a limited number of images could be recorded before dye circulating in the tank started to interfere with the dye coming from the source. Consistent with this explanation is the fact that the scatter for the 15° flows is less than the 30° and the 45° flows, because the smaller angle discharge will have travelled a smaller distance from the source before reaching the point of impact.

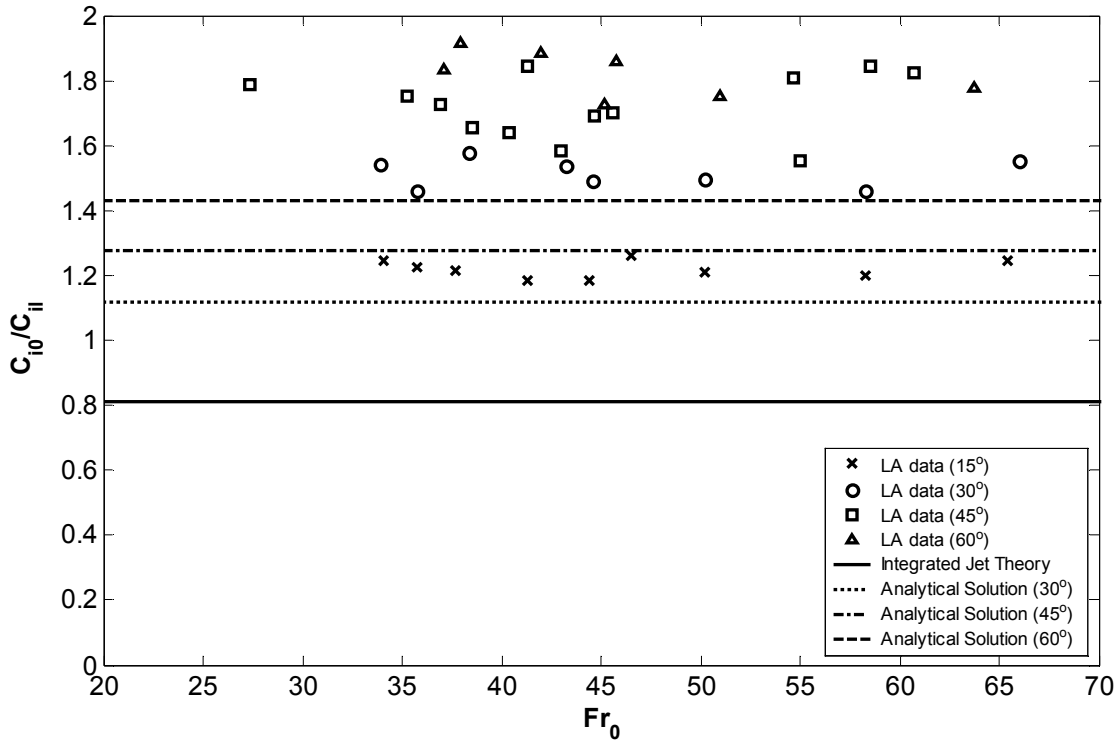

Figure 6.12 - Centreline integrated dilution at impact point for discharges with Reynolds numbers ranging from 2144 to 5207

As for the conditions at the maximum height, the results at the impact point are evaluated by comparing the experimental data with predictions from the analytical solutions for different initial discharge angles. The location coefficient versus the discharge angle is shown in Figure 6.13 and the minimum dilution in Figure 6.14.

The predictions of the location coefficient for the impact point generally underestimate the experimental data (Figure 6.13). However the analytical solutions match the data better for discharges reaching the impact point in the jet region and for relatively high discharge angles, than for the discharges with intermediate initial discharge angles.

As expected from the results in Figure 6.12, the integrated dilution predictions (Figure 6.14) based on the analytical solutions are conservative. The error in the analytical solution for the higher initial angles was approximately 30%. Increasing the analytical prediction by 30% gives the data-fit line as shown in Figure 6.14. This line gives a reasonable prediction for the experimental data at higher discharge angles, and it is interesting to note that when the line is projected towards smaller angles it also picks up the experimental data at 15°. This indicates that the 50% error in minimum integrated dilution at 15° can be divided into 20% due to the close proximity to the transition point and 30% due to the influence of the buoyancy-induced instabilities.

Comparing the minimum dilution results at the maximum height with the results at the impact point, it can be noted that the influence of the buoyancy-induced instabilities has not increased. At both points it was approximately 30%. This is consistent with the cross-sectional profiles shown in Figure 6.3. On the inside of the cross-section the profiles were distorted, away from the theoretical Gaussian profiles. These distortions increased up to the point of maximum height. After the point of maximum height the distortion became approximately constant and the profiles collapsed. Therefore the additional dilution related to the buoyancy-induced instabilities remains constant as the discharge travels from the point of maximum height to the point of impact.

For an initial discharge angle of 60° Zeitoun et al (1972) suggest the point minimum dilution is approximately double that at the maximum height. Roberts and Toms (1987) data suggest a ratio of 2.7 is more appropriate. Comparing the coefficients from equations (6.19) and (6.24), the analytical solutions give a ratio of 2.8, whereas estimates based on the integrated experimental dilution data suggest a value of 3.2. Again it is important to note that point dilution estimates from the present experimental study should be treated with some caution, because it is necessary to assume Gaussian cross-sectional form and that the outer spread is representative of the horizontal spread at the flow centreline.

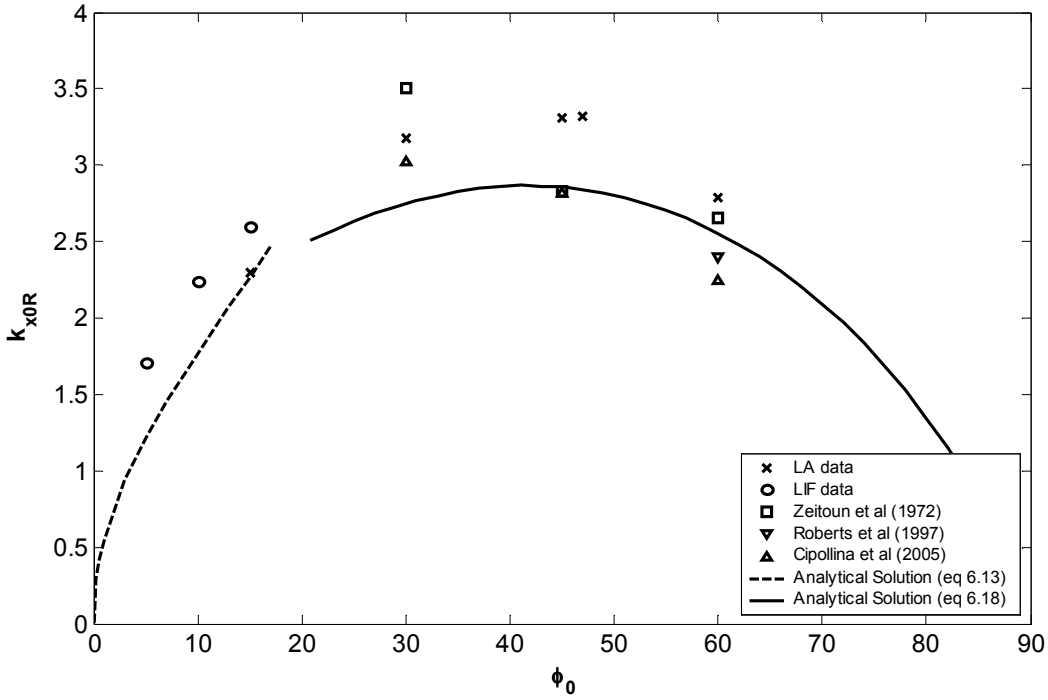

Figure 6.13 - The coefficient for the horizontal centreline location at the impact point as a function of the initial discharge angle

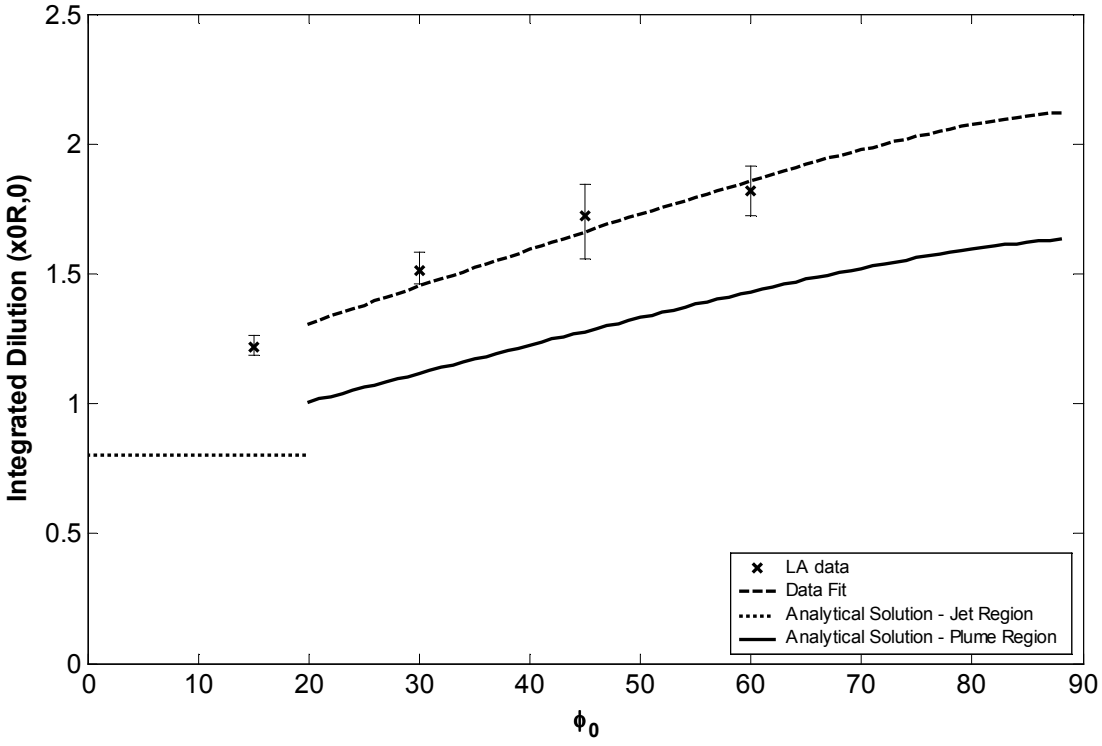

Figure 6.14 - Centreline integrated dilution data at the impact point as a function of the initial discharge angle

6.4.4 – More on the mean properties of negatively buoyant jets

Both VisJet and CorJet are used in practice to predict the trajectory and dilution of buoyant jets. However, both models do not take into account the influence of the buoyancy-induced instabilities and assume axi-symmetric cross-sections. The results from the positively buoyant jet and horizontal buoyant jet in Chapter 5 show the assumption to work for those flow conditions. To further understand the influence of the buoyancy induced instabilities on the negatively buoyant jet, predictions from both models as well as the Momentum Model (also assuming axi-symmetric cross-sections) are compared to the trajectory and dilution results from the experimental investigation. This section also provides an opportunity to view the experimental data in more detail.

The trajectory data, non-dimensionalised by the port diameter and the Froude number, is compared with the model predictions in Figure 6.15. For all angles, the models predict the flow to descend more rapidly than the experimental data indicates. The models assume axi-symmetric cross-sections and therefore overestimate the rate of increase of the buoyancy-generated momentum flux within the flow. It can be seen that the influence on the trajectory is increasing with increasing angle. For the 15° flows, the trajectory prediction from the models are reasonable through to the impact point. For the other three discharge angles, the model predictions only match the data up to the point of maximum height. The exception is the prediction from the Momentum Model at 60°, which is in better agreement with the experimental data than the prediction at 45°. Of the three models, the predictions of the Momentum Model provide the closest match with the experimental data. Unlike the numerical models, the analytical solutions appear to become more consistent with the experimental data with increasing initial discharge angles (30° and above). This difference is caused by the method used to deal with the transition from jet to plume behaviour. The numerical models progressively transform the flow between these regions, whereas the analytical solutions define a distance in the direction of the initial discharge, and transform the flow at this location.

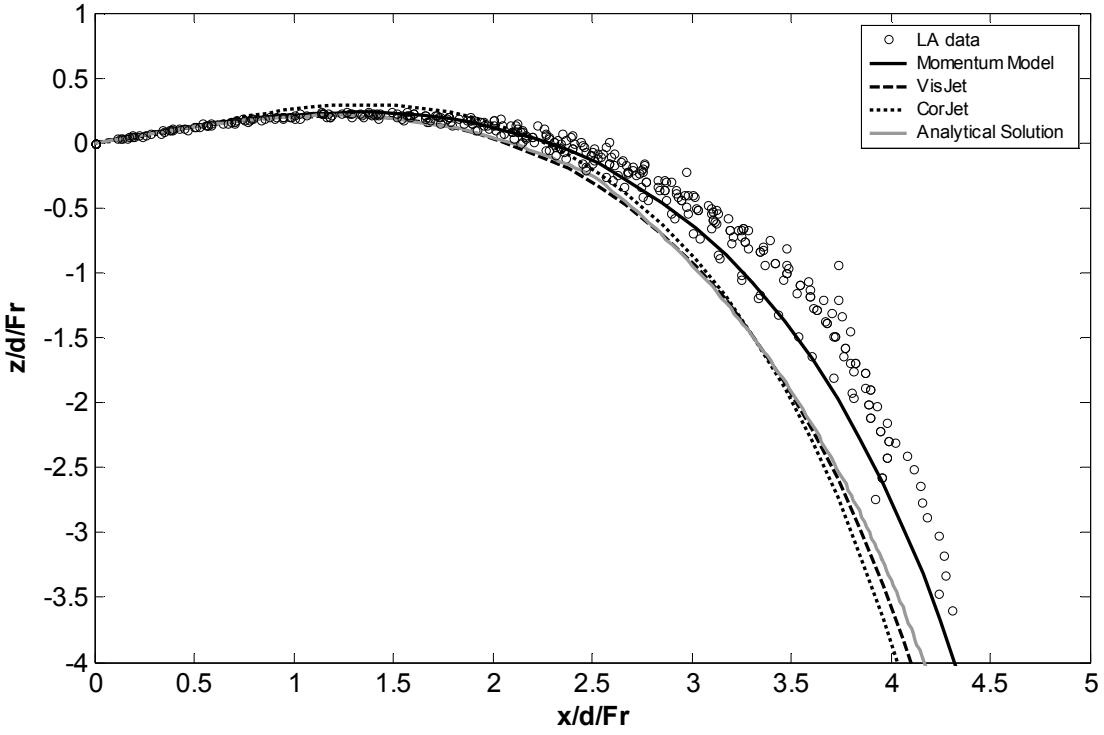

6.15(a) - Initial angle of 15°, Re ranging from 2699 to 5163 and Fr ranging from 34.06 to 65.42

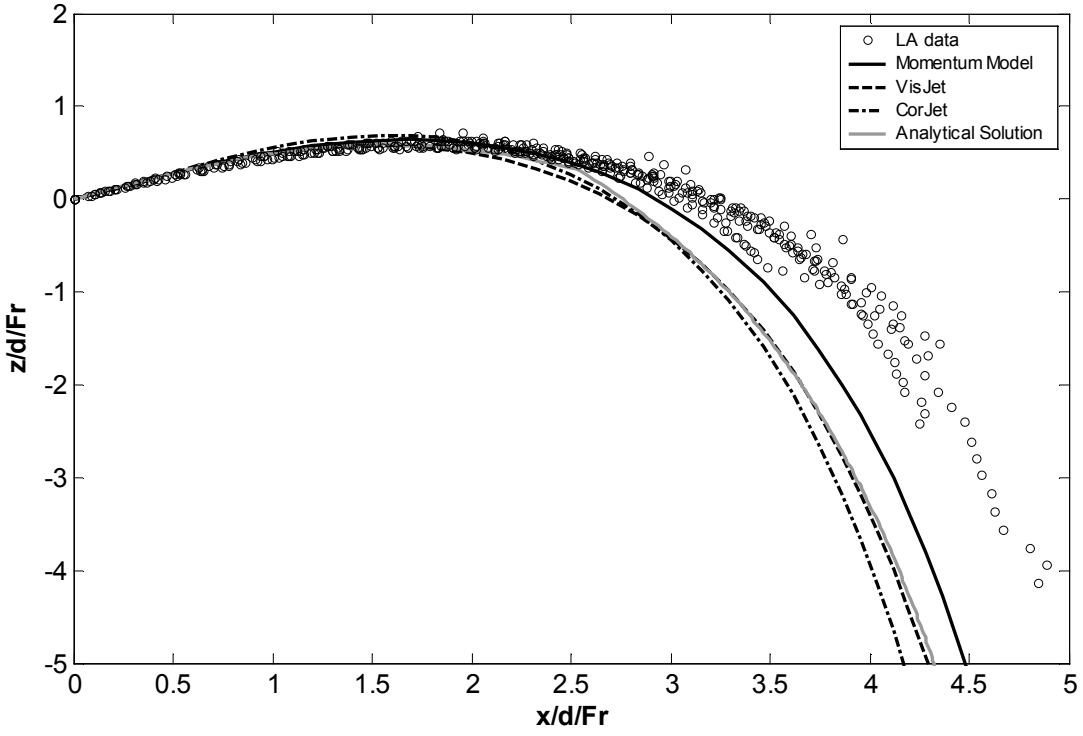

6.15(b) - Initial angle of 30°, Re ranging from 2406 to 5207 and Fr ranging from 29.84 to 65.97

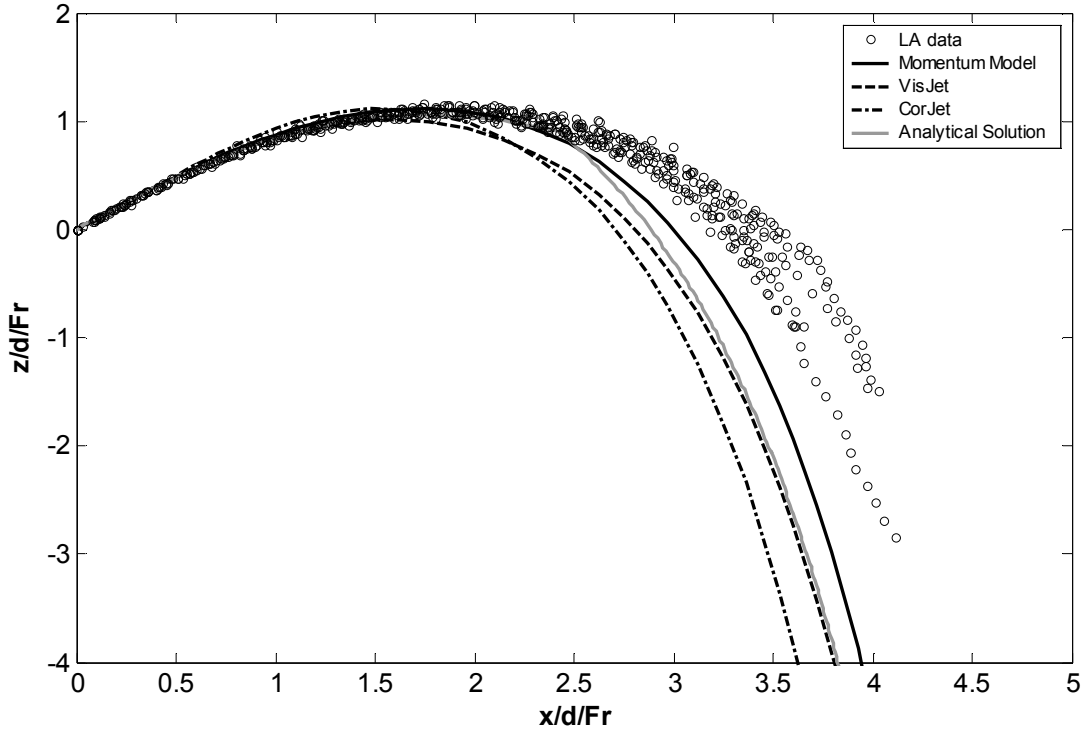

6.15(c) - Initial angle of 45°, Re ranging from 2144 to 4615 and Fr ranging from 27.32 to 60.68

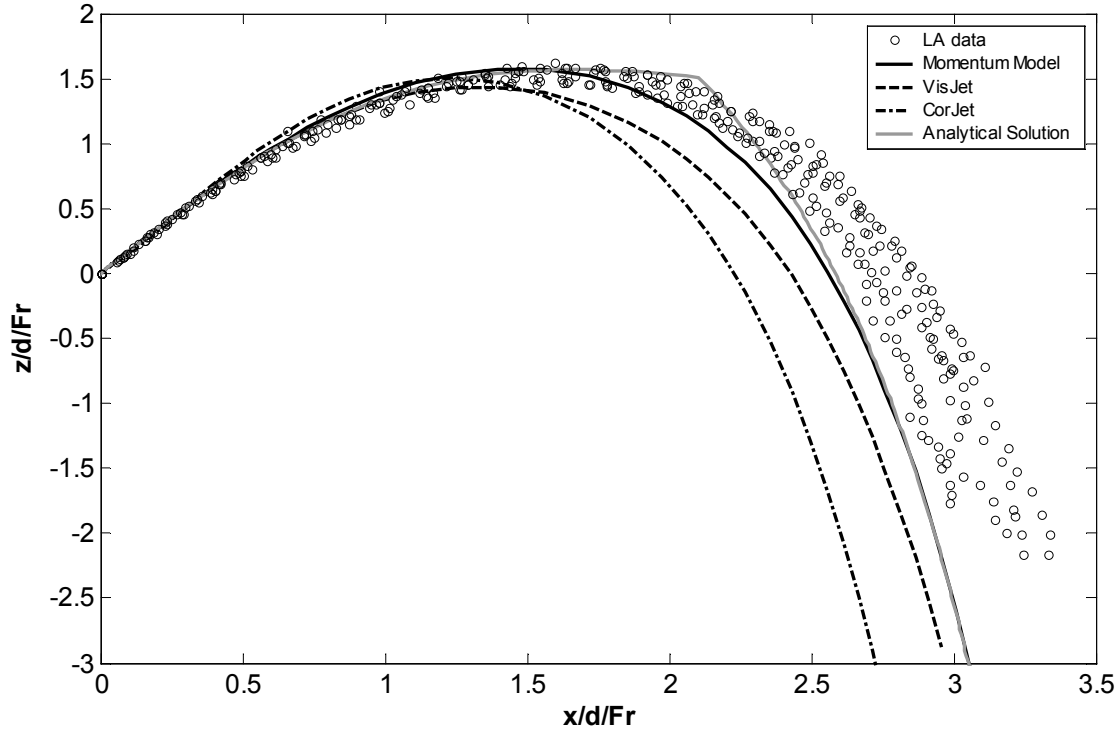

6.15(d) - Initial angle of 60°, Re ranging from 2940 to 5032 and Fr ranging from 37.10 to 63.75

Figure 6.15 – Trajectory results for negatively buoyant jets with discharge angles 15°, 30°, 45° and 60°

A more complete picture of the form of the mean flow is shown in Figure 6.16, where concentration spread and trajectory are presented. Figure 6.16 shows, for the four different initial discharge angles, the trajectory data of a single experiment plus the inside and outside concentration spread. This data is compared with the trajectory and inside and outside concentration spread as predicted by the Momentum Model. From the figure it is clear, particularly for the higher angles, that the inside concentration spread is substantially higher than the predicted values. The 45° flow is arguably affected the most. The buoyancy-generated instabilities have the greatest effect when the flow is moving horizontally. Flows with higher initial discharge angles have less initial momentum flux in the horizontal, and therefore require a shorter distance to change the direction of the trajectory. This relatively quick change leaves less time for the instabilities to affect the flow.

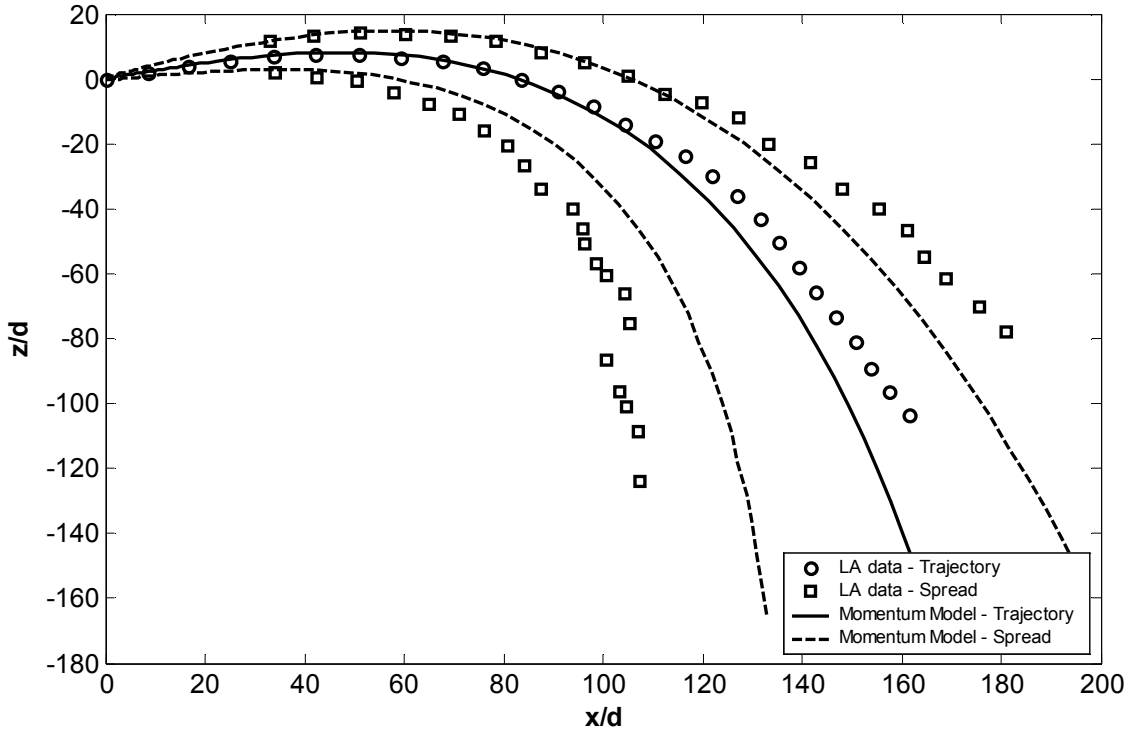

6.16(a) - Initial angle of 15°, Re = 2822 and Fr = 35.76

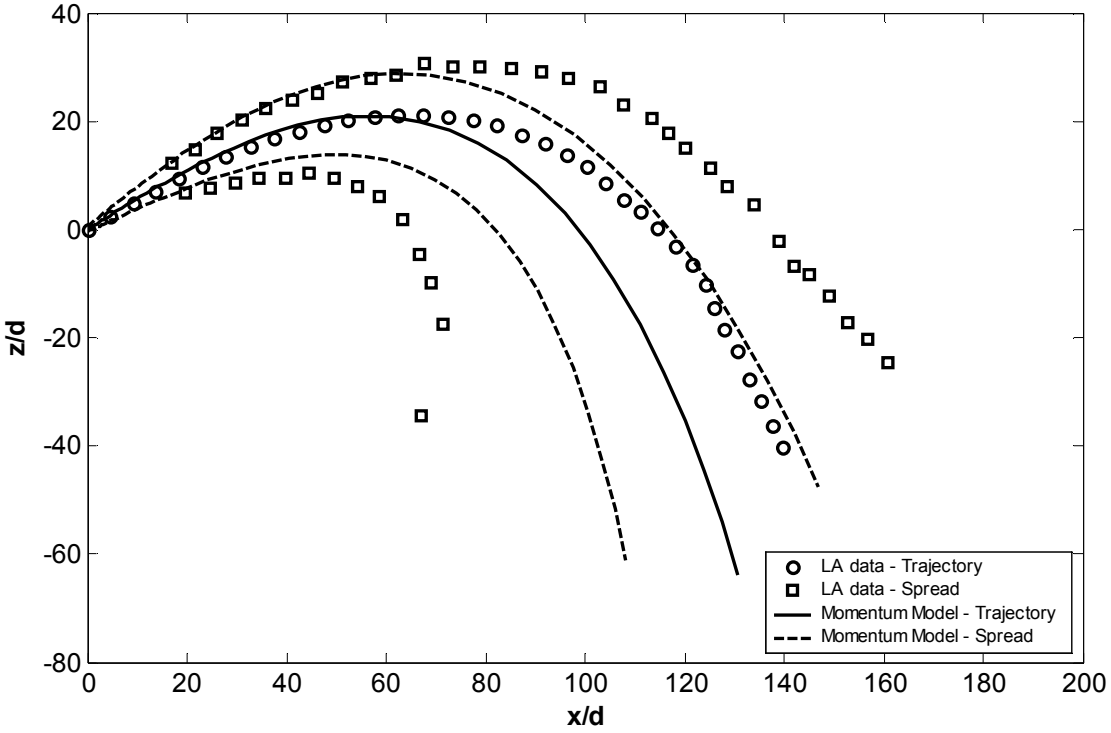

6.16(b) - Initial angle of 30°, Re = 2822 and Fr = 35.76

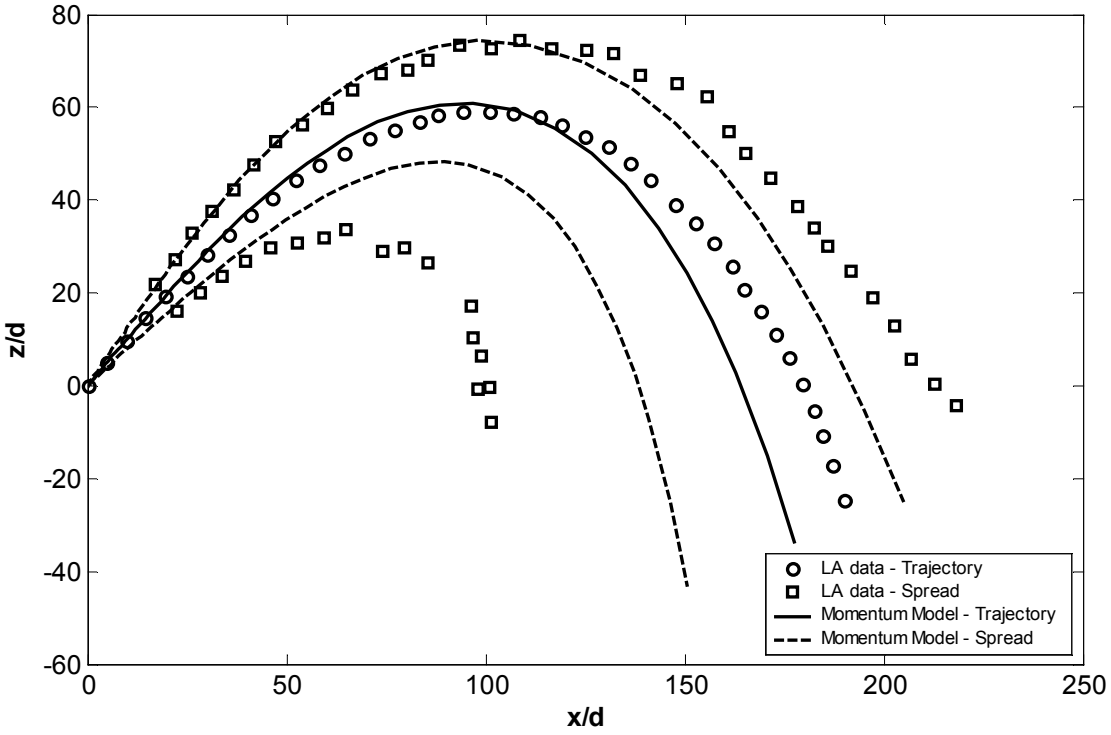

6.16(c) - Initial angle of 45°, Re = 4288 and Fr = 54.65

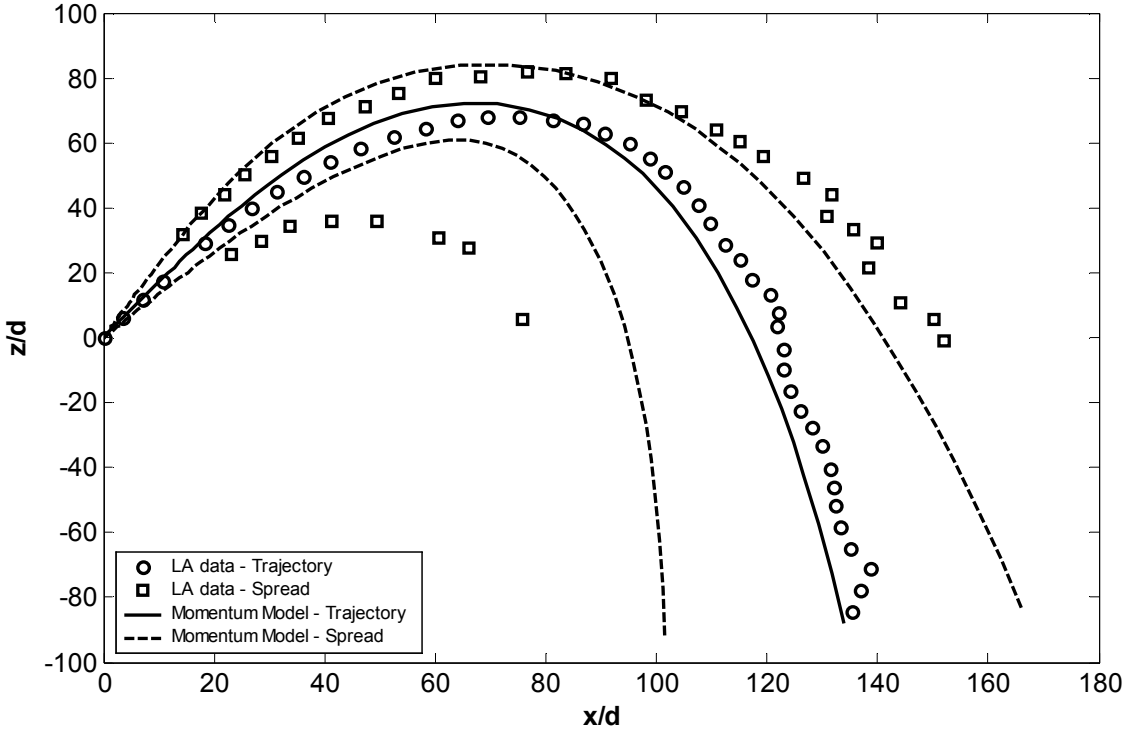

6.16(d) - Initial angle of 60°, Re = 3609 and Fr = 45.74

Figure 6.16 – Spread comparison between experimental data and Momentum Model for discharge angles 15°, 30°, 45° and 60°

The experimental outside concentration spread and the trajectory points appear to have shifted a similar distance when compared to the predicted values. This indicates that the cross-sectional outside concentration spread from both the model and the experiment are similar. This is consistent with the results found in Figure 6.3, where the outside edge of the flow is relatively unaffected by the instabilities and the cross-sectional profiles collapses onto a single Gaussian curve, and is further confirmed by the results presented in Figure 6.17. This Figure shows the concentration spread results as a function of distance from the source, along the flow path. The experimental data from the different initial discharge angles collapses well onto a single line and agree with the theoretical spread assumption.

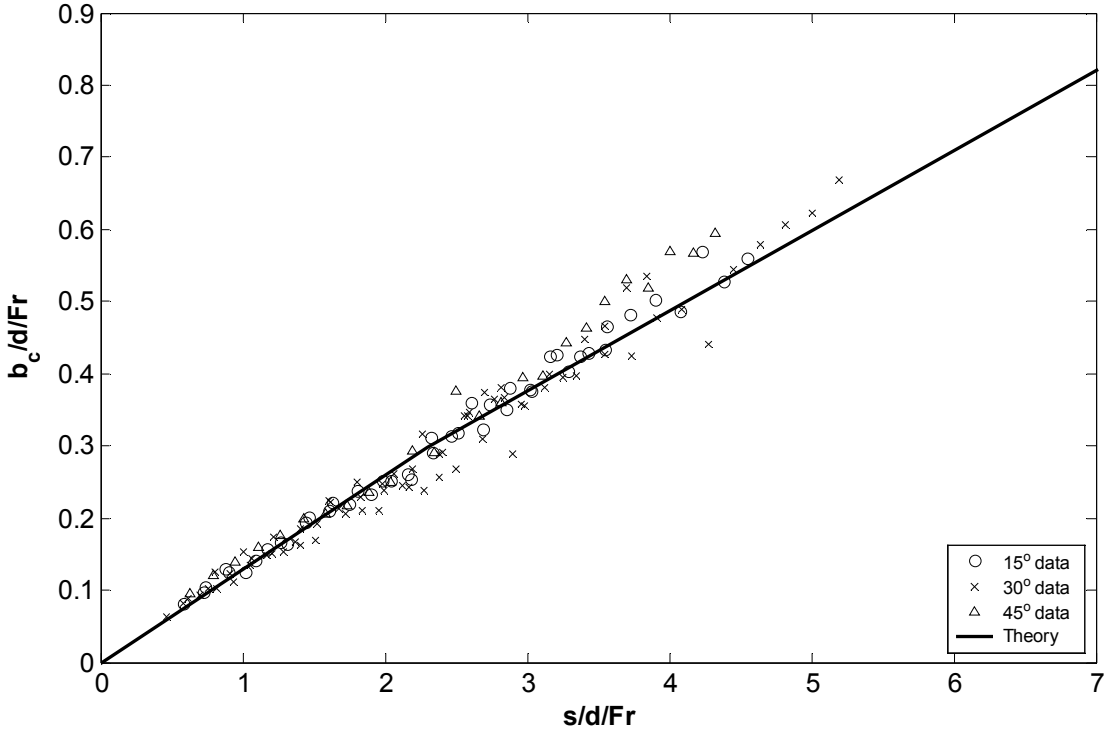

Figure 6.17 - Concentration spread results as a function of distance from source

The dilution results from the experimental investigation are shown in Figure 6.18. The results are presented as integrated centreline dilutions and no attempt has been made to convert these into point centreline dilutions. The internal concentration distribution has to be known to be able to make an accurate conversion and the Gaussian assumption has been shown to be an unrealistic match to the actual cross-sectional concentration distribution for these flows (further evidence of this is given in section 6.4.5). To compare the experimental data with the model predictions the point centreline dilution results given by the models are converted into integrated centreline dilution results. Because of the axi-symmetric spread assumptions used by the models, equation (3.18) can be rearranged to find the conversion relationship between the actual and the integrated centreline dilution.

$$\frac{C_{i0}}{C_{il}} = \frac{d}{b_c\sqrt{\pi}}\frac{C_0}{C_l} \tag{6.21}$$

Figure 6.18 shows that the dilution results predicted by the models are substantially lower than the experimental values found, supporting the observation that the axi-symmetric Gaussian spread assumption no longer gives reasonable answers. The models underestimate the dilution by approximately 30%. No analytical solutions have been developed for predicting the integrated dilution along the centreline of the flow.

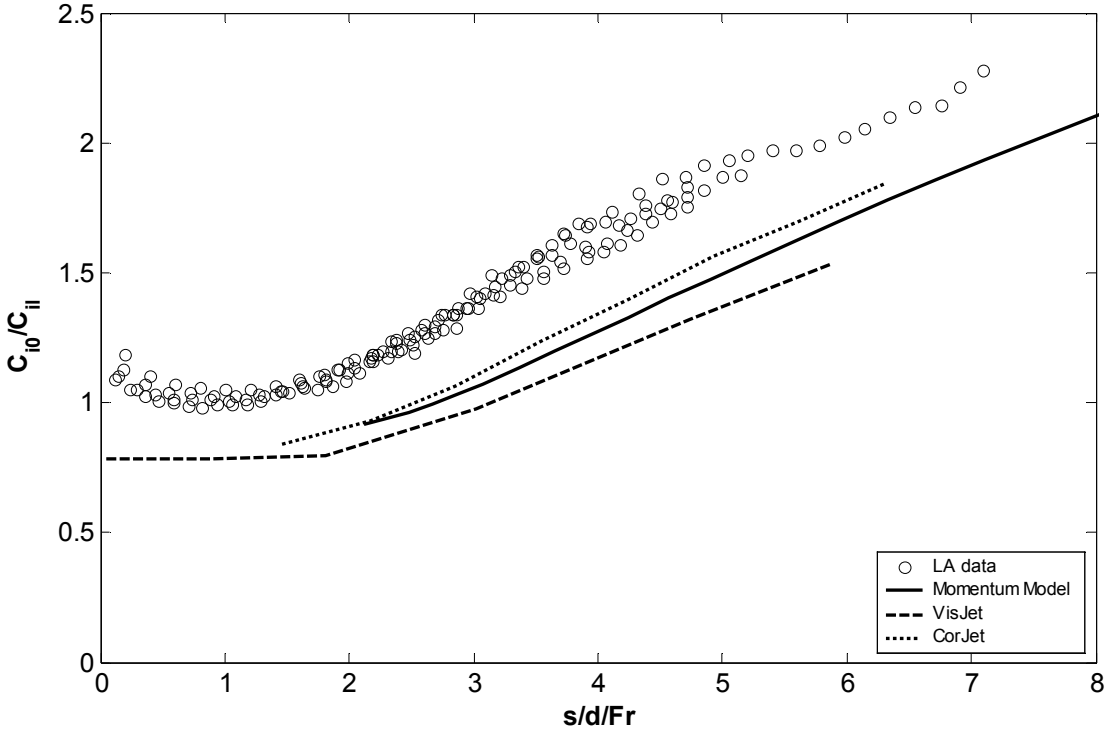

6.18(a) - Initial angle of 15°, Re ranging from 2699 to 5163 and Fr ranging from 34.06 to 65.42

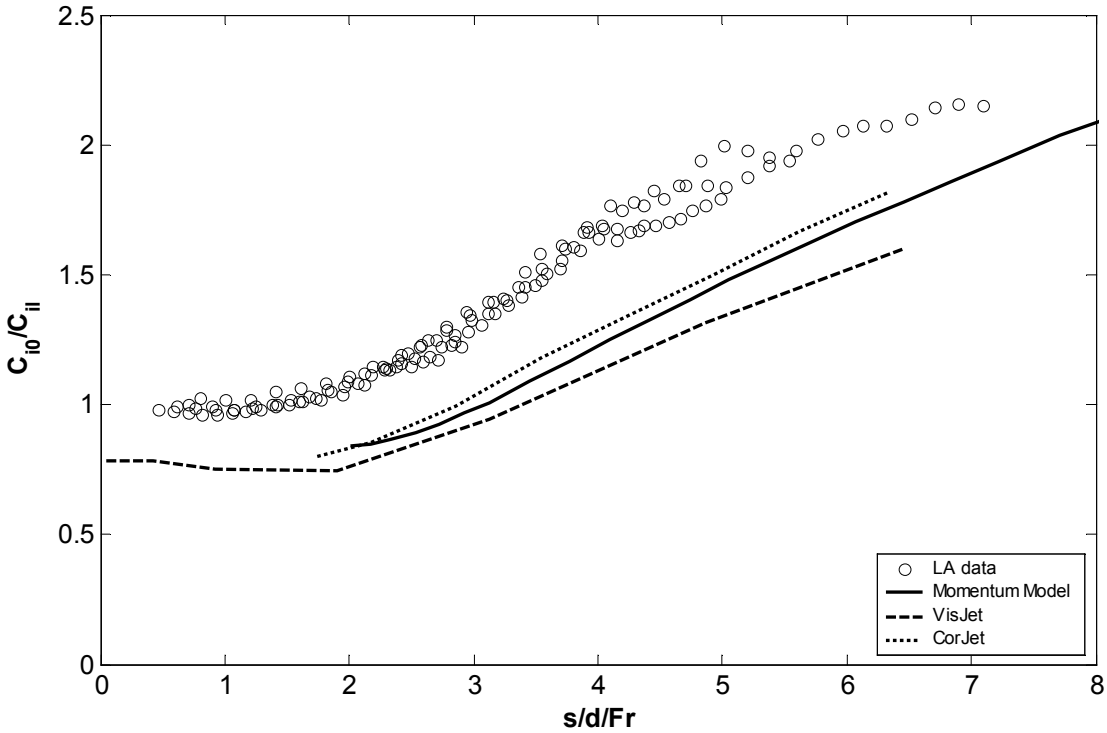

6.18(b) - Initial angle of 30°, Re ranging from 2406 to 5207 and Fr ranging from 29.84 to 65.97

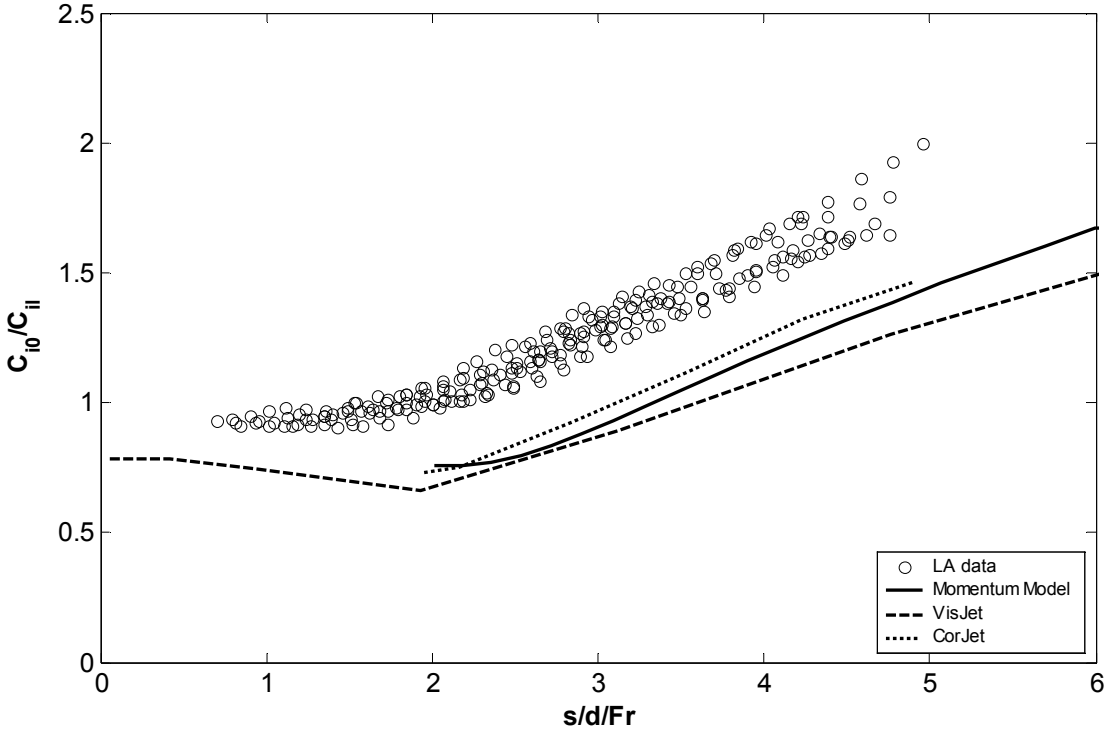

6.18(c) - Initial angle of 45°, Re ranging from 2144 to 4615 and Fr ranging from 27.32 to 60.68

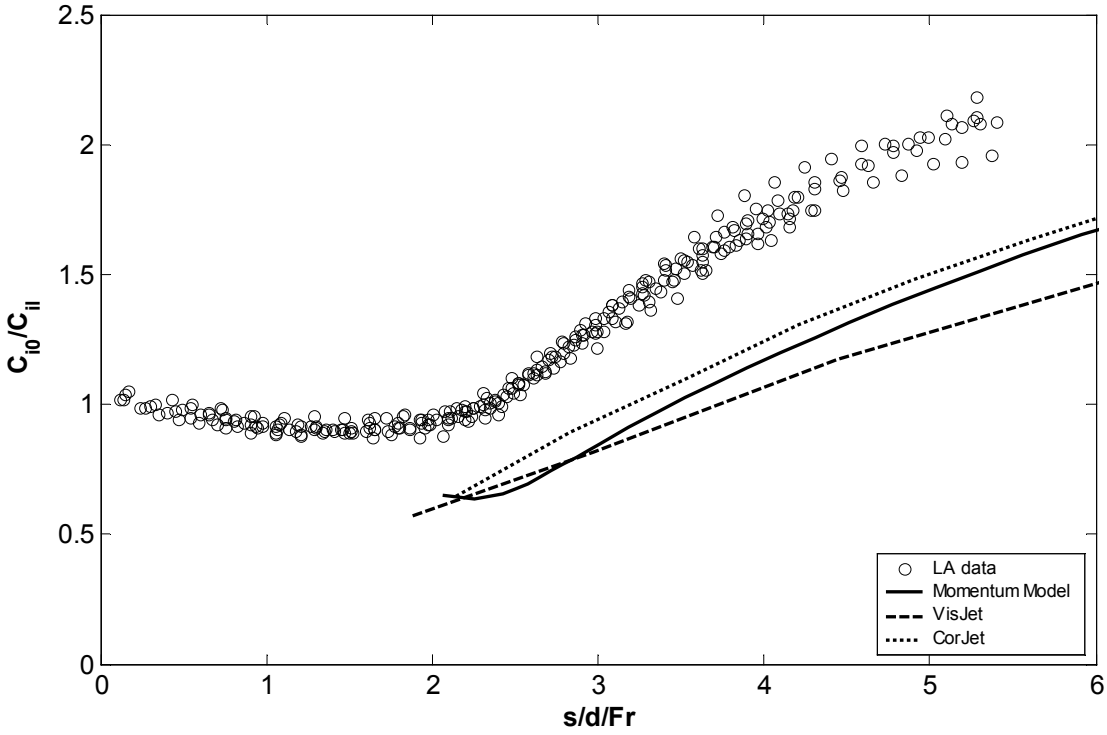

6.18(d) - Initial angle of 60°, Re ranging from 2940 to 5032 and Fr ranging from 37.10 to 63.75

Figure 6.18 - Centreline integrated dilution data as a function of distance downstream for discharge angles 15°, 30°, 45° and 60°

6.4.5 – Preliminary Cross-Sectional Results

The last four runs of the LIF investigation were set up to record various instantaneous cross-sectional profiles of the flow with an initial discharge angle of 45°. The cross-sectional profiles were anticipated to give a different perspective on the effect of the buoyancy-induced instabilities and confirm some of the results that were found earlier. An extensive investigation was not carried out because of the limitations of time. Instead the focus was on gaining a qualitative appreciation of changes to the mean flow cross-sectional structure.

The most accurate cross-sectional profile was recorded perpendicular to the flow at the maximum height. A contour plot of the profile is presented in Figure 6.19 and it clearly shows that the profile is not axi-symmetric. At first glance the top half of the profile seems to still be Gaussian, however a closer look reveals that the width of the profile measured in the horizontal is lower than the width measured in the vertical. This indicates that some of the buoyant fluid that was expected to be at the sides of the profile, near the centreline, has sunk downwards and became part of the tail (inner side of the flow). The concentration profile was integrated in the horizontal direction to find the vertical coordinate of the maximum integrated concentration. This was compared with vertical coordinate of the maximum point concentration. The integrated value (essentially LA) was found to be lower than the point value (LIF) confirming the results shown in Figure 6.3 to Figure 6.6 and the impact of buoyant fluid being removed from the outer edge of the flow near the centreline.

Figure 6.20 shows the contour plot of the horizontal cross-sectional profile at the source height. It does not have any direct relevance to the flow parameters that are normally attributed to describing the flow, however it does show just how much the distortion is influencing the flow behaviour. The plot shows the contour lines at the impact point (the point with the maximum concentration on the right hand side of the image) and 75% of the distance back to the source (on the left). According to the axi-symmetric models, using the assumption that the boundary of the flow is equal to $2*b_c$, their should not be any dye present in the left hand third of the image.

The final cross-section was again recorded at the impact point (see Figure 6.21), however this time the camera was aligned with the direction of the flow at the impact point and the laser sheet was set up perpendicular to the direction of flow. Ignoring the rough edges of the profile, the contour plot as a whole does not differ significantly from the one found at the

maximum height. This matches the conclusions from Figure 6.7 and Figure 6.14 that the distortions, and therefore the increase in dilution associated with those distortions, do not become significantly worse as the flow travels from the maximum height to the impact point. The relatively large width of the profile at the outer edge compared to the sides is more evident at the impact point than it was at the maximum height.

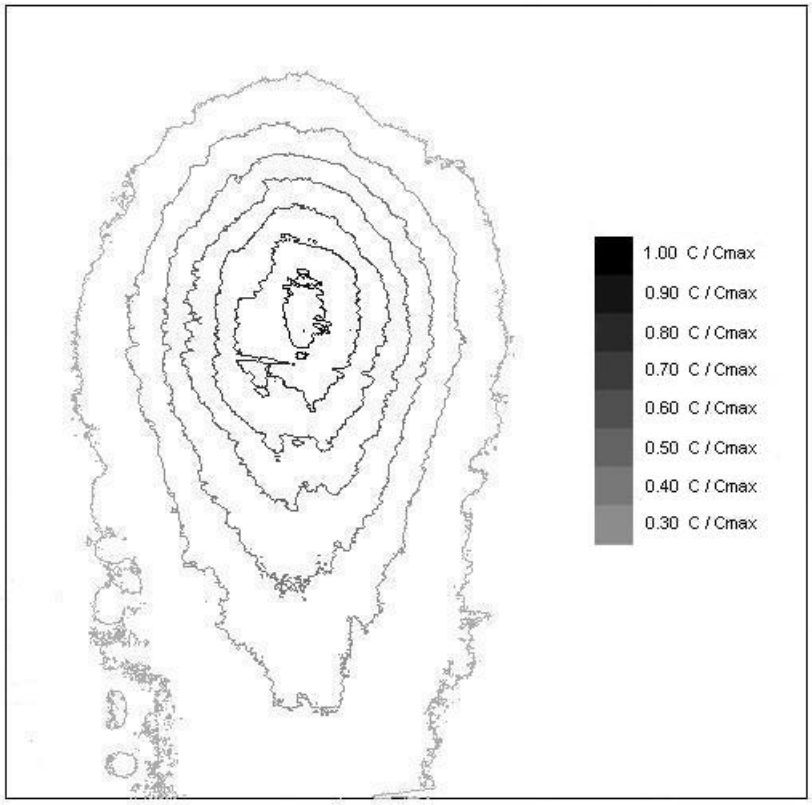

Figure 6.19 - Cross-sectional profile at the maximum height for a 45° buoyant jet

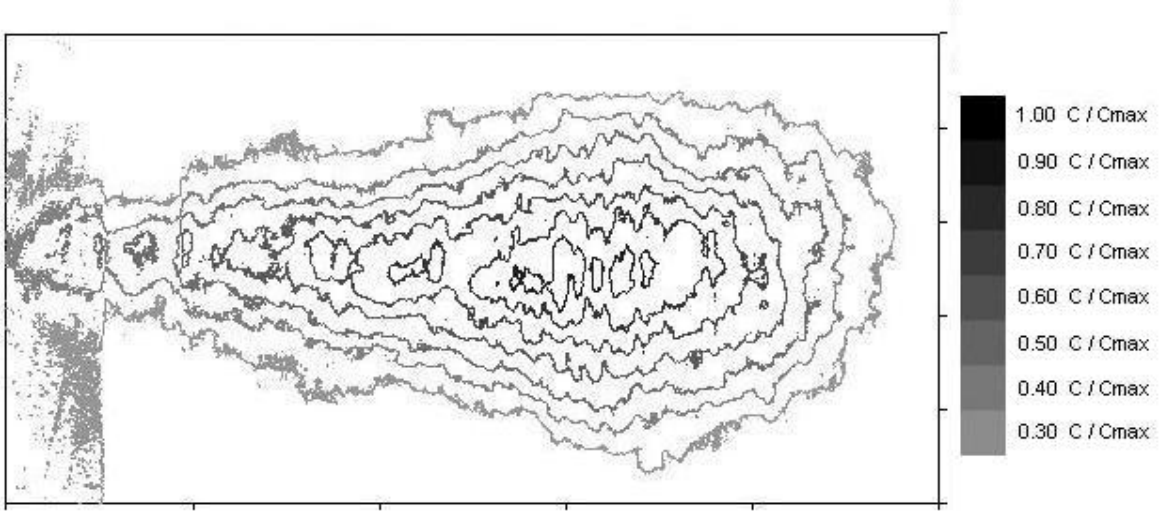

Figure 6.20 - Horizontal cross-sectional profile at source and impact height for a 45° buoyant jet

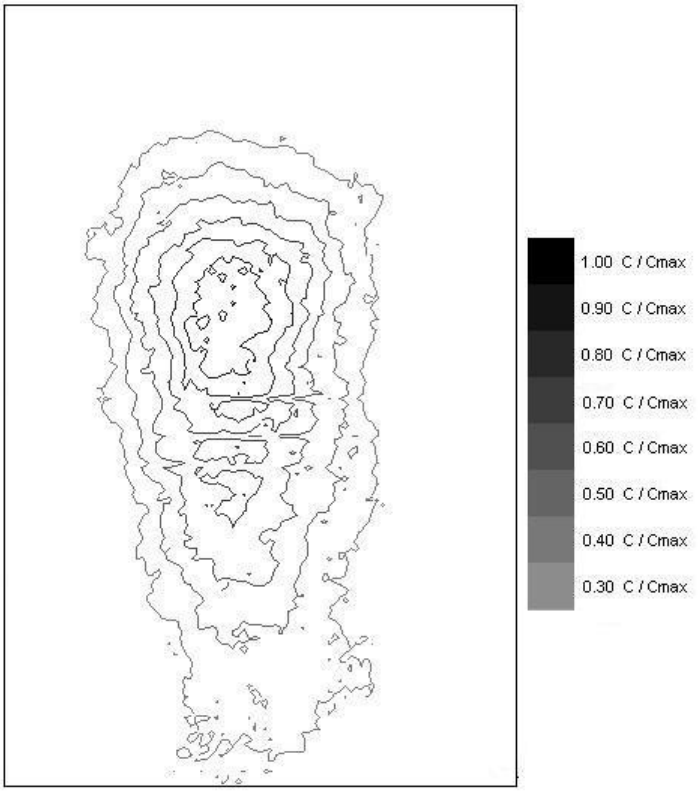

Figure 6.21 - Cross-sectional profile at the impact point for a 45° buoyant jet

6.5 – Summary

Analytical solutions have been developed to predict the behaviour of inclined negatively buoyant discharges for a broad range of initial discharge angles. These relationships complement previously developed empirical relationships of the same form. Predictions from the analytical solutions have been compared with data from previous studies and data obtained from the present experimental study, using both Light Attenuation and Laser Induced Fluorescence techniques, to provide additional information about the behaviour of these flows.

Comparisons show that model predictions of the location of the maximum centreline height fall within the scatter of available experimental data for initial discharge angles ranging from 0° to 75° and initial Froude numbers ranging from 14 to 99. The maximum height of the outer edge of the jet is also predicted with reasonable accuracy, indicating that the assumed growth rate of the outer jet edge is acceptable. This was confirmed by plotting the outer edge concentration spread results versus the distance travelled along the trajectory path and compare it with the expected concentration spread rate for an axi-symmetric buoyant jet.

Comparisons of the predicted location of the impact point with the experimental data show that the analytical solutions generally underestimate the distance to the impact point. In addition minimum integrated dilution predictions at the centreline maximum height and the impact point are shown to be conservative (by about 30% at both points). Both results reflect the influence of buoyancy-induced instabilities on the inner side of the jets, which generate additional vertical mixing and significantly alter the form of the mean concentration profiles in this region.

CorJet and VisJet have been shown to provide trajectory predictions that are similar to those of the analytical solutions presented here, but that they have a tendency to underestimate these values. More significantly the integrated dilution predictions from these numerical models appear to be considerably more conservative than those of the analytical solutions, with these numerical models indicating a reduction in dilution as the flow approaches maximum height. Their integrated dilution predictions also show a dependence on initial discharge angle, which is not evident in either the analytical solutions or the experimental data. VisJet, CorJet and the Momentum Model make the assumption of axi-symmetrical cross-sectional profiles. The present experimental data showed that this assumption is not capable of generating accurate predictions of the behaviour of the negatively buoyant jet. More sophisticated modelling techniques are required to incorporate the effects of the buoyancy-induced instabilities.

A set of preliminary cross-sectional profiles were able to confirm many of the conclusions based on the integrated data. However more detailed investigations into the cross-sectional profiles are needed to provide an in-depth understanding of the changes to the mean-flow structure.

Chapter 7 – Oblique Non-Buoyant Discharges in a Moving Ambient

7.1 - Introduction

In addition to the investigation of the vertically discharged non-buoyant jet in a moving ambient, presented in Chapter 5, a more detailed investigation was carried out to study the behaviour of obliquely discharged non-buoyant jets in a moving ambient.

In the environment, jet discharges are most likely to be buoyant. Even if treated waste water is disposed of in a fresh water lake, only a slight difference in temperature and/or composition between the ambient and the jet fluid is sufficient to produce a buoyant flow. However, for these relatively small density differences the effects of the buoyancy-generated momentum flux are often not felt near the source, where the initial momentum flux and the entrained ambient momentum flux control the flow behaviour. Ultimately the buoyancy-generated momentum flux will have a significant influence on the behaviour of the flow.

Given the ability to produce non-buoyant experimental fluid flows with relative ease, numerous experimental investigators have focused on the non-buoyant discharge in a still and a moving ambient (see Chapter 2). Wang (2000a) and others, as well as results presented in Chapter 5, have shown that in the weakly advected or strong jet region (where the initial excess momentum flux dominates), both the cross-sectional velocity and concentration profiles fit the Gaussian shape well. If there is an ambient flow present, the ambient fluid is entrained into the jet increasing its ambient momentum flux. In the strongly advected region, this entrained ambient momentum flux dominates the behaviour of the flow. Wang (2000b), amongst others, has shown that if the jet fluid is discharged in line with the direction of flow of the ambient fluid, the cross-sectional profiles in the strongly advected region are still Gaussian. This type of flow is referred to as the weak-jet. For jet flows that are discharged perpendicular to the direction of the ambient flow, Chu and Goldberg (1974), and Chu and Lee (1996), amongst others, showed that the self-similar velocity and concentration distributions in the strongly advected region are no longer Gaussian, but resemble that of a vortex pair. The flow is then said to be in the advected line momentum puff region. The

vortex pair distribution enhances the entrainment of ambient fluid and therefore the dilution of the flow.

The above information leads to the conclusion that somewhere between the initial discharge angles of 0° and 90° a change in strongly advected behaviour occurs, from weak-jet to momentum puff. Pun (1998) notes that this changeover cannot be found by length-scale analysis as in both regions the flow is dominated by the same parameters, the initial excess momentum flux and the ambient velocity. The transition between the different strongly advected behaviours must therefore be controlled by the angle of discharge. Experimental studies have been carried out with initial discharge angles between the co-flowing and cross-flowing cases. Margason (1968) studied flows with an initial discharge angle of 60° and 120°. Platten and Keffer (1971) investigated the angles between 45° and 135° with 15° increments, Chu (1975a) studied the same range but in 22.5° intervals and Hung (1998) studied the 15°, 30°, 40° 50°, and 70° cases. However none of the above studies focused on the transition angle.

Current mathematical models capable of predicting buoyant jet flow behaviour are based on a sequence of integral or length-scale solutions of five fully self-similar flow regions. This includes the Momentum Model presented in Chapter 4. In each of these regions either the rate of entrainment or the rate of spread is used to close the system of equations. In the transition region the entrainment or spread assumption is changed to suit the new region. With the angle (or angles) of transition between weak-jet and momentum puff regions currently not precisely determined (Pun 1998), these models lack important information to enable them to accurately predict the flow in this particular area.

This chapter presents an investigation into the behaviour of oblique non-buoyant discharges. Analytical solutions in the weak-jet and momentum puff regions are determined to characterize the flows and estimate the transition angle. An experimental study is carried out to study the flow, focusing on the discharge angles close to the estimated transition angle. The experimental results are compared with the analytical solutions as well as the predictions from the currently available numerical models.

7.2 – Analytical Solutions

As explained above, the current models do not provide a framework for interpreting the experimental data, therefore the expected behaviour is outlined initially in the form of a

hybrid or composite solution model. This type of model is based on relatively simple analytical solutions that are developed within flow regions with a distinct form, such as those described above, and hence is ideal for this type of study.

The discharge configuration adopted for the analytical solutions in Chapter 6 is modified for use with the obliquely discharged non-buoyant jets in a moving ambient, considered here. The investigation focuses on discharges in the *x*-*z* plane. The discharge is ejected at some angle (ϕ_0) to the ambient fluid velocity. The densities of the ambient and discharge fluids are the same. A coordinate system with its origin at the point of discharge can be defined such that the *x* coordinate is in the same direction as the ambient velocity. The *y* coordinate is then perpendicular to the *x* coordinate and lies in the horizontal plane. The *z* coordinate lies in the vertical plane. This information is represented graphically in Figure 7.1.

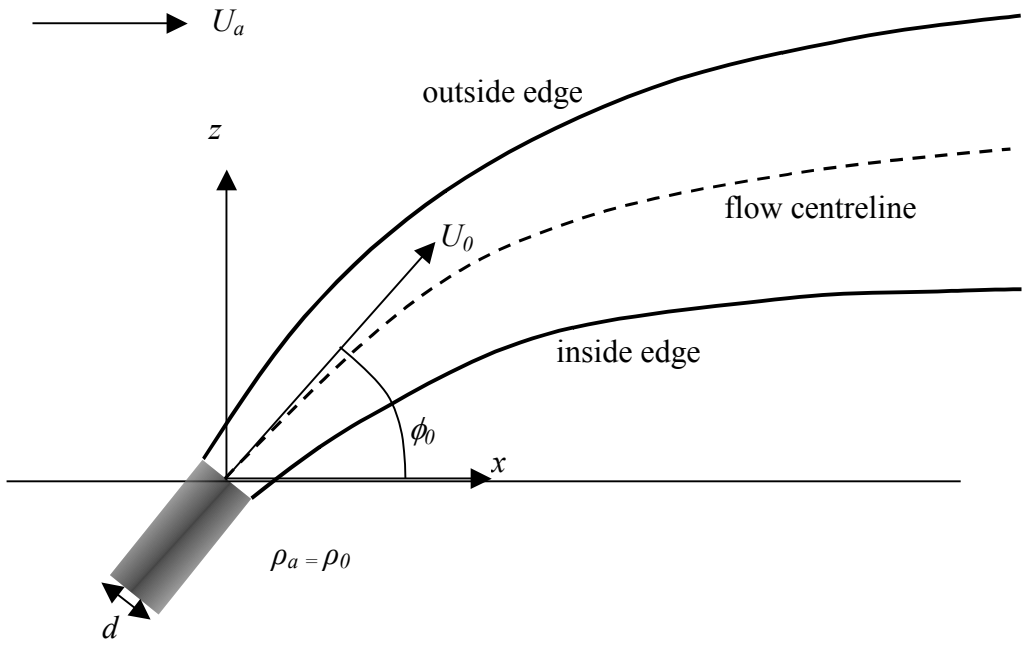

Figure 7.1 - Schematic diagram of the generic discharge configuration for oblique momentum puff

7.2.1 – Weak Jet

In the weak jet region the ambient velocity and the component of the initial excess momentum flux that is parallel to the ambient velocity play important roles in defining the behaviour of the discharge. Application of the equations for conservation of mass and momentum, combined with the spread assumption, yields the following relationships:

$$\frac{b}{M_{e0}^{0.5}/U_a} = \left(\frac{3k\cos\phi_0}{I_q C_{jk}}\right)^{1/3} \left(\frac{x_{wj}}{M_{e0}^{0.5}/U_a}\right)^{1/3} \tag{7.1}$$

$$\frac{U_a}{U_{e0}}\frac{C_0}{C_l} = I_c \left(\frac{3k\cos\phi_0}{I_q C_{jk}}\right)^{2/3} \left(\frac{x_{wj}}{M_{e0}^{0.5}/U_a}\right)^{2/3} \tag{7.2}$$

where I_q and I_c are shape factors with values of π and 7.5 respectively in the weak-jet region, x_{wj} is the distance from the virtual source of the weak jet, and k the Gaussian spread rate (0.106). C_{jk} is a constant in the spread assumption for the weak-jet region and has a value of 1.55. For more detailed derivations see Wang (2000b).

Although the flow is dominated by the component of the excess momentum flux that is parallel to the ambient current and the entrained ambient momentum flux, the component of momentum flux perpendicular to the ambient current will deflect the discharge and thereby alter its trajectory. The relationship for this is given by:

$$\frac{dz_{wj}}{dx_{wj}} = \frac{U_{e0}Q_0\sin\phi_0}{U_a Q + U_{e0}Q_0\cos\phi_0} \tag{7.3}$$

and:

$$\frac{U_{e0}Q_0}{U_a Q} = \frac{M_{e0}}{U_a{}^2\beta_{wj}{}^2\pi b^2} = \frac{1}{\pi\beta_{wj}{}^2\left(\frac{3k\cos\phi_0}{I_q C_{jk}}\right)^{2/3}\left(\frac{x_{wj}}{M_{e0}^{1/2}/U_a}\right)^{2/3}} \tag{7.4}$$

where β_{wj} represents the ratio of the jet edge radius to the nominal radius b. Integration of this equation gives:

$$\frac{z_{wj}}{L_{mz*}} = \frac{3}{\beta_{wj}{}^2\pi}\left(\frac{I_q C_{jk}\tan\phi_0}{3k}\right)^{2/3}\left(\frac{x_{wj}}{L_{mz*}}\right)^{1/3} - \frac{\tan^{1/2}\phi_0 I_q C_{jk}}{\beta_{wj}{}^3\pi^{3/2}k}\tan^{-1}\left(\frac{\beta_{wj}\pi^{1/2}\sin^{1/3}\phi_0}{\cos^{1/2}\phi_0}\left(\frac{3k\cos\phi_0}{I_q C_{jk}}\right)^{1/3}\left(\frac{x_{wj}}{L_{mz*}}\right)^{1/3}\right) \tag{7.5}$$

where

$$L_{mz*} = \frac{\left(M_{e0}\sin\phi_0\right)^{0.5}}{U_a} \tag{7.6}$$

For a more detailed derivation of the trajectory equation, see Appendix F. In the region well beyond the transition zone from the weakly advected to the strongly advected region, the component of the initial excess momentum flux parallel to the ambient current no longer has a significant influence on the path of the discharge, because the motion in this direction is dominated by the entrained ambient momentum flux. This reduces equation (7.5) to

$$\frac{z_{wj}}{L_{mz*}} = \frac{3}{{\beta_{wj}}^2 \pi}\left(\frac{I_q C_{jk} \tan\phi_0}{3k}\right)^{2/3}\left(\frac{x_{wj}}{L_{mz*}}\right)^{1/3} \tag{7.7}$$

For a direct comparison with the analytical solutions in the puff region, the equations for the weak-jet are rewritten as functions of the distance travelled in the *z*-direction instead of the *x*-direction. The concentration spread equation and dilution equation become:

$$\frac{b_c}{{M_{e0}}^{0.5}\sin\phi_0/U_a} = \frac{\lambda k {\beta_{wj}}^2 \pi}{I_q C_{jk}\tan\phi_0}\frac{z_{wj}}{{M_{e0}}^{0.5}\sin\phi_0/U_a} \tag{7.8}$$

$$\frac{U_a}{U_{e0}}\frac{C_0}{C_l} = I_c\left(\frac{{\beta_{wj}}^2 \pi k}{I_q C_{jk}\tan\phi_0}\right)^2\left(\frac{z_{wj}}{{M_{e0}}^{0.5}/U_a}\right)^2 \tag{7.9}$$

As the LA flow visualization technique was used to record the flow during the experimental investigation, the dilution equation has to be integrated to be able to make a direct comparison with the integrated dilution results from the experiments. As mentioned above, the Gaussian assumption fits the cross-sectional concentration profiles well and therefore the integrated results found during the investigation of the simple jet in Chapter 3 can also be applied to the weak-jet solution. Inserting equation (3.18) into equation (7.9) gives the integrated dilution equation for the weak jet region:

$$\left(\frac{U_0}{U_{e0}}\right)^{0.5}\frac{C_{i0}}{C_{il}} = \frac{2I_c}{\lambda}\frac{{\beta_{wj}}^2 k}{I_q C_{jk}\tan\phi_0}\frac{z_{wj}}{{M_{e0}}^{0.5}/U_a} \tag{7.10}$$

7.2.2 – Advected Line Momentum Puff Region

In this region the ambient velocity and the component of the initial excess momentum flux that is perpendicular to the ambient velocity dominate the flow. As indicated previously, it has been shown that the self-similar velocity and tracer distributions in this region resemble that of a vortex pair. For the calculation of the analytical solutions in the puff region, the double-Gaussian approximation, as explained in section 3.2.3.2, has been used for the internal concentration distribution. The cross-sectional profiles are no longer axi-symmetric, and hence the *y*-integrated and the *z*-integrated solutions are not the same. For comparison with the weak-jet solution only the *y*-integrated solutions have been used because the results integrated in the *z*-direction do not show the complete trajectory. Application of the equations of motion and the spread assumption yields:

$$\frac{b_c}{{M_{e0}}^{0.5}\sin\phi_0/U_a} = \lambda h k_{sg}\frac{z_{amp}}{{M_{e0}}^{0.5}\sin\phi_0/U_a} \tag{7.11}$$

$$\frac{U_a}{U_{e0}}\frac{C_0}{C_{peak}} = \frac{I_{cdg}{k_{sg}}^2}{\left(1+e^{-(2f)^2}\right)}\left(\frac{z_{amp}}{{M_{e0}}^{1/2}/U_a}\right)^2 \tag{7.12}$$

The constants h, k_{sg}, f, and I_{cdg} are defined in Chapters 3 and have the values of 1.46, 0.199, 0.88, and 13.65 respectively. z_{amp} is the distance from the virtual source of the advected line momentum puff (see Pun (1998)).

The flow travels in the z-direction due to the initial excess momentum flux in that direction; mean motion in the x-direction is a combined effect of the entrained ambient momentum flux and the appropriate component of the initial excess momentum flux.

$$\frac{dz_{amp}}{dx_{amp}} = \frac{U_{e0}Q_0\sin\phi_0}{U_aQ + U_{e0}Q_0\cos\phi_0} = \frac{U_{e0}Q_0\sin\phi_0}{U_aQ}\left(\frac{1}{1+U_{e0}Q_0\cos\phi_0/U_aQ}\right) \tag{7.13}$$

and

$$\frac{U_{e0}Q_0}{U_aQ} = \frac{M_{e0}}{{U_a}^2{\beta_{amp}}^2\pi b^2} = \frac{1}{\pi{\beta_{amp}}^2{k_{sg}}^2\left(\frac{z}{{M_{e0}}^{1/2}/U_a}\right)^2} \tag{7.14}$$

where β_{amp} represents the ratio of the puff edge radius to the nominal radius b. Integrating this equation, and substituting L_{mz*} as defined by equation (7.6), gives:

$$\frac{x_{amp}}{L_{mz*}} = \frac{{\beta_{amp}}^2\pi{k_{sg}}^2}{3}\left(\frac{z_{amp}}{L_{mz*}}\right)^3 + \frac{1}{\tan\phi_0}\frac{z_{amp}}{L_{mz*}} \tag{7.15}$$

For a more detailed derivation of the puff trajectory equation, see Appendix F. In the region well beyond the transition zone, the component of the initial excess momentum flux parallel to the ambient current no longer has a significant influence on the path of the discharge, because the motion in this direction is dominated by the entrained ambient momentum flux. This reduces equation (7.15) to

$$\frac{x_{amp}}{L_{mz*}} = \frac{{\beta_{amp}}^2\pi{k_{sg}}^2}{3}\left(\frac{z_{amp}}{L_{mz*}}\right)^3 \tag{7.16}$$

Note the limiting trajectory relationship is independent of the initial discharge angle. The dilution equation is again integrated for the comparison with the experimental data to give.

$$\left(\frac{U_0}{U_{e0}}\right)^{0.5}\frac{C_{i0}}{C_{il}} = 2h\lambda k_{sg}\frac{z_{amp}}{{M_{e0}}^{0.5}/U_a} \tag{7.17}$$

For the determination of the theoretical transition angle the limiting trajectory, concentration spread, and integrated dilution solutions of the puff are compared to the limiting trajectory, concentration spread, and integrated dilution solutions in the weak-jet region.

7.2.3 – Theoretical Transition Angle

The analytical solutions have been determined with respect to the vertical distance from the source, and written so that the puff solutions are independent of the initial discharge angle while the weak-jet solutions have a weak dependence on the initial discharge angle. Matching the solutions from the different regions enables a theoretical transition angle to be determined. The trajectory, spread and dilution relationships have the same dependence on the vertical distance from the source, therefore the transition between different strongly advected behaviour is expected to occur when the coefficients have a similar value. This angle, the theoretical transition angle, is an estimate that indicates where the transition is expected to occur.

The theoretical transition angle using the trajectory solution is determined by equating coefficients from equations (7.7) and (7.16), and this gives:

$$\phi_{t1} = \tan^{-1}\left(\frac{{\beta_{wj}}^3 \pi k}{\beta_{amp} k_{sg} I_q C_{jk}}\right) \tag{7.18}$$

Equating coefficients from equations (7.8) and (7.11) gives a second expression for the calculation of the transition angle, based on the concentration spread solutions.

$$\phi_{t2} = \tan^{-1}\left(\frac{{\beta_{wj}}^2 \pi k \lambda_r}{h k_{sg} I_q C_{jk}}\right) \tag{7.19}$$

where λ_r is the ratio of the λ-values for the weak-jet and puff regions. Note that in the above equation the weak-jet concentration spread is set equal to the *y*-integrated concentration spread of the puff region. This is useful for a direct comparison with the experimental data. A second peculiarity is λ_r. Wang (2000b) found values for lambda in the weak jet region to be 30% higher than integral models predicted. This indicates that the value for λ_r is more than one and suggests different theoretical transition angles for the velocity and the concentration spreads. However these differences are unlikely to be significant in the context of estimating the transition location in this way.

Finally equating coefficients from equations (7.10) and (7.17) gives a third expression for the transition angle. This expression is based on equating the integrated centreline dilution in the weak-jet region with the *y*-integrated centreline dilution in the puff region to give:

$$\phi_{t3} = \tan^{-1}\left(\frac{I_c \beta_{wj}{}^2 k}{\lambda_{wj}\lambda_{amp} h k_{sg} I_q C_{jk}}\right) = \tan^{-1}\left(\frac{\beta_{wj}{}^2 k \lambda_r}{h k_{sg} C_{jk}}\right) = \phi_{t2} \tag{7.20}$$

For the calculation of the theoretical transition angles, values have to be assigned to β_{wj}, β_{amp} and λ_r. Combining the weak-jet Gaussian to Top-Hat conversion equation for the momentum flux (equation (4.67)) with the equation for the volume flux (equation (4.68)) gives the following expression for β_{wj}:

$$\beta_{wj} = \sqrt{\frac{I_q}{\pi}\frac{U_e}{U_{eth}}} \tag{7.21}$$

Assuming that the average velocity is half the excess velocity (Pun 1998), makes β_{wj} equal to $\sqrt{2}$. In section 4.4 it was shown that a circle with radius $\sqrt{I_{qdg}/\pi}$ could approximate the area under the double-Gaussian (equation (4.62)). The results in section 5.3.1.2 showed that the predictions of the Momentum Model, based on the double-Gaussian assumption, were consistent with the experimental data for the vertically discharged non-buoyant jet in a moving ambient. This indicates that it is appropriate to multiply the nominal radius by $\sqrt{I_{qdg}/\pi}$ to determine the equivalent puff edge; β_{amp} is therefore assigned the value of 3.00. Wang (2000b) used a value for λ of 1.19, thus the increased value in the weak jet region becomes 1.55. In Chapter 3 the λ in the puff region was left unchanged from that used in the simple jet region. As the theoretical results were a reasonable match with the experimental data, the value for λ in the puff region for the oblique discharges is also set to 1.22. The ratio of the two λ-values is therefore 1.27.

With the above values, the theoretical transition angles are determined to be 18.0° (trajectory) and 31.5° (concentration spread and integrated dilution). These results suggest that for angles higher than 32° the oblique discharge becomes an advected line momentum puff and for angles less than 18° the flow becomes a weak jet in the strongly advected region. This also indicates that there is some form of a transitional region for initial discharge angles between these limits, and that within this region the cross-sectional profiles have a combined strongly advected structure. If a single transition angle is required for modelling purposes, an average angle of 25° for the transition angle seems appropriate. However a second option is to choose either the angle determined by equating the trajectory or the concentration spread and integrated dilution solutions. This choice depends on the purpose of the model and the relative importance of the trajectory, spread and dilution results. The Momentum Model makes use of the average transition angle.

7.2.4 – Weakly Advected to Strongly Advected Transitions and Virtual Sources

Besides the transition between the strongly advected weak-jet and advected line momentum puff regions, the transitions from the weakly advected to the strongly advected regions also have to be determined, to enable comparison of the analytical solutions and the experimental data. These transitions are the strong-jet to weak-jet transition and the strong-jet to puff transition, and are regions where neither the strongly advected solutions nor the weakly advected solutions are reasonable estimates of the flow. Given the lack of detailed knowledge of the transition regions, these regions are modelled as if they occur at a single point. Across this point, it is assumed that the momentum flux is a constant. This requires the creation of a virtual source for the strongly advected regions. Assuming a second dependent parameter of the flow is constant across the transition point enables an estimate of the location of the transition to be determined.

Davidson and Pun (1998) assumed that the flux of excess momentum flux is constant across all transition points in the development of their hybrid model. Three estimates of the location of the transition were determined by matching the spread, the velocity and the dilution. If the three estimates were in reasonable agreement with each other, it indicated that the transition region is relatively short. However for some transition locations there was a wide variation in the estimates, indicating a more gradual transition. In all cases the parameters were compared with available experimental data to verify the estimates. For the current investigation it is assumed that the entrained ambient momentum flux is constant across the transition. As an example, the process of determining the location of the transition by matching the concentration spread in given below.

Given that the analytical solutions are determined with respect to the vertical distance from the source for direct comparisons between the weak-jet and puff solutions, the distance to the transition is therefore stated as a function of the strong-jet to puff transition length-scale $\left(M_{e0}^{0.5}\sin\phi_0 \ /U_a\right)$.

The increase of the concentration spread and entrained ambient momentum flux in the strong jet region are given by the following relationships:

$$\frac{b_c}{M_{e0}^{0.5}\sin\phi_0/U_a} = k\lambda\frac{z_t}{M_{e0}^{0.5}/U_a} \tag{7.22}$$

$$M_a = U_a\pi^{0.5}k_{th}\frac{z_t}{\sin\phi_0}M_{e0}^{0.5} \tag{7.23}$$

where z_t is the vertical distance from the source to the point of transition. The concentration spread relationships for the weak-jet and the puff are given by equations (7.8) and (7.11). The increase in the entrained ambient momentum flux in the weak jet region is:

$$M_a = U_a^2\left(\frac{\lambda k\beta_{wj}^2\pi z_v}{I_q C_{jk}\tan\phi_0}\right)^2\beta_{wj}^2\pi \tag{7.24}$$

where z_v is the vertical distance from the point of transition to the virtual source. In the puff region the entrained ambient momentum flux is given by:

$$M_a = U_a^2 k_{sg}^2\beta_{amp}^2\pi z_v^2 \tag{7.25}$$

Matching the solutions for the concentration spread and the entrained ambient momentum flux at the transition point provides estimates for z_t and z_v and in the weak-jet region these are:

$$\frac{z_t}{M_{e0}^{0.5}\sin\phi_0/U_a} = \frac{k_{th}}{\lambda_j^2 k^2\beta_{wj}^2\pi^{0.5}} = 2.4 \tag{7.26}$$

$$\frac{z_v}{M_{e0}^{0.5}\sin\phi_0/U_a} = \frac{k_{th}I_q C_{jk}}{\lambda_j\lambda_w k^2\beta_{wj}^4\pi^{1.5}}\frac{1}{\cos\phi_0} = \frac{1.46}{\cos\phi_0} \tag{7.27}$$

and for the puff region they are:

$$\frac{z_t}{M_{e0}^{0.5}\sin\phi_0/U_a} = \frac{k_{th}h^2}{k^2\beta_{amp}^2\pi^{0.5}} = 1.7 \tag{7.28}$$

$$\frac{z_v}{M_{e0}^{0.5}/U_a} = \frac{k_{th}h}{kk_{sg}\beta_{amp}^2\pi^{0.5}} = 0.63 \tag{7.29}$$

Thus the transition from strong-jet to weak-jet is predicted to occur at $z = 2.4M_{e0}^{0.5}\sin\phi_0/U_a$. However Wang (2000b) showed that for a co-flowing jet, the transition from strong-jet to weak-jet commences almost immediately after leaving the source at approximately $x = 2.5M_{e0}^{0.5}/U_a$ and continues for several orders of magnitude in the horizontal up to approximately $x = 300M_{e0}^{0.5}/U_a$. Due to the gradual transition from the strong-jet to the weak-jet, assigning a single point to the transition can lead to significant errors. Hence the need for a gradually changing spread function in the Momentum Model (see Chapter 4). The estimate of 2.4 $M_{e0}^{0.5}\sin\phi_0/U_a$ will therefore only be used as an indication of the transition location.

The analytical solutions predict the transition from jet-to-puff to occur at $z_t = 1.7 M_{e0}^{0.5} \sin\phi_0 / U_a$. This estimate is consistent with the results presented in Chapter 5, which show that the transition zone for the vertically discharged non-buoyant jet in a moving ambient begins at approximately 0.5 $M_{e0}^{0.5} \sin\phi_0 / U_a$ and the flow is in the transition region until approximately 3 $M_{e0}^{0.5} \sin\phi_0 / U_a$. Davidson and Pun (1998) determined that matching the dilution at the transition point gave an estimate of 0.54 for the transition constant, and matching the velocity gave an estimate of 0.23. In their hybrid model, they adopted a value of 1.0, based on experimental data. The value of 1.0 $M_{e0}^{0.5} \sin\phi_0 / U_a$ is used in the Momentum Model and this was shown to predict reasonable results for the trajectory, concentration spread and dilution results of vertically discharged non-buoyant jets in a cross-flowing ambient (see Chapter 5). It is also a reasonable average of the theoretical estimates and is therefore employed in the present study as the estimate of the location of the transition from the strong jet to the puff region. This transition point does not match the integrated dilution results from Chapter 3, with these results suggesting a transition point at 1.9 $M_{e0}^{0.5} \sin\phi_0 / U_a$.

Note that when comparing the weak-jet and puff solutions, the analytical solutions use different non-dimensional length-scales for the trajectory, spread and integrated dilution relationships. Therefore the transition length-scale has to be re-written to correspond with the non-dimensional length-scale used.

7.3 – Experimental Design

To look in more detail at the behaviour of oblique discharges in a moving ambient, in particular in the transition region, an experimental investigation was carried out. The experimental data was also used to verify the analytical solutions found above, as well as test the predictions of currently available numerical models. A total of 30 runs consisting of 71 experiments were included in the investigation. The initial conditions for the obliquely discharged non-buoyant jets in a moving ambient are shown in Table D.10

Runs 1 to 14 were carried out as part of a general investigation into the behaviour of non-buoyant obliquely discharged flows. LA was used to visualize the experiments and they were recorded with the Canon MV4i DV. The camera was positioned along side the tank capturing the *y*-integrated view. No attempt was made to record the *z*-integrated view. The runs cover a

range of initial discharge angles from 0° to 140° in ten degree intervals with the exception of the 40° case. The combination of integrated concentration data and a tight turn-around of the flow's trajectory made it difficult to analyse the flow with an initial discharge angle of 140°. Therefore no runs with higher initial discharge angles were carried out. No negative discharge angles were necessary as the flow can be mirrored in the x-axis, and thus the 10° flow is the same as the –10° flow. The initial discharge angle had an accuracy of 0.25°. The diameter of the source was either 3.00 or 2.91 mm, and the initial volume flux was 1.00 or 0.80 l/s, giving a range of Reynolds numbers from 3500 to 4375. The velocity ratio ranged from 0.0220 to 0.0237.

During the initial stages of the analysis of the general investigation, the results suggested that the transition angle separating the weak-jet and momentum puff regions was most likely between 10° and 45°. An additional investigation, made up of runs 15 to 30, therefore focused on flows with initial discharge angles in that range. Each run consisted of three experiments, one more than for the rest of the oblique momentum puff runs, to increase the accuracy of the data. All runs in the additional investigation used a source with a diameter of 2.45 mm. The Reynolds number varied between 3970 and 5154 and the velocity ratio varied between 0.0290 and 0.0392. The camera used to record these flows was the Jai CV M7+, again only the y-integrated view was recorded.

7.4 – Experimental Results and Model Predictions

The experiments generally provided trajectory, concentration spread and integrated dilution results. These results will now be compared with previous experimental studies, the analytical solutions and current model predictions with the aim of identifying the appropriate strongly advected flow regions (advected line momentum puff or weak jet) for a given discharge angle.

7.4.1 - Comparison with Previous Experimental Results

Both Margason (1968) and Platten and Keffer (1971) studied non-buoyant jets discharged at 60° and 120° to the ambient motion. Their trajectory data, non-dimensionalised by the strong jet to puff transition length-scale, has been plotted on Figure 7.2a and is compared with the trajectory results of the current experimental study, as well as predictions of the Momentum Model, VisJet and CorJet. The newly acquired 60° trajectory data matches the previous data

well. In the weakly advected region of the flow, the models are consistent with the experimental data, however in the strongly advected region, they all underestimate the distance travelled in the *z*-direction, suggesting that the influence of the entrained ambient momentum flux on the trajectory results is overestimated. In case of the 120° angle, the current trajectory data is determined to be in the middle of the scatter of the previously acquired data. The Momentum Model prediction is a reasonable match throughout the flow while VisJet is significantly underestimating the distance travelled in the *z*-direction. CorJet was unable to predict this flow configuration.

To date Hung (1998) was the only one to include initial discharge angles in his experimental investigation that, according to the theory above, covered both the momentum puff and weak jet region. In Figure 7.2b, the trajectory results from the current study are compared with the experimental data determined by Hung and the model predictions. For the 30° and 50° angles, Hung's data is higher than the current results, however, the experimental data sets do match well for the 15° and 70° angles.

Note that up to the proposed transition angle, at 25°, the Momentum Model assumes a spread function purely based on weak jet behaviour and a significant change in spread function takes place at the transition angle, while the other models, VisJet and CorJet, assume a gradual transition takes place between the horizontally discharged weak-jet and vertically discharged momentum puff. For the lower angles, the model predictions match the experimental data more closely than for higher angles. The lower angles that, according to the theory, are either in the weak jet region or in the transition between the momentum puff and the weak jet regions. However, the Momentum Model predictions match the 70° experimental data significantly better than the predictions from VisJet and CorJet, indicating that the gradual transition overestimates the influence of the ambient momentum flux on the trajectory results in the puff region.

The transition angle used by the Momentum Model was altered to obtain 30° results with both weak-jet and puff behaviour. The puff result is plotted on Figure 7.2b and is the only prediction of the Momentum Model to match the experimental data. This indicates that choosing the theoretical transition based on equating the trajectory solutions is indeed most accurate for predicting trajectory results.

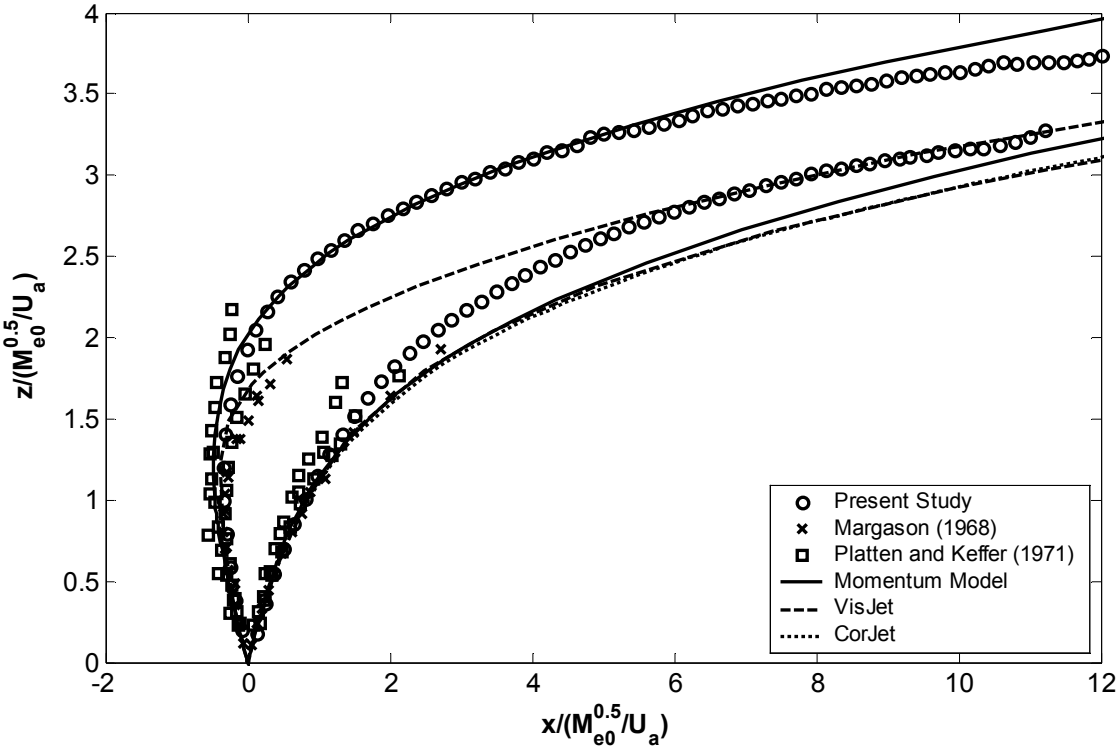

7.2(a) – Initial discharges angles of the flow are 60° and 120°.

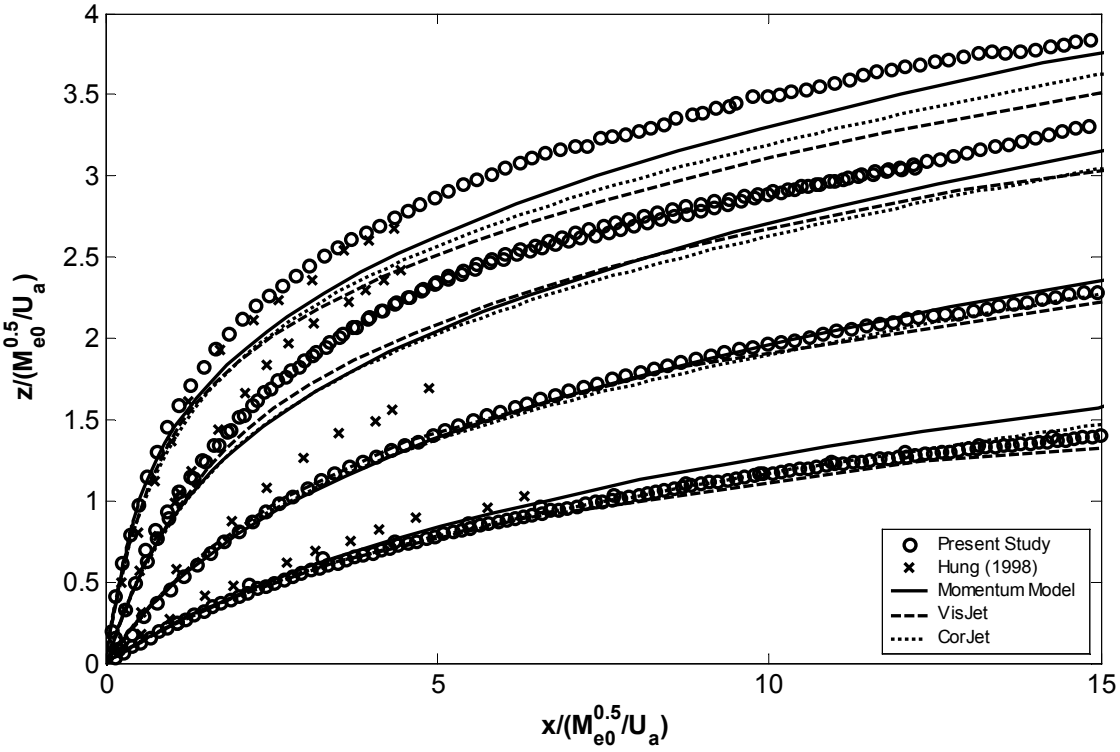

7.2(b) – Initial discharges angles of the flow are 15°, 30°, 50° and 70°.

Figure 7.2 – Trajectory results for oblique discharges in ambient flow

7.4.2 - Comparison with Analytical Solutions

7.4.2.1 – Advected Line Momentum Puff Region

The analytical trajectory solutions are presented with the experimental trajectory results in Figure 7.3. The advected momentum puff solutions were calculated using equation (7.15). The virtual source assumption indicates that the transition point from jet to puff occurs at approximately L_{zm*}, 0.84 L_{zm*} and 0.80 L_{zm*} for the 90°, 45° and 40° cases respectively. The experimental concentration spread results for the puff region are presented in Figure 7.4 and compared with the analytical solutions. The point of intersection between the concentration spread solution in the puff region and the *y*-axis, necessary for plotting the puff solution, is calculated by inserting the transition point into equation (7.22) and equation (7.11) and projecting the puff solution back to the source. The virtual source analysis predicts that the 90° concentration spread puff solution intersects the *y*-axis at approximately –0.24. This is consistent with the analysis of the concentration spread results of the vertically discharged momentum puff flow in Chapter 3. The puff solution intersects the *y*-axis at approximately -0.19 and –0.17 for the 45° and 40° cases respectively. The *y*-integrated dilution results are presented in Figure 7.5. The experimental results are compared with equation (7.17), the advected line momentum puff solution. The vertically discharged non-buoyant jet in a moving ambient suggested the location of the transition point for the *y*-integrated dilution data is at 1.9 transition length-scales from the source. Therefore the puff solution intersects the *y*-axis at –0.54. With the increased distance to the transition point, the ratio of entrained ambient momentum flux after the transition to that before becomes 0.60.

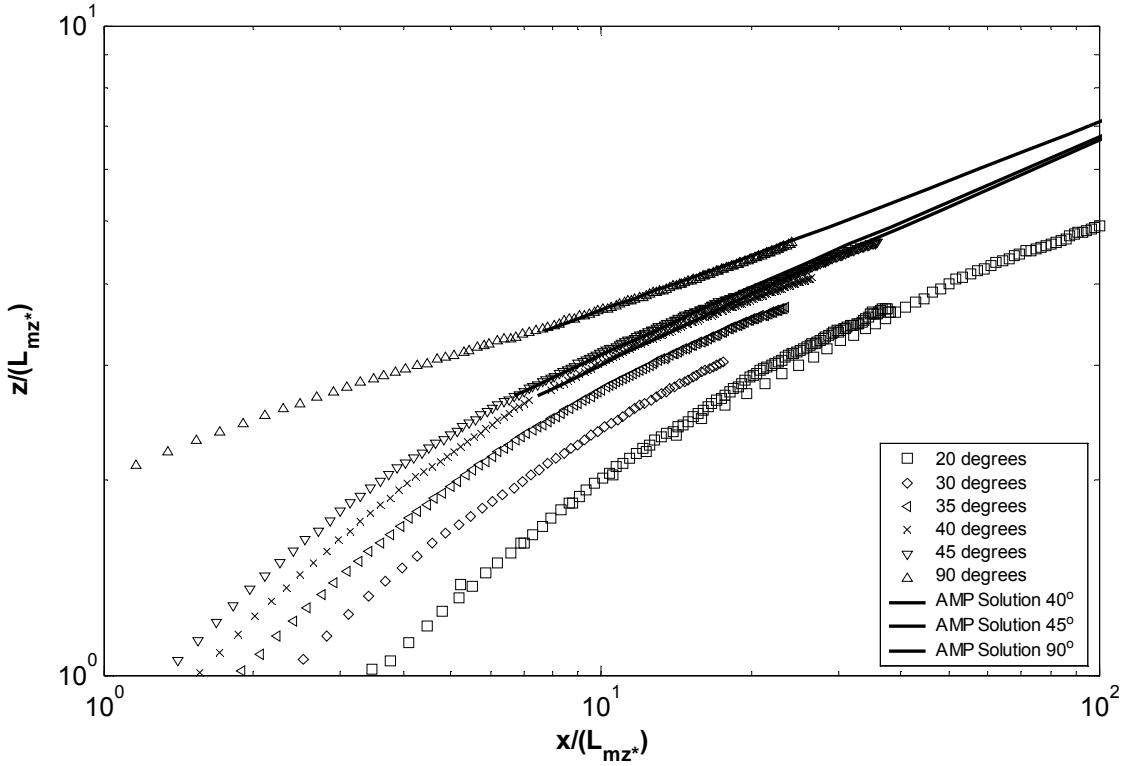

Figure 7.3 - Analytical solutions versus experimental trajectory data for puff region

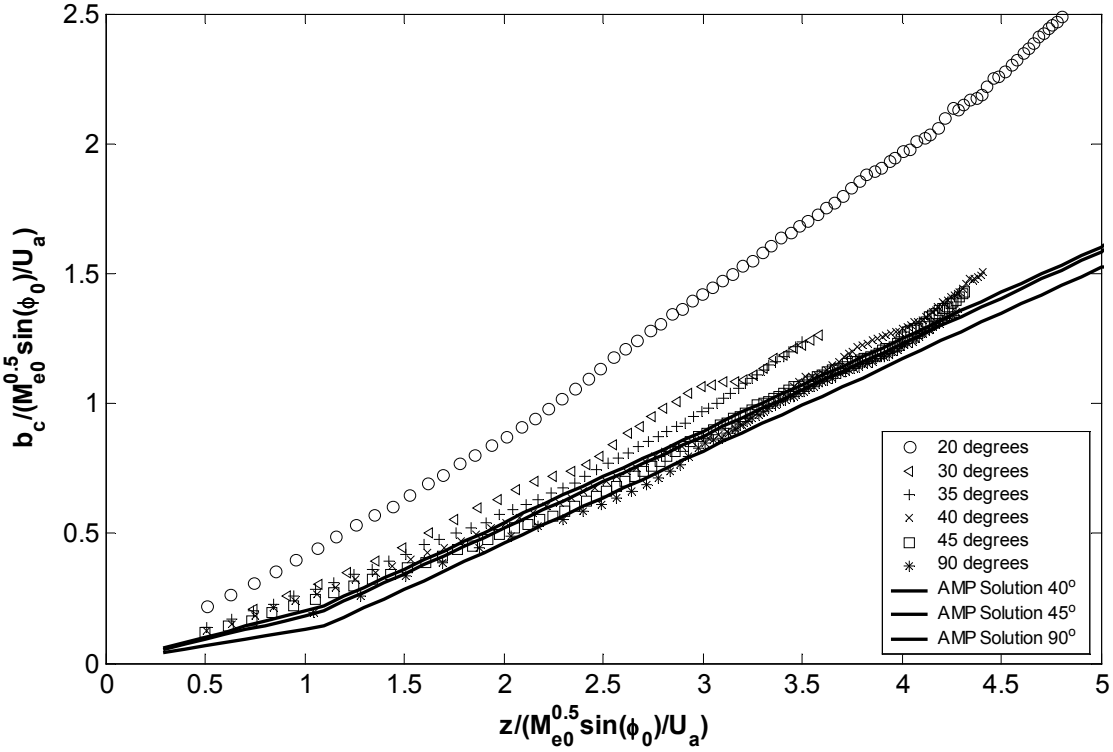

Figure 7.4 - Analytical solutions versus experimental spread data for puff region

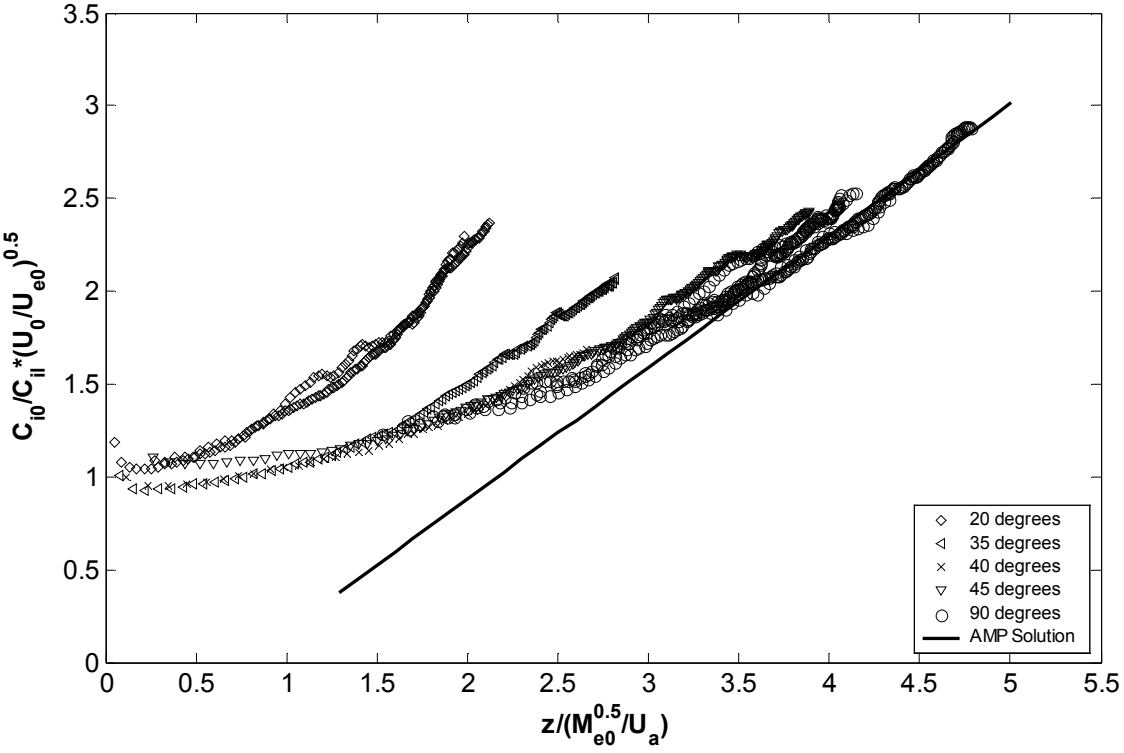

Figure 7.5 – Analytical solutions versus y-integrated centreline dilution results for puff region

Figure 7.3 indicates that the puff solutions will eventually merge to become a single line and thus are independent of the initial discharge angle in the strongly advected region. The 40°, 45° and 90° solutions are reasonable matches with the experimental data. The experimental concentration spread results for 40° and above collapse reasonably well onto the respective analytical puff solutions (Figure 7.4). The 30° and 35° concentration spread data appear to have a similar slope as the analytical puff solutions. The slope of the 20° data in the strongly advected region is significantly greater than the slope of the analytical puff solutions for the concentration spread. The 45° and 90° data collapse well onto the analytical puff solution for the *y*-integrated dilution data (Figure 7.5), and the 40° data collapses onto the 45° and 90° data. Data from the 40° run did not reach far enough downstream to be compared directly to the puff solution. The 35° data does not collapse onto the analytical solution or the 45° and 90° experimental data.

Therefore the 40° data is consistent with the analytical puff solutions for all three parameters, while the 35° integrated dilution data does not match the analytical puff solution. Thus the comparison between the analytical solutions and the experimental data indicates that for angles 40° and above, the flow in the strongly advected region is a puff. The analytical

solutions predicted that for a transition angle higher than 32° the flow in the strongly advected region becomes a puff. This is reasonably consistent with the experimental results.

7.4.2.2 – Weak-Jet Region

The analytical weak jet trajectory solutions, presented in Figure 7.6, were calculated using equation (7.5), inserting the previously discussed value for β_{wj}. As discussed above, the transition from the strong-jet to weak-jet is gradual, and therefore the flow travels a large distance within the transition zone and entrains significant amounts of ambient fluid while doing so. Thus assuming that the flow is a strong-jet up to the transition point, as determined in section 7.2.4, triggers the transition to the weak-jet region too late. The experimental data indicates that the transition point is located at approximately one third of the predicted distance for the 10°, 12°, and 15° discharges. Adopting the decreased distance to the transition point, gives ratios of entrained ambient momentum flux after the transition to that before of 3.0, 2.7 and 3.0. The present experimental trajectory data suggests that the location of the transition point for the 20° is at approximately half the predicted distance. The entrained ambient momentum flux ratio is 2.0

The weak-jet analytical concentration spread results are compared with the experimental data in Figure 7.7. Again the experimental data indicates that the transition point is approximately one third of the predicted distance. Adopting the decreased distance to the transition point, gives ratios of entrained ambient momentum flux after the transition to that before of 2.69, 2.77, 2.68 and 2.80 for the 10°, 12°, 15° and 20° discharge angles respectively. Note that this value appears to be largely independent of the initial discharge angle and they match the values found for the trajectory. The values for the y-axis intercepts become –1.0, -0.80, -0.65 and –0.45.

The weak-jet y-integrated dilution results are presented in Figure 7.8. The experimental results are compared with equation (7.10), the analytical weak jet solution. The present experimental data suggests that the transition point for the 10°, 12°, 15° and 20° weak-jet solutions are at 0.29, 0.34, 0.37, and 0.51 length-scales (approximately two thirds of the predicted distance) and therefore have y-axis intercepts of –0.25, -0.25, -0.10 and –0.10 respectively. The entrained ambient momentum flux ratios are 1.46, 1.45, 1.67 and 1.62. Again these values appear to be reasonably consistent. However they do not match the values

found for the trajectory and concentration spread. This indicates that, when assuming a point transition, the transition from the strong-jet to the weak-jet region, and therefore the virtual source, is not at the same location for all parameters. The transitions of the trajectory and concentration spread appear to occur earlier than the transition of the integrated concentration. This was also the case for the strong-jet to puff transition (see section 3.2.3.2).

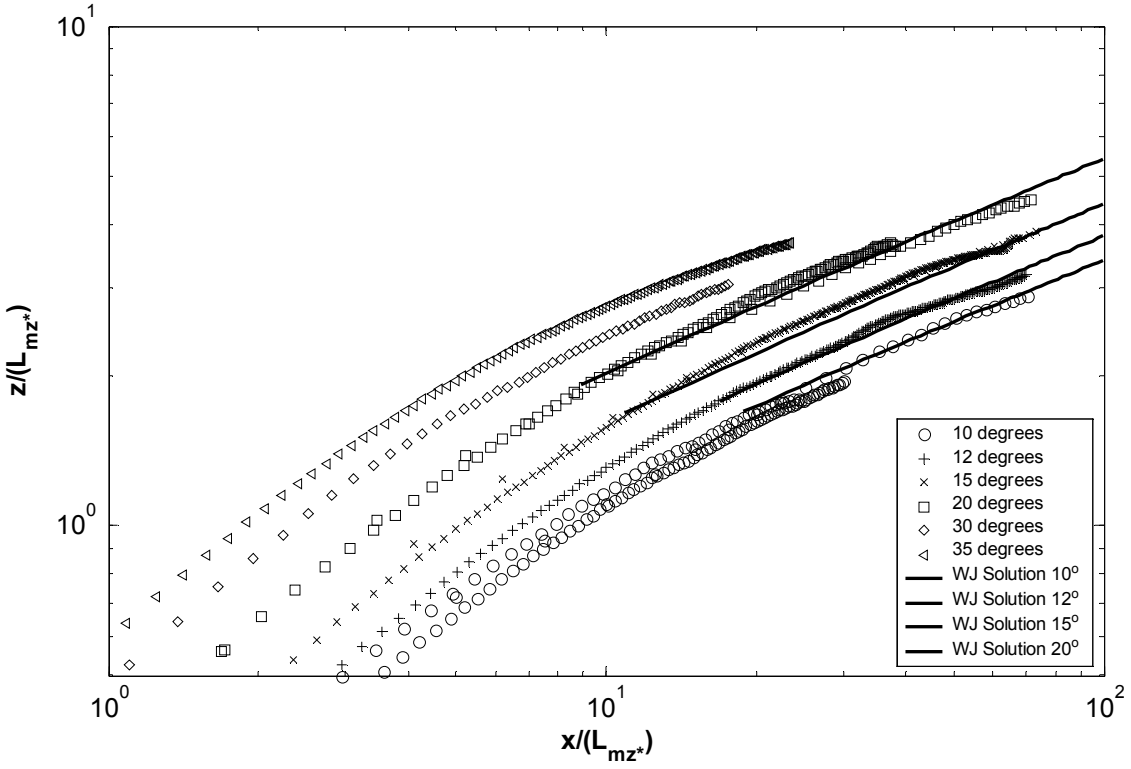

Figure 7.6 - Analytical solutions versus experimental trajectory data for weak-jet region

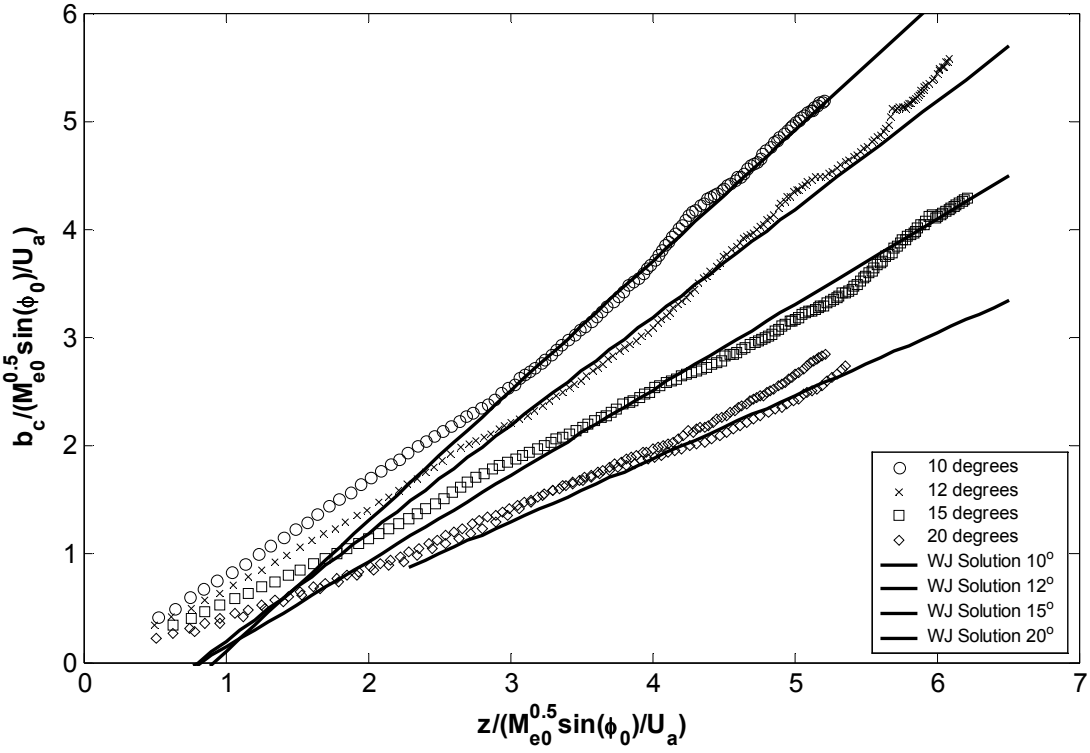

Figure 7.7 - Analytical solutions versus experimental concentration spread data for weak-jet region

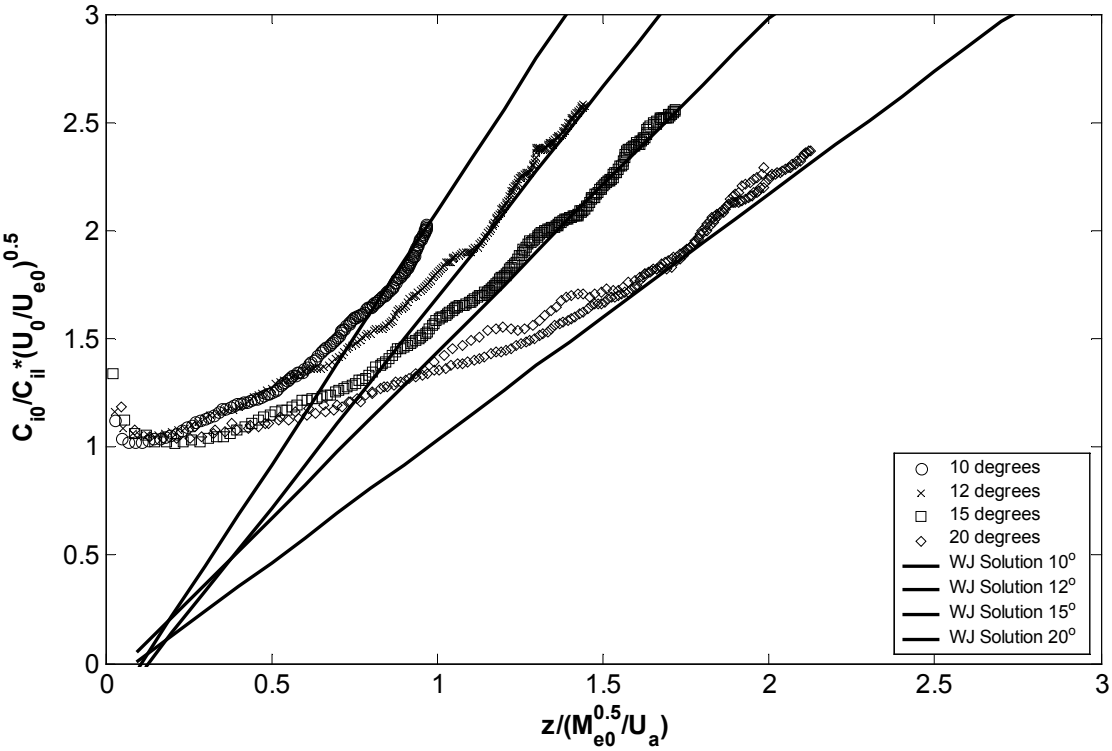

Figure 7.8 – Analytical solutions versus y-integrated centreline dilution results for weak-jet region

The trajectory results (Figure 7.6) show that the analytical solution are consistent with the experimental data of the 10°, 12°, 15° and 20° discharges. There is a good agreement between the experimental weak-jet concentration spread results and the analytical solutions for all angles between 10° and 20° (Figure 7.7), and the weak jet solutions also agree with the integrated dilution experimental data up to and including the 20° run (Figure 7.8).

Therefore up to and including the 20° angle, the experimental trajectory, concentration spread and integrated dilution results match the analytical solutions. Thus the flows with initial discharge angles of 20° or less become a weak-jet in the strongly advected region. This is consistent with the theoretical transition angle, which indicated that for initial discharge angles less than 18° the flow in the strongly advected region becomes a weak-jet.

7.4.2.3 – Transition Region between Weak-Jet and Puff Regions

The experimental results were in reasonable agreement with the theoretically determined range of flows with initial discharge angles that become puffs (≥40°) and that become weak-jets (≤20°) in the strongly advected region. Therefore it also confirmed that there is a transition region in the strongly advected region, where the flow is neither a puff nor a weak-jet. To investigate this further the experimental data from runs with initial discharge angles between 20° and 40° are compared with the analytical solutions.

The trajectory results are presented in Figure 7.9. The virtual source analysis indicates that the transition point from jet to puff occurs at approximately 0.76 L_{zm*}, 0.70 L_{zm*} and 0.58 L_{zm*} in the vertical direction for the 35°, 30° and 20° discharges respectively. The virtual source analysis makes use of the assumption that the trajectory of the flow in the weakly advected region is not affected by the ambient flow. However for lower angles this assumption is no longer appropriate. The entrainment of ambient fluid in the strong-jet region, creates a more gradual transition zone from weakly advected to strongly advected region similar to the strong-jet to weak-jet transition. This was confirmed by the data. For the 40° case, the predicted transition points gave reasonable matches between the experimental data and the puff analytical solutions. However, for the 35°, 30° and 20° cases, it was necessary to reduce the transition point to 0.57 L_{zm*} 0.35 L_{zm*} and 0.29 L_{zm*} for the analytical solution to be consistent with the experimental data. The 30° weak-jet solution employs the same location for the transition point as the 20° weak-jet solution presented in Figure 7.6.

The concentration spread results in the transition region are compared with the experimental data in Figure 7.10. The experimental data suggested entrained ambient momentum flux ratio of 7.5 and a *y*-axis intercept of –0.1 for the 30° weak-jet solution. This experimentally determined transition points does not match the values found earlier for the runs with discharge angles in the weak-jet region. The puff solution intersects the *y*-axis at approximately –0.14 and –0.11 for the 35° and 30° cases respectively.

The *y*-integrated dilution results in the transition region are presented in Figure 7.11. The transition point for the 35° weak-jet solution is located at 0.54 length-scales. This gives an entrained ambient momentum flux ratio of 2.5 at the location of the transition point. This does not match the values found for the discharges in the weak-jet region. No experimental 30° *y*-integrated dilution data was obtained in the current investigation.

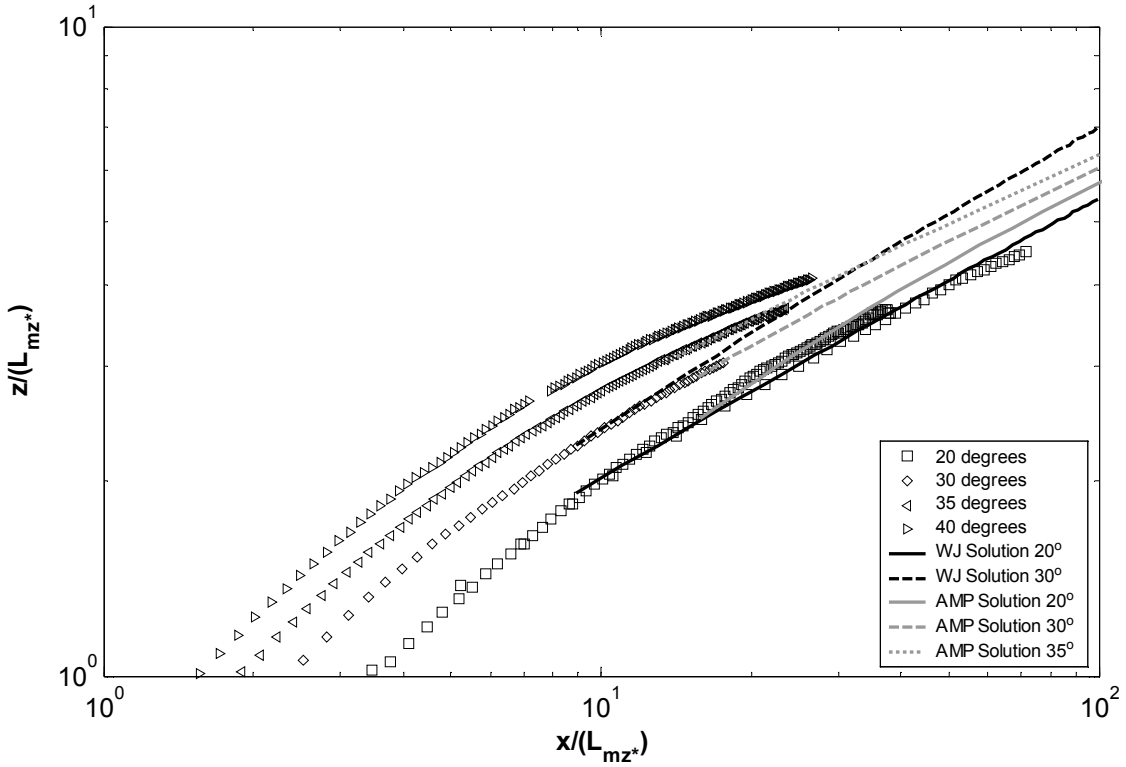

Figure 7.9 - Analytical solutions versus experimental trajectory data for transition region

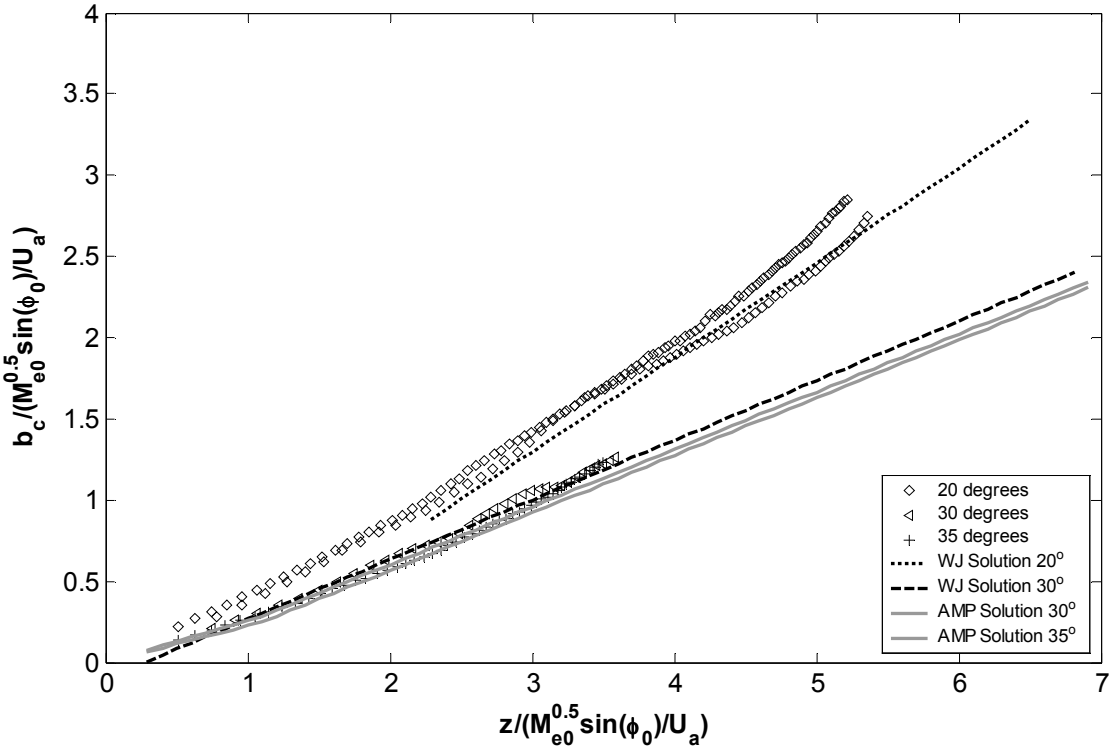

Figure 7.10 - Analytical solutions versus experimental concentration spread data for transition region

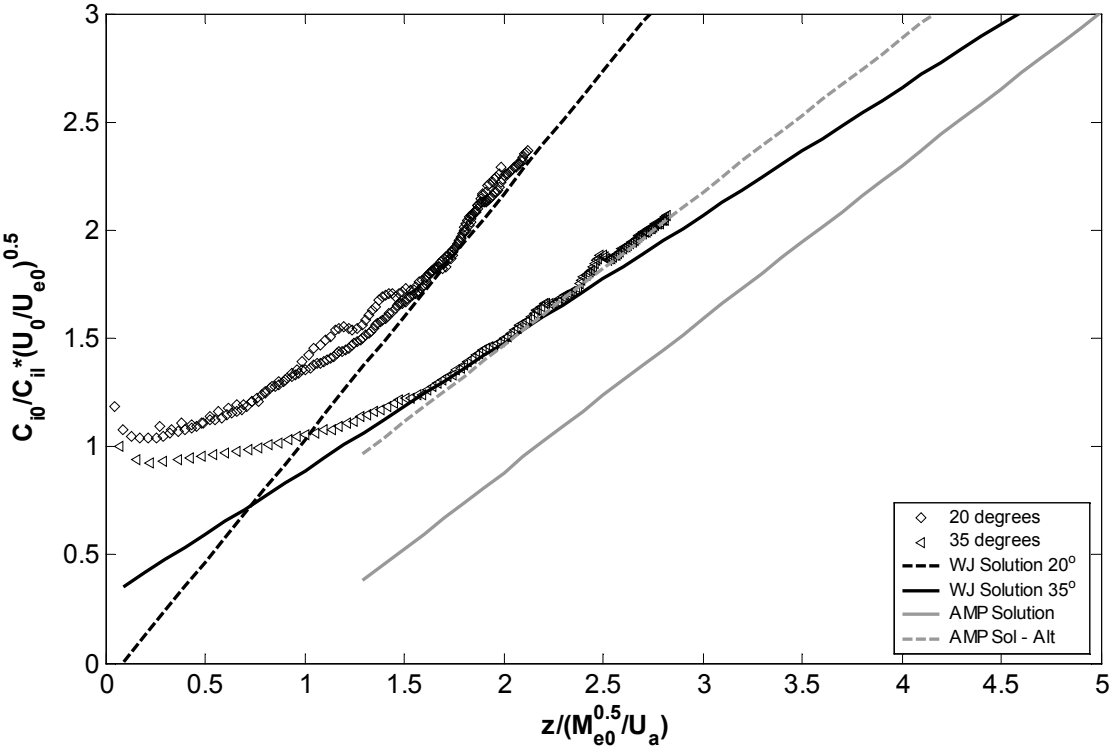

Figure 7.11 - Analytical solutions versus y-integrated centreline dilution results for transition region

Within the transition region the 30° puff solution, with the reduced distance to the location of the transition point, is more consistent with experimental data than the 30° weak-jet solution

(Figure 7.9). This is reversed for the 20° experimental trajectory data. The 30° and 35° puff solutions are consistent with the concentration spread data (Figure 7.10). The 30° weak-jet solution also matches the experimental data reasonably well, but the high entrained ambient momentum flux ratio suggests that the puff solution is more appropriate. The 35° y-integrated dilution data (Figure 7.11) is not consistent with either the 35° weak-jet solution (slope of the solution is too low) or the puff solution (transition to strongly advected behaviour occurs too late). However the puff solution appears to be parallel to the experimental data. This is confirmed by an alternative puff solution, where the distance from the source to the transition point is reduced to 1.0 transition length-scales.

Thus the results in the transition region suggest that the puff solutions match the experimental data for angles of 30° and above, if the location of the transition point is moved closer to the source. This appears to be consistent with the theoretical transition angle estimate of 32° that determines the upper limit of the transition zone.

7.4.3 – Dilution Results

The conversion from integrated to point dilution depends on the internal concentration distribution. As the internal concentration distribution differs between the regions for the weak jet and puff, the region must be determined before the proper conversion can be carried out. The comparison of the analytical solutions with the experimental data showed that the internal concentration distribution in the strongly advected region is double-Gaussian for flows with initial discharge angles of 40 and higher, and Gaussian for flows with initial discharge angles less 20 or less. For flows with initial discharge angles between 20 and 40 , it is expected that the internal concentration distribution has a combined strongly advected structure.

The double-Gaussian and Gaussian assumptions are used to convert the integrated centreline dilution into non-integrated peak dilution. The conversion equations for the puff region and the weak jet region are shown below. Note that b_c in equation (7.30) relates to the spread of the single Gaussian within the double-Gaussian assumption and is not equal to the concentration spread data shown in Figure 7.4. In Chapter 3, the y-integrated concentration spread data was designated hb_c, and the equation has been modified accordingly.

$$\frac{U_a}{U_{e0}}\frac{C_0}{C_l}=\frac{C_{i0}}{C_{il}}\left(\frac{U_0}{U_{e0}}\right)^{0.5}\pi\left(\frac{hb_c}{M_{e0}^{0.5}/U_a}\frac{1}{h}\right) \tag{7.30}$$

Relating the integrated dilution to the peak dilution gives:

$$\frac{U_a}{U_{e0}}\frac{C_0}{C_{peak}}=\frac{C_{i0}}{C_{il}}\left(\frac{U_0}{U_{e0}}\right)^{0.5}\left(\frac{hb_c}{M_{e0}^{0.5}/U_a}\frac{1}{h}\right)\left(\frac{\pi}{1-e^{-(2f)^2}}\right) \tag{7.31}$$

The point centreline dilution in the weak jet region is the peak dilution and the conversion equation is:

$$\frac{U_a}{U_{e0}}\frac{C_0}{C_{peak}}=\frac{C_{i0}}{C_{il}}\left(\frac{U_0}{U_{e0}}\right)^{0.5}\frac{\pi}{2}\frac{b_c}{M_{e0}^{0.5}/U_a} \tag{7.32}$$

The converted experimental results are compared with the model predictions in Figure 7.12. Dilution data from the Momentum Model and VisJet had to be converted from average dilution data to minimum dilution data to be consistent with the notation used in Figure 7.12. Converting the results from VisJet was straightforward as VisJet uses the same conversion factor between the average and minimum dilution in both the weak-jet and advected line momentum puff regions. However, the Momentum Model assumes different cross-sectional profiles, and therefore conversion factors, depending on the value of the transition angle. In the Momentum Model, the theoretical trajectory angle is used to define the strongly advected region. Therefore the theoretical trajectory angle is also used to indicate which conversion is applicable. All data above 25° was treated as momentum puff data, using conversion equation (4.64), and data below that angle as weak-jet data using conversion equation (4.70).

The 90° results in Figure 7.12a are consistent with the earlier results from the vertical momentum puff data. The experimental results fall between the prediction by CorJet and the Momentum Model on the one side and VisJet on the other. The fact that only the Momentum Model predicts the 45° data with reasonable accuracy indicates that the flow is in the puff region and the double-Gaussian cross-sectional profiles are still a reasonable approximation. The gradual change in cross-sectional behaviour by the other two models seems to be inappropriate at 45°. The weak-jet properties are influencing the behaviour of the flow and the dilution is being overestimated.

For the results in the weak-jet region, the models predict the flows with variable success (Figure 7.12b). Close to the source, the predictions from VisJet are a reasonable match with the 15° and 20° data, but significantly overestimate the dilution for the 10° data, while the

prediction from CorJet match the 10° data and overestimate the 15° and 20° data. Neither of the predictions from the Momentum Model match the experimental data close to the source. However, the predicted values were converted with the weak-jet conversion equation, and close to the source the strong-jet conversion equation (equation (4.58)) should be used. Figure 7.12c presents the predictions from the Momentum Model using both conversion equations. This Figure clearly shows that when using the strong-jet conversion equation the predictions from the Momentum Model do match the experimental data up to approximately 0.5 $M_{e0}^{0.5}/U_a$ in the vertical direction. The 20° data reaches sufficiently far enough downstream for the Momentum Model prediction using the weak-jet conversion equation to match up with the experimental. This, in combination with the weak-jet results presented in Chapter 5, indicates that the Momentum Model would also match the dilution for the 10° and 15° discharge angle, had the experimental data extended far enough into the weak-jet region. Further downstream the predictions from VisJet are reasonably consistent with the predictions from the Momentum Model.

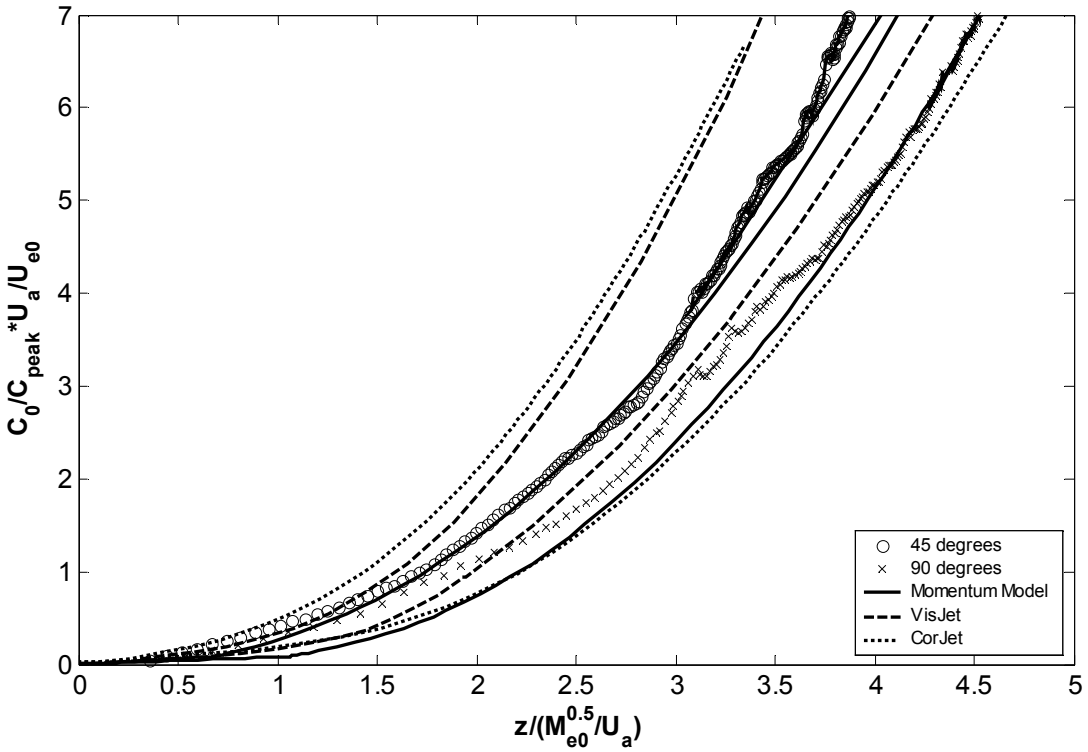

7.12(a) - Peak dilution results for flows in the puff region

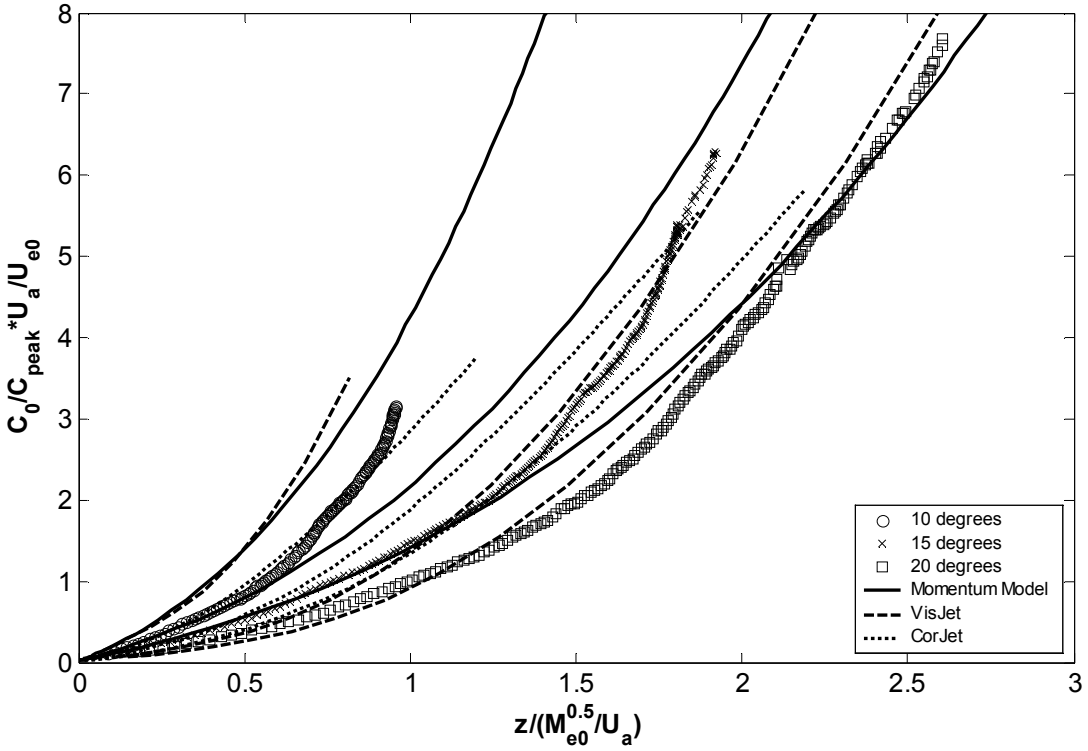

7.12(b) - Peak dilution results for flows in the weak jet region

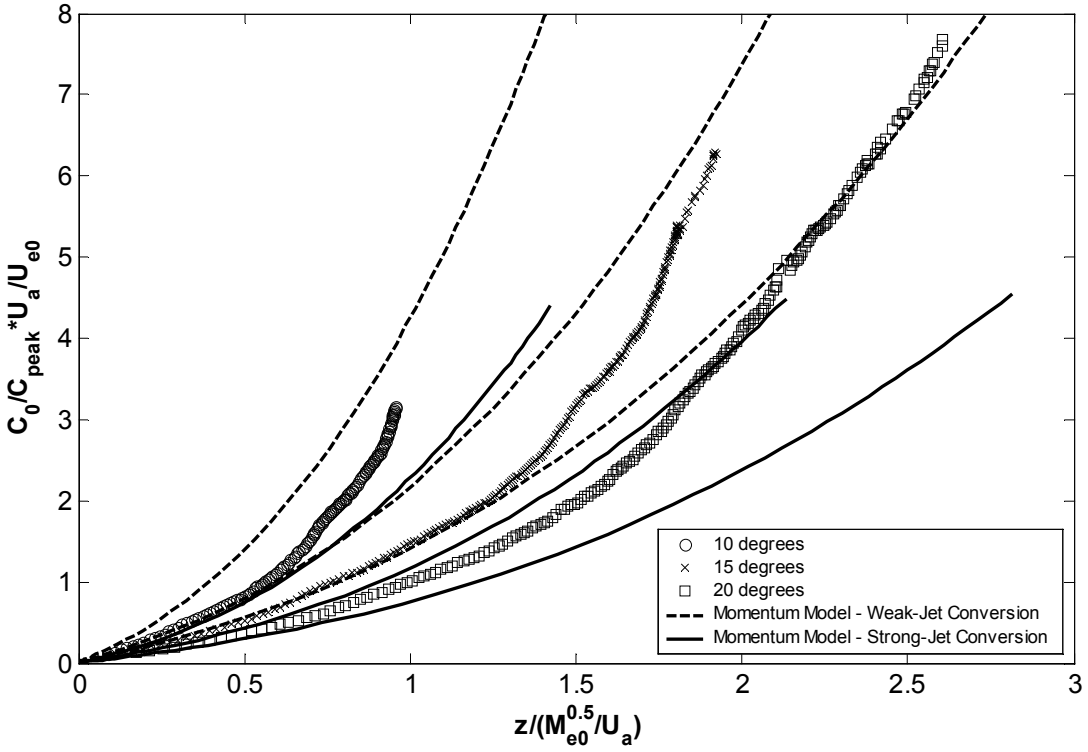

7.12(c) - Peak dilution predictions from the Momentum Model using weak-jet and strong-jet conversions

Figure 7.12 – Peak dilution results for oblique discharges in moving ambient

7.5 - Summary

An experimental investigation was carried out to study the mean behaviour of non-buoyant oblique discharges in an ambient flow. The focus of the research was the angle of discharge that determines whether the flow in the strongly advected region can be classified as a weak-jet or a puff. As an aid in the investigation, analytical solutions were presented for the trajectory, concentration spread and integrated dilution. The theoretical transition angles were determined by equating the weak-jet and puff solutions. The trajectory solutions predicted an angle of 18.0° for the transition. The theoretical transition angle, determined from the concentration spread and the integrated dilution solution, was 31.5°.

Comparison of the experimental data with previous experimental investigations showed that the current results match the previous results. The analytical solutions for the trajectory, concentration spread and the integrated dilution were compared with the experimental data. The experimental data confirmed that for initial discharge angles of 40° and above, the flow is a puff in the strongly advected region, and for initial discharge angles of 20° and less, the flow is a weak-jet in the strongly advected region. The comparison between the analytical solutions and the experimental data also confirmed the existence of a transition region between the strongly advected weak-jet and puff regions for initial discharge angles between 20° and 40°. Within this region the cross-sectional profiles are expected to have a combined strongly advected structure.

The performances of VisJet, CorJet, and the Momentum Model were compared with the results of the experiments. VisJet and CorJet assume a gradual transition between the horizontally discharged weak-jet and vertically discharged puff, while the Momentum Model assumes a Gaussian cross-sectional profile in the strongly advected region up to the transition angle and a double-Gaussian cross-sectional profile for angles above the transition angle. The effect the different assumptions had on the accuracy of the predictions of the weak-jet region was not clearly evident in the trajectory and dilution results. All three models predicted the trajectory for angles up to and including 30° with reasonable accuracy, and the dilution predictions from the Momentum Model and VisJet were similar for lower angles and matched the experimental data reasonably well. However the effect of the different assumptions was more clearly evident in the puff region. The Momentum Model predictions matched several experimental trajectory datasets significantly better than the VisJet and CorJet predictions.

The gradual transition between the horizontally discharged weak-jet and vertically discharged puff appears to underestimate the distance travelled in the z-direction for the flows in the puff region. The dilution results presented similar results. Only the Momentum Model prediction at 45° was consistent with the experimental data, again indicating that the gradual transition is not appropriate in the puff region.

Chapter 8 – Buoyant Jets with Three-Dimensional Trajectories

8.1 - Introduction

Chapters 5, 6 and 7 focussed on discharges with two-dimensional trajectories. However the majority of discharges in the environment are buoyant flows released into a moving ambient, whose direction changes with time. It is important therefore to have the ability to model such buoyant flow behaviour for a wide variety of discharge angles relative to the ambient motion. For the most part these angles are such that the path of the flow is three-dimensional.

Previous studies suggest that a buoyant jet flow can be divided into distinct flow regions (Jirka 2004; Pun 1998). In each of these regions the flow is dominated by a group of independent flow parameters, and the overall flow behaviour can therefore be described by a sequence of these distinct flow regions (see Chapter 4). As the distinct flow regions are the same for buoyant jet flows with two-dimensional and three-dimensional paths, it is assumed that models based on this approach can predict with reasonable accuracy the behaviour of discharges with three-dimensional paths

Currently available numerical models are based on this philosophy and have been verified with experimental data for buoyant jet flows with two-dimensional paths. However even here there are regions where the models do not perform well and Chapters 6 and 7 provide evidence of this. Chapter 6 highlights the fact that these models neglect an important physical process, which results in significant errors in the dilution and trajectory predictions of negatively buoyant jets. Chapter 7 shows the need for the models to incorporate an appropriate entrainment or spread function to match the strongly advected behaviour of obliquely discharged non-buoyant jets in a moving ambient.

As indicated in Chapter 2, reasonably few experimental studies have focused on flows with three-dimensional paths. This is an indication of the difficulty that arises when trying to obtain high quality data from experiments involving buoyant jets with these paths. However, there is some experimental evidence to support the approach taken by the numerical models. Predictions from CorJet (Jirka 2004) were compared with data from Ayoub (1971) and shown to be a reasonable match. Cheung (1991) compared the predictions from VisJet with his own

data and again the model predictions were reasonably consistent with the experimental data. However due to the measurement techniques used during these experimental investigations, a limited amount of data was obtained per experiment (a maximum of six data-points per experiment by Ayoub and four by Cheung), and therefore the coverage of flow regions was limited. Finally the experimental discharge configuration used during the respective experimental investigations was the horizontally discharged buoyant jet in a cross-flow. To the author's knowledge, no other discharge configuration creating three-dimensional paths has been investigated in any detail.

Buoyant jets with three-dimensional trajectories are practically significant flows and it is important to ensure that the above approach remains valid under the circumstances specific to this type of discharge. This chapter describes an experimental investigation into the behaviour of buoyant jets that follow a three-dimensional path. The experimental investigation consisted of five experiments with distinct discharge configurations. The experimental design and analysis are discussed in detail for each experiment. The results are compared with the existing outfall models, where differences are noted and discussed.

8.2 – Flow Configurations

The 3D LA system was employed to record all five experiments. Accurate trajectory results from all five runs were most important, because these could be compared directly with the model predictions. However, a complete calibration was carried out for each experiment as the integrated dilution results would provide information about the internal concentration distribution; even if the point dilution could not be accurately determined, because the internal concentration distribution could not be effectively characterized. For a detailed discussion of the 3D LA system, see section 3.2.4. The coordinate system and corresponding notation for the initial conditions, as defined in Chapter 4 for the Momentum Model, are used for these experiments. The initial conditions of the buoyant jet runs with three-dimensional trajectories are shown in Appendix D, Table D.11.

The density difference between the ambient fluid and the source fluid was kept constant at approximately 2.0% and the diameter of the source was 2.43 millimetres. In order to study the flow through the different regions of behaviour, the ratio of ambient velocity to initial velocity was sufficiently low so that a strongly advected flow did not form immediately after

leaving the source, but this ratio also had to be high enough so that the flow was firmly established in the final flow region by the time the experiment finished.

For the first experiment the source was placed horizontally and perpendicular to the direction of the ambient flow, pointing away from the camera that was located on the side of the tank (see Figure 3.45). This is the most common discharge used when investigating buoyant jets with a three-dimensional trajectory (Ayoub 1971; Cheung 1991). The velocity ratio was 0.038, the Reynolds number was 3400 and the Froude number was 64.8. Before the experiment the initial calibration length-scale at the source was determined for both the y and z-directions. After the experiment the final calibration length-scales were determined using the process as explained in section 3.2.1.2. For the y-direction the initial and final calibration length-scales were 0.465 mm/pixel and 0.489 mm/pixel and for the z-direction 0.492 mm/pixel and 0.517 mm/pixel. The difference between length-scales in a particular direction is approximately 5%. By taking an average length-scale the error could be reduced to 2.5%. However with this approach the maximum error occurred at both the beginning and the end of the experiment, and therefore the location of the source was not known precisely. As the analysis of the rest of the experiment is referenced back to the source location (as it is the only fixed point in the flow), averaging the calibration length-scale was not the preferred option. Instead the experiment was analysed using both length-scales, taking into account the linear relationship between distance and calibration length-scale. Because the calibration length-scale in the x-y plane depended on the distance travelled in the z-direction and the calibration length-scale in the x-z plane depended on the distance travelled in the y-direction, an iterative scheme was needed to determine the actual trajectory path. The error in the final results was $<<1\%$.

Two more experiments were carried out with the source fluid discharged horizontally into the ambient. These configurations were chosen because most rosette diffuser systems discharge effluent horizontally into the ambient at some oblique angle to it. In comparison with the first experiment, the source was rotated horizontally by 45° in the direction of the ambient flow for the second experiment. The velocity ratio was 0.031, the Reynolds number 4100 and the Froude number 77.5. The calibration length-scales in the y-direction were 0.468 mm/pixel and 0.491 mm/pixel, and 0.492 mm/pixel and 0.511 mm/pixel in the z-direction. For the third experiment, the source was rotated horizontally by 45° against the direction of the ambient flow, with respect to the first experiment. For the third experiment the velocity ratio, Reynolds number and Froude number were 0.031, 4075 and 77.0 respectively. The calibration

length-scales were for the *y*-direction 0.468 and 0.492 mm/pixel and for the *z*-direction 0.494 and 0.527 mm/pixel.

The last two experiments were effectively a continuation of the work on negatively buoyant jets discussed in Chapter 6. The source configurations were similar, however where the previous negatively buoyant jet experiments were conducted in a stagnant ambient, the new experiments were discharged in a moving ambient. To tie the results in with the previously described experiments the negatively buoyant fluid was discharged at 45 and 60 to the horizontal, but both discharges were perpendicular to the ambient motion. The velocity ratio, Reynolds number and Froude number were 0.0031, 4100 and 77.0 for both experiments. Given the vertical discharge direction of runs 4 and 5 was opposite to that of the buoyancy force, the direction of flow changed vertically during the experiment. Therefore the initial vertical calibration length-scale was no longer an outermost length-scale. Because the initial calibration length-scale was still needed in the analysis to locate the source, and was a reasonable average length-scale for the entire flow, only the initial calibration length scale was used during the analysis (0.527mm/pixel and 0.524 mm/pixel for runs 6 and 7 respectively). The maximum error due to the calibration length scale in the final results was approximately 2.8% at the point of maximum height. The calibration length-scales in the *y*-direction for run 6 were 0.466 mm/pixel and 0.486 mm/pixel and for run 7 they were 0.467 mm/pixel and 0.480 mm/pixel.

8.3 - Experimental Results and Model Predictions

8.3.1 – Cross-Sectional Behaviour

The final region for the buoyant jet released in a moving ambient with a two-dimensional trajectory is the advected thermal region. Depending on the relative sizes of the buoyancy-generated momentum flux and the entrained ambient momentum flux, the initial strong jet either becomes an advected plume or advected line momentum puff before reaching the advected thermal region. In the strong jet and advected plume regions, the cross-sectional concentration profiles are Gaussian. In the advected line momentum puff and in the advected thermal regions the cross-sectional concentration profiles resemble that of a vortex pair. The double-Gaussian assumption has been used successfully in the present study to approximate this structure (see section 3.2.3.2).

Length-scale theory (Pun 1998) is used to approximately determine where the transition occurs between the various flow regions. The transitions that are initially of particular importance are the transitions from jet to plume (equation 8.1) and jet to momentum puff (equation 8.2).

$$l_{jp} = 2.3\frac{M_{e0}^{3/4}}{\left(Q_{\Delta 0}\right)^{1/2}} = 2.3\left(\frac{\pi}{4}\right)^{1/4} Fr_0 d \tag{8.1}$$

$$l_{jm} = \frac{M_{e0}^{1/2}}{U_a}\sin\phi_0 \tag{8.2}$$

For all runs in the present study, the length-scale from jet to puff is smaller than the length-scale from jet to plume. Therefore the length-scale theory predicts that the flows after the first transition are in the advected line momentum puff region. In this region double-peak integrated cross-sectional concentration profiles are expected to be visible, and the axis of symmetry of the double-peak is parallel to the projection of the initial excess momentum flux in the *y*-*z* plane. In the momentum puff region, the momentum puff to thermal transition length-scale (equation 8.3) indicates when the flow enters the advected thermal region. Again the integrated cross-sectional concentration profiles are expected to show a double-peak structure, with the axis of symmetry in the vertical direction.

$$l_{mt} = 1.35\left(\frac{M_{e0}\left|\sin\phi_0\right|^2}{Q_{\Delta 0}U_a}\right)^{1/3} \tag{8.3}$$

Integrated cross-sectional concentration profiles are used to provide insights into the flow form at particular locations. Figure 8.1 shows the *y*-integrated and *z*-integrated cross-sectional profiles of run 1. Note that x^* is the horizontal distance non-dimensionalised by $Q_0\Delta_0/U_a^3$, the plume to thermal transition length scale. Profiles closer than $x^* = 27.8$ from the source have been omitted from the figure because the assumption that the cross-sections are perpendicular to the camera view is not reasonable.

The ratio of the component of the distance travelled in the direction of the initial discharge, which is perpendicular to the ambient flow, divided by the transition length-scale is used to determine the flow region. For runs 1 to 3 this distance is that travelled in the *y*-direction. According to the length-scale theory, the transition from jet to puff for run 1 occurs before the first cross-sectional profile shown in Figure 8.1. To determine the precise location of the transition to the advected thermal region the location of the puff virtual source should be known. However conservatively assuming that the puff virtual source is at the jet to puff

transition, indicates that the transition from puff to thermal occurs near the first cross-sectional profile. It can therefore be said with confidence that at the first cross-sectional profile, the flow is either in the transition zone from puff to thermal or in the advected thermal region itself.

In Figure 8.1a, the *y*-integrated cross-sectional concentration profiles, a double-peak distribution is not visible at any distance downstream. The cross-sectional profiles closest to the source do however show a significant distortion when compared to the single-Gaussian, but this reduces with increasing distance. These profiles are consistent with the puff to thermal transition taking place in the vicinity of the first cross-sectional profile.

It should be noted that C_{il} in Figure 8.1b, the *z*-integrated cross-sectional concentration profiles, is the integrated centreline concentration of the single Gaussian (see section 3.2.3.2). A Gaussian profile would therefore have a value of 2 at the centreline. In Figure 8.1b, none of the profiles is consistent with the single-Gaussian, and the creation of the double-vortex pair is clearly visible. Therefore the advected thermal dominates the flow in the strongly advected region and that is consistent with length-scale theory. However the peaks travel further apart than was expected, based on the investigation of the advected line momentum puff with a two-dimensional trajectory (section 3.2.3.2). The non-dimensional distance between one of the peaks and the centreline of the cross-section (*f*) had a value of 0.88 in Chapter 3. Figure 8.2 shows *f* as functions of distance in the *y* and *z* directions and verifies that the values for *f* in the cross-sections increased beyond 0.88. From the current data it is unclear whether the value for *f* reaches a maximum value, or if the peaks continue to travel apart until they are separate flows. It is unclear how the advected-thermal region as part of a flow with a three-dimensional path compares with the advected-thermal region as part of a flow with a two-dimensional path. However a higher value for *f* in the advected-thermal region compared to the value for *f* in the puff region seems to match the results in section 5.3.2.2, that showed an increase in spreading rate in the advected thermal region compared to the puff region, but a constant *y*-integrated concentration spread.

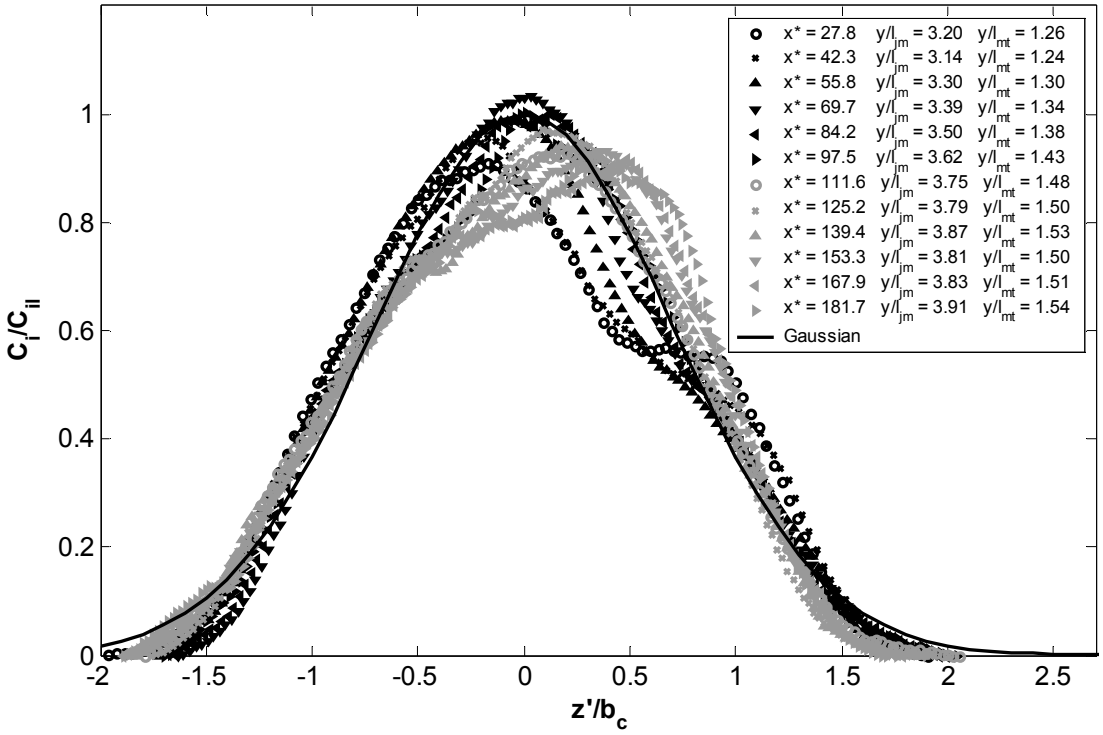

8.1(a) – *y*-integrated concentration profiles

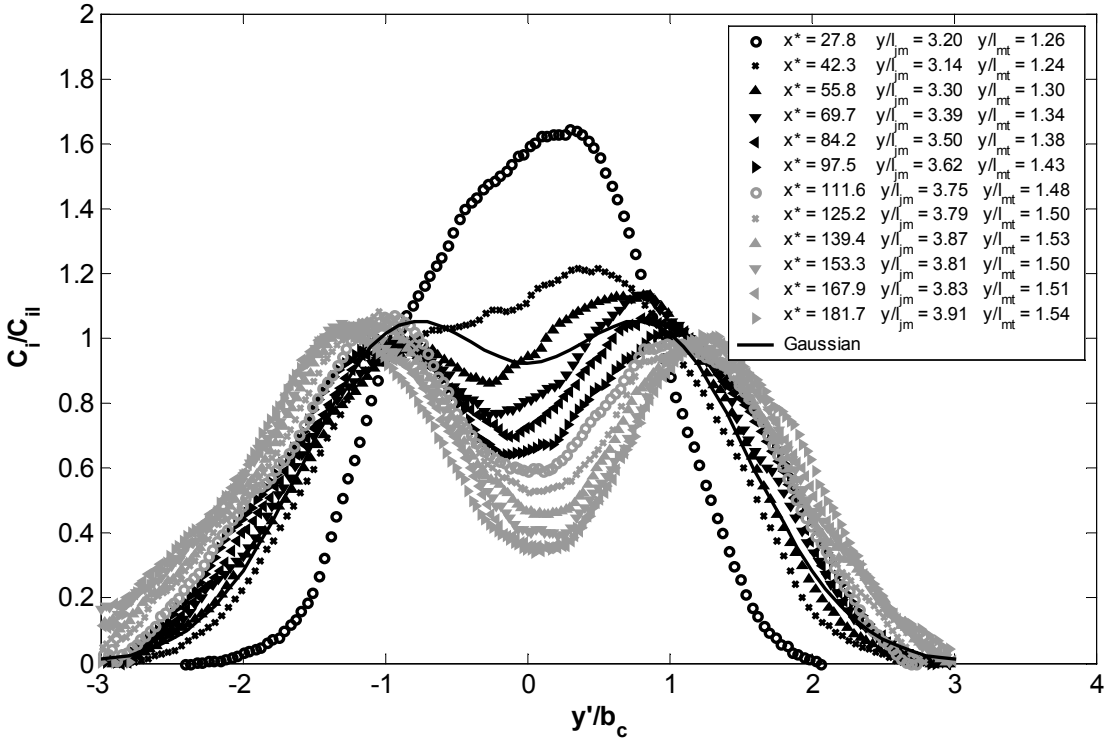

8.1(b) – *z*-integrated concentration profiles

Figure 8.1 – Integrated cross-sectional concentration profiles run 1

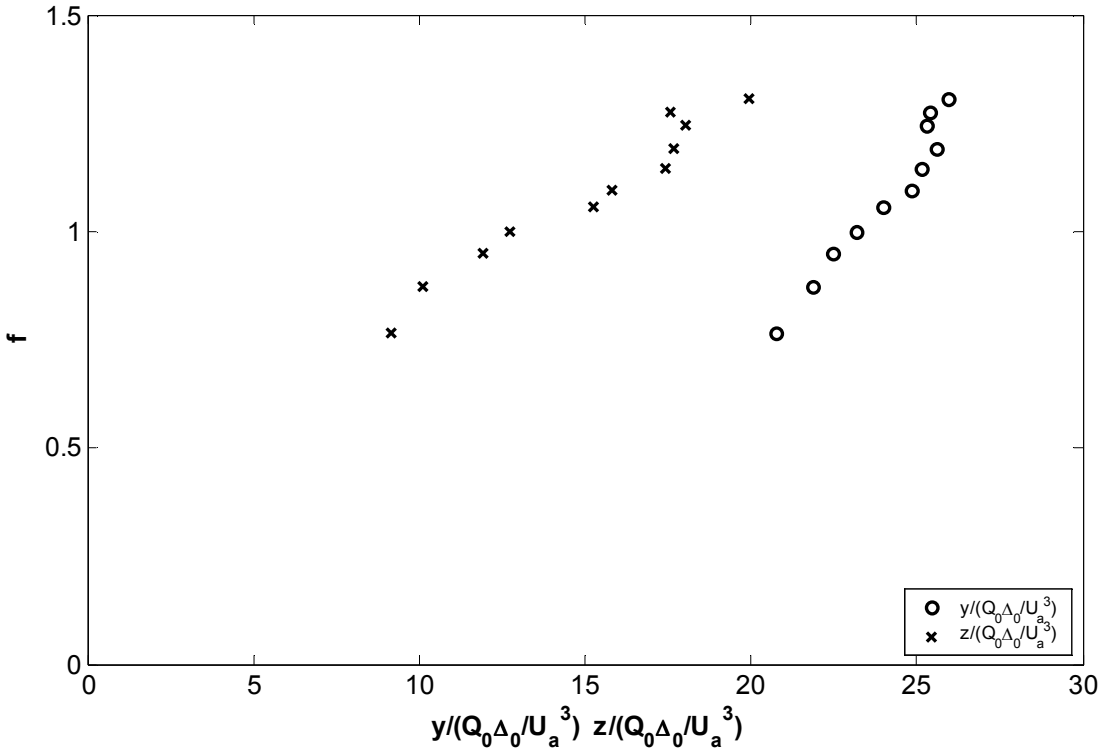

Figure 8.2 - Values for *f* as a function of the distance in the *y* and *z* directions

As indicated, current modelling techniques are based on the assumption that a buoyant jet released in a moving ambient with a three-dimensional trajectory behaves in a similar way to their counterparts with two-dimensional paths, including the cross-sectional structures of the flow. For the flows with a low initial discharge angle this appears to be a reasonable assumption, however for flows with high initial discharge angles there is an important inconsistency. The dominant parameters that cause the vortex pair to be generated in the advected line momentum puff region are U_a and M_{e0}. The vortex-pair is generated in the plane perpendicular to the direction of the ambient flow; with the axis of symmetry of the vortex pair in the direction of the initial excess momentum flux component projected in the *y*-*z* plane. In the advected thermal region the flow is dominated by U_a and M_b and thus in the advected thermal region the axis of symmetry of the vortex-pair is vertical (in the *z*-direction). In the case of a flow with a 2-D trajectory the component of the initial excess momentum flux creating the puff is acting in the vertical direction, and is therefore acting in the same (or opposite) direction as the buoyancy-generated momentum flux. Therefore, no change in the structure of the cross-sectional concentration profiles occurs when the flow changes from an advected line momentum puff to an advected thermal. In the case of a flow with a 3-D trajectory, M_{e0} may act in any direction but the vertical, and therefore does no longer act in the same direction as M_b, creating a discontinuity in the assumed cross-sectional profiles at

the point of transition between these two strongly advected regions. One extreme case is the buoyant jet discharged horizontally and perpendicular to the direction of the ambient flow. The axis of symmetry is expected to be horizontal in the advected line momentum puff region and vertical in the advected thermal region.

The horizontally discharged buoyant jet in a cross-flow experiments by Cheung (1991) were carried out in a flume. The source was at a fixed location and a LIF system was used to obtain non-integrated concentration profiles at cross-sections in the plane perpendicular to the ambient flow. Four cross-sectional concentration profiles were obtained per flow configuration. Based on a length-scale analysis, the initial conditions for all flows indicated that after the first transition the flows became puffs (see Table 8.1, columns 2 and 3). At the first cross-sectional profile all flows had passed this transition point. The theoretical advected thermal transition point was reached by some of the flows before the final cross-sectional profile. The contour plots show a range of different behaviour for the various flows (columns 6). As part of the current investigation the flows are grouped using the ratio of the puff to thermal transition over the jet to puff transition (columns 5). For low ratios (relatively small puff regions), the cross-sectional profiles show definite thermal behaviour with a vertical axis of symmetry for the vortex-pair. With increasing ratios (increasing relative scale of puff regions) the axis of symmetry of the vortex-pair is no longer vertical for the first cross-sectional profile, and rotates towards the vertical in the subsequent cross-sectional images. When the length-scale ratio is increased further the axis of symmetry of the vortex-pair is horizontal in the first cross-sectional profile. The axis rotates towards the vertical further downstream, having an angle of approximately 45° in the final cross-sectional profile. For the flows with the highest length-scale ratios there is no sign in the cross-sectional profiles of the vortex-pair in the first cross-section. The profiles appear to be distorted towards the double-peak structure at the final cross-section, but for a number of flows there is still no indication of the vortex-pair at the end of the experiment. Note that all these flows, at all of the cross-sections, were expected to be strongly advected. And thus the cross-sectional profiles that had a single peak do not match the current theory.

Table 8.1 – Length-scale analysis and observation from buoyant jet in cross-flow experiments, Cheung (1991)

Experiment	l_{jp}	l_{jm}	L_{mt}	L_{mt}/l_{jm}	Visual Observations
H 12-2	0.390	0.026	0.123	4.680	Single peak throughout
H 8-2	0.261	0.026	0.094	3.558	Single peak throughout
H 6-2	0.260	0.036	0.104	2.923	Single peak, but breaking up further downstream
H 16-4	0.522	0.053	0.189	3.561	As H12-6 and H 16-6, but double peak not as apparent
H 12-4	0.390	0.053	0.156	2.928	As H12-6 and H 16-6, but double peak not as apparent
H 16-6	0.519	0.080	0.215	2.704	Double peak in puff region transforming to double peak in thermal region
H 12-6	0.390	0.080	0.178	2.235	Double peak in puff region transforming to double peak in thermal region
H 8-4	0.259	0.054	0.119	2.211	As H4-2, H4-4 and H6-4 but double peak not as obvious
H 4-2	0.173	0.036	0.079	2.217	Double peak already in transition to thermal region
H 6-4	0.258	0.072	0.131	1.817	Double peak already in transition to thermal region
H 4-4	0.173	0.071	0.099	1.405	Double peak already in transition to thermal region
H 2-2	0.087	0.036	0.050	1.398	Double peak in thermal region

The ratio of puff to thermal transition over the jet to puff transition for the current buoyant jet in a cross-flow experiment was 2.54. The establishment of the double-peak in the *z*-integrated profiles is therefore consistent with the observations from Cheung's experiments.

Figure 8.3 shows the integrated cross-sectional concentration profiles of run 2. Given the initial discharge angle between the direction of the initial excess momentum flux and the ambient flow was more than 40°, the flow was expected to become an advected line momentum puff before reaching the advected thermal region (see Chapter 7). The initial excess momentum flux of run 2 was higher than the flux of run 1; however because of the initial discharge angle, the component of the initial momentum flux perpendicular to the cross-flow is significantly reduced. Therefore the ratio of puff to thermal transition length over the jet to puff transition length was 2.81, which is similar to the ratio of run 1, and the flow structure was therefore expected to change in a similar way to run 1. Figure 8.3 shows that in neither direction is there is a definite sign of a double-peak. The *y*-integrated concentration profiles match the Gaussian profile reasonably well, and although the match for the *z*-integrated concentration is not as good, there is still only a single peak. However the profiles from a horizontal distance of $x^* = 113$ onwards show behaviour distinct from the

single Gaussian, and possibly indicate the initial stages of the creation of a double-peak structure. This type of strongly advected cross-sectional behaviour is more consistent with the expectations of the weak-jet region prior to the formation of the advected thermal region, because the cross-sectional profiles in the weak-jet region have been shown to fit the Gaussian shape well (Wang 2000b). One possibility is that the initial transition angle between the weak-jet and advected line momentum puff regions is higher for a flow with a three-dimensional trajectory than was deduced from the study of the initial transition angle in Chapter 7. However a second possibility is that the flow does not reach the strongly advected region until the end of the experiment. In that case the flow would be in the advected plume region where the cross-sectional profiles also match the Gaussian shape (see Chapter 5).

The above visual observations are strengthened by the integrated cross-sectional concentration profiles from run 3. The only difference in the initial conditions was the direction of the component of the initial excess momentum flux parallel to the ambient flow. This switches signs from run 2 to run 3. The expectations therefore were similar to those as for run 2. The theoretical transition from jet to puff was expected to occur $y/l_{jm} \sim 1$, and this corresponds to $x^* = -4$ from the source in the horizontal direction. Again the y-integrated concentration profiles fit the Gaussian shape reasonably, and no double-peak is evident initially in the strongly advected region for the z-integrated concentration profiles. However a definite double-peak structure has started to form at the profile $x^* = 101.5$ from the source, indicating that the flow has reached the transition to the advected thermal region.

There is currently no explanation for the concentration profiles with a single peak for the horizontally discharged buoyant jet in a cross-flow evident in Cheung's results. The same issue is clearly evident for the oblique runs (2 and 3) in the present study. What is however very clear is that the sequence of flow behaviour evident for discharges with two-dimensional paths cannot be simply transferred to the equivalent three-dimensional counterpart.

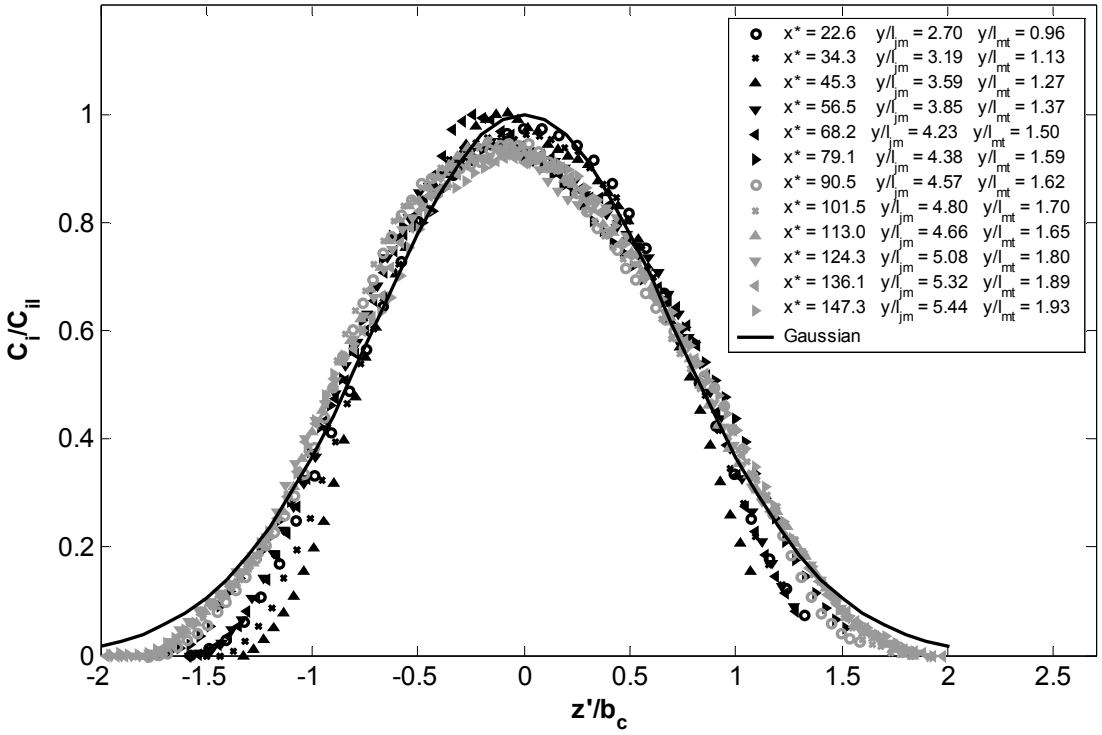

8.3(a) – *y*-integrated concentration profiles

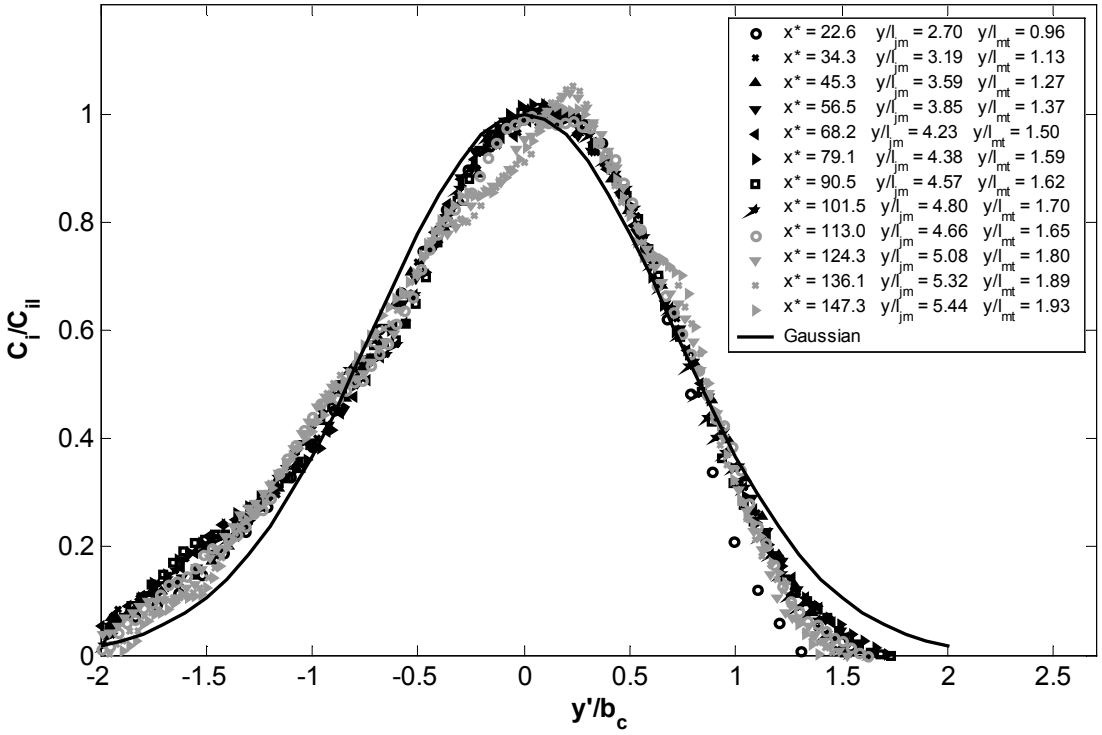

8.3(b) – *z*-integrated concentration profiles

Figure 8.3 – Integrated cross-sectional concentration profiles run 2

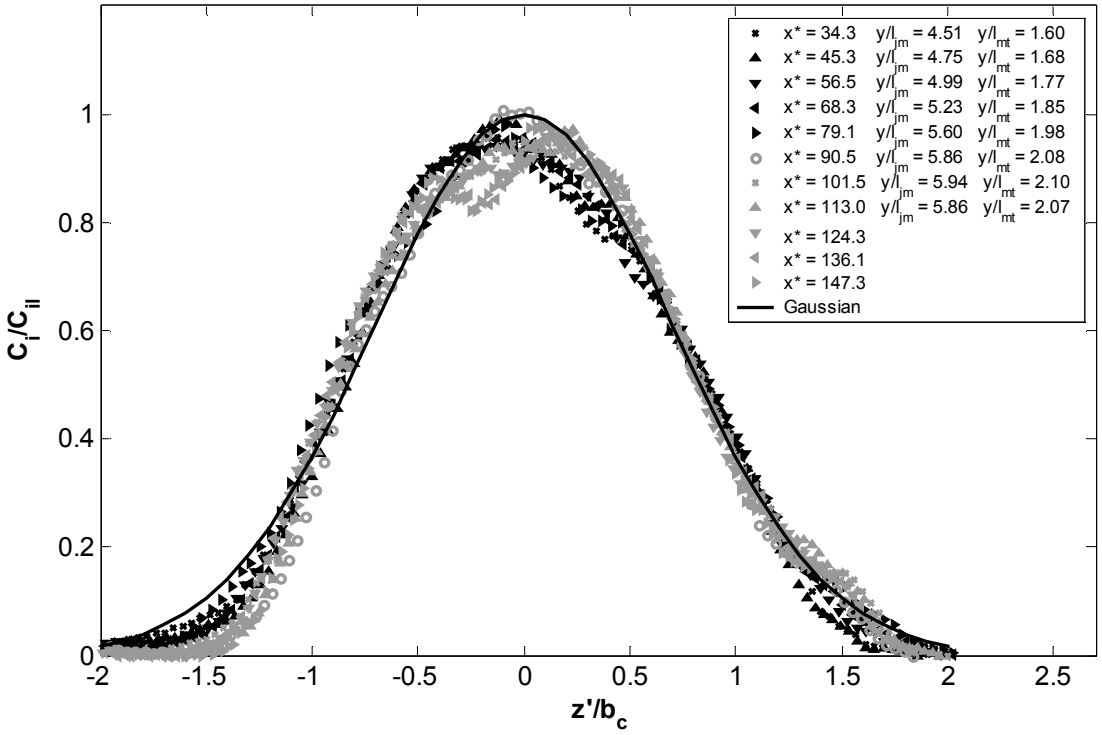

8.4(a) – *y*-integrated concentration profiles

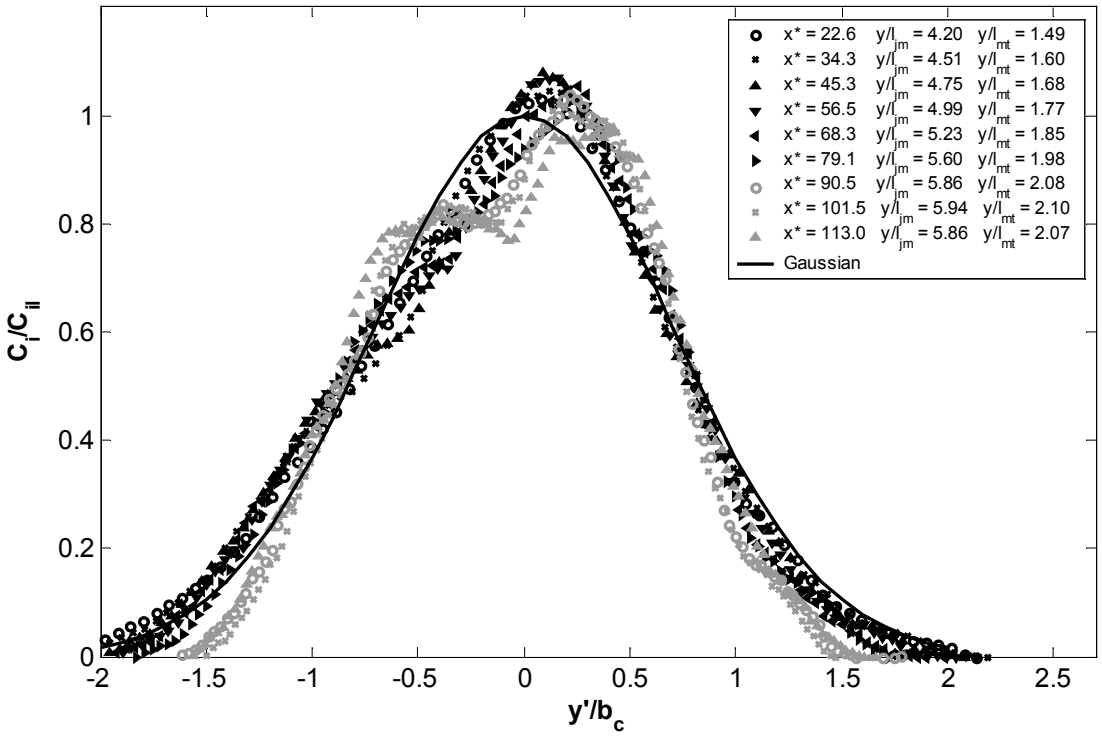

8.4(b) – *z*-integrated concentration profiles

Figure 8.4 - Integrated cross-sectional concentration profiles run 3

For runs 4 and 5, the component of the distance travelled in the direction of the initial discharge that is perpendicular to the ambient is equal to the distance travelled along the projection of the direction of the initial discharge in the *y*-*z* plane (s_{yz}). Because the buoyancy-generated momentum flux acts in the opposite direction to the vertical component of the initial excess momentum flux, the flow changes direction along the s_{yz}-axis. To take this change in direction into account, the cumulative distance travelled along the s_{yz}-axis is used to calculate the ratio of s_{yz} over the transition length-scale.

Again the transition from the jet to the puff region was expected to occur before the first cross-sectional profile. However according to the length-scale theory, the puff to thermal transition was not expected to take place immediately after the jet to puff transition. Therefore double peak puff behaviour was expected to be visible in the *y*-integrated direction. The *y*-integrated plots (Figure 8.5a and Figure 8.6a) show that the cross-sectional profiles are reasonably consistent with the Gaussian assumption, and no double peaks are present. The *z*-integrated plots (Figure 8.5b and Figure 8.6b) show a clear transition between Gaussian profiles close to the source and double-Gaussian profiles further downstream. Therefore, again, the cross-sectional behaviour of the flow does not match the expectations in the puff region. In addition the value for *f* in the advected thermal for runs 4 and 5 increases above 0.88, in a similar way to run 1.

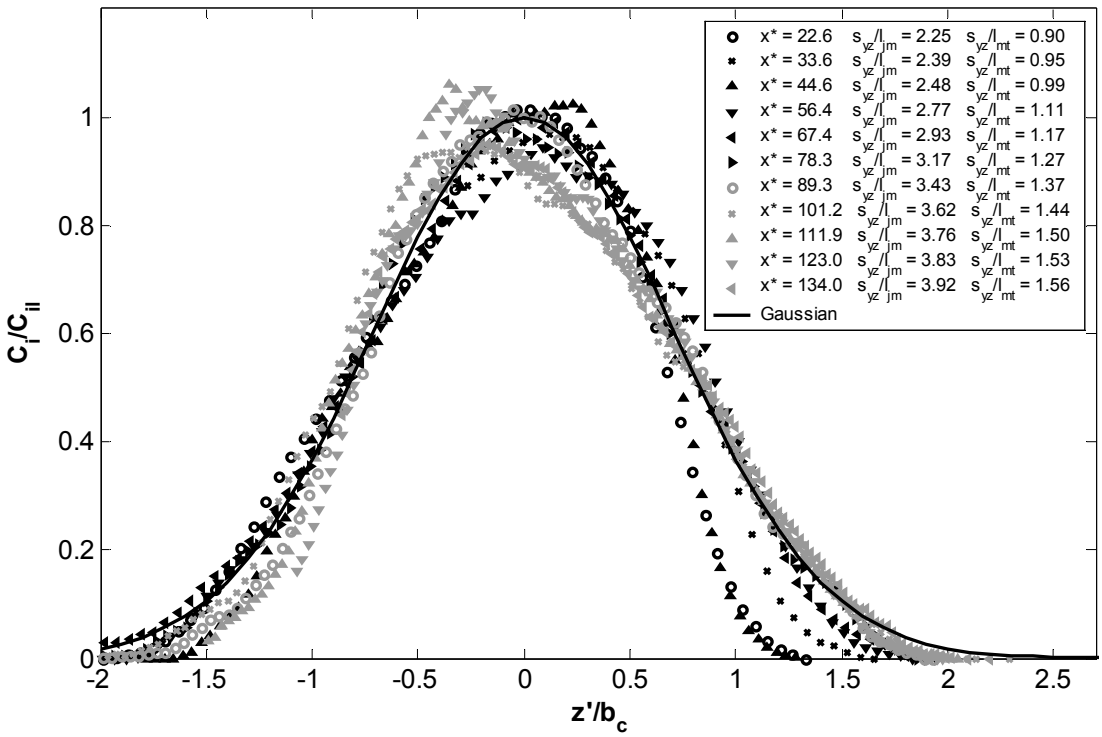

8.5(a) – *y*-integrated concentration profiles

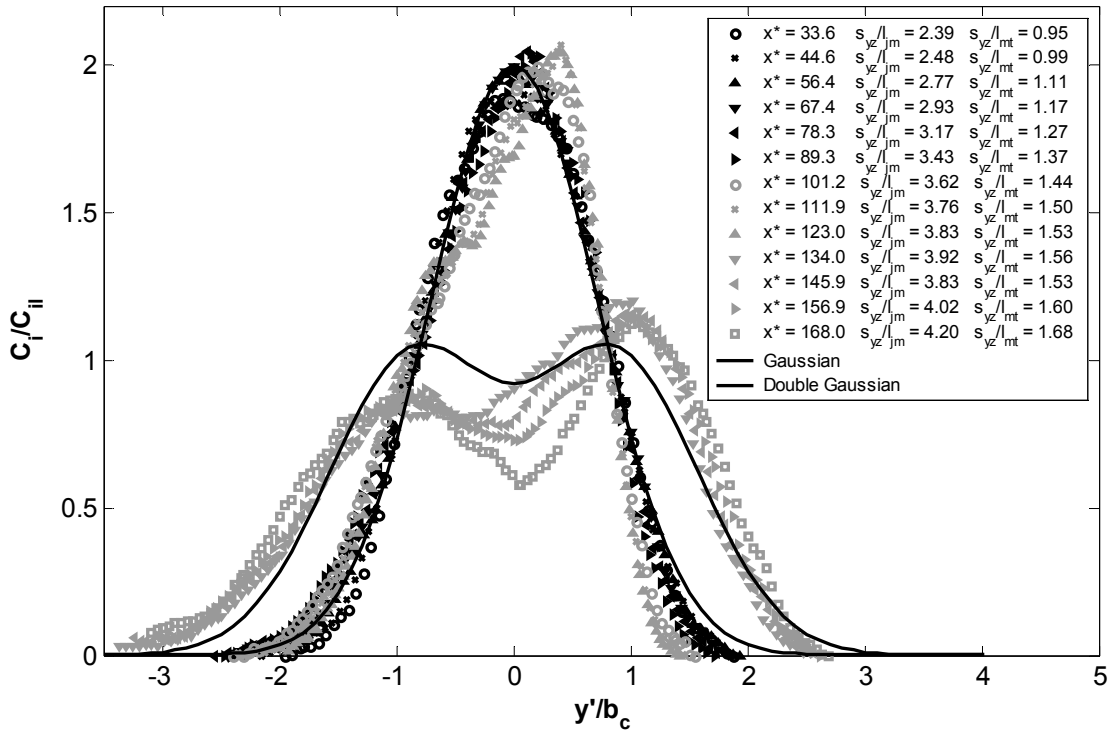

8.5(b) – *z*-integrated concentration profiles

Figure 8.5 - Integrated cross-sectional concentration profiles run 4

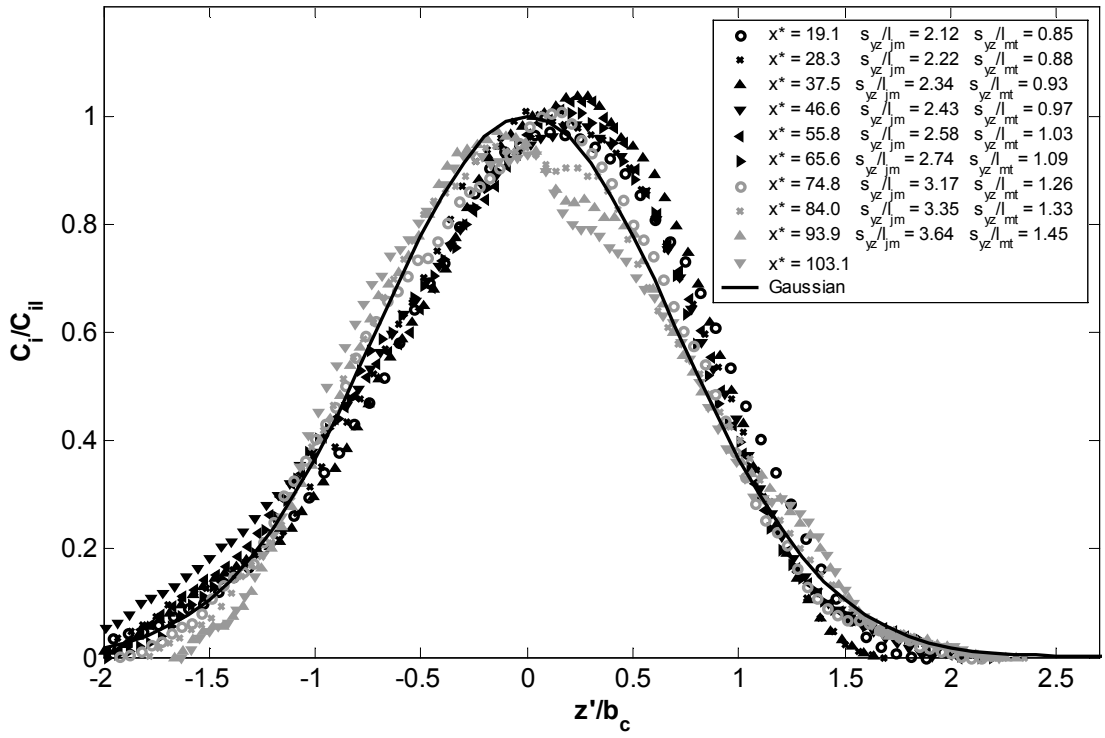

8.6(a) – *y*-integrated concentration profiles

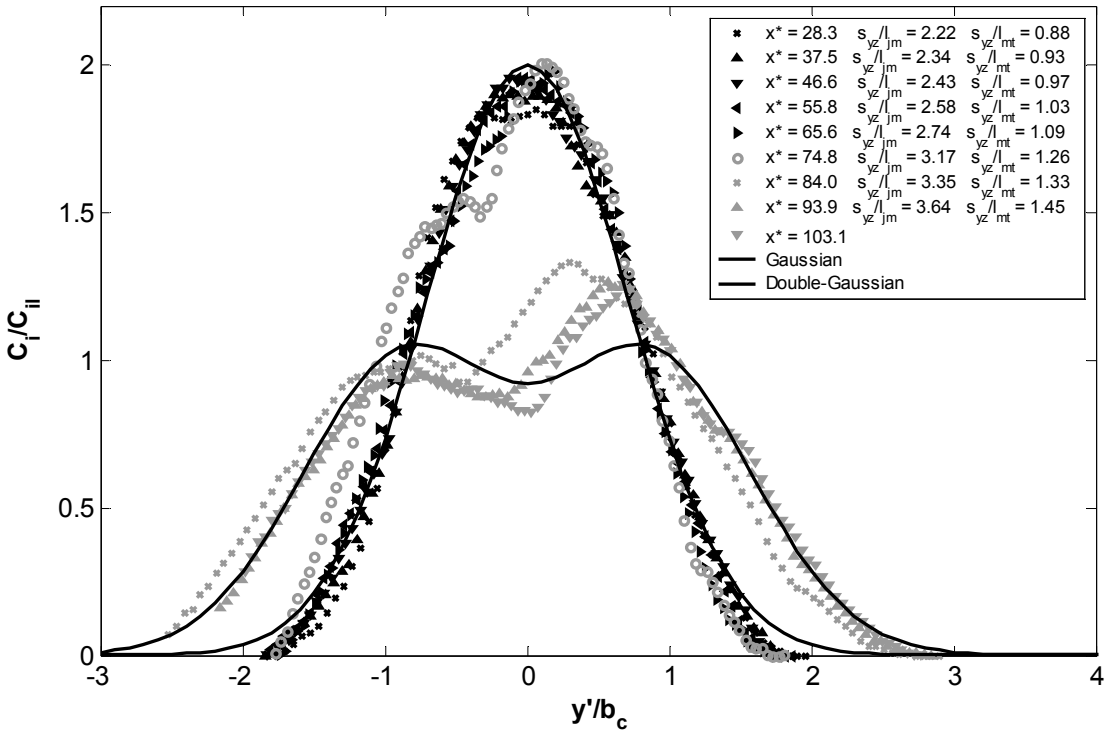

8.6(b) – *z*-integrated concentration profiles

Figure 8.6 - Integrated cross-sectional concentration profiles run 5

8.3.2 – Bulk Properties

The cross-sectional results show that current modelling assumptions have varying degrees of success when applied to the flows with three-dimensional trajectories. To explore the appropriateness of the modelling assumptions further the bulk properties are investigated with the main focus on the trajectory predictions and the interpretation of the integrated dilution results. The horizontally discharged experiments, runs 1 to 3, are discussed first, followed by the negatively buoyant experiments.

8.3.2.1 – Double-Integrated Dilution Results

The double-integrated dilution results have been used in Chapters 3 and 5 to confirm the accuracy of the concentration data as well as determining the end point of the transition from weakly advected to strongly advected flow regions. The double-integrated dilution results of the first three runs are presented Figure 8.7 as functions of the jet to puff transition length-

scale (Figure 8.7a) and the distance in the *x*-direction, non-dimensionalised by the plume to thermal length-scale (Figure 8.7b) The *y*-integrated results refer to the data obtained by integrating the *y*-integrated dilution results in the *z*-direction, the *z*-integrated results refer to the data obtained by integrating the *z*-integrated dilution results in the *y*-direction. Note that if the *y*-integrated data matches the *z*-integrated data, the assumption that the cross-section is perpendicular to the flow direction is reasonable, and that if the double-integrated dilution has a value of 1, the strongly advected region has been reached.

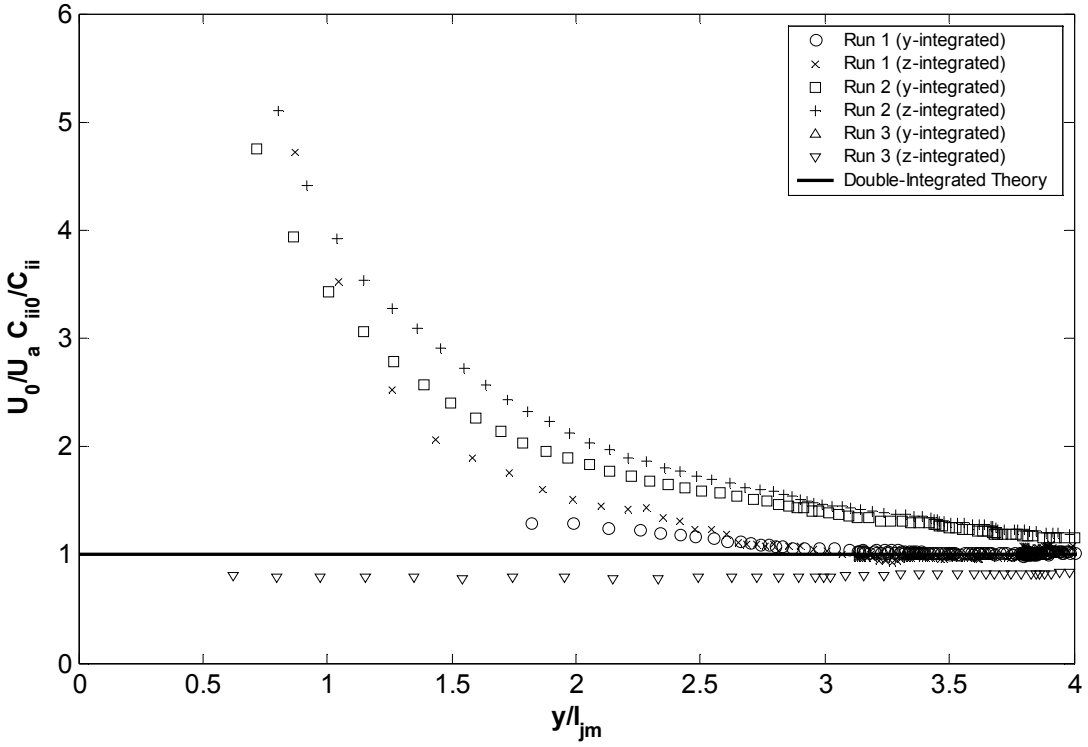

8.7(a) – Double-integrated results as a function of the jet to puff transition length-scale

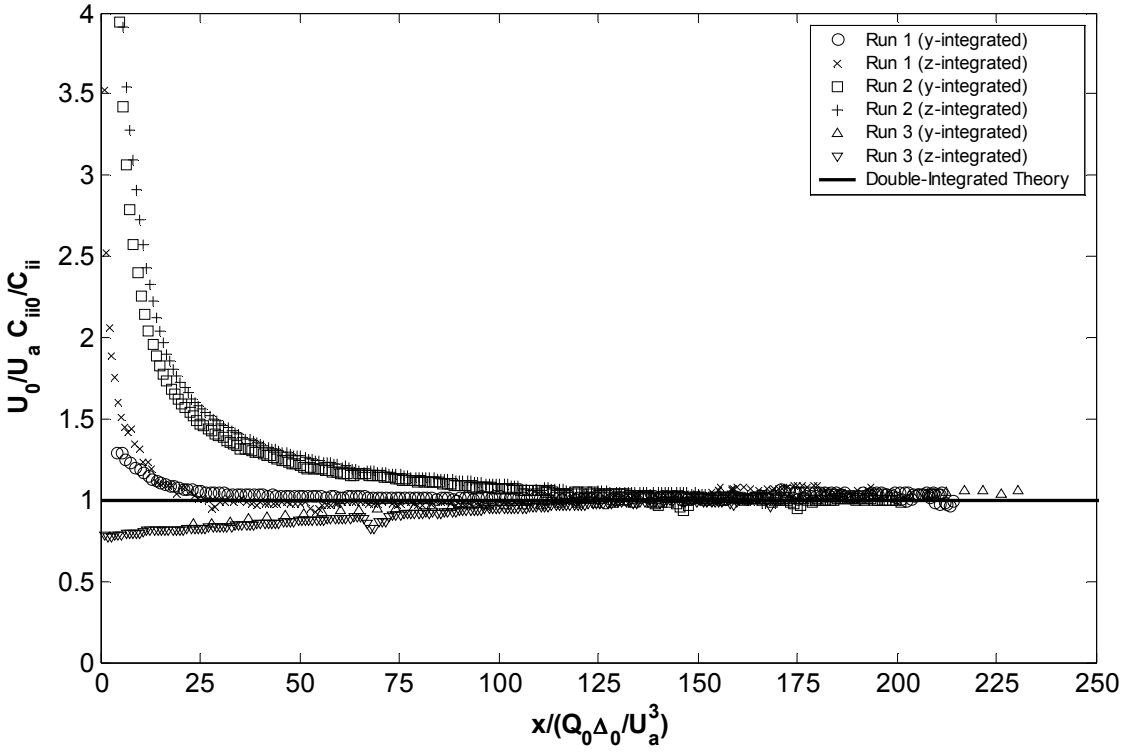

8.7(b) – Double-integrated results as a function of the horizontal distance from the source

Figure 8.7 - Double integrated dilution results from runs 1 and 2

The double-integrated results from run 1 (and to a lesser extend run 2) confirm the quality of the integrated dilution results using the LA technique, because of the accurate match between the experimental results and the value predicted by the double-integrated theory.

The double-integrated results from the vertically discharged non-buoyant jet in a moving ambient showed that the transition from weakly advected to strongly advected flow region is completed at approximately three length-scales (see Chapter 3). Figure 8.7a shows that the double-integrated dilution results from run 1 agree with this, however the results from runs 2 and 3 are significantly different, taking until approximately 5 length-scales for the flow to be completely strongly advected. These observations are consistent with the double-peak structure visible in the cross-sectional profiles of run 1 and the absence of these structures in the profiles from runs 2 and 3 until much further downstream, beyond the transition point determined by the length-scale theory. However whereas the cross-sectional profiles indicate similar behaviour for runs 2 and 3, the double-integrated results show very different behaviour. The double-integrated dilution values less than one indicate that the recorded cross-sectional profiles are not perpendicular to the flow direction. In the case of *z*-integrated dilution, this can only be caused by the buoyancy-generated momentum flux. The differences

between the results from runs 2 and 3 indicate that the buoyancy-generated momentum flux has a higher influence on the flow in run 3. This is expected because the effects of the entrained ambient momentum flux and the initial excess momentum flux will to a large effect cancel each other out in the counter-flowing region of the flow. This process makes it very difficult to determine the location of the transition to strongly advected behaviour from the double-integrated results.

Figure 8.7b shows that run 1 reached the strongly advected region at about $x^* = 28$, coinciding with the first cross-sectional profile presented in Figure 8.1. It was noted, when discussing these profiles earlier, that the Gaussian profile was not a good fit to both the y and z-integrated cross-sectional profiles at any location and that therefore the flow was no longer weakly advected. The double-integrated results confirm these results. The results also indicate that the flow never becomes an established puff. It takes the flow up to the first cross-sectional profile to reach the end of the transition zone to the strongly advected region, however after the first cross-sectional profile, the flow forms a double-peak structure in the z-integrated profiles, indicating the flow is in the advected thermal region. The cross-sectional profiles of run 2 show no sign of double-peak structures before the cross-sectional profile at $x^* = 113$ (Figure 8.3), and this is consistent with the double-integrated results which suggest that run 2 does not reach the strongly advected region until that distance (Figure 8.7b). The cross-sectional profiles of run 3 show definite double-peak structures at $x^* = 90.5$ (Figure 8.4). The double-integrated results are again consistent in that they indicate that the flow reaches the strongly advected region before $x^* = 113$.

The length-scale theory predicts that the results of run 2 are similar to those of run 1. However, the combination of the single Gaussian profiles and the double-integrated dilution results, indicates the flow is weakly advected prior to the formation of the advected thermal, and hence run 2 has an advected-plume region. The sequence of flow regions is therefore jet to plume to thermal instead of the predicted jet to puff to thermal. The results also suggest the jet to plume to thermal flow sequence for run 3. However, because run 3 is discharged into a counter-flow the implications of the flow sequence are not as clear.

8.3.2.2 – Trajectory Results

Froude number and velocity ratio similarities are needed to collapse complete experimental trajectory data sets onto a single line. The Froude numbers and velocity ratios from Cheung's experiments were significantly higher and lower respectively than the values from the current experiments and therefore it was not possible to directly compare the current experimental results with previous experimental results. However by comparing the trajectory results in the *x*-*y* plane with the trajectory results from a non-buoyant discharge in a cross-flow, the assumption that the flow behaviour is essentially independent of the number of dimensions of the trajectory path can be assessed up to the advected thermal region. This comparison is shown in Figure 8.8, the data is non-dimensionalised by the strong jet to puff transition length-scale. The experimental results from run 1 clearly display the double peak structure. An average value for the trajectory of the 3D path experiment has been added for comparison with the 2D path experiment. The trajectory results do not seem to be significantly different up to approximately 3.3 length-scales in the direction of discharge, this point coincides with the transition point from the puff to thermal regions for the 3D path flow. After this point the increased entrainment of ambient fluid in the advected thermal region results in the relative reduction in distance travelled in the *y*-direction for the 3D path flow.

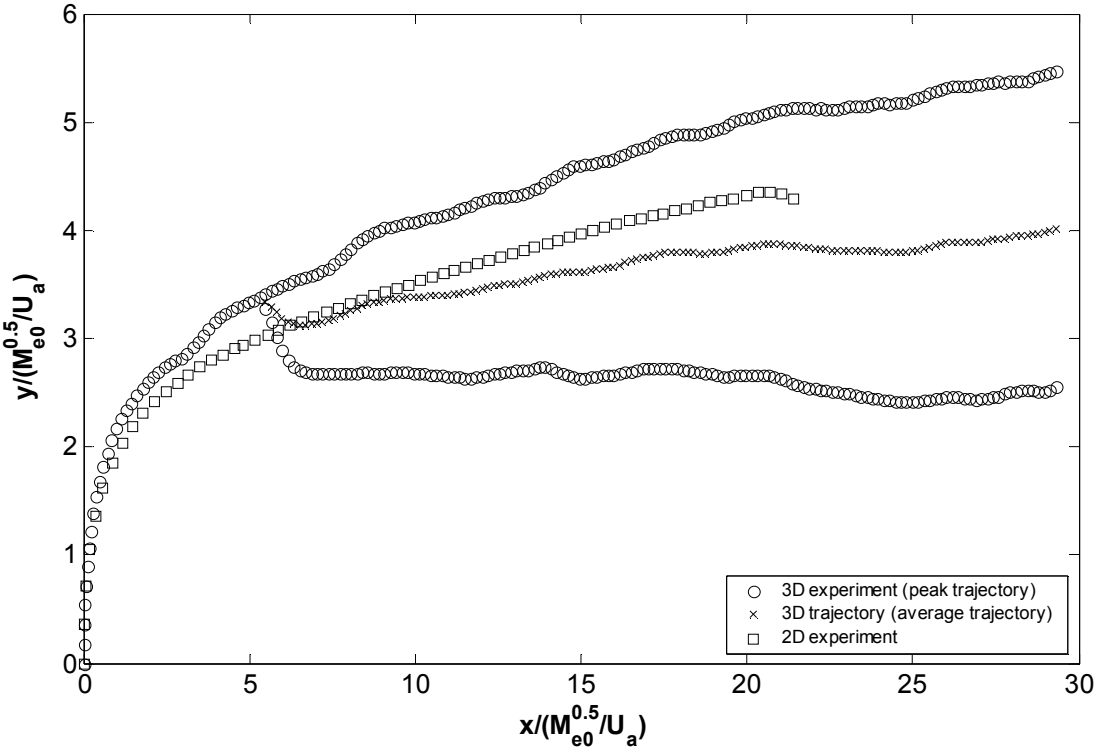

Figure 8.8 - Run 1 trajectory results in x-y plane compared with trajectory results from non-buoyant discharge in moving ambient (Reynolds number = 2133, velocity ratio = 0.033)

The trajectory results in the *x*-*z* plane, non-dimensionalised by the plume to thermal transition length-scale, are presented in Figure 8.9a. None of the model predictions are a good match with the experimental data close to the source. The relatively low slopes of the model lines at the source indicate that the influence of the entrained ambient momentum flux is overestimated and the influence of the buoyancy-generated momentum flux is underestimated. In the advected thermal region the relatively low slope of the experimental data suggests a significantly higher rate of entrainment of ambient fluid relative to that assumed by the models. The trajectory results in the *x*-*y* plane are presented in Figure 8.9b. All model predictions match the experimental results reasonably well in the jet and puff regions of the flow, and the predictions of VisJet and CorJet are also consistent with the average experimental results in thermal region. This is unexpected given the inconsistencies in Figure 8.9a. To show the complete trajectory Figure 8.9c presents a three-dimensional view of the experimental results and the model predictions.

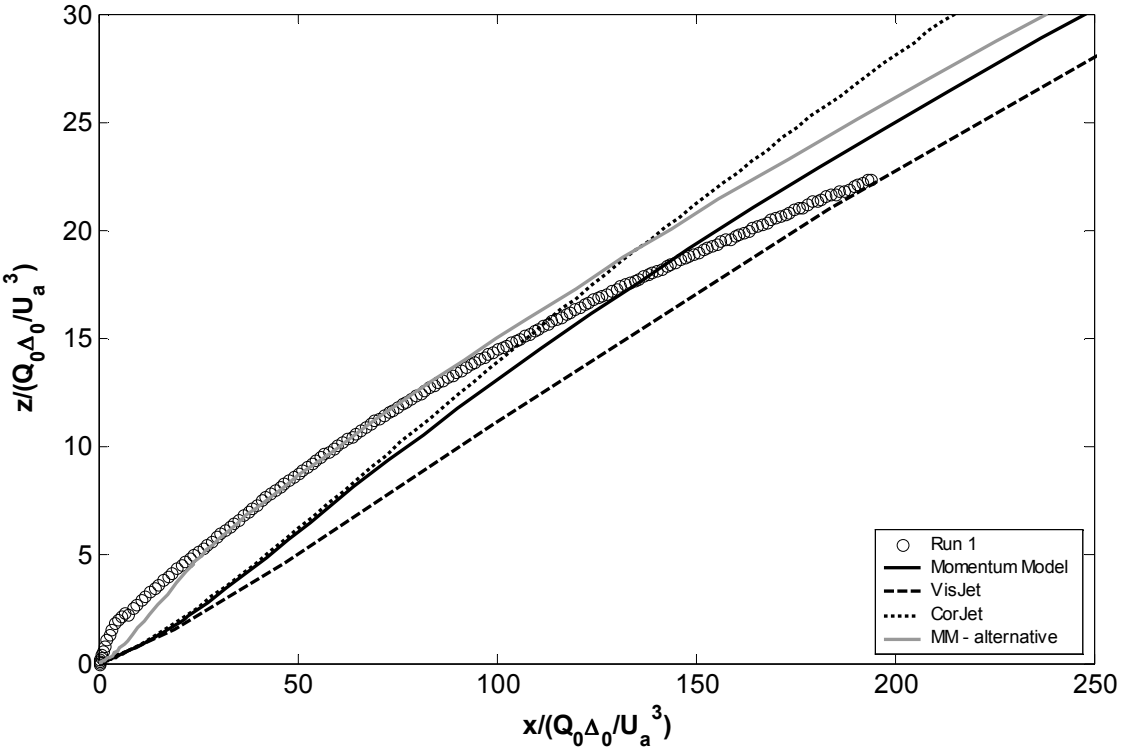

8.9(a) – Trajectory results in *x*-*z* plane

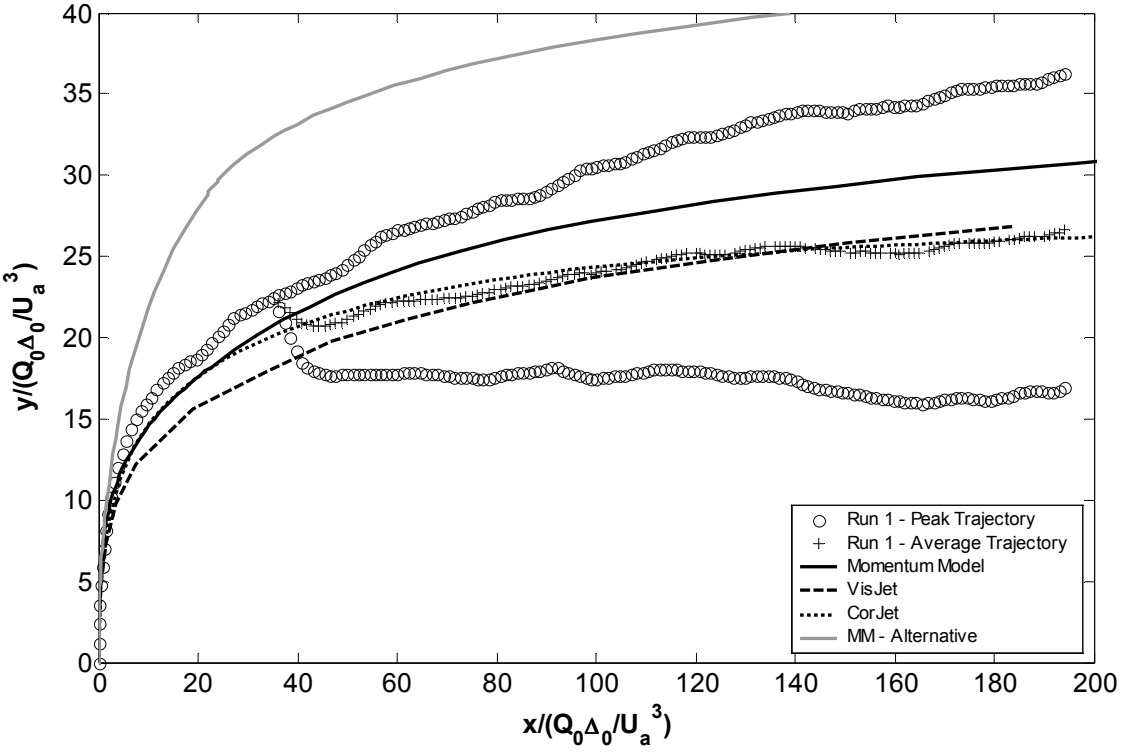

8.9(b) – Trajectory results in *x*-*y* plane

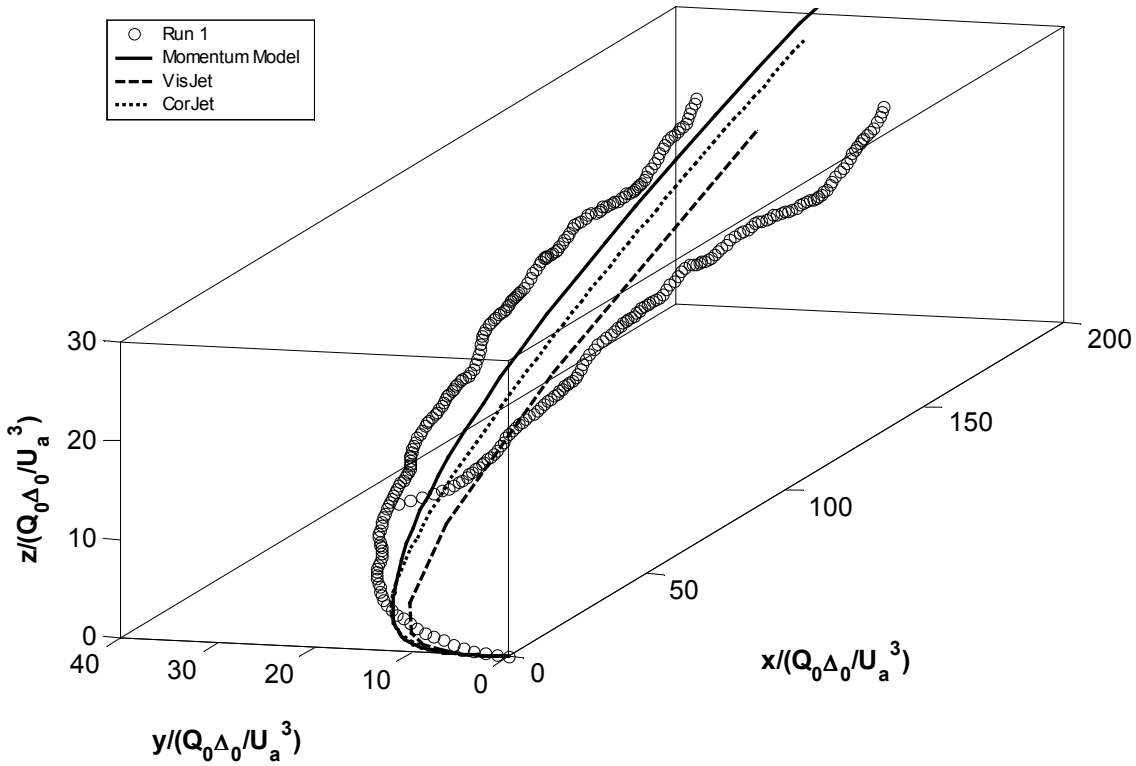

8.9(c) – Three-dimensional view of trajectory results

Figure 8.9 - Trajectory results buoyant jet with three-dimensional trajectories run 1

Based on the observations from Figure 8.8 it was expected that the current mathematical models are capable of reasonably estimating the trajectory of the buoyant jet in a cross-flow in the *x*-*y* plane in the strong jet and puff regions (Figure 8.9b), because it was shown that the model predictions are reasonably consistent with the trajectory results for non-buoyant discharges in a cross-flow (see section 5.3.1.2). However the results from the double-integrated data and the mean cross-sectional concentration data indicated that the puff region was never fully established. The trajectory data in the *x*-*z* plane clearly does not match the model predictions of the trajectory in the strong-jet and puff regions. This also indicates that the behaviour prior to the thermal region for the buoyant jet with a 3D path in a cross-flow cannot simply be based on its 2D counterpart.

The cross-sectional results indicated that the predicted location of the transition from the puff to the thermal region by length-scale theory was a reasonable match with the experimental data. In the advected thermal region of a buoyant jet in co-flow, the trajectory prediction of the Momentum Model matched the experimental values, however VisJet (Cheung et al. 2000) and CorJet (Jirka 2004) overestimated the distance travelled in the *z*-direction (see section 5.3.2.2). In addition, the value for f in the Momentum Model is constant (though currently unknown), while the cross-sectional results show that the value for f increases with increasing distance. The relatively steep slope of the model line of CorJet compared to the slope of the lines of VisJet and the Momentum Model (Figure 8.9a) is consistent with the advected thermal results presented in chapter 5. The slope of the trajectory data predicted by the Momentum Model is approximately the same as the experimental data when the flow enters the thermal region ($x^* = 28$). The two are approximately parallel up to around $x^* = 55$. After this point the slope of the experimental trajectory data reduces. This indicates an increase in entrainment of ambient momentum flux. The distance coincides with the point where the value for f increases above the expected 0.88, suggesting that the increase in f is linked to an increase in the rate of entrainment of ambient fluid.

An alternative prediction from the Momentum Model has also been added to Figure 8.9. By increasing the dominant momentum flux ratio that governs the transition from strong-jet to puff regions in the Momentum Model, the flow was forced to become an advected plume after the strong-jet region. The relatively low entrainment in the plume region compared to the puff region means that the alternative prediction does not match the trajectory in the *x*-*y* plane (Figure 8.9b). However, by increasing the relative importance of the buoyancy-generated momentum flux, the alternative prediction is a reasonable match for the trajectory *x*-*z* plane,

up to $x^* = 70$. This also confirms that when changing from a flow with a 2D path to one with a 3D path, additional complexities are introduced, and these complexities have a significant influence on the behaviour of the flow.

The trajectory results in the *x*-*y* plane from run 2 are compared with the trajectory results from a non-buoyant oblique discharge in a moving ambient (run 26) in Figure 8.10. The Figure shows that the results from the 2D trajectory flow are consistent with the trajectory results of run 2 throughout the flow. This is surprising because the cross-sectional profiles of the 2D trajectory flow matches the double-Gaussian profile (see Chapters 3 and 7), while the cross-sectional profiles of run 2 possess only a single peak, and because the double-integrated dilution results suggest that the 2D flow is strongly advected, while Figure 8.7 suggests that the 3D trajectory flow is still in the weakly advected region.

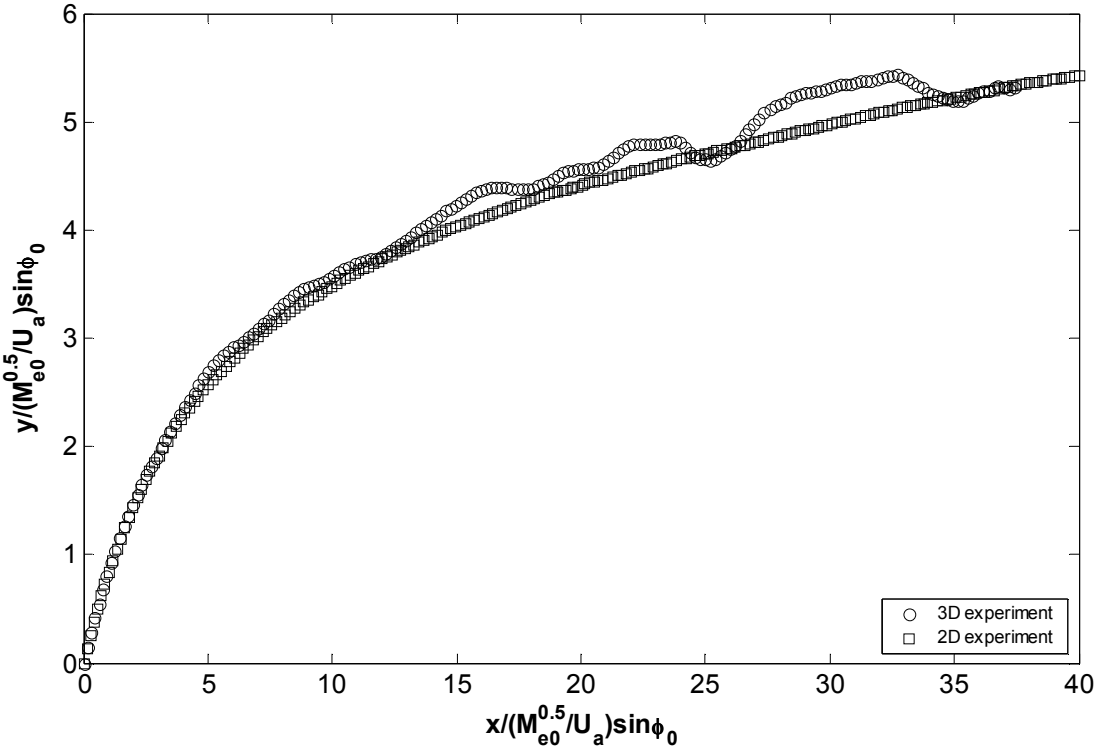

Figure 8.10 - Run 2 trajectory results in *x*-*y* plane compared with trajectory results from non-buoyant discharge in moving ambient (Reynolds number = 4379, velocity ratio = 0.029)

The comparison between the trajectory results from run 2 and the model predictions is presented in Figure 8.11. Again it is surprising that the predictions from the Momentum Model and VisJet match the experimental data well in the *x*-*z* plane (Figure 8.11a), because of the unexpected cross-sectional behaviour. In the *x*-*y* plane (Figure 8.11b) the three models are consistently lower than the experimental data, with the Momentum Model underestimating

the experimental data the least and CorJet the most. The underestimation of the distance travelled in the *y*-direction is in itself not unexpected, the single Gaussian profile leads to a lower than expected entrainment rate of ambient fluid and thus a slower increase in the ambient momentum flux. However this is inconsistent with the results seen in the *x*-*z* plane. A figure showing the three-dimensional trajectory path of run 2 can be found in Appendix E, Figure E.5.

An alternative prediction from the Momentum Model has also been added to Figure 8.11. Because Figure 8.7 indicates that the flow is in the weakly advected region of the flow for a longer distance than expected, the spread relationship has been forced to use the weakly advected spread relationship (equation (4.31)) throughout the flow. This enables a direct comparison between the experimental data and the numerical model based on the observations from the cross-sectional and double-integrated dilution results. Figure 8.11 shows that the alternative prediction from the Momentum Model matches the experimental data well up to $x^* = 110$ in both the *x*-*z* and *x*-*y* plane, however after this point the alternative spread relationship overestimates the entrainment of ambient fluid and therefore the distance travelled in the *y* and *z*-directions is underestimated. $x^* = 110$ coincides with the appearance of double-peak structures in the cross-sectional profiles (Figure 8.4) as well as the end of the transition zone to the strongly advected region (Figure 8.7), and therefore the alternative prediction confirms the cross-sectional and double-integrated results. It also shows that the results in the *x*-*z* plane are significantly less sensitive to the rate of spread than the results in the *x*-*y* plane up to $x^* = 110$.

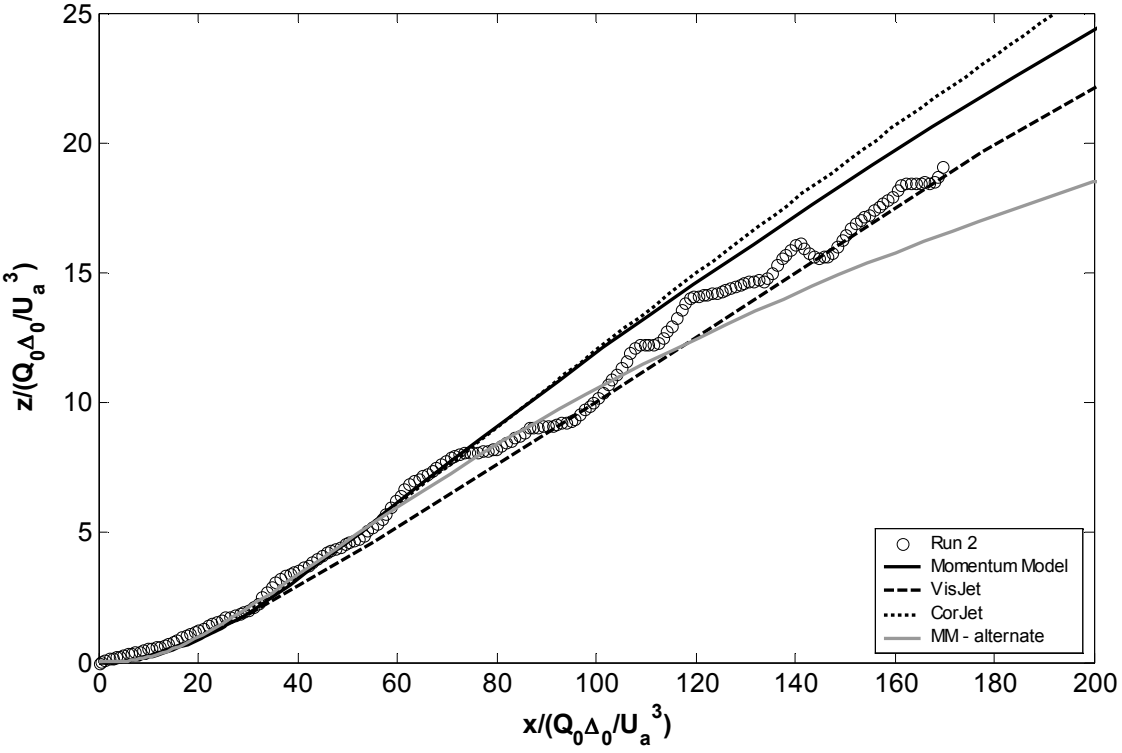

8.11(a) – Trajectory results in *x-z* plane

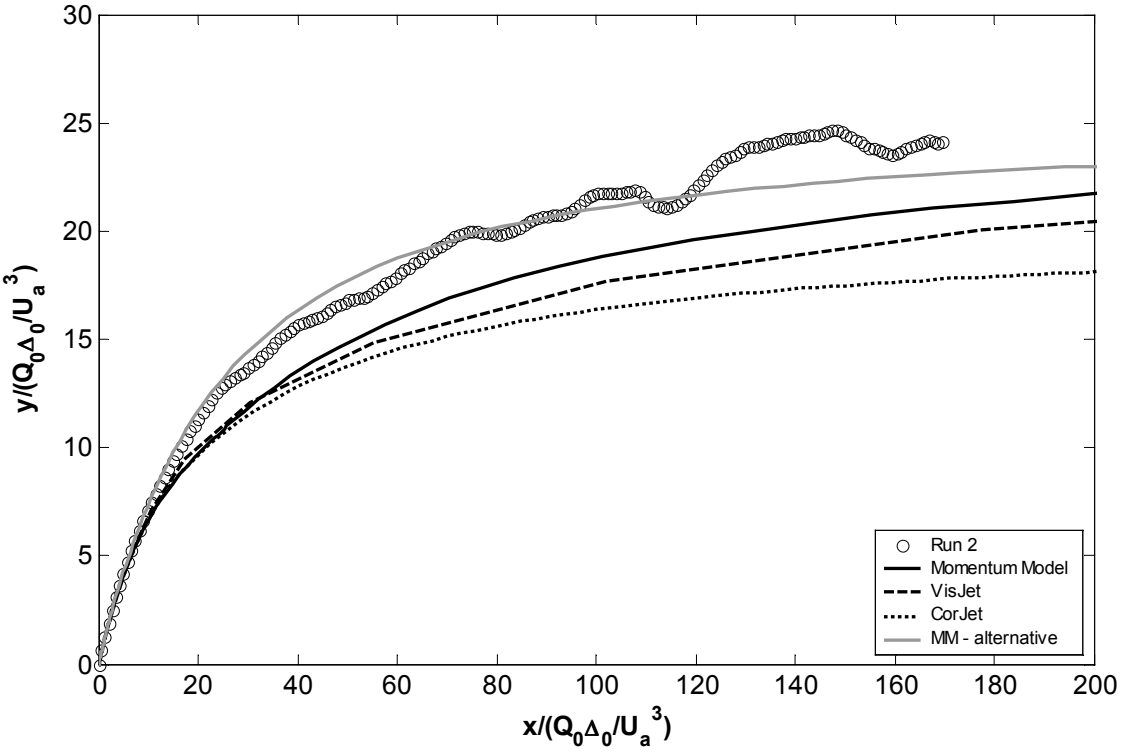

8.11(b) – Trajectory results in *x-y* plane

Figure 8.11 - Trajectory results buoyant jet with three-dimensional trajectories run 2

Figure 8.12 shows the trajectory results of run 3. In this case the horizontal component of the initial excess momentum flux acts in the opposite direction to the ambient flow, and for this reason CorJet could not be used to predict the trajectory results. In Figure 8.12a the trajectory results in the *x*-z plane show similar behaviour to run 1. The influence of the buoyancy-generated momentum flux is underestimated by the models. However, after the change in buoyant flow direction, the predicted trajectories and the experimental results appear to diverge, instead of crossing each other as for run 1. This is consistent with the difference in cross-sectional behaviour between run 1 and 3. The lack of double-peak structures in run 3 leading to less ambient entrainment, and therefore a relatively smaller distance travelled in the *x*-direction. The trajectory results in the *x*-*y* plane (Figure 8.12b) are similar to the results from run 2, with VisJet significantly underestimating the distance travelled in the *y*-direction. The prediction from the Momentum Model is reasonably consistent with the experimental data. A figure showing the three-dimensional trajectory path of run 3 can be found in Appendix E, Figure E.6.

The alternative prediction in Figure 8.12 of the Momentum Model is not based on the same approach as the alternative prediction for run 2. Equation (4.31) could not be used to obtain a reasonable match between the predicted and experimental data. This reflects the differences between run 2 and 3 already discussed in the context of the double-integrated dilution results. As stated above, the model appears to underestimate the buoyancy-generated momentum flux and overestimate the entrained ambient momentum flux. This indicates that the transition from weakly advected flow to strongly advected occurs prematurely (as is confirmed by the double-integrated results). The momentum flux ratio that governs the transition between the weakly and strongly advected regions has therefore been increased by a factor of 1.7 as an indicator of an alternative approach. The results in Figure 8.12 show that again the results in the *x*-*y* plane are less sensitive to the change in the spread relationship, and that the alternative prediction is a better match with the experimental data in the *x*-*z* plane than the prediction of the Momentum Model. However it is not as good as the alternative solution for run 2, and this is indicative of the additional complexities associated with the change in the buoyant flow direction.

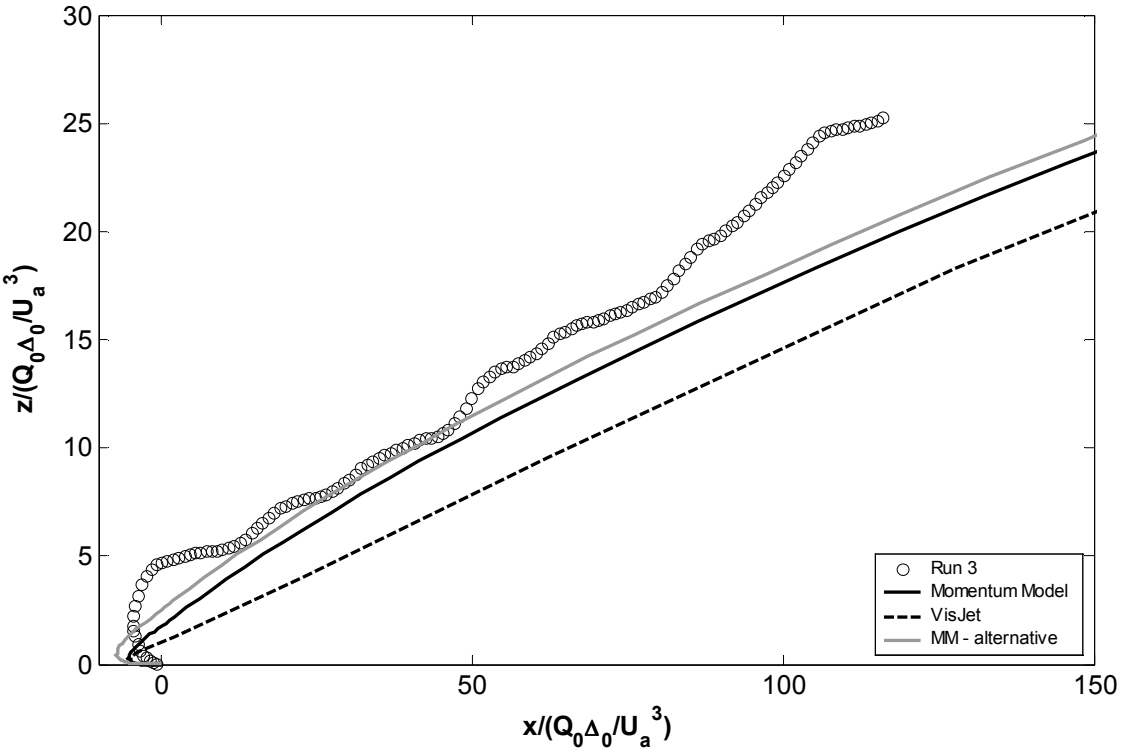

8.12(a) – Trajectory results in *x-z* plane

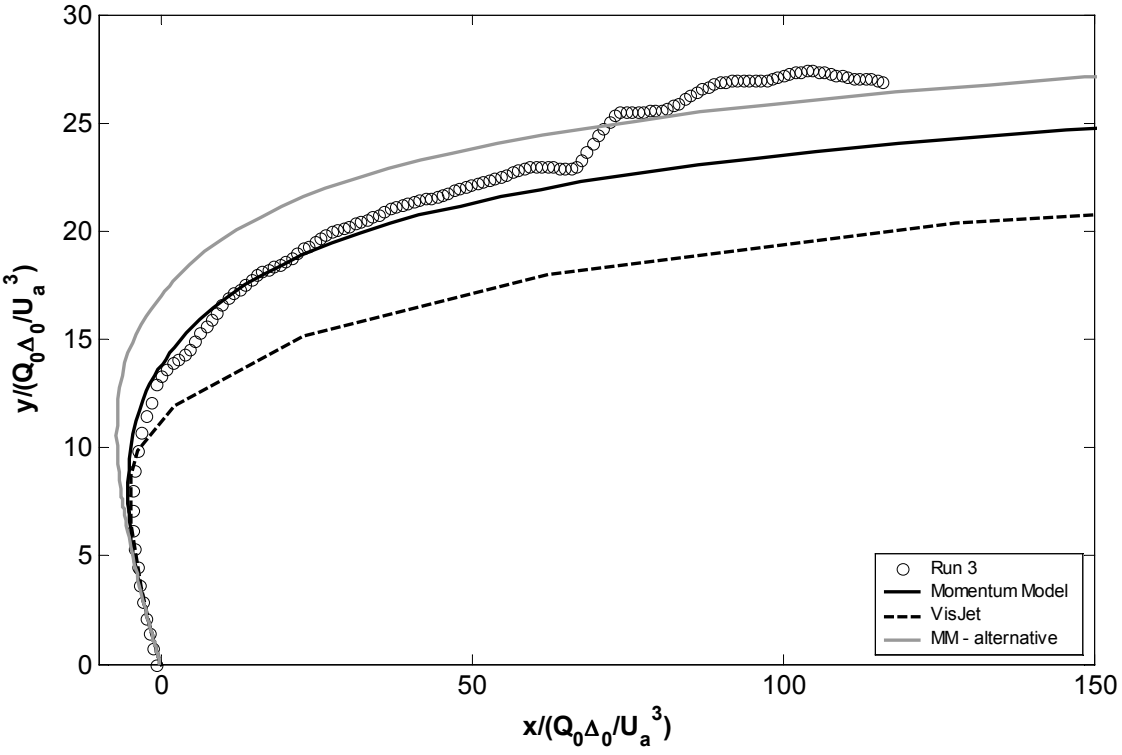

8.12(b) – Trajectory results in *x-y* plane

Figure 8.12 - Trajectory results buoyant jet with three-dimensional trajectories run 3

The trajectory results of the final two runs are presented in Figure 8.13 and Figure 8.14. The predictions from CorJet only went as far as the point at which the flow crossed the *x*-axis. Due to the relatively long transition from single peak to double peak structures there is a discontinuity in the *z*-integrated data (Figure 8.13b and Figure 8.14b). The MatLab analysis automatically followed the trajectory along the peak furthest from the source and the trajectory along the peak closer to the source was found by running the analysis backwards. The discontinuity is created because the single peak moves away from the centreline before a second peak is visible. This process can be seen in Figure 8.5b. Run 5 has a relatively small initial excess momentum flux in the *y*-direction and therefore moves a relatively small distance in this direction, thus errors in the trajectory in *x*-*y* plane are amplified. This can be seen in Figure 8.13b, where the single peak trajectory data moves back towards the source at some locations. Figures showing the three-dimensional trajectory paths of run 4 and 5 can be found in Appendix E, Figure E.7 and Figure E.8.

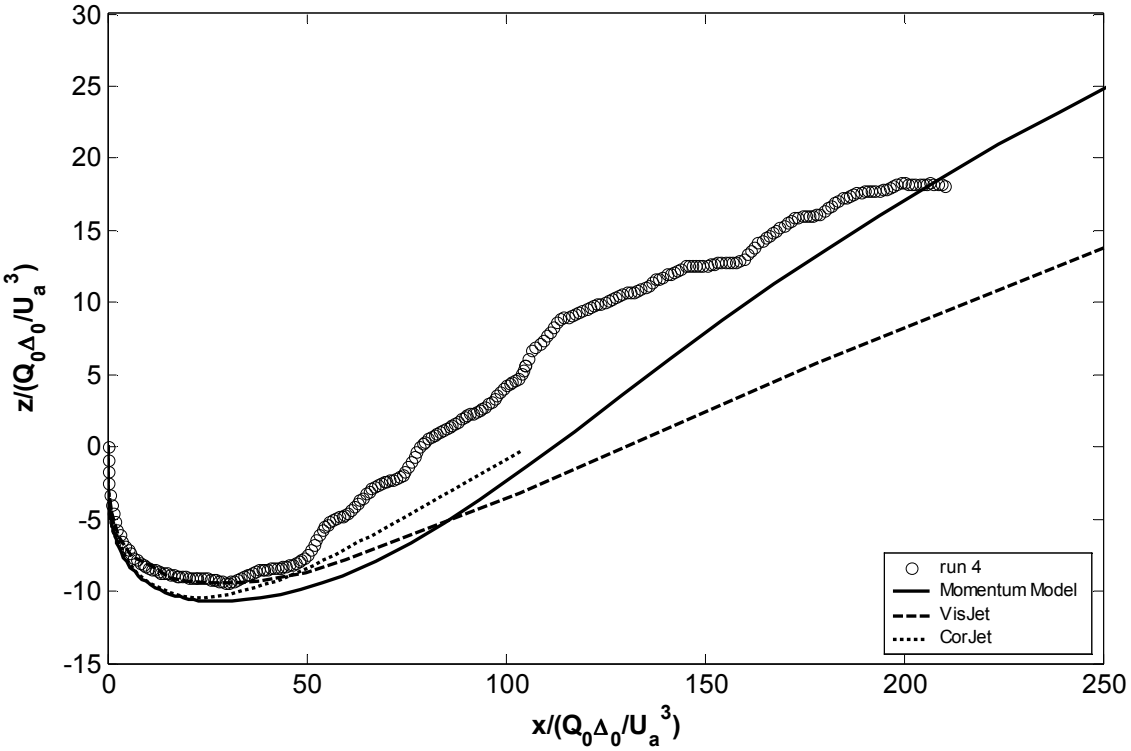

8.13(a) – Trajectory results in *x*-*z* plane

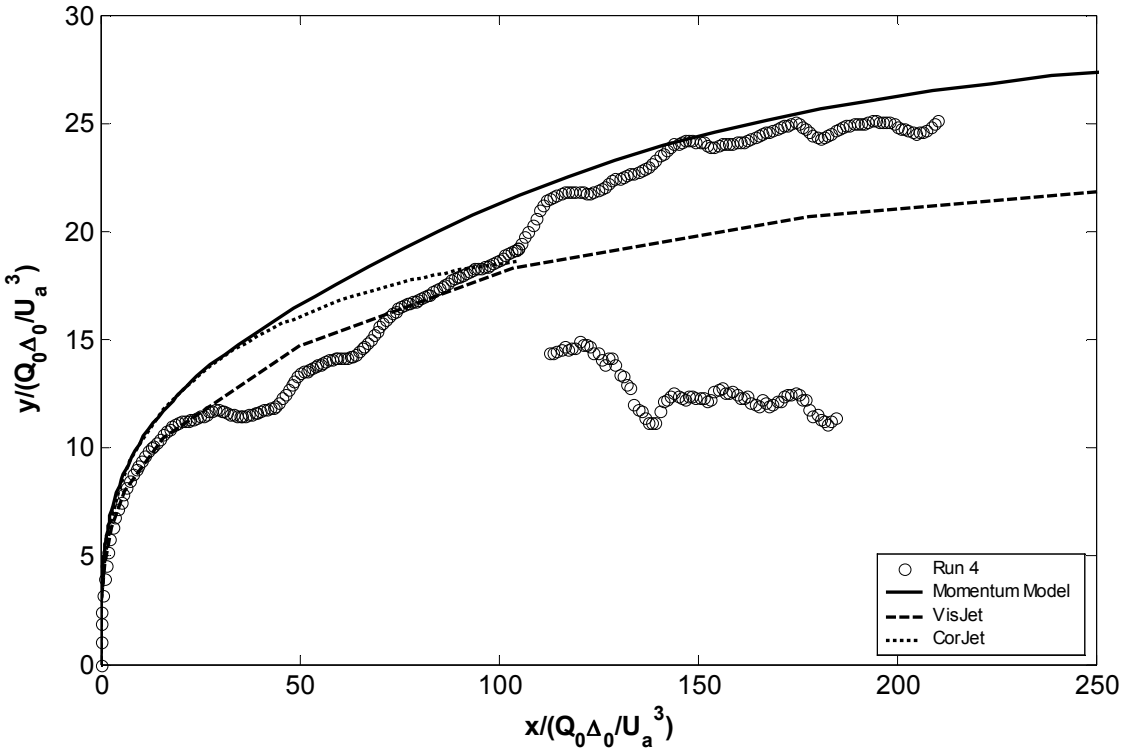

8.13(b) – Trajectory results in *x-y* plane

Figure 8.13 - Trajectory results buoyant jet with three-dimensional trajectories run 4

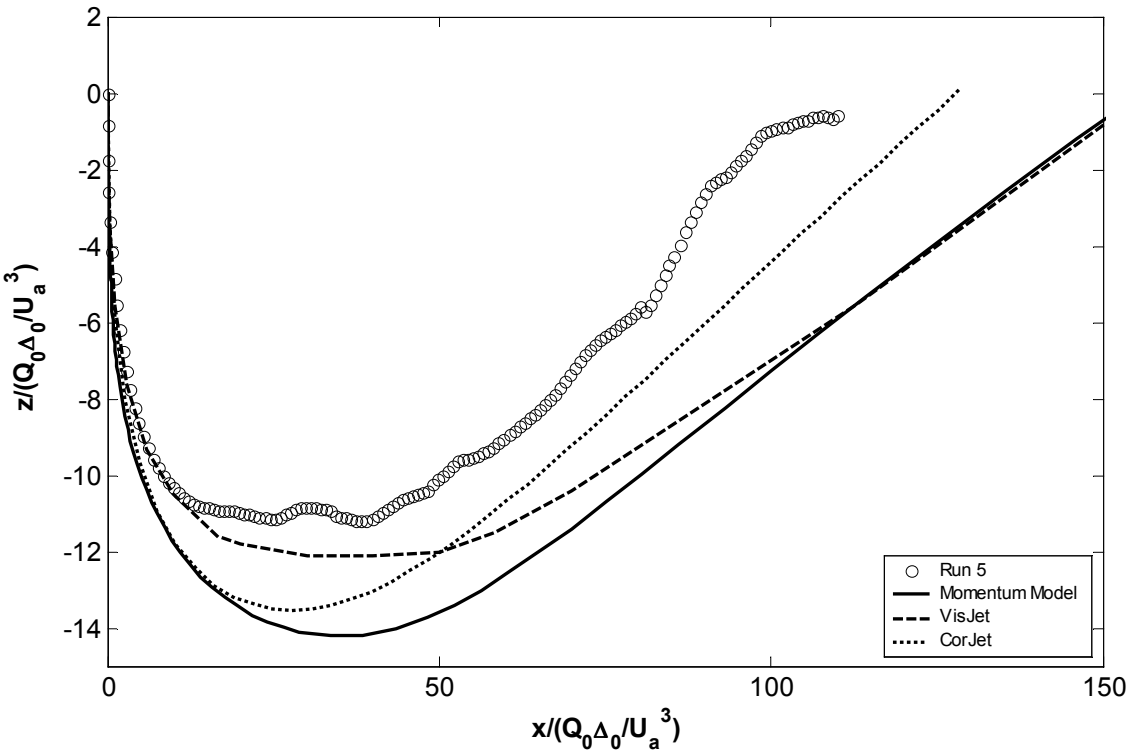

8.14(a) – Trajectory results in *x-z* plane

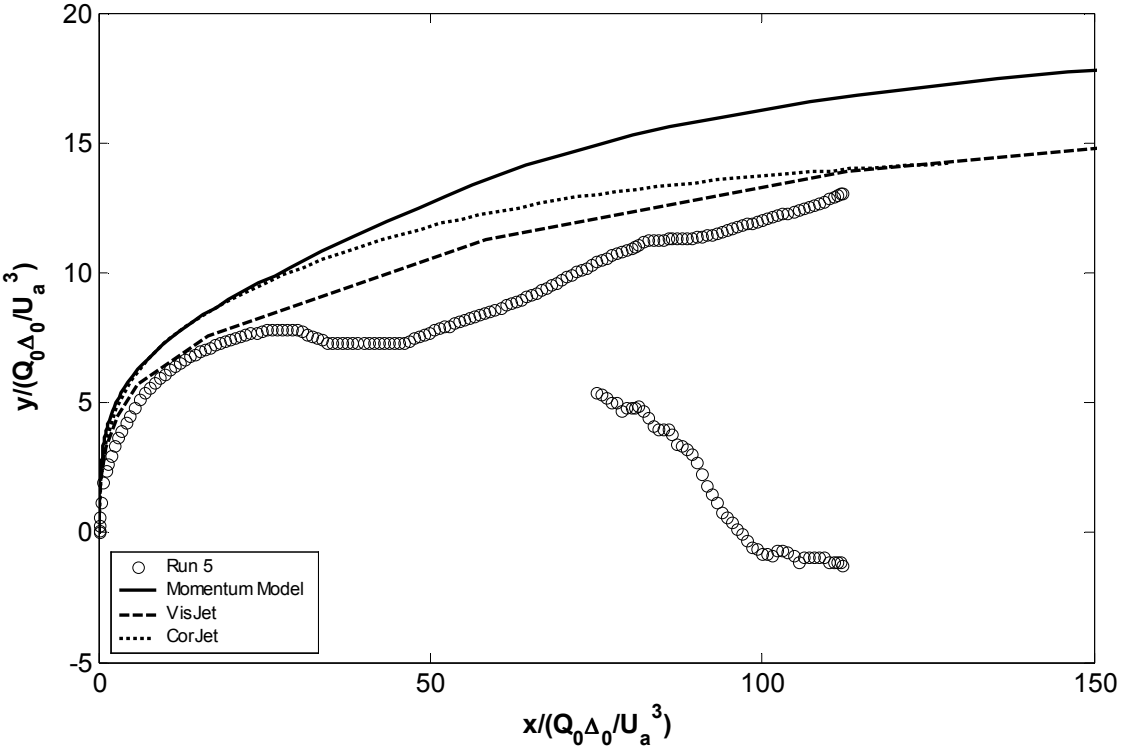

8.14(b) – Trajectory results in *x-y* plane

Figure 8.14 - Trajectory results buoyant jet with three-dimensional trajectories run 5

The dissimilarity of predictions from the models in the advected thermal region, due to differences in the entrainment or spread relationships, are again clearly visible in the *x-z* plane (Figure 8.13a and Figure 8.14a). In the weakly advected region, the models underestimate the influence of the buoyancy-generated momentum flux, which was also seen for runs 1 and 3. The prediction of VisJet is consistent with the experimental data up to the point of minimum height for run 4. The Momentum Model and CorJet match each other up to that point, but they overestimate the vertical distance to the point of minimum height. The prediction of VisJet is also the most consistent with the experimental data for run 5, however, like the predictions from the Momentum Model and CorJet, it overestimates the distance from the source to the minimum height.

The results of the Momentum Model in the strongly advected region of run 4 (Figure 8.13a) are similar to the results of run 1. The prediction lies above the prediction of VisJet, and is perpendicular to the experimental data up to $x^* = 120$. Further downstream the slope of the experimental trajectory data reduces faster than the predicted slope. Contrary to the earlier results, the prediction from CorJet matches the experimental results more closely than the other models in the strongly advected region of run 5 (Figure 8.14a). However, this may no

longer be the case further downstream. Figure 8.13a indicates that the flow trajectory is approximately parallel to the predictions of the Momentum Model after crossing the *x*-axis (as was seen for runs 1 and 2), while the difference between CorJet's prediction and the prediction of the Momentum Model is expected to increase with distance from the source.

The model predictions of the trajectory results in the *x*-*y* plane for runs 4 and 5 (Figure 8.13b and Figure 8.14b) are similar to the results for runs 1 to 3, in that the entrained ambient momentum flux appears to have a smaller influence on the Momentum Model prediction than on the predictions of VisJet and CorJet. The predictions of VisJet and CorJet for run 4 are a reasonable match with the experimental data, predicting approximately the average values when the cross-sectional profiles show a double peak structure. This result is comparable with the result from run 1, and unlike the trajectory results in the *x*-*y* plane from runs 2 and 3, and in addition is consistent with the cross-sectional behaviour. Because the cross-sectional behaviour of run 5 was similar to run 4, it is surprising that the predictions from the models overestimate the distance travelled in the *y*-direction for run 5. A possible explanation is that the buoyancy-induced instabilities, investigated in Chapter 6, affect one run significantly more than the other run due to their different initial discharge angles. However without more information from the *y*-*z* plane, it is not possible to be more specific.

No alternative Momentum Model predictions have been added to the trajectory figures. The combined effect of the single Gaussian cross-sectional behaviour in the puff region of the flow and the buoyancy-induced instabilities make it very difficult to indicate possible alternative approaches to modelling these flows.

8.3.2.3 – Integrated Dilution Results

The *y*-integrated dilution and *z*-integrated dilution results are presented in Figure 8.15 and Figure 8.16 respectively. The *y*-integrated dilution results are plotted versus the vertical distance from the source and the *z*-integrated dilution results are plotted versus the horizontal distance from the source perpendicular to the direction of the ambient flow. Note that the *z*-integrated dilution results are the dilution results at the peak furthest away from the source, because the dilution at this point was generally equal to the cross-sectional minimum dilution.

The *y*-integrated dilution results plotted as a function of the distance in the vertical direction (Figure 8.15) cannot be directly related back to the length-scale analysis, because the length-scales utilized determine the transitions with respect to the direction of the component of the initial excess momentum flux perpendicular to the ambient motion. However it enables the transition to the advected thermal region to be seen. The abrupt change in slope in the *y*-integrated dilution results indicate the flow has reached the advected thermal region. This change can be seen in the experimental results from runs 1, 4 and 5, which are the runs that show double-peak cross-sectional structures. A less abrupt change in slope can be seen for run 3, however the increased rate of dilution does not match that of 1, 4 and 5 within the measured region. Pun (1998) gives the relationship between dilution and distance in the *z*-direction in the advected thermal region, and modified to include the double-Gaussian assumption, this can be written as:

$$\frac{C_0}{C_l}\left(\frac{d}{Q_0\Delta_0/U_a^{\,3}}\right)^2\frac{U_0}{U_a}=\frac{4I_{cdg}k_{sg}^{\,2}}{\pi}\left(\frac{z}{Q_0\Delta_0/U_a^{\,3}}\right)^2 \tag{8.4}$$

Rearranging the double-Gaussian equation (equation (3.25)) for C_l, inserting it into equation (8.4) and integrating in the *y*-direction, gives the relationship for the *y*-integrated dilution in the advected thermal region:

$$\frac{C_{i0}}{C_{ily}}=2h\lambda k_{sg}\frac{z}{M_{e0}^{\,0.5}/U_a}=2h\lambda k_{sg}\frac{z}{l_{jm}} \tag{8.5}$$

Using the values as determined in Chapter 3 (or 5), the *y*-integrated dilution equation has a slope of 0.71. The experimental data gives values of 1.29 and 1.04 for runs 1 and 4 respectively. The value for run 1 is consistent with the results from the trajectory data from run 1, which indicated a higher than expected entrainment of ambient momentum flux in the advected thermal region, and is possibly related to the higher than expected values found for *f*. A significant increase in the entrainment of ambient momentum flux was not visible within the measured region of the trajectory results of run 4, however an increase in the value for *f* was also found for run 5. It has to be noted that the values for *h* and k_{sg} in Chapter 3 are the values for the puff region. However the concentration spread results in Chapter 5 indicated that the product of *h* and k_{sg} has the same value in the puff and thermal regions.

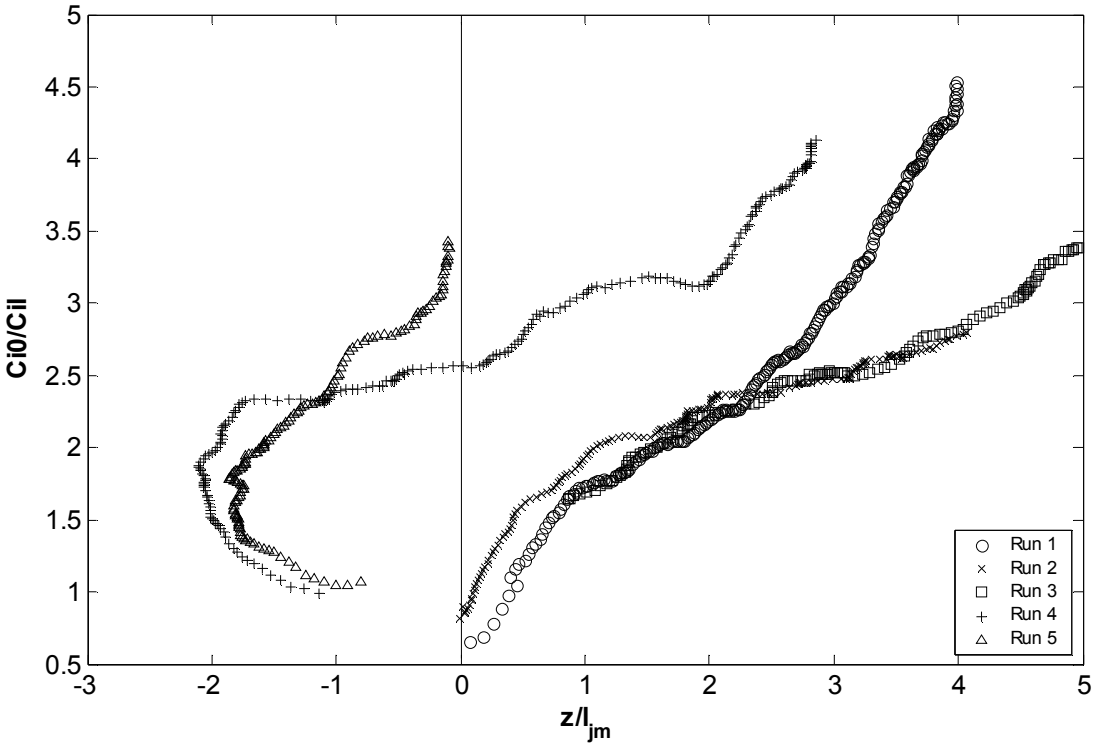

Figure 8.15 - *y*-integrated dilution results

The component of the initial excess momentum flux perpendicular to the direction of the ambient flow for runs 1, 2 and 3 is in the *y*-direction, and thus the jet to puff transition is determined based on the distance in that direction. To enable a direct comparison of runs 1, 2 and 3 with runs 4 and 5, in Figure 8.16, the angle of runs 4 and 5 between this component of the initial excess momentum flux and the *y*-axis has to be taken into account. This is achieved by non-dimensionalising distances moved in the *y*-direction by the component of the jet to puff transition length-scale in *x*-*y* plane ($l_{jm}cos(\beta_0)$). The definition of β_0 is given in Figure 4.1.

In the strong-jet region, the distance between the camera recording the *z*-integrated view and the flow changed continuously with increasing distance, and therefore the trajectory of the flow was not perpendicular to the camera. However runs 1, 2 and 3 were discharged in the plane perpendicular to the camera recording the *z*-integrated view. Therefore the change was only generated by the buoyancy-generated momentum flux and was relatively small. Note that the results from run 3 are lower than the results from run 2 in Figure 8.16, and this is consistent with the lower double-integrated results from run 3 (Figure 8.7). Runs 4 and 5 were discharged at an angle towards the camera recording the *z*-integrated view, and the change was therefore significant. However the theory of the angled jet (section 3.2.3.3) could not be applied to runs 4 and 5, because in the strong-jet region the initial excess momentum flux acts

in the opposite direction to the buoyancy-generated momentum flux, and therefore the angle of the flow in relation to the camera recording the z-integrated view changed rapidly. The results from the strong-jet region from runs 4 and 5 have therefore been omitted. The experimental results from the horizontal discharges (runs 1, 2 and 3) have a *z*-integrated dilution value of approximately 1.2 in the strong-jet region. This is consistent with the value found for the vertically discharged non-buoyant jet in a moving ambient (see Chapter 5).

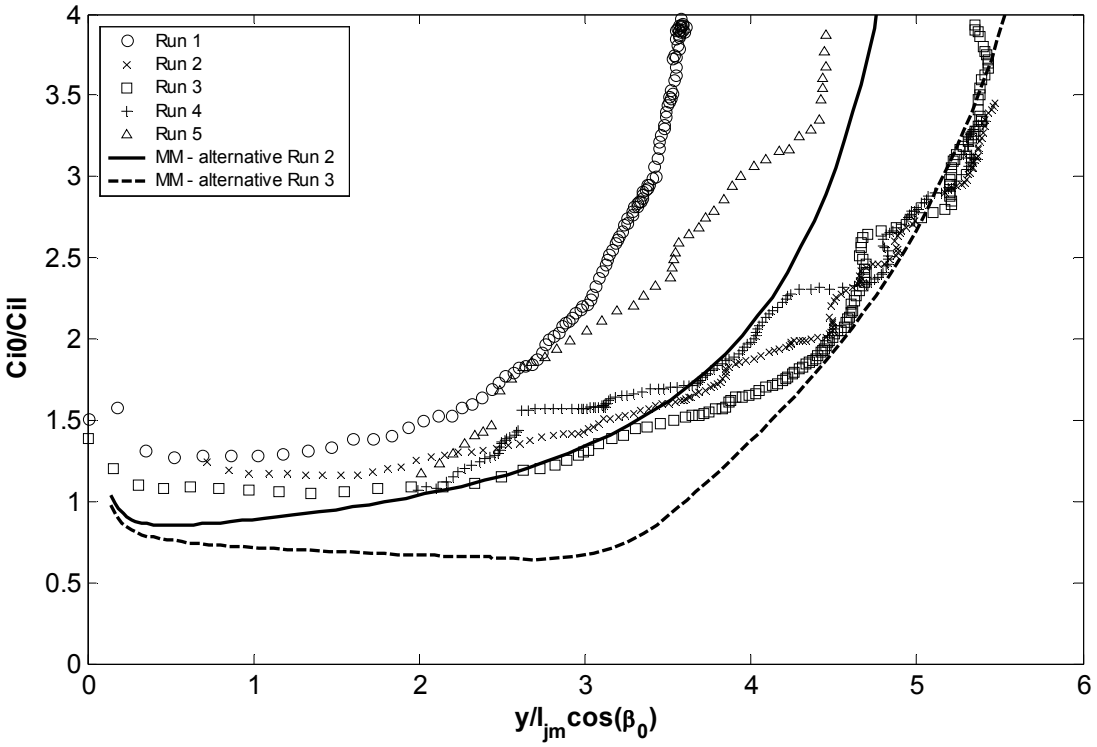

Figure 8.16 - *z*-integrated dilution results

As with Figure 8.15 , the effect of the formation of double-peak structures in the strongly advected region and the corresponding increase in entrainment is clearly visible in the integrated dilution results. This significant increase in integrated dilution is partly due to an increase in entrainment, but also because the increase in entrained ambient momentum flux changes the direction of the flow to travel pre-dominantly in the *x*-direction. The integrated dilution of run 1 is approximately constant up to 1.8 length-scales, agreeing well with the 1.9 length-scales found in Chapter 3. The results from runs 2 and 3 collapse reasonably well. The angle between the *y*-axis and the horizontal component of the initial excess momentum flux perpendicular to the ambient for runs 2, 3 and 4 is the same. Hence by plotting the *z*-integrated minimum dilution results from these runs versus the distance in the *y*-direction, made dimensionless by the projection of the jet to puff transition length-scale in *x*-*y* plane, the results collapse onto a single line. This indicates that the double-peak structures, visible in the

cross-sectional plot from run 4, would also have appeared for runs 2 and 3 if these flows had travelled further in the *z*-direction, and confirms the observations made regarding the cross-sectional plots from 2 and 3, moving towards the creation of a double-peak structure. It also indicates that the conclusions drawn from the double-integrated dilution results from run 2 are applicable to 4, and therefore that run 4 also reaches the advected thermal region via the advected plume region. This is consistent with the cross-sectional profiles of run 4, which did not show double-peak structures in the y-integrated direction (Figure 8.5).

The fact that the results from run 4 collapse reasonably well onto the results from runs 2 and 3 also suggests that the influence from the buoyancy-induced instabilities on the results of run 4 is reasonably small, because it is expected that buoyancy-induced instabilities will have had minimal effects on runs 2 and 3. As with the trajectory results, the *y*-integrated dilution results from run 5 appears not to match the expected behaviour nor the other experimental results.

The alternative *y*-integrated dilution Momentum Model prediction for runs 2 and 3 have been added to Figure 8.16. The alternative prediction of run 2 matches the experimental data reasonably well up to 4.2 length-scales downstream. After this point, the spread relationship predicts a rate of entrainment that is too high. This effect is consistent with the trajectory results of the alternative prediction, which also overestimated the rate of entrainment (Figure 8.11), however it appears to occur further downstream in the trajectory results (at approximately 4.7 length-scales). The alternative prediction for run 3 matches the experimental data reasonably well in the strongly advected region, however the match is not so good in the weakly advected region. The spread relationship used in this region is equation (4.36) and it depends on the angle ϕ_0. The experimental results in the weakly advected region are a better match with the alternative prediction for run 2, which does not depend on the angle ϕ_0. This suggests that the spread relationship in the weakly advected jet and plume regions does not depend on the angle ϕ_0.

8.4 – Summary

The 3D LA technique was used to carry out 5 buoyant jet experiments with a three-dimensional trajectory and each of these experiments had a different initial discharge angle. The first three were discharged horizontally with angles of 45°, 90° and 135° to the ambient flow. The final two, runs 4 and 5, were negatively buoyant jets that were discharged at 90° to the ambient flow, and had vertical angles of –45° and -60°.

Current modelling of buoyant jet flows with a two-dimensional path is based on the assumption that, after the release of the buoyant jet fluid into the receiving ambient, the buoyant jet passes through several distinct flow regions. Length-scales are used to define points of transition between these regions. However the cross-sectional profiles clearly showed that the sequence of flow behaviour evident for discharges with two-dimensional paths cannot be simply transferred to the equivalent three-dimensional flow. Of the experiments carried out as part of the current investigation, only the results from the run discharged horizontally and perpendicular to the ambient flow corresponded well with the assumptions made based on the length-scale theory. The horizontally discharged buoyant jet with an angle of 45° to the ambient flow had single Gaussian mean concentration cross-sectional profiles, where the flow was expected to be in the strongly advected puff and thermal regions and hence these profiles were expected to have a double-Gaussian form. The third horizontally discharged flow demonstrated similar cross-sectional behaviour to the second one. The negatively buoyant discharges were expected to become advected line momentum puffs before reaching the advected thermal region. In the puff region the cross-sectional concentration profiles were expected to have a double-peak. The double-peak was then expected to rotate when entering the advected thermal region as shown by the non-integrated cross-sectional profiles from Cheung. However the cross-sectional results only demonstrated a double-peak in the advected thermal region. In the puff region, the cross-sectional profiles were a reasonable match with the a single Gaussian profile.

The double-integrated dilution results confirmed the quality of the integrated dilution data. The double-integrated results also suggested that the flow sequence for runs 2 and 3 was jet to plume to thermal instead of the expected jet to puff to thermal. This result was consistent with the Gaussian cross-sectional profiles observed for runs 2 and 3. The double-integrated results from run 1 matched the length-scale theory expectations.

The models in their present form are clearly unable to adequately predict the behaviour of the flow with a three-dimensional path. The mixed success of the current theory to predict the cross-sectional and double-integrated dilution behaviour was confirmed by the trajectory results. The experimental trajectory results were compared with the results from the Momentum Model, VisJet and CorJet; these models are essentially based on the same assumptions as the length-scale theory. In all cases, the results showed that the models underestimated the influence of the buoyancy-generated momentum flux on the trajectory results in the x-z plane. However in the strongly advected region the trajectory predictions

from the Momentum Model ran approximately parallel to the experimental data. Further downstream the slope of the trajectory in the *x*-*z* plane of runs 1 and 4 decreased. This indicated that the dilution in the advected thermal region was higher than predicted, and may be linked to the higher than expected values found for *f* during the investigation of the mean cross-sectional profiles of run 1. The horizontally discharged runs with angles of 45°, and 135° to the ambient flow indicated that the models underestimated the distances travelled in the *y*-direction. This is consistent with the lower than expected entrainment of ambient fluid as a result of the single Gaussian cross-sectional profiles. In contrast, the trajectory results in the *x*-*y* plane of the negatively buoyant jet discharged at a vertical angle of –45° matched the model predictions, with the exception of the Momentum Model, reasonably well, while the models overestimated the distance travelled in the *y*-direction for the negatively buoyant jet discharged at a vertical angle of –60°.

Alternative Momentum Model predictions, created by altering the regional spread relationships, were added to the trajectory plots for runs 1, 2 and 3. The results showed that the current models may be capable of predicting the behaviour of buoyant jets with a three-dimensional path with reasonable accuracy, if the regional behaviour can be defined correctly. They also confirmed the extended weakly advected regions for runs 2 and 3

The *z*-integrated dilution results confirmed that runs 1, 4 and 5 reached the advected thermal region. In the advected thermal region, the integrated dilution was higher than the expected dilution. This indicated a higher than expected entrainment of ambient momentum flux in the advected thermal region, and is possibly related to the higher than expected values found for *f*. The *y*-integrated dilution results showed that, using the proper scaling, the results from runs 2, 3 and 4 collapse onto a single line, suggesting that the flow sequence of run 4 was also jet to plume to thermal. In addition the collapse also indicates that the buoyancy-induced instabilities had little effect on the results of run 4. The alternative Momentum Model predictions again indicated the extended weakly advected region evident in runs 2 and 3, as well as the change to the advected thermal region.

Chapter 9 – Conclusions

The overview of relevant research undertaken into the behaviour of buoyant jets released into an unstratified ambient revealed that there was extensive experimental data available, but also that there were flow configurations with limited or no available data. For flows with a two-dimensional trajectory (a flow for which it is possible to define a plane that encompasses the complete trajectory of the flow) these flow configurations were mainly oblique discharges both in a still and a moving ambient. In addition, relatively few studies have focused on the three-dimensional flow trajectory. Useful knowledge was gathered from the past experimental studies, but many of these were limited by the technology available at the time of the research.

A LA (light attenuation) flow visualization technique has been developed to complement the existing LIF (laser induced fluorescence) technique, for the investigation of buoyant jets with two and three-dimensional paths. The LA technique is based upon the relationship between the increase in dye concentration in the fluid and the decrease of light intensity. Calibration experiments have been carried out to determine the relationship between the increase in dye concentration and the loss in intensity, to explore the best possible set up, and to provide insights into the limitations of the method. The results from the calibration experiments show that the accuracy of the LA results is within 5% when employing a pixel-by-pixel calibration, and the integrated concentration is below the upper integrated concentration limit. It has been determined that the attenuation of light due to the presence of dye, depends on the temperature and the clarity of the water. However by keeping the temperature and clarity of the water constant during the calibration and the subsequent experiments, this dependence is taken into account. The main limitation is the relatively low upper limit of concentration of the red dye, which restricts the dynamic range of the system.

LA provides information that has been integrated over a flow depth, which makes the interpretation of the data obtained more challenging. To be able to use the integrated concentration data, the relationships for the non-integrated case are integrated and compared with the data; or alternatively the integrated data is transformed to non-integrated data, based on assumed forms of the concentration distribution, and compared with predictions from existing equations. Investigations into the behaviour of relatively simple weakly advected and

strongly advected flows have been used to examine the interpretation of the integrated information, and to assess the performance of LA in measuring buoyant jet behaviour. The internal concentration structure for a weakly advected flow is assumed to be Gaussian. The experimental concentration spread and integrated dilution results from a weakly advected jet experiment show that the integrated theory based on the Gaussian cross-sectional assumption is consistent with the experimental data. By transforming the data using the Gaussian assumption, the non-integrated dilution data matches existing theory, and the double-integrated dilution data matches the double-integrated dilution theory.

The internal concentration structure for a strongly advected flow resembles that of a vortex-pair. The mean concentration distribution of a vortex-pair has been approximated by a pair of stretched, merging Gaussians. Mean integrated cross-sectional concentration results from strongly advected puff experiments show that the approximation is a reasonable match with the experimental data from both the y-integrated and z-integrated perspective. The z-integrated cross-sectional profiles and the concentration spread results enable the constants, which define the distance between the peaks and the ratio of the spread in the y-direction to the spread in the z-direction, to be determined. Employing the double-Gaussian assumption, the existing relationships describing mean behaviour have been transformed into an integrated framework. The double-integrated, y-integrated, and z-integrated dilution results show that predictions from these transformed relationships are consistent with the experimental data. The alternative approach of transforming the experimental integrated dilution data into non-integrated data and comparing with existing theory also shows reasonable consistency.

An angled jet experiment has been carried out to investigate the accuracy of LA when the flow is no longer perpendicular to the camera view. The results of the experiment show that where the internal concentration profile and the angle between the flow and the camera are known, and the integrated concentration does not exceed the upper integrated concentration limit, LA can be confidently used to quantify the flow. Parallax issues have been investigated using the set up from the angled jet flow. The error due to parallax has been shown to be small and well within the maximum 5% error of the LA system.

The established LA system was also upgraded to a 3D LA system to visualize buoyant jets with a three-dimensional path. Again weakly advected and strongly advected flow experiments, with two-dimensional paths, have been used to help verify the system. The results show that the experimental data is consistent with the theory.

A new numerical model, the Momentum Model, has been developed to assist in the design and to monitor the performance of the experimental investigation. The Momentum Model is an integral model, but unlike existing integral models the behaviour of the flow is determined by the relative magnitudes of the initial excess momentum flux, the buoyancy-generated momentum flux and the entrained ambient momentum flux. Ordinary differential equations based on top-hat cross-sectional profiles have been derived with respect to the distance travelled along the path of the flow, determining the distance travelled in the x, y, and z-directions, the excess momentum flux, buoyancy-generated momentum flux, the entrained ambient momentum flux, the total momentum flux, density deficit flux and the volume flux. To close the set of equations the spread assumption has been employed. Separate expressions have been used for the spread in regions where the flow is Gaussian and double-Gaussian. The application of the relevant spread relationships per region is determined by the relative magnitudes of the momentum fluxes, that control the flow behaviour. The top-hat spreading rates for the model were determined by converting the appropriate Gaussian or double-Gaussian parameters. The use of the double-Gaussian profile as an approximation of the cross-sectional concentration profiles in the strongly advected regions (with the exception of the weak-jet) made it possible to determine minimum cross-sectional and minimum centreline dilutions, and to convert between the two. It also provided the basis for converting dilution predictions from other models, so that direct comparisons could be made.

Experiments investigating buoyant jets with two-dimensional trajectories (including jets and plumes) were carried out to expand available datasets, and to verify the accuracy of the Momentum Model and LA flow visualization technique before they were applied to flows with a three-dimensional path. Results obtained from the experimental investigation included trajectory, concentration spread and dilution data. The data from the current investigation has been compared with data from previous experimental investigations as well as two commercial numerical models, VisJet and CorJet.

The model predictions are generally consistent with each other and the current and previous experimental data, however, there were some notable discrepancies. Close to the transition from the weakly advected to the strongly advected region for vertically discharged non-buoyant jets in a moving ambient, the predictions from the Momentum Model are less accurate. The Momentum Model employs a single-point transition, while the concentration spread data shows that the transition zone begins at approximately 0.5 transition length-scales and ends at approximately 2.7 length-scales. For these flows it was also noted that, in the

transition region, the concentration spread on the downstream side is significantly larger than the concentration spread on the upstream side of the flow. The *y*-integrated dilution results show that in the weakly advected region of the non-buoyant discharge, the experimental data is approximately 50% higher than the prediction from the integrated dilution theory. However, the double-integrated dilution data is consistent with the theory, indicating the difference between the theory and the experimental integrated dilution values is related to the distorted cross-sectional profiles. These distortions are caused by the entrained ambient fluid.

Trajectory data obtained for horizontally discharged buoyant jets in a moving ambient has been used to obtain the top-hat spreading rate in the advected thermal region. This spreading rate is shown to be higher than the spreading rate in the puff region and necessitated separate puff and thermal regions in the spread relationship definitions for the puff and thermal regions in the Momentum Model. Data from these experiments also indicate that the entrainment rates employed by VisJet and CorJet in the advected thermal region result in spreading rates that are too low. The comparison of the trajectory data from the obliquely discharged buoyant jets in a moving ambient with the model predictions shows similar behaviour, although closer to the source the underestimation of the spreading rates by VisJet and CorJet is not as clearly visible. The different spreading rate in the thermal region is not associated with the *y*-integrated spread rate, because the *y*-integrated concentration data for the buoyant jets in a moving ambient indicates that the *y*-integrated concentration spread in the thermal region is the same as that in the puff region.

To provide a relatively simple alternative, analytical solutions have been developed to predict the behaviour of inclined negatively buoyant discharges in a still ambient. The comparison of the predictions from the analytical solutions with experimental data show that, at the location of the maximum centreline height, the predictions fall within the scatter of available experimental data for initial discharge angles ranging from 0° to 75°. The maximum height of the outer edge of the jet was also predicted with reasonable accuracy, indicating that the assumed growth rate of the outer jet edge is acceptable. CorJet and VisJet have been shown to provide trajectory predictions that were similar to, but lower than, those of the analytical solutions. Comparisons of the predicted location of the impact point with the experimental data show that the analytical solutions generally underestimate the distance to the impact point. In addition integrated dilution predictions from the analytical solutions at the centreline maximum height, and the impact point, have been shown to be conservative (by about 30%). More significantly the integrated dilution predictions from VisJet and CorJet appeared to be

considerably more conservative than those of the analytical solutions, with the numerical models indicating a reduction in integrated dilution as the flow approaches maximum height. Their integrated dilution predictions also show a dependence on initial discharge angle, which was not evident in either the analytical solutions or the experimental data. The conservative minimum integrated dilution predictions reflect an increasing influence of buoyancy-induced instabilities on the inner side of the jets, which generates additional vertical mixing and significantly alter the form of the mean concentration profiles in this region. VisJet, CorJet and the Momentum Model make the assumption of axi-symmetric cross-sectional profiles. The new experimental data shows that this assumption is not capable of generating accurate predictions of the behaviour of the negatively buoyant jet.

Analytical solutions have also been developed to study the transition between the different forms of strongly advected behaviour for non-buoyant oblique discharges in a moving ambient. The analytical solutions were employed to determine estimates for the theoretical transition angle. They indicated that for angles less than 18° the flow is in the weak-jet region after the transition from weakly advected to strongly advected region. For angles of 32° and higher, the analytical solutions indicated that the flow behaves like a puff in the strongly advected region. The experimental trajectory, concentration spread and integrated dilution data have been compared with the analytical solutions. The results from this comparison indicated that flows with an initial discharge angle of 20° and less become weak-jets in the strongly advected region, and flows with an initial discharge angle of 40° and above become advected line momentum puffs. These results are in reasonable agreement with the estimates for the theoretical transition angle. Both results suggest that for intermediate angles some form of combined strongly advected structure exists. The numerical models use different approaches to accomplish the transition between the different forms of strongly advected behaviour. The Momentum Model assumes weak-jet behaviour in the strongly advected region for all flows with an initial discharge angle of less than 25°. For higher angles the Momentum Model assumes puff behaviour. VisJet and CorJet assume a gradual transition between the horizontally discharged weak-jet and vertically discharged puff. Both approaches appear to predict the behaviour of the flow in the weak-jet region with reasonable accuracy. However in the puff region, the predictions from the Momentum Model are more consistent with the experimental data than the predictions from VisJet and CorJet. This indicates that the gradual transition approach is not appropriate in the puff region

The numerical models are based on the assumption that buoyant jet flows can be divided in distinct flow regions, and that these distinct flow regions are the same for flows with two-dimensional and three-dimensional paths. Therefore a numerical model capable of reasonably predicting the behaviour of a flow with a two-dimensional path is assumed to be capable of reasonably predicting the behaviour of a flow with a three-dimensional path. The experimental investigation of the buoyant jets with a three-dimensional path studied the validity of this assumption by comparing measured cross-sectional behaviour and the bulk properties of the flow with predictions. The cross-sectional profiles showed that the sequence of flow behaviour evident for discharges with two-dimensional paths cannot be simply transferred to the equivalent three-dimensional counterpart. Single peak structures were found where double-peak structures were expected to be, indicating an extended weakly advected region. The double-integrated results confirmed this and suggested that for some flow configurations the flow sequence was jet to plume to thermal instead of the expected jet to puff to thermal. The trajectory results confirmed these conclusions, as the numerical models underestimated the influence of the buoyancy-generated momentum flux. By altering the regional spread relationship of the Momentum Model it was shown that the current models may be capable of predicting the behaviour of buoyant jets with a three-dimensional path with reasonable accuracy, if the regional behaviour can be defined correctly.

The purpose of this thesis has been to increase the knowledge of the behaviour of buoyant jets with two-dimensional and three-dimensional trajectories. Progress has been made in understanding the behaviour of multiple flow configurations through the extensive experimental investigation carried out as part of the current study. In addition the double-Gaussian assumption, Momentum Model, and analytical solutions for negatively buoyant jets and obliquely discharged non-buoyant jets in a moving ambient have provided additional predictive tools.

However the study was necessarily restricted. The LA flow visualization technique and the Momentum Model both indicate the need for an increased understanding of the behaviour of the flow in transition regions. Without a proper understanding of the cross-sectional profiles within a transition region, it is not possible to determine the non-integrated dilution results from a LA experiment, nor is it possible to effectively convert assumed model concentration, velocity and spread scales to realistic equivalent. The Momentum Model assumes point transitions, therefore nullifying the need to model the flow in the transition region. However it was shown that this assumption limited the ability of the Momentum Model to accurately

predict the behaviour of the flow near the transition, especially for transition regions that are relatively long. The spread relationship of the Momentum Model should be upgraded to include gradual changes during the transitions, as well as defining appropriate conversion factors between the top-hat and equivalent Gaussian or double-Gaussian parameter in these transition regions.

The current study confirmed the existence of a transition region between the different forms of strongly advected behaviour of the non-buoyant jet in a moving ambient. An experimental investigation, including cross-sectional cuts of the flow, needs to be carried out to gain further insight into the combined strongly advected structure that occurs for intermediate angles. The experimental investigation into the behaviour of the negatively buoyant jet in a still ambient showed the effect buoyancy-induced instabilities have on cross-sectional concentration profiles and the bulk flow parameters. The models, based on axi-symmetrical cross-sectional profiles were not capable of accurately predict the behaviour of these flows. More sophisticated modelling techniques are therefore required to incorporate the effects of the buoyancy-induced instabilities.

The experiments with two-dimensional trajectories in a moving ambient showed that the double-Gaussian assumption is a reasonable approximation of the cross-sectional concentration profiles in the puff region. The experiments also determined that the spreading rate in the puff region was lower than the spreading rate in the thermal region, therefore more experimental research is necessary to determine the complete cross-sectional concentration profiles in the advected thermal region. Comprehension of the cross-sectional behaviour in the thermal region may also prove helpful in understanding the differences between the model predictions and the experimental results of the buoyant jets with three-dimensional trajectories. However, the overall understanding of discharges with three-dimensional trajectories is still limited and can only be increased further by additional experimental research.

References

Abbis, J. B., Bradbury, L. J. S., and Wright, M. P. "Measurements on an axisymmetric jet using a photon correlator." *Proceedings LDA Symposium*, Copenhagen, Denmark, 319-335.

Abraham, G. (1960). "Jet diffusion in liquid of greater density." *ASCE -- Proceedings -- Journal of the Hydraulics Division American Society of Civil Engineers -- Proceedings*, 86(HY6, Part 1), 1-13.

Abraham, G. (1963). "Jet diffusion in stagnant ambient fluid." *Publication 29, Series 1, Group 14, Section 14.42*, Delft Hydraulics Laboratory.

Abraham, G. (1967). "Jets with negative buoyancy in homogeneous ???" *Journal of Hydraulic Research*, IAHR 5, 235-248.

Albertson, M. L., Dai, Y. B., Jensen, R. A., and Rouse, H. (1949). "Diffusion of submerged jets." *American Society of Civil Engineers -- Proceedings*, 75(10), 1541-1548.

Anderson, J. L., Parker, F. L., and Benedict, B. A. (1973). "Negatively buoyant jets in a crossflow." Environmental Protection Technology Series, U. S. Environmental Protection Agency, Washington.

Antonia, R. A., and Bilger, R. W. (1973). "An experimental investigation of an axisymmetric jet in coflowing air stream." *Journal of Fluid Mechanics*, 61, 805-822.

Anwar, H. O. (1969). "Experiment on an effluent discharging from a slot into a stationary or slow moving fluid of greater density." *Journal of Hydraulic Research*, 7(4), 411-430.

Ayoub, G. M. (1971). "Dispersion of buoyant jets in a flowing ambient fluid," IPhD Thesis, Department of Civil Engineering, Imperial College of Science & Technology, University of London, London.

Baines, W. D., Turner, J. S., and Campbell, I. H. (1990). "Turbulent Fountains in an Open Chamber." *Journal of Fluid Mechanics*, 212, 557-592.

Baumgartner, D. J., Frick, W. E., and Roberts, P. J. W. (1993). "Dilution models for effluent discharges (second edition)." *EPA/600-R-93/139*, United States Environmental Protection Agency, ERL-Narragansett, Newport Oregon.

Becker, H. A., Hottel, H. C., and Williams, G. C. (1967). "Nozzle-fluid concentration field of round, turbulent, free jet." *Journal of Fluid Mechanics*, 30(Part 2), 285-303.

Birch, A. D., Brown, D. R., Dodson, M. G., and Thomas, J. R. (1978). "Turbulent concentration field of a methan jet." 88(pt 3), 431-449.

Biringen, S. "An experimental investigation of a turbulent round jet in a coflowing airstream." *The ASME winter annual meeting*, Anaheim, California, USA.

Capp, S. P. (1983). "Experimental Investigation of the Buoyant Axisymmetric Jet," University of Buffalo, State University of New York, Buffalo.

Cederwall, K. (1968). "Hydraulics of Marine Water Disposal." Hydraulics Division Report No. 42, Chalmers Institute of Technology, Sweden.

Cenedese, C., and Dalziel, S. (1998). "Concentration and depth fields determined by the light transmitted through a dyed solution." *Private Communication*.

Chen, J. C., and Rodi, W. (1980). *Turbulent buoyant jets - a review of experimental data*, Pergamon Press, Oxford.

Cheung, S. K. B., Leung, D. Y. L., Wang, W., Lee, J. H. W., and Cheung, V. "VISJET - a computer ocean outfall modelling system." *CGI 2000: The 18th Computer Graphics Internationa 'Humans and Nature', Jun 19-Jun 24 2000*, Geneva, Switz, 75-80.

Cheung, V. (1991). "Mixing a round buoyant jet in a current," PhD Thesis, Department of Civil and Structural Engineering, University of Hong Kong, Hong Kong.

Chu, P. C. K. (1996). "Mixing of Turbulent Advected Line Puffs," PhD Thesis, Department of Civil and Structural Engineering, The University of Hong Kong, Hong Kong.

Chu, P. C. K., Lee, J. H., and Chu, V. H. (1999). "Spreading of turbulent round jet in coflow." *Journal of Hydraulic Engineering*, 125(2), 193-204.

Chu, V. H. (1975a). "Three-dimensional forced plumes in a laminar crossflow." *Proceedings of the 16th International Association for Hydraulic Research (IAHR) Congress*, 5(paper 2.1), 31-38.

Chu, V. H. (1975b). "Turbulent dense plumes in a laminar cross flow." *Journal of Hydraulic Research*, 13(3), 263-279.

Chu, V. H., and Goldberg, M. B. (1974). "Buoyant forced plumes in crossflow." *American Society of Civil Engineers (ASCE), Journal of the Hydraulics Division*(122(1)), 27-34.

Chu, V. H., and Lee, J. H. W. (1996). "General integral formulation of turbulent buoyant jets in cross-flow." *American Society of Civil Engineers (ASCE), Journal of the Hydraulics Division*(122(1)), 27-34.

Cipollina, A., Brucato, A., Grisafi, F., and Nicosia, S. (2005). "Bench scale investigation of inclined dense jets." *Journal of Hydraulic Engineering*, 131(11), 1017-1022.

Corrsin, S. (1943). "Investigation of flow in an axially symmetric heated jet of air." *NACA wartime Report W-94*.

Corrsin, S., and Uberoi, M. S. (1950). "Further experiments on the flow and heat transfer in a heated turbulent air jet." *NACA Rep. 998*.

Crow, S. C., and Champagne, F. H. (1971). "Orderly structure in jet turbulence." *Journal of Fluid Mechanics*(48), 547-596.

Davidson, M. J. (1989). "The behaviour of single and multiple, horizontally discharged, buoyant flows in a non-turbulent coflowing ambient," Report 89-3, PhD Thesis, Department of Civil Engineering, University of Canterbury, Christchurch, New Zealand.

Davidson, M. J., Knudsen, M., and Wood, I. R. (1991). "Behaviour of a single, horizontally discharged, buoyant flow in a non-turbulent coflowing ambient fluid." *Journal of Hydraulic Research*, 29(4), 545-566.

Davidson, M. J., and Pun, K. L. (1998). "Hybrid model for prediction of initial dilutions from outfall discharges." *Journal of Hydraulic Engineering*, 124(12), 1188-1197.

Davidson, M. J., and Pun, K. L. (1999). "Weakly advected jets in cross-flow." *Journal of Hydraulic Engineering*, 125(1), 47-58.

Davidson, M. J., and Pun, K. L. (2000). "Locating discharge trajectories in still and moving ambient fluids." *Journal of Hydraulic Engineering*, 126(7), 513-524.

Davidson, M. J., and Wang, H. J. (2002). "Strongly advected jet in coflow." *Journal of Hydraulic Engineering*, 128(8), 742-752.

Doneker, R. L., and Jirka, G. H. (1990). "An expert system for hydrodynamic mixing zone analysis of conventional and toxic submerged single port discharges (CORMIX 1)." *Technical Report EPA/600/3-90/012*, Environmental Research Laboratory, United States Environmental Protection Agency, Athens, Georgia.

Fan, L. N. (1967). "Turbulent buoyant jets into stratified or flowing ambient fluids." *KH-R-15*, W. M. Keck Laboratory of Hydraulic and Water Resources, California Institute of Technology, Pasadena, California.

Fan, L. N., and Brook, N. H. (1969). "Numerical solutions of turbulent buoyant jet problems." *KH-R-18*, W. M. Keck Laboratory of Hydraulic and Water Resources, California Institute of Technology, Pasadena, California.

Fischer, H. B., Imberger, J., List, E. J., and Brook, N. H. (1979). *Mixing in Inland Coastal Waters*, Academic Press, London.

Fisher, T. S. R. (1995). "Dilution of axisymmetric buoyant jets and surface spreading fields," ME Thesis, Department of Civil Engineering, University of Canterbury, Christchurch, New Zealand.

Forstall, W., and Gaylord, E. W. "Momentum and mass transfer in submerged water jet." *American Society of Mechanical Engineers -- Meeting A-38, Nov 28-Dec 3 1954*, 4.

Förthmann, E. (1934). "Uber turbulente Strahlausbreitung." *Ing.-Arch*(5), 42-54.

Frankel, R. J., and Cumming, J. D. (1965). "Turbulent mixing phenomena of ocean outfalls." *American Society of Civil Engineers Proceedings, Journal of the Sanitary Engineering Division American Society of Civil Engineers -- Proceedings*, 91(SA2, Part 1), 33-59.

Gaskin, S. (1995). "Single buoyant jet in a crossflow and the advected line thermal," PhD Thesis, Department of Civil Engineering, University of Canterbury, Christchurch, New Zealand.

Gaskin, S., McKernan, M., and Xue, F. (2004). "The effect of background turbulence on jet entrainment: an experimental study of a plane jet in a shallow coflow." *Journal of Hydraulic Research*, 42(5), 531-540.

Gaskin, S., and Wood, I. R. "Advected line thermals in non-turbulent and turbulent ambient." *11th Australasian Conference on Coastal and Ocean Engineering. Part 1 (of 2), Aug 23-27 1993*, Townsville, Queensland, Australia, 147-152.

George, W. K., Alpert, R. L., and Tamanini, F. (1977). "Turbulence measurements in an axisymmetric plume." *International Journal of Heat Mass Transfer*(20), 1145-1154.

Görtler, H. (1942). "Berechnung von Aufgaben der freien Turbulenz aus Grund eienes neuen Näherungsansatzes." *ZAMM*(22), 244-254.

Hansen, J., and Schroder, H. (1968). "Horizontal jet dilution studies by use of radioactive isotopes." *Acta Polytechnica Scandinavica, Civil Engineering and Building Construction Series Ci 49*, 24.

Hewett, T. A., Fay, J. A., and Hoult, D. P. (1971). "Laboratory experiments of smokestack plumes in a stable atmosphere." *Atmospheric Environment*(5), 767-789.

Hintze, J. O., and van der Hegge Zijnen, B. G. (1949). "Transfer of heat and matter in the turbulent mixing zone of an axially symmetric jet." *Applied Science Research*(A1), 435-461.

Hofer, K., and Hutter, K. (1981). "Turbulent jet diffusion in stratified quiescent ambients, Part II: Experiments." *Journal of Non-Equilibrium Thermodynamics*, 6, 49-64.

Hoult, D. P., Fay, J. A., and Forney, L. J. (1969). "A theory of plume rise compare with field observations." *Journal of Air Pollution Control Association*, 19, 585-590.

Hung, W. K. (1998). "A jet at an oblique angle to a cross-flow," Civil Engineering Department, The Hong Kong University of Science and Technology, Hong Kong.

Hussein, H. J., Capp, S. P., and George, W. K. (1994). "Velocity measurements in a high-Reynolds number, momentum-conserving, axisymmetric, turbulent jet." *Journal of Fluid Mechanics*, 258, 31-75.

James, W. P., Vergara, I., and Kim, K. (1983). "Dilution of a dense vertical jet." *Journal of Environmental Engineering*, 109(6), 1273-1283.

Jirka, G. H. (2004). "Integral Model for Turbulent Buoyant Jets in Unbounded Stratified Flows Part 1: Single Round Jet." *Journal of Environmental Fluid Mechanics*(4), 1-56.

Jordinson, R. (1956). "Flow in a jet directed normal to a wind." *Technical Report R & M*, 3074.

Keffer, J. F., and Baines, W. D. (1963). "The round turbulent jet in a cross-wind." *Journal of Fluid Mechanics*, 15(4), 481-497.

Kikkert, G. A., Davidson, M. J., and Nokes, R. I. (2006a). "Characterising strongly-advected discharges in the initial dilution zone." *Submitted to: Environmental Fluid Mechanics*.

Kikkert, G. A., Davidson, M. J., and Nokes, R. I. (2006b). "Inclined Negatively Buoyant Discharges." *Submitted to: Journal of Hydraulic Engineering*.

Kiser, K. M. (1963). "Material and momentum transport in axisymmetric turbulent jets of water." *A.I.Ch.E. Journal*, 9(3), 386-390.

Knudsen, M. (1988). "Buoyant horizontal jets in an ambient flow," Report 88-7, PhD Thesis, Department of Civil Engineering, University of Canterbury, Christchurch, New Zealand.

Labus, T. L., and Symons, E. P. (1972). "Experimental Investigation of an axisymmetric free jet with an Initially Uniform Velocity Profile." *NASA TN D-6783*.

Lam, K. M., and Chan, C. H. C. (2002). "Time-averaged mixing behavior of circular jet in counterflow: Velocity and concentration measurements." *Journal of Hydraulic Engineering*, 128(9), 861-865.

Lassiter, L. W. (1957). "Turbulence in small air jets at exit velocities up to 705 feet per second." *ASME -- Transactions -- Journal of Applied Mechanics*, 24(3), 349-354.

Law, A. W.-K., and Wang, H. (2000). "Measurement of mixing processes with combined digital particle image velocimetry and planar laser induced fluorescence." *Experimental Thermal and Fluid Science*, 22(3), 213-229.

Liseth, P. (1970). "Mixing of merging buoyant jets from a manifold in stagnant receiving water of uniform density." Hydraulic Engineering Laboratory, College of Engineering, University of California, Berkeley.

Margason, R. J. (1968). "The path of a jet directed at large angles to a subsonic free stream." *NASA TN D-4919*.

McLellan, T. N., and Randal, R. E. (1986). "Measurement of brine jet height and dilution." *Journal of Waterway Port Coastal and Ocean Engineering*, 112, 200-216.

Morton, B. R., Taylor, G. I., and Turner, J. S. (1956). "Turbulent gravitational convection from maintained and instantaneous sources." *Proceedings of the Royal Society of London*(A 234), 1-23.

Muellenhoff, W. P., Soldate, J., A. M., Baumgartner, D. J., Schuldt, M. D., Davis, L. R., and Frick, W. E. (1985). "Initial mixing characteristics of municipal discharges." *Vol. I and II, EPA-600/3-85-073a*, United States Environmental Protection Agency, Newport, Oregon.

Nakagome, H., and Hirata, M. "The structure of turbulent diffusion in an axisymmetrical thermal plume." *Proceedings of 1976 ICHMT Seminar on Turbulent Buoyant Convection*, 361-372.

Nickels, T. B., and Perry, A. E. (1996). "Experimental and theoretical study of the turbulent coflowing jet." *Journal of Fluid Mechanics*, 309, 157-182.

Nokes, R. I. (2005). "ImageStream Version 4.01." Christchurch, Image Processing Software.

Panchapakesan, N. R., and Lumley, J. L. (1993). "Turbulent measurements in axisymmetric jets of air and helium. Part 1: air jet." *Journal of Fluid Mechanics*, 246, 197-223.

Papanicolaou, P. N. (1984). "Mass and momentum transport in a turbulent buoyant vertical axisymmetric jet," PhD Thesis, W.M. Keck Laboratory of Hydraulic and Water Resources, California Institute of Technology, Pasadena, California.

Papanicolaou, P. N., and List, E. J. (1988). "Investigations of round vertical turbulent buoyant jets." *Journal of Fluid Mechanics*, 195, 341-391.

Papantoniou, D., and List, E. J. (1989). "Large-scale structure in the far field of buoyant jets." *Journal of Fluid Mechanics*(209), 151-190.

Papps, D. A. (1995). "Merging buoyant jets in stationary and flowing ambient fluids," PhD Thesis, Department of Civil Engineering, University of Canterbury, Christchurch, New Zealand.

Platten, J. L., and Keffer, J. F. (1971). "Deflected turbulent jet flows." *Journal of Applied Mechanics*, 38(4), 756-8.

Poynton, C. A. (1996). *A technical introduction to digital video*, John Wiley & Sons Inc, New York.

Pratte, B. D., and Baines, W. D. (1967). "Profiles of round turbulent jet in cross flow." *American Society of Civil Engineers Proceedings, Journal of the Hydraulics Division American Society of Civil Engineers -- Proceedings*, 93(HY6), 53-64.

Pun, L. K. (1998). "Hybrid models for jets and plumes in a flowing ambient fluid," PhD Thesis, Department of Civil Engineering, The Hong Kong University of Science and Technology, Hong Kong.

Reichardt, H. (1942). "Gesetzmäßigkeiten der freien Turbulenzen." *VDI-Forschungsheft*(414).

Reichardt, H. (1943). "On new theory of free turbulence." *Royal Aeronautical Society -- Journal*, 47(390), 167-176.

Richards, R. S. (1963). "Experiment on the motion of isolated cylindrical thermals through unstratified surroundings." *International Journal of Air & Water Pollution*(7), 17-34.

Ricou, F. P., and Spalding, D. B. (1961). "Measurements of entrainment by axisymmetrical turbulent jets." *Journal of Fluid Mechanics*, 11(Part 1), 21-32.

Roberts, P. J. W., Ferrier, A., and Daviero, G. (1997). "Mixing in inclined dense jets." *Journal of Hydraulic Engineering*, 123(8), 693-699.

Roberts, P. J. W., and Toms, G. (1987). "Inclined dense jets in flowing current." *Journal of Hydraulic Engineering*, 113(3), 323-341.

Rosler, R. S., and Bankoff, S. G. (1963). "Large Scale Turbulence Characteristics of a Submerged Water Jet." *A.I.Ch.E. Journal*, 9(5), 672-676.

Rouse, H., Yih, C. S., and Humphreys, H. W. (1952). "Gravitational convection from a boundary source." *Tellus*(4), 201-210.

Schmidt, W. (1941). "Turbulente Ausbreitung eines Stromes erhitzter Luft." *ZAMM*(21), 265-271.

Scorer, R. S. (1959). "Behaviour of chimney plumes." *International Journal of Air Pollution*, 1(3), 198-220.

Simoens, S., and Ayrault, M. (1994). "Concentration flux measurements of a scalar quantity in turbulent flows." *Experiments in Fluids*, 16, 273-281.

Smith, D. J., and Hughes, T. (1977). "Some measurements in a turbulent circular jet in the presence of a coflowing free stream." *Aeronautical Quarterly*, 28, 185-196.

Sunavala, P. D., Hulse, C., and Thring, M. W. (1957). "Mixing and combustion in free and enclosed turbulent jet diffusion flames." *Combustion and Flame*, 1(2), 179-193.

Tian, X., and Robert, J. W. (2003). "A 3D LIF system for turbulent buoyant jet flows." *Experiments in Fluids*, 35, 636-647.

Tollmien, W. (1926). "Calculation of turbulent unconfined flow Berechnung turbulenter Ausbreitungsvorgange." *Zeitschrift fur Angewandte Mathematik und Mechanik*, 6(6), 468-478.

Turner, J. S. (1960). "Comparison between buoyant vortex rings and vortex pairs." *Journal of Fluid Mechanics*, 7(Part 3), 419-432.

Turner, J. S. (1966). "Jets and plumes with negative or reversing buoyancy." *Journal of Fluid Mechanics*, 26, 779-792.

van Cruyningen, I., Lozano, A., and Hanson, R. K. (1990). "Quantitative imaging of concentration by planar laser-induced fluorescence." *Experiments in Fluids*, 10(1), 41-49.

Wallingford Hydraulic Research Station. (1977). "Horizontal outfalls in flowing water." Hydraulic Research Station.

Wang, H. (2000a). "Investigations of buoyant jet discharges using digital particle image velocimetry (DPIV) and planar laser induced fluorescence (PLIF)," PhD Thesis, School of Civil and Structural Engineering, Nanyang Technological University, Singapore.

Wang, H., and Law, A. W. K. (2002). "Second-order integral model for a round buoyant jet." *Journal of Fluid Mechanics*, 459, 397-428.

Wang, H. J. (2000b). "Jet interaction in a still or co-flowing environment," PhD Thesis, Department of Civil Engineering, The Hong Kong University of Science and Technology, Hong Kong.

Wong, C.-f., and Lee, J. H. W. "Experiments on advected line thermals." *Proceedings of the International Symposium on Environmental Hydraulics, Dec 16-18 1991*, Hong Kong, 153.

Wood, I. R. (1993). "Asymptotic solutions and behavior of outfall plumes." *American Society of Civil Engineers (ASCE), Journal of the Hydraulics Division*(119(5)), 555-580.

Wright, S. J. (1977). "Effects of ambient crossflow and density stratification on the characteristic behavior of round turbulent buoyant jets." W. M. Keck Laboratory of Hydraulic and Water Resources, California Institute of Technology, Pasadena, California.

Wygnanski, I., and Fiedler, H. (1969). "Some measurements in the self-preserving jet." *Journal of Fluid Mechanics*, 38(pt 3), 577-612.

Yoda, M., and Fiedler, H. E. (1996). "Round jet in a uniform counterflow: Flow visualization and mean concentration measurements." *Experiments in Fluids*, 21(6), 427-436.

Zeitoun, M. A., Reid, R. O., McHilhenny, W. F., and Mitchell, T. M. (1972). "Model studies of ocean outfall systems for desalination plants." Office of Saline Water, U.S. Department of the Interior, Washington D.C.

Zhang, H., and Baddour, R. E. (1998). "Maximum penetration of vertical round dense jets at small and large Froude numbers." *Journal of Hydraulic Engineering*, 124(5), 550-553.

Zhang, J.-B., and Chu, V. H. (2003). "Shallow turbulent flows by video imaging method," American Society of Civil Engineers.

Zimm, W. (1921). "Flow phenomena in free air currents Ueber die Stromungsvorgange." *Forschungsarbeiten auf dem Gebiete des Ingenieurwesens*(234), 36.

Appendix A – Coding and Reproducing Digital Images

The following is an introduction into the relevant operations of coding and reproducing digital images. A more thorough description can be found in Poynton (1996).

When the ray of light reaches the camera, the camera will perceive it as a Spectral Power Distribution (SPD). Visible light for the human eye has a wavelength between 400 nanometres and 700 nanometres and it depends on the SPD what colour the eye perceives. Wavelengths between 400 and 500 nanometres are perceived as blue by the human eye, wavelengths between 500 and 600 nanometres green and between 600 and 700 nanometres red. Figure A.1 is an example of a SPD. This distribution shows what a standard person perceives as a bright yellow-green as determined by the CIE (Commission International de L'eclairage or International Commission on Illumination). The camera will receive a SPD for each pixel and transforms these into digital data. In order to do that the continuous SPD has to be broken up into different components so that a finite amount of data can define the SPD and thus be stored. A possible solution could have been to break a SPD up into 31 components all storing an average value over a range of 10 nanometres. But due to the trichromatic nature of vision, three components are enough if the appropriate spectral weighing functions are used (Poynton, 1996). The three components together are called a tristimulus.

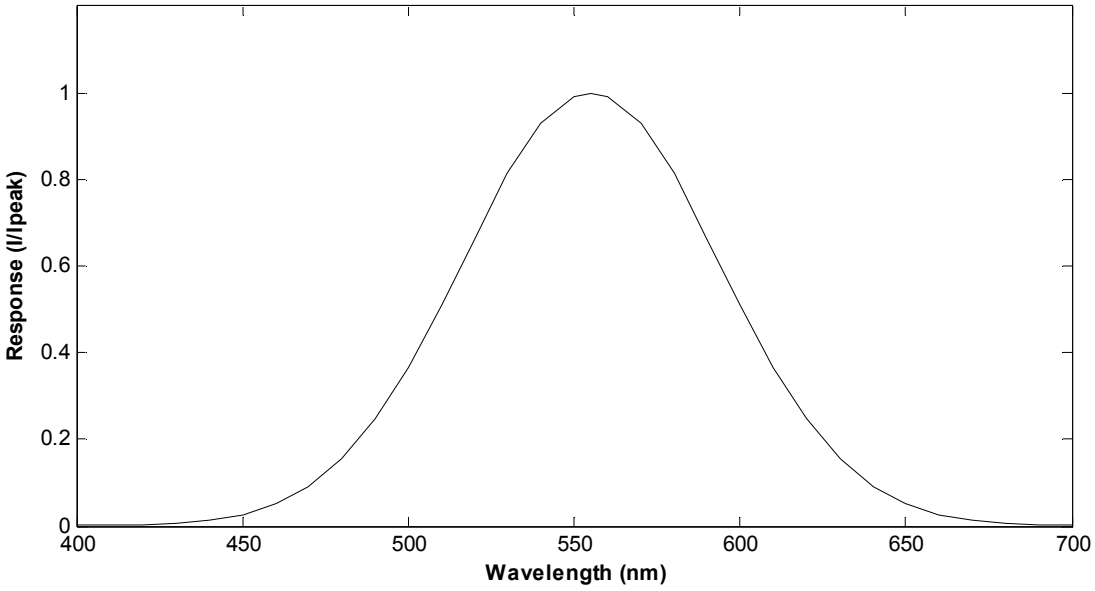

Figure A.1 - The CIE luminous efficiency function

Figure A.2 (figure 7.3, Poynton, 1996) shows that not just any three spectral weighing functions can be chosen. If a wideband filter with three peaks (one in the blue region, in the green and in the red) is chosen, as is shown in the top row of Figure A.2, two monochromatic colours with wavelengths of 610 and 620 nanometres respectively will both be filtered out as red, while in actual fact the first one is orange. If a narrowband filter is chosen, as shown in the middle row in Figure A.2, the problem of the wideband filter is solved but it creates a different problem. The monochromatic colour with a wavelength of 610 nanometres falls between the filters and thus will be reproduced as black.

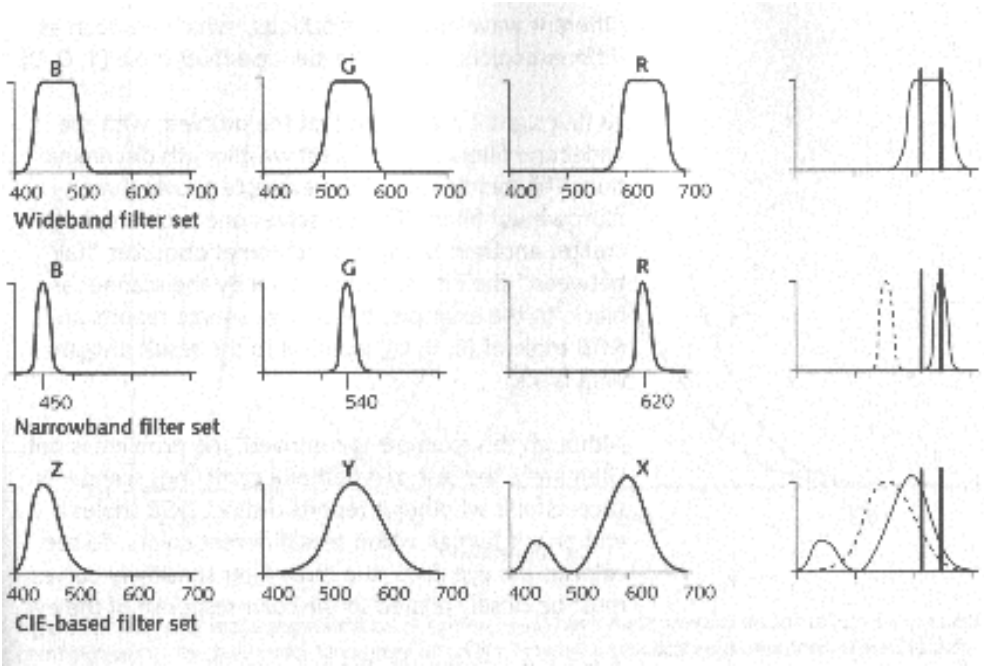

Figure A.2 - Examples of Spectral Weighing Functions (Poynton, 1996)

Thus to always see a colour as the eye would, the response of the filters must be similar to the response of the human eye. The CIE has determined the spectral response curves that do just that for a standard observer, the CIE-based filter set. Together they form the Colour Matching Function enlarged in Figure A.3 (figure 7.4, Poynton, 1996). For a camera to capture all colours, the spectral response curves of the camera must be as shown in Figure A.3 or a linear combination of them. However this is not viable in practice. In practice a different tristimulus XYZ is calculated from x-bar, y-bar, z-bar, where X is obtained by integrating its SPD weighted by the x-bar Matching Function etc. But the tristimulus XYZ turned out to be not perceptual uniform. A system is perceptually uniform if a small perturbation to a component value is approximately equally perceptible across the range of that value. To optimise this further transformations are done to create Tristimuli called L*u*v and L*a*b where L is the luminance or brightness. But complexities make these Tristimuli not suitable for image

coding. Instead R'G'B' is used as it is quite perceptually uniform and is fast enough for interactive applications. R'G'B' is approximately the 0.45 power-law of RGB. RGB is related to XYZ with a 3x3 matrix.

.

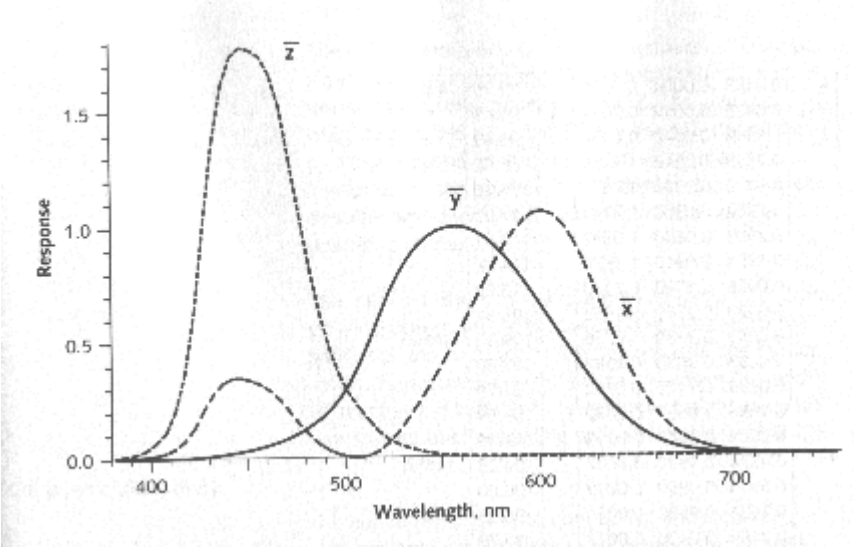

Figure A.3 - CIE colour matching function (Poynton, 1996)

The Tristimulus gives the three components that represent colour. Using these three components it is possible to reproduce the colours (and thus the picture) using the computer. Simplest way of doing that is by adding and mixing the beams of light of the three different colours. There is no need for the original SPD, just the Tristimulus. This is the case with a projector. Computer screens for example work differently. Still the three components are mixed together to form the colours, but the screen itself consists of small dots that produce red, green and blue light. From a distance the viewer will only see the new colours.

The actual transformation that goes on in both the coding of the colour, as well as the reproduction of it are a few steps more complicated than explained above but are based on the same theories.

Appendix B – Analysis of Average Integrated Concentration Image

```
clear;
warning off MATLAB:polyfit:RepeatedPointsOrRescale;

                                % Standard Grid Parameters:
XCoordinateOfGrid = 0;          % Origin x coordinate (mm)          = 0.0
YCoordinateOfGrid = 0;          % Origin y coordinate (mm)          = 0.0
XInterpolationOfGrid = .530;    % Interpolation points x spacing (mm)  = 0.53
YInterpolationOfGrid = .530;    % Interpolation points y spacing (mm)  = 0.53
XPointsInGrid = 1268;           % Number of x points                = 1268
YPointsInGrid = 1024;           % Number of y points                = 1024

XConversion = 1;                % Conversion factor from pixels to mm in x-direction
YConversion = 1;                % Conversion factor from pixels to mm in y-direction
d = 2.45;                       % Enter the diameter of the source (mm)
EndOfSourceXPosition = 342.61;  % Enter the distance from x-boundary to the end of the source outlet (mm)
EndOfSourceYPosition = 987.53;  % Enter the distance from y-boundary to the end of the source outlet (mm)
TrajectoryAngle=90/180*pi;      % Enter Initial Angle of trajectory
CrossSectionPoints=400;         % Enter Amount of point in the cross-section
StepSize = 10;                  % Enter Step size for iteration process (mm)
CrossSectionLength = 400;       % Enter Length of Cross-Section (mm)

Z = dlmread('MP LA - Run 22.txt ', ';');    % Import Average Integrated Concentration Image as txt-file,
                                            % generated in ImageStream

[m,n]=size(Z);                  % Assign the number of columns to n
Z(:,n)=[];                      % Delete last column
Z(:,1)=[];                      % Delete first column

X=Z(1,:)*XConversion;           % Assign horizontal grid numbers to row-vector B and convert in mm
Y=Z(:,1)*YConversion;           % Assign vertical grid numbers to column-vector C and convert in mm

                                % From now on everything is in mm

Z(1,:)=[];                      % Delete horizontal grid numbers from matrix
Z(:,1)=[];                      % Delete vertical grid numbers from matrix
X(:,1)=[];                      % Delete first zero in row-vector
Y(1,:)=[];                      % Delete first zero in column-vector
```

```
[m,n]=size(Z);                  % Reassign the number of columns to n and rows to m

i=1;                            % Step Counter

XPositionOfTrajectory(i,:)=EndOfSourceXPosition;        % Assign value to x-coordinate of first step
YPositionOfTrajectory(i,:)=EndOfSourceYPosition;        % Assign value to y-coordinate of first step
CrossSectionMaximum=interp2(X,Y,Z,EndOfSourceXPosition,EndOfSourceYPosition);
                                                        % Assign value to CrossSectionMaximum
Ci(i,:)=interp2(X,Y,Z,XPositionOfTrajectory(i,:),YPositionOfTrajectory(i,:))
                                                        % Determine integrated concentration at first step

% Using the current x and y coodinates of the trajectory as a center, a vector showing the gradient between the
% current  step and next step is determined as a function of possible trajectory angles

TrajectoryAngleOld=pi/4+0/180*pi;
for j=1:81
        TrajectoryAngle=TrajectoryAngleOld-(j-1)*pi/160
        GradientPositionVector(j,:)=j;
        TrajectoryAngleVector(j,:)=TrajectoryAngle;
        GradientVector(j,:)=(CrossSectionMaximum-
interp2(X,Y,Z,cos(TrajectoryAngle)*StepSize+XPositionOfTrajectory(i,:),sin(TrajectoryAngle)*StepSize+YPos
itionOfTrajectory(i,:)))/(StepSize);
end

% Find minimum gradient and its respective angle. This angle will be thecurrent trajectory angle old.

GradientMinimum=min(GradientVector(:,i),[],1);
                % Find minima in gradient vector
MinimumIsOneInGradientVector=(GradientVector(:,i)==GradientMinimum);
                % Make all non-minimum values zero and minimum-values one in gradient vector
MinimumAdded=MinimumIsOneInGradientVector'*GradientPositionVector(:,i);
                % Multiply inimum gradient vector times position vector
clear Ones
Ones(1:51,1)=1;  % Create ones vector
MinimumMultiplier=MinimumIsOneInGradientVector'*Ones;
                % Multiply minimum gradient vector times ones vector
MinimumGradientPosition=MinimumAdded./MinimumMultiplier;
                % Divide minimum added by minimum multiplier to find position of the minimum gradient

TrajectoryAngleOld(i,:) = interp1(GradientPositionVector,TrajectoryAngleVector,MinimumGradientPosition);
% Find current trajectory angle old by inserting position of minimum gradient in the trajectory angle vector
```

```
while i<7

% For the first seven steps the x and y coordinates and the trajectory angle old are calculated.

   clear MinimumIsOneInGradientVector
   clear GradientPositionVector
   clear GradientVector
   clear TrajectoryAngleVector
   clear Ones
   i=i+1

% Determine current x and y coordinates of trajectory and integrated concentration at those coordinates

   XPositionOfTrajectory(i,:)=XPositionOfTrajectory(i-1,:)+cos(TrajectoryAngleOld(i-1,:))*StepSize;
   YPositionOfTrajectory(i,:)=YPositionOfTrajectory(i-1,:)+sin(TrajectoryAngleOld(i-1,:))*StepSize;
   Cl(i,:)=interp2(X,Y,Z,XPositionOfTrajectory(i,:),YPositionOfTrajectory(i,:))

% Using the current x and y coordinates of the trajectory as a center, a vector showing the gradient between the
%  current step and next step is determined as a function of possible trajectory angles

   for j=1:81
      TrajectoryAngle=TrajectoryAngleOld(i-1,:)+1/4*pi-(j-1)*pi/160;
      GradientPositionVector(j,:)=j;
      TrajectoryAngleVector(j,:)=TrajectoryAngle;
      GradientVector(j,:)=(interp2(X,Y,Z,XPositionOfTrajectory(i,:),YPositionOfTrajectory(i,:))-
interp2(X,Y,Z,cos(TrajectoryAngle)*StepSize+XPositionOfTrajectory(i,:),sin(TrajectoryAngle)*StepSize+YPos
itionOfTrajectory(i,:)))/(StepSize);
   end

% Find minimum gradient and its respective angle. This angle will be the current trajectory angle old.

   GradientMinimum=min(GradientVector,[],1);
                  % Find minima in gradient vector
   MinimumIsOneInGradientVector=(GradientVector==GradientMinimum);
                  % Make all non-minimum values zero and minimum-values one in gradient vector
   MinimumAdded=MinimumIsOneInGradientVector'*GradientPositionVector;
                  % Multiply inimum gradient vector times position vector
   clear Ones
   Ones(1:j,1)=1; % Create ones vector
   MinimumMultiplier=MinimumIsOneInGradientVector'*Ones;
                  % Multiply minimum gradient vector times ones vector
   MinimumGradientPosition=MinimumAdded./MinimumMultiplier;
```

```
                % Divide minimum added by minimum multiplier to find position of the minimum gradient

   TrajectoryAngleOld(i,:)                                                                    =
interp1(GradientPositionVector,TrajectoryAngleVector,MinimumGradientPosition);
% Find current trajectory angle old by inserting position of minimum gradient in the trajectory angle vector
end

while i<700

   clear MinimumIsOneInGradientVector
   clear GradientPositionVector
   clear GradientVector
   clear TrajectoryAngleVector
   clear Ones

% The trajectory angle (new) is recalculated using the trajectory angles (old) from the three steps back to
%  three steps forward in the analysis. The trajectory angle new is less dependent on the grid makeup of
% the data.

   TrajectoryAngleNew(i-2,:)=(TrajectoryAngleOld(i,:)+TrajectoryAngleOld(i-1,:)+TrajectoryAngleOld(i-
2,:)+TrajectoryAngleOld(i-3,:)+TrajectoryAngleOld(i-4,:)+TrajectoryAngleOld(i-5,:)+TrajectoryAngleOld(i-
6,:))/7;

   i=i+1

% Determine current x and y coordinates of trajectory using both trajectory angle old and trajectory angle new

   XPositionOfTrajectory(i,:)=XPositionOfTrajectory(i-1,:)+cos(TrajectoryAngleOld(i-1,:))*StepSize;
   YPositionOfTrajectory(i,:)=YPositionOfTrajectory(i-1,:)+sin(TrajectoryAngleOld(i-1,:))*StepSize;
   XPositionOfTrajectory(i-3,:)=XPositionOfTrajectory(i-4,:)+cos(TrajectoryAngleNew(i-3,:))*StepSize
   YPositionOfTrajectory(i-3,:)=YPositionOfTrajectory(i-4,:)+sin(TrajectoryAngleNew(i-3,:))*StepSize

% Using the current x and y coordinates of the trajectory as a center, based on trajectory angle old , a vector
% showing the gradient between the current step and next step is determined as a function of possible trajectory
% angles

   for j=1:81
      TrajectoryAngle=TrajectoryAngleOld(i-1,:)+1/4*pi-(j-1)*pi/160;
      GradientPositionVector(j,:)=j;
      TrajectoryAngleVector(j,:)=TrajectoryAngle;
```

```
    GradientVector(j,:)=(interp2(X,Y,Z,XPositionOfTrajectory(i,:),YPositionOfTrajectory(i,:))-
interp2(X,Y,Z,cos(TrajectoryAngle)*StepSize+XPositionOfTrajectory(i,:),sin(TrajectoryAngle)*StepSize+YPos
itionOfTrajectory(i,:)))/(StepSize);
  end

% Find minimum gradient and its respective angle. This angle will be the current trajectory angle old.

  GradientMinimum=min(GradientVector,[],1);
                % Find minima in gradient vector
  MinimumIsOneInGradientVector=(GradientVector==GradientMinimum);
                % Make all non-minimum values zero and minimum-values one in gradient vector
  MinimumAdded=MinimumIsOneInGradientVector'*GradientPositionVector;
                % Multiply inimum gradient vector times position vector
  Ones(1:j,1)=1; % Create ones vector
  MinimumMultiplier=MinimumIsOneInGradientVector'*Ones;
                % Multiply minimum gradient vector times ones vector
  MinimumGradientPosition=MinimumAdded./MinimumMultiplier;
                % Divide minimum added by minimum multiplier to find position of the minimum gradient

  TrajectoryAngleOld(i,:)                                                    =
interp1(GradientPositionVector,TrajectoryAngleVector,MinimumGradientPosition);
% Find current trajectory angle old by inserting position of minimum gradient in the trajectory angle vector

% A cross-sectional angle is determined at right-angles to the current trajectory angle new. Using that angle,
% the current x and y coordinates of the trajectory and the cross-section length, the x and y coordinates for the
% begin and end point of the cross-section are determined

  CrossSectionAngleNew(i-3,:)=(TrajectoryAngleNew(i-3,:)+pi/2);
  CrossSectionPoint1(1,1)=XPositionOfTrajectory(i-3,:)-CrossSectionLength*cos(CrossSectionAngleNew(i-
3,:));
  CrossSectionPoint1(1,2)=YPositionOfTrajectory(i-3,:)-CrossSectionLength*sin(CrossSectionAngleNew(i-
3,:));
  CrossSectionPoint2(1,1)=XPositionOfTrajectory(i-3,:)+CrossSectionLength*cos(CrossSectionAngleNew(i-
3,:));
  CrossSectionPoint2(1,2)=YPositionOfTrajectory(i-3,:)+CrossSectionLength*sin(CrossSectionAngleNew(i-
3,:));

% The begin and end point of the cross-section have to be within the limits of the grid. If they are not the
% cross-section length is decreased by 5 mm and the coordinates are recalculated. This is repeated until all
% coordinates are within  the limits of the grid

  for q=1:100;
```

```
    if CrossSectionPoint1(1,1)<0;
        CrossSectionLength=CrossSectionLength-5;
        CrossSectionPoint1(1,1)=XPositionOfTrajectory(i-3,:)-
CrossSectionLength*cos(CrossSectionAngleNew(i-3,:));
        CrossSectionPoint1(1,2)=YPositionOfTrajectory(i-3,:)-
CrossSectionLength*sin(CrossSectionAngleNew(i-3,:));
    end
    q=q+1;
  end
  CrossSectionLength=400;

  for q=1:100;
    if CrossSectionPoint1(1,2)>3500;
        CrossSectionLength=CrossSectionLength-5;
        CrossSectionPoint1(1,2)=YPositionOfTrajectory(i-3,:)-
CrossSectionLength*sin(CrossSectionAngleNew(i-3,:));
        CrossSectionPoint1(1,1)=XPositionOfTrajectory(i-3,:)-
CrossSectionLength*cos(CrossSectionAngleNew(i-3,:));
    end
    q=q+1;
  end
  CrossSectionLength=400;

  for q=1:100;
     if CrossSectionPoint1(1,1)>600;
          CrossSectionLength=CrossSectionLength-5;
        CrossSectionPoint1(1,1)=XPositionOfTrajectory(i-3,:)-
CrossSectionLength*cos(CrossSectionAngleNew(i-3,:));
        CrossSectionPoint1(1,2)=YPositionOfTrajectory(i-3,:)-
CrossSectionLength*sin(CrossSectionAngleNew(i-3,:));
    end
     q=q+1;
  end
  CrossSectionLength=400;

   for q=1:100;
    if CrossSectionPoint1(1,2)<626;
        CrossSectionLength=CrossSectionLength-5;
        CrossSectionPoint1(1,2)=YPositionOfTrajectory(i-3,:)-
CrossSectionLength*sin(CrossSectionAngleNew(i-3,:));
        CrossSectionPoint1(1,1)=XPositionOfTrajectory(i-3,:)-
CrossSectionLength*cos(CrossSectionAngleNew(i-3,:));
```

```
    end
    q=q+1;
  end
  CrossSectionLength=400;

   for q=1:100;
    if CrossSectionPoint2(1,1)<0;
       CrossSectionLength=CrossSectionLength-5;
       CrossSectionPoint2(1,1)=XPositionOfTrajectory(i-
3,:)+CrossSectionLength*cos(CrossSectionAngleNew(i-3,:));
       CrossSectionPoint2(1,2)=YPositionOfTrajectory(i-
3,:)+CrossSectionLength*sin(CrossSectionAngleNew(i-3,:));
    end
    q=q+1;
  end
  CrossSectionLength=400;

  for q=1:100;
    if CrossSectionPoint2(1,2)>3500;
       CrossSectionLength=CrossSectionLength-5;
       CrossSectionPoint2(1,2)=YPositionOfTrajectory(i-
3,:)+CrossSectionLength*sin(CrossSectionAngleNew(i-3,:));
       CrossSectionPoint2(1,1)=XPositionOfTrajectory(i-
3,:)+CrossSectionLength*cos(CrossSectionAngleNew(i-3,:));
    end
    q=q+1;
  end
  CrossSectionLength=400;

  for q=1:100;
     if CrossSectionPoint2(1,1)>600;
          CrossSectionLength=CrossSectionLength-5;
       CrossSectionPoint2(1,1)=XPositionOfTrajectory(i-
3,:)+CrossSectionLength*cos(CrossSectionAngleNew(i-3,:));
       CrossSectionPoint2(1,2)=YPositionOfTrajectory(i-
3,:)+CrossSectionLength*sin(CrossSectionAngleNew(i-3,:));
    end
     q=q+1;
  end
  CrossSectionLength=400;

   for q=1:100;
```

```
    if CrossSectionPoint2(1,2)<626;
        CrossSectionLength=CrossSectionLength-5;
        CrossSectionPoint2(1,2)=YPositionOfTrajectory(i-
3,:)+CrossSectionLength*sin(CrossSectionAngleNew(i-3,:));
        CrossSectionPoint2(1,1)=XPositionOfTrajectory(i-
3,:)+CrossSectionLength*cos(CrossSectionAngleNew(i-3,:));
    end
    q=q+1;
  end
  CrossSectionLength=400;

% Using the coordinates of the begin and end point of the cross-section and the amount of point within the
% cross-section, the cross-section position vector is determined

  for k=0:CrossSectionPoints;
    CrossSectionCoordinatesVector(k+1,1)=((CrossSectionPoint2(1,1)-
CrossSectionPoint1(1,1))/CrossSectionPoints*k+CrossSectionPoint1(1,1));
    CrossSectionCoordinatesVector(k+1,2)=((CrossSectionPoint2(1,2)-
CrossSectionPoint1(1,2))/CrossSectionPoints*k+CrossSectionPoint1(1,2));
  end

        % Use cross-section position vector to calculate integrated concentration values along cross-section

  for k=0:CrossSectionPoints;
    CrossSectionIntensityVector(k+1,i-
3)=(interp2(X,Y,Z,CrossSectionCoordinatesVector(k+1,1),CrossSectionCoordinatesVector(k+1,2)));
    CrossSectionPositionVector(k+1,i-3)=(k)*sqrt((CrossSectionPoint2(1,2)-
CrossSectionPoint1(1,2))^2+(CrossSectionPoint2(1,1)-CrossSectionPoint1(1,1))^2)/CrossSectionPoints;
  end

% Determine the maximum integrated concentration in the cross-section and its position

  Cl(i-3,:)=max(CrossSectionIntensityVector(:,i-3),[],1);
            % Find maximum values of cross section
  MaximumIsOneInCrossSection=(CrossSectionIntensityVector(:,i-3)==Cl(i-3,:));
            % Make all non-maxima values zero and maxima-values one in cross-section
  MaximaAdded=MaximumIsOneInCrossSection'*CrossSectionPositionVector(:,i-3);
            % Multiply maxima-cross-section times position vector
  clear Ones
  Ones(1:CrossSectionPoints+1,1)=1;
            % Create ones vector
  MaximaMultiplier=MaximumIsOneInCrossSection'*Ones;
```

```
                    % Multiply maxima-cross-section times ones vector
   CrossSectionPositionOfTrajectory=MaximaAdded./MaximaMultiplier;
                    % Find maximum along cross section

% Determine integrated concentration (intensity) of cross section at concentration spread 'b_c'

   SpreadIntensity=exp(-1)*Cl(i-3,:);

% Determine distance from point of maximum integrated concentration to 'b' on both sides of the maximum
….
   CrossSectionIntensityVectorDataLimited1=CrossSectionIntensityVector(:,i-3);
   CrossSectionIntensityVectorDataLimited2=CrossSectionIntensityVector(:,i-3);
   CrossSectionPositionVectorDataLimited1=CrossSectionPositionVector(:,i-3);
   CrossSectionPositionVectorDataLimited2=CrossSectionPositionVector(:,i-3);

   j=1;
   k=1;
   while CrossSectionPositionVectorDataLimited2(k,:)<CrossSectionPositionOfTrajectory;
        CrossSectionIntensityVectorDataLimited2(k,:)=[];
        CrossSectionPositionVectorDataLimited2(k,:)=[];
        j=j+1;
   end

   for j=1:CrossSectionPoints+1
      if CrossSectionPositionVector(j,i-3)>CrossSectionPositionOfTrajectory;
         CrossSectionIntensityVectorDataLimited1(j-k+1,:)=[];
         CrossSectionPositionVectorDataLimited1(j-k+1,:)=[];
         k=k+1;
      end
   end

   [m,n]=size(CrossSectionIntensityVectorDataLimited2);

   for k=1:m
   CrossSectionIntensityVectorDataLimited3(k,1)=CrossSectionIntensityVectorDataLimited2(m-k+1,1);
   CrossSectionPositionVectorDataLimited3(k,1)=CrossSectionPositionVectorDataLimited2(m-k+1,1);
   end

SpreadPositionOfCrossSection(1,1)=interp1q(CrossSectionIntensityVectorDataLimited1,CrossSectionPositionV
ectorDataLimited1,SpreadIntensity);
```

```
SpreadPositionOfCrossSection(1,2)=interp1q(CrossSectionIntensityVectorDataLimited3,CrossSectionPositionV
ectorDataLimited3,SpreadIntensity);
   Spread(i-3,1)=CrossSectionPositionOfTrajectory-SpreadPositionOfCrossSection(1,1);
   Spread(i-3,2)=CrossSectionPositionOfTrajectory-SpreadPositionOfCrossSection(1,2);

% Remove all data in cross-section integrated concentration (intensity) and corresponding position vector that
% has an  integrated concentration less than 37% of the maximum

   CrossSectionIntensityVectorDataLimited = CrossSectionIntensityVector(:,i-3);
   CrossSectionPositionVectorDataLimited = CrossSectionPositionVector(:,i-3);

   j=0;
   k=0;
   while j<CrossSectionPoints+1;
      j=j+1;
      k=k+1;
      if CrossSectionIntensityVector(j,i-3)<0.37*Cl(i-3);
         CrossSectionIntensityVectorDataLimited(k,:)=[];
         CrossSectionPositionVectorDataLimited(k,:)=[];
         k=k-1;
      end
   end

% Determine concentration spread by fitting a second-order polynomial through naturally-logged limited cross-
% sectional data

   CrossSectionIntensityVectorDataLimited=log(CrossSectionIntensityVectorDataLimited);
   p = polyfit(CrossSectionPositionVectorDataLimited,CrossSectionIntensityVectorDataLimited,2);
   b(i-3,:) = sqrt(-1/p(1,1))                    % Calculate Spread b
   r0 = p(1,2)*b(i-3,:)^2/2;                     % Calculate Centerline position of Jet in cross-section

% Remove all data in cross-section integrated concentration (intensity) and corresponding position vector that
% makes up the inside edge of the flow

   CrossSectionIntensityVectorDataLimited=CrossSectionIntensityVectorDataLimited2;
   CrossSectionPositionVectorDataLimited=CrossSectionPositionVectorDataLimited2;

   j=0;
   k=0;
   while j<m;
      j=j+1;
```

```
      k=k+1;
      if CrossSectionIntensityVectorDataLimited2(j,1)<0.37*Cl(i-3);
         CrossSectionIntensityVectorDataLimited(k,:)=[];
         CrossSectionPositionVectorDataLimited(k,:)=[];
         k=k-1;
      end
   end

% Determine concentration spread by fitting a second-order polynomial through naturally-logged outer edge
% cross-sectional data

   CrossSectionIntensityVectorDataLimited=log(CrossSectionIntensityVectorDataLimited);
   p = polyfit(CrossSectionPositionVectorDataLimited,CrossSectionIntensityVectorDataLimited,2);
   b2(i-3,:) = sqrt(-1/p(1,1));
end

i=i+1
```

Appendix C – Computer Code Of Momentum Model

MomentumModel7

```
clear;
global FlowRegion
% Input: U0 (m/s),Ua (ms),d (m) , delta0 (m/s2), alpha0, beta0
delta0=0.293755;
d=0.00291;
Ua=0.05;
U0=0.5;
alpha0=-60/180*pi;
beta0=0/180*pi;

x0=0;x=x0;
y0=0;y=y0;
z0=0;z=z0;
b0=0*d;b=b0

% Calculate Phi0;
Phi0=acos(cos(alpha0)*cos(beta0));
% Calculate Mb0
Mb0=0;Mb=Mb0;
% Calculate Q0
Q0=U0*pi*d^2/4;Q=Q0;
% Calculate delta0
delta=delta0;
% Calculate Ma0
Ma0=Ua*(Q0)*cos(Phi0);Ma=Ma0;
% Calculate Me0x
Me0x=(U0*Q0-Ua*Q0*cos(Phi0))*cos(alpha0)*cos(beta0);
% Calculate Me0y
Me0y=(U0*Q0-Ua*Q0*cos(Phi0))*cos(alpha0)*sin(beta0);
% Calculate Me0z
Me0z=(U0*Q0-Ua*Q0*cos(Phi0))*sin(alpha0);
% Calculate Me0
Me0=U0*Q0-Ua*Q0*cos(Phi0);Me=Me0;
% Calculate Ms0
Ms0=((Ma0+Me0x)^2+Me0y^2+Me0z^2)^(1/2);Ms=Ms0;
M=Ma*cos(Phi0)+Me0;
```

```
FlowRegion = 1
c7 = ((Q0*delta0*abs(sin(Phi0)))^2/Me0/Ua^4)^(1/3)

%Non-dimensionalise parameters
M0=U0*Q0;

x=x/d;y=y/d;z=z/d;
Ma=Ma/M0;Mb=Mb/M0;Me=Me/M0;Me0=Me0/M0;Ms=Ms/M0;
Me0x=Me0x/M0;Me0y=Me0y/M0;Me0z=Me0z/M0;
b=b/d;delta=delta/(delta0+eps);Q=Q/Q0;
Ua=Ua/U0;

% Create vector Y:
Y=zeros(1,10);
Y(1)=x;Y(2)=y;Y(3)=z;Y(4)=Mb;Y(5)=Me;Y(6)=b;Y(7)=Ms;Y(8)=Q;Y(9)=delta;Y(10)=Ma;

Fr=U0/((delta0*d)^(1/2));
format short e
[s,Y]=ode45(@dy7,[0,10000],[Y],[],Me0,Me0x,Me0y,Me0z,Fr,Ua,Phi0,c7);
```

dy7

```
function dy7=f(s,Y,Me0,Me0x,Me0y,Me0z,Fr,Ua,Phi0,c7);
global FlowRegion
warning off MATLAB:divideByZero

k=0.106*sqrt(pi/1.7);
mp=0.5979;
mt=0.7294;

%Y(1)=x;Y(2)=y;Y(3)=z;Y(4)=Mb;Y(5)=Me;Y(6)=b;Y(7)=Q;Y(8)=delta;Y(9)=Ma;Y(10)=Ms;

dy7=zeros(10,1);

% dy(1)=(Me0x+Ma)/Ms;
dy7(1)=(Me0x+Y(10))/Y(7);                    % Y(1)=dxds

% dy (2)=Me0y/Ms;
dy7(2)=Me0y/Y(7);                            % Y(2)=dyds

% dy(3)=(Me0z+Mb)/Ms;
dy7(3)=(Me0z+Y(4))/Y(7);                     % Y(3)=dzds
```

```
% dy(4)=4/Fr^2*delta*(b^2);
dy7(4)=4/(Fr+eps)^2*Y(9)*Y(6)^2;                    % Y(4)=dMbds

% dy(5)=(Mb+Me0z)/Me*dy(4)
dy7(5)=(Y(4)+Me0z)/Y(5)*dy7(4);                     % Y(5)=dMe/ds

% SpreadFunction                                    % Y(6)=db/ds

if FlowRegion == 2;
   if Y(4)/Me0<0.673345;
     FlowRegion = 1;
  end;
end;

if FlowRegion == 3;
   if (Y(8)*Ua)/(Me0*sin(Phi0))<(0.255);
     FlowRegion = 1;
  end;
end;

if FlowRegion == 1;
   if abs(Phi0)>25/180*pi;
      if (Y(8)*Ua)/(Me0*sin(Phi0))<(0.255) & Y(4)/Me0<=0.673345;
         dy7(6)=k*abs(Y(5)/Y(8)/(Y(5)/Y(8)+1.55*Ua/2*abs(cos(Phi0))));
      elseif Y(4)/Me0>0.673345;
         FlowRegion = 2;
         dy7(6)=k*abs(Y(5)/Y(8)/(Y(5)/Y(8)+1.55*Ua/2*abs(cos(Phi0))))
      else;
         dy7(6)= mp*abs((Y(2)/sqrt(Y(2)^2+Y(3)^2)*dy7(2)+Y(3)/sqrt(Y(2)^2+Y(3)^2)*dy7(3)));
         FlowRegion = 3;
      end;
   elseif Y(4)/Me0>0.673345;
      FlowRegion = 2;
      dy7(6)=k*abs(Y(5)/Y(8)/(Y(5)/Y(8)+1.55*Ua/2*abs(cos(Phi0))));;
   else dy7(6)=k*abs(Y(5)/Y(8)/(Y(5)/Y(8)+1.55*Ua/2*abs(cos(Phi0))));
   end;
end;

if FlowRegion == 2;
   if Y(10)/Y(4)<=0.3509;
      dy7(6)=k*abs(Y(5)/Y(8)/(Y(5)/Y(8)+1.55*Ua/2*abs(cos(Phi0))));
```

```
   else dy7(6)=mt*abs(dy7(3));
   end;
end;

if FlowRegion == 3;
   if Y(4)/Me0>c7*1.35
   dy7(6)= mt*abs(dy7(3));
   else dy7(6)= mp*abs((Y(2)/sqrt(Y(2)^2+Y(3)^2)*dy7(2)+Y(3)/sqrt(Y(2)^2+Y(3)^2)*dy7(3)));
   end;
end;

% dy(7)=(4*(Me0x+Ma)*Ua*b/Q*dy(6)+(Me0z+Mb)/Ms*dy(4))/(1-2*(Me0x+Ma)*Ua*b^2/Ms/Q);
dy7(7)=(4*(Me0x+Y(10))*Ua*Y(6)/Y(8)*dy7(6)+(Me0z+Y(4))/Y(7)*dy7(4))/(1-
2*(Me0x+Y(10))*Ua*Y(6)^2/Y(7)/Y(8));                    % Y(7)=dMsds

% dy(8)=2*b^2/Q*dy(7)+4*Ms*b/Q*dy(6)
dy7(8)=2*Y(6)^2/Y(8)*dy7(7)+4*Y(7)*Y(6)/Y(8)*dy7(6);    % Y(8)=dQds

% dy(9)=-delta/Q*dy(8);
dy7(9)=-Y(9)/Y(8)*dy7(8);                               %Y(9)=ddeltads

% dy(10)=Ua*dy(8)
dy7(10)=(Ua)*dy7(8);                                    %Y(10)=dMads
```

Appendix D - Initial Conditions for Experiments with 2D and 3D Trajectories

Table D.1 - Initial Conditions for simple jet runs

Jet Run No.	Date	Q_0 (l/s)	d (mm)	U_0 (m/s)	Fr_0	Re_0	ρ_a (kg/m^3)	ρ (kg/m^3)	Camera	Angle (ϕ_0)	Comment
1	21/05/2003	0.0630	10.15	0.78	273	7903	998.85	998.77	Canon	90°	No analysis
2	22/05/2003	0.0425	10.15	0.53		5331	1000.10	1000.10	Canon	90°	No analysis
3	9/06/2003	0.0397	10.15	0.49	100	4980	999.22	998.98	Canon	90°	Investigating LA
4	11/06/2003	0.0460	6.00	1.63	1831	9762	999.22	999.23	Canon	90°	No analysis
5	24/06/2003	0.0460	6.00	1.63	407	9762	999.42	999.15	Canon	90°	Investigating LA
6	25/06/2003	0.0460	6.00	1.63	502	9762	999.50	999.32	Canon	90°	Investigating LA
7	25/06/2003	0.0224	3.20	2.79	1997	8913	999.39	999.32	Canon	90°	Investigating LA
8	26/06/2003	0.0220	3.20	2.74	893	8754	999.35	999.05	Canon	90°	Investigating LA
9	29/06/2003	0.0220	3.20	2.74	1533	8754	999.54	999.43	Canon	90°	No analysis
10	29/06/2003	0.0220	3.20	2.74	1533	8754	999.54	999.43	Canon	90°	Investigating LA
11	30/06/2003	0.0222	3.20	2.76	1296	8833	999.47	999.32	Canon	90°	Investigating LA
12	1/07/2003	0.0220	3.20	2.74	∞!	8754	999.42	999.42	Canon	90°	Investigating LA
13	14/07/2003	0.0206	3.20	2.56	1292	8196	999.59	999.71	Canon	90°	No analysis
14	14/07/2003	0.0207	3.20	2.57	2071	8236	999.61	999.66	Canon	90°	Investigating LA
15	16/07/2003	0.0217	3.20	2.70	1579	8634	999.49	999.40	Canon	90°	Investigating LA
16.1	21/11/2003	0.0100	3.00	1.41	1471	4244	998.91	998.88	Canon	90°	No analysis
16.2	21/11/2003	0.0100	3.00	1.41	1471	4244	998.91	998.88	Canon	80°	No analysis
17.1	1/12/2003	0.0100	3.00	1.41	1037	4244	998.91	998.85	Canon	90°	Investigating Jet on angle
17.2	1/12/2003	0.0100	3.00	1.41	1471	4244	998.91	998.88	Canon	65°	Investigating Jet on angle
18	5/12/2003	0.0100	3.20	1.24	1020	3979	998.91	998.87	Canon	0°	Investigating 3D LA
19	8/12/2003	0.0100	3.00	1.41	1165	4244	998.77	998.72	Canon	90°	Investigating Integrated Theory
20	11/10/2004	0.0094	2.45	1.99	∞	4879	998.87	998.87	Jai CV M7+	90°	Investigating Integrated Theory
21	8/11/2004	0.0072	2.45	1.53	∞	3753	998.82	998.82	Jai CV M7+	90°	Investigating Integrated Theory
22	12/11/2004	0.0069	2.45	1.47	∞	3609	998.91	998.91	Jai CV M7+	90°	Investigating Integrated Theory
23	12/11/2004	0.0069	2.45	1.46	∞	3566	998.90	998.90	Jai CV M7+	90°	Investigating Integrated Theory
24	21/04/2005	0.0058	2.45	1.22	∞	2988	998.70	998.70	Jai CV M7+	0°	Verifying 3D LA
25	21/04/2005	0.0058	2.45	1.22	∞	2988	998.70	998.70	Jai CV M7+ CL	0°	Verifying 3D LA
26	28/04/2005	0.0067	2.45	1.42	∞	3479	999.14	999.14	Jai CV M7+	0°	Verifying 3D LA
27	28/04/2005	0.0067	2.45	1.42	∞	3479	999.14	999.14	Jai CV M7+ CL	0°	Verifying 3D LA

Table D.2 - Initial Conditions for pure plume runs

Plume Run No.	Date	Q_0 (l/s)	d (mm)	U_0 (m/s)	Fr_0	Re_0	$\Delta\rho$	ρ_a (kg/m^3)	ρ (kg/m^3)	Camera	Angle (ϕ_0)	Comment
1	23/07/2003	0.0025	3.20	0.31	10.11	995	0.0301	999.46	1029.50	Canon	90°	
2	25/07/2003	0.0051	3.20	0.63	20.63	2029	0.0301	999.42	1029.50	Canon	90°	
3	14/08/2003	0.0014	3.20	0.17	5.66	557	0.0301	999.27	1029.30	Canon	90°	
4	21/08/2003	0.0020	3.20	0.25	8.09	796	0.0301	999.40	1029.50	Canon	90°	

Table D.3 - Initial Conditions for horizontal buoyant jet runs

Buoyant Jet Run No.	Date	Q_0 (l/s)	d (mm)	U_0 (m/s)	Fr_0	Re_0	$\Delta\rho$	ρ_a (kg/m^3)	ρ (kg/m^3)	l_{jp} (m)	Camera	Angle (ϕ_0)	Comment
1.1	30/07/2003	0.0124	3.20	1.54	50.16	4934	0.0301	999.47	1029.55	0.35	Canon	0°	
1.2	30/07/2003	0.0124	3.20	1.54	50.16	4934	0.0301	999.47	1029.55	0.35	Canon	0°	
2	3/08/2003	0.0034	3.20	0.42	13.75	1353	0.0301	999.19	1029.27	0.10	Canon	0°	
3.1	9/09/2003	0.0061	3.20	0.76	24.68	2427	0.0301	999.05	1029.12	0.17	Canon	0°	
3.2	9/09/2003	0.0061	3.20	0.76	24.68	2427	0.0301	999.05	1029.12	0.17	Canon	0°	

Table D.4 - Initial Conditions for positively buoyant jet runs

Positively Buoyant Jet Run No.	Date	Q_0 (l/s)	d (mm)	U_0 (m/s)	Fr_0	Re_0	$\Delta\rho$	ρ_a (kg/m^3)	ρ (kg/m^3)	l_{jp} (m)	Camera	Angle (ϕ_0)	Comment
1	18/12/2003	0.0060	2.91	0.90	27.15	2625	0.0301	998.77	1028.8	0.1939	Canon	50°	
2	18/12/2003	0.0060	2.91	0.90	27.15	2625	0.0301	998.77	1028.8	0.1939	Canon	60°	
3	18/12/2003	0.0060	2.91	0.90	27.15	2625	0.0301	998.63	1028.7	0.1939	Canon	70°	
4	18/12/2003	0.0060	2.91	0.90	27.15	2625	0.0301	998.63	1028.7	0.1939	Canon	80°	
5	18/12/2003	0.0060	2.91	0.90	27.15	2625	0.0301	998.63	1028.8	0.1939	Canon	90°	
6	18/12/2003	0.0060	2.91	0.90	27.15	2625	0.0301	998.67	1028.8	0.1939	Canon	40°	
7	18/12/2003	0.0060	2.91	0.90	27.15	2625	0.0301	998.67	1028.7	0.1939	Canon	30°	
8	19/12/2003	0.0060	2.91	0.90	27.15	2625	0.0301	998.67	1028.7	0.1939	Canon	20°	
9	19/12/2003	0.0060	2.91	0.90	27.15	2625	0.0301	998.67	1028.8	0.1939	Canon	10°	
10	19/12/2003	0.0060	2.91	0.90	27.15	2625	0.0301	998.67	1028.8	0.1939	Canon	0°	

Table D.5 - Initial Condition for advected line momentum puff runs

Advected Line Momentum Puff Run No.	Date	Q_0 (l/s)	d (mm)	U_0 (m/s)	Fr_0	Re_0	U_a (m/s)	U_r	ρ_a (kg/m^3)	ρ (kg/m^3)	Camera	Angle (ϕ_0)	Comment
1	20/10/2003	0.0181	3.00	2.56	910	7682	0.1041	0.0406			Canon	90°	No analysis
2.1	22/10/2003	0.0062	3.00	0.88	849	2631	0.0336	0.0383	998.96	998.65	Canon	90°	No analysis
2.2	22/10/2003	0.0062	3.00	0.88	1012	2631	0.0338	0.0385	998.74	998.38	Canon	90°	No analysis
2.3	22/10/2003	0.0062	3.00	0.88	1012	2631	0.0334	0.0380	998.67	998.42	Canon	90°	No analysis
2.4	22/10/2003	0.0062	3.00	0.88	2006	2631	0.0339	0.0387	998.67	998.42	Canon	90°	No analysis
3.1	5/11/2003	0.0062	3.00	0.88	1623	2631	0.0333	0.0380	998.90	998.84	Canon	90°	No analysis
3.2	5/11/2003	0.0062	3.00	0.88	1241	2631	0.0338	0.0385	998.87	998.77	Canon	90°	No analysis
3.3	5/11/2003	0.0062	3.00	0.88	2875	2631	0.0337	0.0384	998.84	998.67	Canon	90°	No analysis
4.1	6/11/2003	0.0062	3.00	0.88	2847	2631	0.0333	0.0380	998.91	998.95	Canon	90°	No analysis
4.2	6/11/2003	0.0062	3.00	0.88	1414	2631	0.0338	0.0386	998.90	998.87	Canon	90°	No analysis
5.1	10/11/2003	0.0062	3.00	0.88	2256	2631	0.0327	0.0373	998.79	998.91	Canon	90°	No analysis
5.2	10/11/2003	0.0062	3.00	0.88	∞	2631	0.0331	0.0377	998.75	998.70	Canon	90°	No analysis
6.1	13/11/2003	0.0062	3.00	0.88	3783	2631	0.0337	0.0385	998.53	998.53	Canon	90°	Investigating LA
6.2	13/11/2003	0.0062	3.00	0.88	3772	2631	0.0334	0.0380	998.53	998.55	Canon	90°	Investigating LA
6.3	13/11/2003	0.0062	3.00	0.88	2663	2631	0.0334	0.0381	998.53	998.51	Canon	90°	Investigating LA
6.4	13/11/2003	0.0062	3.00	0.88	2046	2631	0.0334	0.0381	998.53	998.49	Canon	90°	Investigating LA
7.1	19/11/2003	0.0062	3.00	0.88	2923	2631	0.0332	0.0379	998.99	998.93	Canon	90°	Investigating LA
7.2	19/11/2003	0.0062	3.00	0.88	∞	2631	0.0334	0.0380	998.99	999.02	Canon	90°	Investigating LA
8.1	19/11/2003	0.0100	3.00	1.41	3301	4244	0.0334	0.0236	998.99	998.99	Canon	90°	Investigating LA
8.2	19/11/2003	0.0100	3.00	1.41	2899	4244	0.0340	0.0240	998.99	998.93	Canon	90°	Investigating LA
9	21/11/2003	0.0100	3.00	1.41	5029	4244	0.0334	0.0236	998.91	998.84	Canon	90°	Investigating LA
Test 1	4/05/2004	0.0094	2.91	1.41	5083	4113	0.0695	0.0492	999.22	999.19	Jai CV M7+	90°	z-integrated view
Test 2	4/05/2004	0.0095	2.91	1.43	9842	4157	0.0297	0.0208	999.22	999.19	Jai CV M7+	90°	z-integrated view
10.1	13/10/2004	0.0092	2.45	1.95	9842	4770	0.0976	0.0501	998.87	998.85	Jai CV M7+	90°	y-integrated view
10.2	13/10/2004	0.0092	2.45	1.95	∞	4770	0.0977	0.0502	998.87	998.85	Jai CV M7+	90°	y-integrated view
11.1	20/10/2004	0.0098	2.45	2.07	∞	5067	0.0966	0.0467	998.82	998.82	Jai CV M7+	90°	z-integrated view
11.2	20/10/2004	0.0098	2.45	2.07	∞	5081	0.0979	0.0472	998.82	998.82	Jai CV M7+	90°	z-integrated view
12.1	12/11/2004	0.0071	2.45	1.51	5529	3710	0.0546	0.0360	998.99	998.99	Jai CV M7+	90°	z-integrated view
12.2	12/11/2004	0.0071	2.45	1.51	∞	3710	0.0547	0.0361	998.98	998.95	Jai CV M7+	90°	z-integrated view
13.1	23/02/2005	0.0071	2.45	1.50	∞	3667	0.0371	0.0248	998.63	998.63	Jai CV M7+	90°	y-integrated view
13.2	23/02/2005	0.0071	2.45	1.50	∞	3667	0.0372	0.0249	998.56	998.56	Jai CV M7+	90°	y-integrated view
14.1	25/02/2005	0.0071	2.45	1.50	∞	3667	0.0375	0.0251	998.72	998.72	Jai CV M7+	90°	z-integrated view
14.2	25/02/2005	0.0070	2.45	1.48	∞	3623	0.0377	0.0255	998.67	998.67	Jai CV M7+	90°	z-integrated view
14.3	25/02/2005	0.0071	2.45	1.50	∞	3667	0.0377	0.0252	998.67	998.67	Jai CV M7+	90°	z-integrated view
14.4	25/02/2005	0.0070	2.45	1.49	∞	3652	0.0377	0.0253	998.67	998.67	Jai CV M7+	90°	z-integrated view
15.1	14/04/2005	0.0084	2.45	1.79	∞	4374	0.0518	0.0290	999.07	999.07	Jai CV M7+	90°	y-integrated view
15.2	14/04/2005	0.0084	2.45	1.79	∞	4374	0.0518	0.0290	999.07	999.07	Jai CV M7+	90°	y-integrated view
15.3	14/04/2005	0.0083	2.45	1.77	∞	4331	0.0518	0.0293	999.07	999.07	Jai CV M7+	90°	y-integrated view
16.1	14/04/2005	0.0084	2.45	1.79	∞	4374	0.0518	0.0290	999.07	999.07	Jai CV M7+ CL	90°	z-integrated view
16.2	14/04/2005	0.0084	2.45	1.79	∞	4374	0.0518	0.0290	999.07	999.07	Jai CV M7+ CL	90°	z-integrated view
16.3	14/04/2005	0.0083	2.45	1.77	∞	4331	0.0518	0.0293	999.07	999.07	Jai CV M7+ CL	90°	z-integrated view

17.1	18/05/2005	0.0083	2.45	1.77	∞	4331	0.0512	0.0290	999.08	999.08	Jai CV M7+	90°	y-integrated view
17.2	18/05/2005	0.0086	2.45	1.81	∞	4446	0.0513	0.0283	999.05	999.05	Jai CV M7+	90°	y-integrated view
17.3	18/05/2005	0.0084	2.45	1.77	∞	4345	0.0513	0.0289	999.05	999.05	Jai CV M7+	90°	y-integrated view
17.4	18/05/2005	0.0083	2.45	1.77	∞	4331	0.0513	0.0290	999.05	999.05	Jai CV M7+	90°	y-integrated view
18.1	18/05/2005	0.0083	2.45	1.77	∞	4331	0.0512	0.0290	999.08	999.08	Jai CV M7+ CL	90°	z-integrated view
18.2	18/05/2005	0.0086	2.45	1.81	∞	4446	0.0513	0.0283	999.05	999.05	Jai CV M7+ CL	90°	z-integrated view
18.3	18/05/2005	0.0084	2.45	1.77	∞	4345	0.0513	0.0289	999.05	999.05	Jai CV M7+ CL	90°	z-integrated view
18.4	18/05/2005	0.0083	2.45	1.77	∞	4331	0.0513	0.0290	999.05	999.05	Jai CV M7+ CL	90°	z-integrated view
19.1	15/07/2005	0.0066	2.45	1.41	∞	3450	0.0621	0.0441	999.48	999.48	Jai CV M7+	90°	y-integrated view
19.2	15/07/2005	0.0066	2.45	1.41	∞	3450	0.0621	0.0441	999.41	999.41	Jai CV M7+	90°	y-integrated view
19.3	15/07/2005	0.0066	2.45	1.41	∞	3450	0.0621	0.0441	999.41	999.41	Jai CV M7+	90°	y-integrated view
20.1	25/10/2005	0.0078	2.45	1.65	∞	4042	0.0522	0.0317	999.14	999.14	Jai CV M7+	90°	y-integrated view
20.2	25/10/2005	0.0078	2.45	1.65	∞	4042	0.0522	0.0317	999.11	999.11	Jai CV M7+	90°	y-integrated view
20.3	25/10/2005	0.0078	2.45	1.65	∞	4042	0.0522	0.0317	999.07	999.07	Jai CV M7+	90°	y-integrated view
21.1	25/10/2005	0.0078	2.45	1.65	∞	4042	0.0522	0.0317	999.14	999.14	Jai CV M7+ CL	90°	z-integrated view
21.2	25/10/2005	0.0078	2.45	1.65	∞	4042	0.0522	0.0317	999.11	999.11	Jai CV M7+ CL	90°	z-integrated view
21.3	25/10/2005	0.0078	2.45	1.65	∞	4042	0.0522	0.0317	999.07	999.07	Jai CV M7+ CL	90°	z-integrated view
22.1	26/10/2005	0.0098	2.45	2.07	∞	5081	0.0522	0.0252	999.07	999.07	Jai CV M7+	90°	y-integrated view
22.2	26/10/2005	0.0098	2.45	2.07	∞	5081	0.0522	0.0252	999.05	999.05	Jai CV M7+	90°	y-integrated view
22.3	26/10/2005	0.0098	2.45	2.07	∞	5081	0.0522	0.0252	999.04	999.04	Jai CV M7+	90°	y-integrated view
23.1	26/10/2005	0.0098	2.45	2.07	∞	5081	0.0522	0.0252	999.07	999.07	Jai CV M7+ CL	90°	z-integrated view
23.2	26/10/2005	0.0098	2.45	2.07	∞	5081	0.0522	0.0252	999.05	999.05	Jai CV M7+ CL	90°	z-integrated view
23.3	26/10/2005	0.0098	2.45	2.07	∞	5081	0.0522	0.0252	999.04	999.04	Jai CV M7+ CL	90°	z-integrated view

Table D.6 - Initial Condition for advected jet runs

Advected Jet Run No.	**Date**	**Q_0** (l/s)	**d** (mm)	**U_0** (m/s)	**Fr_0**	**Re_0**	**U_a** (m/s)	**U_r**	**ρ_a** (kg/m^3)	**ρ** (kg/m^3)	**Camera**	**Angle** (ϕ_0)	**Comment**
1	1/07/2005	0.0068	2.45	1.43	∞	3508	0.0046	0.00319	999.51	999.51	Jai CV M7+	90°	y-integrated view
2	7/07/2005	0.0066	2.45	1.40	∞	3436	0.0141	0.01005	999.32	999.32	Jai CV M7+	90°	y-integrated view
3	11/07/2005	0.0065	2.45	1.38	∞	3392	0.0104	0.00751	999.49	999.49	Jai CV M7+	90°	y-integrated view
4.1	12/07/2005	0.0066	2.45	1.39	∞	3407	0.0257	0.01845	999.40	999.40	Jai CV M7+	90°	y-integrated view
4.2	12/07/2005	0.0066	2.45	1.39	∞	3407	0.0257	0.01845	999.35	999.35	Jai CV M7+	90°	y-integrated view
5	22/07/2005	0.0076	2.45	1.62	∞	3970	0.0371	0.02292	999.48	999.48	Jai CV M7+	90°	y-integrated view
6	25/07/2005	0.0072	2.45	1.53	∞	3753	0.0125	0.00816	999.48	999.48	Jai CV M7+	90°	y-integrated view

Table D.7 - Initial conditions for buoyant jet in moving ambient runs

Buoyant Jet in Ambient Flow Run No.	Date	Q_0 (l/s)	d (mm)	U_0 (m/s)	Fr_0	Re_0	U_a (m/s)	U_r	ρ_a (kg/m^3)	ρ (kg/m^3)	Camera	Angle (ϕ_0)	Comment
1.1	22/12/2003	0.0060	2.91	0.90	27.15	2625	0.0336	0.0372	998.84	1037.16	Canon	-40°	
1.2	22/12/2003	0.0060	2.91	0.90	27.15	2625	0.0336	0.0372	998.84	1037.16	Canon	-40°	
2.1	23/12/2003	0.0080	2.91	1.20	36.20	3500	0.0339	0.0282	998.84	1037.16	Canon	-30°	
2.2	23/12/2003	0.0080	2.91	1.20	36.20	3500	0.0339	0.0282	998.84	1037.16	Canon	-30°	
3.1	23/12/2003	0.0100	2.91	1.50	45.25	4375	0.0447	0.0297	998.77	1037.42	Canon	-20°	
3.2	23/12/2003	0.0100	2.91	1.50	45.25	4375	0.0451	0.0300	998.77	1037.42	Canon	-20°	
4.1	23/12/2003	0.0100	2.91	1.50	45.25	4375	0.0448	0.0298	998.80	1037.34	Canon	-10°	
4.2	23/12/2003	0.0100	2.91	1.50	45.25	4375	0.0448	0.0298	998.80	1037.34	Canon	-10°	
5.1	23/12/2003	0.0100	2.91	1.50	45.25	4375	0.0448	0.0298	998.80	1037.34	Canon	0°	
5.2	23/12/2003	0.0100	2.91	1.50	45.25	4375	0.0448	0.0298	998.80	1037.34	Canon	0°	
6.1	24/12/2003	0.0100	2.91	1.50	45.25	4375	0.0449	0.0298	998.87	1037.27	Canon	10°	
6.2	24/12/2003	0.0100	2.91	1.50	45.25	4375	0.0453	0.0301	998.87	1037.27	Canon	10°	
7.1	24/12/2003	0.0100	2.91	1.50	45.25	4375	0.0454	0.0302	998.87	1037.27	Canon	20°	
7.2	24/12/2003	0.0100	2.91	1.50	45.25	4375	0.0455	0.0302	998.87	1037.27	Canon	20°	
8.1	29/12/2003	0.0100	2.91	1.50	45.25	4375	0.0450	0.0299	998.84	1037.16	Canon	30°	
8.2	29/12/2003	0.0100	2.91	1.50	45.25	4375	0.0455	0.0302	998.84	1037.16	Canon	30°	
9.1	29/12/2003	0.0100	2.91	1.50	45.25	4375	0.0449	0.0299	998.84	1037.16	Canon	40°	
9.2	29/12/2003	0.0100	2.91	1.50	45.25	4375	0.0450	0.0299	998.84	1037.16	Canon	40°	
10.1	30/12/2003	0.0100	2.91	1.50	45.25	4375	0.0447	0.0297	998.79	1037.34	Canon	50°	
10.2	30/12/2003	0.0100	2.91	1.50	45.25	4375	0.0443	0.0295	998.79	1037.34	Canon	50°	
11.1	30/12/2003	0.0100	2.91	1.50	45.25	4375	0.0444	0.0295	998.79	1037.34	Canon	60°	
11.2	30/12/2003	0.0100	2.91	1.50	45.25	4375	0.0444	0.0295	998.79	1037.34	Canon	60°	
12.1	11/03/2004	0.0086	2.91	1.29	46.44	3741	0.0598	0.0465	998.75	1025.39	Canon	70°	
12.2	11/03/2004	0.0086	2.91	1.29	46.44	3741	0.0598	0.0465	998.75	1025.39	Canon	70°	
13.1	11/03/2004	0.0086	2.91	1.29	46.44	3741	0.0598	0.0465	998.75	1025.39	Canon	80°	
13.2	11/03/2004	0.0086	2.91	1.29	46.44	3741	0.0598	0.0465	998.75	1025.39	Canon	80°	
14.1	12/03/2004	0.0095	2.91	1.43	51.60	4157	0.0598	0.0419	998.67	1025.48	Canon	90°	
14.2	12/03/2004	0.0095	2.91	1.43	51.60	4157	0.0601	0.0421	998.67	1025.48	Canon	90°	
14.3	12/03/2004	0.0095	2.91	1.43	51.60	4157	0.0601	0.0421	998.67	1025.48	Canon	90°	
15.1	16/03/2004	0.0103	2.91	1.55	55.35	4507	0.0595	0.0384	998.84	1026.26	Canon	100°	
15.2	16/03/2004	0.0103	2.91	1.55	55.35	4507	0.0601	0.0388	998.84	1026.34	Canon	100°	
16.1	16/03/2004	0.0096	2.91	1.44	51.59	4200	0.0602	0.0417	998.84	1026.23	Canon	110°	
16.2	16/03/2004	0.0096	2.91	1.44	51.59	4200	0.0603	0.0418	998.84	1026.09	Canon	110°	
17.1	17/03/2004	0.0096	2.91	1.44	51.59	4200	0.0599	0.0415	998.87	1026.13	Canon	120°	
17.2	17/03/2004	0.0096	2.91	1.44	51.59	4200	0.0603	0.0418	998.84	1026.09	Canon	120°	
18.1	17/03/2004	0.0098	2.91	1.47	52.66	4288	0.0594	0.0403	998.87	1026.19	Canon	130°	
18.2	17/03/2004	0.0098	2.91	1.47	52.66	4288	0.0600	0.0407	998.87	1026.18	Canon	130°	
19.1	16/12/2005	0.0079	2.43	1.70	78.16	4119	0.1245	0.0735	998.88	1018.59	Jai CV M7+	0°	Trajectory only
19.2	16/12/2005	0.0079	2.43	1.70	78.16	4119	0.1246	0.0735	998.88	1018.59	Jai CV M7+	0°	Trajectory only
19.3	16/12/2005	0.0079	2.43	1.70	78.16	4119	0.1246	0.0735	998.88	1018.59	Jai CV M7+	0°	Trajectory only
20.1	21/12/2005	0.0060	2.43	1.30	59.93	3158	0.2420	0.1862	998.53	1018.23	Jai CV M7+	0°	Trajectory only
20.2	21/12/2005	0.0060	2.43	1.30	59.93	3158	0.2423	0.1865	998.53	1018.23	Jai CV M7+	0°	Trajectory only
20.3	21/12/2005	0.0060	2.43	1.30	59.93	3158	0.2423	0.1865	998.53	1018.23	Jai CV M7+	0°	Trajectory only

21.1	17/01/2006	0.0033	2.43	0.72	23.62	1747	0.2420	0.3367	998.75	1037.54	Jai CV M7+	0°	Trajectory only
21.2	17/01/2006	0.0033	2.43	0.72	23.62	1747	0.2423	0.3372	998.72	1037.50	Jai CV M7+	0°	Trajectory only
21.3	17/01/2006	0.0033	2.43	0.72	23.62	1747	0.2427	0.3377	998.72	1037.50	Jai CV M7+	0°	Trajectory only
22.1	17/01/2006	0.0061	2.43	1.32	43.31	3202	0.1253	0.0951	998.72	1037.50	Jai CV M7+	0°	Trajectory only
22.2	17/01/2006	0.0061	2.43	1.32	43.31	3202	0.1253	0.0951	998.70	1037.49	Jai CV M7+	0°	Trajectory only
22.3	17/01/2006	0.0061	2.43	1.32	43.31	3202	0.1254	0.0952	998.69	1037.47	Jai CV M7+	0°	Trajectory only
23.1	24/01/2006	0.0024	2.43	0.53	17.32	1281	0.1250	0.2372	998.67	1037.45	Jai CV M7+	0°	Trajectory only
23.2	24/01/2006	0.0024	2.43	0.53	17.32	1281	0.1252	0.2376	998.62	1037.40	Jai CV M7+	0°	Trajectory only
23.3	24/01/2006	0.0024	2.43	0.53	17.32	1281	0.1253	0.2378	998.62	1037.40	Jai CV M7+	0°	Trajectory only

Table D.8 - Initial conditions for LA negatively buoyant jet runs

Buoyant Jet in Ambient Flow Run No.	Date	Q_0 (l/s)	d (mm)	U_0 (m/s)	Fr_0	Re_0	$\Delta\rho$	ρ_a (kg/m^3)	ρ (kg/m^3)	l_{jp} (m)	Camera	Angle (ϕ_0)	Comment
1	19/12/2003	0.0060	2.91	0.90	27.15	2625	0.0301	998.67	1028.73	0.17	Canon	0°	
2	19/12/2003	0.0060	2.91	0.90	27.15	2625	0.0301	998.67	1028.73	0.17	Canon	10°	
3	19/12/2003	0.0060	2.91	0.90	27.15	2625	0.0301	998.67	1028.73	0.17	Canon	20°	
4	19/12/2003	0.0060	2.91	0.90	27.15	2625	0.0301	998.67	1028.73	0.17	Canon	30°	
5	19/12/2003	0.0060	2.91	0.90	27.15	2625	0.0301	998.67	1028.73	0.17	Canon	40°	
6	23/01/2004	0.0105	2.91	1.58	59.47	4594	0.0247	998.84	1023.49	0.37	Canon	47°	
7	23/01/2004	0.0050	2.91	0.74	28.04	2166	0.0247	998.84	1023.49	0.18	Canon	47°	
8	23/01/2004	0.0075	2.91	1.12	42.20	3260	0.0247	998.84	1023.49	0.27	Canon	47°	
9	23/01/2004	0.0025	2.91	0.38	14.16	1094	0.0247	998.84	1023.49	0.09	Canon	47°	
10	23/01/2004	0.0037	2.91	0.56	20.96	1619	0.0247	998.84	1023.49	0.13	Canon	47°	
11	11/02/2004	0.0049	2.91	0.74	27.32	2144	0.0255	998.67	1024.10	0.17	Canon	45°	
12	11/02/2004	0.0098	2.91	1.47	54.65	4288	0.0255	998.67	1024.10	0.34	Canon	45°	
13	11/02/2004	0.0074	2.91	1.11	41.27	3238	0.0255	998.67	1024.10	0.26	Canon	45°	
14	11/02/2004	0.0034	2.91	0.51	18.96	1488	0.0255	998.67	1024.10	0.12	Canon	45°	
15	11/02/2004	0.0010	2.91	0.15	5.58	438	0.0255	998.67	1024.10	0.04	Canon	45°	
16	12/02/2004	0.0065	2.91	0.98	36.25	2844	0.0255	998.80	1024.24	0.23	Canon	75°	
17	12/02/2004	0.0052	2.91	0.78	29.00	2275	0.0255	998.80	1024.24	0.18	Canon	75°	
18	19/02/2004	0.0062	2.91	0.93	33.72	2713	0.0268	998.53	1025.26	0.21	Canon	75°	
19	23/02/2004	0.0055	2.91	0.83	29.84	2406	0.0269	998.72	1025.59	0.19	Canon	30°	
20	23/02/2004	0.0104	2.91	1.56	56.42	4550	0.0269	998.72	1025.59	0.36	Canon	30°	
21	23/02/2004	0.0066	2.91	0.99	35.81	2888	0.0269	998.72	1025.59	0.23	Canon	30°	
22	23/02/2004	0.0034	2.91	0.51	18.45	1488	0.0269	998.72	1025.59	0.12	Canon	30°	
23	23/02/2004	0.0010	2.91	0.15	5.43	438	0.0269	998.72	1025.59	0.03	Canon	30°	
24	3/02/2004	0.0119	2.91	1.79	65.97	5207	0.0258	998.84	1024.57	0.42	Canon	30°	
25	3/02/2004	0.0091	2.91	1.36	50.17	3960	0.0258	998.84	1024.57	0.32	Canon	30°	
26	3/02/2004	0.0065	2.91	0.97	35.76	2822	0.0258	998.84	1024.57	0.23	Canon	30°	
27	3/02/2004	0.0078	2.91	1.17	43.24	3413	0.0258	998.84	1024.57	0.27	Canon	30°	
28	3/03/2004	0.0118	2.91	1.77	65.42	5163	0.0258	998.98	1024.72	0.41	Canon	15°	
29	3/03/2004	0.0091	2.91	1.36	50.17	3960	0.0258	998.98	1024.72	0.32	Canon	15°	

30	3/03/2004	0.0065	2.91	0.97	35.76	2822	0.0258	998.98	1024.72	0.23	Canon	15°	
31	4/03/2004	0.0081	2.91	1.21	44.63	3522	0.0258	998.96	1024.70	0.28	Canon	45°	
32	4/03/2004	0.0070	2.91	1.04	38.53	3041	0.0258	998.96	1024.70	0.24	Canon	45°	
33	8/03/2004	0.0083	2.91	1.24	45.74	3610	0.0258	998.79	1024.52	0.29	Canon	60°	
34	8/03/2004	0.0069	2.91	1.03	37.98	2997	0.0258	998.79	1024.52	0.24	Canon	60°	
35	8/03/2004	0.0115	2.91	1.73	63.75	5032	0.0258	998.79	1024.52	0.40	Canon	60°	
36	25/03/2004	0.0089	2.91	1.34	46.79	3894	0.0287	999.02	1027.65	0.29	Canon	0°	
37	25/03/2004	0.0071	2.91	1.07	37.33	3107	0.0287	999.02	1027.65	0.24	Canon	0°	
38	25/03/2004	0.0108	2.91	1.62	56.51	4704	0.0287	999.02	1027.65	0.36	Canon	0°	
39	12/04/2004	0.0066	2.91	0.99	38.29	2888	0.0235	999.22	1022.73	0.24	Canon	0°	
40.1	13/04/2004	0.0077	2.91	1.16	44.40	3369	0.0238	998.98	1022.77	0.28	Canon	15°	Investigate time-averaging
40.2	13/04/2004	0.0077	2.91	1.16	44.40	3369	0.0238	998.98	1022.77	0.28	Canon	15°	Investigate time-averaging
41	14/04/2004	0.0073	2.91	1.09	40.86	3172	0.0249	999.22	1024.14	0.26	Canon	15°	
42	29/10/2004	0.0085	2.94	1.26	48.64	3699	0.0233	999.02	1022.32	0.31	Jai CV M7+	45°	
43	29/10/2004	0.0096	2.94	1.42	54.97	4181	0.0233	999.02	1022.32	0.35	Jai CV M7+	45°	
44	29/10/2004	0.0106	2.94	1.57	60.68	4615	0.0233	999.02	1022.32	0.39	Jai CV M7+	45°	
45	29/10/2004	0.0106	2.94	1.57	60.68	4615	0.0233	999.02	1022.32	0.39	Jai CV M7+	45°	
46	29/10/2004	0.0096	2.94	1.42	54.97	4181	0.0233	999.02	1022.32	0.35	Jai CV M7+	45°	
47	26/01/2005	0.0064	2.94	0.95	35.28	2796	0.0253	998.49	1023.77	0.22	Jai CV M7+	45°	
48	26/01/2005	0.0107	2.94	1.58	58.54	4639	0.0253	998.49	1023.77	0.37	Jai CV M7+	45°	
49	26/01/2005	0.0107	2.94	1.58	58.54	4639	0.0253	998.49	1023.77	0.37	Jai CV M7+	45	
50	26/01/2005	0.0083	2.94	1.23	45.62	3615	0.0253	998.49	1023.77	0.29	Jai CV M7+	45	
51	26/01/2005	0.0083	2.94	1.23	45.62	3615	0.0253	998.49	1023.77	0.29	Jai CV M7+	45	
52	27/01/2005	0.0068	2.94	1.00	37.10	2940	0.0253	998.58	1023.87	0.24	Jai CV M7+	60°	
53	27/01/2005	0.0077	2.94	1.13	41.97	3326	0.0253	998.58	1023.87	0.27	Jai CV M7+	60°	
54	27/01/2005	0.0083	2.94	1.22	45.16	3579	0.0253	998.58	1023.87	0.29	Jai CV M7+	60°	
55	27/01/2005	0.0093	2.94	1.38	50.94	4037	0.0253	998.58	1023.87	0.32	Jai CV M7+	60°	
56	27/01/2005	0.0106	2.94	1.57	58.24	4615	0.0253	998.49	1023.77	0.37	Jai CV M7+	60°	
57	27/01/2005	0.0106	2.94	1.57	58.24	4615	0.0253	998.49	1023.77	0.37	Jai CV M7+	60°	
58	28/01/2005	0.0062	2.94	0.92	33.91	2687	0.0253	998.56	1023.85	0.22	Jai CV M7+	30°	
59	28/01/2005	0.0081	2.94	1.20	44.55	3531	0.0253	998.56	1023.85	0.28	Jai CV M7+	30°	
60	28/01/2005	0.0070	2.94	1.03	38.32	3037	0.0253	998.56	1023.85	0.24	Jai CV M7+	30°	
61	28/01/2005	0.0106	2.94	1.57	58.24	4615	0.0253	998.56	1023.85	0.37	Jai CV M7+	30°	
62	28/01/2005	0.0106	2.94	1.57	58.24	4615	0.0253	998.56	1023.85	0.37	Jai CV M7+	30°	
63	31/01/2005	0.0062	2.94	0.92	34.06	2699	0.0253	998.49	1023.77	0.22	Jai CV M7+	15°	
64	31/01/2005	0.0069	2.94	1.02	37.71	2988	0.0253	998.49	1023.77	0.24	Jai CV M7+	15°	
65	31/01/2005	0.0085	2.94	1.26	46.53	3687	0.0253	998.49	1023.77	0.30	Jai CV M7+	15°	
66	31/01/2005	0.0085	2.94	1.26	46.53	3687	0.0253	998.49	1023.77	0.30	Jai CV M7+	15°	
67	31/01/2005	0.0106	2.94	1.57	58.24	4615	0.0253	998.46	1023.74	0.37	Jai CV M7+	15°	
68	31/01/2005	0.0106	2.94	1.57	58.24	4615	0.0253	998.46	1023.74	0.37	Jai CV M7+	15°	
69	7/02/2005	0.0068	2.94	1.00	36.95	2928	0.0253	998.60	1023.88	0.23	Jai CV M7+	45°	
70	7/02/2005	0.0074	2.94	1.09	40.45	3205	0.0253	998.67	1023.96	0.26	Jai CV M7+	45°	
71	7/02/2005	0.0079	2.94	1.16	43.03	3410	0.0253	998.67	1023.96	0.27	Jai CV M7+	45°	

Table D.9 - Initial conditions for LIF negatively buoyant jets

Buoyant Jet in Ambient Flow Run No.	Date	Q_0 (l/s)	d (mm)	U_0 (m/s)	Fr_0	Re_0	$\Delta\rho$	ρ_a (kg/m^3)	ρ (kg/m^3)	l_{jp} (m)	Camera	Angle (ϕ_0)	Comment
1	14/09/2004	0.0069	2.45	1.47	54.69	3595	0.0299	998.99	1028.91	0.29	Pulnix TM 1010	5°	
2	14/09/2004	0.0092	2.45	1.94	72.48	4764	0.0299	998.99	1028.91	0.38	Pulnix TM 1010	5°	
3	14/09/2004	0.0060	2.45	1.28	47.66	3133	0.0299	998.99	1028.91	0.25	Pulnix TM 1010	5°	
4	14/09/2004	0.0081	2.45	1.71	63.91	4201	0.0299	998.99	1028.91	0.34	Pulnix TM 1010	5°	
5	16/09/2004	0.0061	2.45	1.28	47.88	3147	0.0299	998.99	1028.91	0.25	Pulnix TM 1010	10°	
6	16/09/2004	0.0090	2.45	1.91	71.16	4677	0.0299	998.99	1028.91	0.38	Pulnix TM 1010	10°	
7	16/09/2004	0.0065	2.45	1.38	51.61	3392	0.0299	998.99	1028.91	0.27	Pulnix TM 1010	10°	
8	16/09/2004	0.0080	2.45	1.70	63.47	4172	0.0299	998.99	1028.91	0.34	Pulnix TM 1010	10°	
9	20/09/2004	0.0061	2.45	1.30	48.32	3176	0.0299	998.96	1028.87	0.26	Pulnix TM 1010	15°	
10	20/09/2004	0.0090	2.45	1.91	71.16	4677	0.0299	998.96	1028.87	0.38	Pulnix TM 1010	15°	
11	20/09/2004	0.0068	2.45	1.44	53.59	3522	0.0299	998.96	1028.87	0.28	Pulnix TM 1010	15°	
12	20/09/2004	0.0080	2.45	1.70	63.47	4172	0.0299	998.96	1028.87	0.34	Pulnix TM 1010	15°	
13	21/09/2004	0.0062	2.45	1.31	48.76	3205	0.0299	998.98	1028.89	0.26	Pulnix TM 1010	30°	
14	21/09/2004	0.0090	2.45	1.91	71.16	4677	0.0299	998.98	1028.89	0.38	Pulnix TM 1010	30°	
15	22/09/2004	0.0060	2.45	1.27	47.44	3118	0.0299	998.99	1028.91	0.25	Pulnix TM 1010	41.4°	
16	22/09/2004	0.0067	2.45	1.42	52.93	3479	0.0299	998.99	1028.91	0.28	Pulnix TM 1010	41.4°	
17	23/09/2004	0.0061	2.45	1.28	47.88	3147	0.0299	998.98	1028.89	0.25	Pulnix TM 1010	37.5°	
18	23/09/2004	0.0093	2.45	1.97	73.58	4836	0.0299	998.98	1028.89	0.39	Pulnix TM 1010	37.5°	
19	23/09/2004	0.0071	2.45	1.51	56.23	3696	0.0299	999.12	1029.04	0.30	Pulnix TM 1010	37.5°	
20	23/09/2004	0.0082	2.45	1.74	65.01	4273	0.0299	999.12	1029.04	0.34	Pulnix TM 1010	37.5°	
21	23/09/2004	0.0059	2.45	1.26	47.00	3089	0.0299	998.98	1028.89	0.25	Pulnix TM 1010	52.5°	
22	23/09/2004	0.0093	2.45	1.97	73.58	4836	0.0299	998.98	1028.89	0.39	Pulnix TM 1010	52.5°	
23	23/09/2004	0.0069	2.45	1.47	54.69	3595	0.0299	998.98	1028.89	0.29	Pulnix TM 1010	52.5°	
24	23/09/2004	0.0083	2.45	1.75	65.23	4287	0.0299	998.98	1028.89	0.35	Pulnix TM 1010	52.5°	
25	23/09/2004	0.0062	2.45	1.32	49.20	3234	0.0299	998.98	1028.89	0.26	Pulnix TM 1010	60°	
26	23/09/2004	0.0082	2.45	1.73	64.57	4244	0.0299	998.98	1028.89	0.34	Pulnix TM 1010	60°	
27	24/09/2004	0.0059	2.45	1.26	47.00	3089	0.0299	998.98	1028.89	0.25	Pulnix TM 1010	65.5°	
28	24/09/2004	0.0071	2.45	1.50	56.01	3681	0.0299	998.98	1028.89	0.30	Pulnix TM 1010	65.5°	
29	24/09/2004	0.0085	2.45	1.81	67.43	4432	0.0299	998.98	1028.89	0.36	Pulnix TM 1010	65.5°	
30	24/09/2004	0.0091	2.45	1.93	71.82	4721	0.0299	998.98	1028.89	0.38	Pulnix TM 1010	65.5°	
31	6/01/2005	0.0046	2.45	0.97	39.46	2388	0.0254	998.72	1024.08	0.21	Pulnix TM 1010	45°	
32	6/01/2005	0.0057	2.45	1.20	48.66	2945	0.0254	998.72	1024.08	0.26	Pulnix TM 1010	45°	
33	6/01/2005	0.0068	2.45	1.44	58.44	3537	0.0254	998.72	1024.08	0.31	Pulnix TM 1010	45°	
34	6/01/2005	0.0083	2.45	1.77	71.56	4331	0.0254	998.72	1024.08	0.38	Pulnix TM 1010	45°	
35	6/01/2005	0.0104	2.45	2.20	88.97	5385	0.0254	998.72	1024.08	0.47	Pulnix TM 1010	45°	
36	6/01/2005	0.0092	2.45	1.94	78.71	4764	0.0254	998.72	1024.08	0.42	Pulnix TM 1010	45°	
37	6/01/2005	0.0108	2.45	2.30	93.02	5630	0.0254	998.72	1024.08	0.49	Pulnix TM 1010	45°	
38	12/01/2005	0.0072	2.45	1.53	62.02	3753	0.0254	998.72	1024.08	0.33	Pulnix TM 1010	45°	
39	12/01/2005	0.0083	2.45	1.77	71.56	4331	0.0254	998.72	1024.08	0.38	Pulnix TM 1010	45°	
40	17/01/2005	0.0058	2.45	1.23	49.61	3003	0.0254	998.70	1024.06	0.26	Pulnix TM 1010	45°	

Table D.10 - Initial condition for non-buoyant oblique discharges in moving ambient

Oblique Discharge Run No.	Date	Q_0 (l/s)	d (mm)	U_0 (m/s)	Fr_0	Re_0	U_a (m/s)	U_r	ρ_a (kg/m^3)	ρ (kg/m^3)	Camera	Angle (ϕ_0)	Comment
1.1	9/12/2003	0.0100	3.00	1.41	1471	4244	0.0330	0.0233	998.91	998.88	Canon	70°	
1.2	9/12/2003	0.0100	3.00	1.41	1471	4244	0.0330	0.0233	998.91	998.88	Canon	70°	
2.1	10/12/2003	0.0100	3.00	1.41	941	4244	0.0334	0.0236	998.91	998.99	Canon	100°	
2.2	10/12/2003	0.0100	3.00	1.41	2090	4244	0.0335	0.0237	998.91	998.93	Canon	100°	
3.1	11/12/2003	0.0100	2.91	1.50	850	4375	0.0335	0.0223	998.96	998.85	Canon	60°	
3.2	11/12/2003	0.0100	2.91	1.50	2256	4375	0.0335	0.0223	998.91	998.93	Canon	60°	
4.1	11/12/2003	0.0100	2.91	1.50	1307	4375	0.0336	0.0223	998.96	998.91	Canon	110°	
4.2	11/12/2003	0.0100	2.91	1.50	1009	4375	0.0337	0.0224	998.96	998.88	Canon	110°	
5.1	12/12/2003	0.0100	2.91	1.50	1587	4375	0.0337	0.0224	998.91	998.88	Canon	120°	
5.2	12/12/2003	0.0100	2.91	1.50	1015	4375	0.0333	0.0222	998.91	998.99	Canon	120°	
6.1	12/12/2003	0.0100	2.91	1.50	1587	4375	0.0332	0.0221	998.91	998.88	Canon	130°	
6.2	12/12/2003	0.0100	2.91	1.50	842	4375	0.0332	0.0221	998.91	998.80	Canon	130°	
7.1	12/12/2003	0.0100	2.91	1.50	583	4375	0.0331	0.0220	998.63	998.87	Canon	30°	
7.2	12/12/2003	0.0100	2.91	1.50	1515	4375	0.0332	0.0221	998.63	998.67	Canon	30°	
8.1	15/12/2003	0.0100	2.91	1.50	∞	4375	0.0332	0.0221	998.63	998.63	Canon	20°	
8.2	15/12/2003	0.0100	2.91	1.50	∞	4375	0.0334	0.0222	998.63	998.63	Canon	20°	
9.1	16/12/2003	0.0100	2.91	1.50	983	4375	0.0330	0.0220	998.84	998.75	Canon	10°	
9.2	16/12/2003	0.0100	2.91	1.50	∞	4375	0.0331	0.0220	998.84	998.84	Canon	10°	
10.1	16/12/2003	0.0100	2.91	1.50	1562	4375	0.0331	0.0220	998.84	998.80	Canon	140°	
10.2	16/12/2003	0.0100	2.91	1.50	983	4375	0.0331	0.0220	998.84	998.75	Canon	140°	
11.1	17/12/2003	0.0100	2.91	1.50	1273	4375	0.0329	0.0219	998.84	998.79	Canon	50°	
11.2	17/12/2003	0.0100	2.91	1.50	1273	4375	0.0331	0.0220	998.84	998.79	Canon	50°	
12.1	17/12/2003	0.0100	2.91	1.50	1273	4375	0.0330	0.0219	998.84	998.79	Canon	0°	
12.2	17/12/2003	0.0100	2.91	1.50	1273	4375	0.0331	0.0220	998.84	998.79	Canon	0°	
13.1	17/12/2003	0.0080	2.91	1.20	712	3500	0.0330	0.0275	998.80	998.70	Canon	80°	
13.2	17/12/2003	0.0080	2.91	1.20	548	3500	0.0331	0.0275	998.80	998.63	Canon	80°	
14.1	18/12/2003	0.0100	2.91	1.50	828	4375	0.0337	0.0224	998.84	998.72	Canon	50°	No analysis
14.2	18/12/2003	0.0100	2.91	1.50	983	4375	0.0338	0.0225	998.84	998.75	Canon	50°	No analysis
15.1	21/10/2004	0.0099	2.45	2.10	∞	5154	0.0804	0.0382	999.02	999.02	Jai CV M7+	10°	No dilution results
15.2	21/10/2004	0.0099	2.45	2.10	∞	5154	0.0809	0.0385	999.02	999.02	Jai CV M7+	10°	No dilution results
16.1	22/10/2004	0.0098	2.45	2.07	∞	5081	0.0800	0.0386	999.12	999.12	Jai CV M7+	12.5°	No dilution results
16.2	22/10/2004	0.0098	2.45	2.07	3536	5067	0.0809	0.0391	999.12	999.11	Jai CV M7+	12.5°	No dilution results
17.1	26/10/2004	0.0097	2.45	2.06	3567	5038	0.0798	0.0388	999.18	999.16	Jai CV M7+	15°	No dilution results
17.2	26/10/2004	0.0097	2.45	2.06	∞	5038	0.0807	0.0392	999.18	999.18	Jai CV M7+	15°	No dilution results
18.1	27/10/2004	0.0097	2.45	2.06	∞	5053	0.0805	0.0390	999.11	999.11	Jai CV M7+	17.5°	No dilution results
18.2	27/10/2004	0.0098	2.45	2.07	∞	5067	0.0808	0.0391	999.11	999.11	Jai CV M7+	17.5°	No dilution results
19.1	28/10/2004	0.0099	2.45	2.10	∞	5154	0.0805	0.0383	999.02	999.02	Jai CV M7+	20°	No dilution results
19.2	28/10/2004	0.0099	2.45	2.10	∞	5154	0.0809	0.0384	999.02	999.02	Jai CV M7+	20°	No dilution results
20.1	22/03/2005	0.0076	2.45	1.62	∞	3970	0.0512	0.0316	998.87	998.87	Jai CV M7+	13.5°	
20.2	22/03/2005	0.0077	2.45	1.63	∞	3999	0.0517	0.0317	998.87	998.87	Jai CV M7+	13.5°	
20.3	22/03/2005	0.0077	2.45	1.64	∞	4013	0.0518	0.0316	998.84	998.84	Jai CV M7+	13.5°	
21.1	24/03/2005	0.0083	2.45	1.77	∞	4331	0.0516	0.0292	998.77	998.77	Jai CV M7+	15°	
21.2	24/03/2005	0.0083	2.45	1.76	∞	4302	0.0517	0.0294	998.70	998.70	Jai CV M7+	15°	

21.3	24/03/2005	0.0084	2.45	1.79	∞	4374	0.0517	0.0289	998.70	998.70	Jai CV M7+	15°
22.1	4/04/2005	0.0083	2.45	1.76	∞	4316	0.0519	0.0294	998.84	998.84	Jai CV M7+	12.5°
22.2	4/04/2005	0.0083	2.45	1.77	∞	4331	0.0518	0.0293	998.84	998.84	Jai CV M7+	12.5°
22.3	4/04/2005	0.0083	2.45	1.77	∞	4331	0.0518	0.0293	998.82	998.82	Jai CV M7+	12.5°
23.1	29/04/2005	0.0084	2.45	1.79	∞	4374	0.0517	0.0290	999.30	999.30	Jai CV M7+	0°
23.2	29/04/2005	0.0084	2.45	1.78	∞	4360	0.0517	0.0291	999.27	999.27	Jai CV M7+	0°
23.3	29/04/2005	0.0084	2.45	1.79	∞	4374	0.0517	0.0289	999.26	999.26	Jai CV M7+	0°
24.1	5/05/2005	0.0083	2.45	1.77	∞	4331	0.0516	0.0292	998.93	998.93	Jai CV M7+	10°
24.2	5/05/2005	0.0084	2.45	1.78	∞	4360	0.0518	0.0291	998.93	998.93	Jai CV M7+	10°
24.3	5/05/2005	0.0084	2.45	1.77	∞	4345	0.0518	0.0292	998.93	998.93	Jai CV M7+	10°
25.1	6/05/2005	0.0083	2.45	1.77	∞	4331	0.0517	0.0293	999.19	999.19	Jai CV M7+	20°
25.2	6/05/2005	0.0084	2.45	1.77	∞	4345	0.0517	0.0292	999.15	999.15	Jai CV M7+	20°
25.3	6/05/2005	0.0084	2.45	1.79	∞	4374	0.0518	0.0290	999.14	999.14	Jai CV M7+	20°
26.1	9/05/2005	0.0084	2.45	1.79	∞	4374	0.0517	0.0290	999.30	999.30	Jai CV M7+	45°
26.2	9/05/2005	0.0085	2.45	1.81	∞	4432	0.0517	0.0286	999.27	999.27	Jai CV M7+	45°
26.3	9/05/2005	0.0083	2.45	1.77	∞	4331	0.0517	0.0293	999.27	999.27	Jai CV M7+	45°
27.1	10/05/2005	0.0083	2.45	1.77	∞	4331	0.0517	0.0293	999.34	999.34	Jai CV M7+	15°
27.2	10/05/2005	0.0084	2.45	1.77	∞	4345	0.0517	0.0292	999.34	999.34	Jai CV M7+	15°
27.3	10/05/2005	0.0084	2.45	1.79	∞	4374	0.0518	0.0290	999.34	999.34	Jai CV M7+	15°
28.1	11/05/2005	0.0083	2.45	1.76	∞	4316	0.0517	0.0294	999.30	999.30	Jai CV M7+	12°
28.2	11/05/2005	0.0084	2.45	1.77	∞	4345	0.0517	0.0292	999.30	999.30	Jai CV M7+	12°
28.3	11/05/2005	0.0084	2.45	1.79	∞	4374	0.0518	0.0290	999.30	999.30	Jai CV M7+	12°
29.1	30/08/2005	0.0084	2.45	1.78	∞	4360	0.0521	0.0293	999.39	999.39	Jai CV M7+	40°
29.2	30/08/2005	0.0083	2.45	1.76	∞	4316	0.0522	0.0296	999.32	999.32	Jai CV M7+	40°
29.3	30/08/2005	0.0083	2.45	1.76	∞	4316	0.0521	0.0296	999.32	999.32	Jai CV M7+	40°
30.1	31/08/2005	0.0083	2.45	1.77	∞	4331	0.0521	0.0295	999.40	999.40	Jai CV M7+	35°
30.2	31/08/2005	0.0083	2.45	1.76	∞	4316	0.0522	0.0296	999.34	999.34	Jai CV M7+	35°
30.3	31/08/2005	0.0084	2.45	1.78	∞	4360	0.0522	0.0293	999.32	999.32	Jai CV M7+	35°

Table D.11 - Initial Condition for buoyant jets with 3D trajectories

Buoyant Jet Run No.	Date	Q_0 (l/s)	d (mm)	U_0 (m/s)	Fr_0	Re_0	U_a (m/s)	U_r	ρ_a (kg/m^3)	ρ (kg/m^3)	Camera (Jai CV)	Angle (α_0)	Angle (β_0)	View
1.1	19/09/2005	0.0065	2.43	1.40	64.79	3391	0.0052	0.0374	999.37	1018.83	M7+	0°	90°	y-integrated
1.2	19/09/2005	0.0065	2.43	1.40	64.79	3391	0.0052	0.0374	999.37	1018.83	M7+ CL	0°	90°	z-integrated
1.3	19/09/2005	0.0064	2.43	1.38	63.95	3348	0.0052	0.0379	999.30	1018.75	M7+	0°	90°	y-integrated
1.4	19/09/2005	0.0064	2.43	1.38	63.95	3348	0.0052	0.0379	999.30	1018.75	M7+ CL	0°	90°	z-integrated
1.5	19/09/2005	0.0063	2.43	1.37	63.40	3319	0.0052	0.0383	999.30	1018.75	M7+	0°	90°	y-integrated
1.6	19/09/2005	0.0063	2.43	1.37	63.40	3319	0.0052	0.0383	999.30	1018.75	M7+ CL	0°	90°	z-integrated
2.1	06/10/2005	0.0078	2.43	1.69	77.51	4104	0.0052	0.0309	999.30	1019.20	M7+	0°	45°	y-integrated
2.2	06/10/2005	0.0078	2.43	1.69	77.51	4104	0.0052	0.0309	999.30	1019.20	M7+ CL	0°	45°	z-integrated
2.3	06/10/2005	0.0078	2.43	1.68	77.24	4090	0.0052	0.0311	999.29	1019.19	M7+	0°	45°	y-integrated
2.4	06/10/2005	0.0078	2.43	1.68	77.24	4090	0.0052	0.0311	999.29	1019.19	M7+ CL	0°	45°	z-integrated
2.5	06/10/2005	0.0078	2.43	1.68	77.24	4090	0.0052	0.0311	999.30	1019.16	M7+	0°	45°	y-integrated
2.6	06/10/2005	0.0078	2.43	1.68	77.24	4090	0.0052	0.0311	999.30	1019.16	M7+ CL	0°	45°	z-integrated
3.1	10/10/2005	0.0078	2.43	1.68	76.96	4075	0.0052	0.0311	999.32	1019.23	M7+	0°	135°	y-integrated
3.2	10/10/2005	0.0078	2.43	1.68	76.96	4075	0.0052	0.0311	999.32	1019.23	M7+ CL	0°	135°	z-integrated
3.3	10/10/2005	0.0078	2.43	1.68	76.96	4075	0.0052	0.0311	999.31	1019.21	M7+	0°	135°	y-integrated
3.4	10/10/2005	0.0078	2.43	1.68	76.96	4075	0.0052	0.0311	999.31	1019.21	M7+ CL	0°	135°	z-integrated
3.5	10/10/2005	0.0078	2.43	1.68	76.96	4075	0.0052	0.0311	999.26	1019.16	M7+	0°	135°	y-integrated
3.6	10/10/2005	0.0078	2.43	1.68	76.96	4075	0.0052	0.0311	999.26	1019.16	M7+ CL	0°	135°	z-integrated
4.1	17/10/2005	0.0078	2.43	1.68	76.96	4075	0.0052	0.0311	999.32	1019.23	M7+	45°	90°	y-integrated
4.2	17/10/2005	0.0078	2.43	1.68	76.96	4075	0.0052	0.0311	999.32	1019.23	M7+ CL	45°	90°	z-integrated
4.3	17/10/2005	0.0077	2.43	1.67	76.41	4046	0.0052	0.0312	999.31	1019.21	M7+	45°	90°	y-integrated
4.4	17/10/2005	0.0077	2.43	1.67	76.41	4046	0.0052	0.0312	999.31	1019.21	M7+ CL	45°	90°	z-integrated
4.5	17/10/2005	0.0078	2.43	1.68	76.96	4075	0.0052	0.0311	999.30	1019.20	M7+	45°	90°	y-integrated
4.6	17/10/2005	0.0078	2.43	1.68	76.96	4075	0.0052	0.0311	999.30	1019.20	M7+ CL	45°	90°	z-integrated
5.1	18/10/2005	0.0078	2.43	1.68	76.96	4075	0.0052	0.0310	999.32	1019.23	M7+	60°	90°	y-integrated
5.2	18/10/2005	0.0078	2.43	1.68	76.96	4075	0.0052	0.0310	999.32	1019.23	M7+ CL	60°	90°	z-integrated
5.3	18/10/2005	0.0078	2.43	1.69	77.51	4104	0.0052	0.0309	999.32	1019.23	M7+	60°	90°	y-integrated
5.4	18/10/2005	0.0078	2.43	1.69	77.51	4104	0.0052	0.0309	999.32	1019.23	M7+ CL	60°	90°	z-integrated
5.5	18/10/2005	0.0078	2.43	1.68	76.96	4075	0.0052	0.0311	999.29	1019.19	M7+	60°	90°	y-integrated
5.6	18/10/2005	0.0078	2.43	1.68	76.96	4075	0.0052	0.0311	999.29	1019.19	M7+ CL	60°	90°	z-integrated

Appendix E – Additional Figures

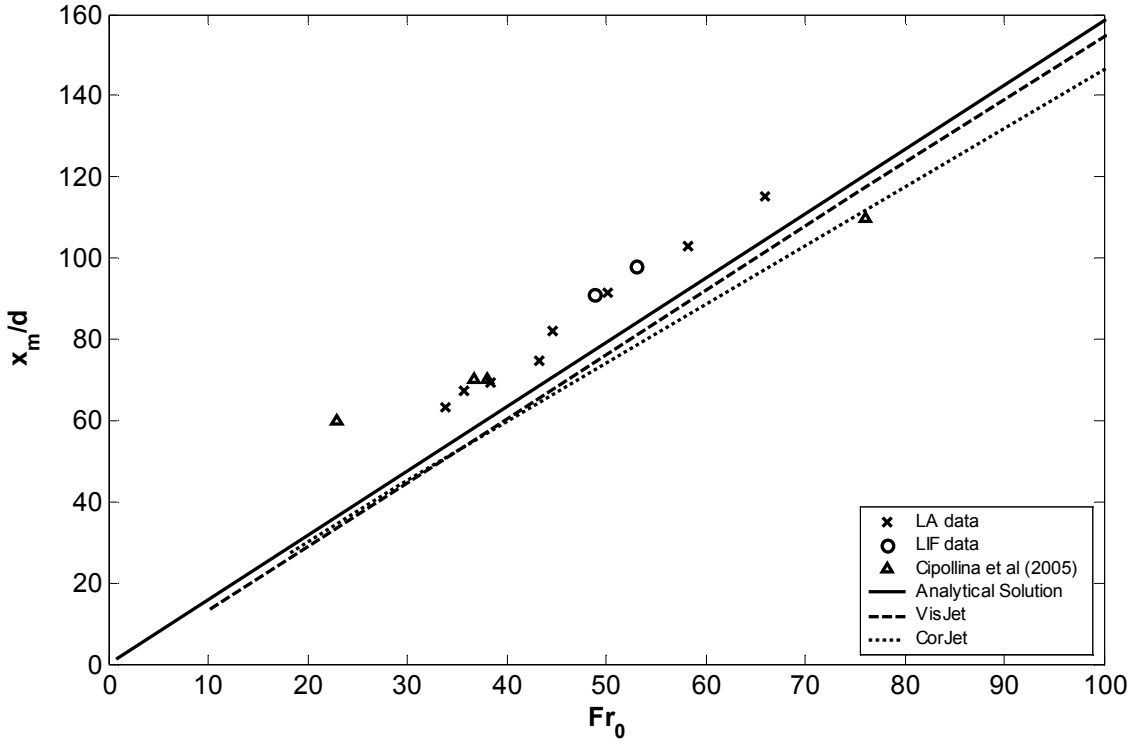

E.1(a) - Initial angle of 30° and Reynolds numbers ranging from 2406 to 5207

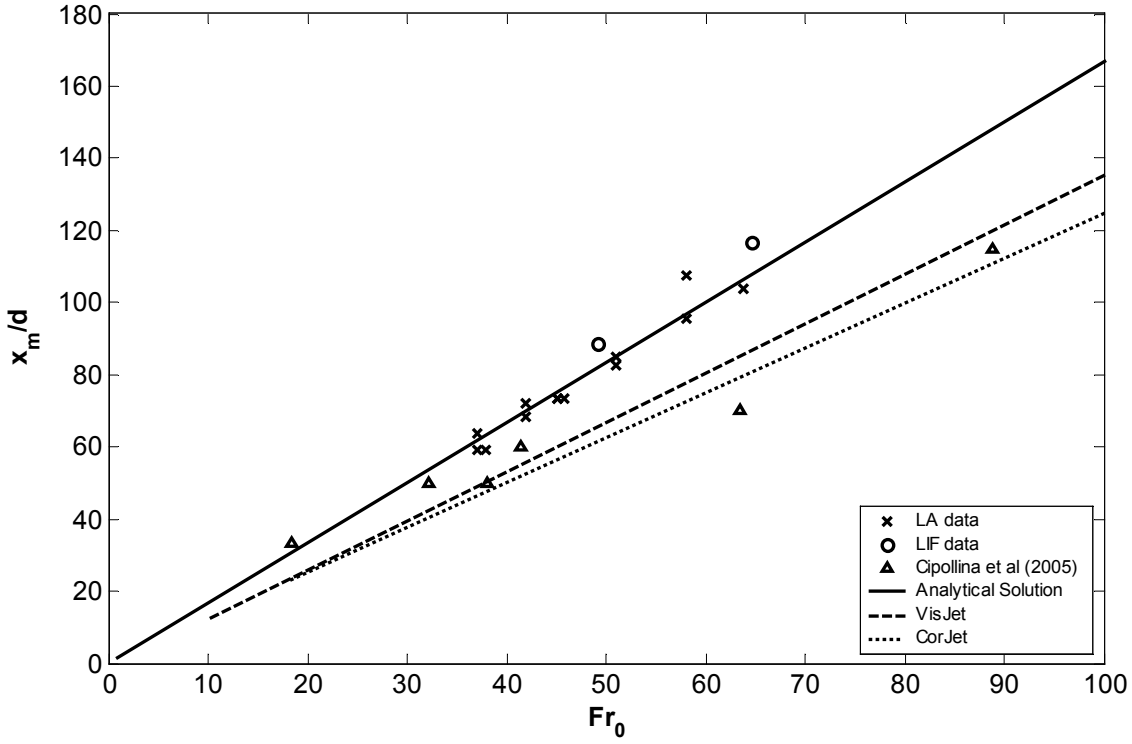

E.1(b) - Initial angle of 60° and Reynolds numbers ranging from 2997 to 5032

Figure E.1 – Horizontal location of maximum centreline height for flows with initial angles of 30° and 60°

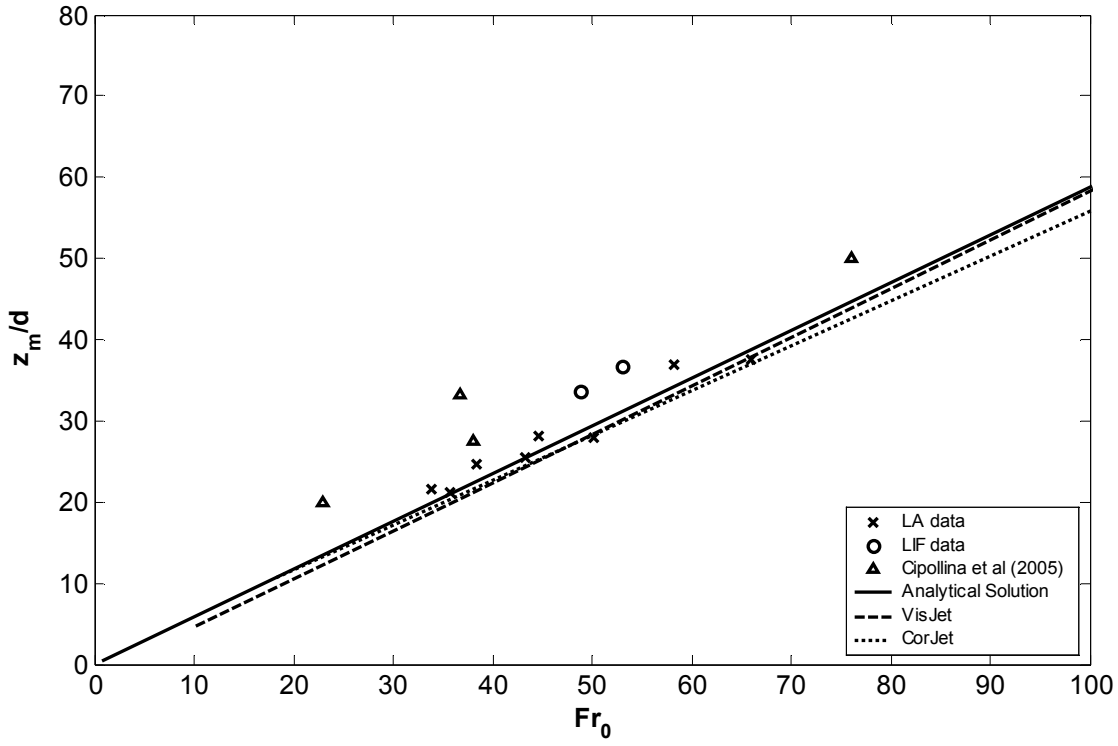

E.2(a) - Initial angle of 30° and Reynolds numbers ranging from 2406 to 5207

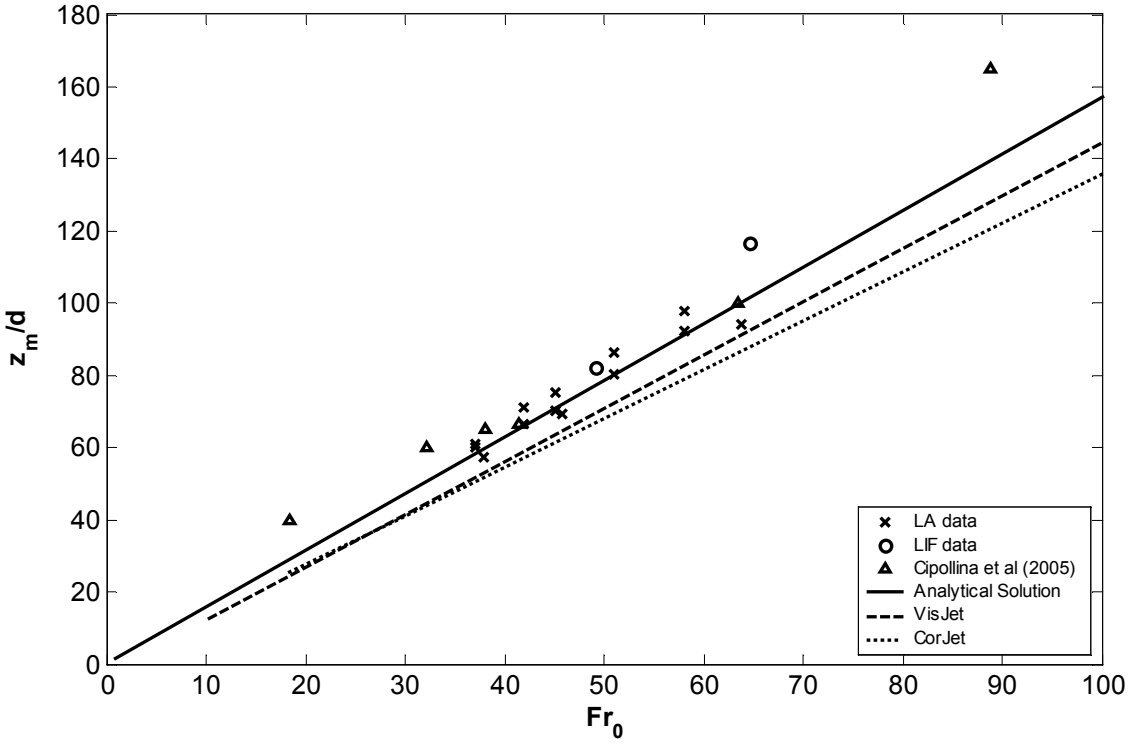

E.2(b) - Initial angle of 60° and Reynolds numbers ranging from 2997 to 5032

Figure E.2 - Vertical location of maximum centreline height for discharges with initial angles of 30° and 60°

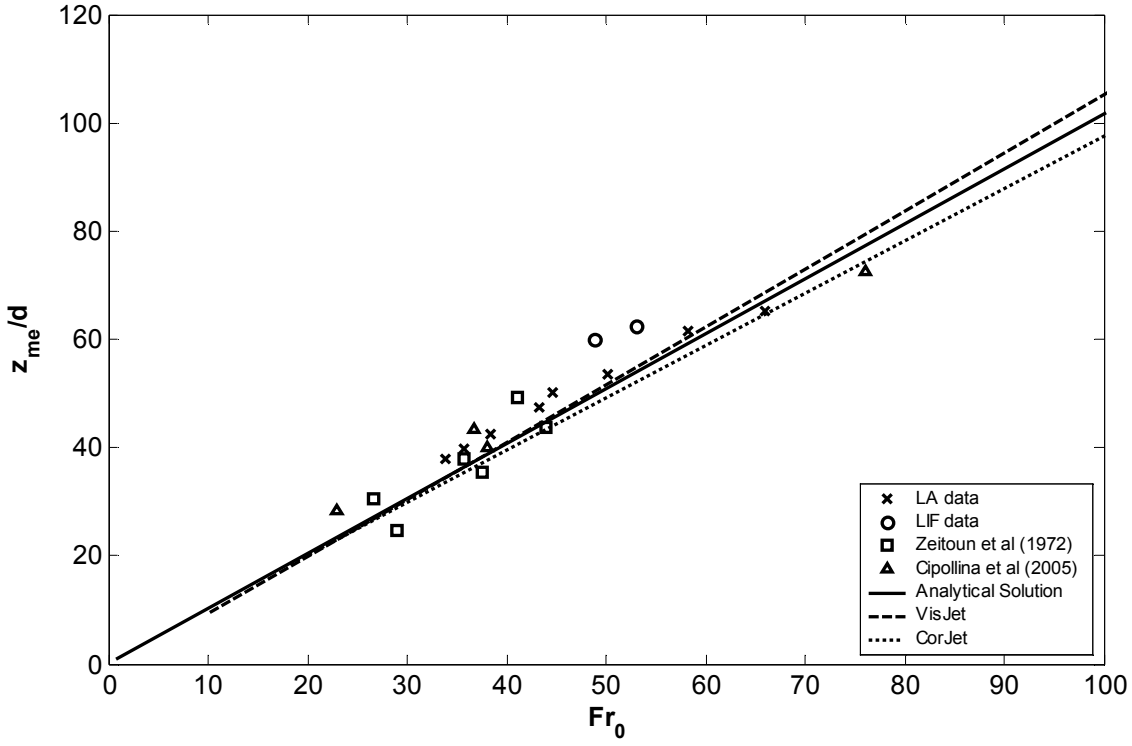

E.3(a) - Initial angle of 30° and Reynolds numbers ranging from 2406 to 5207

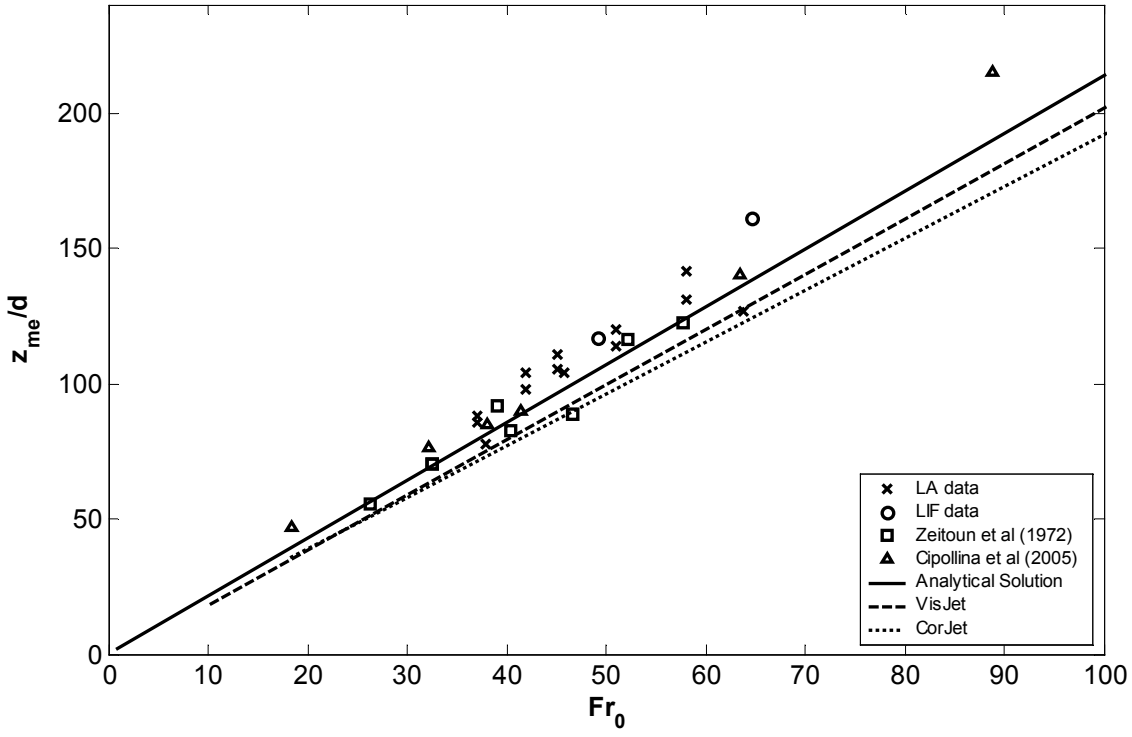

E.3(b) - Initial angle of 60° and Reynolds numbers ranging from 2997 to 5032

Figure E.3 - Maximum height of edge of jet for discharges with initial angles of 30° and 60°

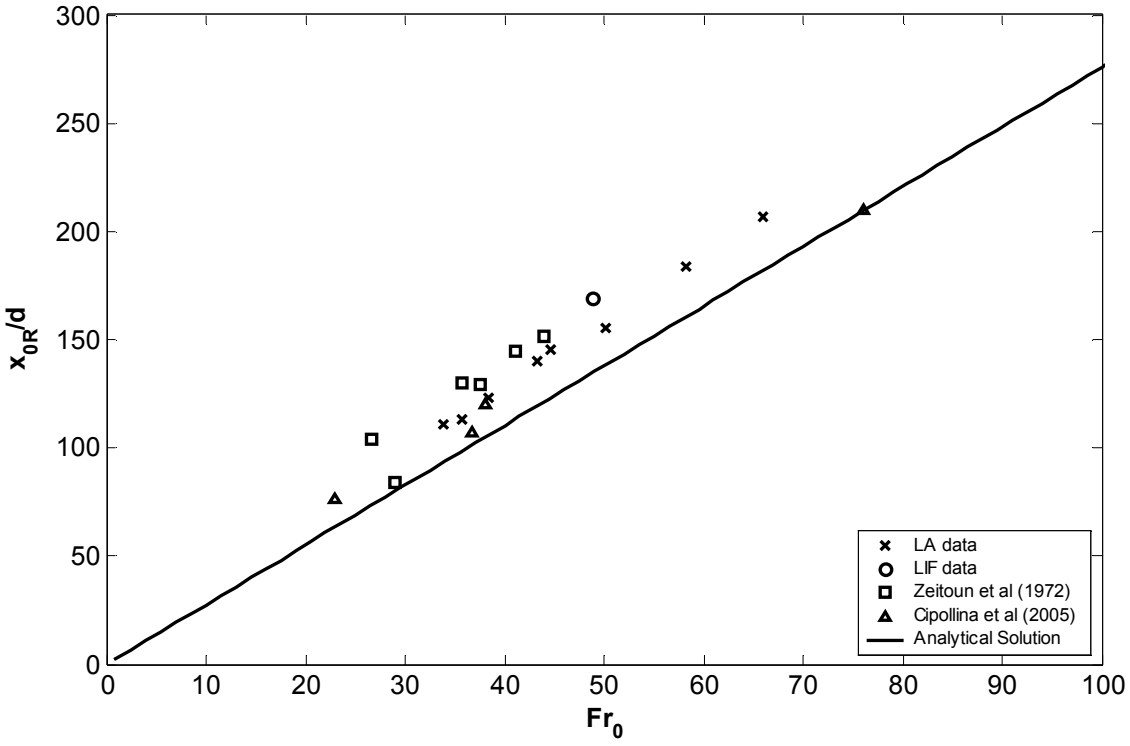

E.4(a) - Initial angle of 30° and Reynolds numbers ranging from 2406 to 5207

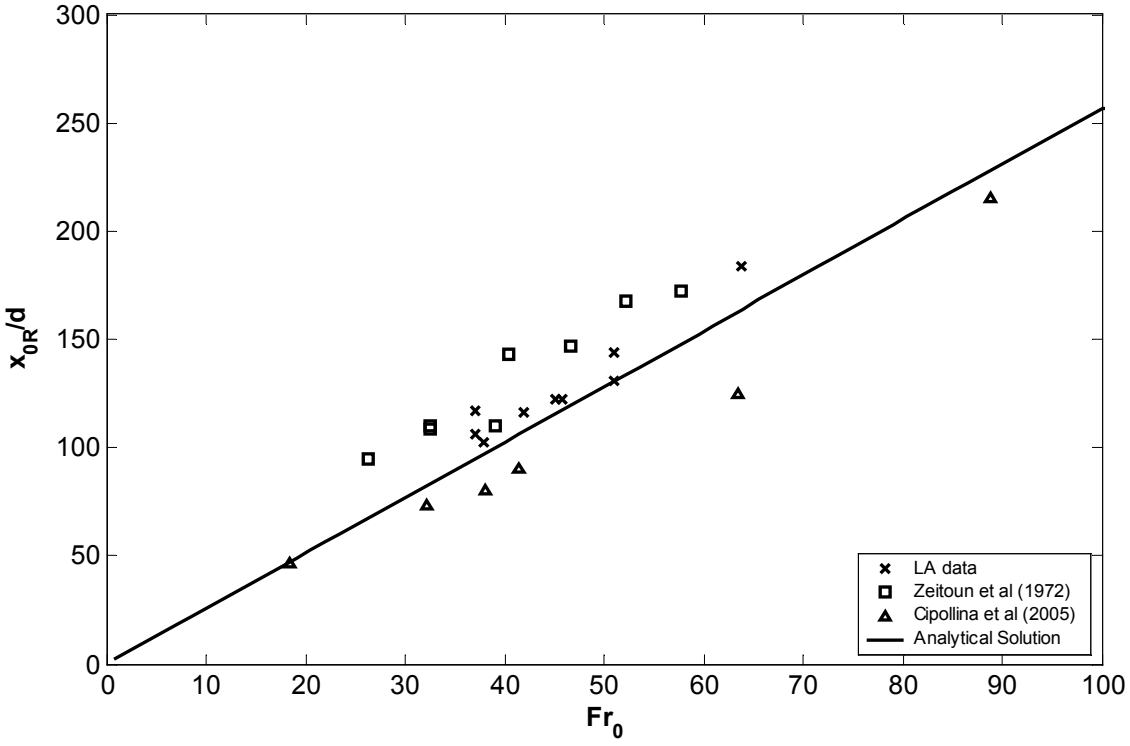

E.4(b) - Initial angle of 60° and Reynolds numbers ranging from 2997 to 5032

Figure E.4 - Horizontal location of impact point for flows with initial angles of 30° and 60°

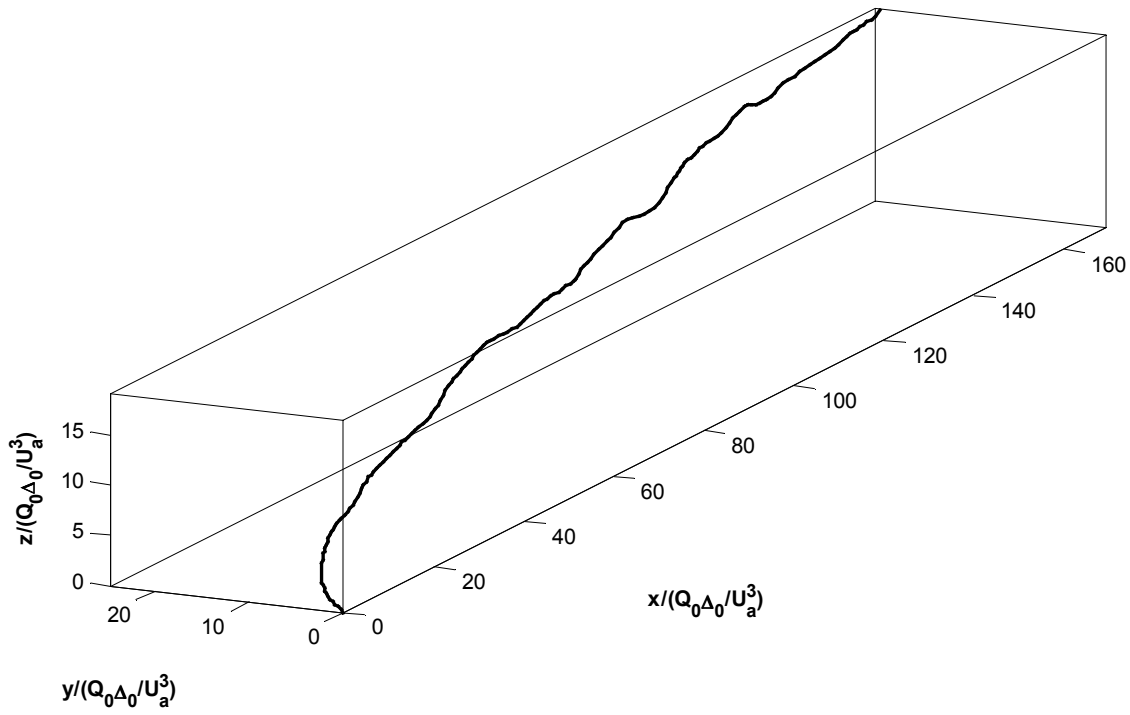

Figure E.5 - Three-dimensional view of trajectory results
buoyant jet with three-dimensional trajectories run 2

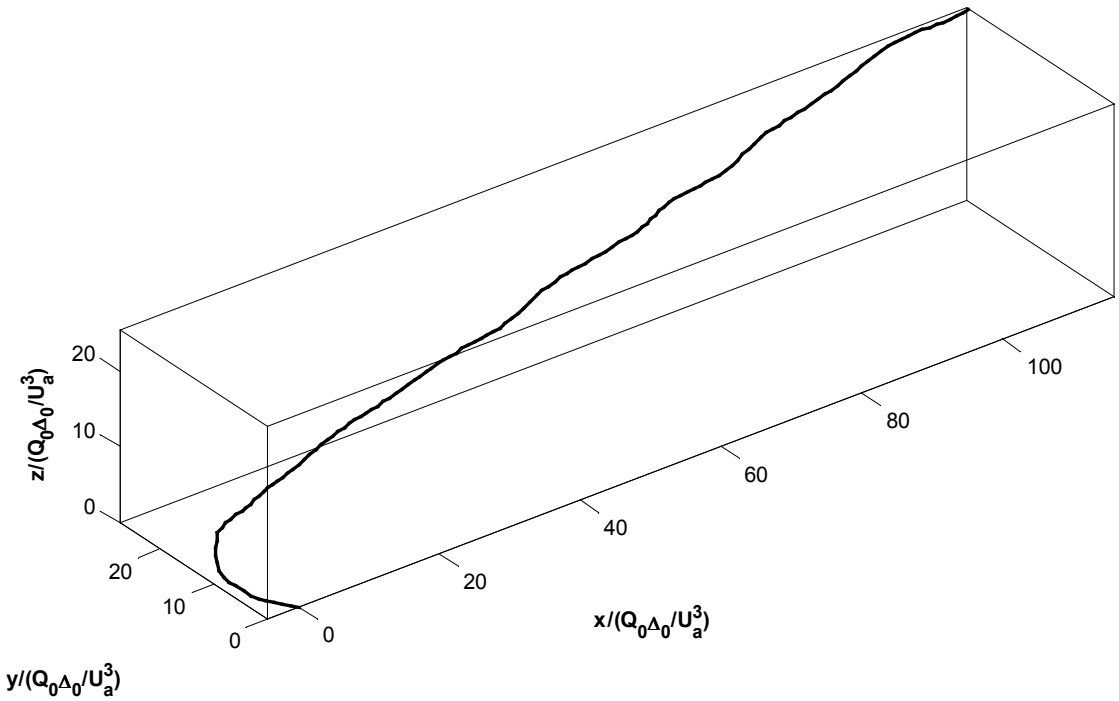

Figure E.6 - Three-dimensional view of trajectory results
buoyant jet with three-dimensional trajectories run 3

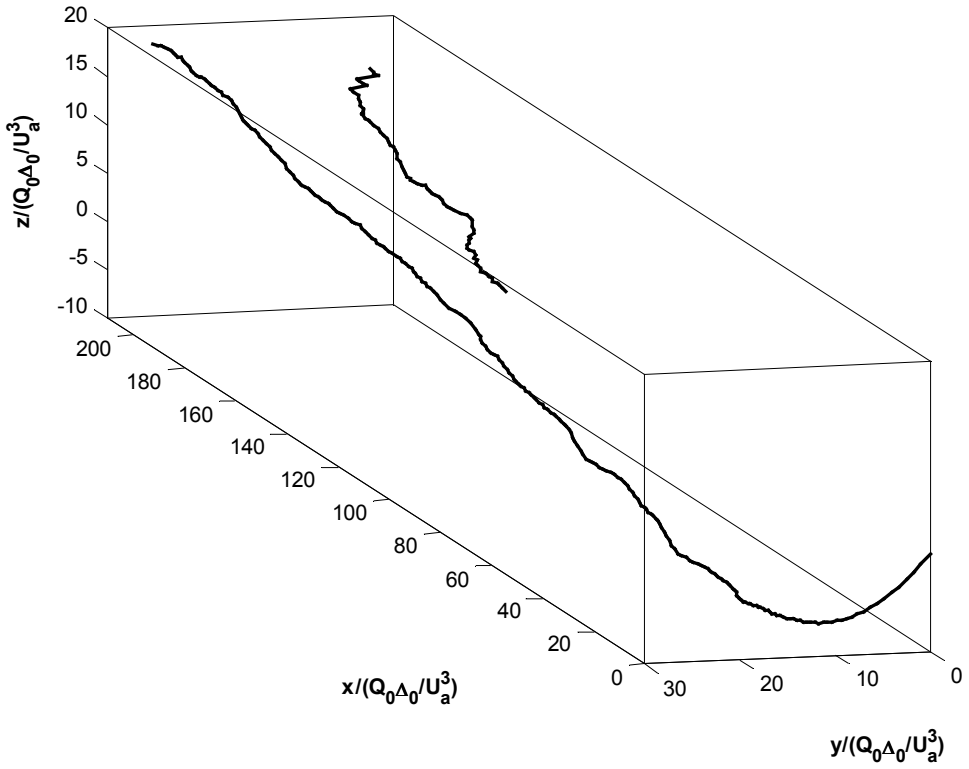

Figure E.7 - Three-dimensional view of trajectory results
buoyant jet with three-dimensional trajectories run 4

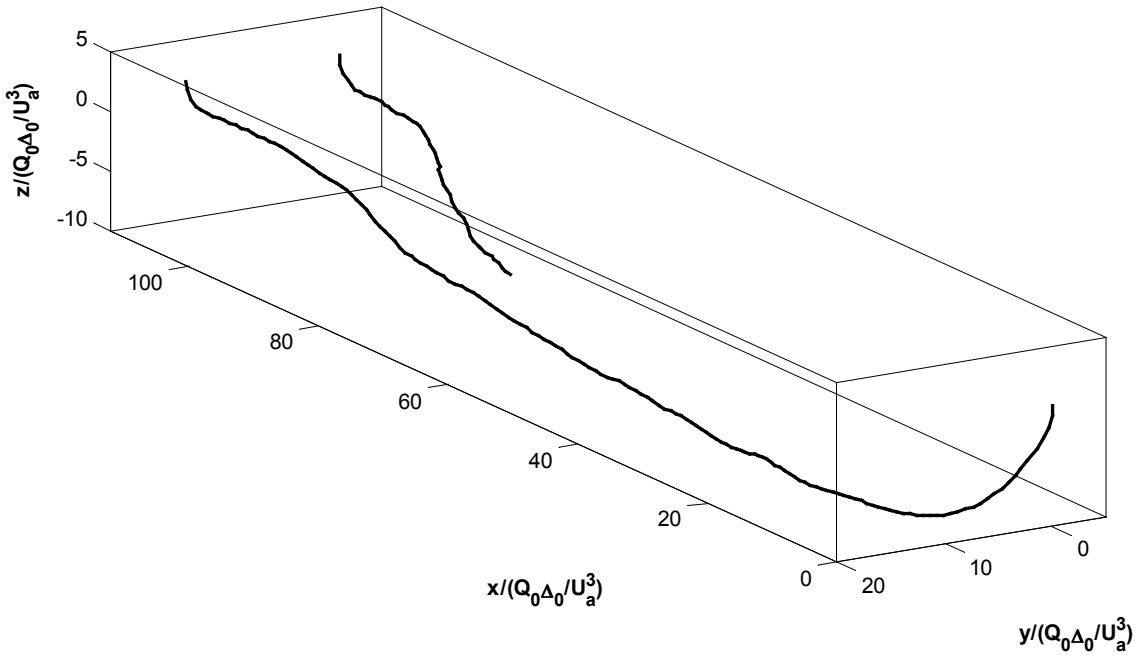

Figure E.8 - Three-dimensional view of trajectory results
buoyant jet with three-dimensional trajectories run 5

Appendix F – Trajectory Solutions for Weak-Jet and Puff Regions

Weak-Jet Region

In the weak-jet region, the flow is dominated by the component of the excess momentum flux that is parallel to the ambient current and the entrained ambient momentum flux. The component of momentum flux perpendicular to the ambient current will deflect the discharge and thereby alter its trajectory. The relationship for this is given by:

$$\frac{dz_{wj}}{dx_{wj}} = \frac{U_{e0}Q_0 \sin\phi_0}{U_a Q + U_{e0}Q_0 \cos\phi_0} \tag{F.1}$$

where

$$\frac{U_{e0}Q_0}{U_a Q} = \frac{M_{e0}}{U_a{}^2 \beta_{wj}{}^2 \pi b^2} \tag{F.2}$$

Application of the equations for conservation of mass and momentum, combined with the spread assumption, yields the following relationship for the spread in the weak-jet region (Wang 2000b):

$$\frac{b}{M_{e0}{}^{0.5}/U_a} = \left(\frac{3k\cos\phi_0}{I_q C_{jk}}\right)^{1/3} \left(\frac{x_{wj}}{M_{e0}{}^{0.5}/U_a}\right)^{1/3} \tag{F.3}$$

Inserting equation (F.3) into (F.2) gives:

$$\frac{U_{e0}Q_0}{U_a Q} = \frac{1}{\pi\beta_{wj}{}^2 \left(\frac{3k\cos\phi_0}{I_q C_{jk}}\right)^{2/3} \left(\frac{x_{wj}}{M_{e0}{}^{1/2}/U_a}\right)^{2/3}} \tag{F.4}$$

Equation (F.1) can be re-written as:

$$\frac{dz_{wj}}{dx_{wj}} = \frac{\frac{U_{e0}Q_0 \sin\phi_0}{U_a Q}}{1 + \frac{U_{e0}Q_0 \cos\phi_0}{U_a Q}} \tag{F.5}$$

Inserting equation (F.4) into (F.5) gives:

$$\frac{dz_{wj}}{dx_{wj}} = \frac{\frac{\sin\phi_0}{\pi\beta_{wj}{}^2 \left(\frac{3k\cos\phi_0}{I_q C_{jk}}\right)^{2/3} \left(\frac{x_{wj}}{M_{e0}{}^{1/2}/U_a}\right)^{2/3}}}{1 + \frac{\cos\phi_0}{\pi\beta_{wj}{}^2 \left(\frac{3k\cos\phi_0}{I_q C_{jk}}\right)^{2/3} \left(\frac{x_{wj}}{M_{e0}{}^{1/2}/U_a}\right)^{2/3}}} = \frac{\frac{c_{wj2}}{x_{wj}{}^{2/3}}}{1 + \frac{c_{wj1}}{x_{wj}{}^{2/3}}} \tag{F.6}$$

Therefore:

$$dz_{wj} = \frac{\dfrac{c_{wj2}}{x_{wj}^{2/3}}}{1+\dfrac{c_{wj1}}{x_{wj}^{2/3}}} dx_{wj} = \frac{c_{wj2}}{x_{wj}^{2/3} + c_{wj1}} dx_{wj} \tag{F.7}$$

Let $w = x_{wj}^{1/3} \Rightarrow dx = 3w^2 dw$. Thus:

$$dz_{wj} = \frac{c_{wj2}}{w^2 + c_{wj1}} 3w^2 dw = 3c_{wj2}\left(\frac{w^2/c_{wj1}}{1+w^2/c_{wj1}}\right)dw = 3c_{wj2}\left(1 - \frac{1}{1+w^2/c_{wj1}}\right) \tag{F.8}$$

$$dz_{wj} = 3c_{wj2}\left(1 - c_{wj1}\frac{1}{c_{wj1}+w^2}\right)dw \tag{F.9}$$

Integrating equation (F.9), and applying the virtual source assumption gives:

$$z_{wj} = 3c_{wj2}\left(w - \sqrt{c_{wj1}}\tan^{-1}\left(\frac{w}{\sqrt{c_{wj1}}}\right)\right) \tag{F.10}$$

$$z_{wj} = 3c_{wj2}\left(x_{wj}^{1/3} - \sqrt{c_{wj1}}\tan^{-1}\left(\frac{x_{wj}^{1/3}}{\sqrt{c_{wj1}}}\right)\right) \tag{F.11}$$

Inserting c_{wj1} and c_{wj2} into equation (F.10) gives the analytical trajectory solution for the weak-jet region:

$$\frac{z_{wj}}{l_{mz*}} = \frac{3\sin^{2/3}\phi_0}{\pi\beta_{wj}^{\ 2}}\left(\frac{I_q C_{jk}}{3k\cos\phi_0}\right)^{2/3}\left(\frac{x_{wj}}{l_{mz*}}\right)^{1/3} - \frac{\tan^{1/2}\phi_0 I_q C_{jk}}{\pi^{3/2}\beta_{wj}^{\ 3}k}\tan^{-1}\left(\frac{\pi^{1/2}\beta_{wj}\sin^{2/3}\phi_0}{\cos^{1/2}\phi_0}\left(\frac{3k\cos\phi_0}{I_q C_{jk}}\right)^{1/3}\left(\frac{x_{wj}}{l_{mz*}}\right)^{1/3}\right) \tag{F.12}$$

where

$$L_{mz*} = \frac{\left(M_{e0}\sin\phi_0\right)^{0.5}}{U_a} \tag{F.13}$$

Puff Region

In the puff region, the flow travels in the *z*-direction due to the initial excess momentum flux in that direction; mean motion in the *x*-direction is a combined effect of the entrained ambient momentum flux and the appropriate component of the initial excess momentum flux. The relationship for this is given by:

$$\frac{dz_{amp}}{dx_{amp}} = \frac{U_{e0}Q_0\sin\phi_0}{U_a Q + U_{e0}Q_0\cos\phi_0} = \frac{U_{e0}Q_0\sin\phi_0}{U_a Q}\left(\frac{1}{1+U_{e0}Q_0\cos\phi_0/U_a Q}\right) \tag{F.14}$$

where

$$\frac{U_{e0}Q_0}{U_aQ} = \frac{M_{e0}}{{U_a}^2{\beta_{amp}}^2\pi b^2} \tag{F.15}$$

The spread assumption, based on the double-Gaussian approximation (see 3.2.3.2) yields the following relationship for the spread in the puff region:

$$\frac{b_c}{{M_{e0}}^{0.5}\sin\phi_0/U_a} = \lambda h k_{sg}\frac{z_{amp}}{{M_{e0}}^{0.5}\sin\phi_0/U_a} \tag{F.16}$$

Inserting equation (F.16) into (F.15) gives:

$$\frac{U_{e0}Q_0}{U_aQ} = \frac{1}{\pi{\beta_{amp}}^2{k_{sg}}^2\left(\dfrac{z}{{M_{e0}}^{1/2}/U_a}\right)^2} \tag{F.17}$$

Inserting equation (F.17) into (F.14) gives:

$$\frac{dz_{amp}}{dx_{amp}} = \frac{\dfrac{\sin\phi_0}{\pi{\beta_{amp}}^2{k_{sg}}^2\left(\dfrac{z_{amp}}{{M_{e0}}^{1/2}/U_a}\right)^2}}{1+\dfrac{\cos\phi_0}{\pi{\beta_{amp}}^2{k_{sg}}^2\left(\dfrac{z_{amp}}{{M_{e0}}^{1/2}/U_a}\right)^2}} = \frac{\dfrac{\sin\phi_0}{\pi{\beta_{amp}}^2{k_{sg}}^2}\left(\dfrac{{M_{e0}}^{1/2}/U_a}{z_{amp}}\right)^2}{1+\dfrac{\cos\phi_0}{\pi{\beta_{amp}}^2{k_{sg}}^2}\left(\dfrac{{M_{e0}}^{1/2}/U_a}{z_{amp}}\right)^2} \tag{F.18}$$

Therefore:

$$dx_{amp} = \frac{1+\dfrac{\cos\phi_0}{\pi{\beta_{amp}}^2{k_{sg}}^2}\left(\dfrac{{M_{e0}}^{1/2}/U_a}{z_{amp}}\right)^2}{\dfrac{\sin\phi_0}{\pi{\beta_{amp}}^2{k_{sg}}^2}\left(\dfrac{{M_{e0}}^{1/2}/U_a}{z_{amp}}\right)^2}dz_{amp} = \frac{1}{\tan\phi_0}+\frac{\pi{\beta_{amp}}^2{k_{sg}}^2}{\sin\phi_0}\left(\frac{z_{amp}}{{M_{e0}}^{1/2}/U_a}\right)^2 dz_{amp} \tag{F.19}$$

Integrating equation (F.19), and applying the virtual source assumption gives:

$$x_{amp} = \frac{1}{\tan\phi_0}z_{amp}+\frac{\pi{\beta_{amp}}^2{k_{sg}}^2}{3\sin\phi_0}\left(\frac{1}{{M_{e0}}^{1/2}/U_a}\right)^2{z_{amp}}^3 \tag{F.20}$$

or

$$\frac{x_{amp}}{l_{mz*}} = \frac{1}{\tan\phi_0}\frac{z_{amp}}{l_{mz*}}+\frac{\pi{\beta_{amp}}^2{k_{sg}}^2}{3}\left(\frac{z_{amp}}{l_{mz*}}\right)^3 \tag{F.21}$$